FS SONNE
FAHRTBERICHT SO138
CRUISE REPORT SO138

GINCO-2

GEOSCIENTIFIC INVESTIGATIONS ON THE ACTIVE CONVERGENCE ZONE BETWEEN THE EAST EURASIAN AND AUSTRALIAN PLATES ALONG INDONESIA

JAKARTA - JAKARTA
29.12.1998 - 28.01.1999

Edited by
Ernst R. Flueh, Bernd Schreckenberger, and Jörg Bialas
with contributions of cruise participants

GEOMAR
Forschungszentrum
für marine Geowissenschaften
der Christian-Albrechts-Universität
zu Kiel

KIEL 1999

GEOMAR REPORT 81

GEOMAR
Research Center
for Marine Geosciences
Christian Albrechts University
in Kiel

Redaktion dieses Reports:
Ernst R. Flueh, Bernd Schreckenberger und
Jörg Bialas

GEOMAR REPORT
ISSN 0936 - 5788

GEOMAR
Forschungszentrum
für marine Geowissenschaften
Wischhofstr. 1-3
D - 24148 Kiel
Tel. (0431) 600-2555, 600-2505

Editors of this issue:
Ernst R. Flueh, Bernd Schreckenberger, and
Jörg Bialas

GEOMAR REPORT
ISSN 0936 - 5788

GEOMAR
Research Center
for Marine Geosciences
Wischhofstr. 1-3
D - 24148 Kiel
Tel. (49) 431 / 600-2555, 600-2505

TABLE OF CONTENTS

1.1 ZUSAMMENFASSUNG

Das Hauptziel der FS SONNE Ausfahrt SO138 - GINCO II (Geoscientific Investigatios on the active convergence zone between the east Eurasian and Australian plates along Indonesia) vom 29. Dezember 1998 bis 28. Januar 1999 war es, die seewärtigen Untergrundstrukturen des Kontinentalrandes vor Sumatra und Java sowie im Bereich der Sunda Straße zu untersuchen. Entlang von 9 Profilen mit einer Gesamtlänge von 1860 km wurden Ozeanboden Hydrophone (OBH) und Ozeanboden Seismometer (OBS) an insgesamt 111 Lokationen abgesetzt und mit einer Ausnahme erfolgreich wieder geborgen. Gleichzeitig wurde Einkanal-Reflexionsseismik entlang der Profile aufgenommen. Um die Qualität der gewonnenen Daten zu kontrollieren sowie erste wissenschaftliche Interpretationen zu ermöglichen, wurden die gesamten seismischen Daten während der Ausfahrt bearbeitet, dargestellt, analysiert und archiviert. Eine kontinuierliche Datenerfassung der Hydroakustik und Gravimetrie erfolgte während der gesamten Fahrt. Magnetische Messungen mit Hilfe eines empfindlichen Gradientenmagnetometers wurden auf einer Gesamtstrecke von 2700 km vorgenommen. In Ergänzung zu den auf der vorangegangenen Ausfahrt SO137 gewonnenen Daten wurde eine gute Überdeckung von bathymetrischen, gravimetrischen und magnetischen Daten entlang des Sunda Grabens, insbesondere aber in den drei für SO138 ausgewählten Arbeitsgebieten erhalten. Vor Sumatra wurde eine Teilfläche landwärts der Grabenachse detailliert vermessen. Auch für die Sunda Straße konnte eine detaillierte bathymetrische Karte erstellt werden.

Eine erste Analyse aller Daten wurde bereits an Bord begonnen. Wenn auch diese Ergebnisse nur vorläufig sind, so lassen sich schon jetzt einige Aussagen machen. Im Arbeitsgebiet vor Sumatra wurde eine auffällige Krustenverdickung der ozeanischen Kruste unmittelbar vor dem Tiefseegraben gefunden. Inwieweit es sich dabei um eine ausgedehntere Struktur oder nur eine lokale Anomalie handelt, kann aus den Daten nicht abgeleitet werden. Der gesamte Akkretionskeil zeichnet sich durch hohe seismische Geschwindigkeiten aus, die ein bis zu 12 km mächtiges Paket ausmachen. Die Mentawai Störung trennt diesen Akkretionskeil von einem tiefen Forearc Becken mit einer bis zu 5 km mächtigen Füllung. Die kontinentale Moho liegt hier in ca. 24 km Tiefe. An der Akkretionsfront herrscht eine chaotische Topographie vor, viele kleine steile Rücken und Rutschungen sind zu beobachten. Erst weiter landwärts werden größere topographische Einheiten erkannt. Auffallend ist zudem ein deutlicher Versatz von nahezu 10 km an der Deformationsfront, dessen Ursache jedoch nicht erkannt wurde.

Im Arbeitsgebiet vor Java wurde ebenfalls ein bis zu 15 km mächtiger Akkretionskeil gefunden, der sich auch durch hohe seismische Geschwindigkeiten auszeichnet, unterhalb von einer Tiefe von 5 km unter dem Meeresboden jedoch noch einen Geschwindigkeitssprung zu höheren Geschwindigkeiten aufweist. Diese Einheit kann auch dem javanesischen Inselbogen zugeordnet werden. Das Forearc Becken zeigt eine bis zu 5 km mächtige Füllung, die tieferen Krustenstockwerke vor Java sind jedoch durch ein anderes Geschwindigkeitsfeld als vor Sumatra gekennzeichnet. Die Moho wird küstennah in einer Tiefe von ca. 25 km angetroffen.

Auch im Bereich der Sundastraße konnte die abtauchende Platte abgebildet werden, erneut zeichnet sich der Akkretionskeil durch hohe Geschwindigkeiten aus. Der Neigungswinkel der Platte nimmt von 5° an der Grabenachse auf 8.5° im Bereich der Sunda Straße zu.

Die magnetischen Anomalien zeigen ein ruhiges Feld über dem Akkretionskeil und starke Anomalien über dem Forearc-Becken. Es gibt keine Anzeichen für einen magnetisierten Körper direkt über dem Outer Arc Ridge, der den aus der Reflexionsseismik ersichtlichen "Oceanic Crustal Splinters" entsprechen könnte. Die Interpretation der Schwereanomalien erfordert allerdings auf einigen Profilen eine geringe Dichtezunahme im Bereich dieser Strukturen. Die Modellierung der magnetischen Anomalien über dem Forearc-Becken hat noch nicht zu endgültigen Ergebnissen geführt. Die Interpretation der Schwereanomalien soll durch die aus den seismischen Weitwinkeldaten erhaltenen Geschwindigkeitsmodellen weiter verbessert werden.

Die weitere Datenbearbeitung, Modellierung und Integration von Erkenntnissen anderer Ausfahrten in dieses Gebiet sollte es dann ermöglichen, detaillierte und zuverlässige Modelle zu erstellen. Damit wird eine Beschreibung der Struktur und Evolutionsgeschichte in diesem Untersuchungsgebiet möglich sein.

1.2 SUMMARY

The main goal of RV SONNE cruise SO138 - GINCO II (Geoscientific Investigations on the active convergence zone between the east Eurasian and Australian plates along Indonesia) from 29. December 1998 to 28. January 1999 was to investigate the large scale structure of the offshore parts of the continental margins of Sumatera and Java and within Sunda Strait. Along 9 profiles with a total length of 1860 km, ocean bottom hydrophones (OBH) and seismometers (OBS) were deployed at 111 positions. All of them except one were safely recovered. Single channel seismic data were also recorded along the seismic profiles. All seismic data were preprocessed and displayed onboard for quality assurance, archiving and preliminary interpretation. Continous recordings of gravity and hydroacoustic soundings were made throughout the entire cruise. Magnetic measurements using a state-of-the-art gradient magnetometer were carried out along 2700 km of trackline. Together with the data from the previous cruise SO137, a good coverage of bathymetric, magnetic and gravity data is obtained along the Sunda trench, which is especially dense in the three working areas of cruise SO138. Off Sumatera, an area landward of the trench has been fully covered. A detailed bathymetric map was produced for Sunda Strait.

A first analysis of the data was accomplished onboard. Although the results are preliminary, some key observations can already be made. Off Sumatera, a pronounced thickening of the oceanic crust immediately seaward of the ttrench is found. From the data collected during the cruise it cannot be deduced if this crustal thickening extends further or is only a local anomaly. The accretionary complex, which is up to 12 km thick, is characterized by high seismic velocities. The Mentawai fault separates the accreationary complex from a deep forearc basin, which contains up to 5 km of young infill and is underlain by continental crust, with the Moho found at 24 km depth. The accretionary front shows a chaotic topography with many small ridges and numerous slides. Further landward, larger bathymetric units are visible such as elongated ridges and basins. There is also a pronounced retreat of the accretionary wedge of about 10 km, for which no obvious explanation is known.

In the working area off Java we encountered a 15 km thick wedge above the downgoing plate, also characterized by high seismic velocities. About 5 km below the sea floor a marked velocity discontinuity can be observed within the wedge. This lower unit may be part of the Javanese crust. The forearc basin has about 5 km infill, but the crustal velocities differ significantly from those off Sumatera.. Close to the coast, the Moho is found at a depth of about 25 km. Near Sunda Strait, the downgoing plate was investigated. Again, the accretionary complex is characterized by high seismic velocities. The dip of the downgoing slab increases from 5° near the trench to 8.5° near the shelf edge.

The magnetic data generally show only smooth variations across the accretionary complexes, contrasting strong anomalies across the forearc basin. There are no indications for lateral differences in magnetization of the accretionary wedge across the outer arc high, which had previously been interpeted as oceanic crustal rocks, scratched off the downgoing plate during subduction in earlier times. This contradicts interpretations of the gravity field, which indicate a density increase asscociated with these structures in some locations. Modelling of the magnetic anomalies in the forearc basin has not yet been conclusive. Further gravity modelling will be carried out using the seismic wide-angle velocity field as additional constraints.

Further processing, modelling and integration of the data collected on this cruise with those from other cruises in this region will enable us to derive more detailed and better constrained models, from which the structure and evolution of the surveyed area can be deduced with more confidence.

2. INTRODUCTION

Being located at the point of directional change of the Sunda arc, Sunda Strait marks a transition zone between oblique subduction off Sumatra to orthogonal subduction off Java. It thus presents a key element in understanding the dynamics and changes in deformation and seismicity along this subduction zone, as well as the structural differences associated with the change in subduction obliquity along the margin.

2.1 AIMS OF THE PROJECT

(E. Flueh)

Within the scope of the bilateral agreement between Germany and Indonesia on economical and technological cooperation in marine sciences, the active plate boundary off Sumatra and Java is the focus of the project "GINCO" (*G*eoscientific *IN*vestigation on the active *CO*nvergence zone between the East Eurasian and Indo-Australian plates along Indonesia). Three legs of the German Research Vessel SONNE (SO 137, SO 138 and SO 139) are dedicated to this area. Different methods are used on each leg. Cruise SO 137 was focussed on the collection of multichannel seismic reflection (MCS) data. On cruise SO 138, certain profiles of the MCS survey were selected for coincident seismic wide-angle measurements. The main task of the third leg (SO139) will be geological and geochemical analyses and collection of samples. On all three cruises, continuous recordings are made of hydroacustic data. The magnetic and gravity field are measured on the first two cruises.

Due to their enormous potential for natural hazards (earthquakes, volcanoes and tsunamis), subduction zones are a threat for the social and economic development of the nations concerned in all over the world. With an ever increasing population density in such high risk regions, a better assessment of the risks is required. A sound risk analysis can be used for future planning purposes such as establishing rules for emergencies, and ultimately for the development of useful warning systems by which potential losses can be minimized.

Although substantial progress has been made over the past decades, fundamental questions concerning the processes and their causes in subduction zones still need to be explored in detail. This requires multidisciplinary and international cooperation, and new initiatives such as the MARGINS Program have been launched recently. The GINCO project is one step towards this aim. The Sunda arc subduction zone is suited particularly well for studying some of the key questions related to the mechanics and development during plate convergence because there are significant lateral variations along the arc which also imprint the architecture of the system. Pronounced lateral differences are known along the Sunda Graben. The age of the subducting crust decreases from south-east to north-west, while the sedimentary cover increases in the same direction. One of the key elements within the study area is the transition from orthogonal subduction off Java to an oblique collision off Sumatra, giving rise to the Sumatra and Mentawai strike slip faults. This transition is mainly believed to occur in Sunda Strait, giving rise to a pull apart basin above the downgoing plate. Volcanism is more widespread and active on Java than on Sumatra, but large earthquakes ($M > 7.5$) are only known from Sumatra. It is still unknown how the different parameters (crustal age, obliquity, sediment input etc.) are related to these observations.

During cruise SO138, seismic wide-angle data were to be collected to study the crustal structure and architecture of the incoming plate and the continental margin with its pronounced outer arc high and forearc basin. The profiles were chosen coincident with MCS profiles collected by BGR during SO 137 (Reichert, in prep.), and additional strike lines were shot to calibrate the interpretation of the dip lines. Three working areas were chosen:

1. off Sumatra, where part of the convergence is taken upwards along the Mentawa and Sumatra faults
2. within Sunda Strait and the adjacent margin, where the transition occurs and
3. off Java, where normal subduction is taking place.

The wide-angle seismic profiles were to be completed by additional magnetic observations as well as swathmapping and gravity measurements to complete the coverage of certain key areas and to provide a detailed base map for the geological sampling program of the following cruise SO139. Most of the objectives for the project were met during the cruise.

2.2 REGIONAL BACKGROUND

(H. Lelgemann)

2.2.1 TECTONIC EVOLUTION OF THE WESTERN INDONESIAN REGION

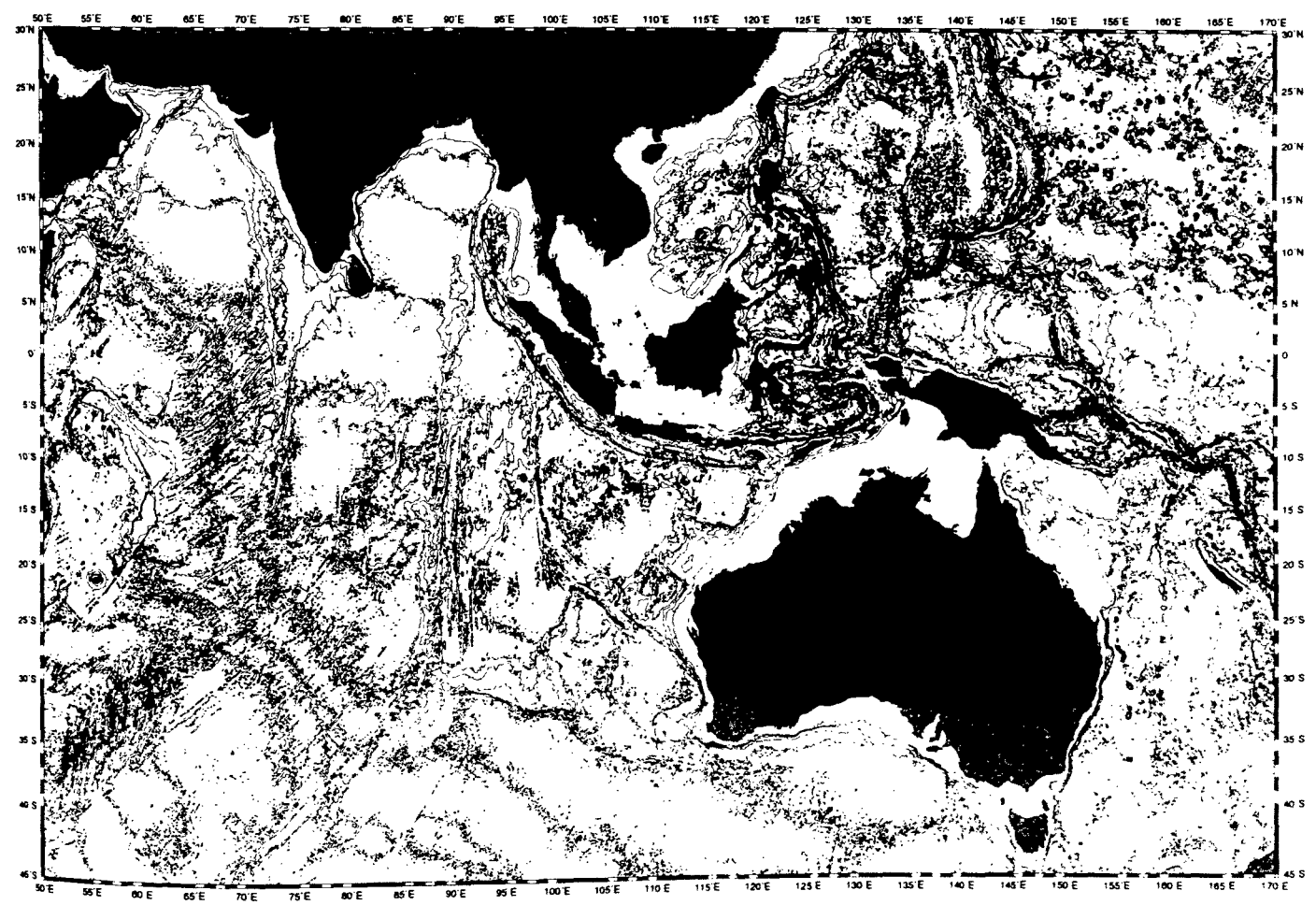

Figure 2.2.1.1: Bathymetry map of the Indian Ocean and western Pacific. The Sunda Arc subduction zone, which runs along the islands of Sumatra and Java in Indonesia, shows up clearly in the bathymetry, as does the Ninety East Ridge in the Indian Ocean.

The evolution of the large tectonic units of the Indian ocean (Fig. 2.2.1.1) is well confined by seafloor-spreading isochrons. Much of the Indonesian region is however characterized by the interaction of several smaller lithospheric plates, the movement of which within the complex is not well constrained. Several continental terranes were identified in SE Asia (Metcalfe, 1996), which are entirely allochthonous to central and northern Asia, although there is still some disagreement as to the number of terranes and their boundaries. Comparative studies of palaeontology, palaeomagnetism and stratigraphy suggest that the various pre-Cretaceous continental terranes were derived from Gondwanaland (Gasparon, 1995, Nishimura, 1997). The evolution of Gondwanaland and Tethys during the Palaeozoic and Mesozoic involved the rifting of continental slivers/fragments from northern Gondwanaland and their northwards drift and accretion, accompanied by the opening and destruction of the Tethys ocean system, to form proto-SE Asia (Fig. 2.2.1.2) (Metcalfe, 1996). The continental terranes are bounded by sutures (representing former oceans), by narrow mobile belts or major fault zones (Fig. 2.2.1.3) (McCourt, 1996). The formation of present-day SE Asia involved the progressive suturing of terranes to each other during Late Palaeozoic to Cenozoic times and their subsequent disruption, principally caused by the collision of India with Eurasia. The ages of sutures in SE Asia become younger to the south and south-east.

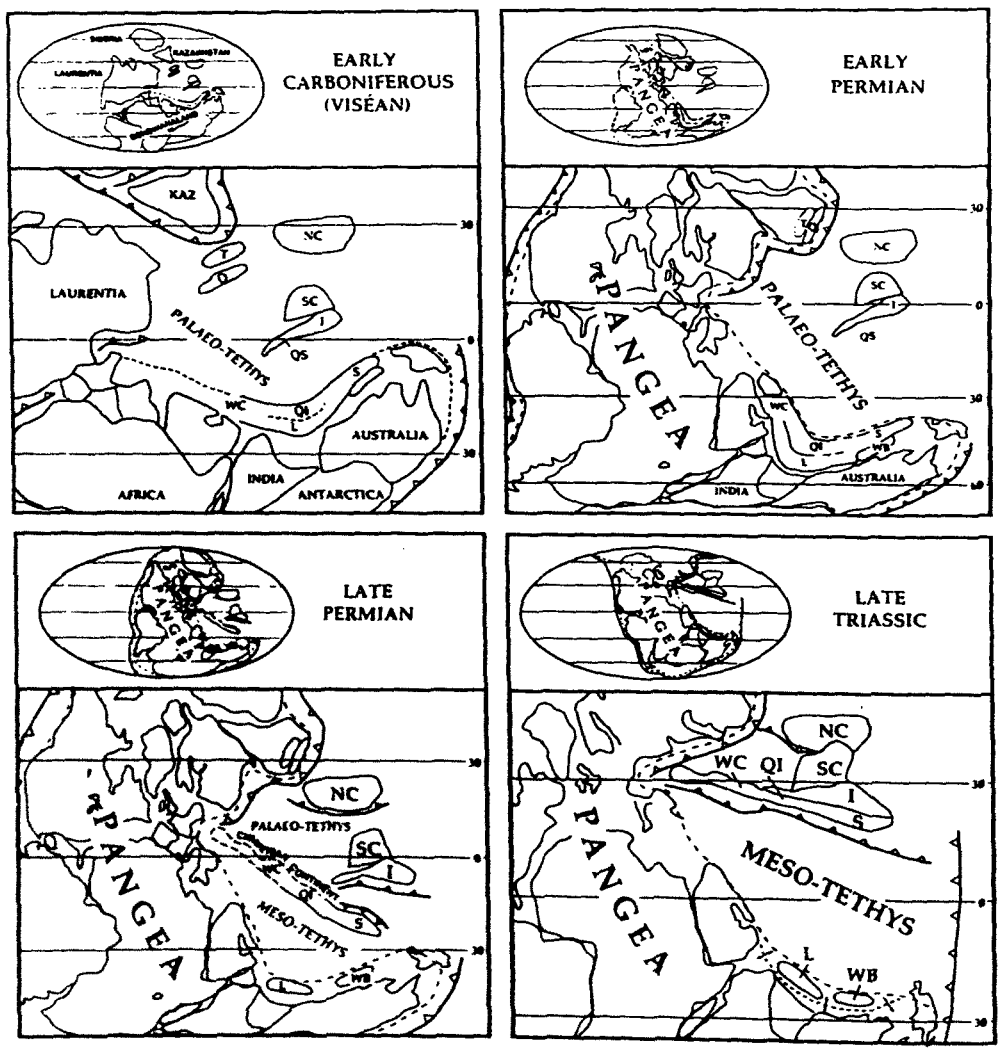

Figure 2.2.1.2: Palaeographic reconstructions of the Tethyan region for Early Carboniferous, Early Permian, Late Permian and Late Triassic showing the postulated positions of SE Asian terranes. Present day outlines are for reference only. NC: North China, SC: South China, T: Tarim, I: Indochina, Q: Qaidam, WC: Western Cimmerian Continent, Qi: Qiantang, L: Lhasa, S: Sibumasu, WB: West Burma (after Metcalfe, 1996).

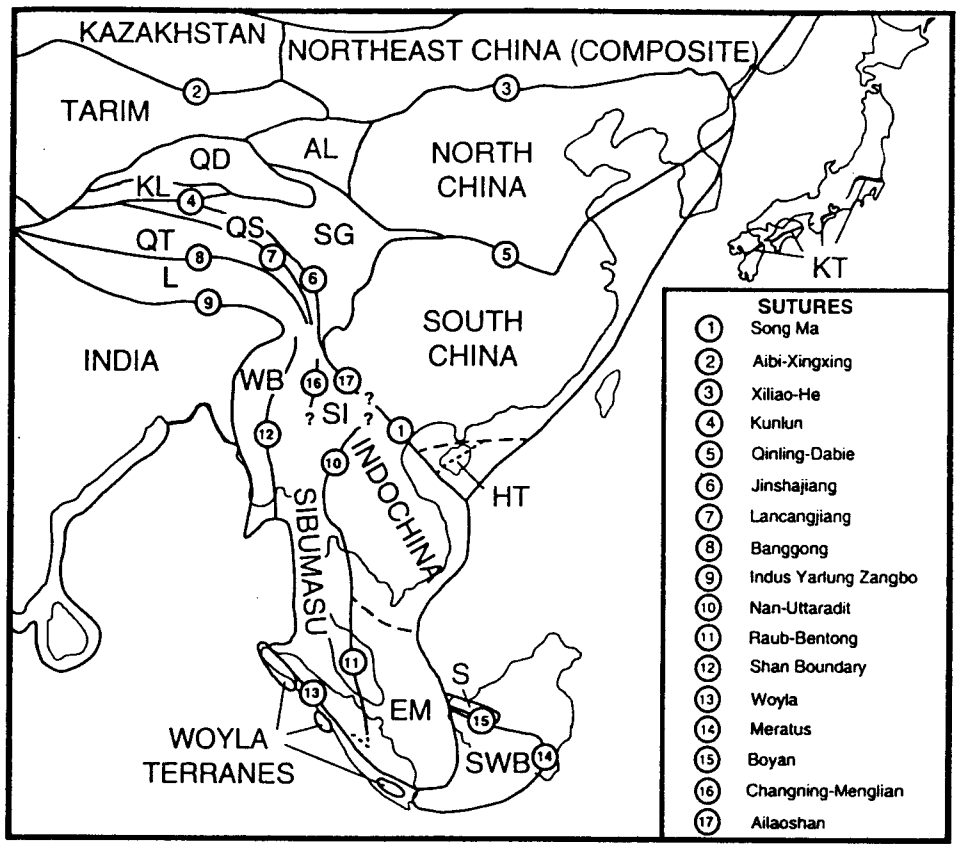

Figure 2.2.1.3: Distribution of principal continental terranes and sutures in East and SE Asia. EM: East Malaya, WB: West Burma, SWB: South West Borneo, S: Semitau Terrane, HT: Hainan Island terranes, L: Lhasa terrane, QT: Qiantang Terrane, QS: Qamdo-Simao Terrane, SI: Simao Terrane, SG: Songpan Ganzi accretionary complex, KL: Kunlun Terrane, QD: Qaidam Terrane, AL: Ala Shan Terrane, KT: Kurosegawa Terrane (after Metcalfe, 1996).

It is generally agreed, as shown in Figure 2.2.1.3 after Metcalfe (1996), that South Tibet, Burma, western Thailand, Malaysia and Sumatra reveal strong geological correlations and formed a geological province, the Sibumasu terrane, which is bounded to the west by the Shan Boundary Fault and the Andaman Sea basin and to the south-west by the Woyla suture in Sumatra (Audley-Charles, 1988, Hutchinson, 1989, Metcalfe, 1996, McCourt, 1996). Its eastern boundary is formed by the Raub-Bentong suture in Peninsular Malaysia, and the Changning-Menglian and Lancangjian Sutures in western Yunnan. The eastern boundary of Sibumasu in North Thailand and Burma is still not clear (Metcalfe, 1996). Paleomagnetic data along with Gondwanaland faunas (Cambrian to Lower Permian) with NW Australian affinities on Sibumasu strongly suggest a NW Australian origin for the Sibumasu terrane (Metcalfe, 1996, Nishimura, 1997). The predicted paleolatitude for Sibumasu, if placed adjacent to NW Australia, would be about 40°S in the Late Carboniferous.

A major rifting phase occured on the northern margin of Gondwana in the Early Permian (Fig. 2.2.1.2), as is indicated by the occurrence of calc-alkaline volcanics and granitic plutons of Permo-Triassic age (248-218 Ma), (Nishimura, 1997). Paleomagnetic data indicate that Sibumasu travelled rapidly from southern to northern paleolatitudes in Permian times (Metcalfe, 1996), followed by collision of the Sibumasu Block with East Malaya along the Raub-Bentong suture in the earliest Triassic (McCourt, 1996). The Raub-Bentong suture thus represents the palaeo-Tethys. Metcalfe (1996) suggested a collision time of Sibumasu with Indochina in the latest Permian or Triassic, but the exact suturing age is still controversial.

The late Triassic to Late Jurassic saw renewed rifting on the north-east margin of Gondwanaland, leading to the destruction of the Meso-Tethys (Fig. 2.2.1.2). The Woyla terrane split from Gondwana in the Late Jurassic and by Late Cretacous had accrected to proto-SE Asia. This terrane consisted of several small continental fragments, including the Sikuleh and Natal blocks, now located along the Woyla suture along the south-west margin of Sumatra, as shown in Fig. 2.2.1.3, which comprises Cretacous ophiolites and accretionary complex material (Metcalfe, 1996). Stratigraphic similarities with the Exmouth Plateau of the NW Australian shelf and palaeomeagnetic data from the Sikuleh block suggest palaeolatitudes of 26°S for the Late Triassic and 10°S in the Late Mesozoic which is consistent with a NW Australian origin of these terranes (Metcalfe, 1996).

The time of initiation of northward subduction of the Izangi Plate, which underlay the Mesozoic Tethys Ocean along the proto-Sunda trench is still enigmatic, but magmatism and ophiolite emplacement date back to the Cretaceous (Widiyantoro, 1996). Cretaceous subduction complexes around margins of the Eurasian continent are identified in western and central Java and south-western Sulawesi (Nishimura, 1997). The location of these subduction complexes and paleomagnetic measurements indicate that the position of pre-Tertiary subduction was at the front of the Eurasian continent. A waning or cessation of subduction along the proto-Sunda Arc was proposed by Hamilton (1979) for the Late Cretaceous to Early Tertiary, based on the magmatic record. From middle Tertiary times on, subduction of the Indian sea plate occurred again along Sumatra and became connected to the Java Trench during the Late Miocene (10-8 Ma).

The present distribution and geometry of SE Asia is the result of the effects of the collision of Indian and Eurasia, i.e. indention, extrusion and strike-slip faulting. The island continent of India collided with the Tethyan margin in Eocene time (Fig. 2.2.1.4), about 40 million years ago, and since then has continued to move northward at a velocity of about 5 cm/yr relative to Eurasia. The great Pakistan and Assam syntaxes at west and east corners of the Indian plate indicate northward motion of India relative to the Middle East to the west, and to South-East Asia to the east. About half the northward motion of India relative to north-west Eurasia is being accommodated by continental underthrusting of the Tibetan plateau and by compressive thickening of the entire continental crust (Hamilton, 1979). The other half is compensated primarily by the eastward motion of China, obliquely out of the way of the advancing southern continent, along a complex series of strike-slip faults and other structures. The resulting escape tectonics in south-eastern Asia included clockwise rotation of tectonic units in Indochina and Indonesia, as implied by the plasticene indentation experiments of Tapponier et al (1982) presented in Fig. 2.2.1.4a.

The present day position of Sumatra is the result of its clockwise rotation by about 20° in the late Cenozoic. Nishimura (1997) concluded from existing paleomagnetic data from south Sumatra and west Java that Sumatra underwent clockwise rotation relative to Java of about 20° during the period 5-1 Ma.

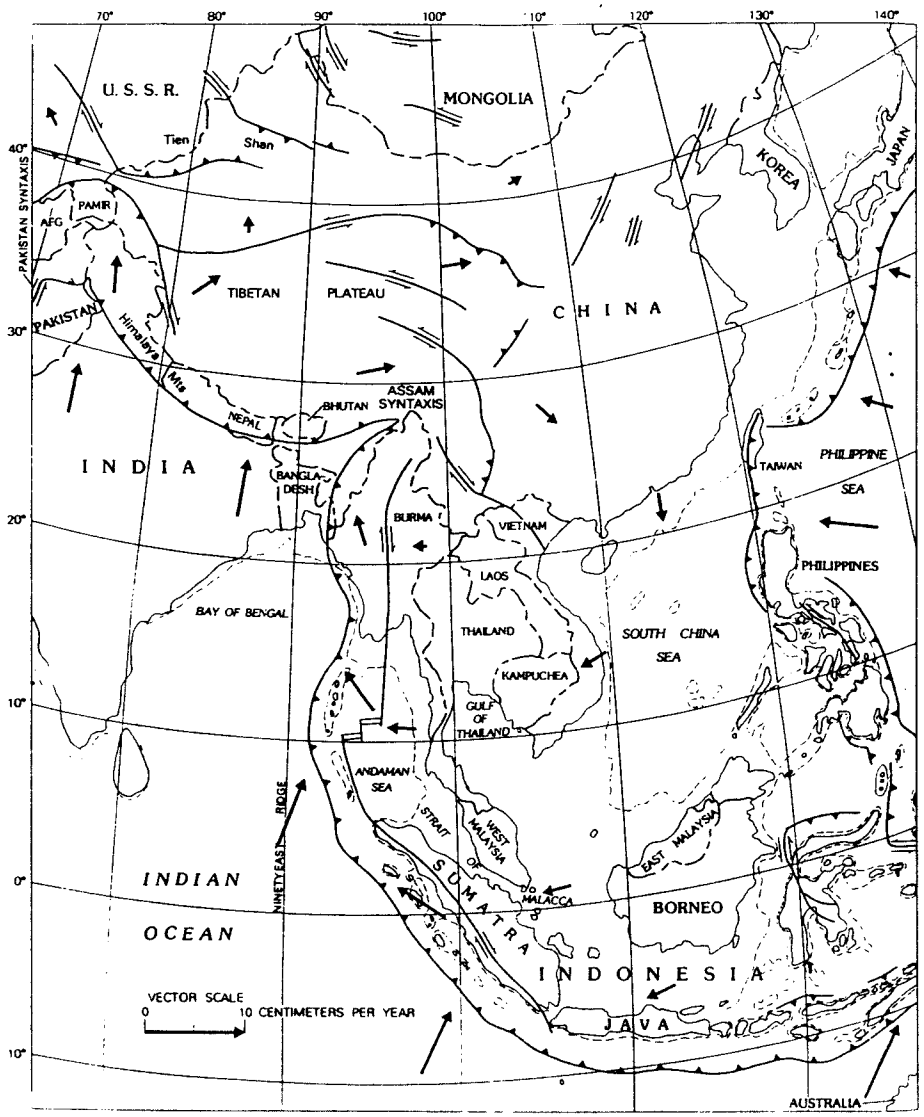

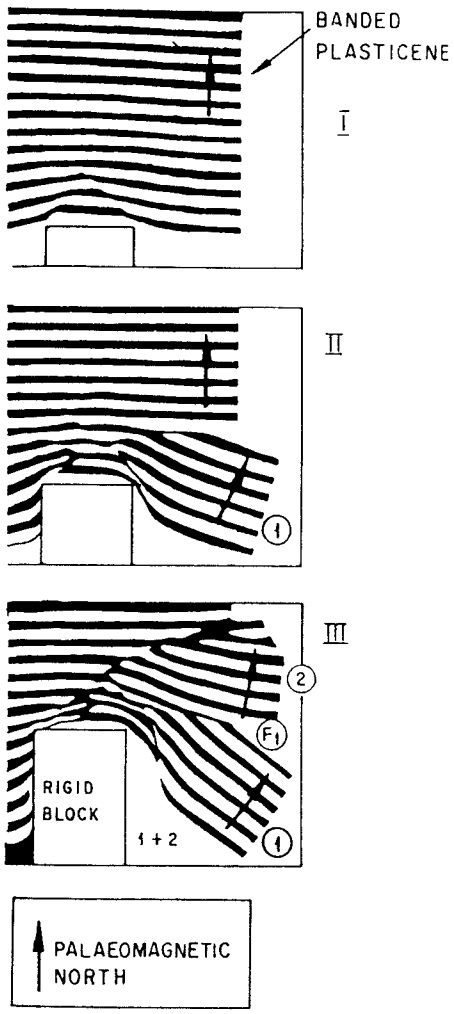

Figure 2.2.1.4: a) some active structures of the Chinese-Indonesian region. Perhaps half the norhtward motion of India relative to northwest Eurasia is being taken up by underthrusting of the Tibetan Plateau by India and by compressive thickening of the entire continental crust. The other half is compensated primalrily by the eastward motion, relative to northwestern eurasia, of China. Southeast Asia and western Indonesia are swinging clockwise, pivoted near the Assam syntaxis, over the Indian ocean and the northern Bay of Bengal. Large arrows show direction and velocity of motion relative to northwestern Eurasia (after Hamilton, 1979).
b) Three successive stages of an indentation experiment on plasticene (plan view). The free side is on the right. The rigid block is modelled as India. 1 is taken as the Indochina-south-east Asian block, 2 as south China. 1 is the opening of the South China Sea and 1+2 as the Andaman Sea. F_1 is the Red River Fault (after Taponnier et al, 1989).

2.2.2 SUNDA ARC

Introduction

Sunda Arc, which extends over 5600 km between the Himalayan syntaxis in the north-west and the Banda Arc to the east, is a classic convergent or subduction margin with the Indian-Australian plate underthrusting the Eurasian or South-East Asian plate (Fig. 2.2.2.1). Changes of orientation of the plate margin result in a change of subduction obliquity from Java to Sumatra. The nature of the transition between these two subduction regimes is of major interest. Many characteristics of the Sunda Arc change significantly along strike, most notably the direction of the convergence relative to the overriding plate. Thus it provides a good opportunity to study the effects of the along strike lateral variations in subduction geometries and structures on the subduction process.

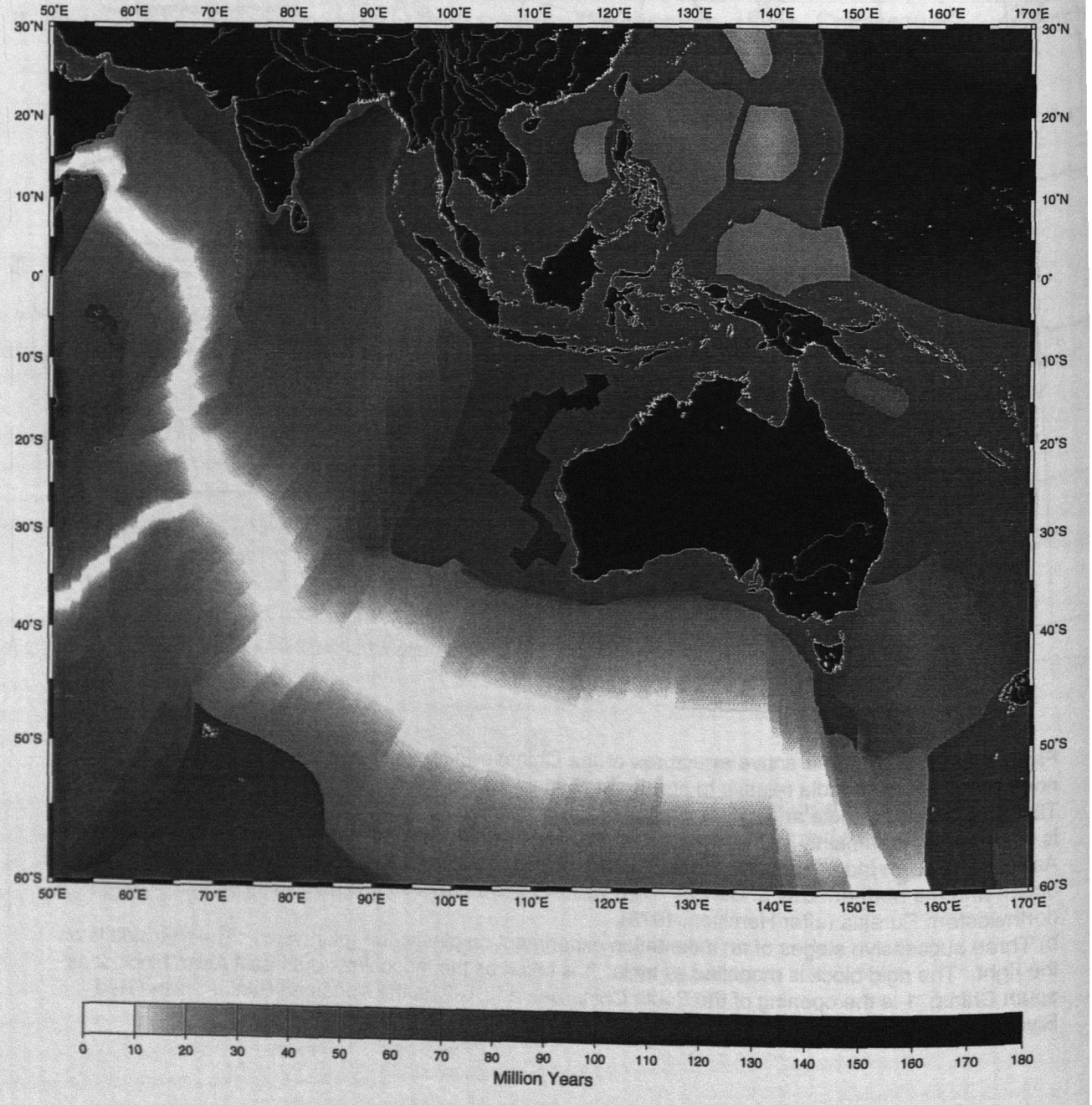

Figure 2.2.2.1: Age of the oceanic crust (after Müller et al., 1997) for the Indian Ocean and western Pacific ocean in million years.

The major variations which occur along the arc are principally a function of two parameters: direction and speed of convergence across the subduction zone, and thickness of sediment on the underthrusting plate (Curray, 1989). Sunda Strait marks the structural transition of frontal subduction off Java to oblique subduction off Sumatra, which becomes essentially subparallel along the Andaman Islands in the north (Fig. 2.2.2.2). The convergence rate along the margin varies from 60 mm yr^{-1} near Sumatra to 78 mm yr^{-1} in the easternmost part of the Sunda arc, in accordance with the relative plate velocity of 71±2 mm yr^{-1} between Australia and Eurasia according to NUVEL-1 (DeMets, 1990), which does not use data from the Sunda Arc.

The arc-trench system changes from ocean-continent, where the oceanic lithosphere subducts beneath the continental platform of Sumatra and western Java, through transitional off central Java to oceanic in the eastern Sunda arc. Whereas the arc east of the Sunda Strait is an island arc, the Sumatran sector is a truly cordilleran margin.

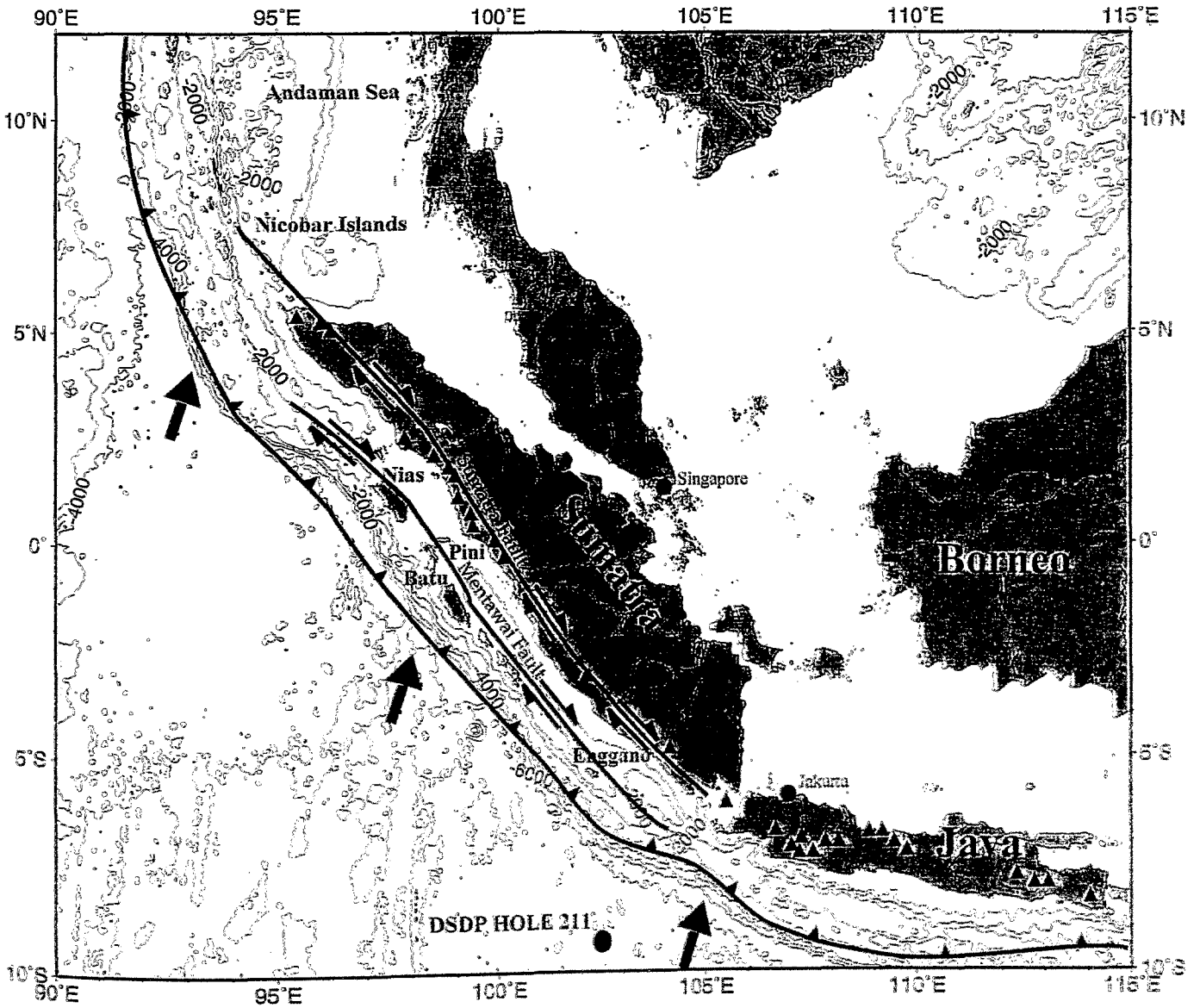

Figure 2.2.2.2: Plate tectonic setting and kinematic motion along the Sunda Arc. The Central Sumatran Fault which runs along the volcanic chain of Sumatra and the parallel Mentawai Fault offshore Sumatra are the tectonic response to the obliquity of the subduction. Note the region of scarce volcanic activity in Java around 110°E which coincides with a zone of low seismicity.
Thick arrows indicate motion of the subducted oceanic lithosphere with respect to Sumatra and Java, thin arrows give the relative motion along strike-slip faults. Triangles show the location of active volcanoes on Sumatra and Java.

Cenozoic arc-trench system

The present arc-trench system evolved during the late Oligocene after the late Eocene collision of India with Asia. Subduction has been occuring intermittantly at least since the Cretaceous, with the current episode of subduction beginning or accelerating in late Oligocene (Hamilton, 1979). The age and thickness of the subducting ocean floor varies along the Sunda Arc from 50 to 90 Ma along Sumatra to 100 to 135 Ma and 140 to 160 Ma near Java and Flores along the Banda Arc, where continental Australian lithosphere is being subducted (Widiyantoro, 1996).

Transversely, Sunda Arc displays a classic morphology of outer arc rise, the Sunda trench, outer-arc ridge which ponds the forearc basin, and volcanic arc (Fig. 2.2.2.3). The along strike lateral change of subduction parameters and the range of up to 15 km of sediment thickness being carried into the trench are manifested in many important variations in the character of the forearc region, including morphology of the trench, morphology and volume of the accretionary prism/outer arc ridge, style and intensity of deformation within the accretionary prism, and tectonic effects on the edge of the overthrusting plate which result from the variable oblique convergence. The depths of the forearc basins, the trench slope break, and the trench increase towards Java. The sediment thickness on top of the subducting plate ranges from 15 km in the north-west, where the sedimentary influx coming from the Bengal deep-sea fan is larger, to 400-600 m in the south-east (Curray, 1989). This variation of over 15 km of sediment passing into the subduction zone in the north to a few hundred meters off Java is manifested in the height, width, and volume of the accretionary prism. Estimates of the volume of the various parts of the accretionary prism by Curray (1989) show the volume variations to be compatible with the sediment thicknesses on the lower plate and with rates, speeds, and duration of convergence. Most of the sediment carried into the subduction zone since early Cretaceous can still be accounted for in the accretionary prism.

South of West Java, the forearc basin is poorly developed, while the outer arc ridge is deeply submerged and narrow, being about 2-3 km deep with isolated highs of 1 km. The ridge emerges intermittently above sea leavel in a chain of islands off Sumatra, including Nias, Batu, Pini, and Enggano, and even more so in the Andaman-Nicobar Ridge (Fig. 2.2.2.2).

Subduction along the Sunda Arc

The change of orientation of the arc near the Sunda Strait imposes a large change in the ratio of parallel to normal slip. Along the western arc this ratio progressively increases toward the Andaman region in the north, whereas along the eastern arc it remains nearly constant at a low rate (Fitch, 1972). Along Sumatra, the Indian Ocean convergence azimuth deviates up to 15° from perpendicular incidence on the Sumatran Trench. Oblique subduction induces partitioning of the motion into convergent motion and north-westward strike-slip motion. This partitioning results from the coupling effect between the dipping oceanic slab and the upper plate lithosphere. The coupling can be identified by study of slip vectors at the subduction zone which indicates the true direction of relative movement of the oceanic slab with respect to the forearc (McCaffrey, 1992). The subduction can thus be resolved into two components, one perpendicular component, calculated at between 5.7 and 7.0 cm /yr, and a transform component of slippage parallel to the trench axis of up to 2.1 cm/yr (Hutchinson,

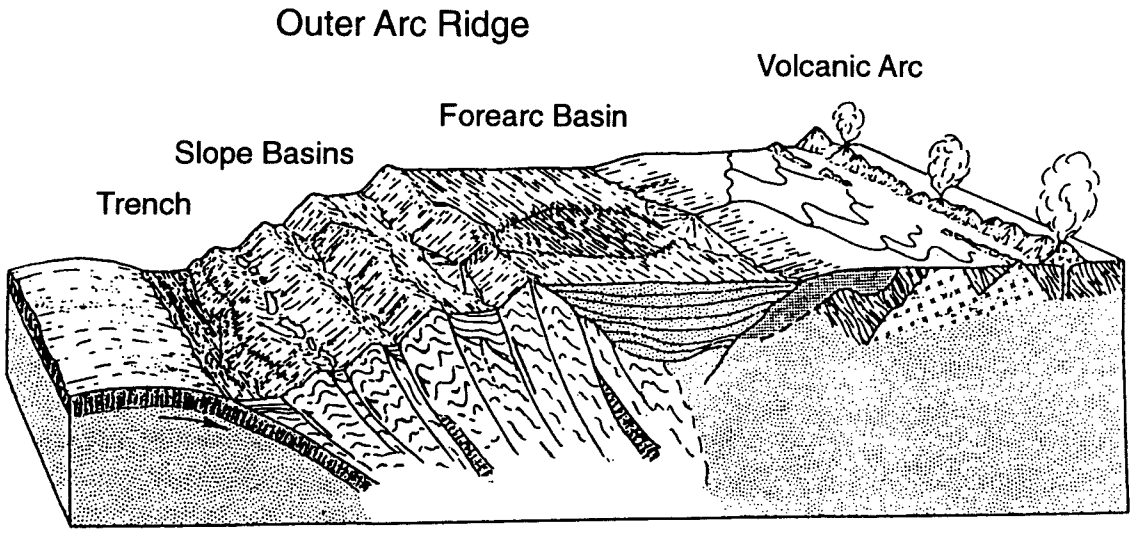

Figure 2.2.2.3a: Diagrammatic section across the Sunda Arc (modified after Curray, 1989).

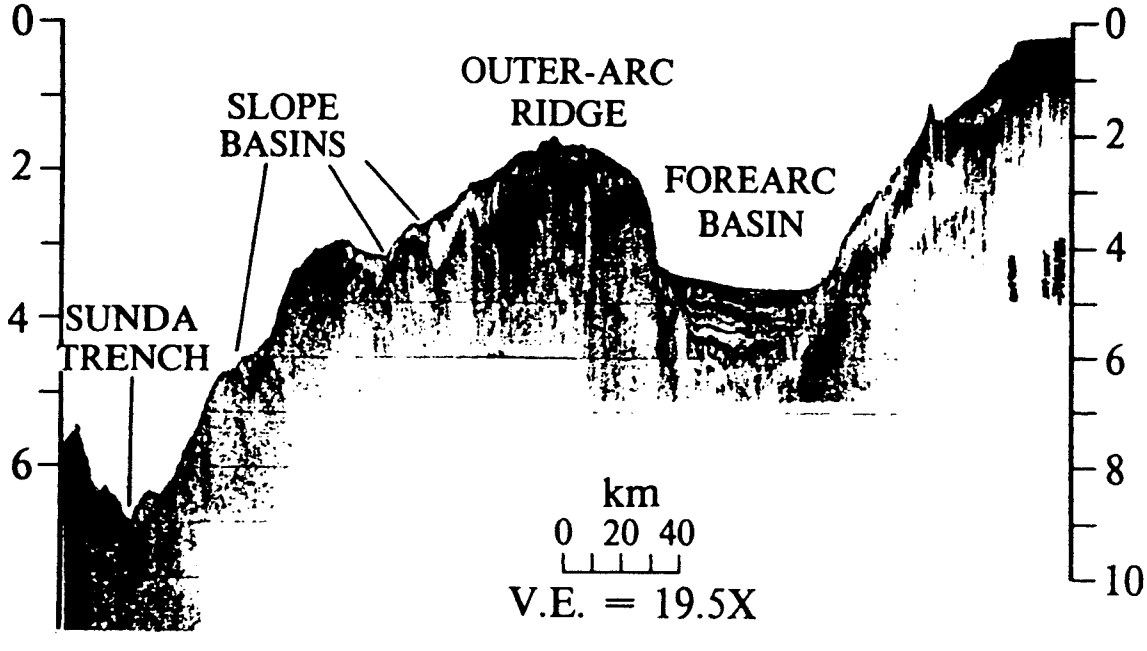

Figure 2.2.2.3b: Single-channel analog seismic reflection profile across the Sunda Trench slope south of Java, collected on the SIO Eurydice expedition in 1979. The classic morphology of trench, outer arc ridge, and forearc basin is clearly imaged (from Moore et al., 1980).

1989). The lateral movement results in the formation of a microplate sliver, while the movement perpendicular to the margin, mainly taken up by subduction, is also expressed by compressional deformation within the accretionary prism or the forearc. The obliquity of the Sumatra subduction zone is mainly compensated by dextral strike-slip movement along the Central Sumatra or Semangko fault (Fig. 2.2.2.4), which runs parallel to the long axis of Sumatra and offsets right laterally the Sumatra island, thus forming the Sumatra plate sliver between the trench of the Sunda Arc and the Sumatran Fault. It has also been proposed that the Mentawai fault off Sumatra takes part in the compensation (Diament, 1992, Malod, 1996) (Fig. 2.2.2.2). Offshore northern Sumatra, the Mentawai Fault is relayed and connected to the Sumatra fault by the Batee Fault. The slip rate along the Mentawai Fault is currently still unknown (Malod, 1996). Thus at least a fraction of slip parallel to the plate margin results in transcurrent movements on the nearly vertical Central Sumatra fault, which consists of about 20 separate en echelon segments, extending 1600 km along the volcanic chain of western Sumatra (Newcomb, 1987). The Sumatran Fault has been explained as a lithospheric scale fault zone that cuts the lithosphere vertically down to the asthenospheric wedge (Bellier et al., 1995) The Central Sumatra fault may be traced into the forearc of South Sumatra and appears to turn into a complex pattern of extensional faults (Huchon and Le Pichon, 1984). North of Sumatra it extends into the Andaman Basin, where it most likely joins the fracture zones of the back arc spreading center near the Andaman Islands (Fig. 2.2.2.2).

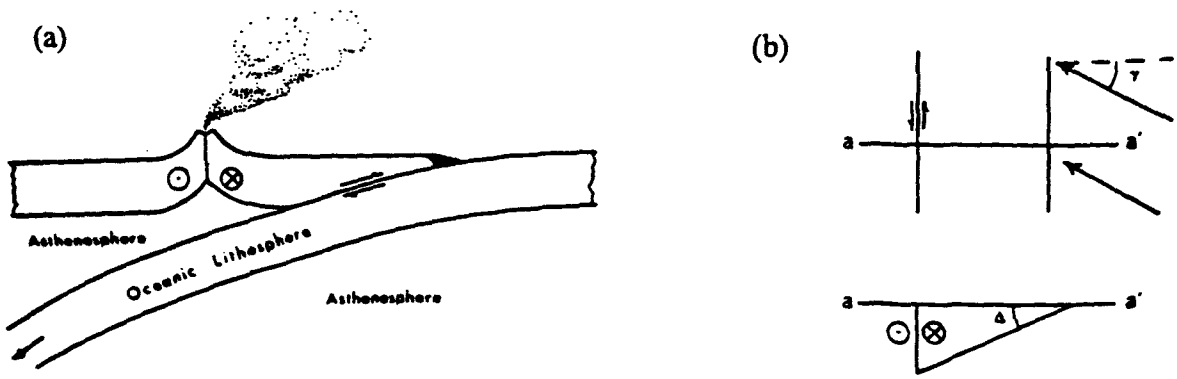

Figure 2.2.2.4 (a): (modified from Fitch, 1972) illustrates the formation of the transcurrent fault along a thermally-thinned zone coincident with the axis of the magmatic arc. Oblique conversion is converted into a subduction-zone transcurrent-fault pair west of Sunda Strait where the angle of convergence between the Indian and Asian plates becomes markedly oblique.
(b) is a cartoon illustrating the geometry of a Sunda-style margin. γ and Δ are the angle of convergence and the dip of the Wadati-Benioff zone, respectively.

It has been proposed that the northward increase in convergence obliquity along the Sumatran margin leads to a north-westward increase of the forearc motion relative to the upper plate which could increase from zero, east of the Sunda Strait, to 45-60 mm/yr, in northern Sumatra; thus the varation in obliquity along the arc produces a variation in slip rate along the Sumatran Fault (Bellier et al., 1995). This would result in a longitudial extension of the forearc sliver plate between the trench and the Sumatra fault. This model may partly explain the discrepancy between extension at the two ends of the Sumatra fault, from more than 460 km in the Andaman Sea (Curray et al., 1978) compared to only 50-70 km in the Sunda Strait (Diament et al., 1992). The exact slip rate along the Sumatran Fault is still a matter of debate.

To the east, opposite Java, subduction is normal and a typical, yet poorly developed forearc basin exists (Arifin, 1987), while the outer arc ridge is well developed. This was interpreted as the effect of the continuation of the Sumatra Fault within the active margin. On land, a large fault zone known as the Cimanderi Fault is interpreted as a sinistral strike-slip fault initiated during the Miocene (Dardji et al., 1994). In the transition zone, the curvature of the margin induces a north-westward increase of the obliquity of subduction and consequently of the lateral component of the partitioned motion. It has been proposed that the transition between the two regimes of subduction occurs to the south-west of Java, raising the question of the continuation of the Sumatra and Mentawai Faults into the accretionary prism and their connection with the structures of western Java.

Seismotectonics and Mantle Structure of the Sunda Arc

Given the tectonic setting of the Sunda Arc, it can be expected that the junction of island arcs and continental platform overlies a strongly heterogeneous mantle, as is evident from regional seismicity. The character of subduction related seismicity changes abruptly between east and west of Sunda Strait. Seismicity displays a distinct Wadati-Benioff zone, which exists all the way around the arc, but dramatically changes in depth and pattern (Curray, 1989) (Fig. 2.2.2.5). Active andesitic volcanism occurs along most of the arc, and age and thickness of the subducted oceanic lithosphere increases from Sumatra to Java. For young subducting lithosphere (with age less than 70 Ma) the thickness increases with age (Parsons and Sclater, 1977). Eastward from near Sunda Strait the age of the oceanic crust is over 70 Ma (Hamilton, 1979). The thick slab off Java and further east extends to greater depth and exerts significant slab pull force which supplements the outer arc bending related extensional stress to cause the tensional earthquakes oceanward off the trench of Java. The increasing dip and depth of penetration of the Benioff zone (as shown in Fig. Fig. 2.2.2.5, profiles JJ'-OO') reflect this change. Steplike increase in the depth of the deepest earthquakes from 150 km west of the strait to >600 km east of it suggests that the rate of underthrusting in this region has a similar step-like increase. Fitch (1972) pointed out that an abrupt change in the orientation of the arc near the Sunda Strait can account for such a change in the rate of underthrusting and thus can account for the configuration of the inclined seismic zone beneath this part of the arc in general.

Deep focus earthquakes down to almost 700 km occur underneath the Sunda Shelf, but end abruptly near the Sunda Strait (Fig. 2.2.2.6). Moreover, south of Java the maximum depth of the trench is greater than 6000 m, and decreases towards the Sumatra trench. Underneath Java, seismic activity extends from the surface to a depth of 670 km. The seismic zone is steeply dipping here at an angle of about 60°. A pronounced seismic gap exists below Java in a depth interval of about 300-500 km. It has been inferred from tomographic images that the slab is continuous across the seismic gap beneath Java and that there is a pronounced seismic anomaly in the lower mantle with higher than average seismic velocities with small amplitudes. This amplitude reduction in the seismic gap suggests a thinning or "necking" of the Java slab. Widiyantoro et al., 1996, modeled a kink in the slab which gradually decreases from Java towards the west, where the lower mantle slab is almost vertically below the north-western tip of Sumatra (Fig. 2.2.2.7). They suggested the clockwise rotation of tectonic units in Indonesia as a cause for the kinking of the slab.

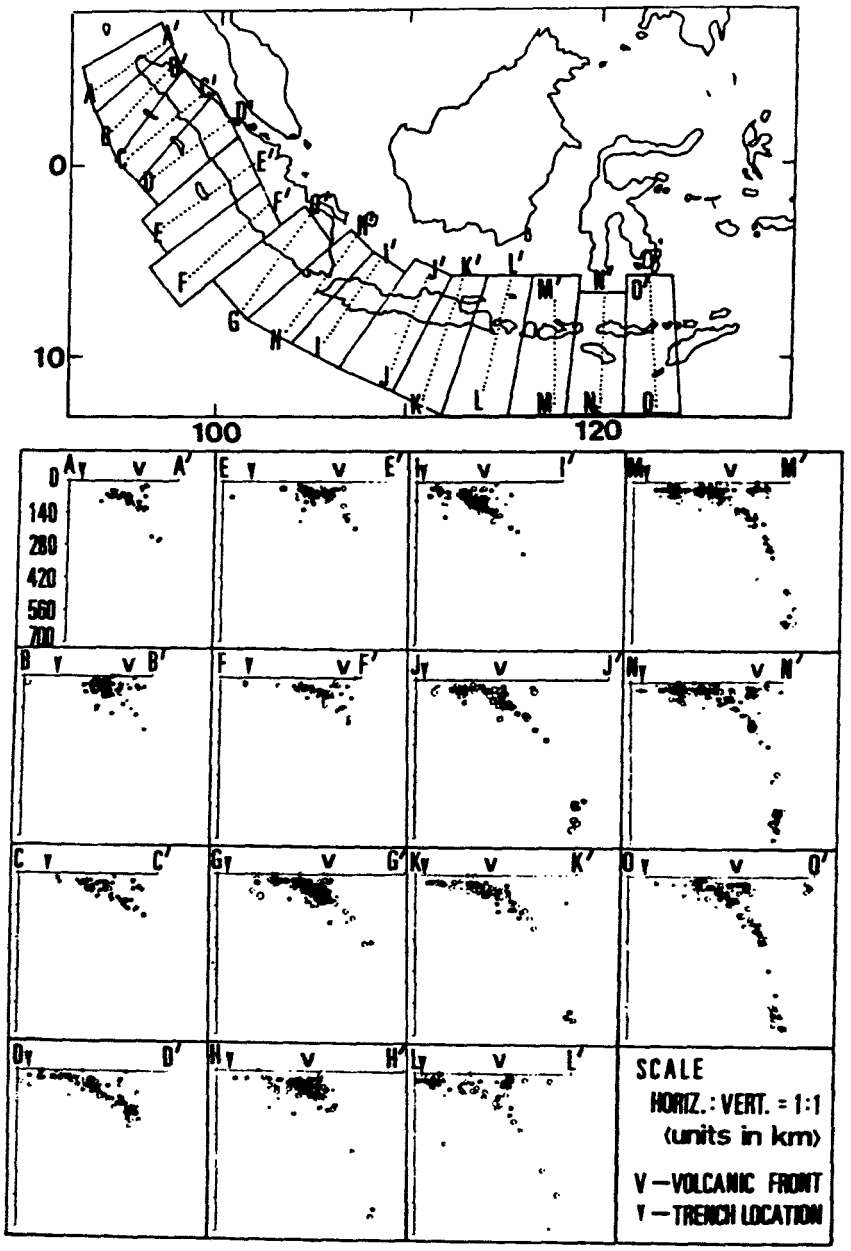

Figure 2.2.2.5: Benioff zone structure along the Sunda arc. Earthquakes reported by 15 or more stations from the ISC Data File (1971-1983) are plotted against depth. The depth variation of the Benioff zone along the arc ranges from ca. 300 km in northern Sumatra (profile A-A') to ca. 700 km beneath Java (profiles JJ', NN', KK', and OO'). The gap in seismic continuity beneath Java between 300 and 500 km is imaged in profiles MM', NN' and OO' (from Ghose et al., 1990).

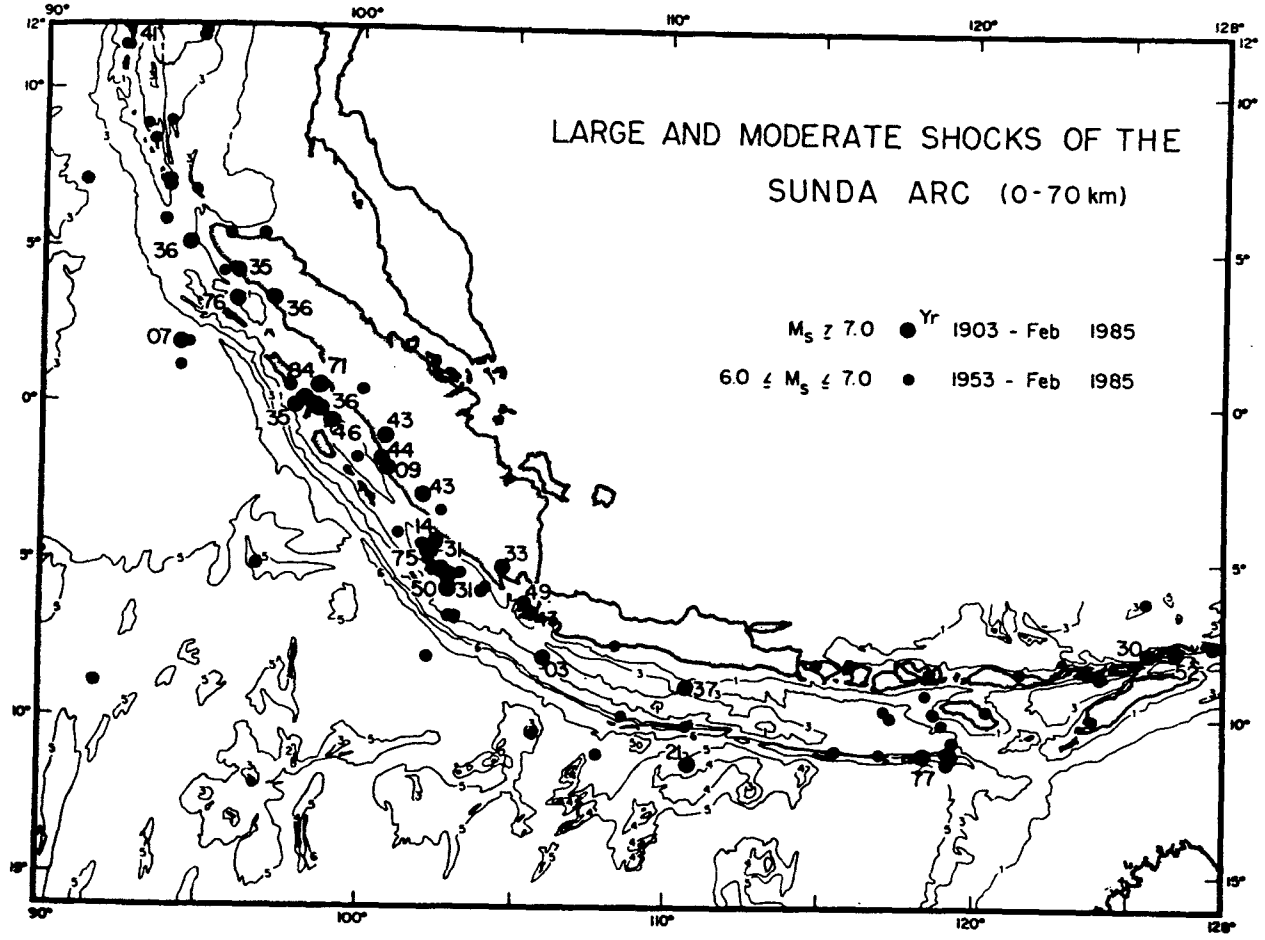

Figure 2.2.2.6: Large shallow earthquakes (Ms > 7.0, z < 70 km) of this century are plotted with year indicated beside the epicentral location. All events since 1921 have been relocated. The catalog of large and moderate events was developed by Newcomb and McCann (1987).

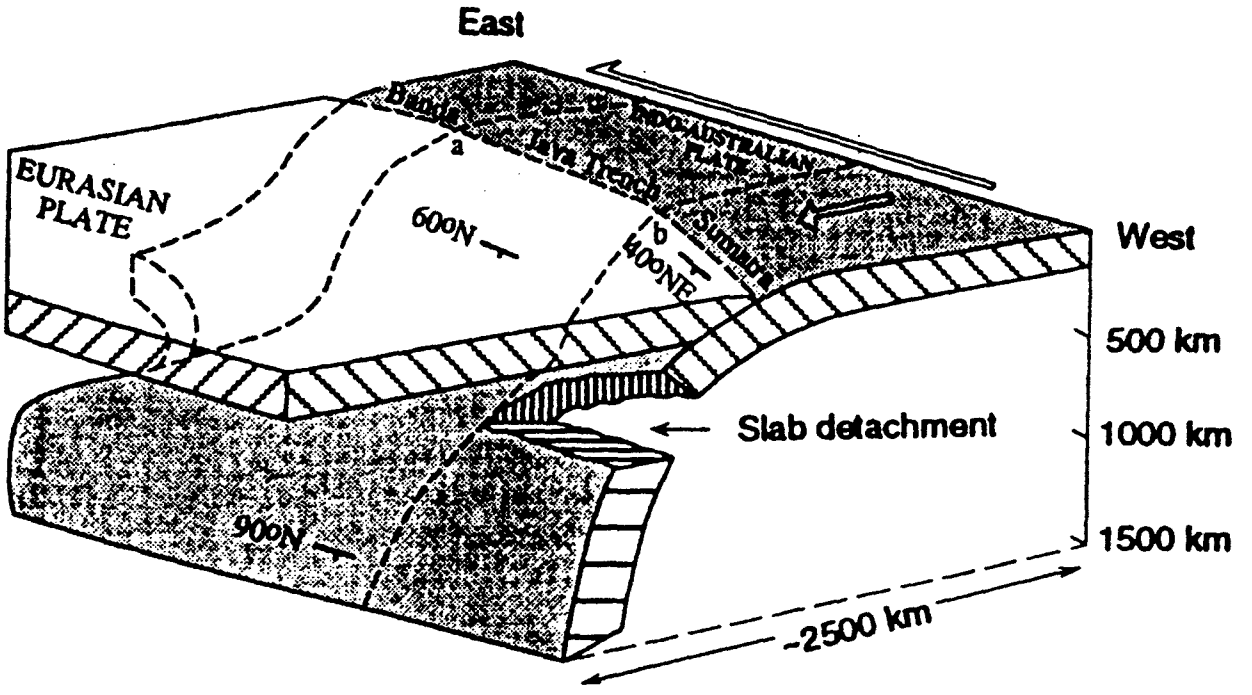

Figure 2.2.2.7: Slab structure beneath the Sunda and western Banda arcs. The shallow slab dips in a northeast direction at an angle of ca. 40° below Sumatra and in a north direction at an angle of ca. 60° below Java; the deep slab sinks almost vertically into the lower mantle. Notice the slab detachment below Sumatra.

Farther to the west and north, earthquake foci do not exceed a depth of 300 km. Slab configuration is ambiguous in northern Sumatra while in the south a plane dipping 40-50° is apparent, which has been attributed to the relatively young age of subducted lithosphere. The subduction process here has a much younger history than Java, where the subducting oceanic crust is very old, and the slab has penetrated much deeper down. The detection of a positive velocity anomaly in the lower mantle beneath Sumatra (Widiyantoro et al, (1996) suggests that the deep part of the slab is detached from the seismogenic slab (Fig. Fig. 2.2.2.7). This might have been caused by the buoyancy of the young lithosphere and the change to oblique subduction because of the rotation of Sumatra, which reduced flow in the vertical direction and may have combined to temporarily cease subduction, while the deep, old slab continued to sink to larger depths.

The shallowest earthquakes (0-20 km) near Sumatra (Fig. Fig. 2.2.2.6) immediately adjacent to the Sunda trench are commonly associated with strain release occurring within the subducted lithosphere. At Sumatra, the interplate seismic coupling is very high, and thus causes the large thrust events. The majority of strong earthquakes in both the historic and instrumental catalogues of the Sunda Arc (Mw = 8.75, in 1833, and Mw = 8.4, in 1861) are located in the forearc of Sumatra (Fig. Fig. 2.2.2.6). At Java, subduction occurs between two strongly coupled plates, causing more aseismic slip. It is striking that at Sumatra, although the plates are strongly coupled, the shallow seismicity does not extend far into the continental platform, whereas the whole of Java experiences many such shallow events. The difference in slab penetration between Sumatra and Java cannot completely account for this difference in shallow seismicity inlands of Sumatra and Java. However, the distance from the trench to inland Sumatra exceeds that of Java (Fig. 2.2.2.2) As a matter of fact, the line of active volcanoes (which usually corresponds to the 120 km depth contour for the inclined seismic zone) passes through the centre (E-W) of Java, whereas for Sumatra it runs close the the Indian ocean coast (Fig. 2.2.2.2).

The occurence of numerous large earthquakes near Sumatra and the absence of such events near Java (Fig. Fig. 2.2.2.6) correlate with changes in tectonic style along the arc and support the variation in mode of interplate motion (seismic vs. aseismic). The maximum magnitude of great interplate earthquakes in Sumatra (Mw = 8.5-9) contrasts sharply with that of interplate earthquakes in Java (M = 7.2). The variation in maximum magnitude of earthquakes in the world's subduction zones is similar to the variation in seismic slip rate (Newcomb et al., 1987). In regions that have great earthquakes, seismic slip rates are comparable to the rate of relative plate motion. Sumatra's great earthquakes account for a majority of slip between the two plates. The lack of such events near Java indicates differential motion at the plate margin which is principally being taken up aseismically or by small magnitude earthquakes.

A strong correlation of earthquake size with both age of the subducted lithosphere and convergence rate has been found (Newcomb et al., 1987). High convergence rates and subduction of younger seafloor are associated with regions of great thrust earthquakes (Fig. Fig. 2.2.2.6), while regions with fewer such events tend to subduct older seafloor at low rates. Convergence rates along the Sunda Arc do not change substantially, but the difference in age of the subducted lithosphere is almost 100 my between Sumatra and Java. The basis for this correlation may be interpreted in terms of the subducted plates' trajectory, where convergence rate controls the horizontal component and slab age controls the vertical component. The average density of an oceanic plate increases as it ages, since more high-density mantle is

underplated with time. The difference in vertical velocity upon subduction causes changes in coupling along the plate boundary and hence changes in the ability to generate great earthquakes. The vertical force acting on an old and dense subducted plate (like the one beneath Java) will minimize coupling in an interface thrust zone, resulting in the absence of great thrust earthquakes (Ghose et al., 1990).

In the Sunda Arc, the width of the plate interface, as measured from the trench axis to the 100 km depth contour, indicates a more broad zone of contact at Sumatra, where great interplate earthquakes occur, and a relatively narrower zone at Java, where shallow portions of the Benioff zone dip more steeply (Fig. Fig. 2.2.2.6). These observations are consistent with the concept of coupling in that younger lithosphere being subducted at a higher convergence rate has a more shallow dip, a greater area of contact, and a greater shear traction applied to the plate boundary. Thus the variation in age of the subducted seafloor correlates with the variation in mode of strain energy release, as reflected in the amount of seismic activity and the maximum magnitude of earthquakes, as well as the dip of the shallow portion of the Benioff zone.

Fault plane solutions in the forearc of Sumatra are all thrust mechanism at the appropriate depth of and with one nodal plane coincident to the plate interface (Ghose et al., 1990).

The Roo Rise

Another feature which draws attention is that, out of many scattered localities of enhanced seismic activity and of relative seismic quiescence, around 110°E longitude, there is a remarkably silent zone south off Java (Fig. 2.2.2.8). This seismically quiet zone for small (Mb>5.5) events is about 75 km in width and trends almost N-S from the trench to inland Java between 104.1°E and 116.4°E. There are few moderate to large earthquakes that are clearly associated with deformation in the forearc. Although minor seismic activity might be present here, absence of earthquakes with magnitude >5.5, even in the inner thrust zone is certainly noteworthy. Relevantly, a buoyant oceanic high - the Roo rise - is subducting just south of this locality (Fig. 2.2.2.9). The Roo Rise is a prominent bathymetric high which appears to be interacting with the forearc. This feature was formed at a ridge crest and is more buoyant, and thus more difficult to subduct, than the surrounding seafloor. It is commonly more than 2.5 km higher than the surrounding seafloor, composed of anomalously thickened crust with an average thickness of about 11.5 km with a maximum of about 16.4 km (Ghose et al., 1990). The unusual thick layer has been interpreted as thrust faulting with a basal thrust plane possibly located at the base of the crust (Curray et al., 1977). However, thickening caused by compressional tectonism is unlikely, since the free-air gravity signature of this region shows no departure from the normal outer rise gravity high associated with bending of the lithosphere. The anomalously thick crust and the absence of a free-air expression of the relief of the Roo Rise suggest that this rise is a compensated feature supported by a low-density root, as features formed on ridge crests. Anomalously thick oceanic crust, formed after continents have rifted, is found on many of the world's passive margins (Newcomb et al., 1987).

The Roo Rise probably continues into the trench since the axis of the trench is deflected 50-60 km landward and the crust is very thick there. It also appears to be interacting with the forearc. In contrast to adjacent regions where forearc basins show undisturbed sedimentary

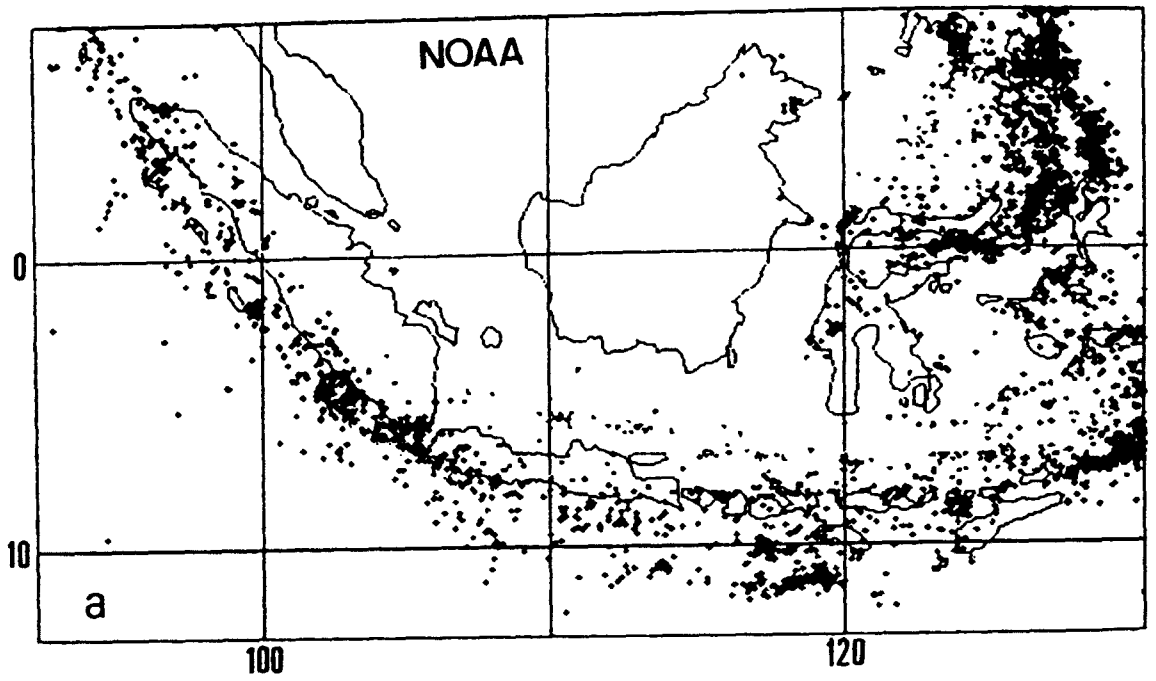

Figure 2.2.2.8: Distribution of earthquakes in the Sunda Arc region during 1900 - May, 1981, from NOAA Hypocentre Data File. Notice the area of scarce seismicity around 109°E beneath Java.

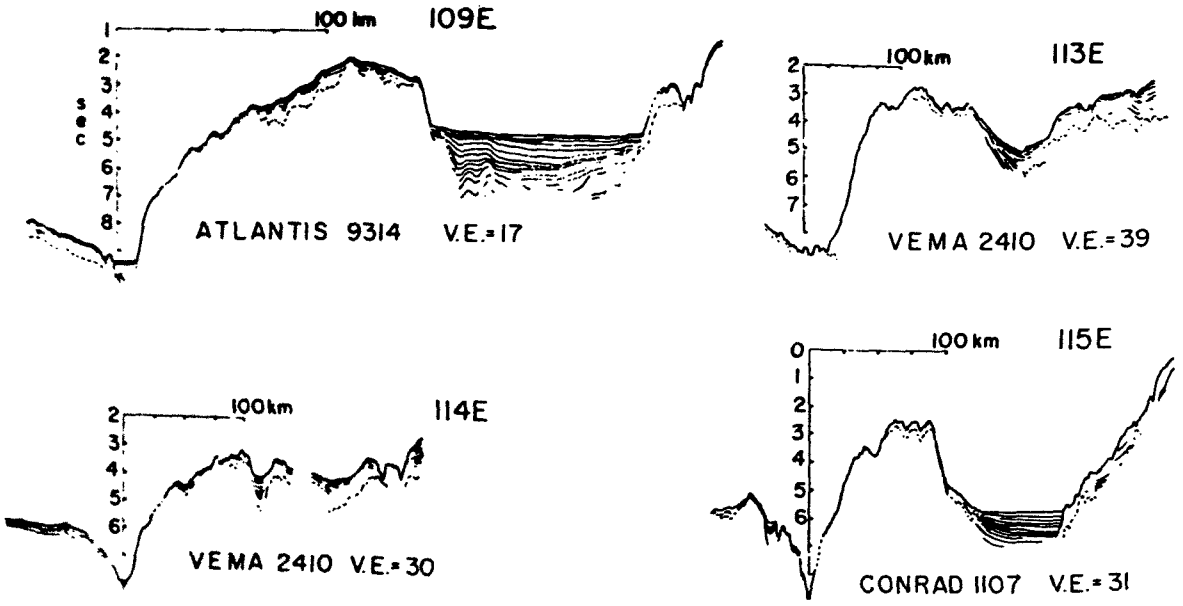

Figure 2.2.2.9: Line drawings from four successive seismic profiles crossing the forearc south of Java at longitudes 109°E, 113°E, 114°E, and 115°E. Vertical scale is equivalent in all profiles; vertical exaggeration is indicated. Forearc basins at 109°E and 115°E are undisturbed. Profile at 113°E shows progressively onlapping horizons implying recent uplift of the trench slope break. At 114°E the forearc basin appears folded and faulted, indicating recent tectonism. Sites of distrubed forearc basins occur where the along-strike extension of the Roo Rise intersects the trench.

fill, the forearc basins of Java indicate that there has been recent uplift of the trench slope break in an isolated region immediately landward of the Roo Rise. Four records by Newcomb et al., 1987, at approximately 109°E, 113°E, 114°E, and 115°E (Fig. Fig. 2.2.2.9) show this transition. The trench slope break at 109°E appears to have been more active in the past as indicated by the small compressional folds at depth in the basin strata; the shallowest strata of the basin are generally undisturbed and away from the trench slope break, deeper reflectors are only broadly warped. It is apparent in section 113°E that the seaward margin of the basin is actively rising; basin strata that onlap the trench slope break are strongly tilted landward. The point of intersection of the along-strike extension of the Roo Rise with the forearc is just reaching this longitude. At 114°E the forearc basin strata are discontinuous and have been severely disturbed. This section has been most recently affected. Section 115°E shows flat lying sediments in a relatively undisturbed forearc basin.

The low density root of the Roo Rise should cause this bathymetric feature to be more buoyant than the surrounding seafloor and therefore more difficult to subduct. The depth to which the Roo Rise penetrates into the thrust zone and the exact limits of the Roo Rise are still unclear. Subduction of lighter oceanic rise material has been correlated to a number of observed peculiarities in subduction zones, e.g. outer arc uplift, modification of slab dip, discontinuity in the volcanic line and lack of moderate to large earthquakes (Ghose et al., 1990, Newcomb et al., 1987). In the case of Roo Rise subduction, any change in slab dip in the shallower region is not readily decipherable from the seismicity data alone. However, a clear gap in the line of active volcanoes around the north extension of the interacting Roo Rise is apparent, which coincides with the zone of scarce seismic activity around 109°E.

Ghose et al. (1990) modelled the subduction of a buoyant ridge to investigate the influence of Roo Rise on the regional stress level. Using a density contrast between the ridge and the slab of 0.42 g cm^{-3} (Ghose, 1990) they calculated the stress field in 75 km depth for a subducting low-density Roo Rise and found a clear rise in the stress level near the location of ridge subduction. This is quite expected since the low-density root of the Roo Rise ought to cause the rise to be more buoyant than the surrounding sea floor and therefore more difficult to subduct. When it interacts with the crystalline material of the overriding plate, the increased interplate coupling might be expected to cause enhanced seismic activity relative to adjacent areas subducting old abyssal plains. With the model parameters and the assigned material properties used by Ghose et al., (1990) it was thus not possible to justify the narrow seismic quiescence at 109°E as to be due to the subduction of the Roo Rise. The seismic quiescene may imply that the Roo Rise is only in the initial stages of subduction.

Regional Stress Field Along the Sunda Arc

In regions of active interplate collision or subduction, plate tectonic forces dominate the stress field. The dominance of plate tectonic forces over those inducing local stresses (e.g., those associated with flexure of those induced by lithosphereic cooling as in ridge areas) is greater if there is a concentration of stresses due either to lithospheric age variations encountered along trench systems or to angular or curved geometry of plate boundaries (Cloetingh and Wortel, 1985). The principal forces driving subduction are the slab pull force resulting from the density contrast between the slab and the surrounding asthenosphere and the ridge push force arising from the elevation of the spreading ridge above the adjacent sea floor and the thickening of the lithosphere with cooling.

For the Sunda Arc, the age of the descending oceanic lithosphere varies significantly along the strike of the trench. Thus it is very important to consider the age dependency of the boundary forces for stress field calculations. Cloetingh and Wortel (1985) have calculated a regional stress field for the Indian plate. The calculated stress field displays significant variation along the strike of the Sunda Arc. Compression occurs seaward and parallel to the Sumatra trench segment, while off Java, extension perpendicular to the trench is dominant. The change from a compressive stress field parallel off Sumatra to a tensional stress field normal to Java is caused by the contrast in the age of the subducted lithosphere under Sumatra (40-70 Ma) and Java (140 Ma). The driving forces considered to act on the plate are the pull on the downgoing oceanic lithosphere at trenches and the ridge push, where slab pull is proportional to the age of the subducted lithosphere. The lateral variation in the component of the regional stress field perpendicular to the trench as proposed by Cloetingh and Wortel is in accordance with the varying style of trench tectonics along the Sunda Arc.

2.2.3 SUNDA STRAIT

Introduction

Sunda Strait, which separates Sumatra from Java, serves as a major boundary between two different geodynamic regimes. The trench itself is curved landward west of Sunda Strait, so that the strait appears to be a transition zone between two different regions (Fig. 2.2.2.2). Major tectonic trends in Java and Sumatra are disrupted across the strait. This setting implies that the Sunda Strait region is a key to the understanding of the geodynamic processes involved. Huchon and Le Pichon (1984) propose that the formation of Sunda Strait results from extension due to the north-westward motion of the Sumatra sliver plate along the Central Sumatra Fault, away from the north-east Sumatra and west Java block. The evolution of Sunda Strait would then be related to the 20° clockwise rotation of Sumatra relative to Java during Late Cenozoic time, which initiated the change to oblique subduction along the Sumatra part of the Sunda Arc. The Sumatran fault is related to this oblique subduction, which is at least in part compensated by the dextral strike slip motion along the fault.

Sunda Strait represents a tectonic as well as a physiographic break in the arc. It is 25 km wide in the east and approximatly 100 km wide in the west with the active Anak Krakatau volcano in its center (Fig. 2.2.3.1). The region is characterized by north-north-east trending transverse structures (Ghose et al., 1990). Sunda Strait is one of the most active regions in Indonesia in terms of volcanism, seismicity, and vertical motion. A concentration of shallow earthquakes in Sunda Strait region is further evidence for a tectonic break in this region (Fig. 2.2.3.2). Possibly this activity results from extension on the seaward side and convergence on the landward side of the strait as suggested by the opposite sense of motion on faults adjacent to the strait (Fitch, 1972).

This shallow seismicity is especially dense in a narrow, N20°E trending zone through Krakatau volcano (Fig. Fig. 2.2.3.2). This seismic belt coincides with a volcanic lineament about 200 km long from Panaitan, Anak Krakatau, Sebesi and Mt. Rajabasa, through to the Sukadana basalt area of SE Lampung (Fig. 2.2.3.3). It has been proposed that this lineament represents a fracture zone. This seismic zone is nearly parallel to the direction of convergence; thus, it may be interpreted as a giant tension gash.

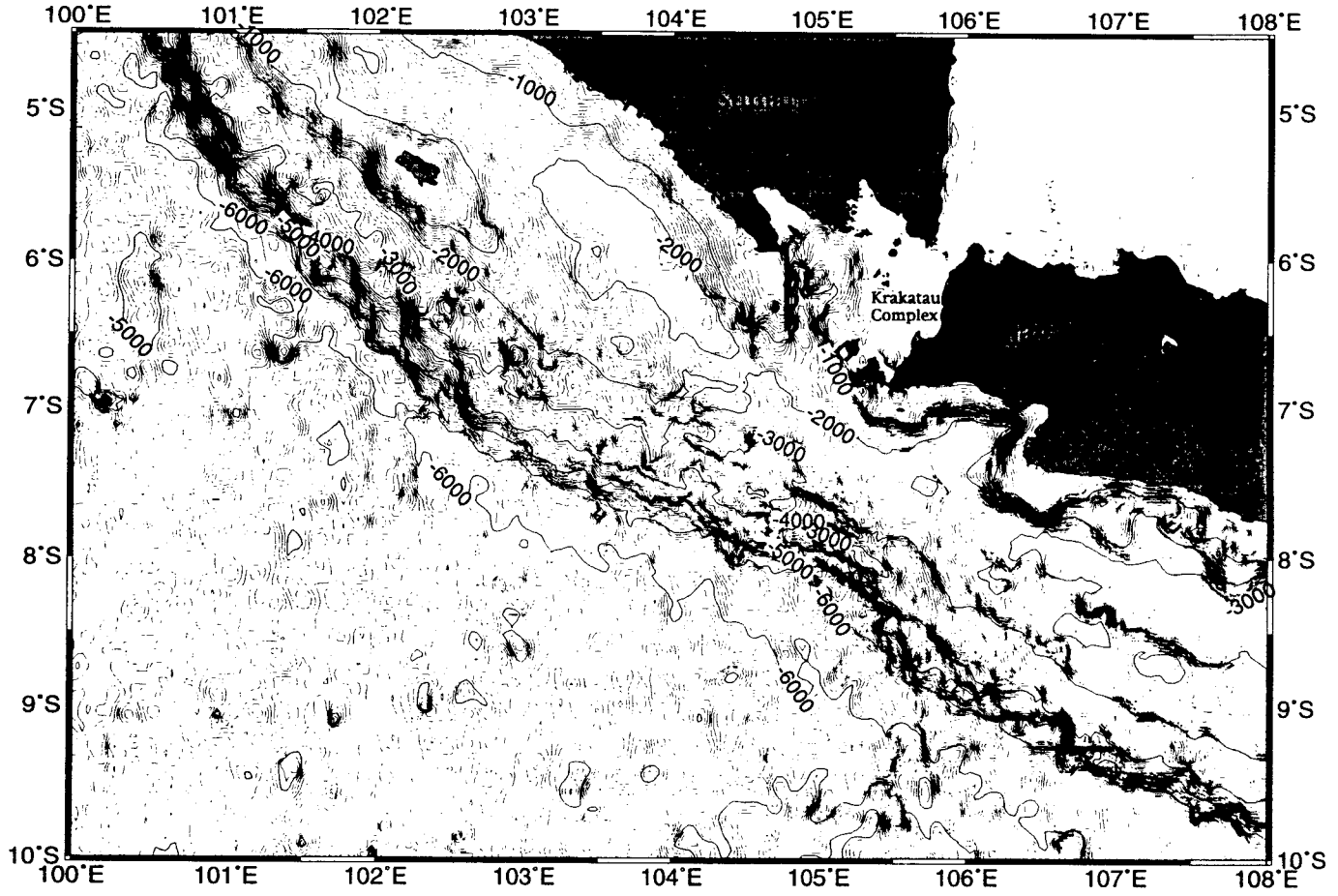

Figure 2.2.3.1: Bathymetry of the study region. Waterdepth reaches 1500 m at the western entrance to Sunda Strait.

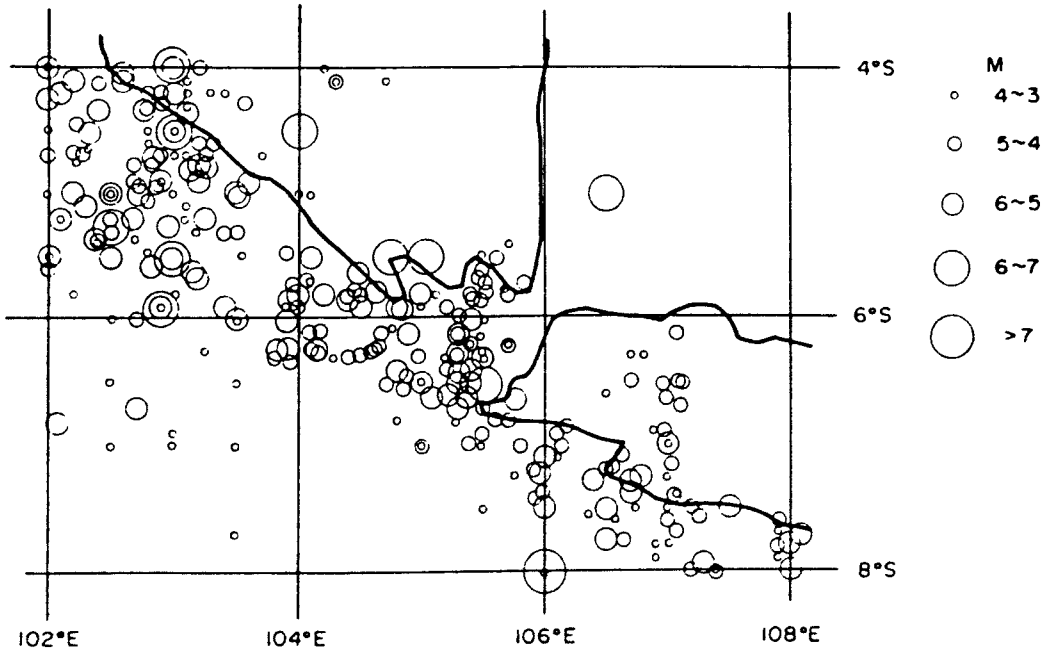

Figure 2.2.3.2: Shallow earthquakes (h<100 km) 1961-1981 located by the International Seismological Center. Notice the north-south trending band of enhanced seismic activity along the volcanic lineament.

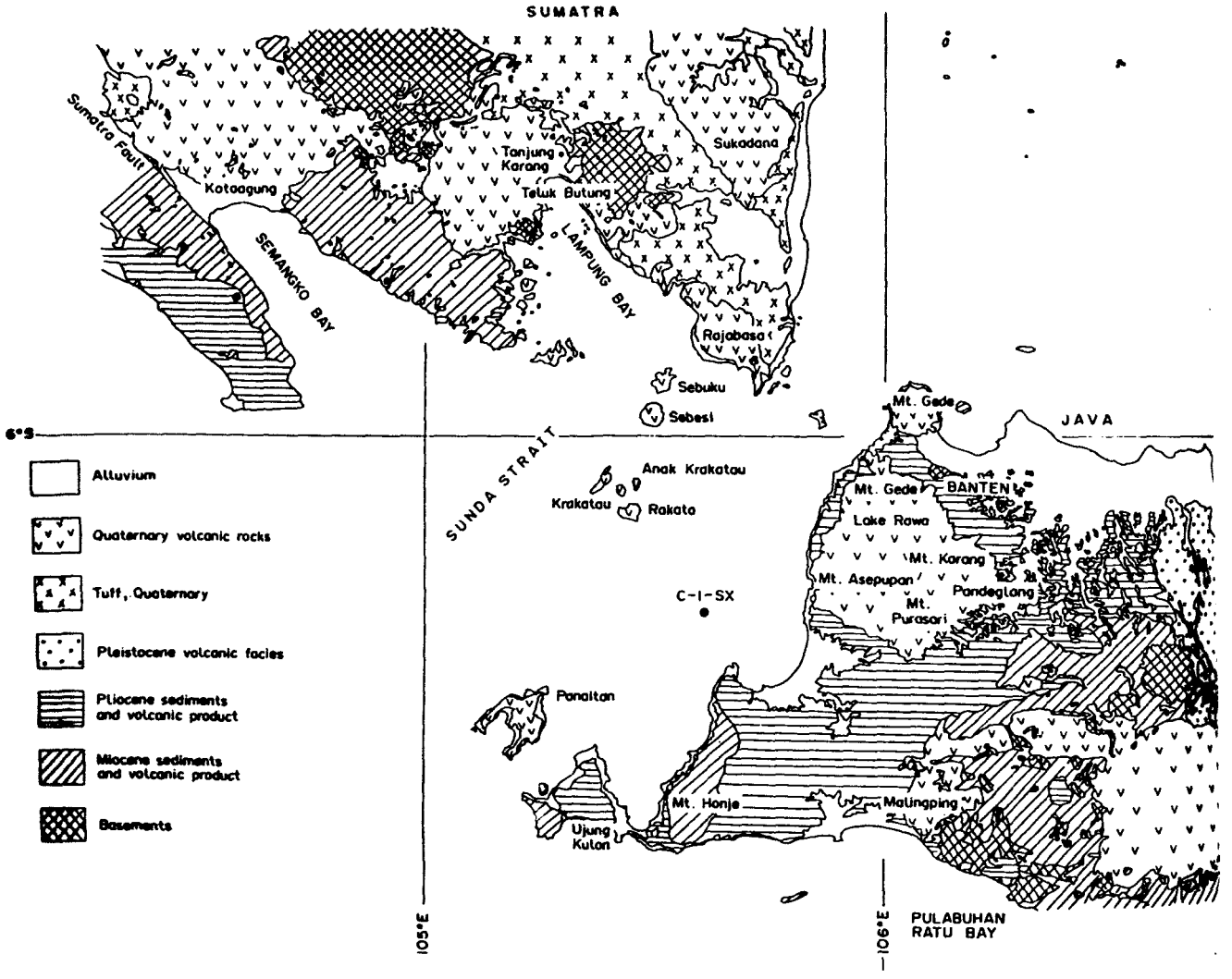

Figure 2.2.3.3: Geological map around the Sunda Strait (modified from Peta Geologi; Director Geologi, 1978). The geology of Western Java shows close relationships to South Sumatra. C-I SX denotes one of nine wells drilled within the Sunda Strait.

The bathymetry of Sunda Strait is divided into two distinct domains. To the east of Krakatau, the depth of water is less than 120 m deep except for the Krakatau complex, where the bottom of the caldera reaches a depth of 200 m. A large amount (> 2000 m) of volcanics and volcaniclastics has been deposited in a small basin. Nine wells were drilled in the S and E part of Sunda Strait (Asikin, 1987). One well, C-1 SX (lat 6°23'9"S; long 105°36'7"E, 31.9 m under sea-level) penetrated an apparently continuous sedimentary sequence ranging in age from Quaternary to upper Pleistocene (shown in Fig. Fig. 2.2.3.3), indicating strong subsidence during this time. The rocks encountered were mostly marine clays and claystone which generally contain good formaminiferan fossils. They were thinly interbedded with quartz sandstone, siltstone and altered clastics of volcanic origin. These sediments were deposited in an environment in which water depth varied from inner sublittoral to upper bathyal. One of the most unusual features of the section is the aforementioned great thickness of upper Pliocene sediments encountered (555-3005 m). Therefore, this area of the Sunda Strait must have formed in a rapidly subsiding trough in which vast thickness of clastic sediments derived from adjacent areas accumulated. Evidence of contemporaneous nearby volcanism comes from the scattered volcanic debris in the claystones and from the occasional tuffaceous beds. The small basins in this area are further evidence for the extensional

character of the strait. The volume of volcanic material was insufficient to keep up with the extension, so that basins were created by subsidence. The Pliocene subsidence rate has been found to be of the order of 400 m/my. It has been proposed that the strait opened 5 Ma ago with a maximum displacement of 50 to 70 km parallel to the Sumatran fault. The extension in the Sunda Strait probably began in Oligo-Miocene time following the initiation of N-S faults and remained limited until the Pliocene. In Pliocene time, extension became much more important.

To the west, water depth reaches 1500 m at the entrance to the strait (Fig. Fig. 2.2.3.1). The continental slope is steep and cut by several canyons. One of them lies in the prolongation of the Sumatra fault (Hamilton, 1979) and probably explains why this part of the strait has not been filled by sediments. Stratigraphic interpretations of the eastern flank of this graben clearly reveal rapid subsidence since Pliocene (Harjono et al., 1991), in correspondence with the subsidence in the eastern part of the strait. This large N-S trending graben trends parallel to the Sumatra fault (Nishimura et al., 1992). The exact location of the Sumatra fault system within the Sunda Strait is still enigmatic. Hamilton (1979) assumed that the fault continues southward and intersects the trench, while Huchon and Le Pichon (1984) proposed that the fault ends in the Sunda Strait within the mentioned graben.

Seismicity

Seismicity in the Sunda Strait is not correlated with the bathymetry, but does correlate with the Krakatau volcanic belt (Fig. Fig. 2.2.3.2). Underneath Krakatau volcano, a cluster of shallow earthquakes exists. It has been proposed that these events are of tectonic rather than volcanic (tremors) origin. Earthquakes associated with a volcanic origin such as magma movements normally have low frequencies as compared to tectonic ones. Also, there is common evidence that volcanic earthquakes are not generated by a double couple as are tectonic ones. The Krakatau events show both high frequencies and up and down first motions. Their vertical distribution and focal mechanism show that these events correspond to displacement along faults controlled by the deep geometry of the calderas (Hajorno et al., 1991).

A second seismicity cluster within the Sunda Strait coincides with the eastern flank of the N-S trending graben and is connected to the Krakatau cluster by a fault striking N50°E-N60°E. Results from focal mechnism investigations (Hajorno et al., 1991) support the notion that Sunda Strait is under an extensional tectonic regime, the direction of extension being parallel to the Sumatra fault.

A third cluster composed of small magnitude earthquakes has been recorded south of Sumatra. Their centroid moment tensor solutions mostly represent strike-slip faulting with an extensional component (Hajorno et al., 1991). The extension direction is roughly parallel to the Sumatra fault. It has been proposed that the direction of faulting is the one that gives rise to a right lateral fault, in accordance with the dextral movement of the Sumatra Fault. Such a fault, the Batee fault, has been described for northern Sumatra, connecting the Mentawai and Sumatra faults. These faults, transverse to the fore arc basin probably delineate blocks that rotate along the Sumatra fault.

Volcanism

The most prominent volcanoes within Sunda Strait compose the Krakatau complex. It consists of four islands: Serung, Panjang, Rakata and Anak Krakatau (Fig. Fig. 2.2.3.3). This configuration results form at least two historical destructive eruptions and from the recent emergence of Anak Krakatau. Anak Krakatau (child of Krakatau) is an active volcanic cone born in August 1927, 44 years after the famous 1883 explosion. This volcano is characterized by a bimodal basalt-dacite composition, different from the common pattern of volcanoes in Indonesia which generally show a uniform composition common to most island arc volcanoes. Krakatau thus exhibits a peculiar chemistry when compared to that of the rocks from Java and the main part of Sumatra. This is very probably related to the tectonic setting of the Sunda Strait as an extensional regime. The Krakatau complex lies on the N-S trending volcanic lineament, of which Anak Krakatau is presently the only active volcano (Fig. Fig. 2.2.3.2). The recent volcanic activity around the Sunda Strait occurred along this Krakatau volcanic line. According to several authors it started in the north by alkali basaltic emplacement at Sukadana, continued to the south through Rajabasa, Sebesi, Sebuku, Panaitan, and finally ended at Krakatau (Fig. Fig. 2.2.3.3). Nevertheless it must be noted that no dating has been done on Panaitan. The K-Ar age determination of the Sukadana basalt is between 0.8 and 1.2 Ma. Compared to the other Quaternary volcanic rocks in the region, the source of this basaltic plateau is more primitive.

From attenuation of S-waves the existence of magma bodies beneath Krakatau volcano could be inferred (Hajorno, 1989). According to petrological and volcanological analysis, the magma reservoir for recent eruptions should be at shallow depth, less than 15 km beneath the Krakatau complex. It could be demonstrated that an attenuating body is located beneath Krakatau, which consists of two anomalous zones which are assumed to correspond to two distinct magma reservoirs. The deeper one is located just beneath the Moho at about 22 km depth and presents a large horizontal extension. The upper one, located at a depth of about 9 km, has a smaller extension but is large enough to allow the differentiation of the volume of dacite of the 1883 eruption (Deplus et al., 1995). It is divided into three parts that were interpreted as magma pockets. The present shape of the upper attenuation zone could be related to the internal structure of the volcano, controlled by the successive collapses of calderas. The volcanic history of the Krakatau complex can be divided into three periods:

Formation of a shield volcano (Proto-Krakatau) about 2000 m high and 10-12 km in diameter. A destruction of the primitive volcano would have resulted in the formation of a large submarine caldera whose diameter is approximately 7 km. The islands of Sertung and Panjang and the basement of Rakata are remnants of the rim of this caldera. The destruction occurred about 60 000 years ago according to Ninkovich (1979). In the second period, the formation of a 800 m high basaltic cone on the edge of the prehistoric caldera was followed by the growth of two andesitic cones. These three overlapping volcanoes merged into one elongated volcanic island, Krakatau. The Krakatau island largely disappeared on 27 August 1883, leaving only half the cone of Rakata and a small rock pinnacle exposed above sea level. Following the eruption, pyroclastic deposits have greatly increased the area of the islands of Sertung and Panjang. The emission of a huge volume of ignimbrite covered the islands and the surrounding seafloor, where a submarine caldera was formed. The emergence of Anak Krakatau characterized the third stage. A tuff ring (basic andesite) was constructed up to 152

pyroclastics in the Late Quaternary. The south-eastern part of the Sunda Strait is also a submerged extension of the Sumatra fault zone. The large quantities of pyroclastics in south Lampung and Banten could well be the products of the volcano-tectonic depression in the Sunda Strait, including the acid pyroclastics of Sertung and Panjang and the basement of the Sunda Strait. The fission-track age of the pyroclastics is 0.1 Ma (Nishimura, 1989). The fissure eruption of Sukadana basalt in Lampung could be connected with the trend along the north-south fracture zone in Sunda Strait, which coincides with the volcanic lineament.

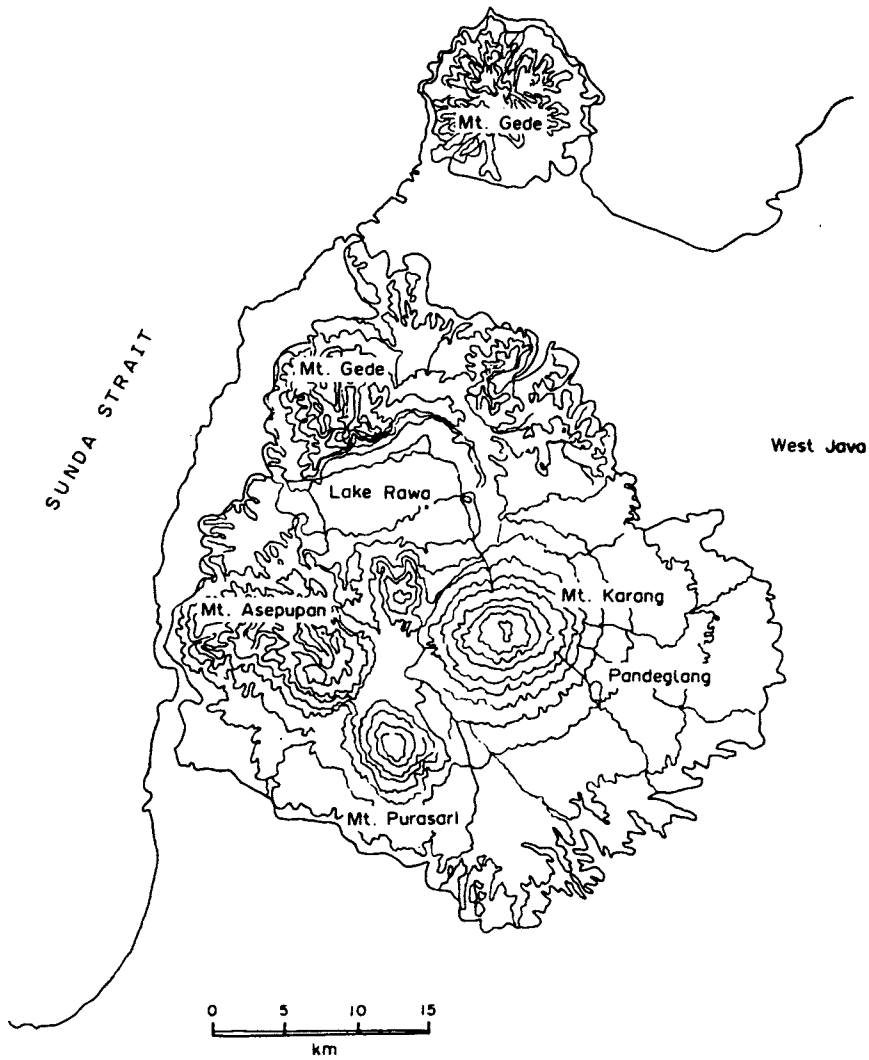

Figure 2.2.3.4: Topographical map around Lake Rawa, West Java.

2.2.4 INDIAN OCEAN: DSDP HOLE 211

The deep Indian Ocean lies south and west of the Sunda Arc, with waterdepths mostly near 5000 m. Thick clastic sediments overlie the oceanic crust in the north-west due to the influx of the Bengal fan, but most of the ocean floor has only a thin cover of pelagic sediments. Between the east flank of the Ninetyeast Ridge and the Sunda Arc extends the abyssal Wharton Basin. Water depths exceed 6000 m in the central part of the basin. The basin typically has a rough oceanic basement thinly covered by pelagic sediments. However, extensive abyssal turbidites forming the eastern part of the Bengal fan, come into the basin from the Ganges-Brahmaputra Delta region far to the northwest.

The floor of the Wharton Basin is of Late Jurassic and Early Cretaceous age near Australia and of progressively younger Cretaceous and early Tertiary age westward and northward.

Nine of the Deep Sea Drilling Project (DSDP) drillholes lie at abyssal depths in the Wharton Basin, most of which reached basalt. In hole 211 (Fig. 2.2.2.2), south of South-east Sumatra (lat 9°47'S, long 102°42'E) Quaternary and upper Pliocene pelagic silicic ooze and minor ash overlie Pliocene turbidite pelagic brown clay; at the base of the section is nannofossil ooze and clay of Maestrichtian and early Campanian (Late Cretaceous) age, and under that altered basalt. The basement rocks of DSDP hole 211 consist of diabase intrusive into thin basaltic lava flows that are variably amphibolitized and that have a whole-rock K-Ar age of about 71 my (Hamilton, 1979).

2.3 PRELIMINARY RESULTS OF CRUISE SO-137 (GINCO I)

(B. Schreckenberger)

During the first leg of the GINCO cruise (SO-137) multichannel seismic (MCS), magnetic, gravity, and bathymetric measurements were made across the offshore area of the Sunda Arc. The measurements provide an overview over the variable structures related to the subduction zone off southern Sumatra starting at Bengkulu north of the island Pulau Enggano down to westernmost Java at about 107°E (Fig. 2.3.1). Most of the seismic profiles were processed (velocity analysis and stack) and interpreted on board of R.V. SONNE. They are contained as linedrawings in Reichert and Shipboard Science Party (in preparation).

In general, the seismic records show structures that are very similar if we compare the profiles off Java (SO137-01, -03, and -34) with those off Sumatra (from NW to SE, SO137-14, -09, -12, -19, and -06). The oceanic crust SW of the trench shows few reflectors, and a faint Moho reflection is only visible on one of the lines. With 300 to 400 m, the sediment cover of the oceanic crust is very thin and also the trench is filled with sediments of only about 1000 m thickness. The basement reflection of the oceanic crust can be traced up to 100 km landward below the accretionary wedge. After a relatively steep slope the accretionary wedge reaches a more or less pronounced plateau which off Java lies deeper (3.5 km waterdepth; Fig. 2.3.2) than off Sumatra (2.5 km waterdepth; Fig. 2.3.3). The wedge is strongly imbricated at a scale of 5 to 10 km visible in the seafloor topography and from internal reflections. The stacked sections that were used in the interpretation and for preparing the linedrawings (Fig. 2.3.2 and 2.3.3) show many overlapping diffractions in the frontal part of the wedge. Its internal structure will be better resolved after migration of the sections.

Landward of the plateau there is another rise to the outer arc ridge which again is less pronounced off Java than off Sumatra. In contrast to the outer part of the accretionary wedge this ridge shows a clear internal structure. There is a strong reflector under a sedimentary cover of variable thickness which indicates a clearly jointed and sometimes imbricated structure. The whole unit, in Figs. 2.3.2. and 2.3.3 it is called 'oceanic crustal splinters', is 50 to 75 km wide. In the NE part of the survey area it is located at a water depth of about one kilometre and has a very plain surface (Fig. 2.3.3, also on line SO138-09) which may be an indication of a former erosive stage near the sea surface. The proximity of the lines to the island chain off Sumatra, in this case to Pulau Enggano, makes it reasonable to compare the geology of the islands with the bodies under discussion. Hamilton (1979) describes the geology of Enggano and of most other islands as middle Miocene to Oligocene melanges. For one of the islands (Pulau Nias) he mentions also ophiolites. Moore and Karig (1980) found two main geological units on Nias, one is described as melange complexes the other unit are less deformed neogene sediments of marine origin. The melange complexes contain oceanic crustal and mantle rocks (pillow basalt, gabbro, peridotite) that Moore and Karig (1980) interpret as slices of oceanic crust and mantle that were accreted together with strongly deformed trench fill turbidites at the inner trench slope during the Miocene. The term 'oceanic crustal splinters' used in Fig. 2.3.2 and 2.3.3 is based on a similar interpretation.

We suggest that oceanic crustal splinters were indeed incorporated into the wedge during a certain phase (e.g. the Miocene) but we consider it as unlikely that there are compact and intact units of oceanic crust because they do not cause a magnetic anomaly (Fig. 2.3.2, 2.3.3, upper panels). Particularly the SW transition to the less structured part of the accretionary wedge should cause an edge anomaly, even if the source bodies have only low magnetization intensities. Nevertheless, the transition on all profiles occurs in an area with a very quiet magnetic field even though the questionable bodies on some profiles (SO137-14 and –09) lie

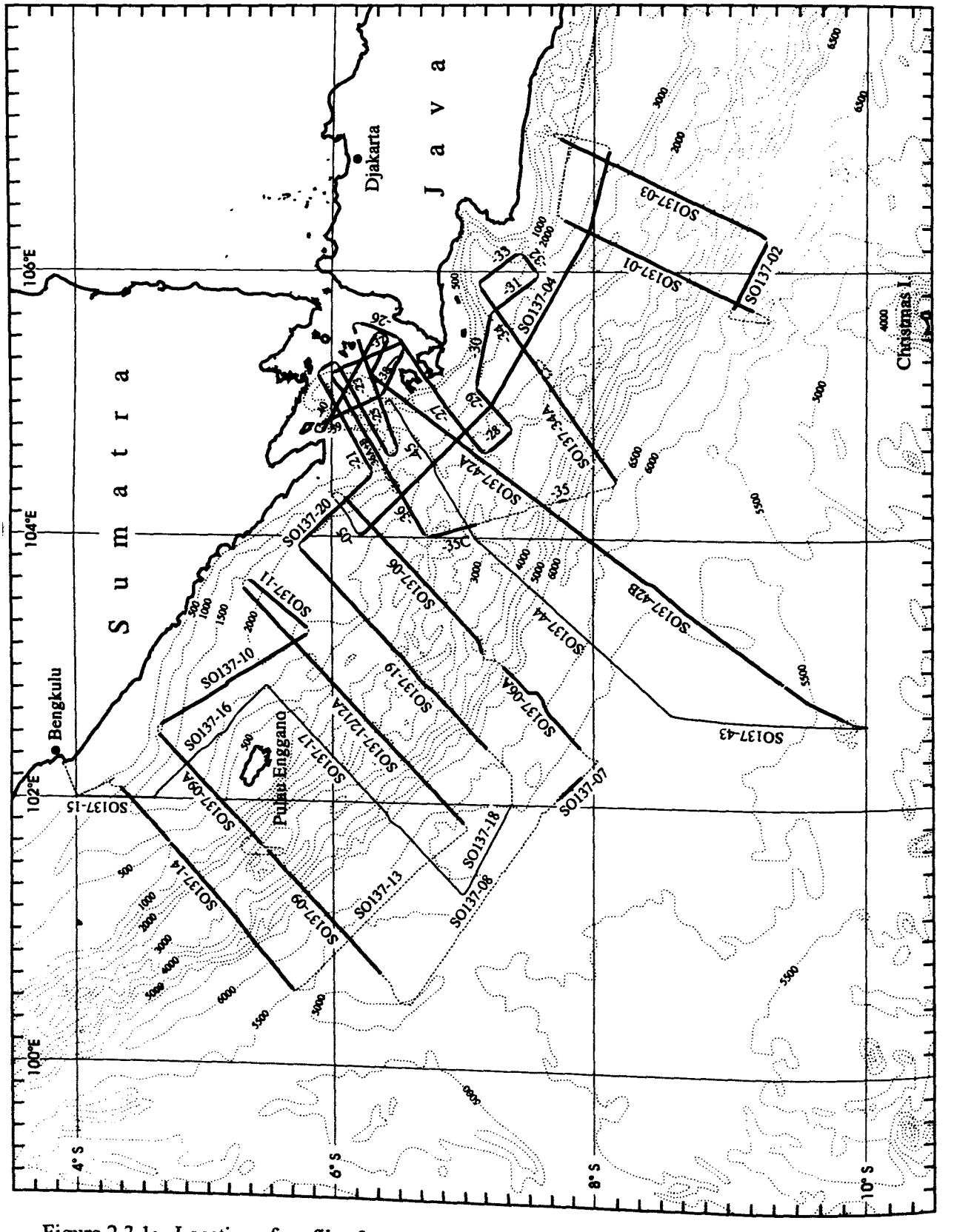

Figure 2.3.1: Location of profiles from SONNE cruise 137 (GINCO I). Thick lines with multichannel seismics, magnetics; thin lies without MCS but with magnetics; stippled lines without MCS and magnetics. Gravity and hydroacoustics was measured on all lines.

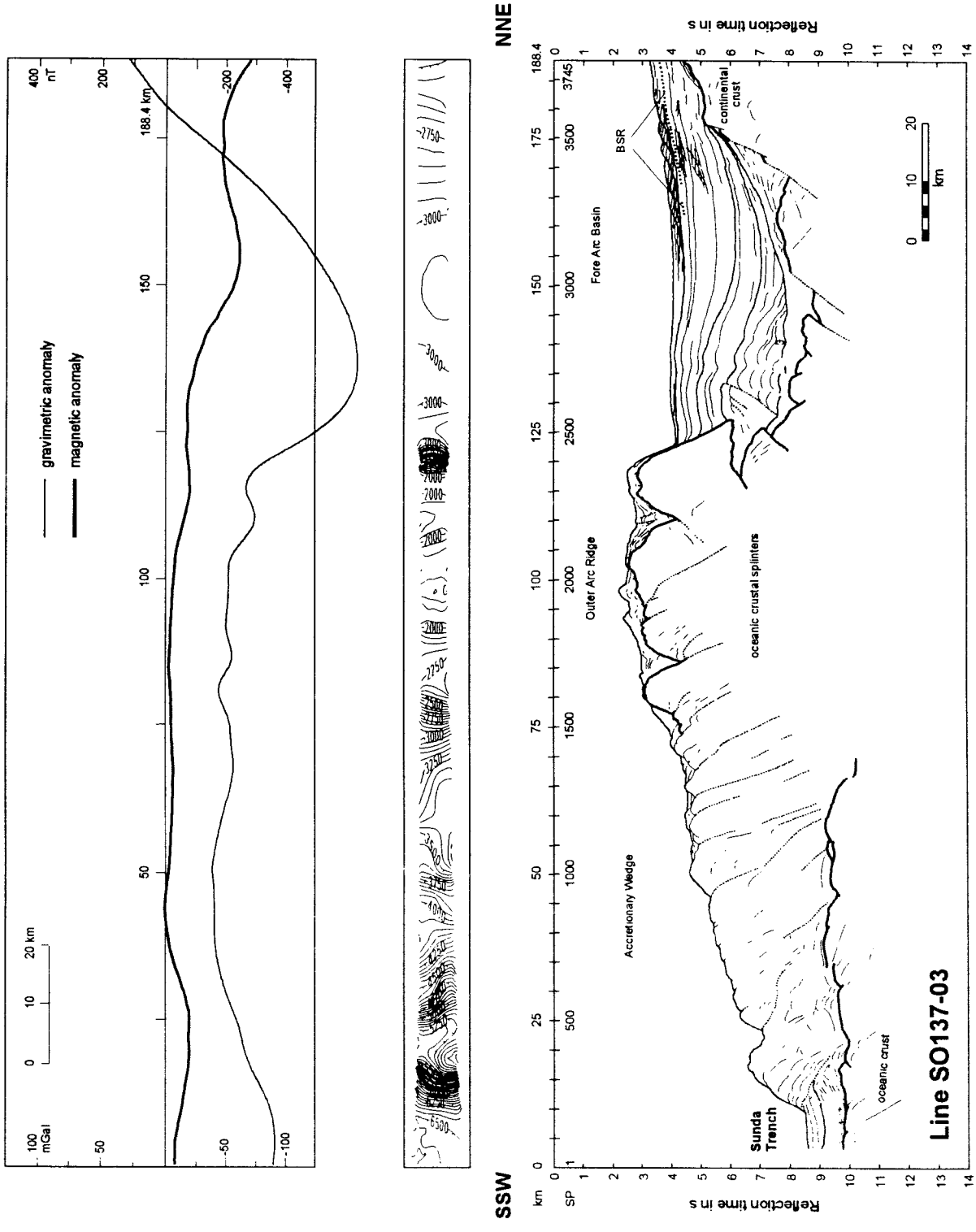

Figure 2.3.2: Seismic linedrawing (lower panel), water depth from Hydrosweep (center panel), and gravimetric and magnetic anomalies (upper panel) for Profile SO137-03 off Java from cruise SO-138 (GINCO I).

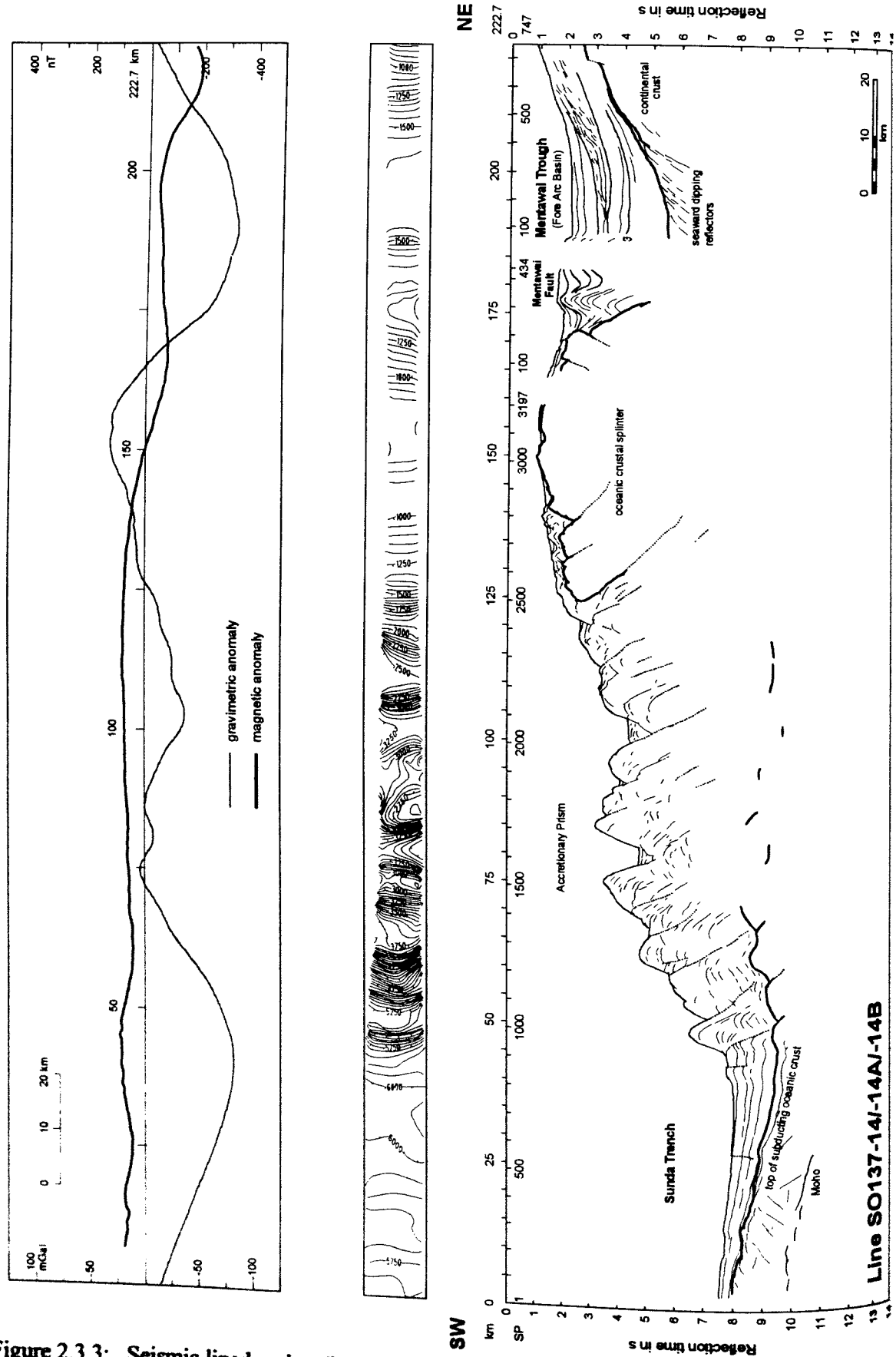

Figure 2.3.3: Seismic linedrawing (lower panel), water depth from Hydrosweep (center panel), and gravimetric and magnetic anomalies (upper panel) for Profile SO137-14/14A off Sumatra from cruise SO-138 (GINCO I)

less than one kilometre below the sea surface. Possibly it is more conceivable that the bodies correspond to the melange complexes of Nias. There, about 20% of the inclusions in the melange consist of oceanic crustal rocks (Moore and Karig, 1980). The fragments would be randomly distributed in their matrix of sedimentary rocks and would have scattered magnetic directions that cancel out the remanent magnetic field of the whole body, leaving only the induced part of the magnetization. The strength of the induced magnetization of oceanic crust is in the order of 1 A/m. A body that contains not more than 20% of that material would have a mean magnetization of less than 0.2 A/m, a value that would be compatible with the amplitude of the magnetic anomalies over the inferred crustal splinters. The seismic stacking velocities show fairly high values (4 km/s) within the bodies and gravity modelling also indicates a higher density compared to the rest of the accretionary complex. The values of these parameters are compatible with the nature of the bodies proposed here but compact bodies of oceanic crust would have even higher values and it would be difficult to bring them in agreement with the velocity determinations and the free-air gravity anomaly.

Subsequently, in the landward continuation of the profiles, we crossed the forearc basin between the outer arc ridge and the main lands of Sumatra and Java. The sediment basin on line SO137-03 (Fig. 2.3.2) reaches a thickness of at least 4 s TWT. The basin in the area of profiles SO137-12 and –19 is only a little bit shallower, but the depth and the width of the forearc basin decreases more distinctively to the north (SO137-09 and –14; Fig. 2.3.3). The reflection pattern in the MCS sections shows chaotic sequences in the lower parts of the basins, which after Hamilton (1979) may represent deformed pre-subduction strata formed by gravitational flow from the outer arc high. Large parts of the basin infill consist of undeformed strata while near to the landward slope disturbed sediment layers reappear, e.g. contourites on line SO137-03 (Fig. 2.3.2 around SP 3500; see also Reichert and Shipboard Science Party, in preparation).

There is a typical deformation of the sediments on all profiles off Sumatra (e.g. in Fig. 2.3.3 between profile kilometre 175 and 190) that can be associated with the transpressional Mentawai Fault (Fig. 2.2.6) and that is always located on the NE edge of the inferred 'oceanic crustal splinter' unit. To what extend the inferred fault penetrates into the lower parts of the crust can not yet be decided because the shallow disturbances obstruct the view into the lower levels of the crust. On line SO137-01 off Java we found a similar but more narrow structure which probably has another origin because there are no such structures on the neighbouring lines SO103-03 and –34. It is noticeable that in most cases bottom simulating reflectors (BSR) can be observed in conjunction with the Mentawai Fault (profiles SO137-09, -12, -19, and –06). More BSR are visible at the landward slope of the fore arc basins (e.g. Fig. 2.3.2) but no such reflections can be seen on the inner trench slope.

Many of the structures observed on the profiles mentioned so far, like the forearc high and the forearc basins, are not present or at least not clearly visible on line SO137-42, which runs from the SW across the accretionary wedge into the Sunda Strait. Because this profile has not yet been processed the following conclusions trust in the single channel near trace records. The sedimentary trench infill and the first slope to the plateau of the accretionary wedge are very similar to all other profiles. Then a terraced slope follows to reach another plateau at 1700 m waterdepth where we would expect structures equivalent to the 'oceanic crustal splinters' on the other lines but it seems that they are much less distinct. Without having a bathymetric low we observe a further steep increase to the continental crust or to a volcanic structure near the island of Panaitan, where quaternary volcanic rocks are abundant (Fig. 2.3.17). This part of line SO137-42 is characterised by a strong magnetic anomaly, also indicative of a volcanic origin of the observed structures. There is a small sediment basin at

the foot of the steep flank from the plateau to the volcanic structure which is only 15 km wide and 2 s TWT deep.

In the NE part of all profiles we can identify the continental crust of Sumatra and Java partly down to a depth of 8 s TWT. On all lines off Sumatra (SO137-14, -09, -12, -19, and –06) we found subbasement reflections below the centre of the sediment basins that resemble the seaward-dipping reflector sequences (SDRS) which are well known from many passive continental margins. If that pattern represents similar structures and processes like that at volcanic passive margins then we are able to observe basalt flows that presumably have been emplaced on both sides of an eruption centre within a continental rift or during an initial phase of seafloor-spreading. This means that we see remnants of the break-up of the Sibumasu terrane from Gondwana, possibly representing a Permian volcanic passive margin (see chapter 2.2.1).

With profile SO137-04 and some shorter lines (SO137-31 and –33) we crossed the Pelabuhan Ratu fault zone which seems to represent the seaward continuation of the Cimandiri fault on Java (chapter 2.2.2; Malod et al., 1995). It appears in the reflection seismic sections as a distinctively steep fault with a height of 5 s TWT on line SO137-31 and at least 7 s TWT on line SO137-33.

The tectonically complicated situation in the Sunda Strait will be discussed very briefly because only a small part of the lines have been processed and interpreted so far. On profiles SO137-21 and –25 (Fig. 2.3.4), which were processed on board, and on line SO137-23 (location see Fig. 2.3.1) we see small sediment basins as well as highs that are at least partially of volcanic origin. On the eastern part of line SO137-25 (Fig. 2.3.4), near to the Krakatau volcanic complex, we observe a 2 s TWT thick cover of mostly disturbed sediments over a faint basement reflection of unknown origin. At the eastern end of the profile about 6 km SE of the Krakatau island Rakata we see a volcanic pipe that causes a distinct magnetic anomaly (upper panel of Fig. 2.3.4). Deep reflections (8-9 s TWT) on line SO137-21 and also on line SO137-25 (in Fig. 2.3.4 at SP 300) may indicate the southern continuation of the Sumatra Fault (Fig. 2.2.6) into the Sunda Strait.

In conclusion it can be said that more than 4000 km of MCS data and 5500 km with gravity, magnetics and hydroacustics provide a sound basis for interpretation and for the planning of the following legs. Also the recordings of the parasound system, not mentioned so far, will be most valuable for geochemical and geological work.

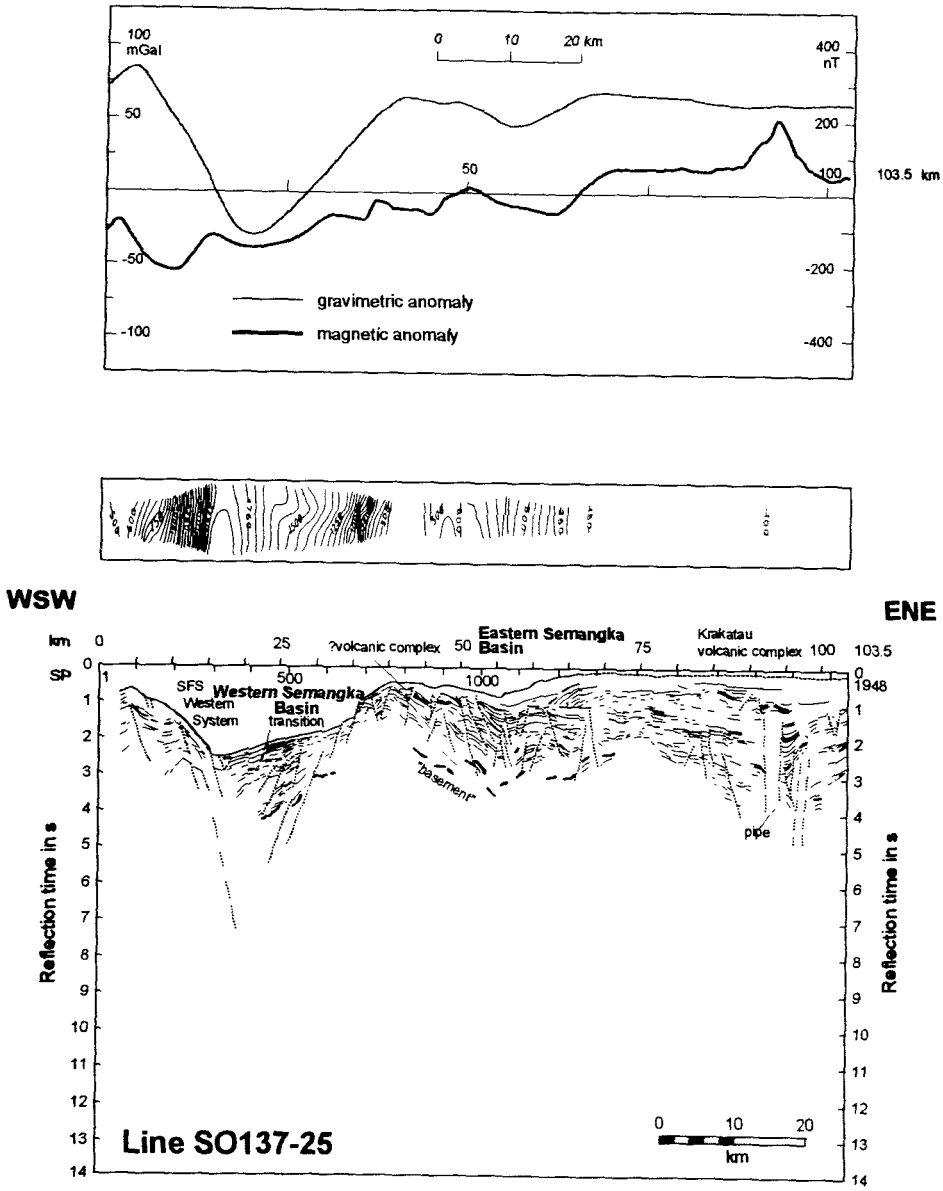

Figure 2.3.4: Seismic linedrawing (lower panel), water depth from Hydrosweep (center panel), and gravimetric and magnetic anomalies (upper panel) for Profile SO137-25 in the Sunda Strait from cruise SO-138 (GINCO I).

3. PARTICIPANTS

3.1. SCIENTISTS

Ernst R. Flüh, GEOMAR, chief scientist
Bernd Schreckenberger, BGR, co-chief scientist
Hans-Otto Bargeloh, BGR
Arnim Berhorst, GEOMAR
Jörg Martin Bialas, GEOMAR
Moh. Nurjaman Dadan, BPPT (29.12.98 - 14.01.99)
Andrea Hampel, GEOMAR
Abdul Haris, UI (29.12.98 - 14.01.99)
Ingo Heyde, BGR
Katrin Huhn, GEOMAR
Stephan Husen, GEOMAR
Leonard Jill, UI (14.01.99 - 27.01.99)
Günter Kallaus, BGR
Kawit, Liaison Officer, DTNI
Heinz-Peter Kewitsch, BGR
Heidrun Lelgemann, GEOMAR
Thomas Leythaeuser, GEOMAR
Carl Jörg Petersen, GEOMAR
Tanja Petersen, GEOMAR
Rahardian, BPPT (14.01.99 - 27.01.99)
Syamsu Rosid, UI (29.12.98 - 14.01.99)
Silke Schenck, GEOMAR
Uwe Schrader, BGR
Joachim Sievers, BGR
Klaus-Peter Steffen, GEOMAR
Supriyanto, UI (14.01.99 - 27.01.99)
Iim Trimanadi, BPPT
Michael Zeibig, BGR

3.2. CREW

Henning Papenhagen	Master
Stefan Bülow	Chief Officer
Wolfgang Becker	1st Officer
Wilfried Osterhues	Radio Officer
Anke Walther	Surgeon
Andreas Martin	Chief Engineer
Werner Guzman	2nd Engineer
Eberhard Bochnik	2nd Engineer
Achim Köhler	Engineer
Burkhard Rehberg	Electrician
Rainer Duthel	Chief Electronic Engineer
Helmut Vöhrs	Electronic Engineer
Volkmar Gebhardt	System Operator
Andreas Klein	System Operator
Rudolf Tscharnke	Fitter
Michael Koch	Motorman
Klaus Teichert	Motorman
Johannes G. Arronet	Motorman
Frank Tiemann	Chief Cook
Adolf Cwienk	2nd Cook
Johann Bronn	Chief Steward
Gerlinde Grübe	Stewardess
Jan Hoppe	2nd Steward
Karl-Heinz Lohmueller	Boatswain
Hans-Jürgen Vor	Able Bodied Seaman
Siegfried Becker	Able Bodied Seaman
Peter Schober	Able Bodied Seaman
Bernd Neitzsch	Able Bodied Seaman
Günther Ventz	Able Bodied Seaman
Herman Röpti	Able Bodied Seaman

3.3. ADDRESSES OF PARTICIPATING INSTITUTIONS

GEOMAR: GEOMAR
Forschungszentrum für
marine Geowissenschaften der
Christian-Albrechts-Universität zu Kiel
Wischhofstraße 1-3
24148 Kiel
Germany
Tel. 0049 - 431 - 600 - 2972
Fax. 0049 - 431 - 600 - 2922
e-mail: nn@geomar.de

BGR: Bundesanstalt für Geowissenschaften und Rohstoffe
Stilleweg 2
Postfach 510153
30631 Hannover
Germany
Tel. 0511/643-0
Fax. 0511/643-3663
e-mail: nn@bgr.de

BPPT: BPP Teknologi
Gedung II BPPT Lt. 19
Jln. MH. THamrin 8
Jakarta Pusat - 10340
INDONESIA
Phone: (62-21) 316 9711
Fax: (62-21) 316 9720
e-mail: nn@bppt.go.id

UI: Dept. of Physics
Faculty of Math and Sciences
University of Indonesia
Depok 16424
INDONESIA
Phone: (62-21) 7270160
Fax: (62-21) 684819
e-mail: ziyan@makara.cso.ui.ac.id

DTNI: Dishidros TNI AL
Jl. Pantai Kuta V No. 1 Ancol Timur
Jakarta Utara
INDONESIA
Phone: (62-21) 684810
Fax: (62-21) 684819
e-mail: infohid@indo.net.id

4. AGENDA OF SONNE CRUISE SO 138

(E. Flueh)

SONNE cruise SO 138 started on 29 December 1998 in Jakarta, Indonesia, and ended on 27 January 1999, again in Jakarta. After equipment had been loaded and installed, SONNE left the pier on 29 December at 16:00 and reached the Sunda Strait on 30 December at 01:30 Continuous recordings of hydroacoustics and gravity started here and ended on leaving the Sunda Strait on 26 January 1999 at 24:00 with hydroacustic profile SO138-175. A complete trackchart of cruise SO 138 is shown in Figure 4.1.

Due to the short port time, most of the instrument preparation had to be performed at sea. The required time was used to complement the hydroacoustic and potential field survey of the previous cruise SO 137 in Sunda Strait. The magnetometer was deployed on 30 December at 04:00, and eight profiles (SO138-101 to 108) were completed by noon on 31 December 1998. After two runs for testing the releasers of the ocean bottom hydrophones (OBH), using the W06 winch to 6000 m, 16 OBH were deployed along line SO138-01 (coincident with the BGR MCS line SO137-12). Five out of 23 releasers did not work properly, and were not available for the cruise after a third unsuccessful test at 5500m. This imposed a slight restriction on the following work.

The deployment of 16 OBH was finished in the evening of 01 January 1999, and shooting along the nearly 200 nm long profile lasted until 12:00 on 03 January1999. The transit between the first resp. last instrument and the start/end of the shooting line was run along parallel courses with the magnetometer deployed (profiles SO138-110 and 111). The OBH recovery took about 24 hours, all but one instrument (OBH06) could be released promptly, sometimes from distances of more than five miles. OBH06 interrogated and transmitted the execute command, but did not rise. Unfortunately, the seismic data recovery was rather poor.

Next, two strike lines were covered with nine instruments at 3 nm spacing each. The shooting of these lines (SO138-02,02Q, and 03) was started in the morning of 05 January 1999. One of the lines was located on the outer arc high, the more landward one in the forearc basin. Structural information from the MCS survey of the previous cruise SO137 was used to locate the profiles in an optimum position. Parts of profile SO138-03 were shot twice, the second time a reduced shot interval of 40 s outside the recording array and 20 s along the recording array was chosen. These additional data should help to avoid aliasing problems when trying to apply imaging techniques. Shooting was terminated in the evening of 06 January 1999, and subsequently all instruments were recovered without delay within 14 hours.

With the magnetometer deployed, a swathmapping survey of the accretionary front around profile SO138-01 was started on 07 January 1999 and lasted until 10 January 1999 in the morning. During this period, three attempts were made to dredge the non-recovered OBH06. Since the instrument responded, we could determine its position to within 40 m. We had noticed that all instruments recovered were picked up at a noticeble distance of up to 0.5 nm from their deployment position, which indicated that the currents reached to great depth. After the first dredging attempt had failed, we attached another release unit to one of the two dragons, in order to determine the position of the dragon relative to the instrument. Much to our surprise, it had also drifted quite noticably, and thus was far from the instrument. Therefore another attempt was made on 09 January 1999, this time both dragons were equipped with an acoustic release for navigational purposes. After some careful manouvering, we had placed the two dragons, separated by 750 m to the south of OBH06, and we were very optimistic about a successful dredge haul. A total 7500 m of wire were deployed, and when trying to pull the dragons, the force on the wire increased slightly to about 7 kN, without any apparent motion of the dragons. Unfortunately, the wire broke close to the ship while trying to stretch the wire. Although equipped with their own buoyancy, both release units could not be recovered and were also declared lost. No further attempt was made to recover the lost instruments or the wire. The swathmapping survey was subsequently continued and included the transit along the trench axis to the next working area of Sunda Strait.

Between 14:30 on 10 January and 04:00 on 11 January 1999, sixteen instruments (OBH35 to 50), including the vertical array, the OBS and a newly designed light weight OBS were deployed along SO138-04. Shooting started close to Krakatau volcanoe in the morning of the same day and took until the evening of 12 January 1999. Line SO138-04 was chosen

coincident with MCS line SO137-42 of the previous cruise. All instruments had been recovered without any delay in the evening of 13.01.1999. Several profiles were run in Sunda Strait to increase the coverage for swathmapping, gravity and magnetics until the morning of 14 January, when three Indonesian scientists were exchanged at Cigading port. During the transit to the next seismic profile, a safety drill of the life boats was made. Later that day, problems were encountered with the magnetometer cable, the magnetometer was not deployed for most of the transit.

A deployment of 16 instruments along profile SO138-05 started on 15.01.1999 at midday. Along this profile, shooting was again performed at a speed of 5.5 kn with a shot interval of 60 s and terminated on 17 January 1999 at 11:30. All instruments were safely recovered within 24 hours. This profile was chosen coincident with MCS line SO137-03, but was extended seaward by some distance. Problems encountered with the shipboard power supply made most of the streamer recordings useless.

Immediately after recovery of the instruments from profile SO138-05, ten OBH were deployed along a strike line close to the coast of Java (Profile SO138-06). Between the deployments, a test of a deep towed streamer was made using the W6 winch. The streamer with its recording unit was put out to 2500 m cable length, a pinger attached to the depressor indicated a depth of 300 m above ground (2500 water depth). A single airgun was used as source. A later analysis of the data showed that towing the streamer created considerable noise and that even the direct arrivals were difficult to see

Shooting along the 75 nm long line (So138-06) lasted from 03:00 to 17:00 19.01.1999, with increasing winds and swell, which continued to the end of the cruise. Due to a nearby fishing vessel, the magnetometer and the portside airgun array had to be pulled in for a short while during the profile. For the first time during this cruise, a 400 m long vertical array was deployed (OBH78). All instruments were routinely recovered by 05:00 the next morning.

After a short transit with the magnetometer deployed another strike line was occupied with 12 instruments, again including the 400 m long vertical array. Shooting along this line (SO138-07) was made with the usual parameters and finished on 21.01.1999 at 13:00. All instruments were subsequently recovered within 9 hours.

The transit back to the Sunda Strait was used for additional swathmapping and magnetic profiles along the trench axis, and was interrupted for four hours in the morning of 22.01.1999 for a CTD measurement to 3900 m. Heavy winds and swell forced SONNE to slow down to less than 9 knots, and the plan to get a complete hydrosweep coverage of the trench and deformation front was given up to gain time for the seismic work program. A gap of 20 miles of the trench axis remains unsurveyed.

A total of 16 instruments, including an 800 m long vertical array, were deployed along profile SO138-08 running exactly north-south into Sunda Strait, where we encountered calm waters again. No fishing activity was apparent, therefore shooting along this profile could be started close to the island of Pulau Tabuan in Semanka Bay. The usual shooting parameters were used, and shooting was terminated on 24.01.1999 at 08:20. The magnetometer remained deployed on the transit back to the first instrument of this profile to be recovered. The recovery was finished by midnight on 24.01.1999, except for the 800 m long vertical array, which we intended to recover in daylight.

The seismic program was terminated with a short profile to test a small volume airgun array for high resolution work. For this test a short profile (SO138-09) was covered with six ocean bottom recorders. Shooting with one BGR airgun array into the recorders and the streamer was performed in the morning of 25 January 1999. The profile was then shot in reverse direction using both the BGR and the GEOMAR high resolution array in alternating mode. The instruments were all recovered on the same evening, finishing off the seismic work of SO138 with a total of 111 ObH positions covered and more than 11.000 airgun shots fired along 1864 km. The vertical array (OBH100) from profile SO138-08 was released in the early afternoon of 25 January 1999. It was sighted soon afterwards and the normal recovery procedure started. After about 200 m of cable including the head buoy with the recording package were onboard, the cable suddenly broke, just when the first additional floatation reached the surface. Although the nominal strength of the cable is about one ton, apparently

the sudden downward force of the buoyancy due to the heavy swell caused the cable to break. The cable sank back to the seafloor, including the releaser and the two hydrophones with their amplifier boxes, as well as the cable and the floats.

During the night of 25/26 January, additional magnetic observations were made along selected profiles in Sunda Strait to complete the coverage. On 26 January 1999 at 04:20 the magnetometer had to be retrieved for storage so that the magnetic measurements of the cruise ended. An attempt was made to dredge the vertical array at OBH100 in the morning of 26 January. The releaser could be located to within 50 m on the seafloor by acoustic ranging (minimum range 1713 m), Altogether 4100 m of cable were lowered to the seafloor at 1720 m depth in a circle around the instrument. Sonne sailed another 180° around the suspected instrument position and when hieving the cable it soon became apparent that the instrument was moving and had got tangled in the cable. Despite of gail winds, it was safely recovered at noon, with all components intact.

The remaining hours before depature were used to fill some gaps in the hydrosweep coverage in Sunda Strait, before SONNE headed for Jakarta on 26 January 1999 at 24:00. She arrived at the pilot station of Jakarta at 08:00 and docking at the pier at 08:50 the cruise ended after 4680 miles and 28 days at sea.

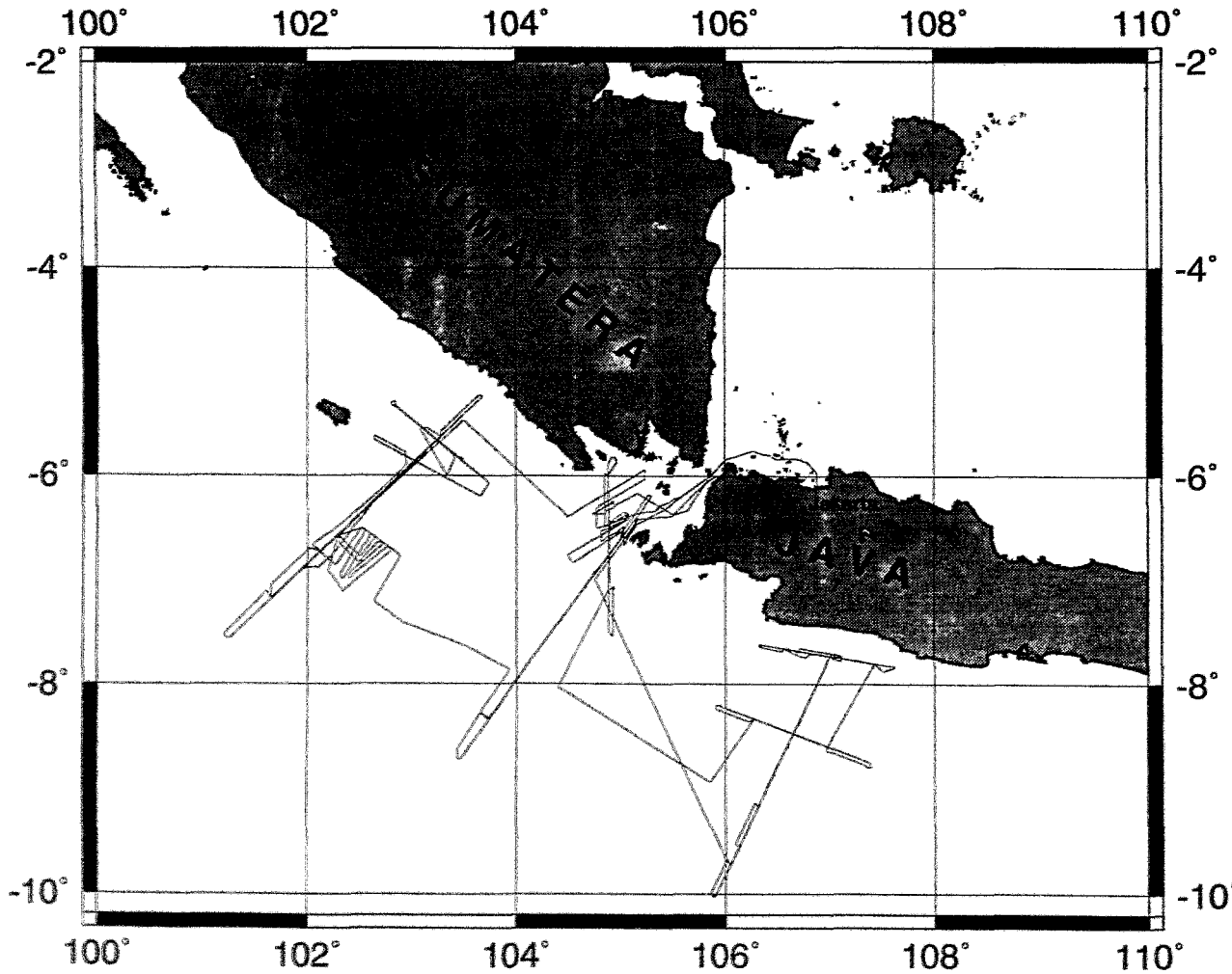

Figure 4.1: Track chart of SO 138-GINCO II.

5. SCIENTIFIC EQUIPMENT

5.1 COMPUTER FACILITIES

5.1.1 THE GEOMAR COMPUTER NETWORK

(J. Bialas)

Both BGR and GEOMAR set up various computer systems aboard RV SONNE. Due to the heavy load of data transmission via the computer network GEOMAR set up its own LAN in the „Wet Chemistry Lab" (WCL). This network connects workstations from Sun Microsystems, 1 X-screen and one MS-Windows based PC. A Macintosh and a second X-screen were set up in the Hydrosweep lab as well as another Macintosh in the „Dry Chemistry Lab". All computers were directly connected to a 12 port ethernet switching hub (3COM-SuperstackII 1000) with dedicated 10 Mbps ports. The fast link of this switch (100 Mbps) was connected to the workstation "Moho". This Sun operated as a NIS server and provided general home accounts doubled from GEOMAR enabling every user to find his/her familiar user interface. With a second network interface Moho served as router to the shipboard network. Therefore the shipboard network could be kept undisturbed from heavy network load during data playback and copying operations. A detailed list of the GEOMAR computer equipment is given in Table 5.1.1. For plotting and printing, two HP Postscript Laserprinters (papersize A4 and A3) were included into the local network.

Two of the workstations (Galicia, Laurentia) were equipped with the older SunOs-4.x operating system required to run the GEOSYS seismic processing system. All other Sun workstations were operated under the Solaris operating system. Software packages such as GMT, Seismic Unix (SU), MB System (Hydrosweep processing) as well as custom designed software for refraction seismic data processing and interpretation were installed on all stations. Data playback of the Methusalem DAT data cassettes (see 5.2.2) was performed at the Galicia workstation. A spare playback unit was available with the Laurentia workstation. Several DAT and Exabyte drives were available for data backup purposes. A Pentium II PC (Mbs) was equipped with three PCMCIA slots which were used for playback of the PC Flashcards used with the new MBS seismic recorders (see 5.2.2). It should be noted that the three PCMCIA slots could only be operated under MS-Windows 95-b version simultanuously. 2-D raytracing and word processing was performed on two additional PowerMacintosh computers.

Name	Operating system	Processor	Disk space	External drives
Moho (Neolithikum)	Solaris	Sparc 20	16 GB	1 DAT 1 Exabyte
Devonia	Solaris	Sparc Ultra	105 GB	2*DAT 2*Exabyte
Avalonia	Solaris	Sparc 5	8 GB	1 Playback 1 DAT
Laurentia	SunOs 4.x	Lx	8 GB	
Galicia	SunOs 4.x	Sparc 10	6 GB	1 DAT 1 Exabyte
Mbs	MS-Win 95-b	Pentium II	4 GB	3 PCMCIA 1 Zip
2 X Screen				
Eastonia	MacOs 7.5.5	PCI 8200	1 GB	1 Zip
Quepos	MacOs 7.5.5	PCI 7200	500 MB	

Table 5.1.1: List of computers connected in the GEOMAR LAN aboard R/V SONNE

5.1.2 COMPUTER SYSTEMS FOR NAVIGATION, GRAVITY, AND MAGNETICS

(B. Schreckenberger, H.-O. Bargeloh)

The BGR's marine gravity/magnetics group operates two DIGITAL AlphaServer computers that run under the operating system OpenVMS 7.1. On board of R/V SONNE they are connected with the ship's computers and terminal servers via thinwire or twisted pair Ethernet. One of the computers is used for data acquisition from the network and from terminal servers and for realtime data display. Data processing and interpretation is done on the other Alpha Server. It would be possible to do everything with only one computer but the second server is kept running also as a spare system in case of a failure of the data acquisition server.

The following list contains the hardware used for data acquisition and data processing:

- Workstation for data acquisition: AlphaServer 1000A 5/333, 128 MB memory, 2 GB and 4 GB hard disks, magneto optical drive, DAT tape drive, CD-ROM drive, floppy disk drive. Operating system OpenVMS 7.1.
- Workstation for data processing and interpretation: AlphaServer 1000A 5/333, 256 MB memory, 2 GB and 2x4 GB hard disks, magneto optical drive, DAT tape drive, CD-ROM drive, floppy disk drive. Operating system OpenVMS 7.1.
- 2 Terminal servers Digital DECserver 700
- 3 PC systems (Windows NT)
- 2 Plotters (1 DIN A0 Inkjet plotter HP Draftmaster 750C, 1 ink-jet printer/plotter DEC LJ250)
- 3 printers (1 laser printer DEClaser 3500, 1 dot-matrix printer Fujitsu DL-2400, 1 dot-matrix-printer DEC LA50)
- 2 graphic terminals, 1 alphanumeric terminal
- 1 precision digitizer Kontron Summagraphics (DIN A1)
- 1 Scanner Hewlett-Packard ScanJet 4c
- 1 GPS controlled clock Meinberg GPS 166
- 1 uninterruptable power supply Victron NetPro 1500

All computers were integrated into the LAN of the ship.

Equipment of the ship used during the survey

The list contains only the most important systems:

- 2 GPS receivers Ashtec LD-XII
- 1 GPS receiver Trimble 4000 DS
- 1 DGPS system Racal Skyfix incl. MultiFix 2 software
- 1 interface processor belonging to the ANP2000 navigation system
- 1 general purpose minicomputer MicroVax 3100 ('WISVAX')
- 3 Digital terminal servers
- 1 plotter Graphtec MP 4300 (DIN A3)
- 1 ink-jet plotter Hewlett-Packard DesignJet 650C
- 1 precision digitizer Kontron Summagraphics (DIN A0)
- Alphanumeric terminals

- PC systems (text processing and graphic data processing)

Data acquisition

All data are read into the computer via serial interfaces or over the Ethernet network. There is a number of real time programs that write the data into the memory as soon as they are available. The main data acquisition program checks, reformats, and collects the data items to one data set each 20 seconds and writes it to direct access files on magnetic disk.

The navigation data come via the ship's WISVAX computer over an Ethernet link once per second. On this cruise the following data were received from the ship's navigation system:

- position, speed and course from GPS
- heading from the gyro
- speed from the doppler-sonar (DO-Log)
- water depth values from HYDROSWEEP (the central beam only) and PARASOUND
- weather data, water temperature, and salinity.

The following data are read over serial lines:

- precise time marks (UTC) from a GPS controlled clock once per second
- shot point numbers and shot point times from the seismic system
- magnetic total intensity for both sensors from the gradient magnetometer
- heading of the magnetometer array from the compass between the sensors
- raw gravity values, Eötvös corrected gravity and free air gravity from the marine gravimeter

The data acquisition program provides online navigation data for the following systems:

- once per second to the marine gravity meter where they are used to support the gyro system
- for every shotpoint to the seismic system

Analog recordings are produced for the magnetic total intensity, the gradient, and the raw gravity. Moreover, we use a small navigation program (Roeser et al., 1992) for plotting the planned profile lines and a continuous online track plot on a DIN A3 plotter.

5.2 SEISMIC DATA AQUISITION
5.2.1 MINI STREAMER
(J. Bialas)

During the cruise, all shots were also recorded by a short streamer. It is a three channel unit originally built by Prakla-Seismos, Hannover, Germany for the Deutsches Hydrographisches Institut (German Institute of Hydrography) in 1979. The system comprises three parts, a 50 m long active length, a 50 m long stretch length and a 150 m long towing cable. The active length is separated into three groups of 16 HHOC type hydrophones. The construction of the first and third group are identical while the middle one has a smaller hydrophone separation. Within group one and three the hydrophones are 1.2 m apart building a 18 m long unit. This selection results in an antenna directivity which is sensitive to high frequency wavefronts impinging from the near vertical. The -3 dB point is found to be at 48 Hz for wavefronts traveling at 90° (measured from the vertical), 66 Hz / 30°, 190 Hz / 11.5° and 380 Hz / 5.7°. The central group is only 6 m long with 16 hydrophones each 0.4 m apart. The -3 dB point is found at 110 Hz / 90°, 220 Hz / 30 °, 550 Hz / 11.5° and 1.1 kHz / 5.7°. Adding up all three groups, the total directivity is (-3 dB) 18 Hz / 90°, 36 Hz / 30°, 90 Hz / 11.5°, 180 Hz / 5.7°. At the tail, a depth sensor is installed which indicates the actual depth modulated as frequency changes. With a base frequency of 990 Hz at the surface it increases by 100 Hz per bar (100 Hz per 10 m). As there is only one depth sensor at the tail, a pressure pipe was attached to the towing length during deployment for profile 05 in order to messure the water depth at the stretch length connection. Unfortunately, the switchboard of the winch broke after half the streamer had been deployed. It therefore did not reach normal towing depth. At this time the tail was measured at 1 – 2 m depth while the stretch length was at 4 m depth. Although this was not the ordinary measuring configuration it can be assumed that the active length will be almost horizontal during profiling. The whole unit is stored and operated from a hydraulic winch at the stern of RV SONNE, between the two airgun arrays (see 5.3).

For data recording, one of the four channel MBS recording units (see 5.2.2) was used. The streamer signals were sampled with a 250 Hz interval resulting in a Nyquist frequency of 125 Hz, which is well above the expected maximum energy of 100 Hz. Playback was done using 32 bit data samples to keep the possible dynamic range during all routine processes.

Based on experiences from cruise SO-131 SINUS (Flueh and Reichert), it was decided to add only a small weight (10 kg) 60 m in front of the stretch length, well separated from the hydrophones, resulting in a towing depth of 16 m. In order to suppress the wave state induced low frequency noise (up to 5 Hz), the input impedance of the channel separator was set to adjust the -3 dB point at 15 Hz. Further, a set of three Low Noise 20 preamplifiers were prepared in a shielded housing to adjust the streamer signals for the MBS analogue input range. Due to the calm sea states the low frequency influence on the streamer was very small and enabled undisturbed recordings on channels 2 and 3. Channel 1 was much noisier during all of the lines. A reason for this could not be detected during the cruise. The streamer provided useful information during the cruise and added reflection information for those parts of the lines which had not been covered on the first leg of GINCO by BGR reflection seismic acquisition (Reichert and shipboard party, in prep.). The sedimentary structure was well imaged. These data are essential for detailed interpretation of the wide-angle data and helped to determine near vertical reflection times on the refraction seismic sections during onboard seismic modelling.

5.2.2 THE GEOMAR OCEAN BOTTOM HYDROPHONE (OBH)

(E. Flueh and J. Bialas)

The Instrument

The first GEOMAR Ocean Bottom Hydrophone was built in 1991 and tested at sea in January 1992. A total of 18 OBH instruments were available for SO138. This type of instrument has proved to have a high reliability; in fact more than 800 successful deployments have been made.

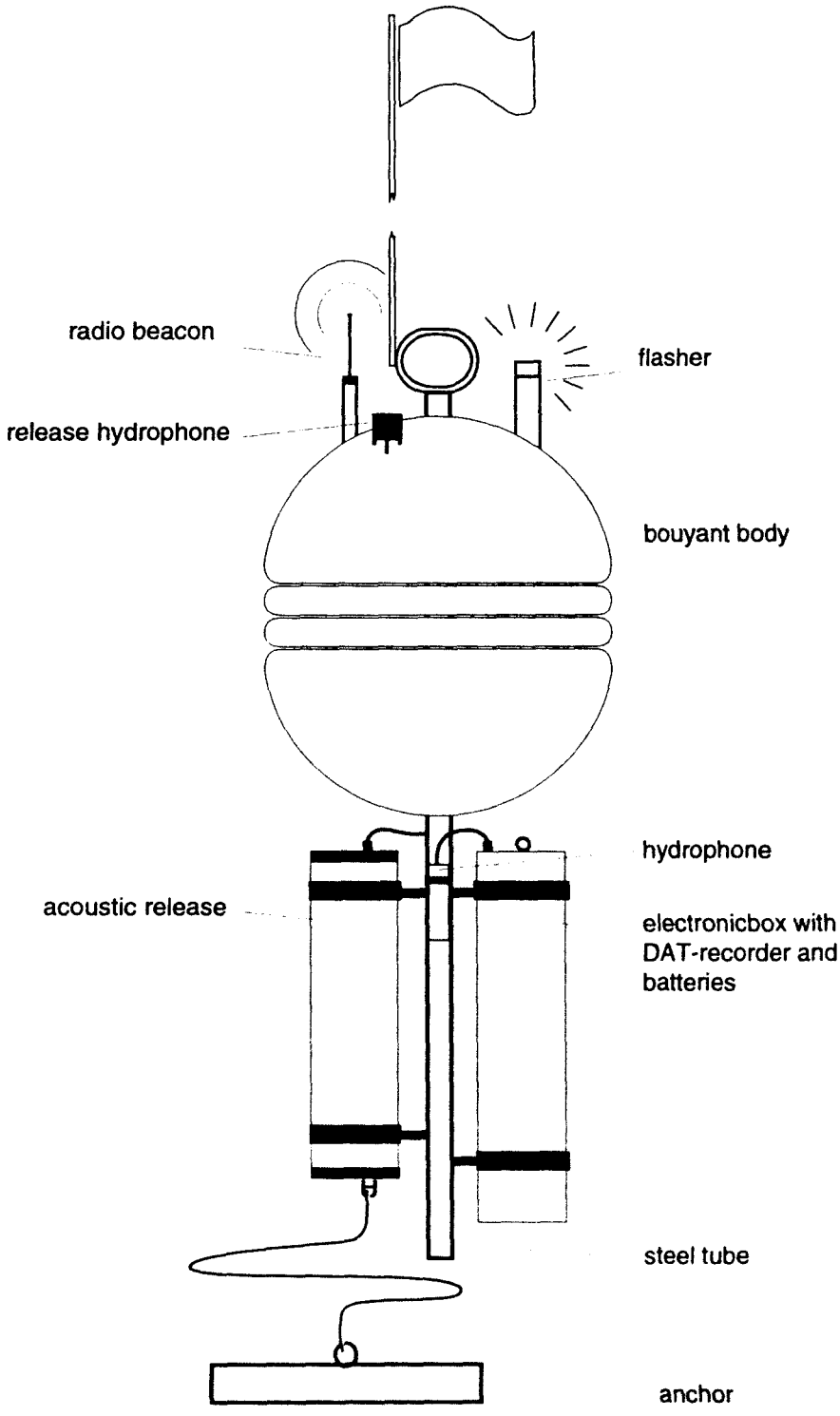

Figure 5.2.2.1: Principle design of the GEOMAR OBH

A total of 111 sites were occupied during the GINCO cruise.

The principle design of the instrument is shown in Figure 5.2.2.1, and a photograph showing the instrument upon recovery can be seen in Figure 5.2.2.2. The design is described in detail by Flueh and Bialas (1996).

The system components are mounted on a steel pipe which holds the buoyancy body on its top. The buoyancy is made of syntactic foam and is rated, as are all other components of the system, for a waterdepth of 6000 m, except for the pressure cylinders holding the recording electronics. Here, various models for variable depths (2500 m, 3000 m, and 6000 m) are available. Attached to the buoyant body are a radio beacon, a flash light, a flag and a swimming line for retrieving from aboard the vessel. The hydrophone for the acoustic release is also mounted here. The release transponder is a model *RT661CE* made by *MORS Technology*. Communication with the instrument is possible through the ship's transducer system, and even at maximum speed and ranges of 4 to 5 miles release and range commands are successful. For anchors, we use pieces of railway tracks weighing about 40 kg each. The anchors are suspended 2 to 3 m below the instrument. The sensor is an *E-2PD* hydrophone from *OAS Inc.*, and the recording device is a *Methusalem* recorder of *DELTA t*, which is contained in its own pressure tube and mounted below the buoyant body opposite the release transponder (see Figure 5.2.2.1). *Two alternate hydrophones were also tested during this cruise (see chapter 6.3.4.3).* The *Methusalem* consists of a preamplifier (26 dB), a highpass and antialias filter, a 13 bit A/D converter and a core memory of 0.768 MB. Signals are sampled at 800 Hz, and after FIR-decimation filtering, a resolution of 14 to 15 bits is achieved. Data are stored as 16 bit integers on a DAT cassette, which is run in audio-mode to save power consumption and which can store about 1.1 GB of data. The power supply is from alkaline batteries for long term deployments or from rechargeble lead batteries for short term deployments (up to 3.5 days). The instrument can be programmed before deployment through an RS232 interface. Up to 4 channels with different amplifications and sampling rates can be recorded. A DTCXO (0.05 ppm accuracy) is checked against GPS time before and after deployment. The DAT cassettes are read from a playback system, which simulates a SCSI interface, to a workstation for data reduction and analysis (see Chapter 6.3.2).

Marine Broadband Seismic Recorder (MBS)

Apart from the older DAT recording units a new generation of digital seismic recorders was used. The so-called *Marine Broadband Seismic recorder (MBS)*, manufactured by *SEND GmbH*, was developed based upon experience with the DAT based recording unit Methusalem (Flueh and Bialas, 1996) over the last years. This new recorder avoids mechanically driven recording media, and the PCMCIA technology enables static flash memory cards to be used as unpowered storage media. Read/write errors due to failure in tape handling operations should not occur any more. In addition, a data compression algorithm is implemented to increase the data capacity. Redesign of the electronic layout enables a decreased power consumption (1.5 W) of about 25% compared to the *Methusalem* system. Depending on the sampling rate data output could be in 16 to 18 bit signed data. Based on digital decimation filtering the system was developed to serve a variety of seismic recording requirements. Therefore, the bandwidth reaches from 0.1 Hz for seismological observations to the 50 Hz range for refraction seismic experiments and up to 10 kHz for high resolution seismic surveys. The basic system is adapted to the required frequency range by setting up the appropriate analog front module. Alternatively, 1, 2, 3 or 4 analogue input channels may be processed. Operational handling of the recording unit is similar to the *Methusalem* system or by loading a file via command or automatically after power-on. The time base is based on a DTCXO with a 0.05 ppm accuracy over temperature. Setting and synchronizing the time as well as monitoring the drift is carried out automatically by synchronization signals (DCF77 format) from a GPS-based coded time signal generator. Clock synchronization and drift are checked after recovery and compared with the original GPS units. After software preamplification the signals are low-pass filtered using a 5-pole Bessel filter with a -3 dB corner frequency of 10 kHz. Then each channel is digitised using a sigma-delta A/D converter at a resolution of 22 bits producing

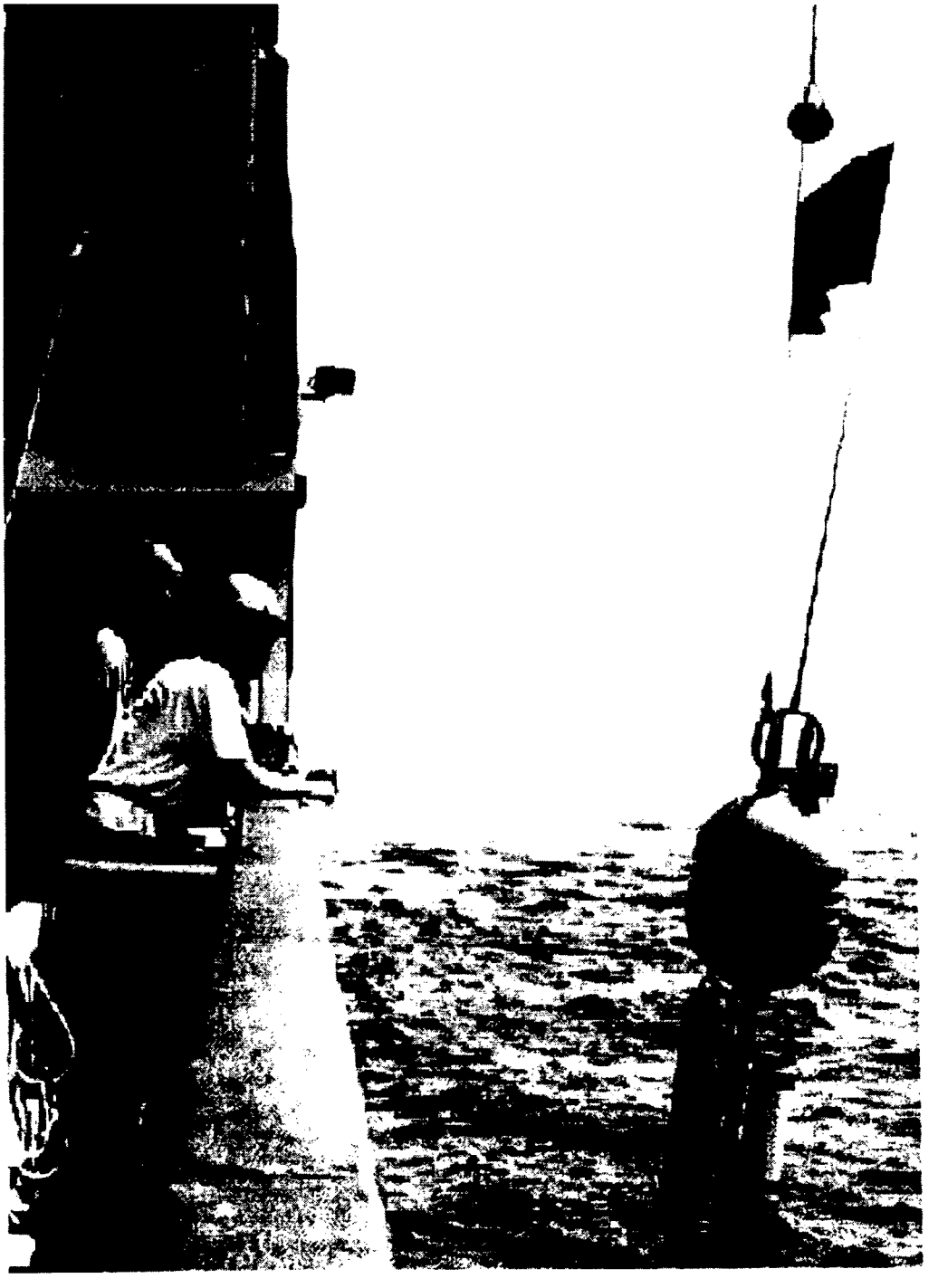

Figure 5.2.2.2: The GEOMAR OBH upon recovery.

32-bit signed digital data. After delta modulation and Huffman coding the samples are saved on PCMCIA storage cards together with timing information. Up to 4 storage cards may be used. Currently, up to 400 MB per card are available. Data compression allows more than 2 GB data capacity. After recording the flashcards need to be copied to a PC workstation. During this transcription the data are decompressed and data files from a maximum of four flash memory cards (up to 400 Mbyte each) are combined into one data set and formatted according to the PASSCAL data scheme used by the *Methusalem* system. This enables full compatibility with the established processing system. While the *Methusalem* system did provide 16 bit integer data, the 18 bit data resolution of the *MBS* can be fully utilized using a 32 bit data format.

Data Processing

The OBH data recorded on the *Methusalem* and the *MBS* have to be converted into standard SEG-Y format for further processing. The necessary program structure was mainly taken from the existing REFTEK routines and modified for the OBH requirements and GEOMAR´s hardware platforms. Because the GEOMAR OBH works in a continuous mode, most of the modifications on the existing program package had to be done in the program parts handling continuous data streams.

A flow chart shown in Figure 5.2.2.3 illustrates the processing scheme applied to the raw data. A detailed description of the main programs follows below:

• mbs2pass

For the PC-cards used with the MBS recorder data expansion and format conversion into PASSCAL data format is performed with DOS based PC. The program mbs2pass reads the data from the set of up to four flashcards used during recording. Decompressed data are written onto the PC´s hard disk using the PASSCAL data format, either 16 or 32 bit storage is available. This enables compatibility with the DAT recordings (s.b.). After ftp transmission to a sun workstation ref2segy and all other software can be used to handle and process the data files and store them as SEG-Y traces.

• ref2segy

Downloading the raw data from DAT tape on a hard disk of a SUN workstation is done by the program ref2segy. It will produce a pseudo SEG-Y trace consisting of one header and a continous data trace containing all samples. For each channel (different amplifications) one file will be created. The name of this file contains the start time, the serial number of the *Methusalem* and the channel number. In addition a log and an error file will track the download process. In a second mode PASSCAL disk files written by *mbs2pass* in either 16 or 32 bit format can be read in and included into the standard processing scheme. The file size of the data is directly related to the recording time. For example, a recording time of one hour sampled with 200 Hz will produce a file size of 1.44 MB per channel. A record with two channels and a recording time of two days will get a total data volume of 70 MB.

• merge

If a tape error has occurred during the download process, the ref2segy program has to be restarted. This will lead to several data files with different starting times. Merging these files into a single file is done by the merge program. The gap between the last sample and the first sample of the consecutive data trace will be filled up with zeros. Overlapping parts will be cut out.

• segy2trig

The trigger signal, which is provided by the airgun control system, is recorded simultaneously on an additional *Methusalem* during the shooting period. This tape is treated as a regular data tape and downloaded to the hard disk via the ref2segy program. The segy2trig program detects the shot times in the data stream. It determines the shot times by detecting the trigger signal through a given slope steepness, duration and threshold of the trigger pulse. The output is an ASCII table consisting of the shot number and the shot time. The accuracy of the shot time is one

of the most crucial matters in seismic wide-angle work. It has to be reproduced with a precision of 5 ms. Due to this demand the shot times have to be corrected with the shift of the internal recorder clock. As additional information the trigger file contains the profile number and the start/end time of the profile and the trigger recording. The shot times are part of the UKOOA file which links the coordinates of the source and the hydrophones with the shot times.

• **ukooa**
The ukooa program is used to establish the geometric data base. It requires the trigger file containing the shot times, the ship's navigation and the position of each OBH for input. The ship's navigation is stored in a database about every two seconds (see Chapter 5.4.3). The program calculates the coordinates of each shot and creates a file in the UKOOA-P84/1 format as output. This file will be used when creating a SEG-Y section via the dat2segy program. During the cruise, the BGR system provided shot tables which already connected shot time, DGPS position and water depth. The ukooa program was therefore used to transform this table into UKOOA-P84/1 format.

• **dat2segy**
The dat2segy program produces standard SEG-Y records either in a 16 or 32 bit integer format by cutting the single SEG-Y trace (from the merged ref2segy file) into traces with a certain time length. It reads both the ukooa file with the geometry informations and the downloaded raw data as produced with the ref2segy program. In addition, the user can use several parameters for controlling the output. These parameters are information about the profile and the receiver station, number of shots to be used, trace length, time offset of the trace and reduction velocity (to determine the time of the first sample within a record (see Chapter 6.3.2)). Also the clock drift of the recorder is taken into account and corrected for. The final SEG-Y format consists of the file header followed by the traces. Each trace is built up by a trace header followed by the data samples. The output of the dat2segy program can be used as input for further processing with GEOSYS or Seismic Unix (SU).

Apart from these main programs for the regular processing sometimes additional features are needed for special handling of the raw data:

• **divide**
The program divide cuts the raw data stream in traces with a given length without offset and time informations. The output is stored as SEG-Y format. The routine is useful for a quick scan at the raw data or if a timing error has occured.

• **segyhdr**
The routine segyhdr prints all the header values of the raw data on the screen.

• **segyshift**
The program segyshift modifies the time of the first sample, which means that the whole raw data trace can be shifted by a given value. This is very useful when shifting the time base from Middle European Time to Greenwich Mean Time or any local time. Because of recording problems, the data sometimes show a constant time shift, which can be corrected as well with segyshift.

• **castout**
The program castout allows you to cut out a specified time window from the raw data stream. When the shooting window is much smaller than the recording time, one can reduce the data volume by cutting out only the useful information. This will reduce the demand on diskspace.

• **relobs**
Due to a drift of the OBH during deployment and errors of the ship's GPS-navigation system the OBH positioning may have a mislocation of up to several 100 m. As this error leads to an asymmetry and wrong traveltime information in the record section it has to be corrected, which is done with the program relobs.

As input the assumed OBH location, snot locations and the picked traveltimes of the direct wave near to its apex are needed. By shifting the OBH position relobs minimizes the deviation between computed and real traveltimes using a least mean square fitting algorithm assuming a constant water velocity.

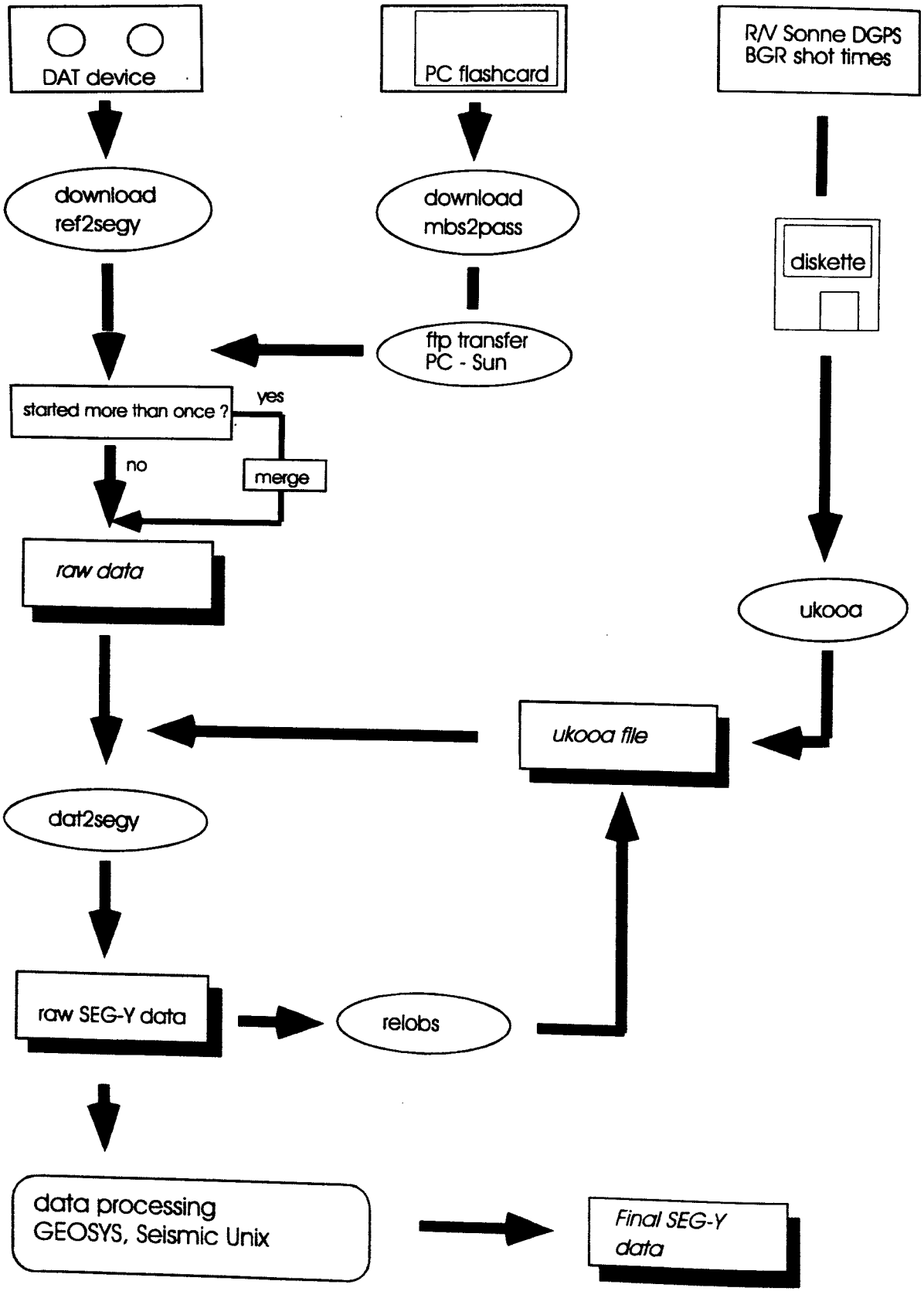

Figure 5.2.2.3:processing flow from raw data to SEG-Y records.

5.2.3 THE GEOMAR OCEAN BOTTOM SEISMOMETER

(J. Bialas, K. P. Steffen and E. Flueh)

The Ocean Bottom Seismometer (OBS) construction (Fig. 5.2.3.1) is based on experience with the GEOMAR OBH. It was built by *GTG*, Kiel, Germany. For system compatibility, acoustic release, pressure tubes, and hydrophone are identical to those used for the OBH. Syntactic foam was again used as floatation, but of larger diameter due to the increased payload. In contrast to the OBH, the OBS has three legs around its center post to which the anchor weight is attached. While the OBH floats about 1 m above the sea bottom, the OBS touches the sea bottom to avoid collision of the the seismometer cable with the anchor. The sensitive seismometer is deployed about 1 m to the side of the system once the sea floor is touched. During diving of the system the footplate of the seismometer release lever is about one meter below the base of the anchor and will therefore hit the seafloor first. During touchdown the baseplate forces an upward movement of the lever which will lay out the seismometer hook until the seismometer anchor is about 0.5 m above the seafloor. At about 45 degrees to the vertical the seismometer is released from its hook and falls to the sea floor from about 1 m height. This should ensure coupling of the seismometer to the sea floor. At this time the only connection from the seismometer to the instrument is a cable and an attached wire which will take the pull load while rising to the sea surface later. Thus, mechanical transmission of movements or currents on the instrument to the seismometer is ruled out. All three channels are preamplified within the seismometer housing and recorded by the standard *MBS* recorder as used in the OBH units. Parallel to these three channels the standard hydrophone is recorded on the fourth channel.

During this cruise a new OBS with a different anchor design (OBS-light) was tested (Fig. 5.2.3.2). For this unit a standard OBH frame was equipped with two additional traverses which were clamped to the center post. One of the standard railway track anchors was equipped with a rectangular shape metal plate providing a fixing for the two traverses. This way, the OBS will touch the sea floor with the fixed anchor. A 1.5 m long lever is attached to the lower end of the center post and kept at about 30° angle to the horizontal by the anchor. The 3 component seismometer hangs from the end of this lever on a wire long enough to enable touchdown to the seafloor. As with the three leg version (s.a.) the only connection between seismometer and instrument is the electric cable. After release of the anchor the lever turns down into the vertical and ensures that the seismometer can not be damaged during recovery operations from the vessel. First recordings showed good results on the standard hydrophone as well as the 3 component seismomete. High noise levels on the 3 components might be caused by cable loops lying on top of the housing. Further improvement of the cable fixing should avoid this. Once further succesful dives are achieved, this construction might be an easy way to transform standard OBH units into lightweight OBS.

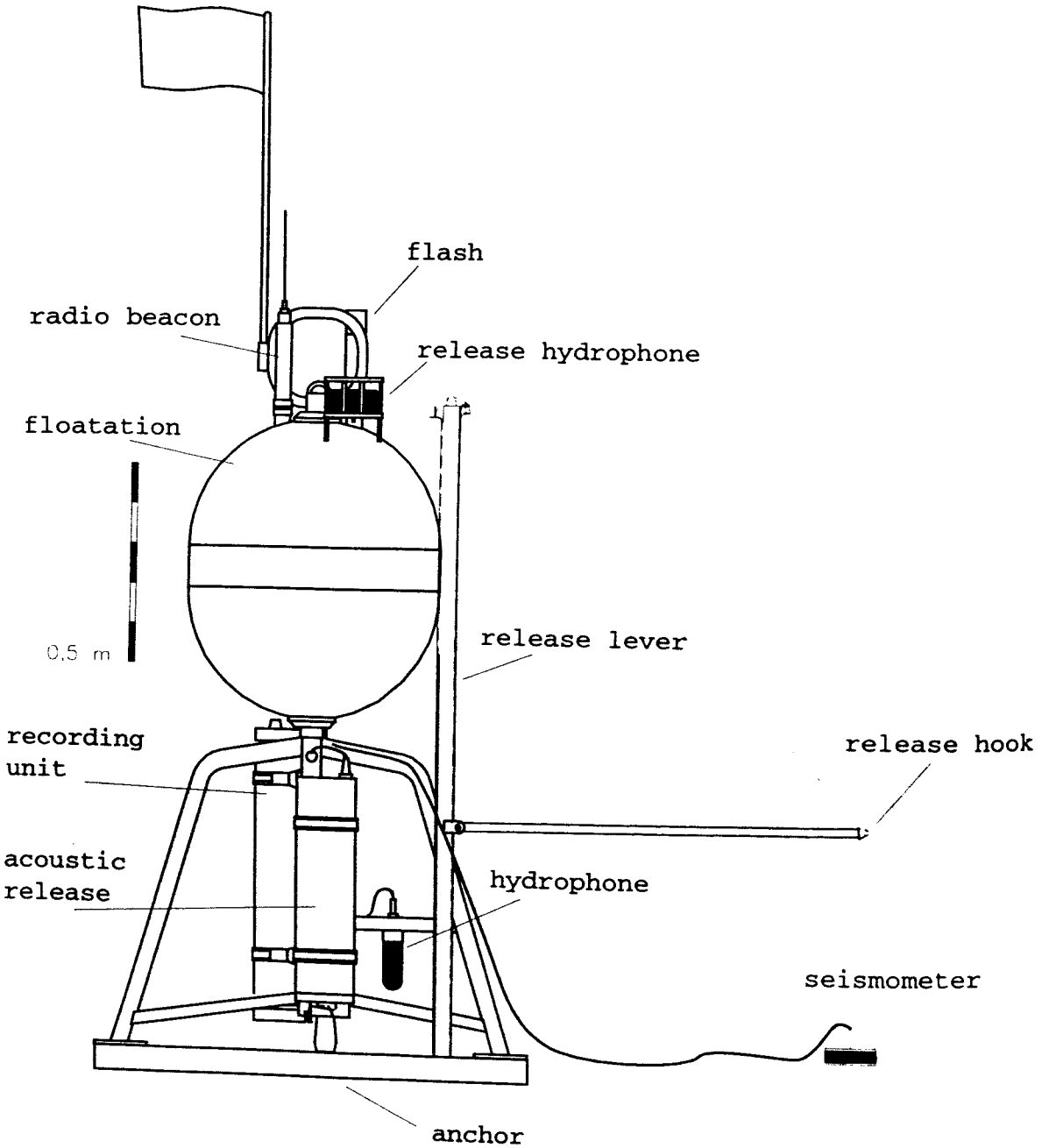

Figure 5.2.3.1: Design of the GEOMAR Ocean Bottom Seismometer.

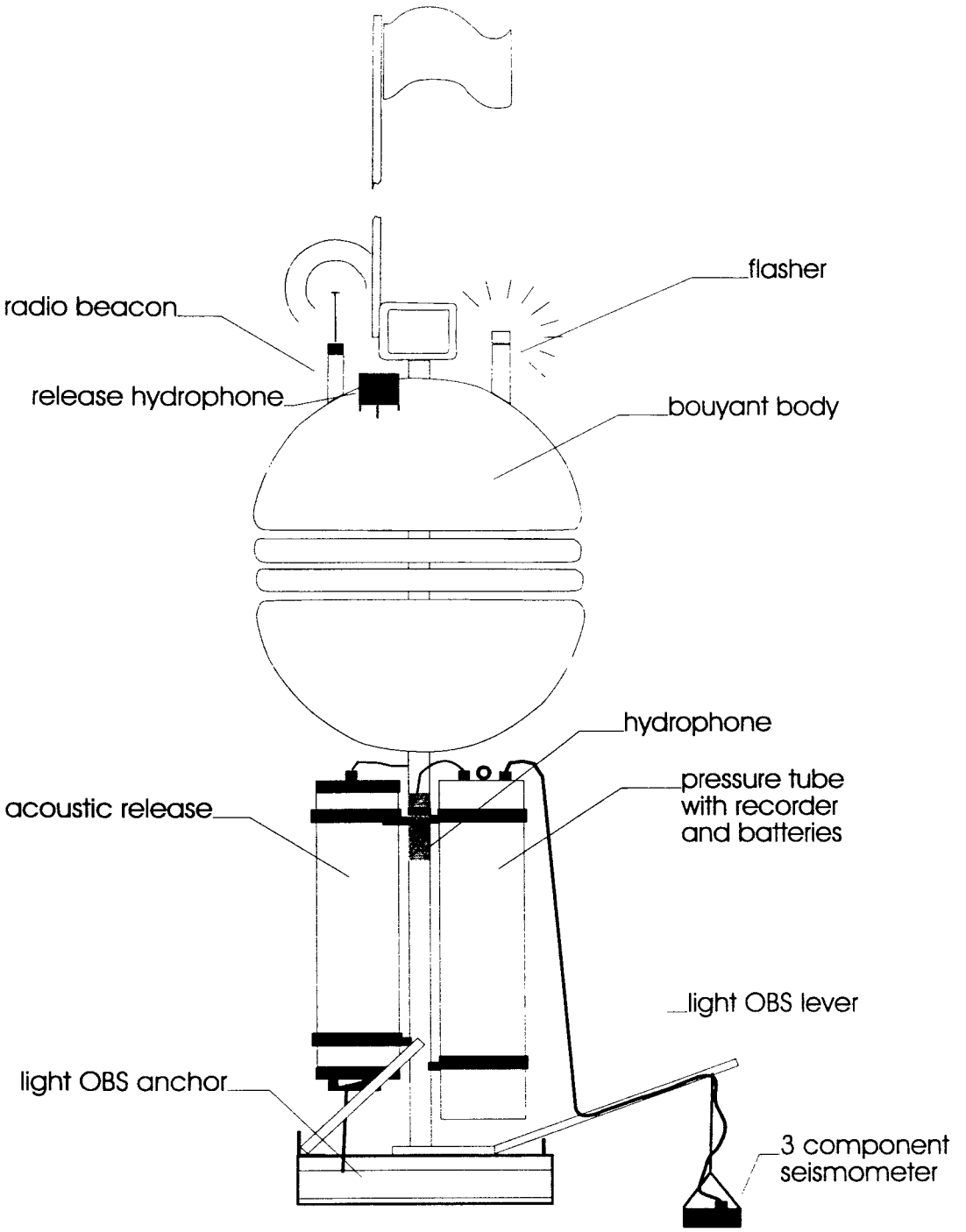

Figure 5.2.3.2: Design of the GEOMAR Ocean Bottom Seismometer "light"

5.2.4 Vertical Arrays

(J. Bialas, K.-P. Steffen, E. Flueh)

Apart from hydrophone and seismometer sensors we operated two vertical arrays, one of which was used successfully on earlier cruises (Flueh and Fisher, 1996). It is a 100 m long cable with four groups of AQ-1 hydrophones manufactured by *BENTHOS*. Each group contains ten hydrophones and a AQ-302 preamplifier. The bouyancy is slightly enlarged while the electronic equipment is the same type as for the OBH system. On previous cruises. the array worked well and stacking of the single channels could improve the data quality. During this cruise several problems occurred which could be repaired with the help of the ship's electronic shop (WTD). Most sections show high noise levels which might have been caused by the strong currents that were observed during the cruise (up to 1 kn). Nevertheless, at least two useful data channels were available on all occupied locations. Recordings on profile 5 showed good quality data on all four channels.

The second array is a 1200 m long cable with 3 channels. An enlarged OBH type float with two disks is used at the top of the cable to carry the electronics pressure cylinder and the recovery aids. Below this, three consecutive 400 m long sections of cable are connected to the bottom where an acoustic release transponder carries the anchor weight. Major components were taken from the OBH system and therefore the individual channels are set up by one *OAS* hydrophone each. Every 400 m a small pressure tube acts as a connector between two cables. The tube houses batteries, a preamplifier, hydrophone and two cable connectors. Each case feeds its hydrophone connection into channel number one and shifts all other channels taken from the cable over by one. This system enables installing the tube at any position and ensures that the closest hydrophone will always be channel one. During cruise SO131 SINUS (Flueh and Reichert, 1998), a first test deployment was done. Bouyancy was added to each of the three preamplifier housings and right on top of the release unit. At the time of recovery, the system did not pop up although the acoustic release stated the execution of anchor release. Luckily, the array cable could be dredge thanks to skillful operations by the ship's crew. Probably the release with the anchor attached sank slower towards the seafloor than the array cable. As a result the anchor might have been dropped on top of a part of the cable keeping it at depth after release. As a consequence, this time, a bouyant sphere from an OBH (without disks) was attached approx. at the middle of one 400 m cable length. On the first test deployment only one 400 m cable section was attached in order to gain experience in deployment handling and measuring results.

After deploying the top buoy from the stern, SONNE sailed slowly along the profile while the cable was pulled out to sea. This ensures that the system was deployed along the scheduled line although the exact inline position needed to be relocated after recovery. At the time of recovery the release transponder answered promptly and the array popped up. After pick up of the top bouy the remaining cable was pulled using a shipboard winch.

Playback of the data from location 76 on profile SO138-06 showed clear signal arrivals for the standard hydrophone while the second channel from the long cable was dead due to a failure of the preamplifier. A second deployment at location 89 on profile SO138-07 was more successful. For the third deployment at location 100 on profile SO138-08 two 400 m sections with two hydrophones were attached to the top buoy. Three disks were attached to the middle of the second cable section taking account for the increased payload. Due to heavy weather conditions and the difficult recovery operation for such a cable it was decided to postpone the recovery of the vertical array to daylight time. Therefore recovery started after the shooting test profile SO138-09. The top bouy popped up after acoustic release and was recovered following the routine OBH recovery procedure. Once on board the remaining cable was pulled with the shipboard winch as done before. After 200 m of cable, the first bouy came out of the water but fell back immediately due to the heavy sea. As a result, the cable broke a few meters above the bouy and the cable sank again as the remining bouyancy was not enough to carry the whole array. Distance ranging with the acoustic release indicated that the release had sunk down to the seafloor and that the array kept stable at its position. As it could be assumed that the remaining 600 m of cable were held almost vertical in the water column by the attached floatations it was decided to return the next

day for a dredge operation. Thanks to skillful handling by the ship's crew this trial was successful and the whole equipment could be recovered. This time the cable withstood the heavy pull load during dredging and recovery. Although there are no indications for external damage the only explanation for the break of the cable is the sudden increase in load while the bouy fell back into the waves. As a result, the distribution and size of bouyancy along the cable must be further improved.

5.3 SEISMIC SOURCES

5.3.1 THE BGR AIRGUN ARRAY

(B. Schreckenberger, J. Sievers)

The seismic signals were generated by a tuned set of 20 airguns (VLF, Prakla-Seismos) grouped in two identical linear sub-arrays 10 m apart on starboard and port side, respectively (Fig. 5.3.1.1). The total volume of the BGR airgun array is 51.2 litres (3,124 cu. in.) filled by pressured air of some 135 bar (1,920 psi). Each sub-array consists of 3 groups (from stern to tail):

- 4 x 3.0 L + 2.5 L
- 2.5 L + 2.3 L + 2.0 L
- 2.3 L + 2.0 L

The total length of each sub-array is 19.6 m starting 40 m behind the stern. The geometrical airgun centre is 50 m behind the stern and 120 m behind the positioning reference point (satellite antenna on the main mast). Three buoys per sub-array keep the airguns at 7 m water depth.

Exact shot timing of the particular airguns is ensured by a microprocessor-controlled airgun-synchronisation unit type Prakla VZAD and VZAC2 with storage oscilloscope. The system was externally triggered by a Meinberg clock GPS 166 during SONNE cruise SO-138.

The pressured air was provided by one of SONNE's LMF compressors, manufactured by Leobersdorfer, Austria, with a capacity of 25 m^3/minute. In case of a malfunction the identical LMF alternate compressor was used.

Quality control during airgun operation consisted of:

- continuous control of the airgun pressure
- control of the airgun operation (autopops, misfires, delays) and sensor signal
- duly maintenance of particular airgun assembly parts during off-times (e.g. gaskets, valves etc.).

With very few exceptions all 20 airguns were properly working, the air pressure was always in the range 134-135 bar (1,900 psi).

Time Reference

The Meinberg clock GPS 166 provided the absolute universal time corrected (UTC) from the GPS system. The minute and second pulses bear an accuracy of < 1 ms. This time reference was fed into the shooting PC, into the mini-streamer recording system and into the PC that was used for calibration of the internal quartz clock installed in the respective OBH systems. Thus, an identical time base was provided for all seismic systems.

VZAD and VZAC

The VZAD unit controls synchronisation and triggering of up to 20 airguns. According to external trigger pulses a 20 ms TTL pulse is generated and sent to the VZAC unit. Here, it is transformed to 60 V and sent to the magnetic airgun valves. The valves do open and in the same instant a sensor sends the time break signal to the VZAD. The deviation (offset) between this response pulse and the target value is determined and used for correction of the trigger pulse sent to the airguns providing optimum synchronisation. This procedure automatically compensates for time delays produced by worn-out assembly parts of particular airguns in the course of operation.

Shooting PC programme

The so-called shooting PC keeps control on all systems. It is connected to the VZAD, to the positioning system and - in case of multi-channel seismics - to the recording system. The programme code TIMER22 used to run this PC is an upgrade of an earlier version TIMER21 by J. Adam (Sievers and Adam, 1997). The programme internally generates a series of suitable trigger signals for the VZAD with selectable intervals between 10,000 and 65,535 ms on the PC quartz clock time base. Simultaneously, a random time shift of up to ± 300 ms can be superimposed on the shot interval. In combination with multi-channel seismics and related stacking this is used to suppress seafloor multiple reflections from previous shots.

Alternatively, an external input (e.g. the Meinberg clock GPS 166) can be used. In this mode, TIMER22 generates a series of trigger signals with selectable intervals between 10 and 65,535 seconds based on an absolute time base. The random function superposition option is inactive in this case. This mode was used for the operation during SO-138.

The trigger signals are sent to the VZAD that fires the airguns with a constant time delay of 73.8 ms due to electronic and mechanical components and returns a time break pulse to the shooting PC. The time break sent to the mini streamer system also contains the 73.8 ms delay.

Simultaneously, different data are read via 9 serial RS232 interfaces. The data are compiled in 'external header' records which are saved in a protocol file. The records comprise the following information:

- shot no, status, GPS time, GPS date, PC date, PC time, actual time, nominal time, half random width
- error code, GPS latitude, GPS longitude, course, speed, shot interval
- error code, shot no, trigger mode, gun delay average interval, gun offset
- gun no, status, offset, delay, error code
- error code, sign, starboard air pressure, label
- error code, sign, port air pressure, label
- error code, latitude, longitude, altitude (corrected by BGR navigation system)
- extension
- software version no

Shot triggering during SO-138

Generally, the shots were triggered in time intervals of 60 seconds on full minutes UTC. At a speed of 5.5 knots this results in a shot point distance of 167 m. One exception was made on line SO138-S3. This line was shot with the normal 60 seconds interval from east to west and in the direction from west to east partly with 40 seconds and partly with 20 seconds interval. Details for every seismic line can be found in Appendix 9.2.

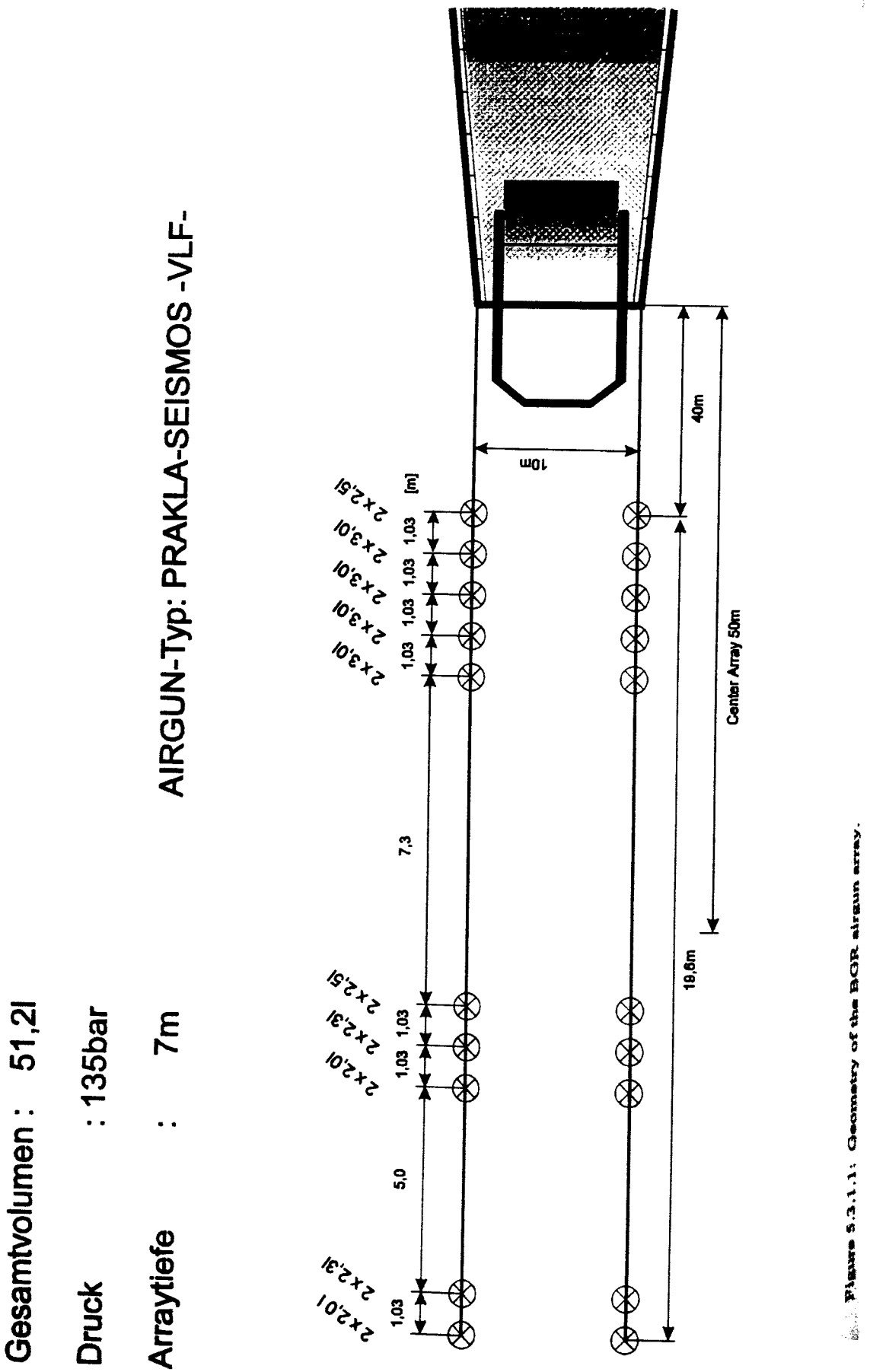

Figure 5.3.1.1: Geometry of the BGR airgun array.

5.4 GRAVIMETER AND MAGNETOMETER

5.4.1 GRAVITY MEASUREMENTS AT SEA

(I. Heyde, P. Kewitsch, and B. Schreckenberger)

Short description of the seagravimeter system

The BGR owned gravimeter system KSS31 is a high performance instrument for marine gravity measurements, manufactured by the BODENSEEWERK GEOSYSTEM GmbH. While the sensor is based on the ASKANIA type GSS3 seagravimeter designed by Prof. Graf in the 60ties, the development of the horizontal platform and the corresponding electronic devices took place by the BODENSEEWERK GEOSYSTEM in the second half of the 70ties. The KSS31 system consists of two main assemblies: the gyro-stabilized platform with gravity sensor and the data handling subsystem.

The gravity sensor (Fig. 5.4.1.1) consists of a tube-shaped mass that is suspended on a metal spring and guided frictionless by 5 threads. It is non-astatized and particularly designed to be insensitive to horizontal accelerations. This is achieved by limiting the motion of the mass to the vertical direction. The main part of the total gravity acceleration is compensated by the mechanical spring, but gravity changes are compensated and detected by an electromagnetic system. A displacement of the spring-mass assembly with respect to the outer casing of the instrument is measured using a capacitance transducer. The output from the transducer is fed back into an electromagnetic moving coil system used for feedback control. A P-I feedback (P=Proportional, I=Integration) suppresses the accelerations of sea motion. An I-acting feedback provides a signal which drives the system to the zero position and represents an overcritical damping of the system. The current flowing through the moving coil is the measure for the gravity change.

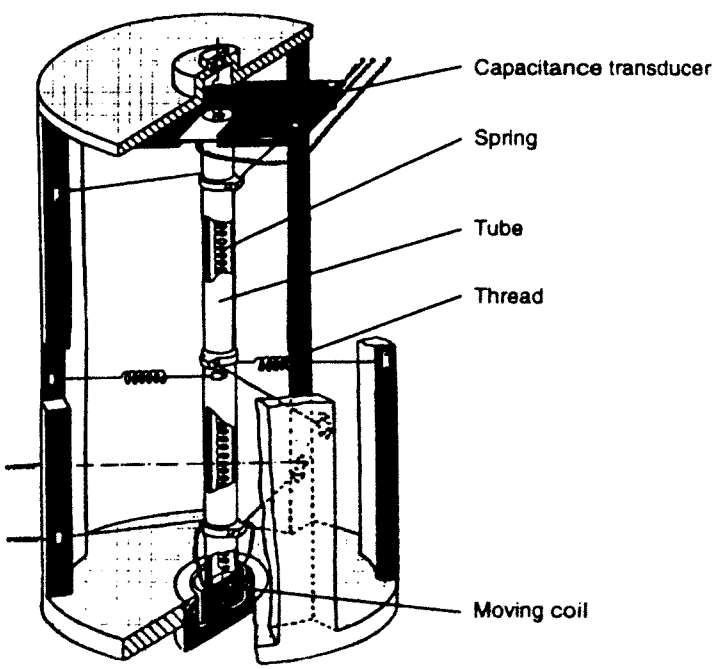

Fig.5.4.1.1: Gravity Sensor GSS30 of the seagravimeter-system KSS31

In addition to the spring-mass assembly, as the gravity detector, the sensor housing contains the control electronics that converts the current signal to voltage output and forwards it to the data handling subsystem. The power supply of the gravity sensor contains a sealed buffered battery unit with sufficient capacity to maintain the internal temperature stabilization of the sensor for 24 hours in case of main power loss. In case of system failure the sensor electronics automatically activates a caging mechanism preventing the spring-mass assembly from damage.

The levelling subsystem consists of a platform stabilized in two axes by a vertical electrically erected gyro. The stabilization during course changes can be improved by providing the system online navigation data. The control electronics and the power supply of the platform are located in the data handling subsystem unit. Functions like gyro run-up and -down sequences and the automatic platform caging are performed by the system controller unit located in the data handling subsystem, too.

Additionally the data handling subsystem provides functions for filtering, logging and pre-processing of the data as well as self-testing sequences of the instrument and the platform. It also contains the power supply for the sensor and the platform.

On board R.V. SONNE the seagravimeter system KSS31 is installed in the so-called gravimeter room which is located near the geometrical centre of the ship. The data are transmitted to the BGR data acquisition and processing system (see 5.1.2) in the gravity/magnetic laboratory. The KSS31 receives from this system the online navigation data used to support the stabilising platform.

Processing of the gravity data

Processing of the gravity data consists essentially of the following steps:
- a time shift of 175 seconds due to the overcritical damping of the sensor,
- conversion of the output from reading units (r.u.) to mGal by applying a conversion factor of 0.94542 mGal/r.u.,
- connection of the harbour gravity value to the world gravity net IGSN 71(see 6.4.1)
- correction for Eötvös effect using the navigation data,
- correction for the instrumental drift (not performed until completion of the cruise)
- subtraction of the normal gravity (WGS67).

As a result, we get the so-called free-air anomaly (FAA) which in the case of marine gravity is simply the observed gravity minus the normal gravity. According to the selectable time interval of the data acquisition system, gravity values are available every 20 seconds.

5.4.2 THE GRADIENT MAGNETOMETER

(B. Schreckenberger and P. Kewitsch)

Generally all marine magnetometer measurements suffer from the lack of base stations that can be used in order to reduce the temporal magnetic variations as it is routine for land and airborne surveys. In the past only on a few cruises we had the opportunity to install a base station on adjacent islands or coasts. Unfortunately, permanently operating magnetic

distant from our survey areas in remote oceanic regions. Particularly the short period variations can not be reduced in this way.

In order to avoid these problems and to obtain variation-free magnetic measurements on the ship we use the gradient magnetometer Geometrics G-811G. The instrument consists of two proton magnetometers which are towed 150 meters apart as a longitudinal array about 600 meters astern of the ship (Fig. 5.4.2.1). Many parts of the instrument have been modified, especially the towing system including all connections of the sensors and the splitter box to the cables. We use plugs from seismic streamer technology instead of the original fixed connectors at all these connections in order to enable fast replacement of defective cables and sensors and easy handling.

Both sensors measure the total intensity of the magnetic field simultaneously. The difference between the two measurements is an approximation for the longitudinal gradient of the field in the direction of the profile line. It is free from temporal variations and its integration restores the variation-free total intensity or magnetic anomaly (apart from a constant value). The practical procedure that reconstructs the anomaly from the gradient is by no means trivial because several kinds of measuring errors have severe effects during the integration.

The remanent, viscous, and induced magnetizations of the ship are much more critical for gradiometer than for normal marine magnetic measurements. Because the two sensors have different distances to the ship a systematic error is generated in the gradient depending on the course and even on the time due to the viscous part of the ship's magnetization. This long-period errors can have a disastrous effect during the reconstruction of the magnetic field from the gradient. Because mathematical models for the magnetic effect of the ship are by far not precise enough, we are towing the sensors at a greater distance behind the ship than it is standard for normal marine magnetic surveys (Fig. 5.4.2.1).

Another source of error is the deviation of the magnetometer array from the profile line and its unknown azimuth as well as the different depth of the sensors. In order to obtain information about the location and orientation of the array behind the ship we installed a fluxgate compass in the middle of the cable between the two sensors.

A more detailed discussion of errors can be found in Eilers et al. (1994). For example, magnetic fields are induced by the movement of sea water within the earth's magnetic field. This results in a distinctively raised noise level of the records during times of rough seas. However, due to the statistical character of the disturbing fields and the smoothing effect of the integration this hardly reduces the quality of the reconstructed anomaly.

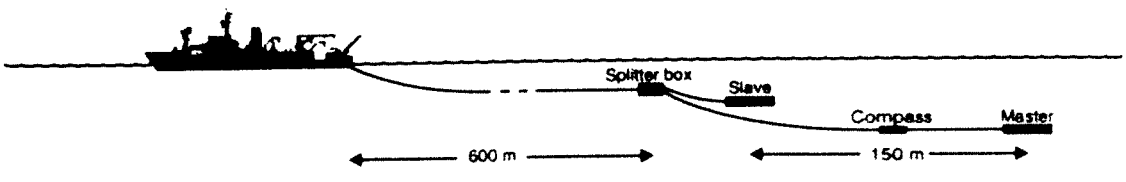

Figure 5.4.2.1: Gradient magnetometer configuration.

In addition to the spring-mass assembly, as the gravity detector, the sensor housing contains the control electronics that converts the current signal to voltage output and forwards it to the data handling subsystem. The power supply of the gravity sensor contains a sealed buffered battery unit with sufficient capacity to maintain the internal temperature stabilization of the sensor for 24 hours in case of main power loss. In case of system failure the sensor electronics automatically activates a caging mechanism preventing the spring-mass assembly from damage.

The levelling subsystem consists of a platform stabilized in two axes by a vertical electrically erected gyro. The stabilization during course changes can be improved by providing the system online navigation data. The control electronics and the power supply of the platform are located in the data handling subsystem unit. Functions like gyro run-up and -down sequences and the automatic platform caging are performed by the system controller unit located in the data handling subsystem, too.

Additionally the data handling subsystem provides functions for filtering, logging and pre-processing of the data as well as self-testing sequences of the instrument and the platform. It also contains the power supply for the sensor and the platform.

On board R.V. SONNE the seagravimeter system KSS31 is installed in the so-called gravimeter room which is located near the geometrical centre of the ship. The data are transmitted to the BGR data acquisition and processing system (see 5.1.2) in the gravity/magnetic laboratory. The KSS31 receives from this system the online navigation data used to support the stabilising platform.

Processing of the gravity data

Processing of the gravity data consists essentially of the following steps:
- a time shift of 175 seconds due to the overcritical damping of the sensor,
- conversion of the output from reading units (r.u.) to mGal by applying a conversion factor of 0.94542 mGal/r.u.,
- connection of the harbour gravity value to the world gravity net IGSN 71(see 6.4.1)
- correction for Eötvös effect using the navigation data,
- correction for the instrumental drift (not performed until completion of the cruise)
- subtraction of the normal gravity (WGS67).

As a result, we get the so-called free-air anomaly (FAA) which in the case of marine gravity is simply the observed gravity minus the normal gravity. According to the selectable time interval of the data acquisition system, gravity values are available every 20 seconds.

5.4.2 THE GRADIENT MAGNETOMETER

(B. Schreckenberger and P. Kewitsch)

Generally all marine magnetometer measurements suffer from the lack of base stations that can be used in order to reduce the temporal magnetic variations as it is routine for land and airborne surveys. In the past only on a few cruises we had the opportunity to install a base station on adjacent islands or coasts. Unfortunately, permanently operating magnetic

distant from our survey areas in remote oceanic regions. Particularly the short period variations can not be reduced in this way.

In order to avoid these problems and to obtain variation-free magnetic measurements on the ship we use the gradient magnetometer Geometrics G-811G. The instrument consists of two proton magnetometers which are towed 150 meters apart as a longitudinal array about 600 meters astern of the ship (Fig. 5.4.2.1). Many parts of the instrument have been modified, especially the towing system including all connections of the sensors and the splitter box to the cables. We use plugs from seismic streamer technology instead of the original fixed connectors at all these connections in order to enable fast replacement of defective cables and sensors and easy handling.

Both sensors measure the total intensity of the magnetic field simultaneously. The difference between the two measurements is an approximation for the longitudinal gradient of the field in the direction of the profile line. It is free from temporal variations and its integration restores the variation-free total intensity or magnetic anomaly (apart from a constant value). The practical procedure that reconstructs the anomaly from the gradient is by no means trivial because several kinds of measuring errors have severe effects during the integration.

The remanent, viscous, and induced magnetizations of the ship are much more critical for gradiometer than for normal marine magnetic measurements. Because the two sensors have different distances to the ship a systematic error is generated in the gradient depending on the course and even on the time due to the viscous part of the ship's magnetization. This long-period errors can have a disastrous effect during the reconstruction of the magnetic field from the gradient. Because mathematical models for the magnetic effect of the ship are by far not precise enough, we are towing the sensors at a greater distance behind the ship than it is standard for normal marine magnetic surveys (Fig. 5.4.2.1).

Another source of error is the deviation of the magnetometer array from the profile line and its unknown azimuth as well as the different depth of the sensors. In order to obtain information about the location and orientation of the array behind the ship we installed a fluxgate compass in the middle of the cable between the two sensors.

A more detailed discussion of errors can be found in Eilers et al. (1994). For example, magnetic fields are induced by the movement of sea water within the earth's magnetic field. This results in a distinctively raised noise level of the records during times of rough seas. However, due to the statistical character of the disturbing fields and the smoothing effect of the integration this hardly reduces the quality of the reconstructed anomaly.

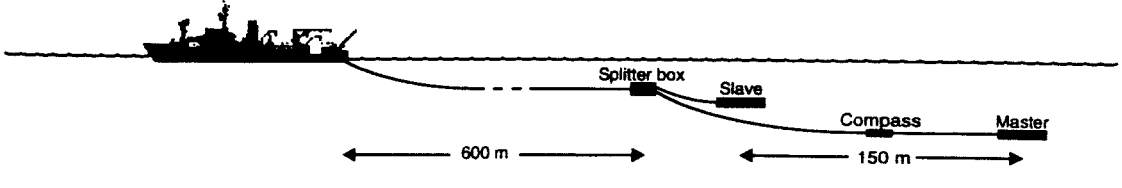

Figure 5.4.2.1: Gradient magnetometer configuration.

5.5 SHIPBOARD EQUIPMENT
(K. Huhn)

5.5.1 HYDROSWEEP

For continuous bathymetric profiling the HYDROSWEEP multibeam system from ATLAS-ELEKTRONIK is available on board of RV SONNE. Using a frequency of 15.5 kHz and 59 beams in a swath of 90° it can map the seafloor with a scanline width of up to twice the water depth. The range of the central beam is up to 10,000 m with an error of 1% and of the outer beams up to 7,000 m with a precision of about 1% if roll is less than 10° and pitch less than 5°. Corrections for roll, pitch, and heave are automatically applied. Due to the fixed angle between beams, the resolution depends on the water depth and varies from about 170 m to 200 m in water depths of 5,000 m to 6,000 m.

To calculate depths from echo time delays, the velocity of sound in the different waterlayers is required. HYDROSWEEP uses a second set of transducers and a calibration scheme with soundings alongtrack to determine an average water sound velocity profile (Schreiber und Schencke, 1990). Yet in certain areas this algorithm fails (c.f. Flueh and von Huene, 1994). So for better results, direct measurement of sound velocity at different depths using a CTD is required.

Postprocessing of HYDROSWEEP data comprises merging navigational data, calculating depth and positions of the footprints of the beams, removing artifacts and erreoneous datapoints, and generating a digital terrain model (DTM). The ATLAS HYDROMAP software, based on the CARIS software package, is available on board for that purpose. However, for several reasons outlined in Flueh and von Huene (1994) and Weinrebe (1997), the academic software MB-System (Caress and Chayes, 1996) from Lamont-Doherty Earth Observatory is used for HYDROSWEEP data processing.

5.5.2 PARASOUND

For geological mapping of the uppermost sedimentary layer, the parametric echosounder PARASOUND from ATLAS ELEKTRONIK is available on board of R/V SONNE. This system uses a parametric signal generated by the superposition of two, slightly offset, high frequencies to gain deeper penetration and higher resolution compared to that of ordinary echosounders. One signal is generated with a fixed frequency of 18 kHz, the other can be set to values between 20.5 kHz and 23.5 kHz (at 0.5 kHz increments), thus yielding a parametric signal of 2.5 kHz to 5.5 kHz with a (narrow) beam angle of about 4°. The footprint of a beam ensonifies an area of approximately 7% the water depth. Due to the narrow beam, no echos from the sea bottom or sedimentary layers will reach the receiver if the seafloor is inclined more than 2°, restricting the application of PARASOUND to relatively flat areas.

5.5.3 NAVIGATION

(B. Schreckenberger and H.-O. Bargeloh)

Since 1996, SONNE has been using the differential GPS (DGPS) system SkyFix by Racal Survey. Data from several reference stations are processed at a land-based station and correction values are broadcasted via INMARSAT satellites to the users. On board of SONNE the special software package MultiFix 2 receives the signals from a special decoder and from the GPS receiver Trimble 4000 DS for the calculation of the DGPS positions. The reference stations Jakarta, Singapore, and Darwin were used by MultiFix on this cruise. We estimated a mean error of a few meters, in general below 5 meters, for the final position solution. Therefore, Navigation by SkyFix overcomes all former problems with Selective Availability and it is possible to use the GPS position without further postprocessing.

The only problem on cruise SO-138 were short gaps of one or two minutes on a few lines because of problems with the rotation of the INMARSAT antenna beyond 360° and because of its possible shadowing by the mast of the ship. Unfortunately, under this conditions the SkyFix system does not use the uncorrected GPS position but simply stops the data output.

All navigation data refer to the GPS antenna on the main mast of the vessel and are given in the WGS 84 system. The position of the airgun array and the streamer relative to the antenna is described in the chapter about the seismic system (5.3.1).

Shooting was done in one minute intervals on most of the lines (exception line SO138-03). In general the speed was 5.5 knots through the water. Using the BGR computer system for data acquisition and data processing and the procedures described in 5.1.2, shotpoint lists have been prepared for every seismic line. The lists contain the profile name, shotpoint number, date, time, position (GPS antenna), and waterdepth for every shot. In general it was not necessary to make a postprocessing of the positions, in the case of the gaps described above a linear interpolation algorithm turned out to be satisfactory.

6. WORK COMPLETED AND FIRST RESULTS

6.1 HYDROSWEEP

(K.Huhn and watch standers)

Work performed, data quality

Hydrosweep multibeam data were continuously recorded during the entire SONNE138 cruise. The instrument worked nearly all time without any problems. Only in times of bad weather conditions with too much heave and pitch the data quality was unsatisfactory. Lesser data quality was obtained in the S-E area of our working area around profile 5.6, and 7. In summary, during the cruise multi beam data were recorded along 4680 track miles.

The water sound velocity was taken from literature (Flueh & Reichert, 1998). In addition, a new calibration of sound velocity was obtained from a CTD tool on January 23, 1999 during cruise SONNE138 - GINCO (Figure 6.1.1). These correspond closely to the used profile.

The HYDROSWEEP data were processed onboard using the MB System software developed at Lamont-Doherty Earth Observatory (Caress and Chayes, 1996). MB System is a package of programs and macros for processing multibeam data on UNIX system. The raw data sets were transferred by the onbord computer network to a Sun Solaris work station. With the given water sound velocity the raw HYDROSWEEP echo time data were converted to depth by complete ray tracing through the different water layers. The multibeam sweeps, including all 59 beams, were edited using the MB system to eliminate erratic points. Edited sweeps were then assembled, gridded, and contoured with the GMT software (Wessel and Smith, 1991). No filters were applied to smooth the edited data. There is no limitation on grid size and spacing. The HYDROSWEEP data were processed to generate contour maps of water depth and perspective images of the morphology which was done using the GMT software. Data from cruise SO131 (Flueh and Reichert, 1998) and SO137 (Reichert and shipboard scientific party, in prep.) were also processed and included in this data set.

Sound velocity profiles obtained with the CTD

For calibration of the water sound velocity to transfer the echo times of the HYDROSWEEP data into water depth, a CTD tool was run in deep water south of the Sunda Street. The obtained sound closely resembles earlier measurements.

The velocity profile shows the typical curvature (Fig. 6.1.1) with the same characteristics as CTD profiles measured elsewhere. Sound velocity in shallow water has a very high negative gradient in the first 200m. In this depth it reaches a sound velocity of 1495 ms^{-1}. This strong gradient is typical for this region as seen in other velocity profiles. Beneath this depth the velocity decrease is slower up to a minimum value at about 1000m (1483ms^{-1}). Then the sound velocity increases up to the maximal depth of 4000m (1517ms^{-1}) nearly linear from 1800m. Significant for the velocity are numerous small excursions from the global trend between 300m and 1700m.

Also the temperature curve shows such a significant strong gradient in first 200m until 10°C. Beneath this depth the temperature decreases continuously. The salinity shows large

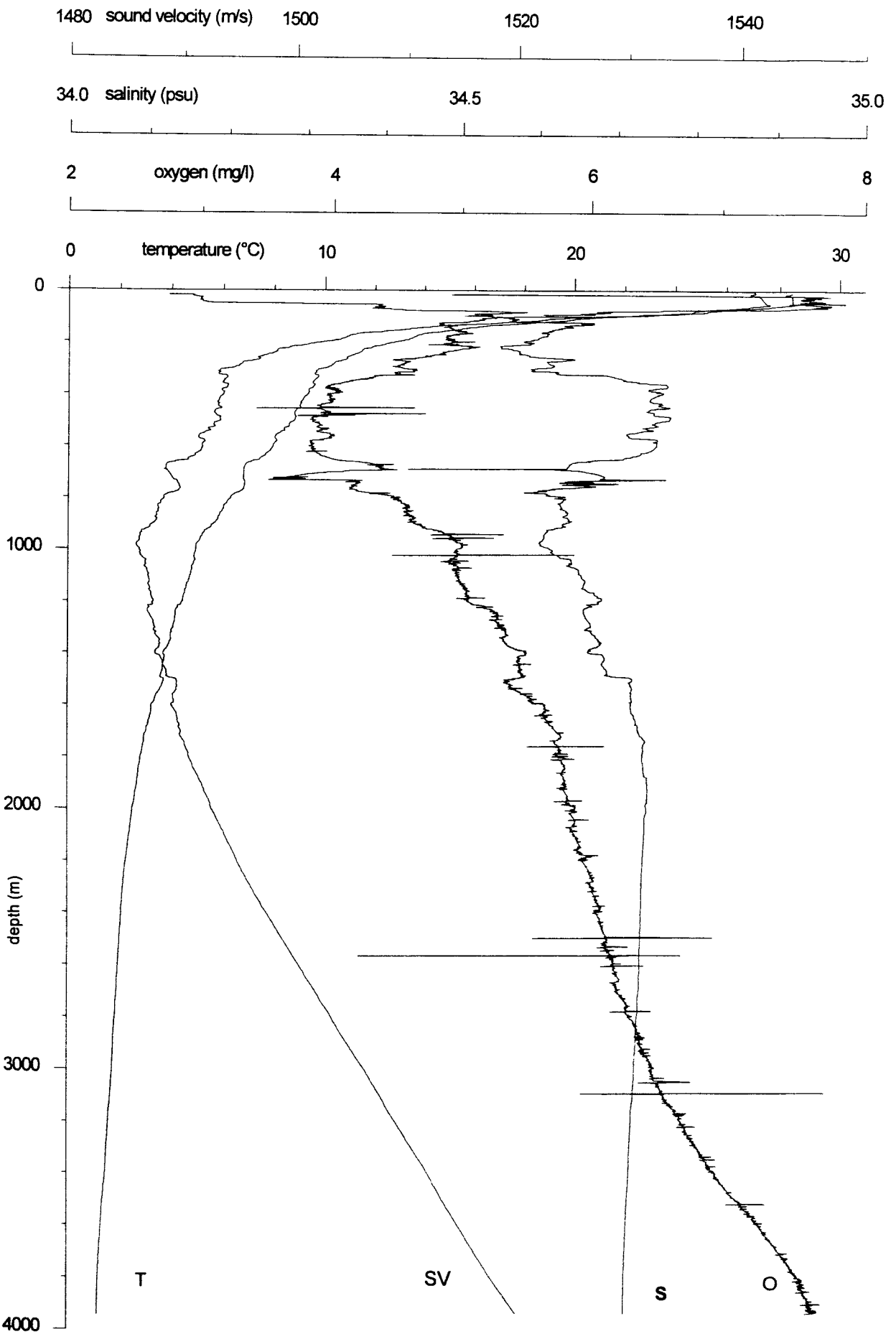

Figure 6.1.1: Water sound velocity, temperature, and salinity profiles from the CTD tool.

variations with great periods until 1500 m. Beneath this depth, salinity reaches a nearly constant value of 34.69psu. The oxygen tool did not work properly.

The Sunda Trench

About 10000 km of the Sunda Trench between 102°E/ 103°S and 6°25'S/ 7°10'S were surveyed with HYDROSWEEP during SONNE cruise SO138. A contour map of this area is shown in Figure 6.1.2 and three perspective illuminated images in Figures 6.1.3, 6.1.4 and in Figure 6.1.5.

The actual deformation front is clearly indicated in the bathymetrical data by the first ridge of the accretionary wedge. Two remarkable segments of the wedge – an upper and a lower part - could be imaged by a significant change in morphological style. The upper segment is mainly intact and massive and shows a classical wedge structure. The topography is smooth with a small slip angle and accretionary ridges trending NW - SE with lengths of up to 35km as seen at the most landward accretionary ridge (Fig. 6.1.4). But also large slides are recognized which mark active tectonism as clearly visible in Figure 6.1.3. The 5000m isoline separates the upper wedge with a significantly rougher topography. This segment is characterized by numerous cuts.The topography shows strong disturbances. No typical subparallel ridge system can be imaged. Large slides and short ridge fragments can be identified. This remarkably rough topography indicates recent active tectonical processes.

The most important structure and also the most interesting feature of this accretionary system is a displacement of the deformation front at 102°15'E/6°53'S (Fig. 6.1.3). A strong cut separates the western part of the upper accretionary wedge from an eastern part displaced nearly 8 km to the SW. Both segments show different topography. There is no typical ridge system to be observed on the western upper accretionary ridge but large slides are seen everywhere. On the eastern segment short ridge segments with lengths of up to 16 km can be recognized (Fig. 6.1.5). Both upper segments also show different slopes. This is indicated by two cross sections through the wedge on both sides of the displacement. The western upper segment has a remarkably higher slope angle of 5.4° (Fig. 6.1.6) compared to the eastern segment with 4.6°. The deformation front is well imaged on the N-W profile through the wedge by a steep rise of 1300m. This part of a wedge with a higher slope angle in the upper part shows vast disturbances, displaying none of the classical structures of an accretionary wedge. In the cut of the southern profile the deformation front can not be imaged by such a step. The upper wedge shows a significantly lower slope angle with a much rougher topography. Neither are there typical subparallel ridge systems. Only short ridge segments could be imaged.

An interpretation of the displacement as a slide is contradicted by an especially steeply bordered cut. Based on this marked border it does not show the typical fan structure. In addition, a fan could not have such dimensions. On the other hand, there is yet no tectonical explanation to interpret this displacement as a result of a transform fault. New results from our other measurements may provide an answer to this question.

In summary, the structure of the wedge is not classical. Two main segments, an upper and an lower slope, could be imaged and the upper segment could also separated into a western and an eastern segment.

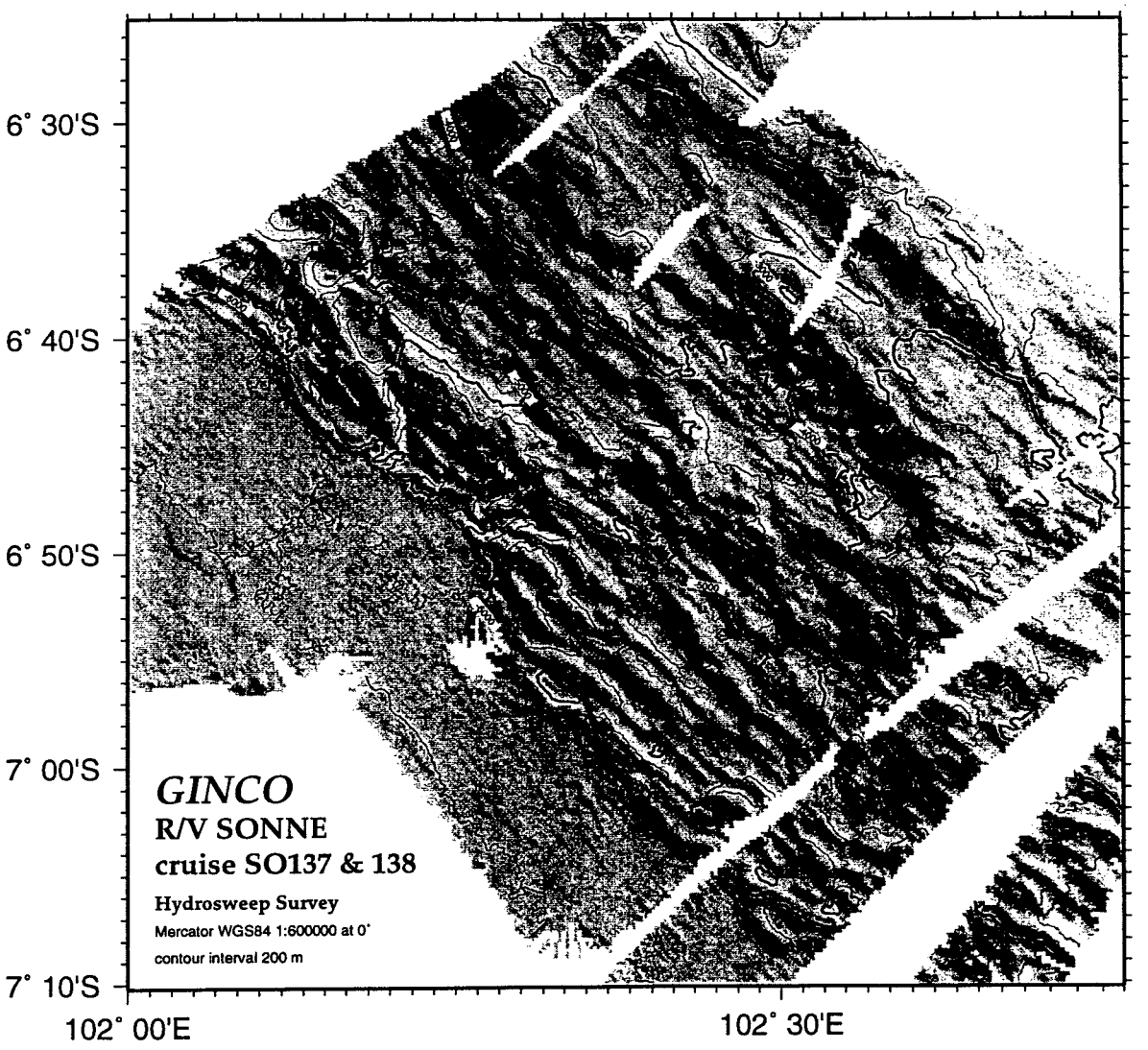

Figure 6.1.2: Bathymetrical contour plot of the entire Sunda trench surveyed during SO138. Contour spacing 200m. Grid size 0.002°.

Figure 6.1.3: 3d plot perspective view of surveyed Sunda trench. Viewpoint 270°.

Figure 6.1.4: 3d plot perspective view of surveyed Sunda trench. Viewpoint 210°.

Figure 6.1.5: 3d plot perspective view of surveyed Sunda trench. Viewpoint 160°.

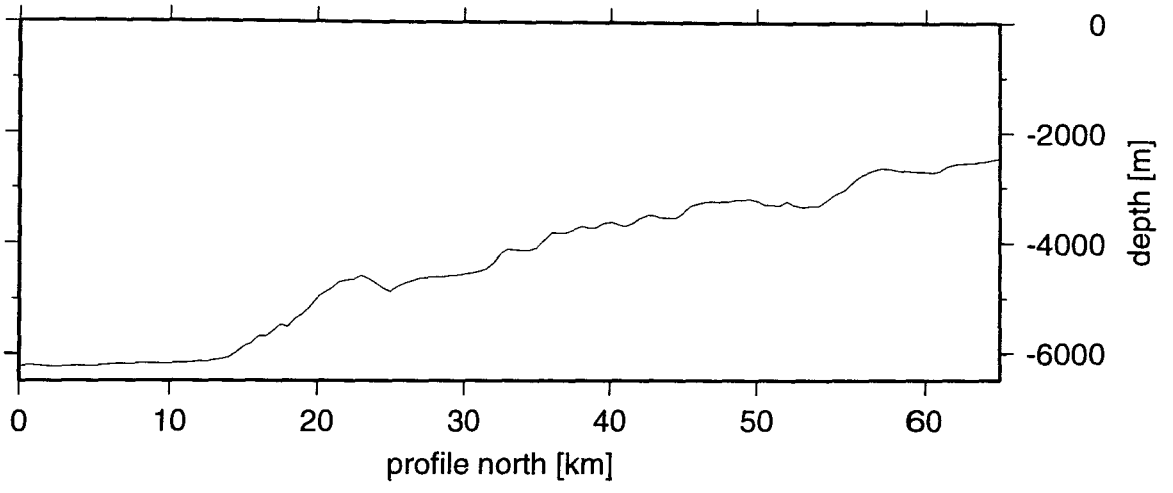

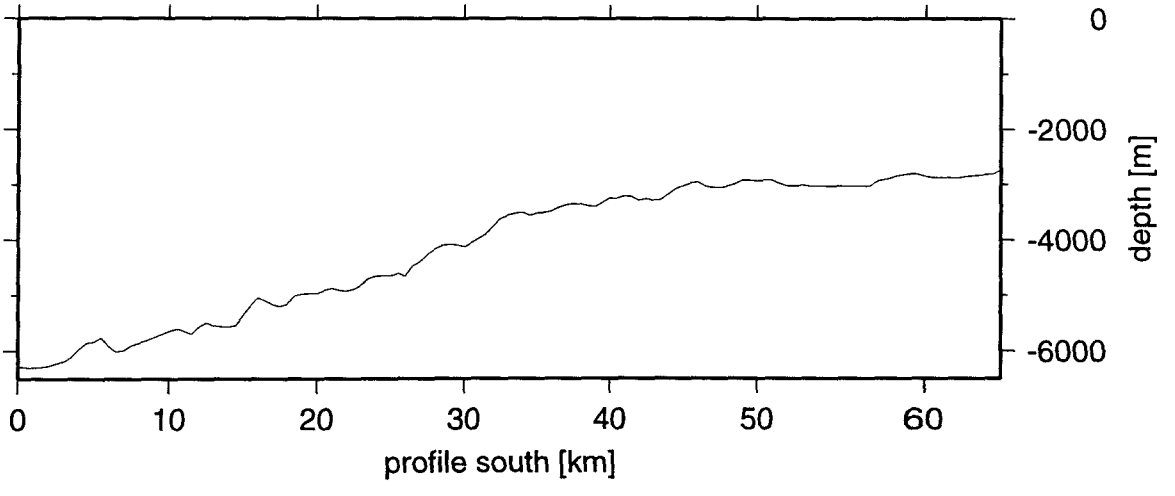

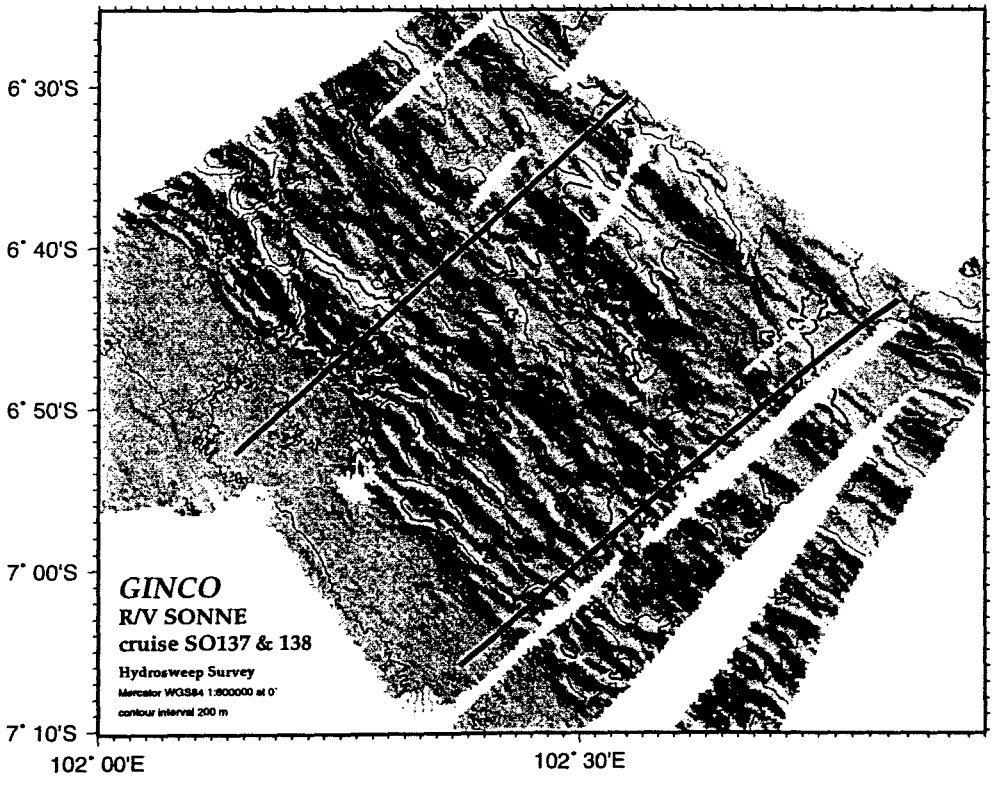

Figure 6.1.6: Cross sections along the surveyed accretionary wedge, located as shown in the bathymetrical contour plot below.

The Sunda Strait

Hydrosweep mapping was not planned for the Sunda Strait, however, in addition to the data obtained during shooting, magnetic measurements, and transits, several HYDROSWEEP profiles were recorded to cover great parts of Sunda Strait. A contour map of the observed area is shown in Figure 6.1.7.

Bathymetry variations within Sunda Strait are clearly imaged in the bathymetrical contour map. A deep north-south trending graben structure along 104°51' is marked by depth values of up to 1800 m in its center. This graben is bordered by steep flanks on both sides. As can be infered from the narrow placement of the contour interval, the dip angle of the western flank is much steeper than on the eastern side, representing a clear cut transition to the shallower topography at the western entrance of the strait. Some authors have interpreted this graben structure as a pull apart basin in continuation of the Sumatra strike-slip fault (Huchon and Le Pichon, 1984).

On the eastern side the graben is not as clearly constrained. Around 6°20' the flank is not continuous, a broad almost east-west trending gully ends in the graben. A bit further north on the eastern side at 6°10' a circular structure is visible in the bathymetry map which is interpreted as a cone of volcanic origin. East of the graben the bathymetry becomes more and more shallow, reaching depths of less than 50 m near the Krakatau volcanic complex. This variation of the seafloor depth can also be witnessed from the track width of the sonar rays, which become extremely narrow in the central and eastern part of Sunda Strait.

At its southern end the graben gradually opens and terminates in a broad basin extending from southwest of Panaitan towards the Sunda Arc.

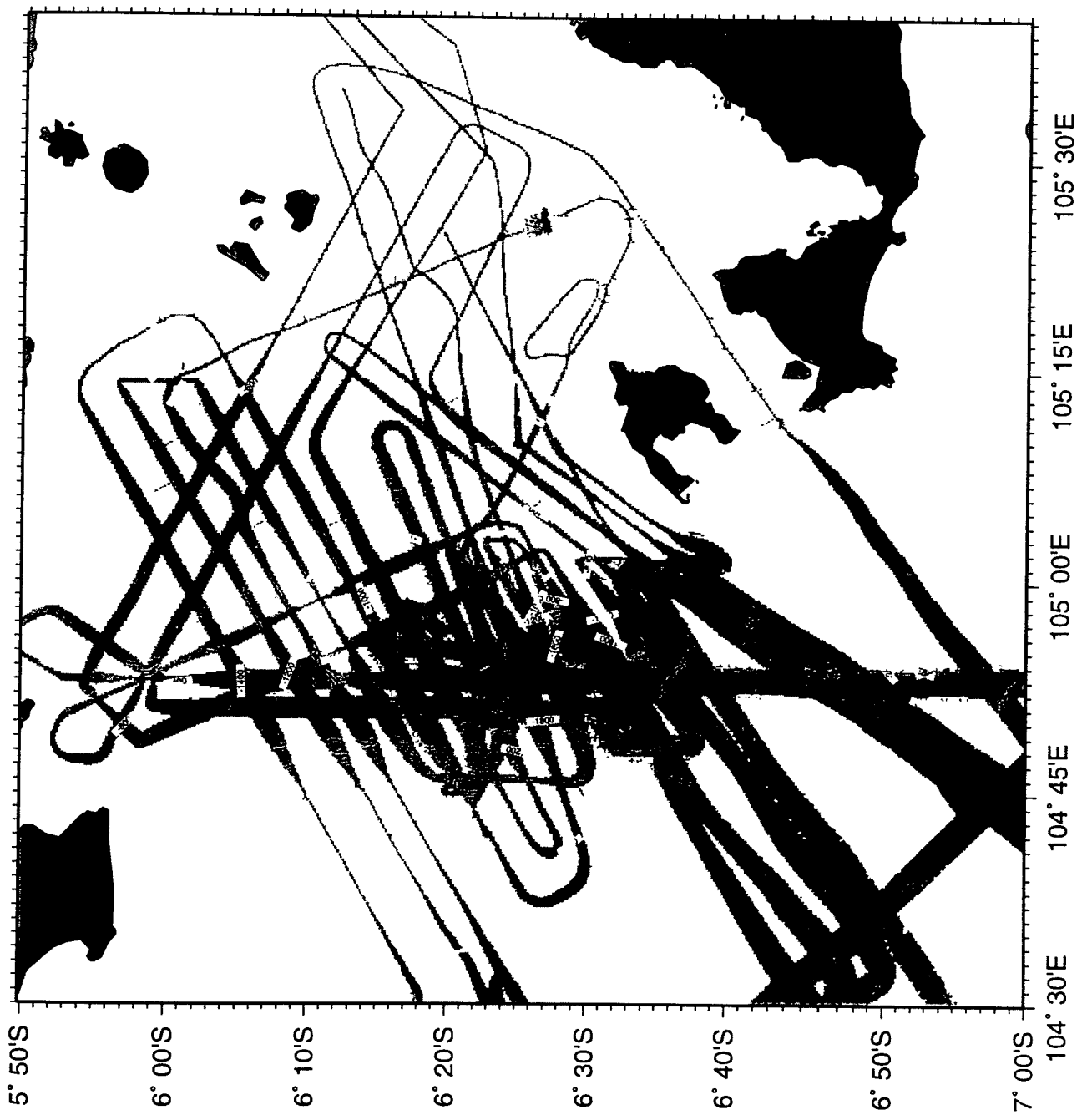

Figure 6.1.7: Bathymetrical contour plot of the entire Sunda Strait surveyed during SO137 and SO138. Contour spacing 200m. Grid size 0.002°.

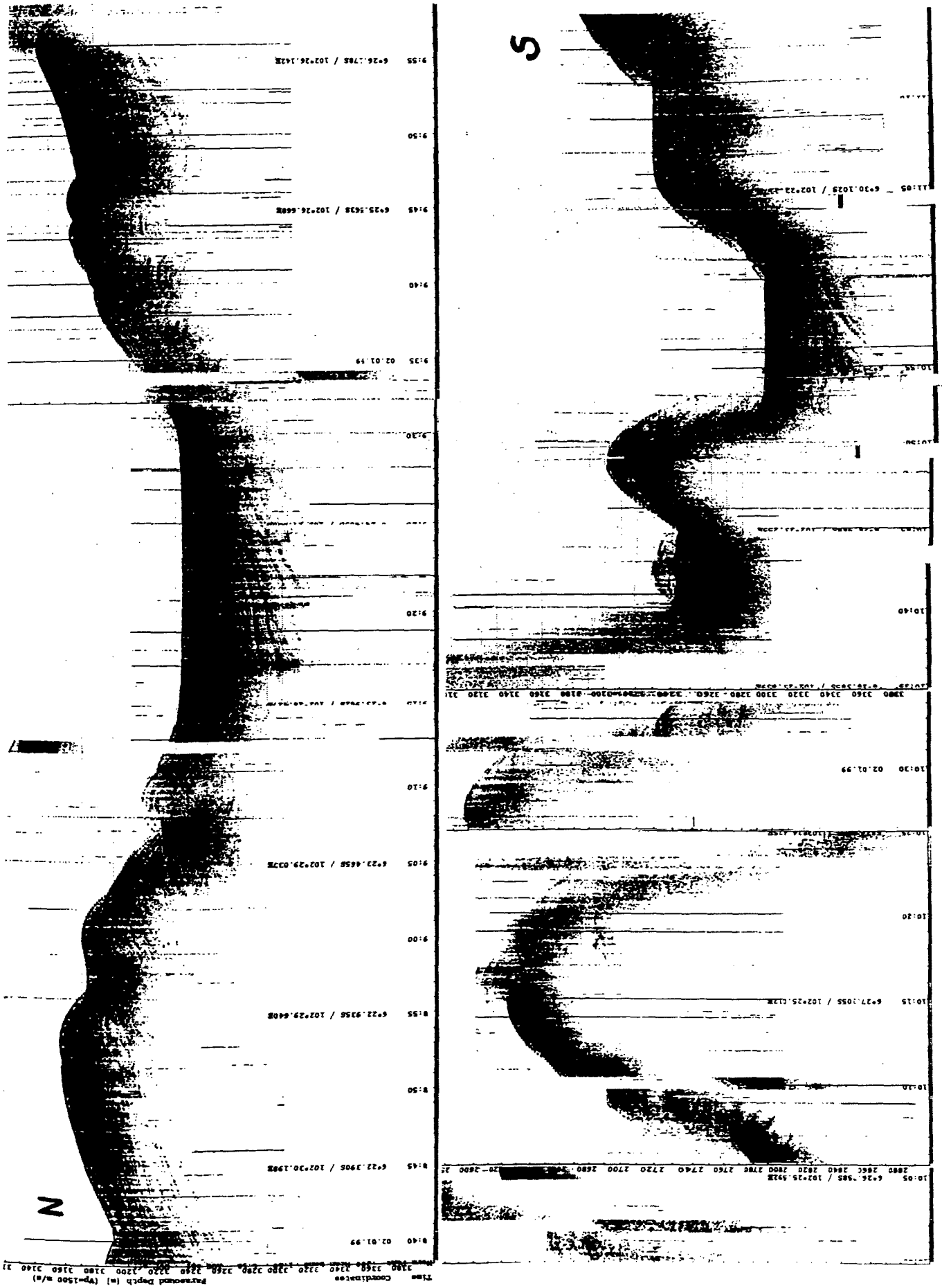

Figure 6.2.1: Parasound anologue recordings along profile 1 of a faulted zone at the accretionary wedge. This section shows typical ridge deformation and portions of layered sediments inbetween.

6.2 PARASOUND

PARASOUND data were collected during the HYDROSWEEP and magnetic surveys and along all seismic lines. Data were recorded continuously analog on a white and black plotter as well as a color plotter. Where the slope was sufficiently shallow, the data quality was good throughout the cruise at the ship's speed of maximally 12 knots. Lesser data quality was only obtained in areas of maximum slope and under bad weather conditions. In flat areas, a penetration of up to 130 m into the uppermost sedimentary layers was achieved.

Ridge systems and sediment ponds

Good Parasound images were obtained from the accretionary wedge south of Sumatra. Typical ridge systems and flat portions between this ridges can be recognized on the NE-SW profile1 between 6°22'S/102°30'E and 6°30'S/102°22'E (Fig. 6.2.1). On the parallel profile 4 and 5 and the NW-SE trending profiles about the wedge, sediment filling between the accretionary ridges is also well imaged. Penetration into the sediments is about 80m. These sediments are highly reflective and in the flat area no deformation is visible. The layering of the sediment infill is nearly parallel to the sea bottom, as well seen in Figure 6.2.1. Perhaps this style of undisturbed layering of sediments characterizes young post tectonic sedimentation after the shortening and faulting of the ridges, but this cannot be decided yet. Another style of sedimentation can be imaged by filled sediments which are not quite parallel to the sea bottom. They follow the flanks of the ridges nearly subparallely. This indicates that this sedimentations is much older, overlayn by younger sediments. The underlying sediments were tiled during formation of the ridge.

Mud diapirs and gas lenses

At several locations within the wedge mud diapirs have been identified in the Parasound recordings (Fig. 6.2.2). They reach highs of up to 35m. These structures are found on the entire wedge, mostly in the western part of our measuring area south of Sumatra. Mud volcanoes are often found on the flanks of the ridges marking zones of actual deformation processes.

Parasound measurements in other areas show such diapires in the vicinity of blank zones which were interpreted as zones of methane accumulation (Flueh & Reichert, 1997). Although such structures are not visible in our data, the presence of methan gas is quite possible. This is confirmed by the presence of gas lenses (Fig. 6.2.3). The gas lenses marked by an arrowhead in Figure 6.2.3 are visible as blank lense-shaped zones. These lenses are covered with about 20m of sediment. These sediments are quite undisturbed and they are layered subparallel to the seabottom. The blank zones follow the slope. These sediments are only disturbed by short fractures in distances of a few meters.

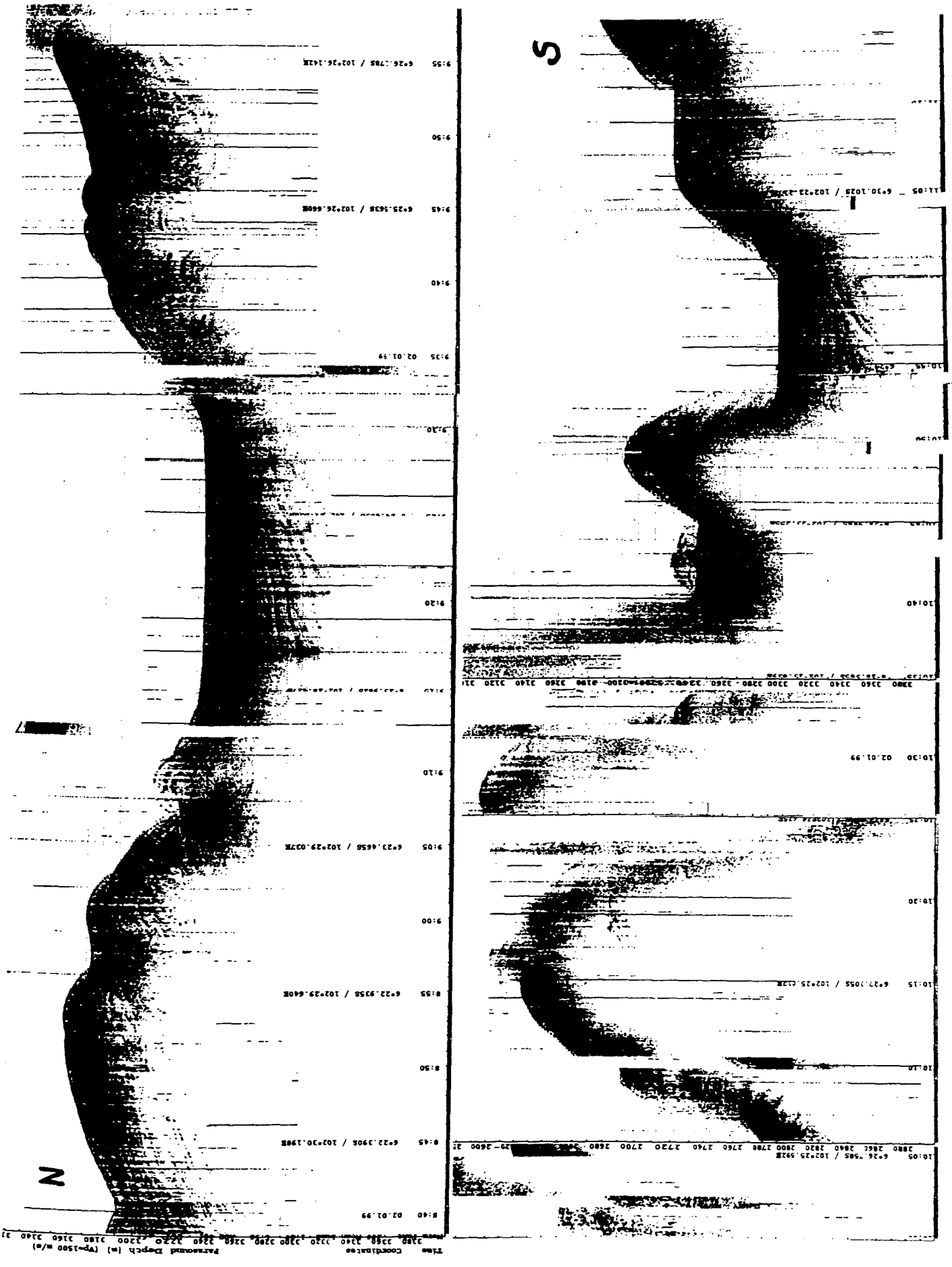

Figure 6.2.1: Parasound anologue recordings along profile 1 of a faulted zone at the accretionary wedge. This section shows typical ridge deformation and portions of layered sediments inbetween.

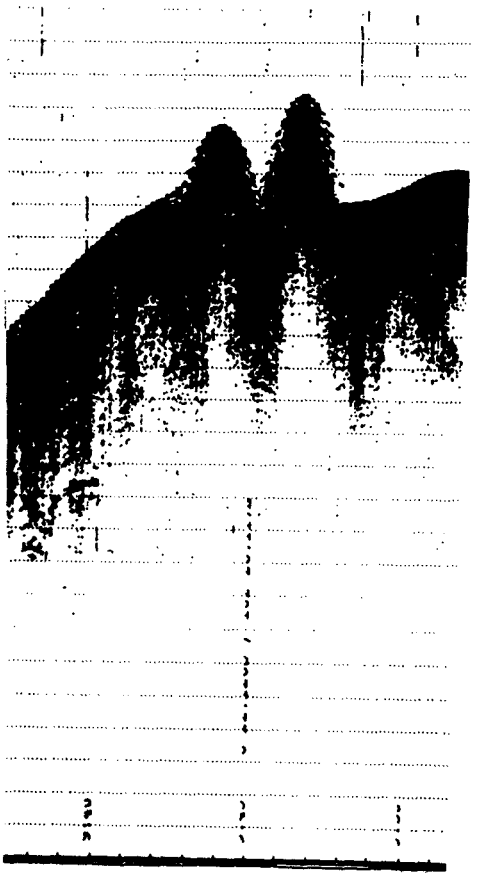

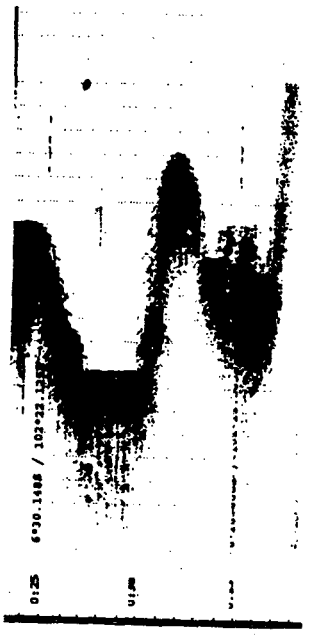

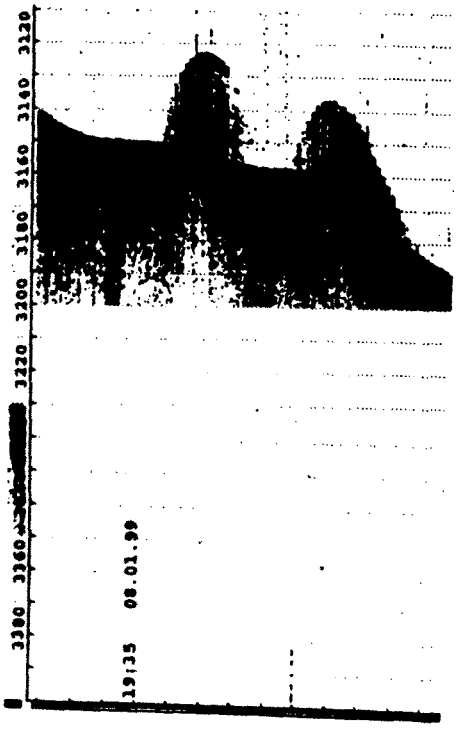

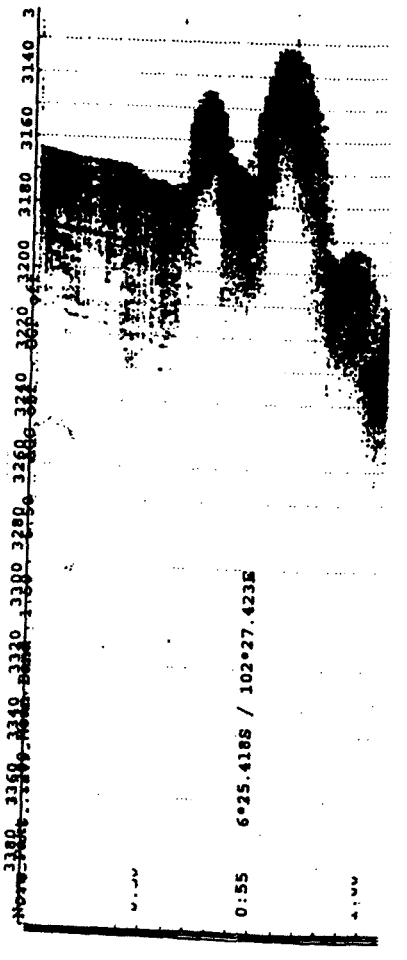

Figure 6.2.2: Parasound recordings of typical mud diapirs across the entire accretionary wedge.

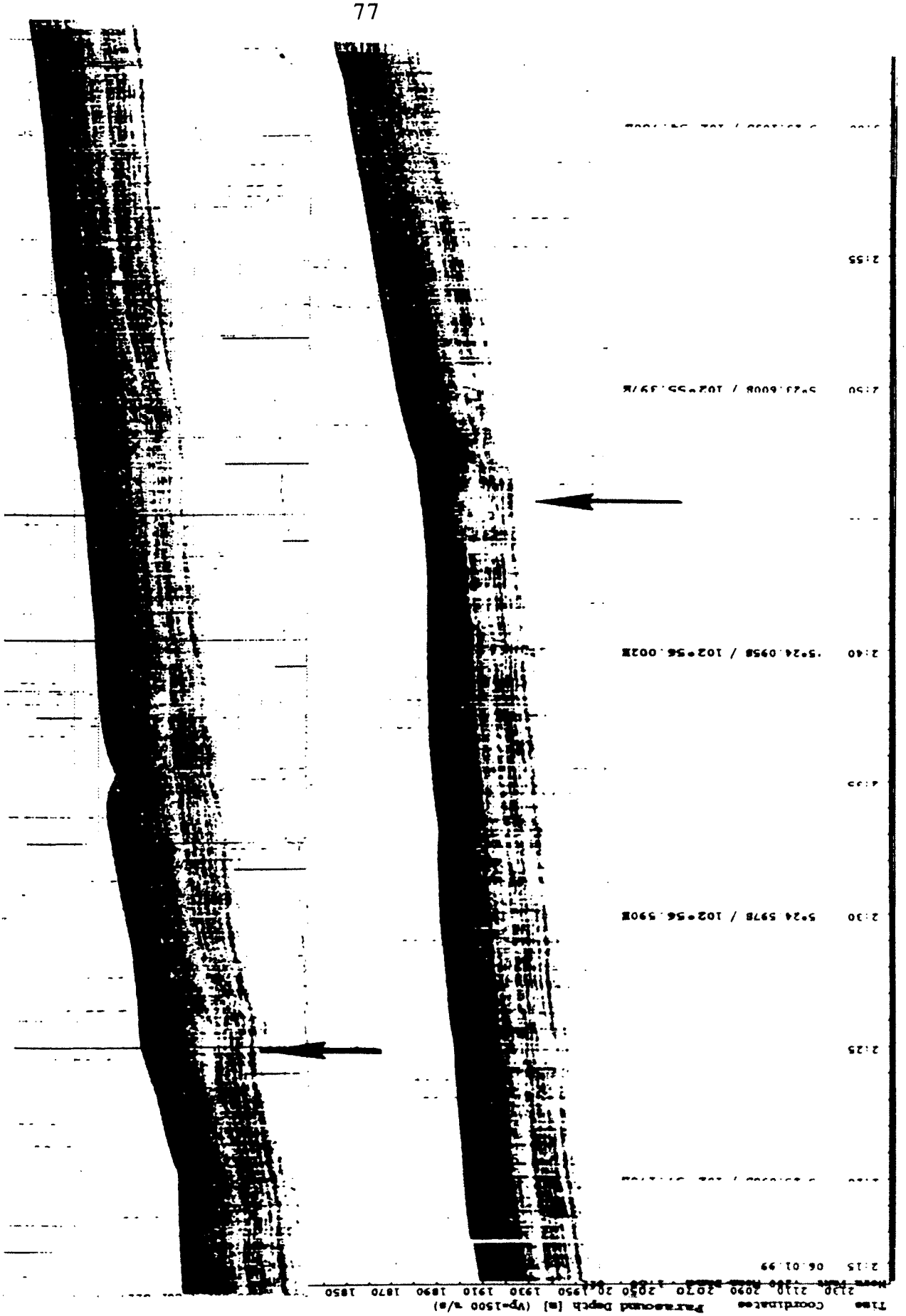

Figure 6.2.3: Parasound data recorded at the NW end of line SO138-3. Blank zones marked by an arrowhead are interpreted as gas lenses.

6.3 SEISMIC WIDE-ANGLE WORK

6.3.1 INTRODUCTION

(E. Flüh)

The major work during SO138-GINCO II was devoted to the collection of seismic wide-angle data. A total of 97 OBH and 14 OBS were deployed along 9 lines, one of the lines (SO138-9) being a short test line for a new airgun array. All instruments except one were safely recovered. The rgwvertical array (OBH 100) broke after 200 m of cable had been taken on board. The remaining part was successfully recovered using a dredge hook. A summary of all deployment sites and profiles is shown in Figure 6.3.1, technical details are summarized in Appendix 9.1. The data quality is variable, on some of the strike lines it is excellent. We experienced more problems with recording errors than usually, mainly with the deepest deployments near the trench. Some of these failures were apparently due to mechanical weaknesses of the new equipment (pressure cylinders and recorders), which had never been tested in deep water before. All instruments that failed to record data on deployment worked fine in the laboratory.

Shooting was performed without any problems or delays using the well tuned BGR airgun array. No malfunctions of the guns were observed. Details on the profiles with a total number of more than 11.000 shots along the profiles with a total length of 1860 km are given in Appendix 9.2.

The short three-channel streamer was deployed along all profiles. After some initial malfunction of the recording system due to noise in the ship's power supply it provided valuable data, especially when shooting in previously unexplored regions.

New equipment like the long vertical array or a modified OBS, a deep towed streamer and a high resolution airgun array were tested during the cruise with variable success, but promise possible improvements on future cruises.

All seismic data collected were copied, processed and plotted during the cruise. They are stored in standard SEG-Y format and copies could be made for the participating institutions which created a heavy load on workstation space and time. The excellent cooperation between the scientific parties onboard and the ship's crew enabled a very smooth operation. Preliminary interpretations were made for some of the profiles, especially for those collected early during the cruise. In the following chapters the applied processing (chapter 6.3.2) and modelling techniques (chapter 6.3.3) are described first. This is followed by a description of each profile, which includes the chronology of the experiment (all times given correspond to local times), the most important data and some first initial results. Naturally, these first results should be read with great care. Further processing, and especially the incorporation of the MCS data from cruise SO137 (Reichert and shipboard scientific party, in prep.) will lead to a much more detailed image of the crustal structure and its variation along the Sunda Graben and margin. The data needed to achieve the aims of the project were acquired during the cruise and the interpretation to be done in the forthcoming months is based on a solid foundation. Once more, it became apparent that the combination of MCS (cruise SO137) and wide-angle seismic data, together with potential field and hydroacustic data, rules out many of the ambiguities inherent to a single data set. In this respect, also the results of the forthcoming cruise aimed at geological and geochemical investigations on the Sunda Trench and margin (SO139) will provide significant additional information.

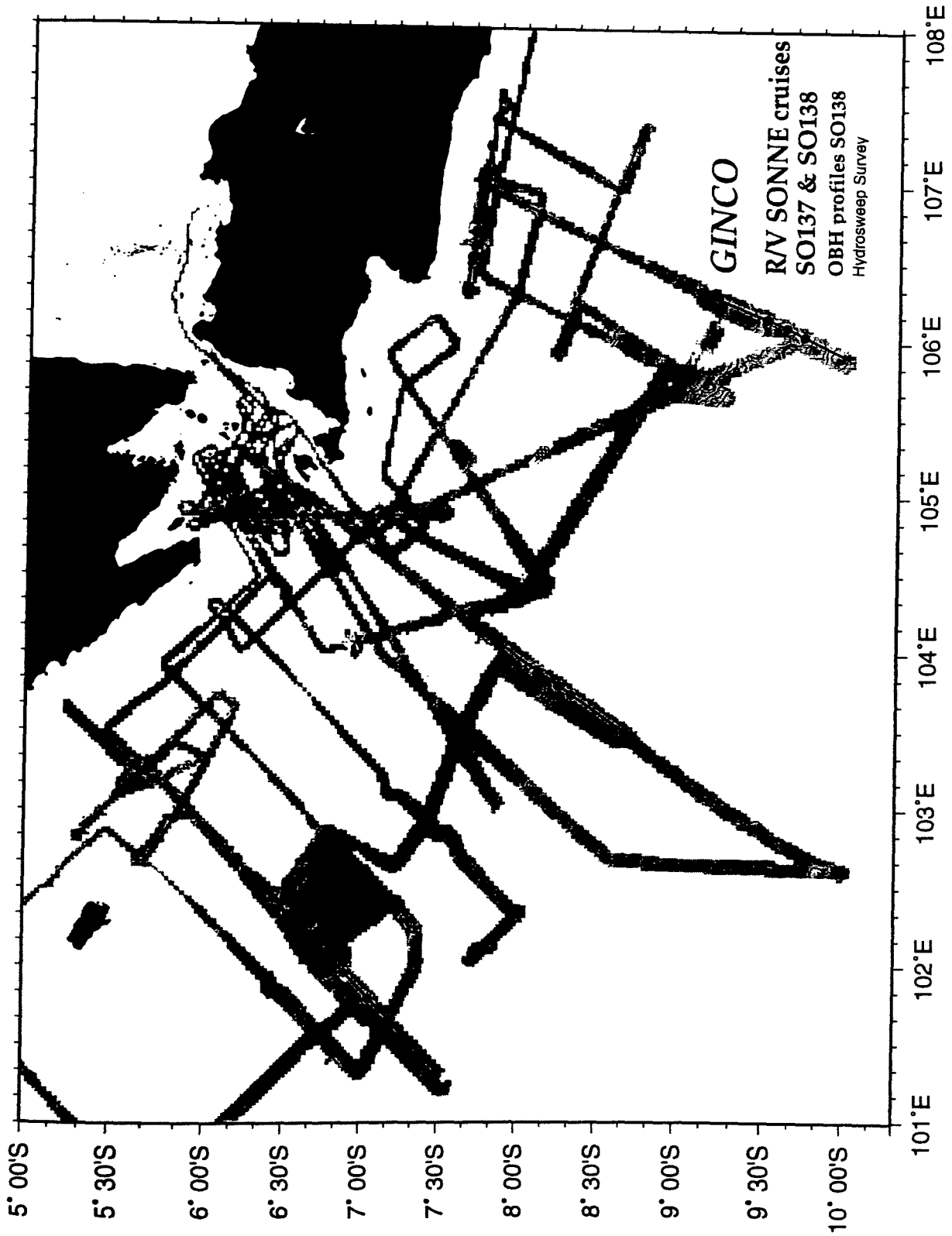

Figure 6.3.1: Location map of OBH-positions and seismic lines with results from swathmapping during SO137 and SO138 underlain.

6.3.2 SEISMIC PROCESSING AND DATA EXCHANGE

(H. Lelgemann)

6.3.2.1 MINI-STREAMER DATA

Raw data: As a data example, channel 3 of profile SO138-04 is presented in Figure 6.3.2.1.1.

Frequency filtering: Due to the limited onboard time, no extensive testing of different parameters for the frequency filter was applied. Instead, we relied on filter parameters which had been used during recent cruises (e.g. SO 131 at the Ninety East Ridge (Flueh and Reichert, 1998)) and which had proved to be especially stable when applied to the mini-streamer data. These comprised an Ormsby frequency filter, which is characterized by linear slopes. The filter is described by four corner frequencies:

Lower stop/ pass band boundary and upper pass/ stop band boundary. As a broad frequency range is contained in the data, time dependent filtering was applied based on the seafloor topography.

Deconvolution: To improve the temporal resolution of the seismic data a deconvolution is applied to compress the basic seismic wavelet. The recorded wavelet has many components, including the source signature, recording filter, and hydrophone response. Ideally, deconvolution should compress the wavelet components, leaving only the earth's reflectivity in the seismic trace. The deconvolution algorithm which was applied is the Wiener deconvolution in sucessive trace segments which is based on the following assumptions:

1. The earth's reflectivity is 'white'.
2. The wavelet shows the minimum-delay phase behavior

As in near-vertical data the amplitude spectra of the seismic traces vary with time, the deconvolution must be capable of following these time variations. Each trace is therefore divided into 3 s data gates with a 1.5 s overlap, in which time-invariant deconvolution operators are computed from the autocorrelation function of the data segments and subsequently applied to the data. As the signal-to-noise ratio tends to be relatively poor especially at later travel times, the autocorrelation function is laterally averaged over 11 traces. The overall deconvolved trace results from a weighted merging of the independently deconvolved gates. For the dataset collected during SO138, an operator length of 240 ms and a predictive length of 80 ms was chosen.

After deconvolution a time variant Ormsby filter was applied. As the depth of the seafloor changes rapidly along the seismic lines, each trace was staticly corrected to a fictive seafloor travel time of 11 s based on the water depth. This information is available in the trace headers. After applying the time variant filter a spherical divergence correction was used with an interval velocity of 1500 m/s at the seafloor and 6000 m/s 2 s below the seafloor followed by a trace normalization along the seafloor event. After this spatially invariant pre-processing each trace was shifted back again to the original travel times, NMO corrected by water velocity and stacked along the profile. After stacking a Butterworth filter was applied for the final data representation. This filter shows only a small amount of ringing compared to other filter techniques. The Butterworth filter is characterized by a lower and upper corner frequency of 8 and 90 Hz. At these frequencies the amplitudes are reduced by a factor of 0.5.

Processing sequence:

- Input: SEGY-data, 4 ms sample rate, with complete geometry information
- Gated Wiener deconvolution: gate length 3s, overlap 1.5 s, 11 traces for averaging the autocorrelations, operator length 240 ms, prediction interval 80 ms
- static correction to a fictive seafloor travel time of 11 s
- time dependent Ormsby frequency filter (on time shifted traces)

100%-time TWT (s)	lower stop/pass	upper pass/stop band (Hz)
11.3	7/10	90/110
11.6	7/10	50/60
14.0	5/8	30/40

- spherical divergence correction based on interval velocities: 1500m/s at 11 s TWT time and 6000 m/s at 13 s TWT time (on time shifted traces)
- trace normalization: 2 s window length with a center time at 11 s TWT time
- static correction to original travel times
- nmo-correction based on water velocity of 1500 m/s
- stacking in offset bins along the profile
- Butterworth frequency filter: 8-90 Hz

Processed data: A comparison of the pre-processed data in Figure 6.3.2.1.1 to the unprocessed data in Figure 6.3.2.1.2 shows a clear reduction of noise especially at later traveltimes. The ringing resulting from the shots could be compressed. The noise within the water column was eliminated fairly well. The stacking of the different channels further enhanced the data quality.

6.3.2.2 OBH/OBS-DATA PROCESSING

Raw data: As a data example, OBH station 01 of profile SO138-01 is shown in Figure 6.3.2.2.1.

Frequency filter : The selection of frequency filter parameters was based on experience from earlier cruises on which the well tuned BGR airgun array was also used as a source. An Ormsby frequency filter was used to suppress unwanted frequencies of the seismic energy. This filter is comprised of four corner frequencies:

Lower stop / pass band boundary and upper pass / stop band boundary. As a broad frequency range is contained in the data, a time and offset dependent filtering was applied.

Deconvolution: To improve the temporal resolution of the seismic data a deconvolution method is applied to compress the basic seismic wavelet.

As in wide-angle data the amplitude spectra of the seismic traces vary with time and offset, so that the deconvolution must be capable of following these time and offset variations. Each trace is therefore devided into 2 s data gates with 1 s overlap, in which time invariant deconvolution operators are computed from the autocorrelation function of the data segment and subsequently applied to the data. The overall deconvolved trace results from a weighted merging of the independently deconvolved gates. For the data collected during SO138 an operator length of 480 ms with a predictive length of 80 ms was chosen.

After deconvolution a time variant Ormsby filter was applied. As the seafloor depth changes rapidly along the seismic lines, each trace was staticly corrected to a fictive seafloor

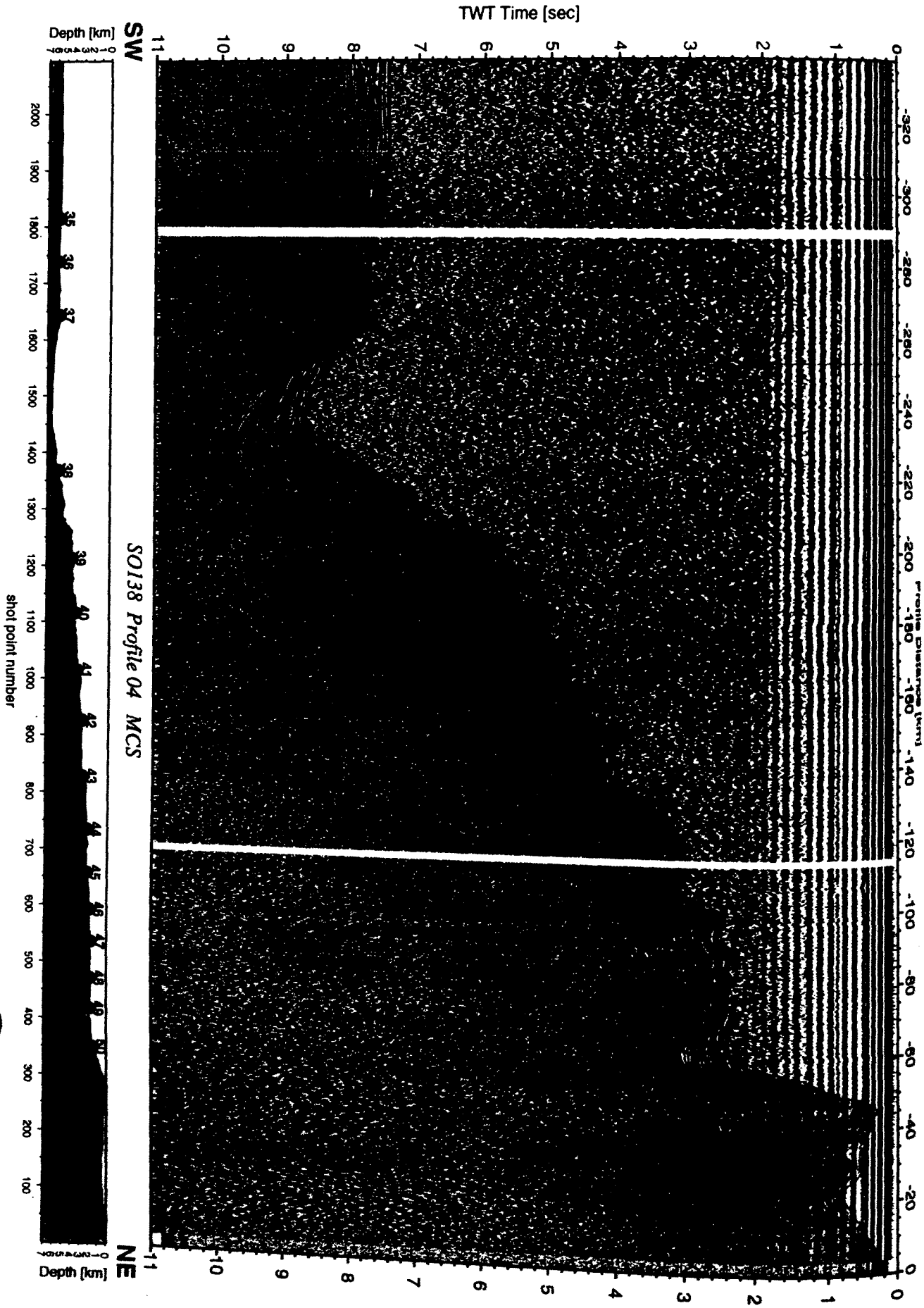

Figure 6.3.2.1.1: Seismic section from un-processed MCS channel 3, Profile 04.

Figure 6.3.2.1.2: Seismic section from pre-processed MCS channel 3, Profile 04.

travel time of 6 s based on the water depth. This information is available in the trace headers. After application of the time and offset variant filter depending on the applied reduction velocity the data were shifted back to their original travel times.

Processing sequence:

- Input: SEGY data, 5 or 4 ms sample rate with complete geometry information
- low cut frequency filter 5Hz with 48 db slope
- Gated Wiener deconvolution: gate length 2s, overlap 1 s, operator length 480 ms, prediction interval 80 ms
- static correction to a fictive seafloor travel time of 6 s
- time and offset dependent Ormsby frequency filter (on time shifted traces with a reduced time scale of 6 km/s):

offset (km)	100%-time (s)	lower stop/pass	upper pass/stop (Hz)
0	7.5	3/5	35/50
0	9.5	3/5	20/40
0	11.5	3/5	10/20
30	4.755	3/5	35/50
30	6.755	3/5	20/40
30	8.755	3/5	10/20
60	2.01	3/5	35/50
60	4.01	3/5	20/40
60	6.01	3/5	10/20
90	0.005	3/5	35/50
90	1.265	3/5	20/40
90	3.265	3/5	10/20
120	0.005	3/5	35/50
120	0.01	3/5	20/40
120	0.52	3/5	10/20

- time and offset dependent Ormsby frequency filter (on reduced time scale with 8km/s):

offset (km)	100%-time (s)	lower stop/pass	upper pass/stop (Hz)
0	4.0	3/5	35/55
0	6.0	3/5	20/35
0	8.0	3/5	10/20
40	2.0	3/5	35/55
40	0.5	3/5	20/35
40	1.0	3/5	10/20
60	2.0	3/5	35/55
60	1.0	3/5	20/35
60	0.0	3/5	10/20

- linear time and offset scaling (on unreduced time scale only for plotting).

Processed data: Comparison of the pre-processed data in Figure 6.3.2.2.1 to the unprocessed data in Figure 6.3.2.2.2 shows a clear reduction of the high frequency noise on the far offset traces and a compression of the wavelet signal. For picking of events and model building by raytracing both sections were used to keep all the available seismic information.

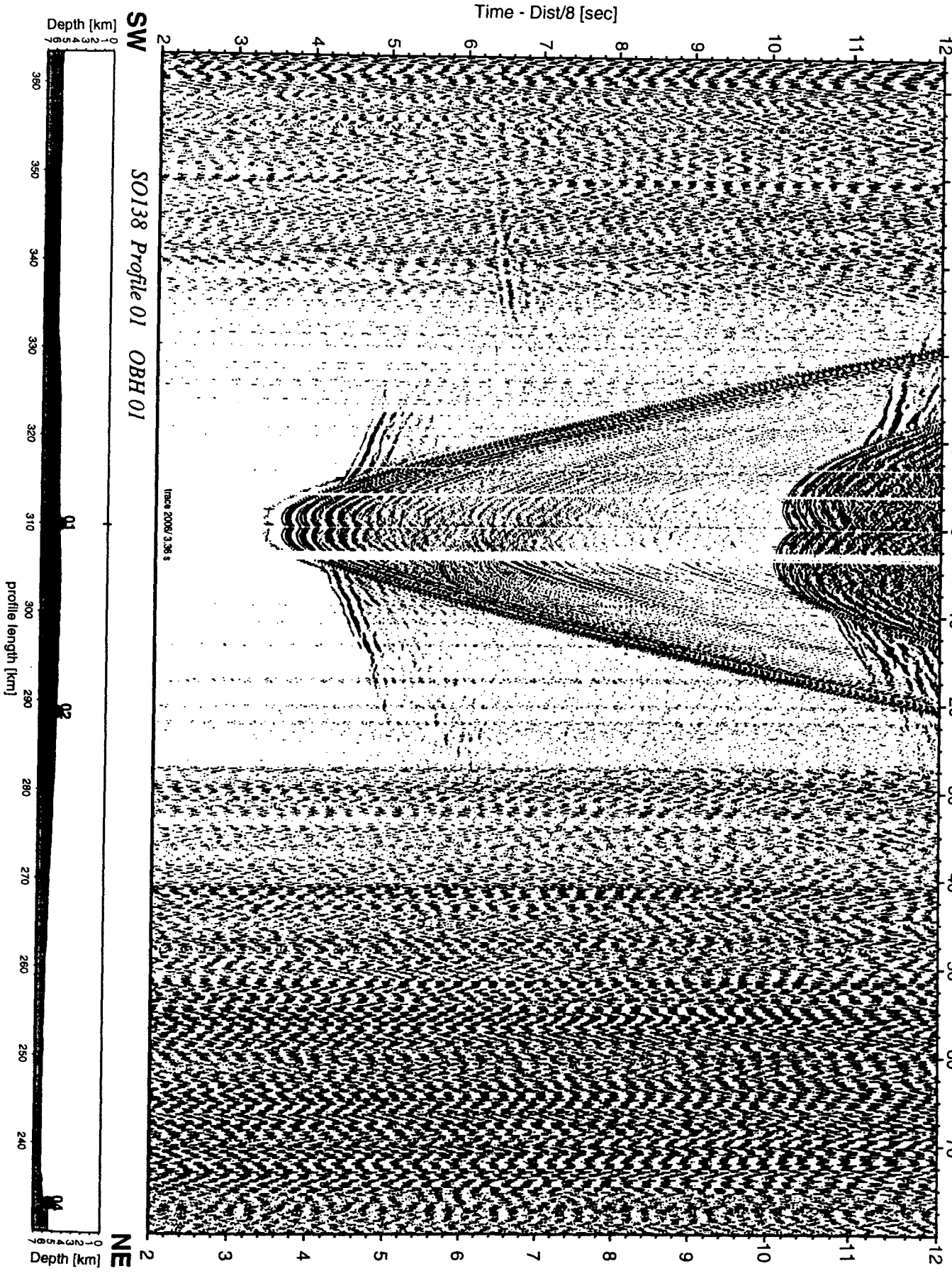

Figure 6.3.2.2.1 Un-processed record section from OBH 01 , Profile 01.

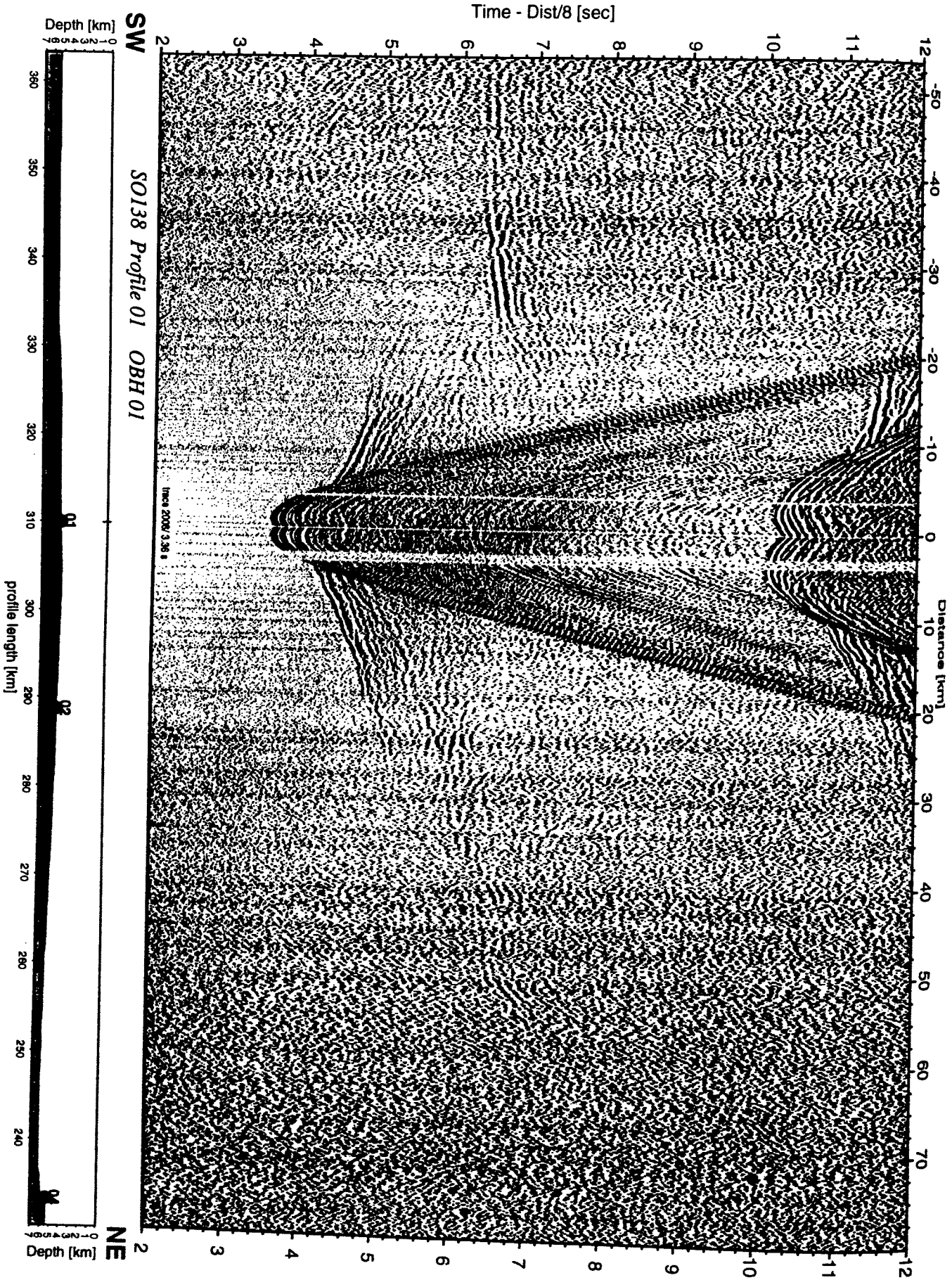

Figure 6.3.2.2.2 Pre-processed record section from OBH 01 , Profile 01.

DATA EXCHANGE

For exchange of the OBH/OBS data, the SEGY-format on disk in a Sun-tar-format was chosen. The trace length for the raw data is 20 s, a reduction velocity of 8000 m/s was used. The complete geometry information is positioned in the SEGY-trace header:

Inform.	Receiver No.	Shot No.	Offset	Red. Vel.	Water Depth
Byte:	13-16	21-24	37-40	93-94	61-64

6.3.3 WIDE-ANGLE DATA MODELLING

(The Modelling/Interpretation Group)

The OBH/OBS data were analyzed for sediment crust and upper mantle velocity structures. The modelling sequence of the wide-angle data involves three different steps:

A) Picking: The traveltimes of the observed phases are picked interactively on the workstation's screen using Seismic Unix Software. This provides ASCII files containing offsets and traveltimes of phases for each record, which are used for the modelling.

B) 1-D modelling: 1-D velocity-depth modelling was performed on some of the record sections. This first approach to determine the velocity structure along the different lines allows a definition of preliminary velocity-depth models, which are used as starting point for 2-D modelling. The software used for this purpose is an interactive program "MacR1D" (Luetgert, 1992) for calculating travel-time curves from 1-D velocity-depth functions. It allows a quick manipulation of velocity-depth functions, the resulting travel times can be seen immediately. Thus, "MacR1D" gives useful insights into the effects of changing gradients, low-velocity zones, etc.

C) 2-D modelling: Models have been created for some of the lines. The water depth is taken from UKOOA-files. The models are capable of predicting the correct offset/time of as many of the observed phases as possible. During the cruise, we used the program "MacRay" (Luetgert, 1992), an interactive application for calculating travel-time curves from 2-D velocity models. It is based upon the RAY84 and RAY86 seismic raytracing programs written for the DEC VAX/VMS environment and adapted to the Apple Macintosh graphical interface for display and manipulation of the velocity models.

Velocity models are defined by two or more interfaces extending across the model. Any pair of successive interfaces describes a layer, within which the velocity may be defined in terms of the velocity at the top and bottom of the layer. Within any layer the velocity may be inhomogeneous but continuous. First or second order discontinuities in velocity may occur at the interfaces. A ray tracing algorithm calculates the propagation of rays within a layer by the stepwise integration of a system of first order differential equations (Cerveny et al., 1977). Lithologic interfaces are represented in the model as first or second order velocity discontinuities. When an interface is encountered in the calculation of a ray, Snell's law is applied and the calculation is continued. "MacRay" is very useful for quick manipulation of velocity models.

6.3.4.1 PROFILE SO138-01

(T. Leythaeuser, S. Husen, E. Flueh, B. Schreckenberger)

Profile SO138-011 is a dip line across the Sumatra margin and trench and was chosen coincident with MCS line SO137-12, but was extended seawards across the trench to ensure full coverage of the downgoing oceanic plate. The location of the OBH and the extent of shooting is shown in Figure 6.3.4.1.1. A total of sixteen OBH (OBH01 to OBH16) were deployed at variable spacing (5 to 15 nm) between 22:00 on 31 December 1998 and 17:00 on 01 January1999. Exact locations and instrument numbers are summarized in Appendix 9.1.1. Shooting started on 01 January at 20:47. and ended on 03.01 at 12:00. During shooting, the streamer was also deployed, and the section is shown in Figure 6.3.4.1.2. Due to an interference with a laptop, the recording unit of the streamer did not store the data properly, and they could not be recovered. Instruments were recovered within 24 hours starting on 03 January on 17:00. OBH06 acknowledged the releaser command and indicated the right distance and release command, but for unknown reasons it stayed at the seabottom and could not be released. Several instruments had recording errors, which limits the total number of recordings to 11. The signal-to-noise-ratio is rather poor on some records.

The OBH data were processed as described in chapter 6.3.2, the record sections for the data are shown in Figures 6.3.4.1.3 to 6.3.4.1.13.

A line drawing of MCS Profile SO137-12 (Reichert and shipboard sientific party, in prep) with the positions of the successful OBH recordings is shown in Figure 6.3.4.1.14. The plate boundary, accretionary wedge, the outer arc high and forearc basin are clearly seen. The forearc basin is interpreted by Reichert and shipboard scientific party (in prep) to be underlain by a sequence of seaward dipping reflections, and the outer arc high to be composed of ophiolithic rocks (crustal splinters). Preliminary modelling of the wide-angle data was carried out on board of SONNE. Velocities and structure at the crossings of SO138-02 and SO138-03 are in good agreement with the results of SO138-01.

Necessarily, the analyses on board of FS SONNE remain uncompleted. More detailed modeling and in-depth studies still have to be done.

Modeling results and interpretation

P-wave first arrivals, major wide angle reflections and near-vertical reflections were picked from the seismic sections. Based on the traveltime data of these 11 OBH, a ray tracing forward modelling was performed using the interactive *MacRay* program (Luetgert, 1992). Subsequently a velocity model of profile SO138-01 was achieved, which is shown in Figure 6.3.4.1.15 .

At the south-west end of profile SO138-01 OBH01 and OBH02 are located ridgeward of the subduction front. Both OBHs are lying on a small scale bathymetric high, water depth increasing in north-east dircetion towards the Sunda trench and in south-west direction towards the deep sea as shown in the mini streamer data (Fig.: 6.3.4.1.2). On both seismic sections no first arrival of a sedimentary layer can be seen. Instead, on the mini streamer data, a relatively thin sediment sequence can clearly be noticed. For modeling purposes a P-wave velocity of 1.7-1.8 km/s was assumed in the vicinity of OBH01 and OBH02. The very first arrival seen on both sections corresponds to the acoustic basement. To the south-west at an offset of ~25 km this traveltime branch dies out suddenly. This dramatic change in amplitude behaviour is caused by the energy absorbing effect of a sedimentary filled half graben structure south-west of OBH01, clearly visible in the ministreamer data. A similar effect can be recognized towards the north-east, caused by the sediment sequence within the Sunda trench. Modeling reveals a oceanic crust composed of a thin layer 2 (5.5-6.2 km/s) and thicker layer 3 (6.2-7.2 km/s). On the seismic section of OBH01, between 6-7 seconds towards the south-west, a very clear PmP and Pn phase is evident. Less clear, but still visible PmP, and Pn phases could be identified on OBH02 as well and in the north-east OBH01 . Pn phases were modeled using an upper mantel velocity of 8.2-8.3 km/s. PmP arrivals reveal a Moho depth of 17,5 km beneath OBH01. To the south-west, the depth of the Moho decreases to15 km, to the north-east it decreases to 13,5 km. This results to an abnormal thickness

of the oceanic crust of up to 12 km beneath OBH01. The observation of a locally deeper moho suggests that the small scale bathymetric high is not originated by the bulge of the subducting oceanic plate, but furthermore gives evidence of the existance of a seamount or ridge in this area. The half graben south-west of this ridge shows a similar width and depth as the Sunda trench in front of the subduction zone (see ministreamer data, Fig.: 6.3.4.1.2). Its location at the south-east flank of the rigde reveals its tectonic uplift. The increased Moho depth beneath the ridge and the prominent half graben structure may indicate an additional strike-slip fault within the Sunda subduction zone, similar to the huge strike-slip fault systems found landwards of the Sunda trench. Apart from this our observations may as well indicate an early stage in the development of a new subduction zone seawards of the ridge. If a new subduction zone should evolve, the ridge itself would probably not be subducted as it is mergly to large and buoyant, but rather would be obducted and form an ophiolitic complex within the new accretionary wedge. These hypotheses can only be constrained further by new intensive geophysical surveys within the area.

The seismic sections of OBH 05, 07, 08, 09 , located at the frontal part of the accretionary wedge, all show a strong asymmetric pattern, corresponding to the topography of the accretionary wedge and its asymmetrical structures. Three sedimentary layers could be identified in this part of the wedge, all showing nearly no lateral variation. The first layer having a P-wave velocity of 1.7-1.8 km/s, the second one showing velocities between 3.0-3.3 km/s. The third sedimentary layer shows a velocity of 3.7-4.1 km/s at the front of the subduction zone, only gradually increasing to 3.8-4.2 km/s landwards. Beneath OBH05 in a depth of 8.3 km the top of the subducting oceanic plate, corresponding to a 5.5-6.2 km/s velocity layer , is recognized. PmP arrivals suggest a oceanic crustal thickness of only 7 km in this part of the plate. A very clear near-vertical reflection of the top of the lower plate can be found in the seismic section of OBH07 at 6.2 seconds, thus giving good control over the depth of the downgoing slap in this location. Refractions and wide angle reflections of the oceanic crust allow to identify the subducting oceanic plate to a depth of 15 km beneath OBH12. Further to the north-east no oceanic crustal refractions can be found in the seismic sections. Based on a clear PmP phase in the south-west direction of OBH13, the Moho of the downgoing plate is found at a depth of 22.5 km. Further to the north-east no PmP Phases can be seen in the seismic sections.

Underneath OBH11 the sediments of the accretionary wedge reach a thickness of 13.5 km. The sediment velocities remain basically the same as in the frontal part of the wedge, giving no hint of a change within the wedge as suggested by an interpretation of the MCS data along SO137-12 by Reichert and shipboard scientific party (in prep).

The sedimentary velocity of the second layer changes at OBH12 to 2.1-2.6 km/s. Beneath OBH12 the crustal structure changes and in north-east direction a continental crust can be found. North-east of OBH13 a forcarc basin filled with 2 sedimentary layers (1.7-2.4 km/s; 2.8-3.0 km/s) is evident. This basin is underlain by continental crust with a velocity of 6.0-7.2 km/s. No PmP phases of the upper mantle could be found in the seismic sections, so that the Moho is not visible in this part of the profile. Within the forearc basin a layer with 5.4 - 5.9 km/s P-wave velocities can be found. Because of its distinct velocities and its high gradient, this layer could correspond to the seaward dipping reflectors shown in the interpretation of the MCS data of line SO137-12 (Fig.: 6.3.4.1.14).

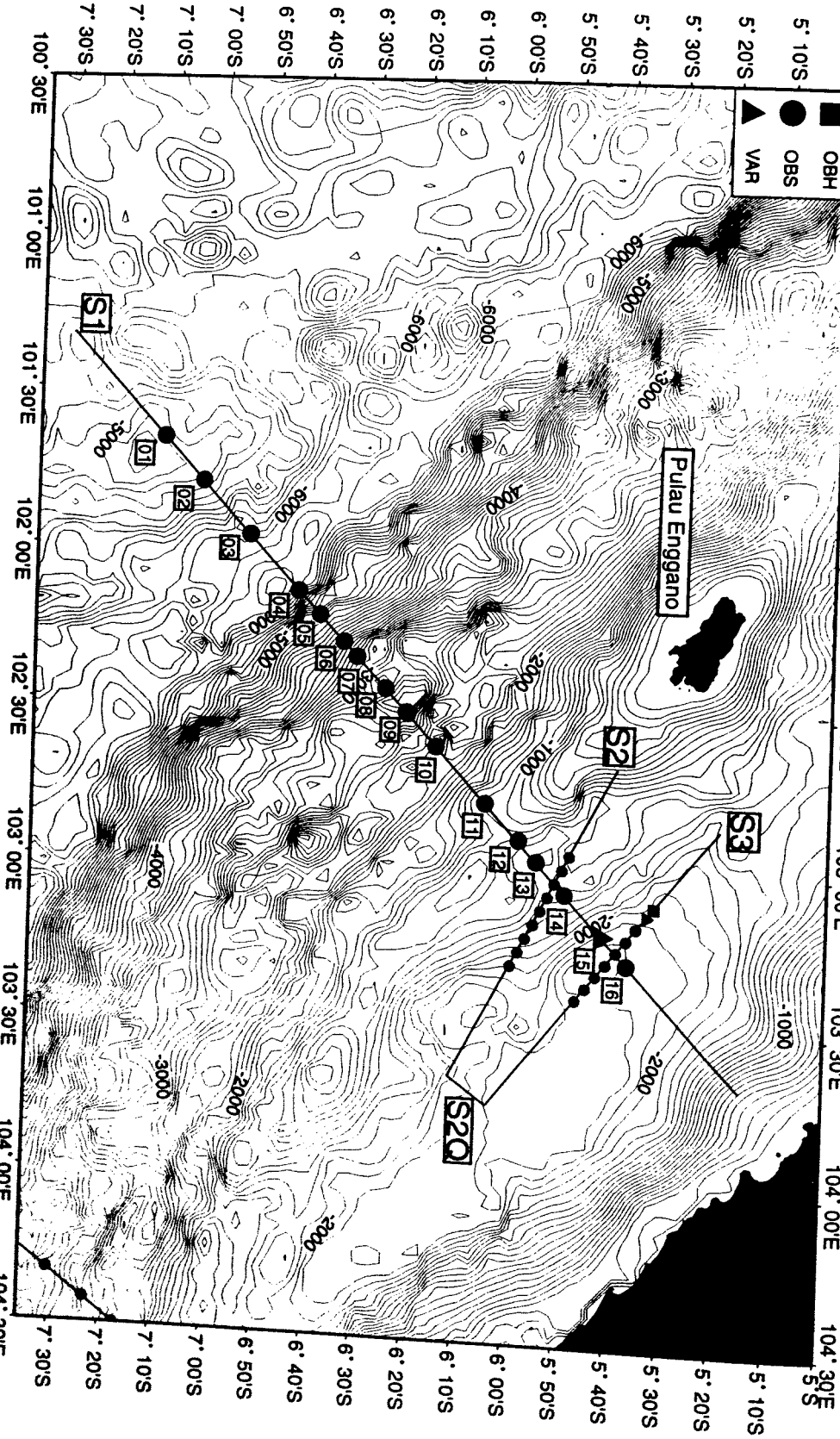

Figure 6.3.4.1.1: Location map of seismic profile S1.

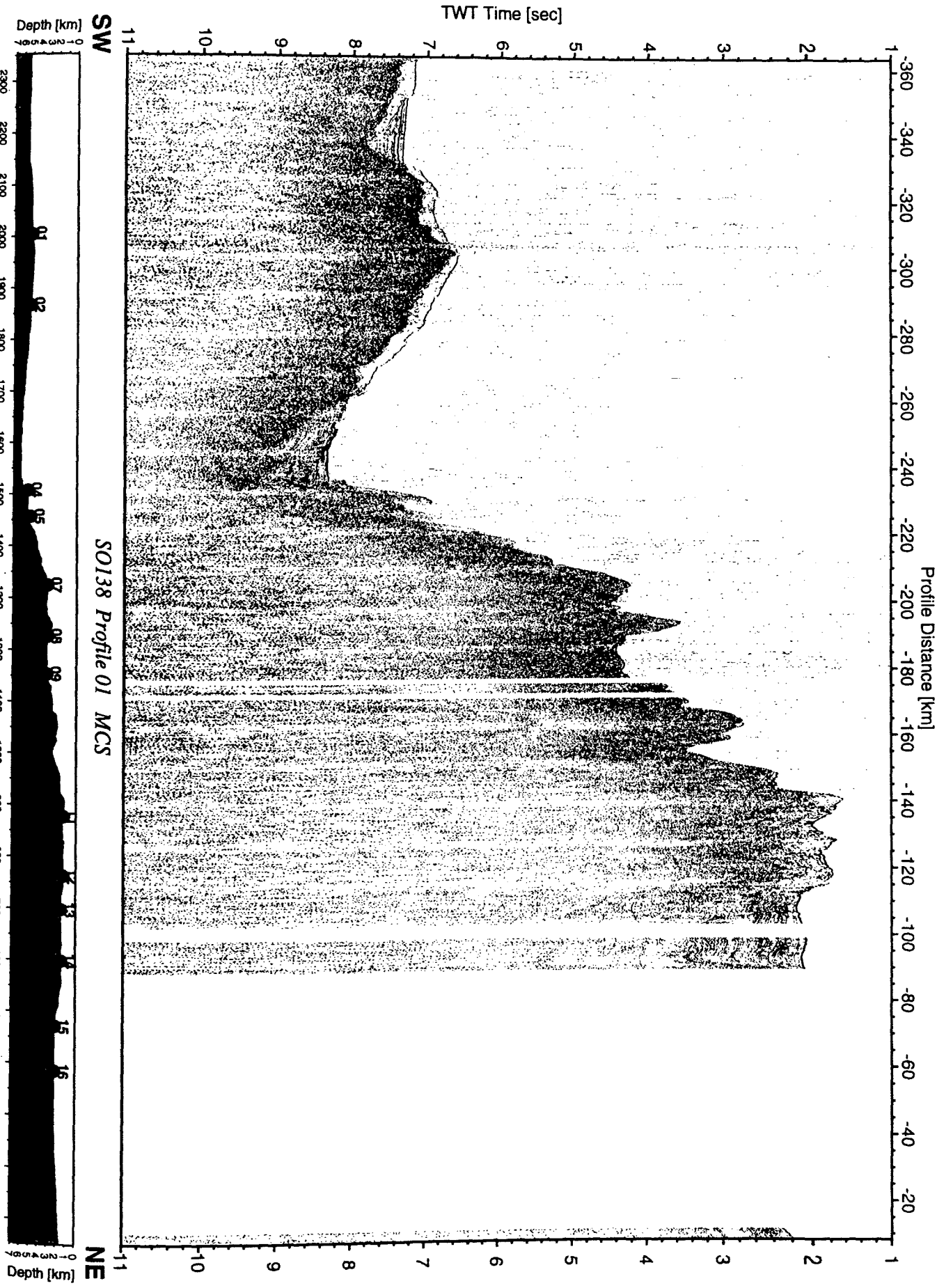

Figure 6.3.4.1.2: Seismic section from MCS stack, Profile 01.

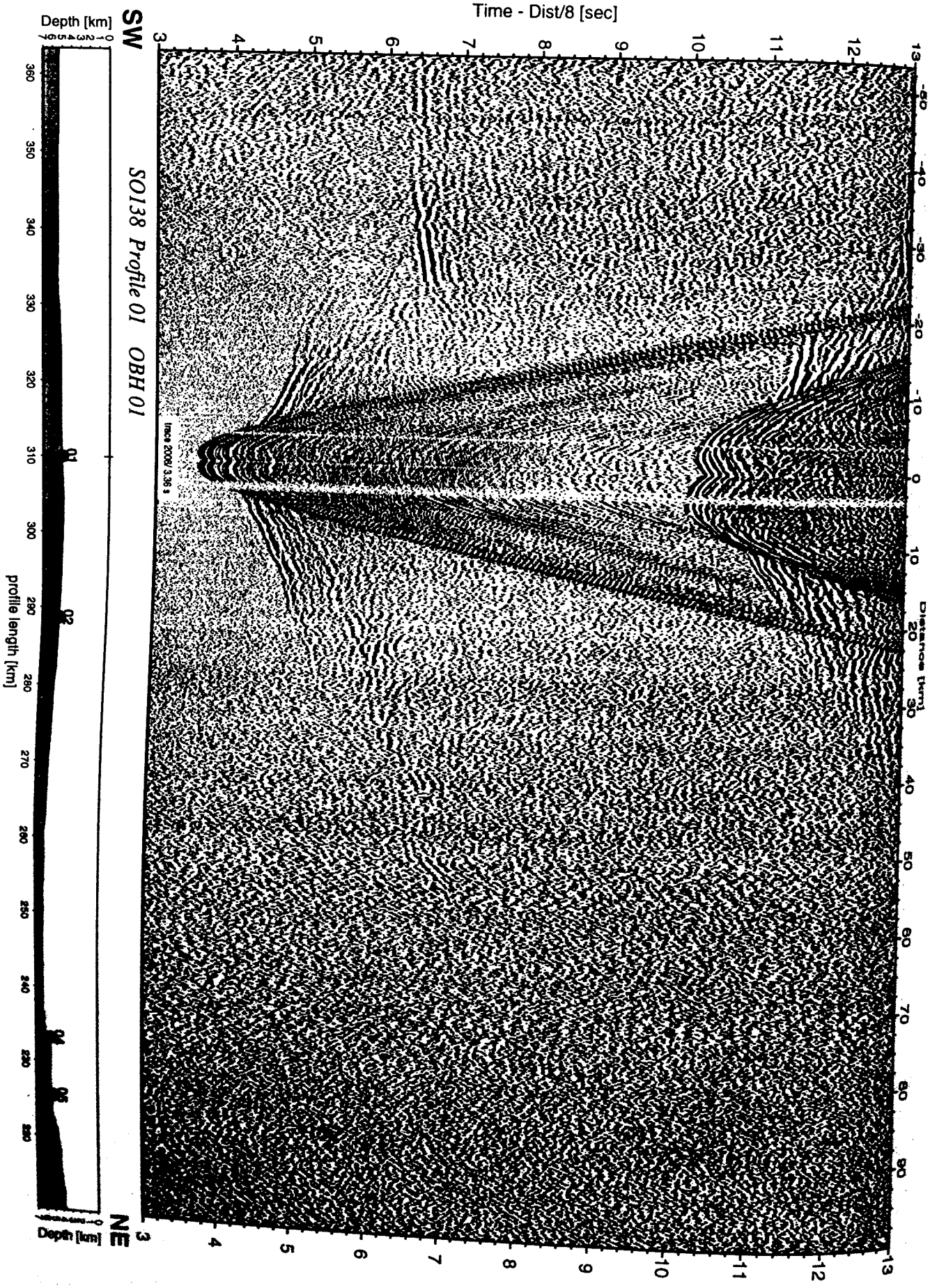

Figure 6.3.4.1.3: Record section from OBH 01 , Profile 01.

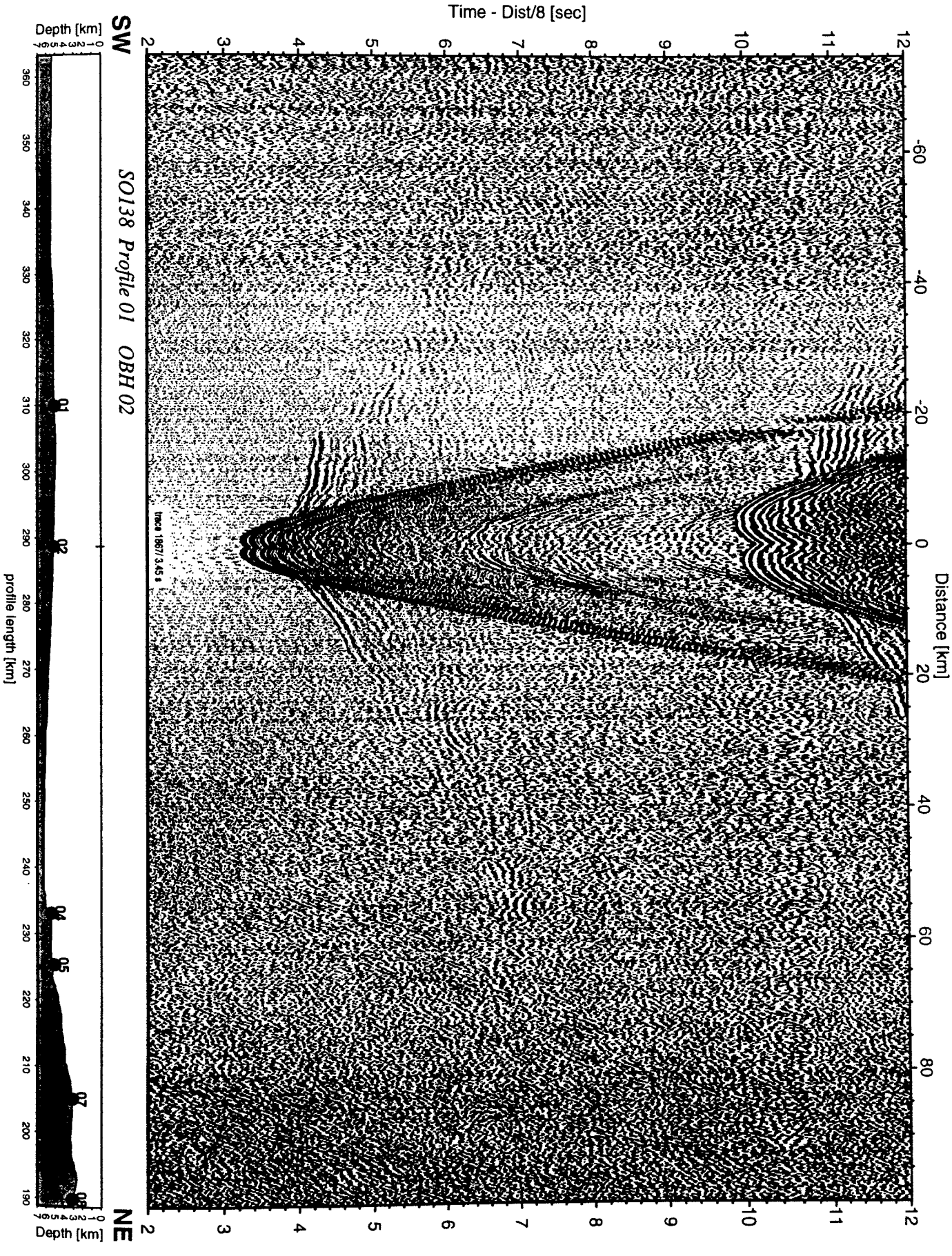

Figure 6.3.4.1.4: Record section from OBH 02 , Profile 01.

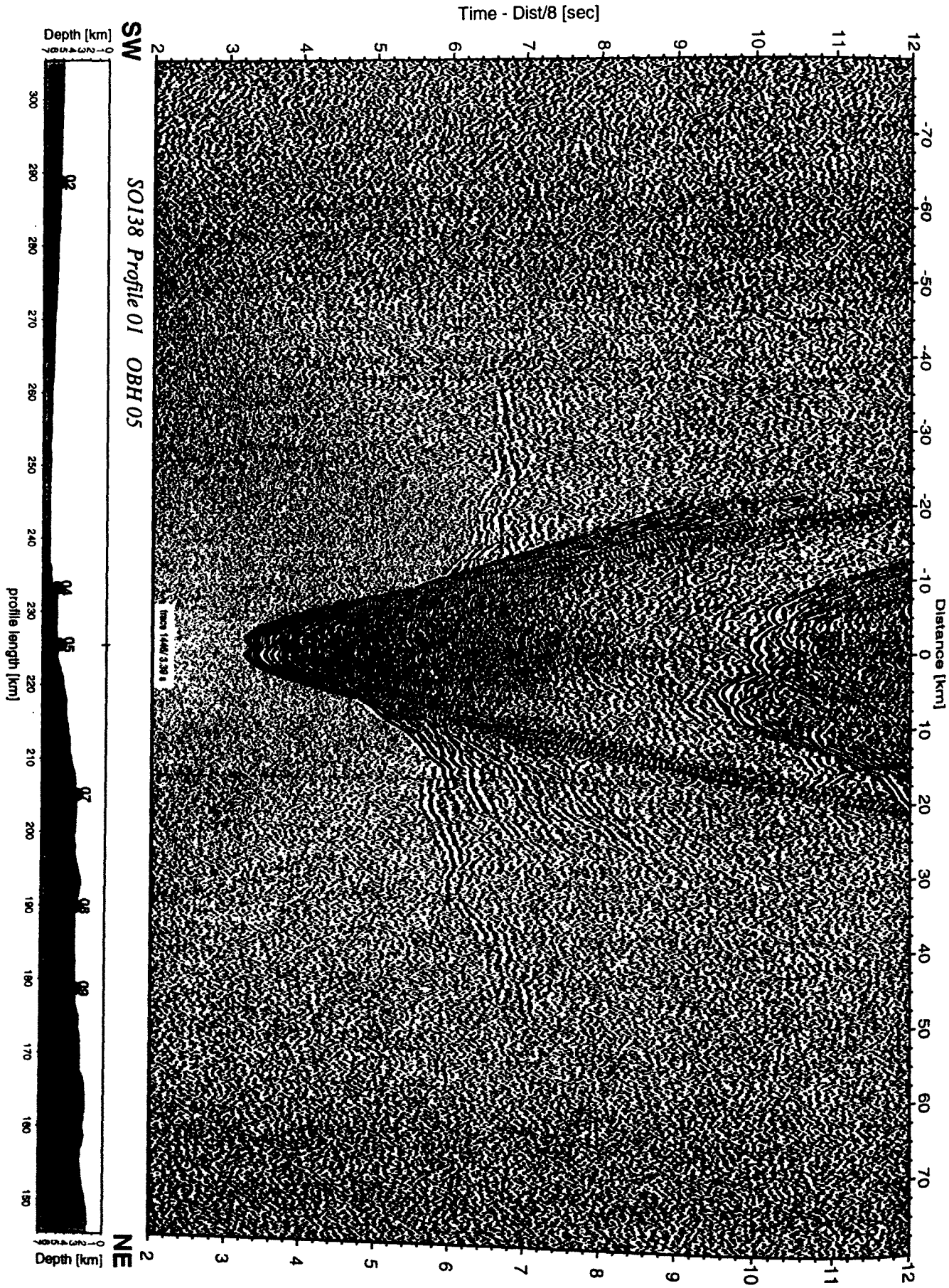

Figure 6.3.4.1.5: Record section from OBH 05 , Profile 01.

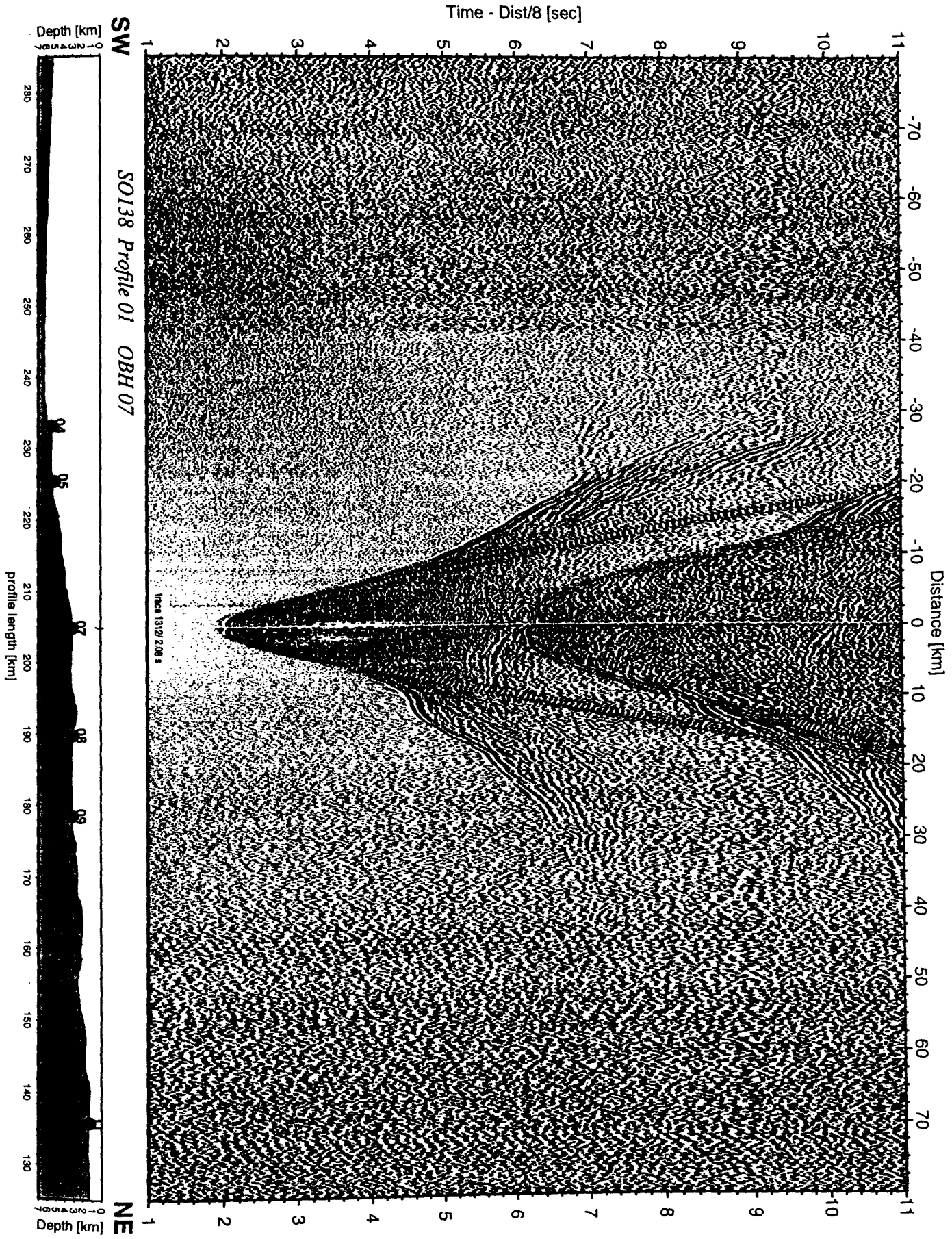

Figure 6.3.4.1.6: Record section from OBH 07 , Profile 01.

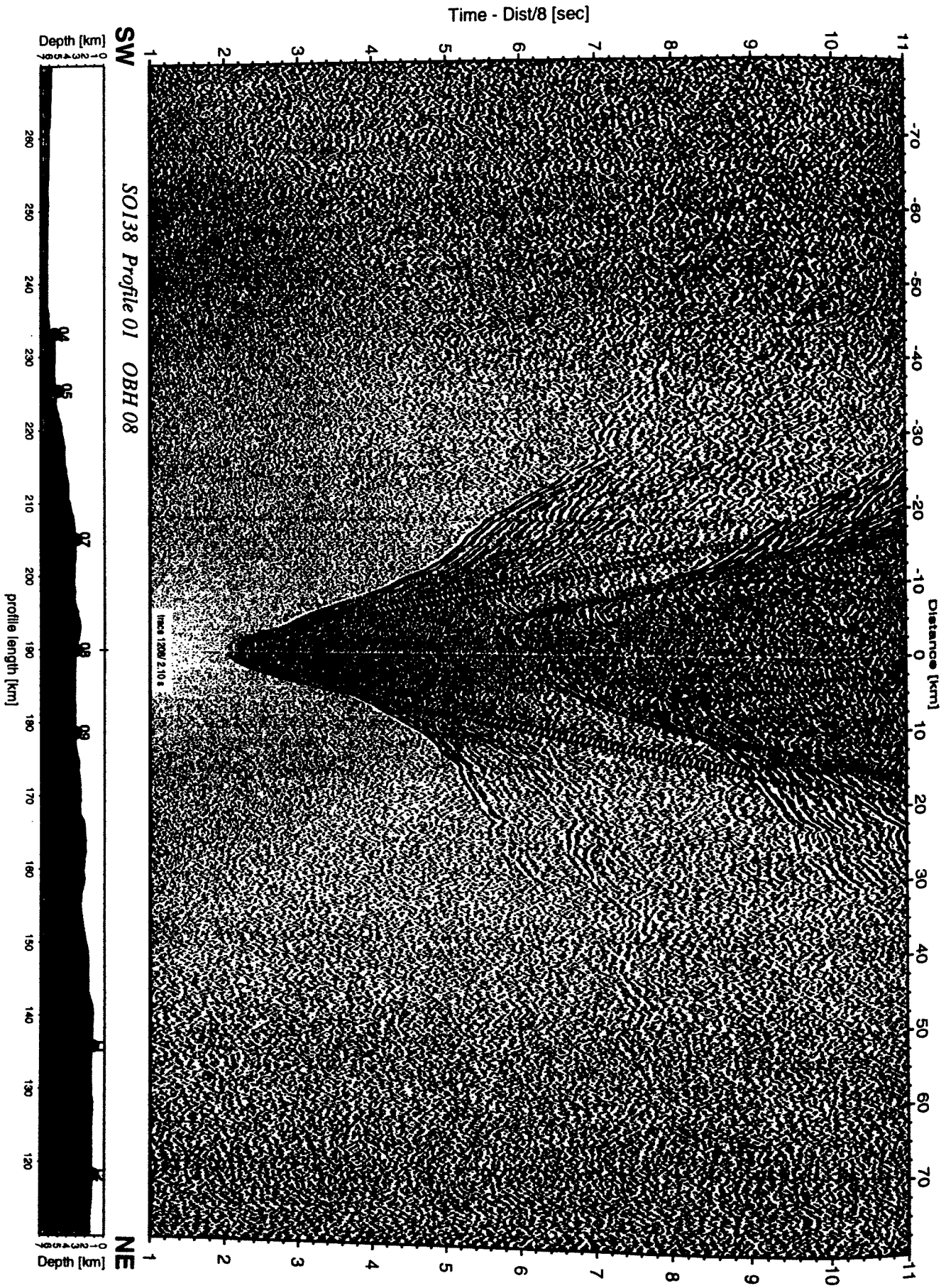

Figure 6.3.4.1.7: Record section from OBH 08 , Profile 01.

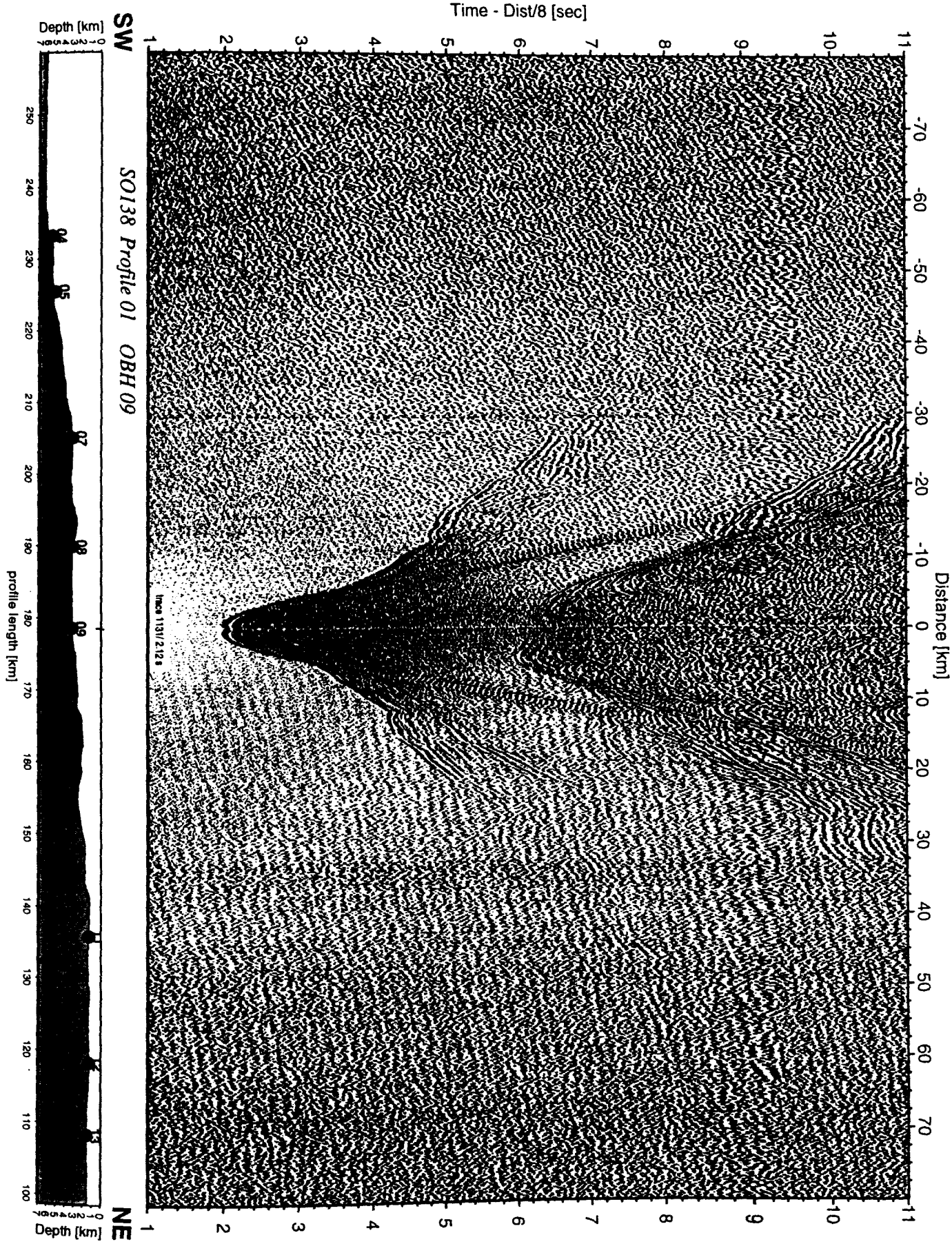

Figure 6.3.4.1.8: Record section from OBH 09 , Profile 01.

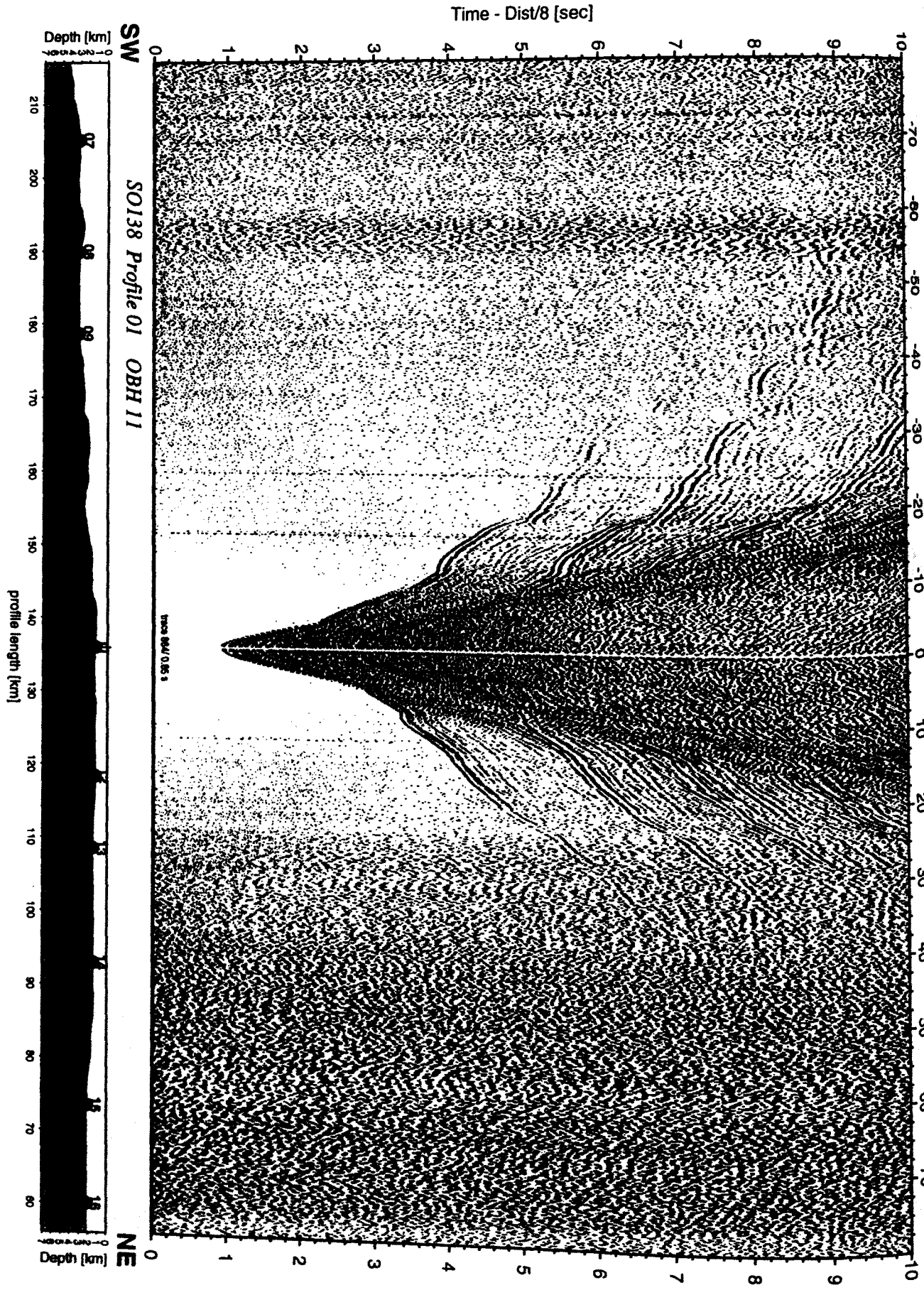

Figure 6.3.4.1.9: Record section from OBH 11 , Profile 01.

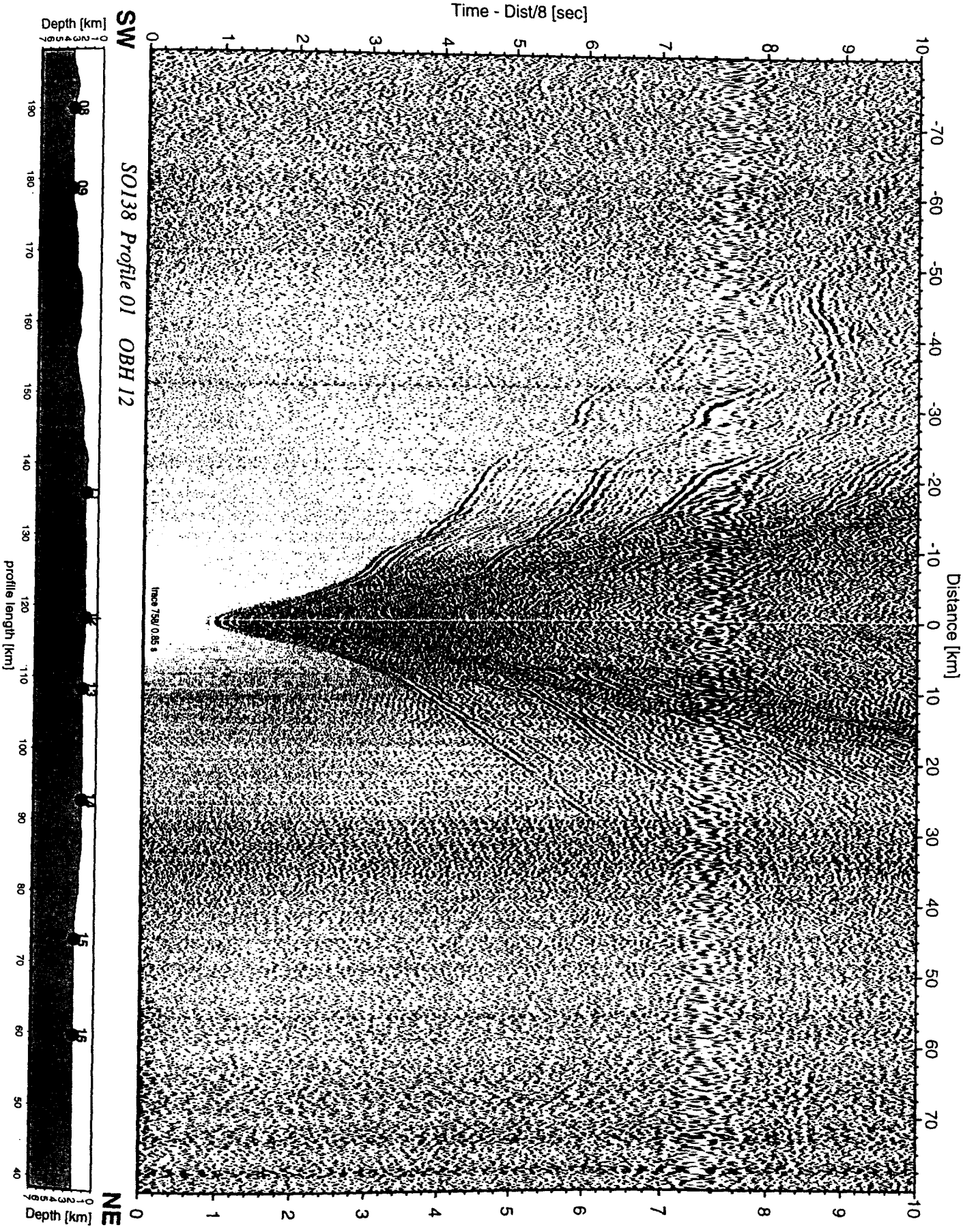

Figure 6.3.4.1.10: Record section from OBH 12 , *Profile 01*.

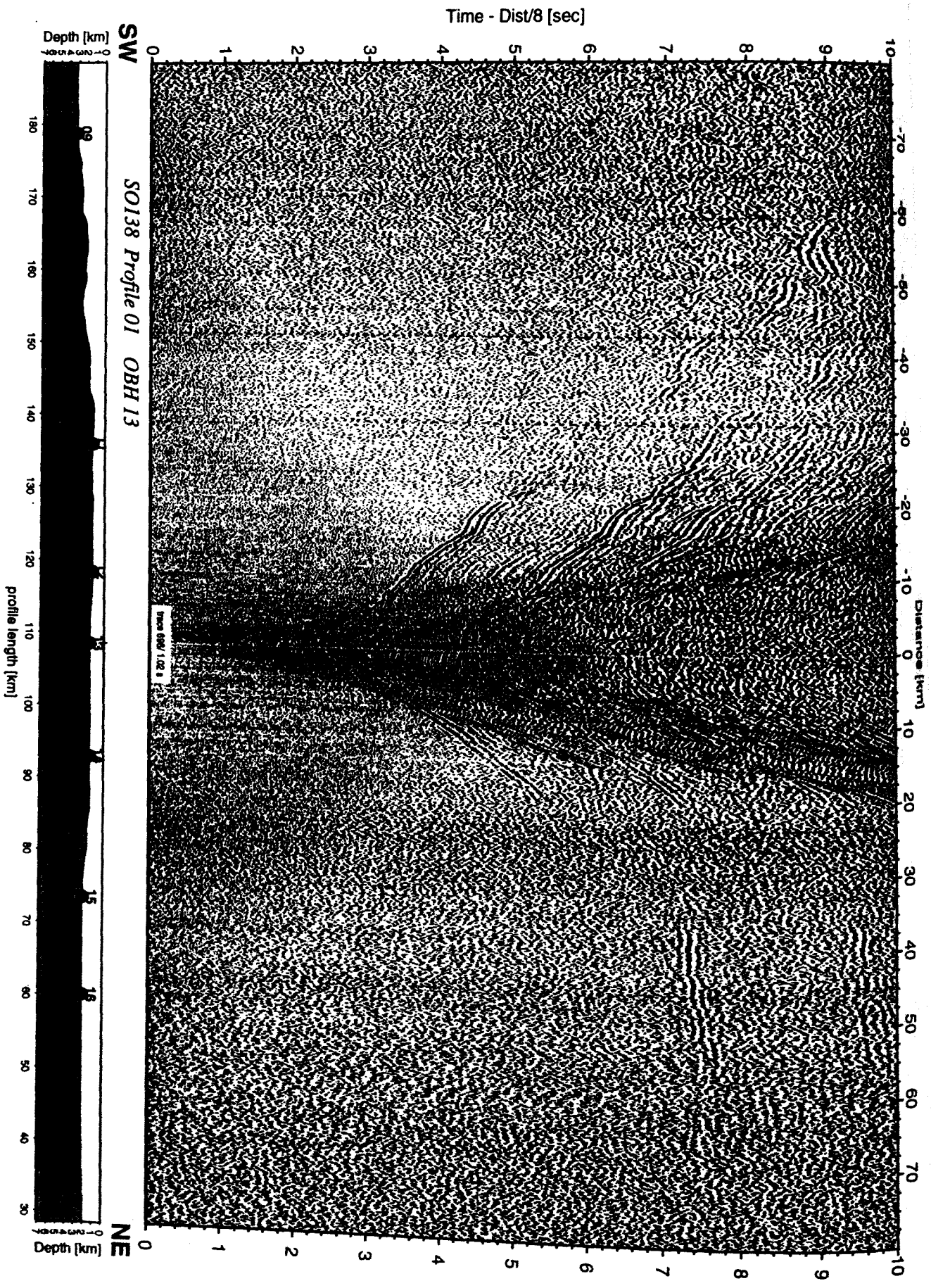

Figure 6.3.4.1.11: Record section from OBH 13 , Profile 01.

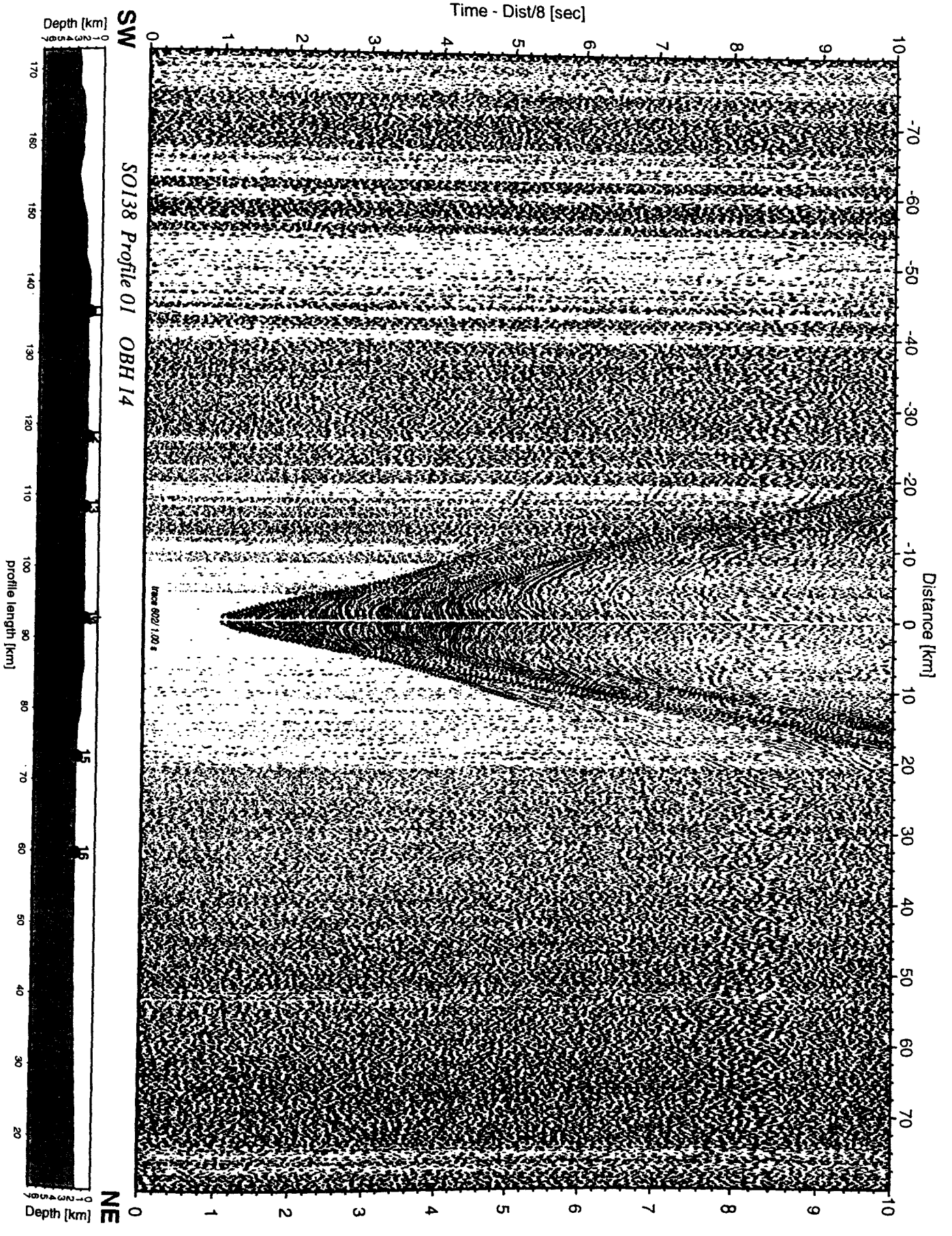

Figure 6.3.4.1.12: Record section from OBH 14 , Profile 01.

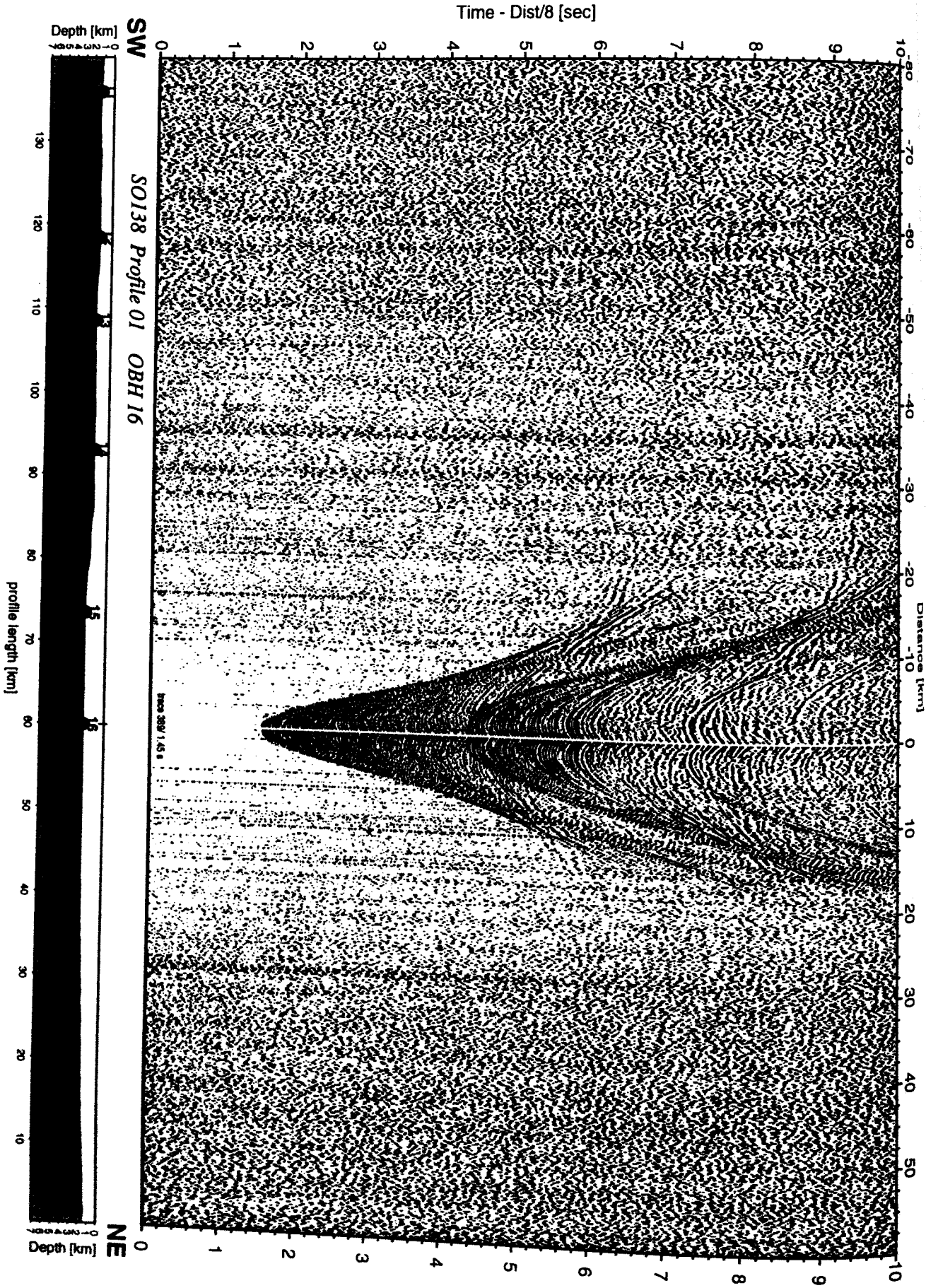

Figure 6.3.4.1.13: Record section from OBH 16 , Profile 01.

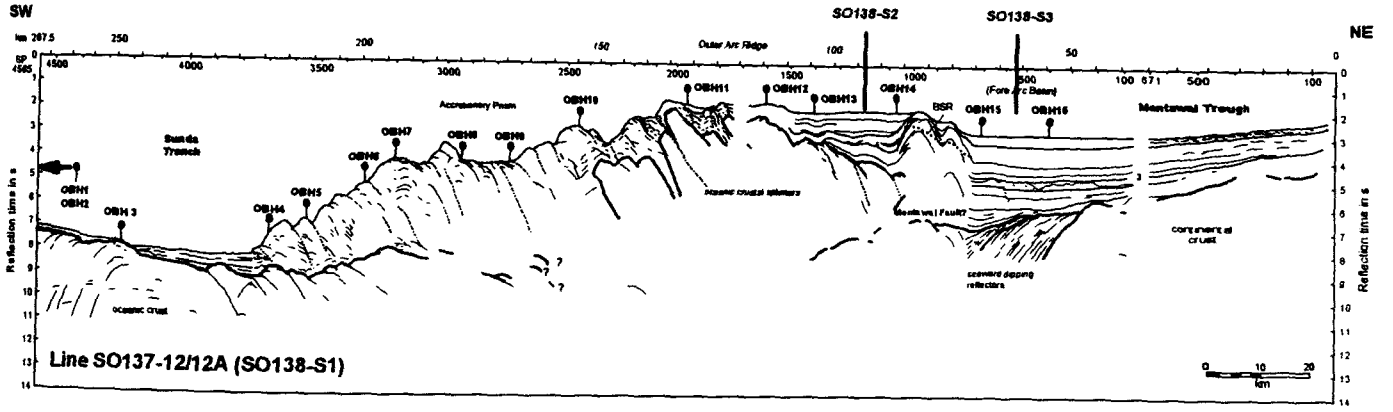

Figure 6.3.4.1.14: Interpretation of the MCS data along profile SO138-12 by Reichert and sientific shipboard party (inprep).

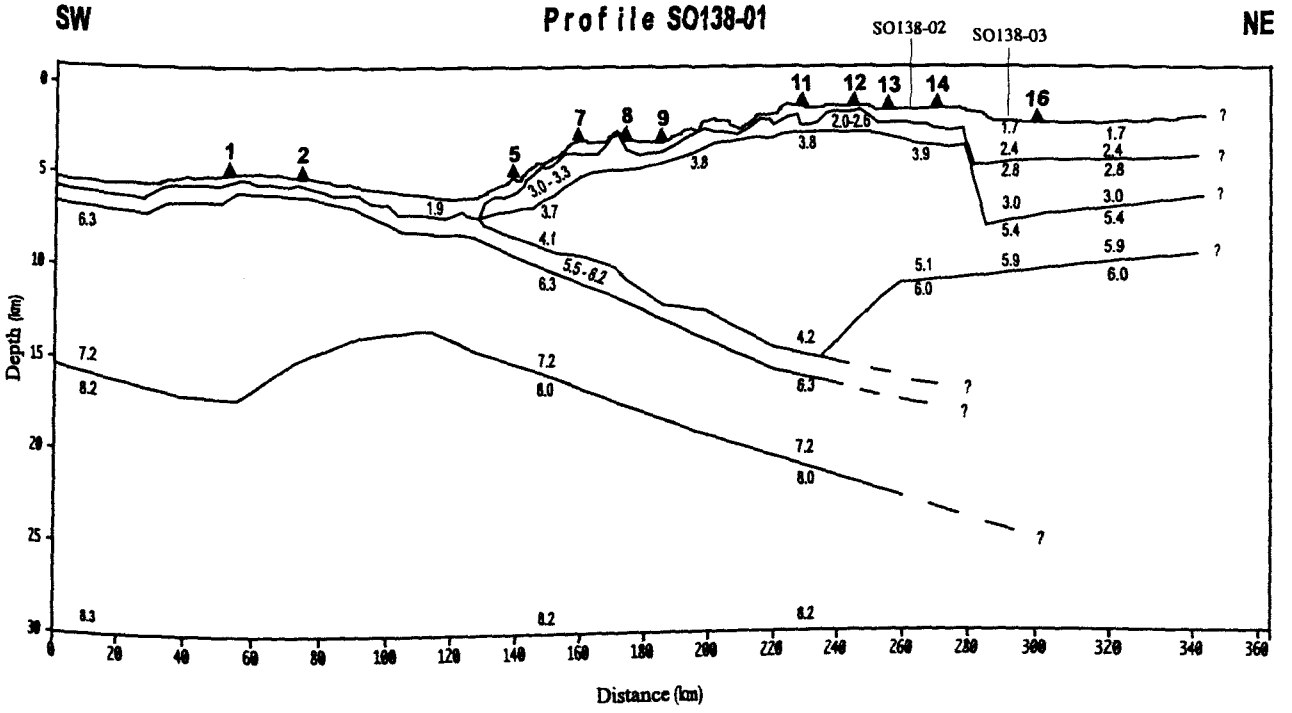

Figure 6.3.4.1.15: 2D - velocity-depth-model derived from profile SO138-01 displaying the Sunda trench subduction zone offshore Sumatra. See Figure 6.3.4.1.1 for exact location of the profile. P-wave velocity values in km/s.

6.3.4.2 PROFILES SO138-02 AND SO138-03

(A. Hampel, A. Berhorst, E. Flueh)

Profiles 2 and 3 are two strike lines on the Sunda shelf. They were located according to results of the MCS data from SO137, wich indicated a series of seaward dipping reflections beneath the Mendawai forearc basin (profile 3) and landward dipping strucutres below the outer arc high, preliminarily interpreted as ocean crustal splinters forming the backstop (Reichert and shipbord scientific party , in prep).

Along each profile, 9 instruments were placed at 3.0 nm spacing, including one OBS and the small vertical array (OBH17 and 18). Further details on instrumentation can be found in Appendix 9.1.2, the location of the instruments and the extension of the shooting lines is given in Figure 6.3.4.2.1. The instruments were deployed during the night 04/05.01.1999. Shooting started 20 miles ahead of the first instrument on 05.01.1999 at 06:50 at shot intervals of 60s along Profile SO138-02. It was continued during the transit between the two lines (Profile SO138-02) and was terminated on 06.01.1999 at 11:00 about 20 miles north-east of the recording array on line 3. Line 3 was shot again with a shorter shooting interval of 40 s from the start of the profile to about 6 miles north-east of the array and with 20s shot interval further along the line to about 3 miles south-east of the OBH array. It was terminated on 06.01.1999 at 19:45. The streamer was deployed throughout the shooting, the record sections are shown in Figures 6.3.4.2.2 to 6.3.4.2.4.

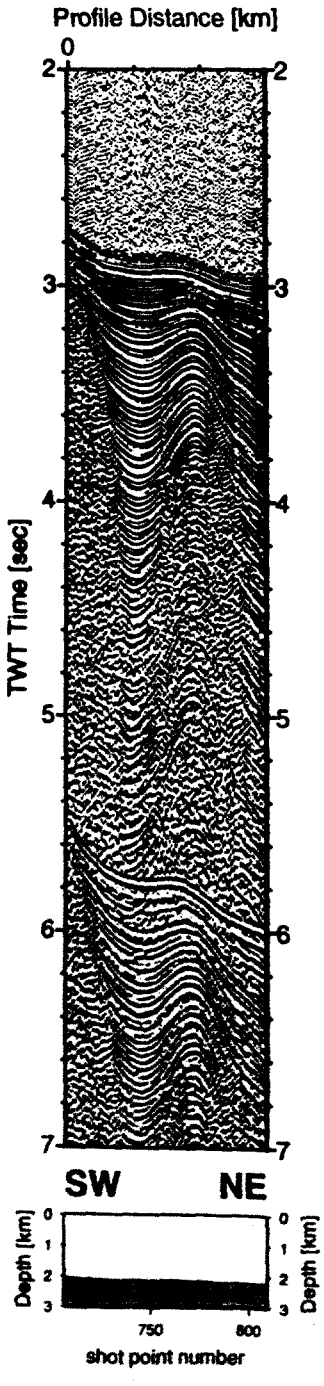

All instruments were recovered before noon on 07.01.1999, and all but three recorded well. Record sections from the inline observations are shown in Figures 6.3.4.2.5 to 6.3.4.2.19. Generally, the data quality is rather good, except for the OBS recordings that indicate a rather poor coupling or high noise. It is interesting to note that nearly all instruments were recovered about 0.5 miles south-east of their deployment position, which indicates rather strong currents even at large depths. The shorter shooting intervals of 40 and 20 s along parts of profile 3 were mainly used for later imaging techniques. A comparison for one instrument (OBH20) is shown in Figures 6.3.4.20 and 21. While with the 60 s shot interval (Figure 6.3.4.3.21) a rather constant signal-to-noise-ratio is observed, the 40 s shot interval data (Figure 6.3.4.2.20, offsets 50 to 25 km) show an increased noise level, and the 20 s shot interval data suffer from wrap-around multiples. However, at near-vertical offsets they are clearly superior to the 60 s shot interval data and reflections can be picked with more confidence.

Modelling and interpretation of profile SO138-02

For modelling and interpretation of profile SO138-02, the record sections of OBH 26 to 31 were used, which show arrivals of up to 50 km offset. The main phases to be identified on all record sections are the water-wave, two refracted phases from the sediment and a refracted and a reflected phase from the basement. By comparison with the seismic section from MCS stack (Figure 6.3.4.2.2), three other reflections and the associated refracted phases could be identified. All record sections show a slight asymmetry.

To obtain an idea of the corresponding layers and the velocity field, arrivals of the record sections of OBH 26 to 29 were analysed by forward modelling using ray tracing program techniques. Mainly OBH 26, 28 and 31, located at the south-eastern end, in the middle and at the north-western end of the profile, respectively, were used to fit the modelled arrivals to the observed phases. Afterwards, the other OBH record sections were checked and no apparent misfit was noticed.

Figure 6.3.4.2.3: Seismic section from MCS stack, Profile 02Q.

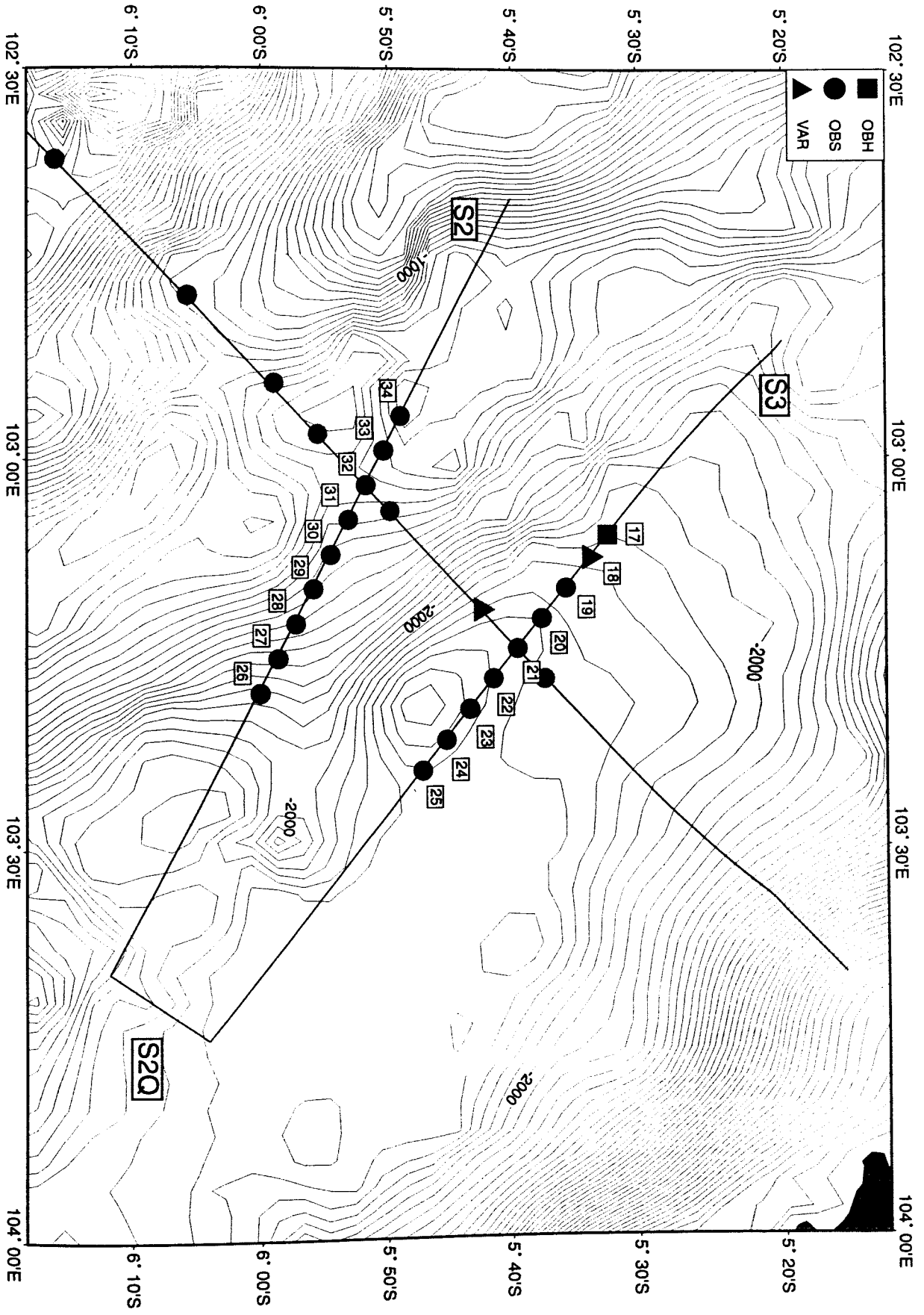

Figure 6.3.4.2.1: Location map of seismic profiles S2, S2Q, and S3.

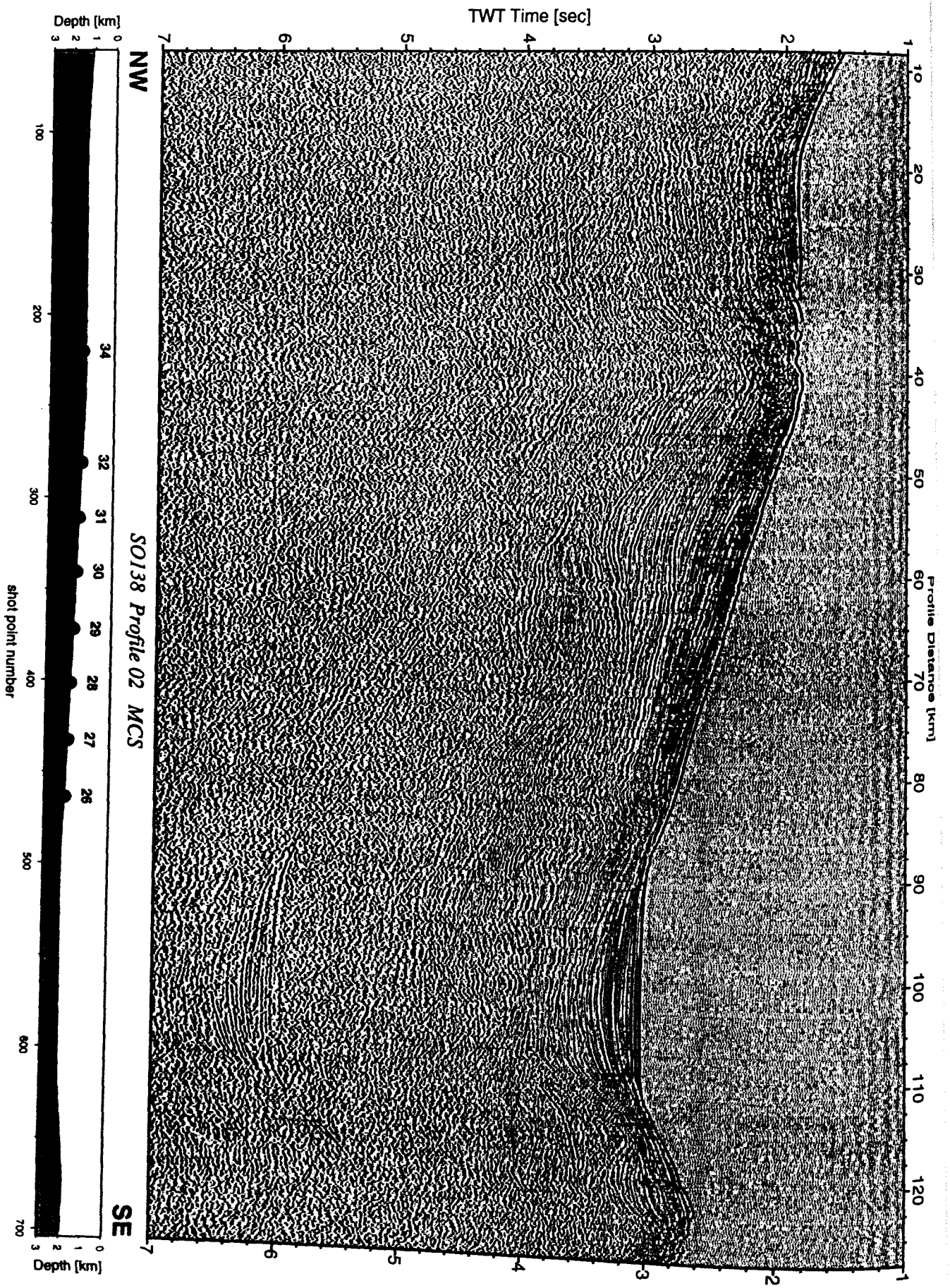

Figure 6.3.4.2.2: Seismic section from MCS stack, Profile 02.

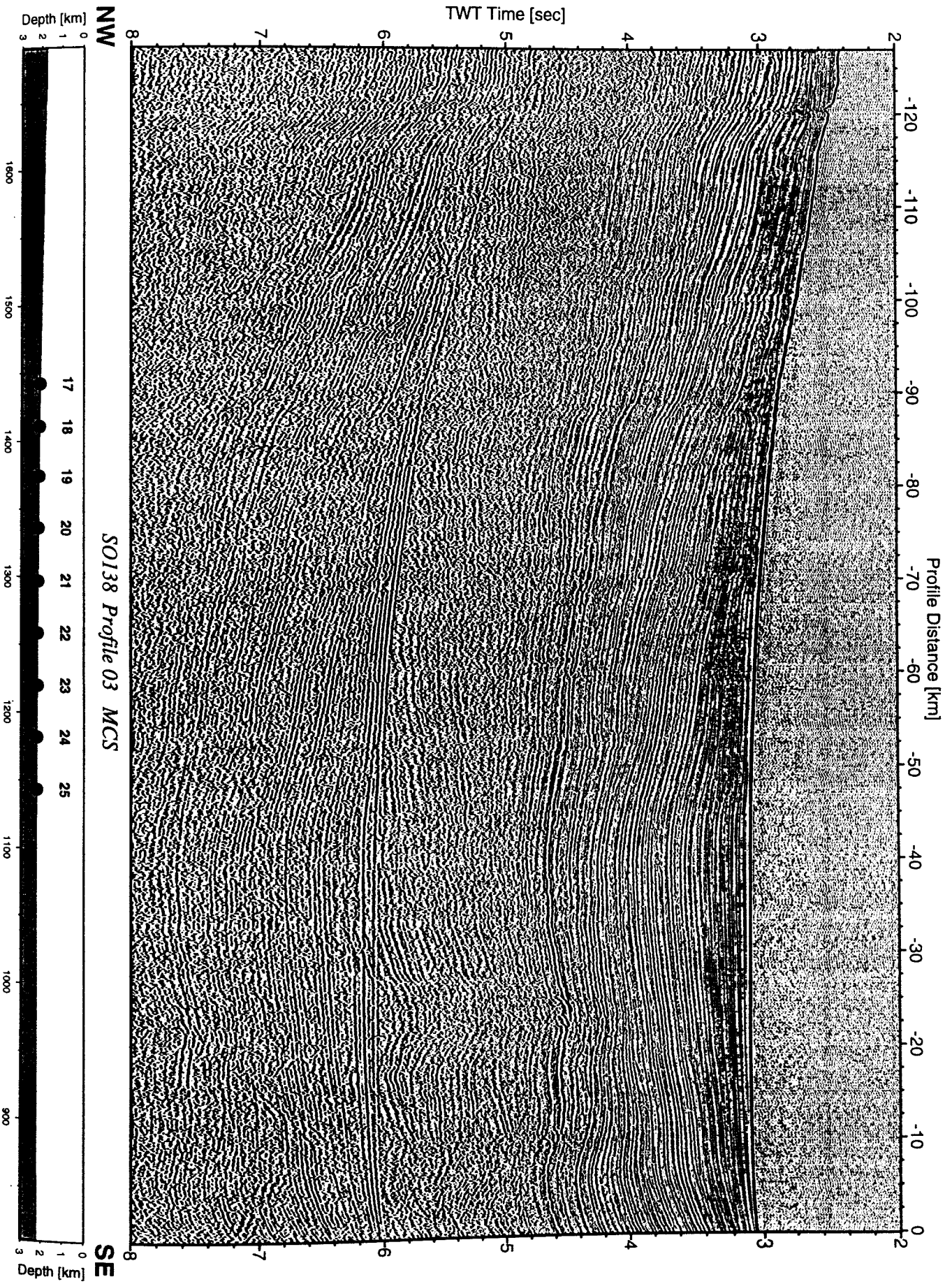

Figure 6.3.4.2.4: Seismic section from MCS stack, Profile 03.

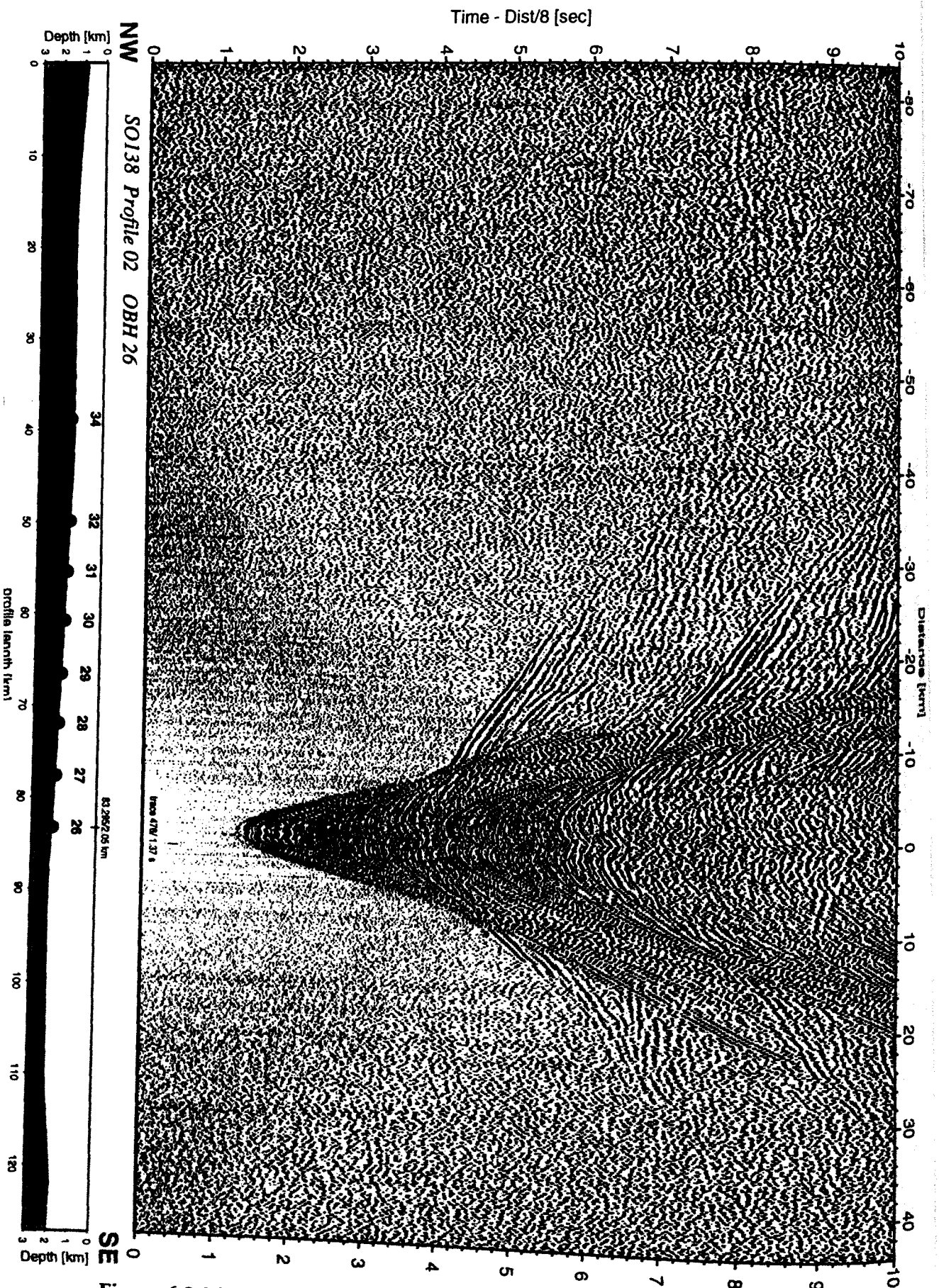

Figure 6.3.4.2.5: Record section from OBH 26 , Profile 02.

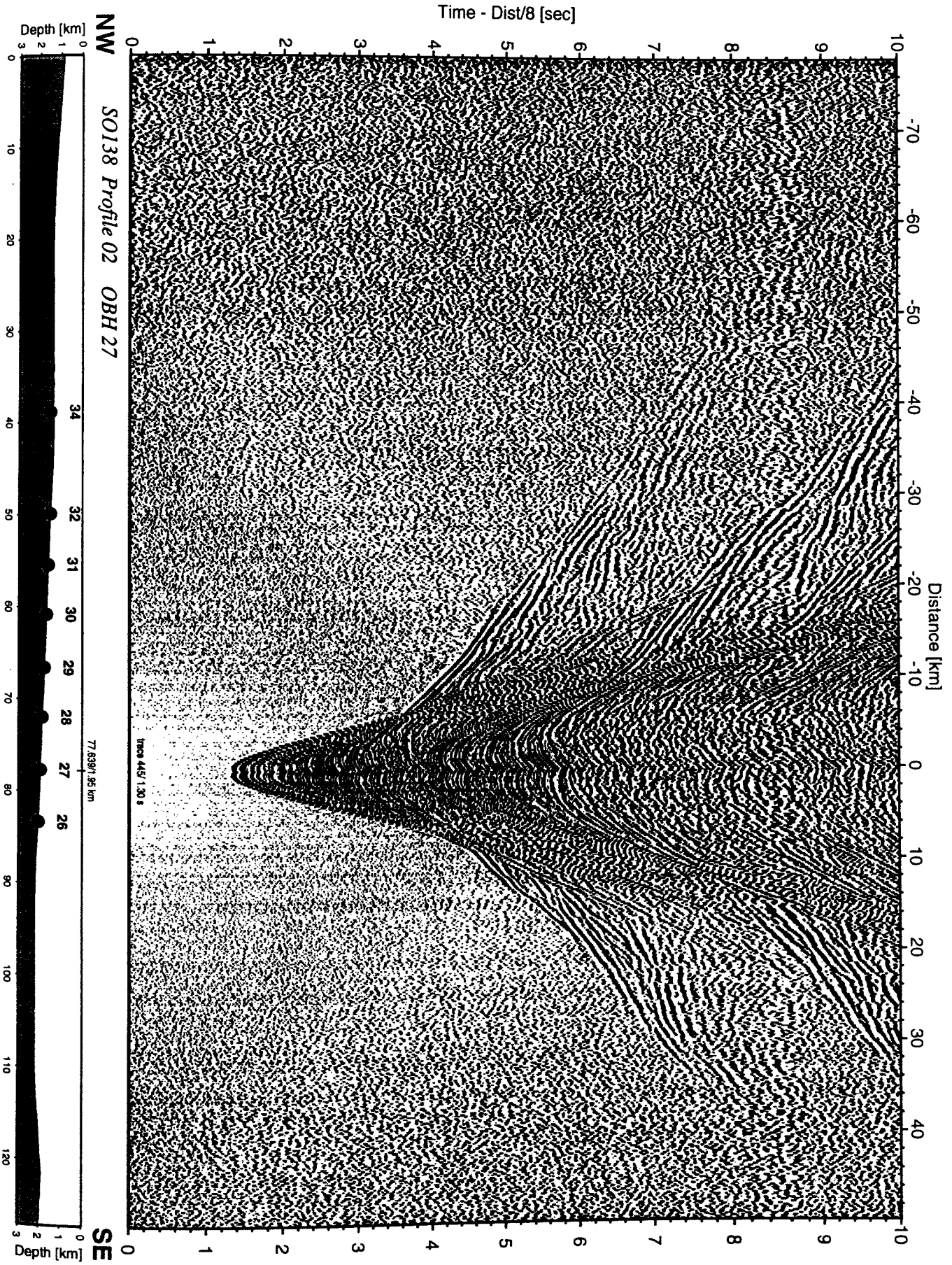

Figure 6.3.4.2.6: Record section from OBH 27 , Profile 02.

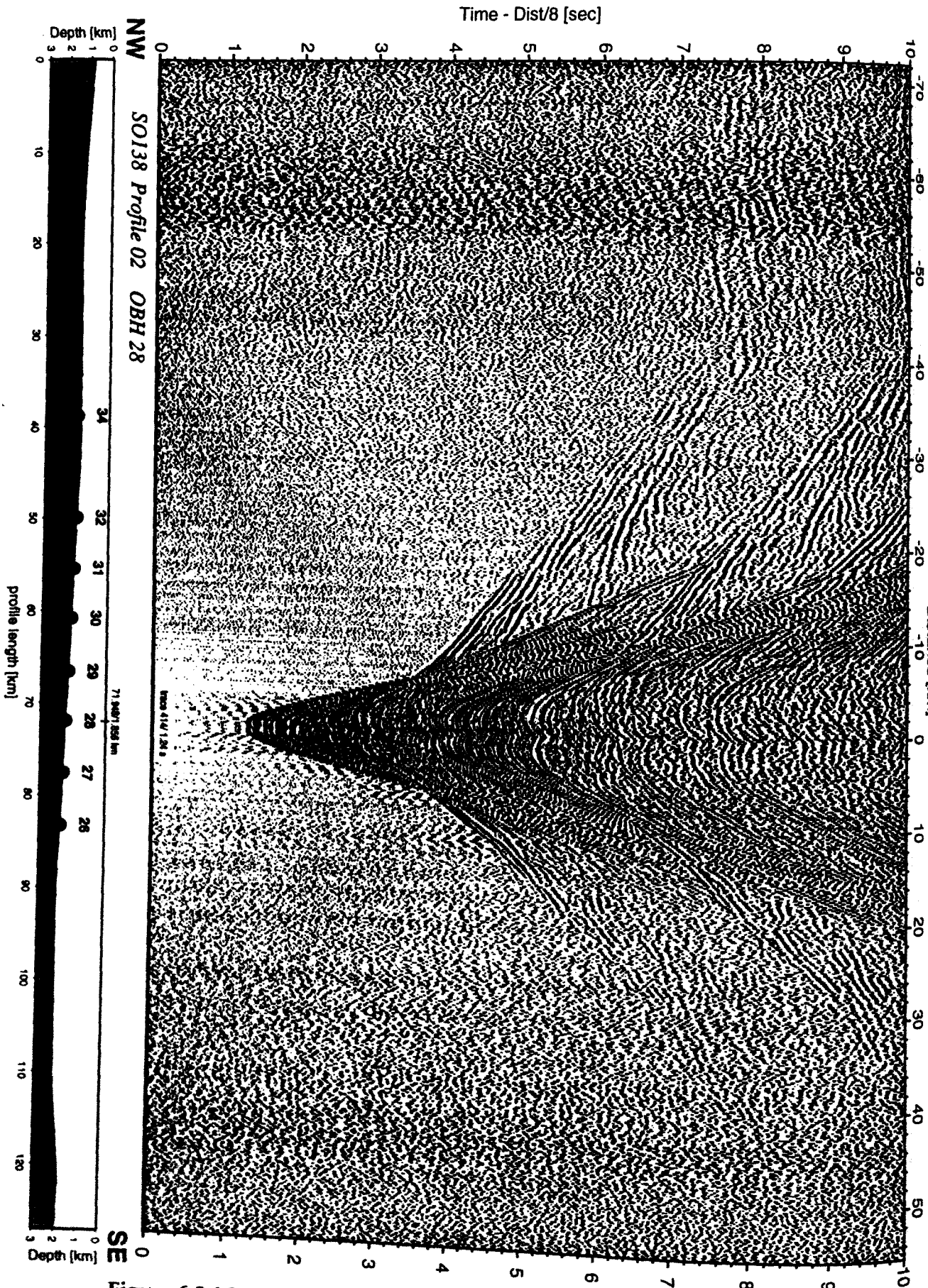

Figure 6.3.4.2.7: Record section from OBH 28 , Profile 02.

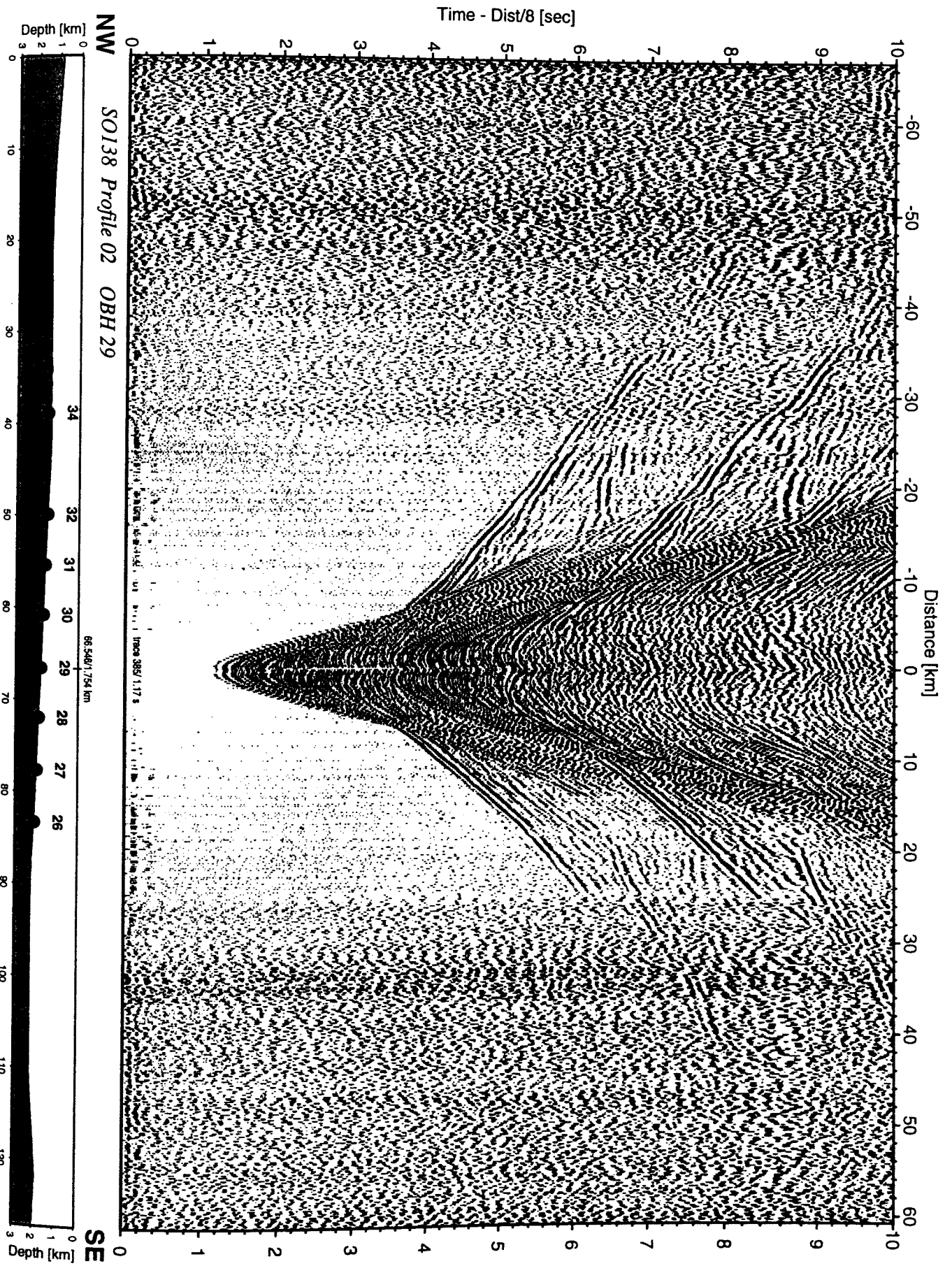

Figure 6.3.4.2.8: Record section from OBH 29 , Profile 02.

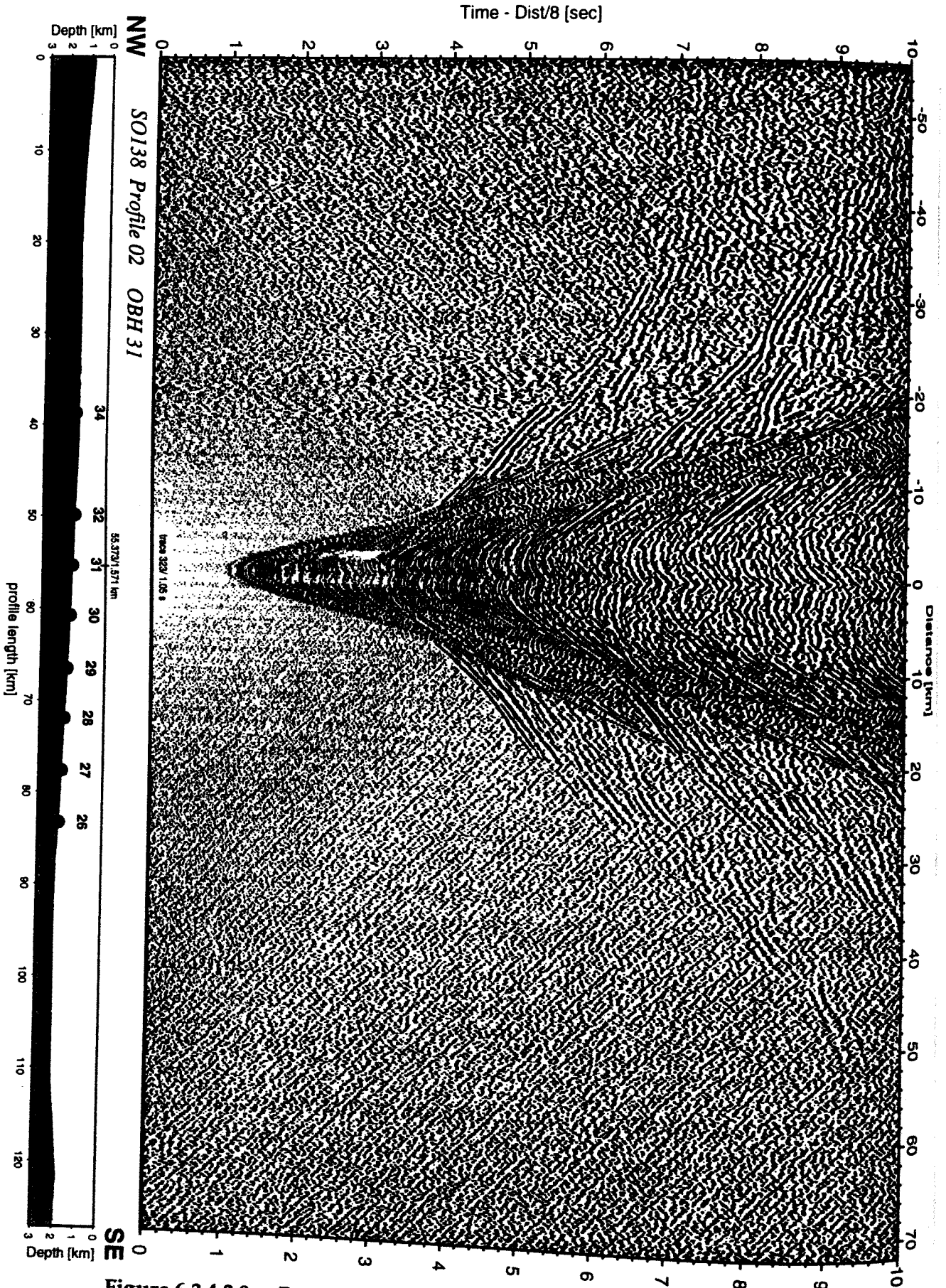

Figure 6.3.4.2.9: Record section from OBH 31 , Profile 02.

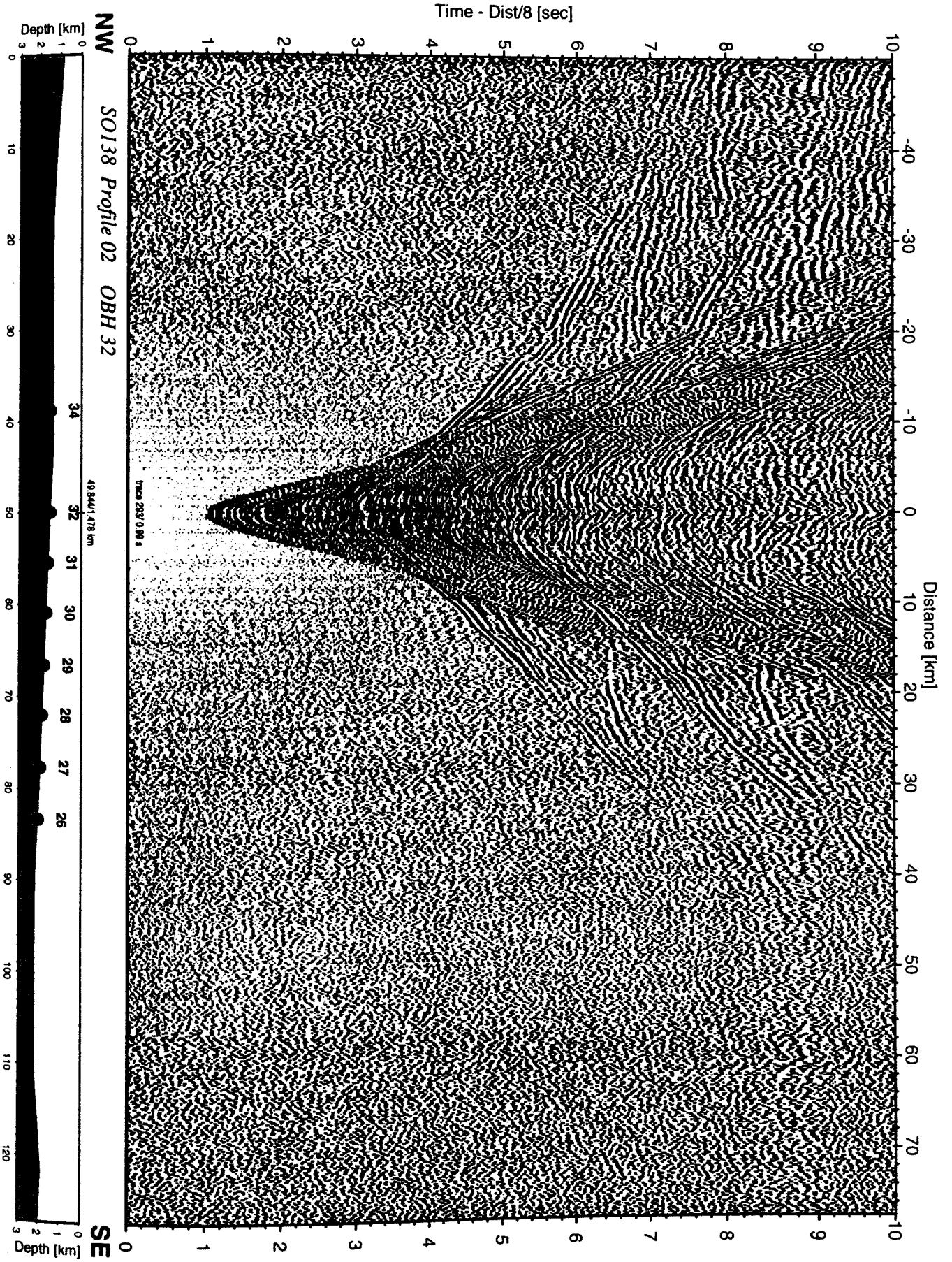

Figure 6.3.4.2.10: Record section from OBH 32 , Profile 02.

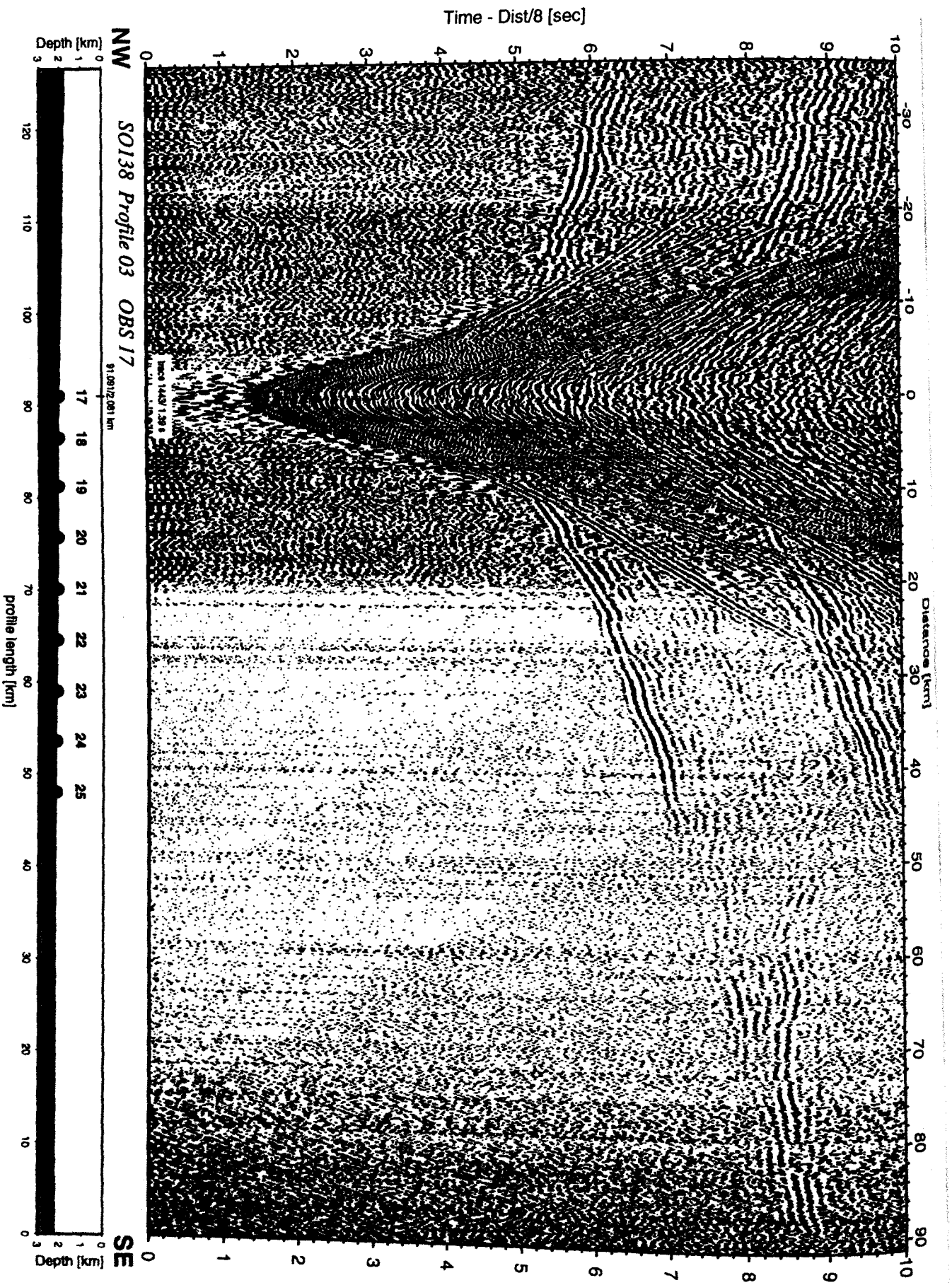

Figure 6.3.4.2.11: Record section from OBS 17 vertical component, Profile 03.

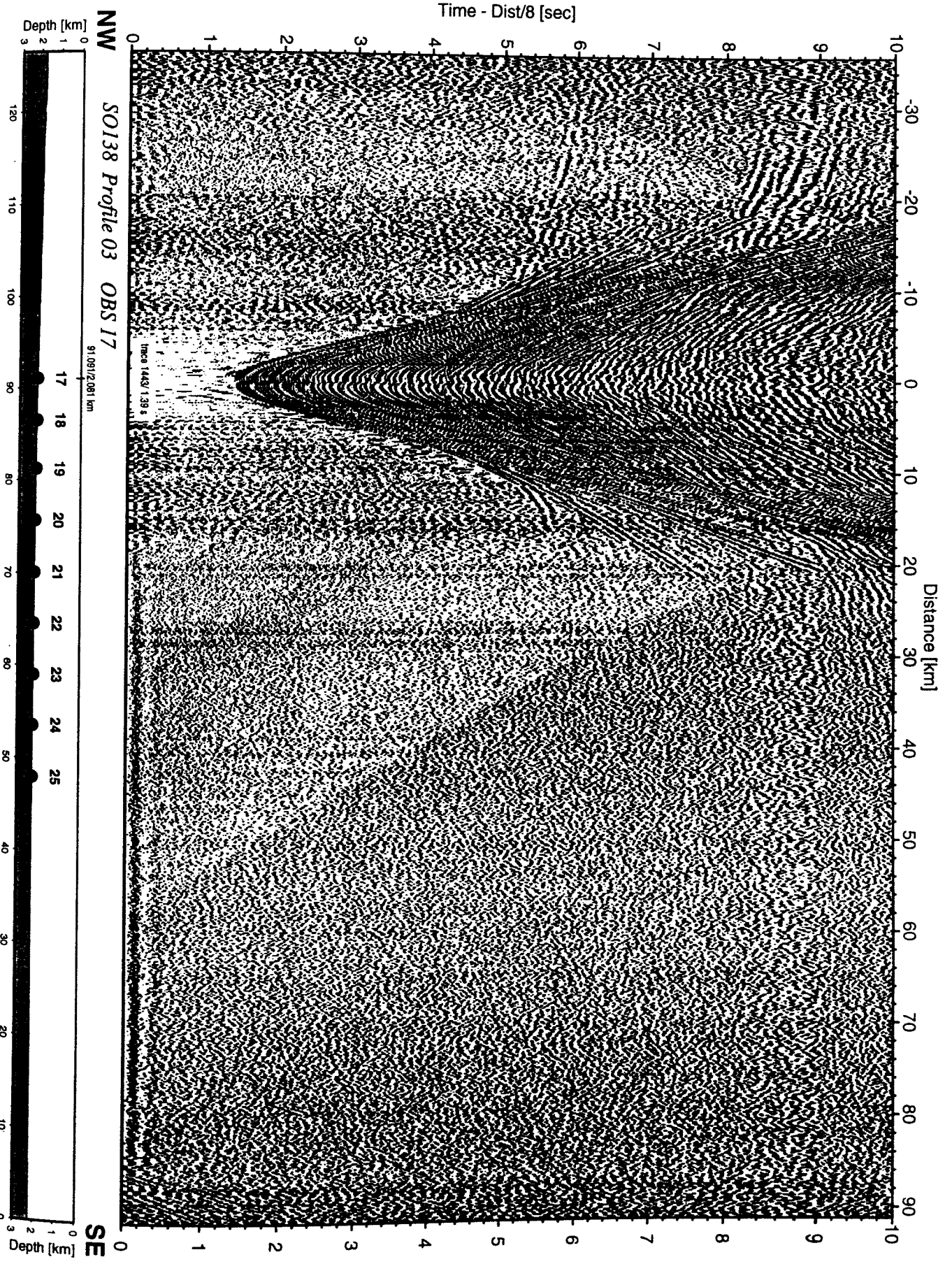

Figure 6.3.4.2.11a: Record section from OBS 17 horizontal component 1, Profile 03.

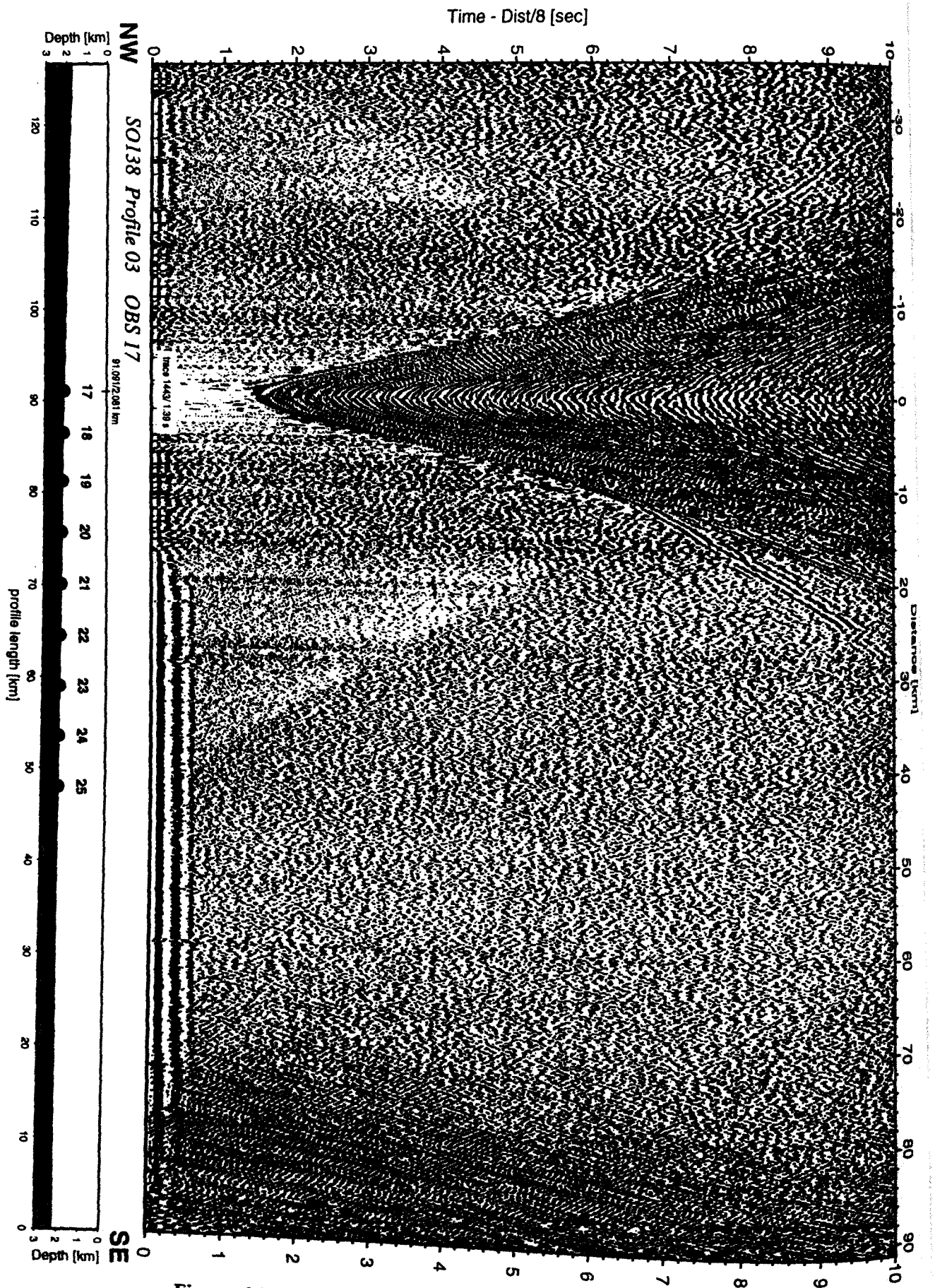

Figure 6.3.4.2.11b: Record section from OBS 17 horizontal component 2, Profile 03.

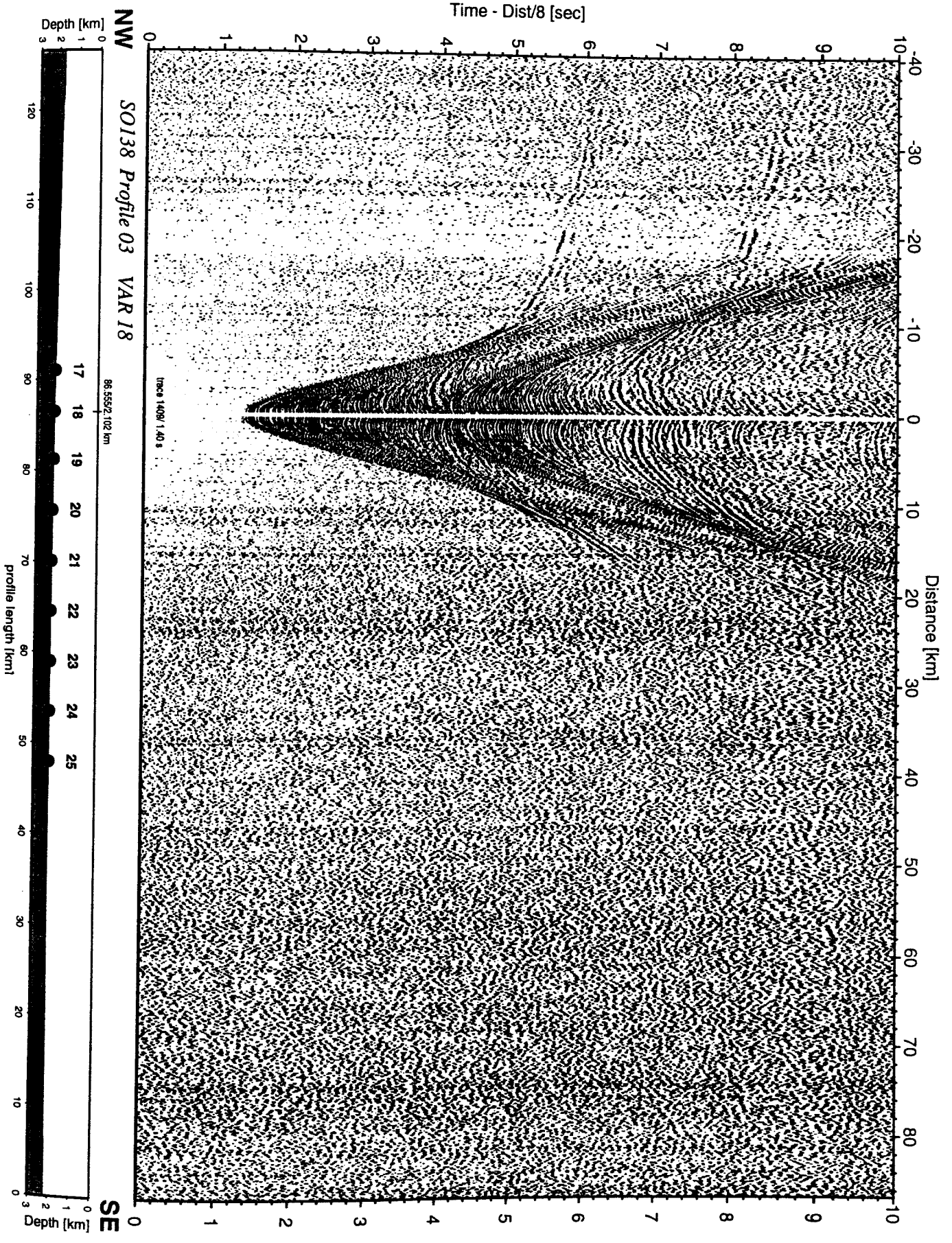

Figure 6.3.4.2.12: Record section from VAR 18 channel_1, Profile 03.

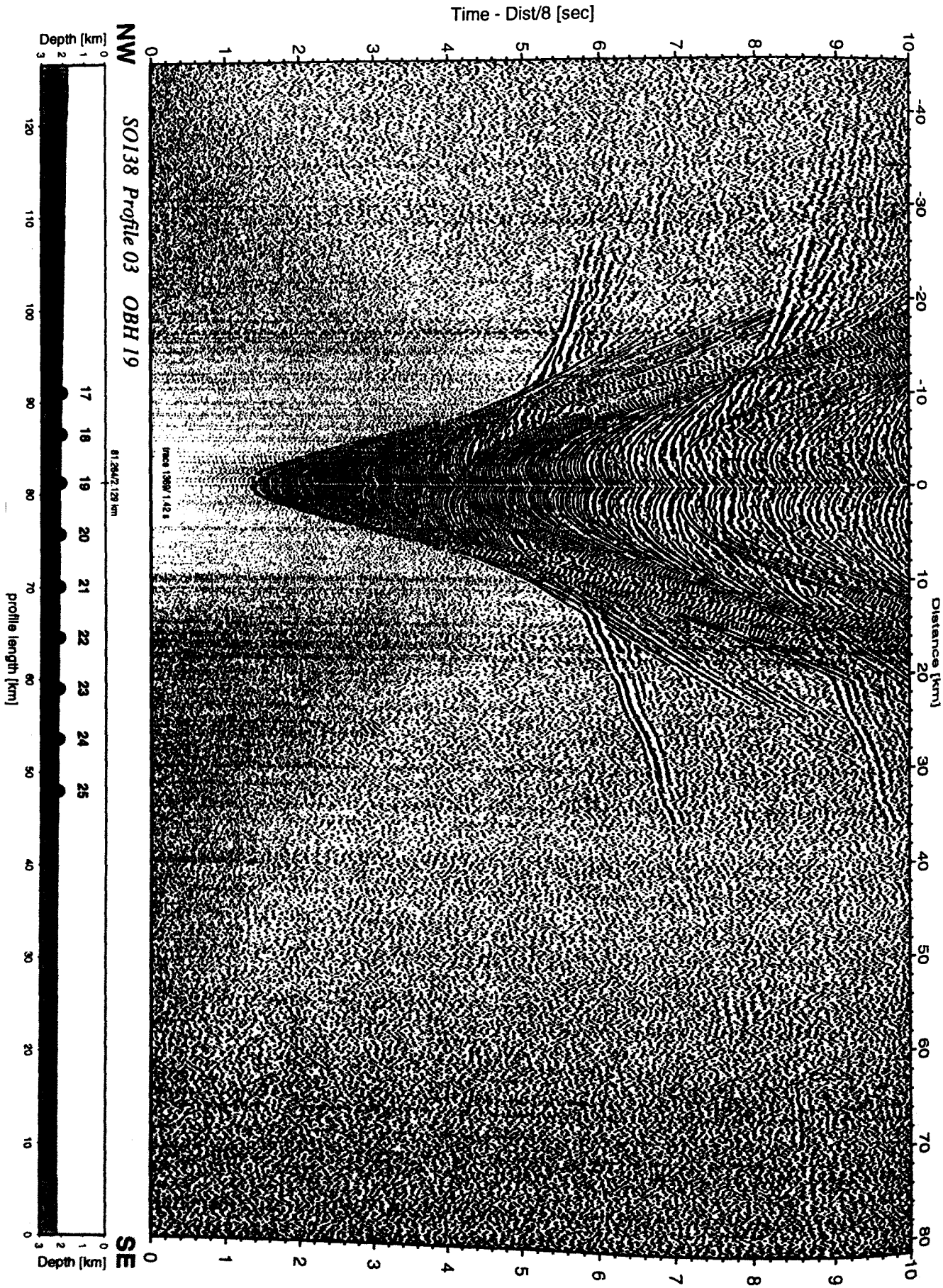

Figure 6.3.4.2.13: Record section from OBH 19 , Profile 03.

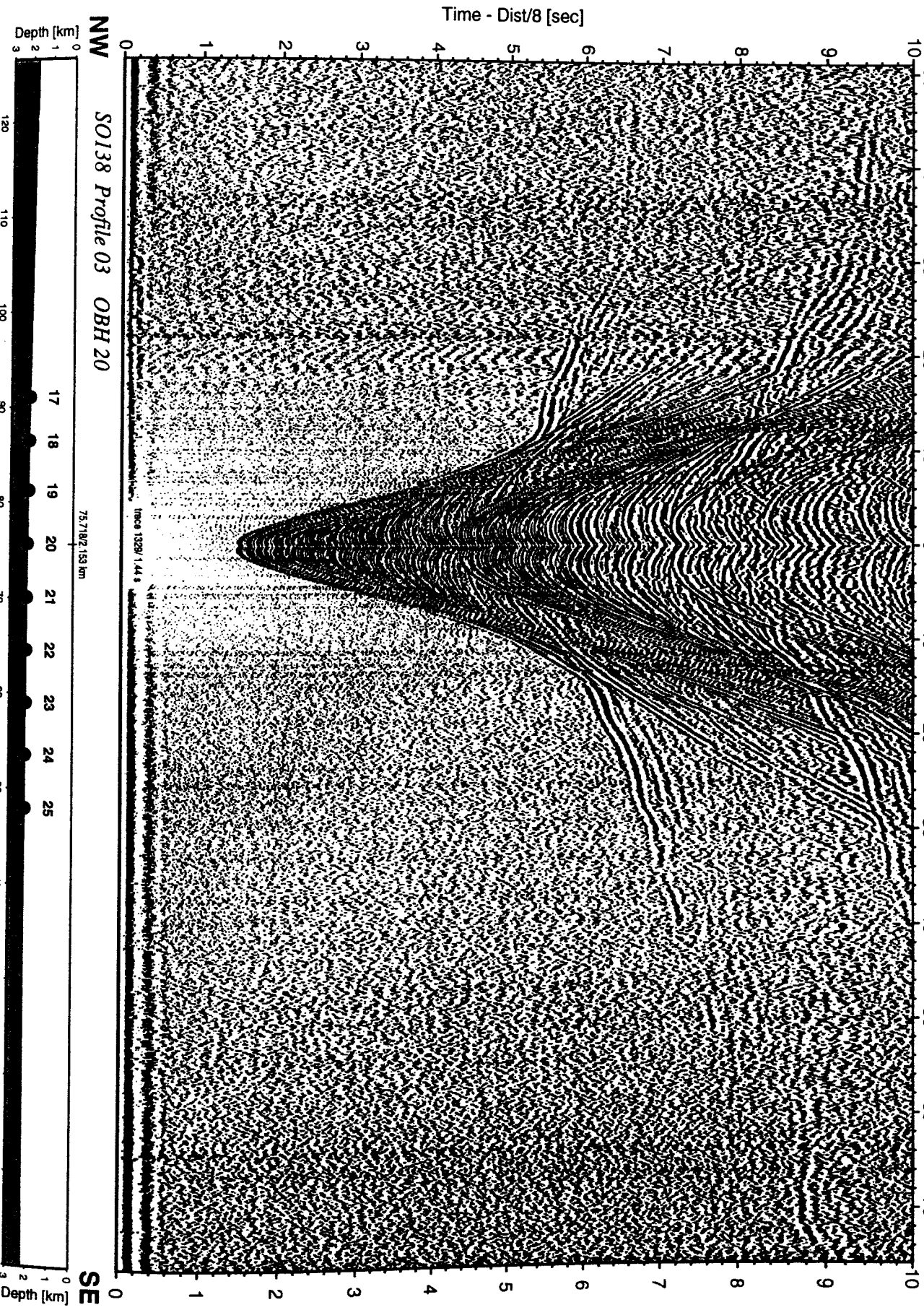

Figure 6.3.4.2.14: Record section from OBH 20 , Profile 03.

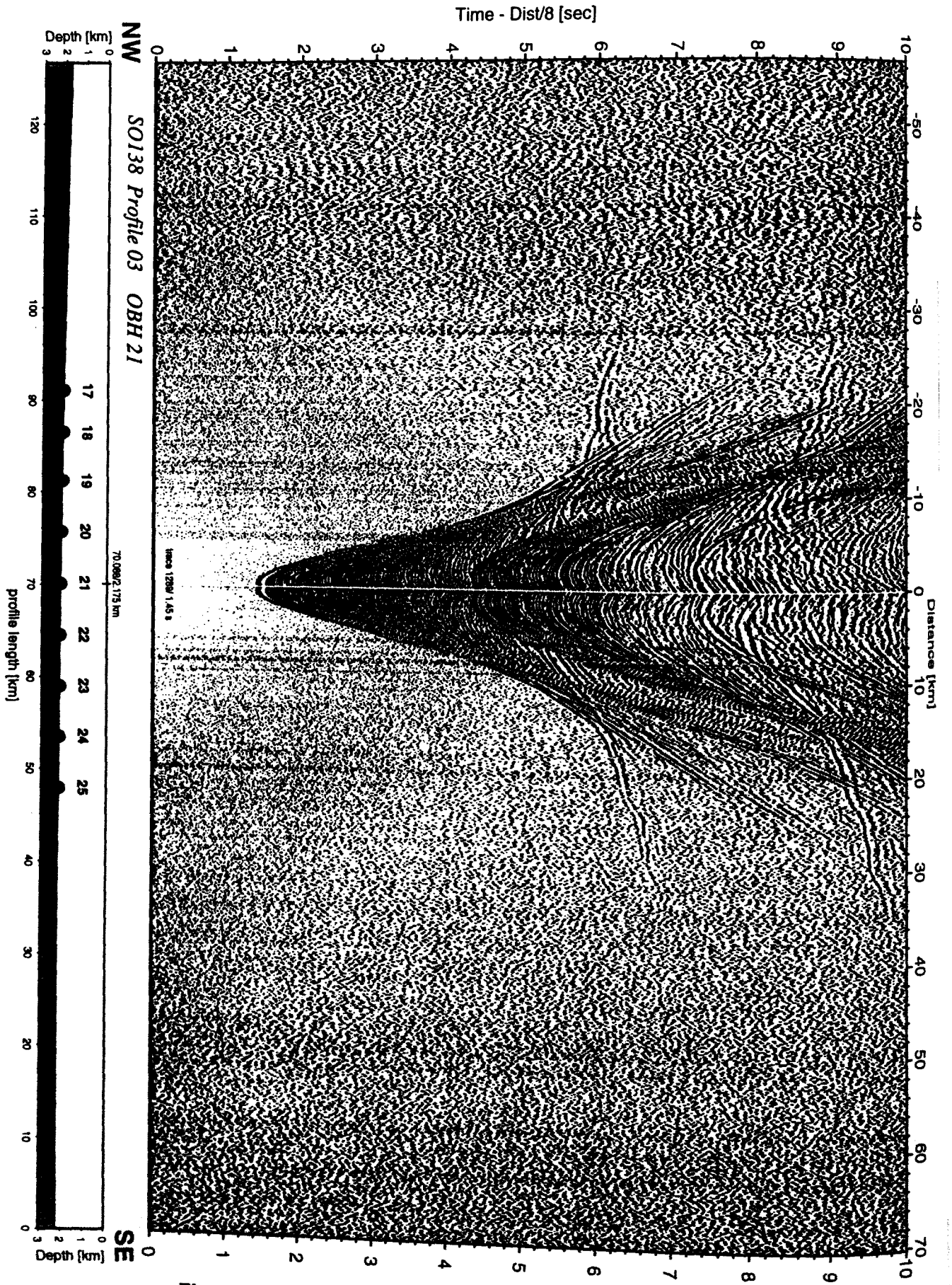

Figure 6.3.4.2.15: Record section from OBH 21 , Profile 03.

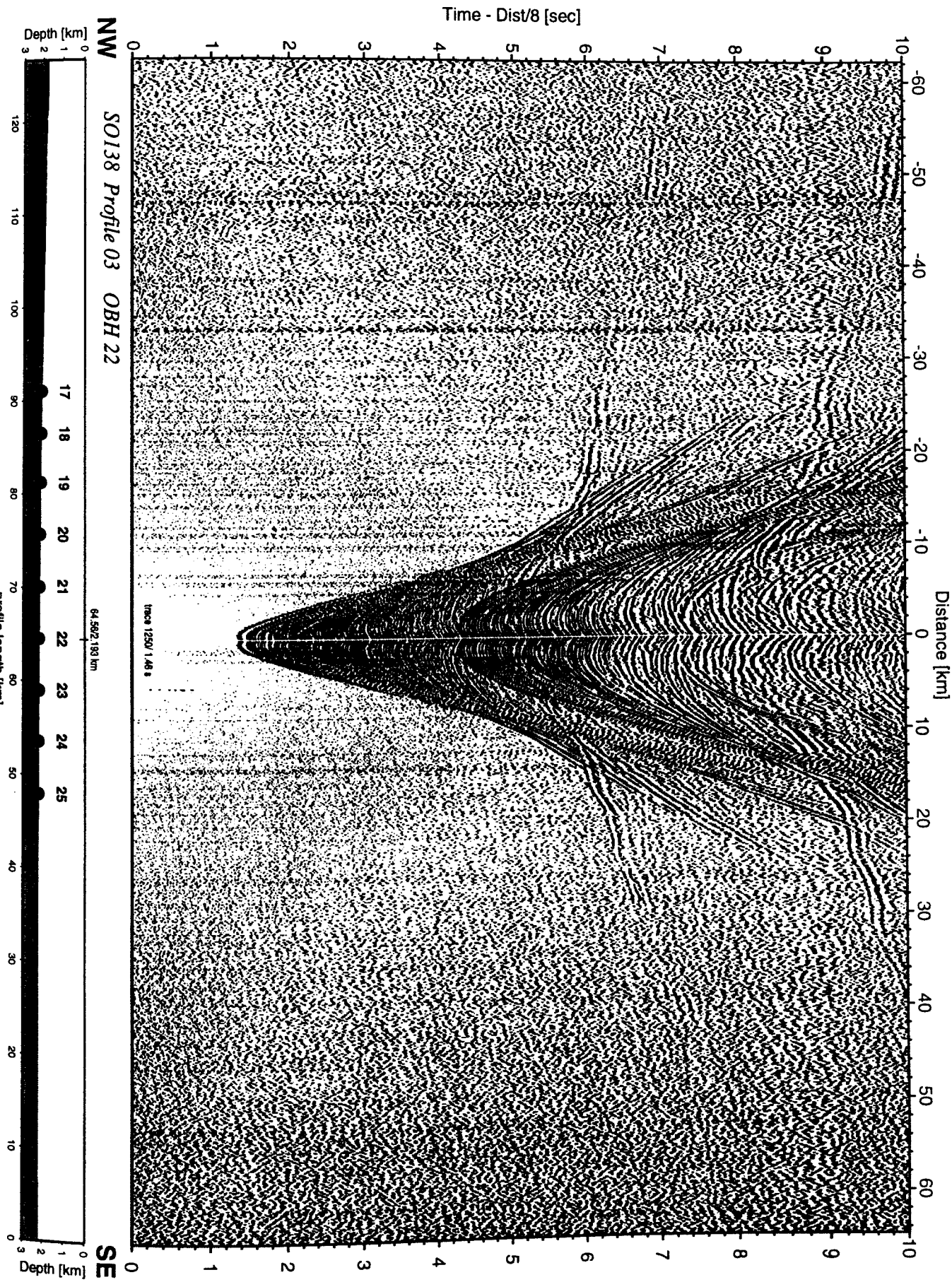

Figure 6.3.4.2.16: Record section from OBH 22 , Profile 03.

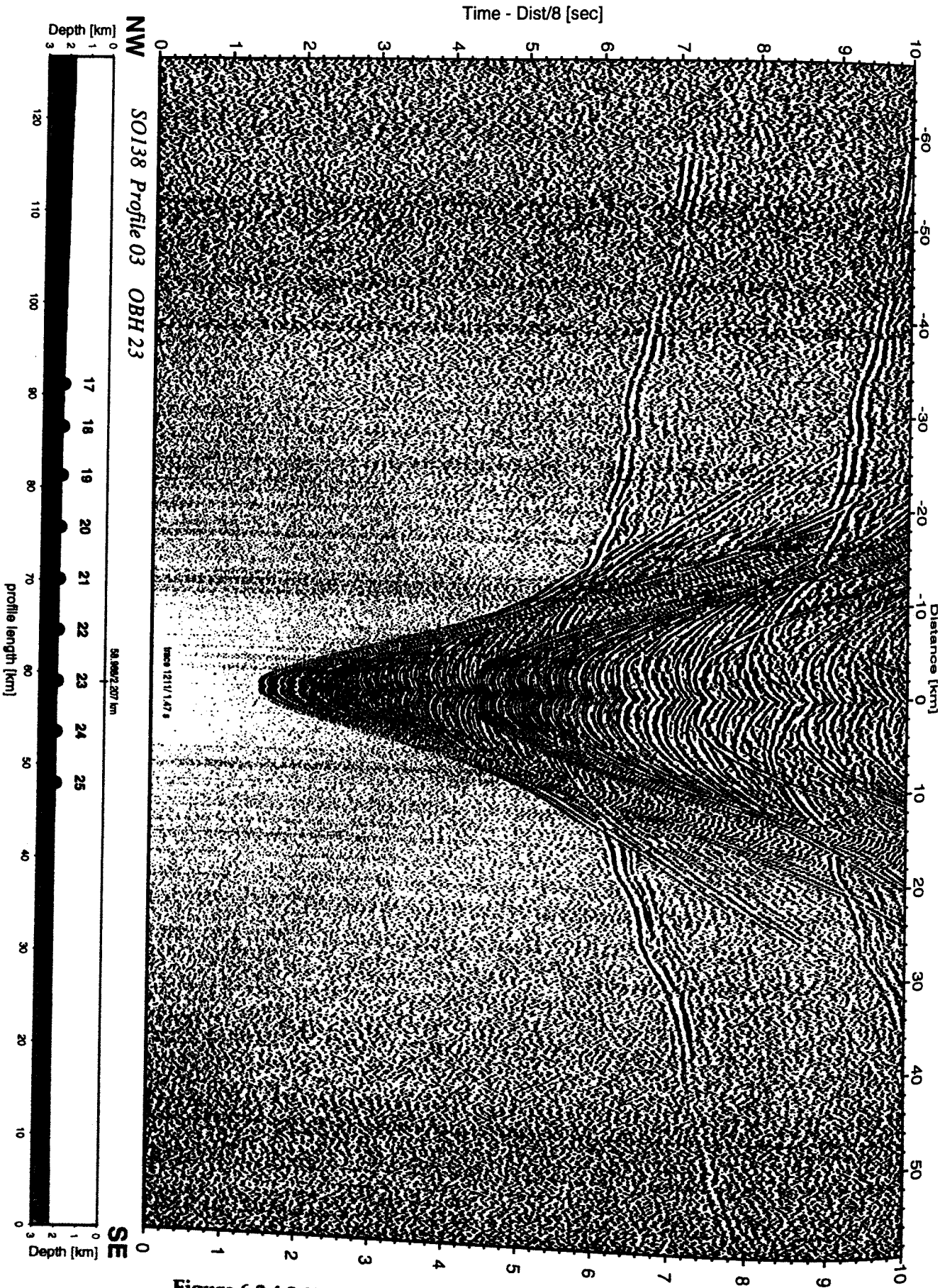

Figure 6.3.4.2.17: Record section from OBH 23 , Profile 03.

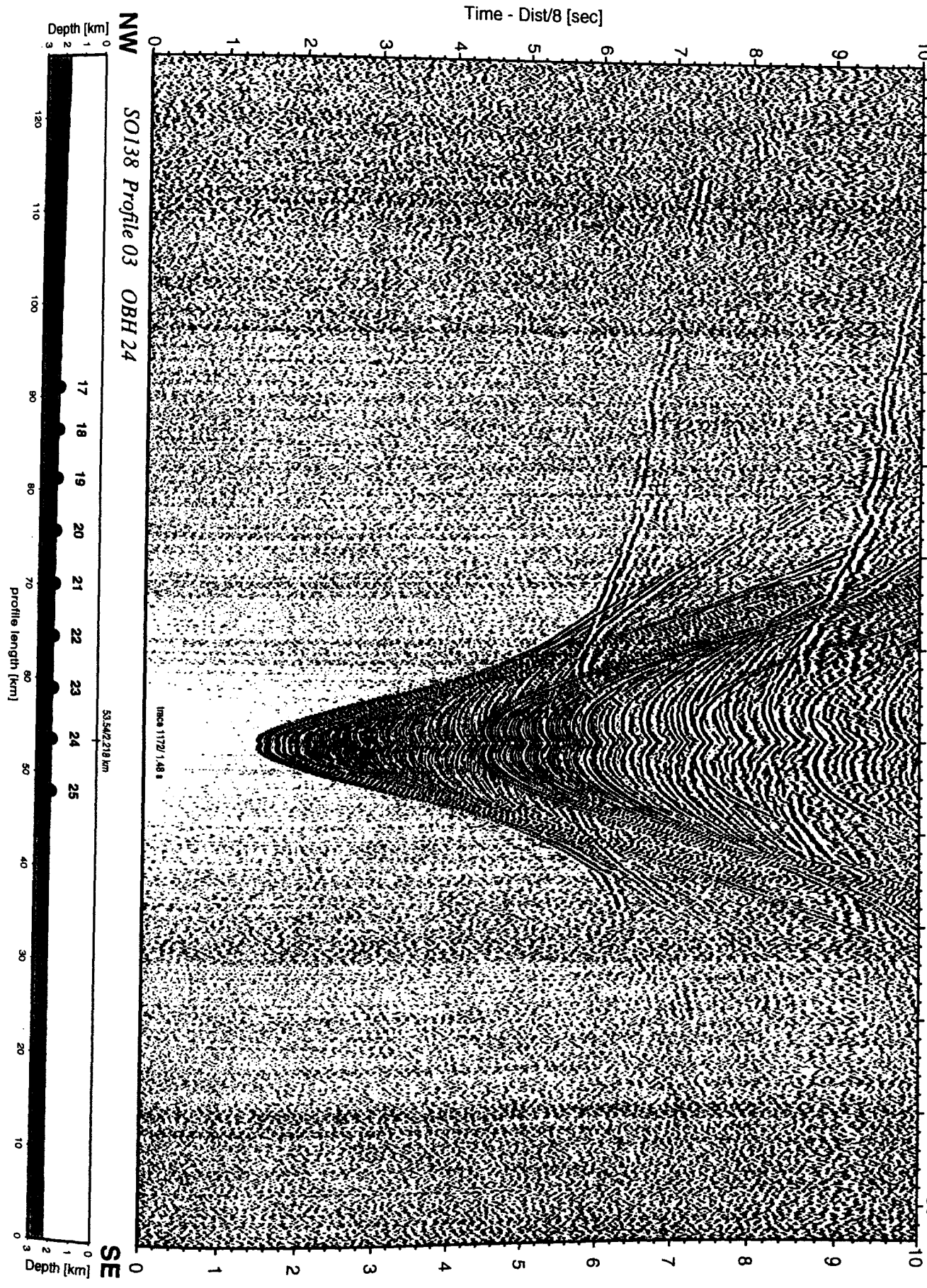

Figure 6.3.4.2.18: Record section from OBH 24 , Profile 03.

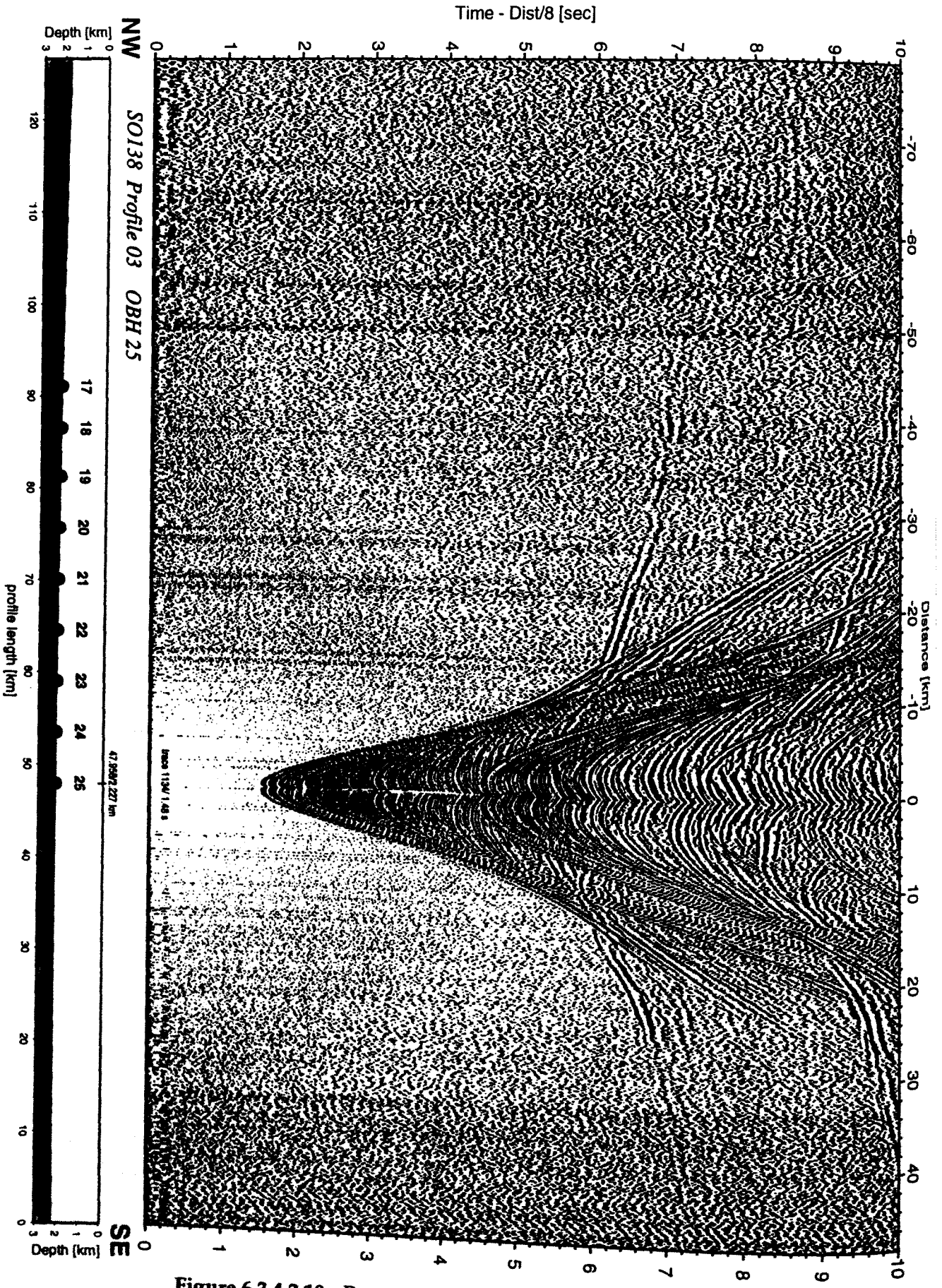

Figure 6.3.4.2.19: Record section from OBH 25 , Profile 03.

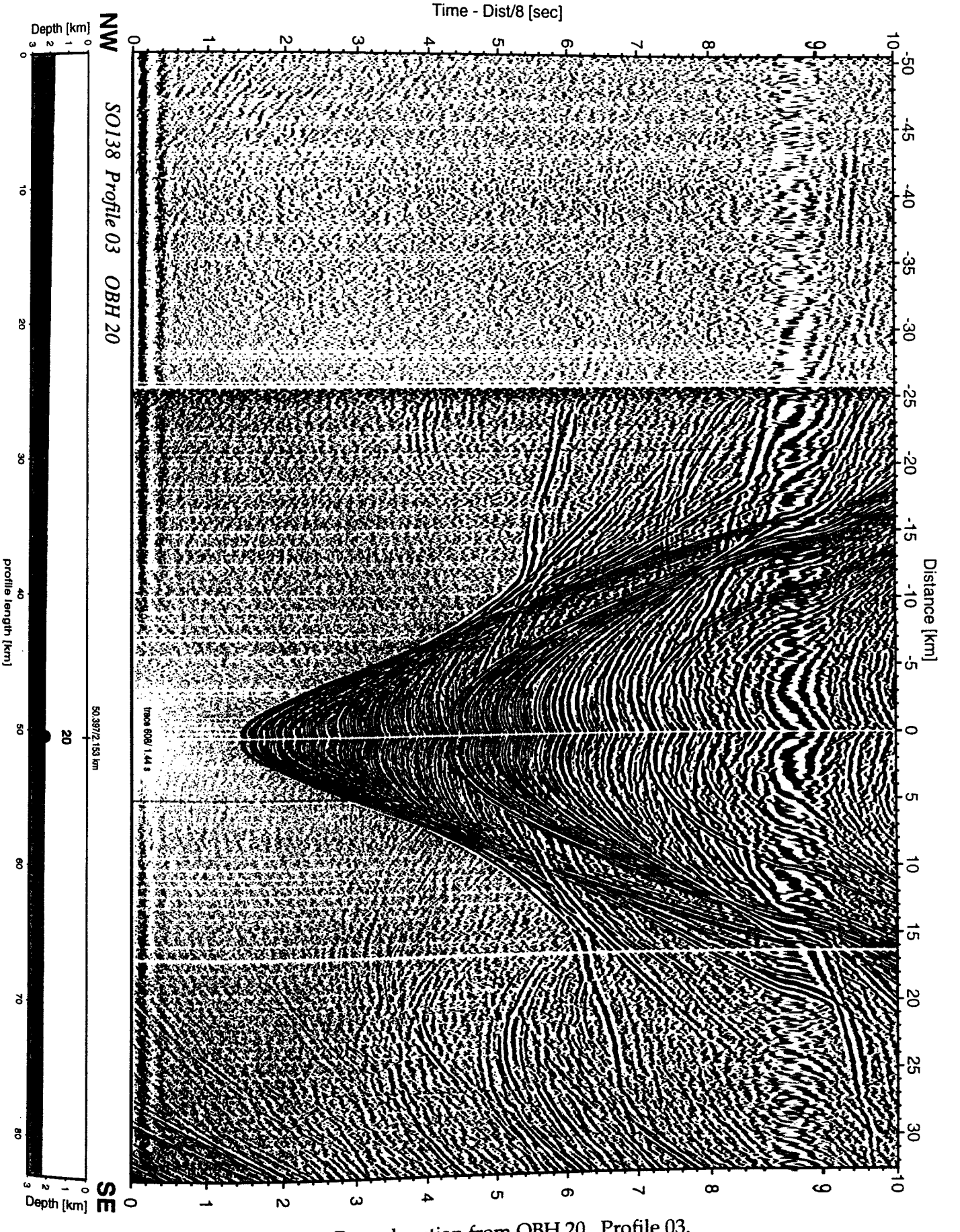

Figure 6.3.4.2.20: Record section from OBH 20 , Profile 03.

40 s shot interval(-50 km to -25 km), 20 s (-25 km to 32 km)

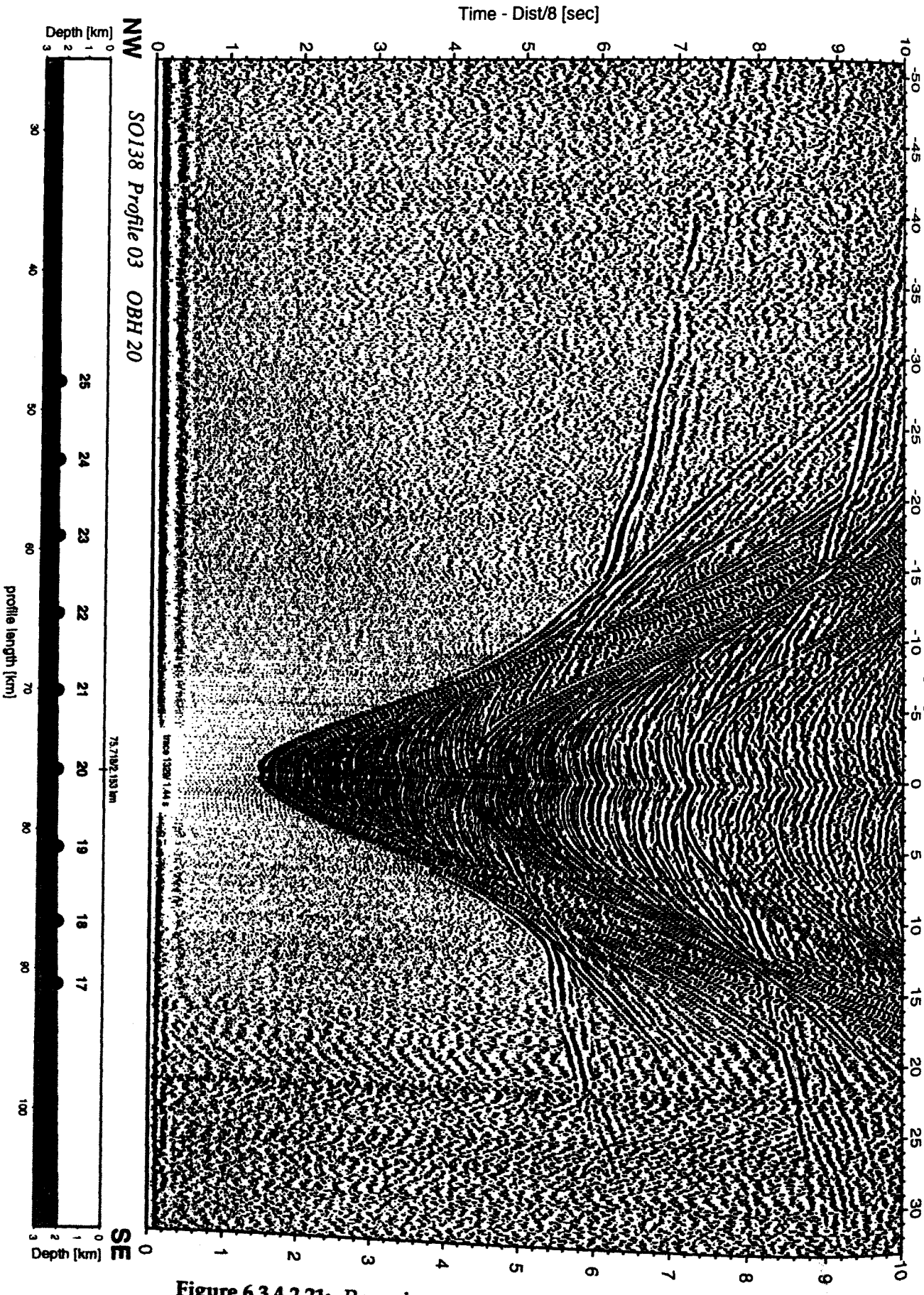

Figure 6.3.4.2.21: Record section from OBH 20 , Profile 03.

The preliminary model with its five layers is shown in figure 6.3.4.22, imposed on the seismic section from MCS stack. The three upper sediment layers from the model with velocities of 1.7 km/s, 1.9 km/s and 2.5 km/s coincide well with the marker horizons in the seismic section. They have a varying thickness, generally dipping to the SE. Together, the three upper sediment layers are about 3 km thick, 3 km in the NW, 2 km in the middle of the profile and 4 km in the SE.

The fourth layer, beginning at a depth of about 4 km, is characterized by a velocity of 4.1 km/s at the top rising to 5.1 km/s at the bottom . It is about 8 km thick at the north-western end of the profile and 5 km at the south-eastern end. The top of this fourth layer can partly be seen on the seismic section, between profile km 30 and 120. It shows a topographic high in the middle of the profile, which is constrained by refracted phases of OBH 26, 28 and 31.

At a depth of about 11 to 13 km, the top of the basement is marked in all OBH record sections by refracted phases and clear wide angle reflections of high amplitude, which are produced by a velocity change from 5.1 km/s to at least 6.0 km/s. On Profile SO138-02, no arrivals from deeper parts of the basement or the Moho could be observed. So there is no information about the velocity field within the basement.

Figure 6.3.4.2.23 shows the ray coverage of profile SO138-02. For modeling with MacRay, the sources are located at the OBH positions 26, 28 and 31.

The high gradient layer between 4 and 12 km depth was interpreted along the crossing MCS profile SO 137-12 to represent ophiolite material, obducted onto the continental margin (Reichert and ship board scientific party, in prep.). The velocities found here support such a lithology. The basement depth from the MCS data is in close agreement with our modelling results.

Modelling and interpretation of profile SO 138-03

For onboard interpretation of this profile, OBH 25 to 19, the record section of the vertical component of OBS 17 and channel 1 of the vertical array were analysed. All record sections show the water-wave, two refracted phases from sediments and two refractions from the basement. In addition, the record sections of OBH 20, 21 and 25 show a third sediment layer. The reflections of three sediment layers can also be verified by comparison with the seismic section of MCS stack (Figure 6.3.4.2.4).

Only in the record section of OBS 17 (Figure 6.3.4.2.11), a refracted phase at 7.8 s and a wide angle reflected phase at 8.5 s, both at an offset of 60 km, can be observed. These arrivals are interpreted to mark the Moho, which is found at a depth of 24 km.

For forward modelling, the program MacRay (Luetgert, 1992) was used mainly on OBH 19, 22 and 25, located in the north-western part, the center and at the south-eastern end of the profile, respectively. The resulting model was cross-checked with the other record sections and no major disagreement became apparent.

The preliminary model for profile SO138-03 is superimposed on the seismic section in figure 6.3.4.2.24.

The three upper layers of sediment with velocities of 1.7 km/s, 2.0 km/s and 2.4 km/s are together 2 –3 km thick and dip to the SE. A fourth, thicker sediment layer with a velocity of 2.8 km/s at the top and 3.0 km/s at the bottom resulted from modelling the refracted and reflected arrivals in the OBH record sections, but its bottom can hardly be recognized in the seismic section because it is masked by the multiple.

The boundary separating the fourth sediment layer from the underlying basement is characterized by a change of velocity from 3.0 km/s to 5.3 km/s. The top of the basement is located in a depth of 7 km in the SE and rises to 5 km from profile km 80 north-westward. The location and structure of the top of the basement is constrained by refracted phases in all OBH record sections and explains the asymmetry and variations observed by these refracted

phases. Along MCS profile SO 137-12, a layer corresponding in depth to the high gradient upper basement was interpreted by Reichert and ship board scientific party (in prep.) to represent a sequence of seaward dipping reflections, as commonly observed on passive margins. The velocities determined from the wide angle data do not contradict this interpretation.

The basement is divided into two parts, separated by a moderate velocity change from 6.0 km/s to 6.2 km/s at a depth of 10 to 11 km. This is indicated by a slight change of the apparent velocities of the refracted phases in the record sections.

Only OBS 17 shows a refracted and wide angle reflected phase at a large offset of 60 km. These phases are interpreted to be Moho reflections, based on the critical distance of these wide angle reflections.

Figure 6.3.4.2.25 shows the ray coverage for SO 138-03 with rays propagating from OBHs 25, 22 and 19 as sources.

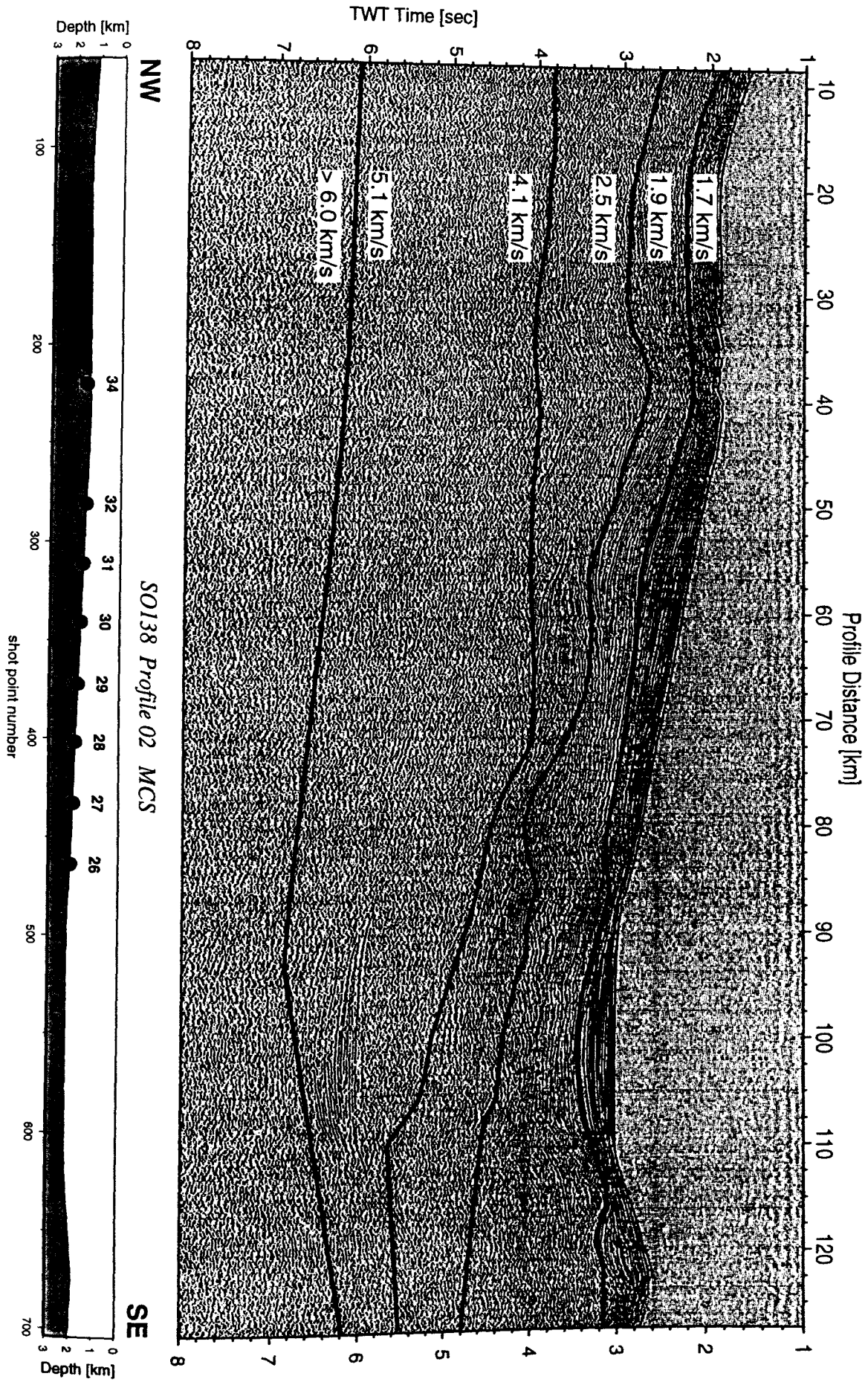

Figure 6.3.4.2.22: Seismic section from MCS stack, Profile 02.

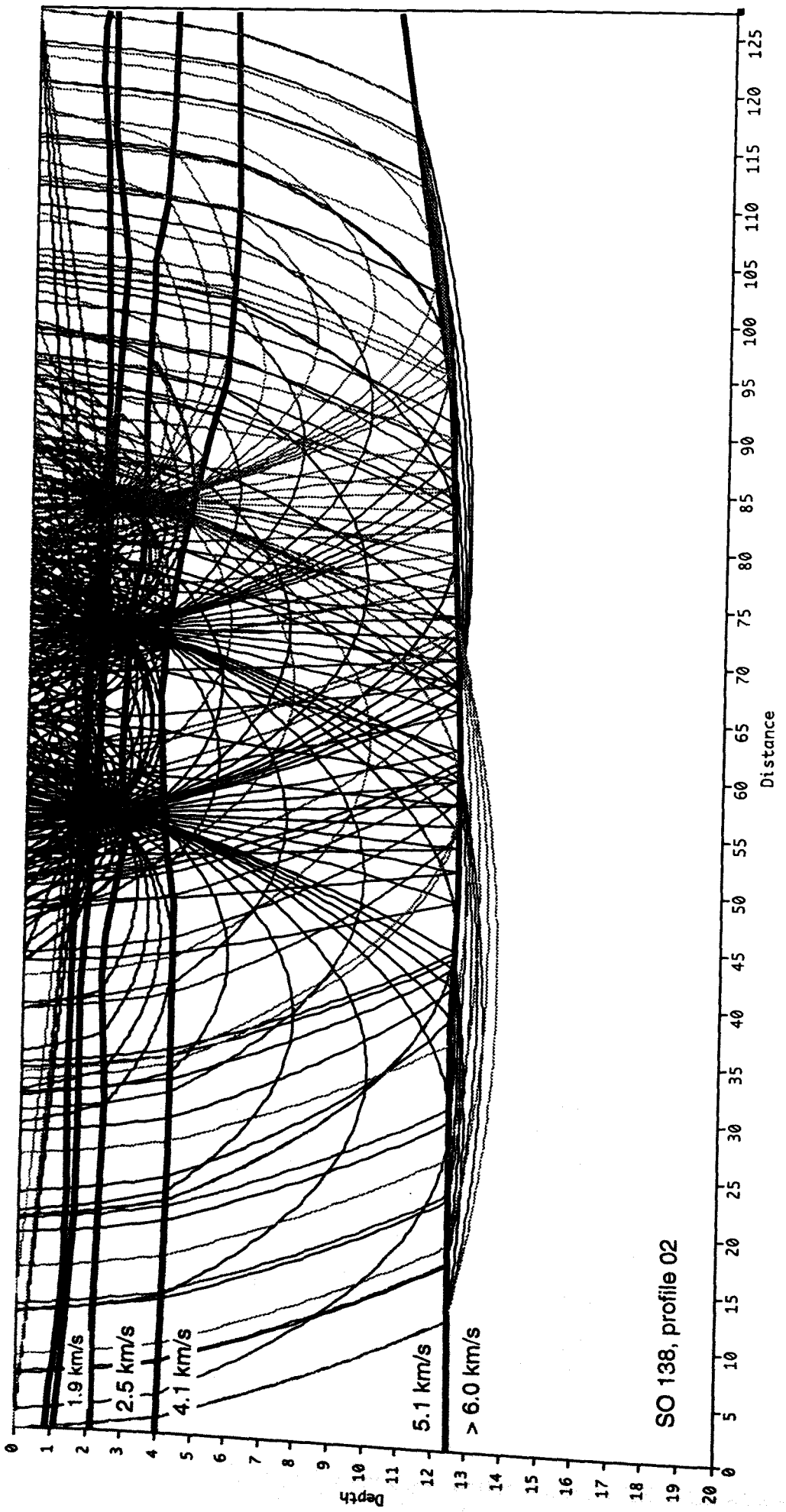

Figure 6.3.4.2.23: Ray coverage from OBH 26, 22, and 31

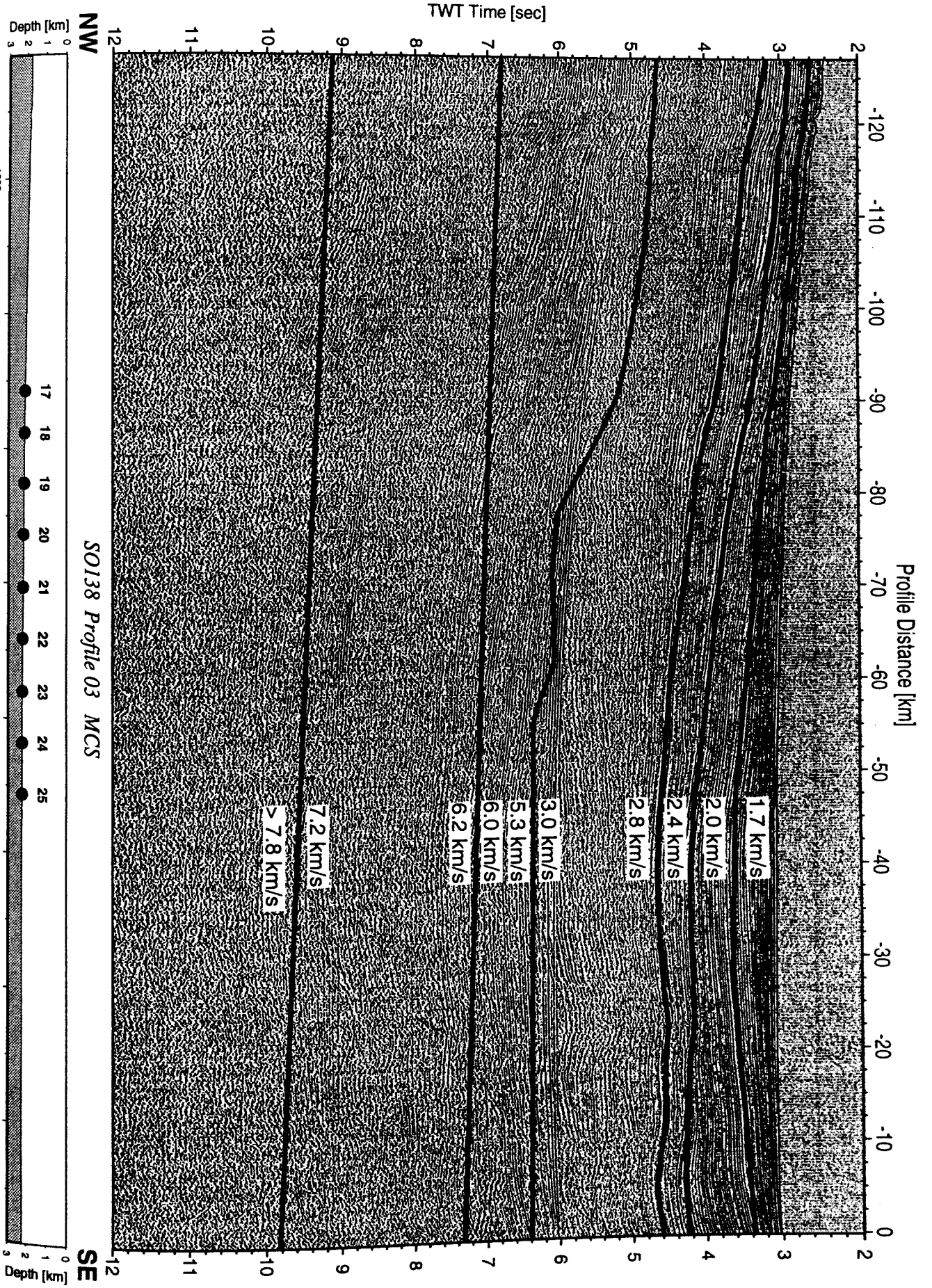

Figure 6.3.4.2.24: Seismic section from MCS stack, Profile 03.

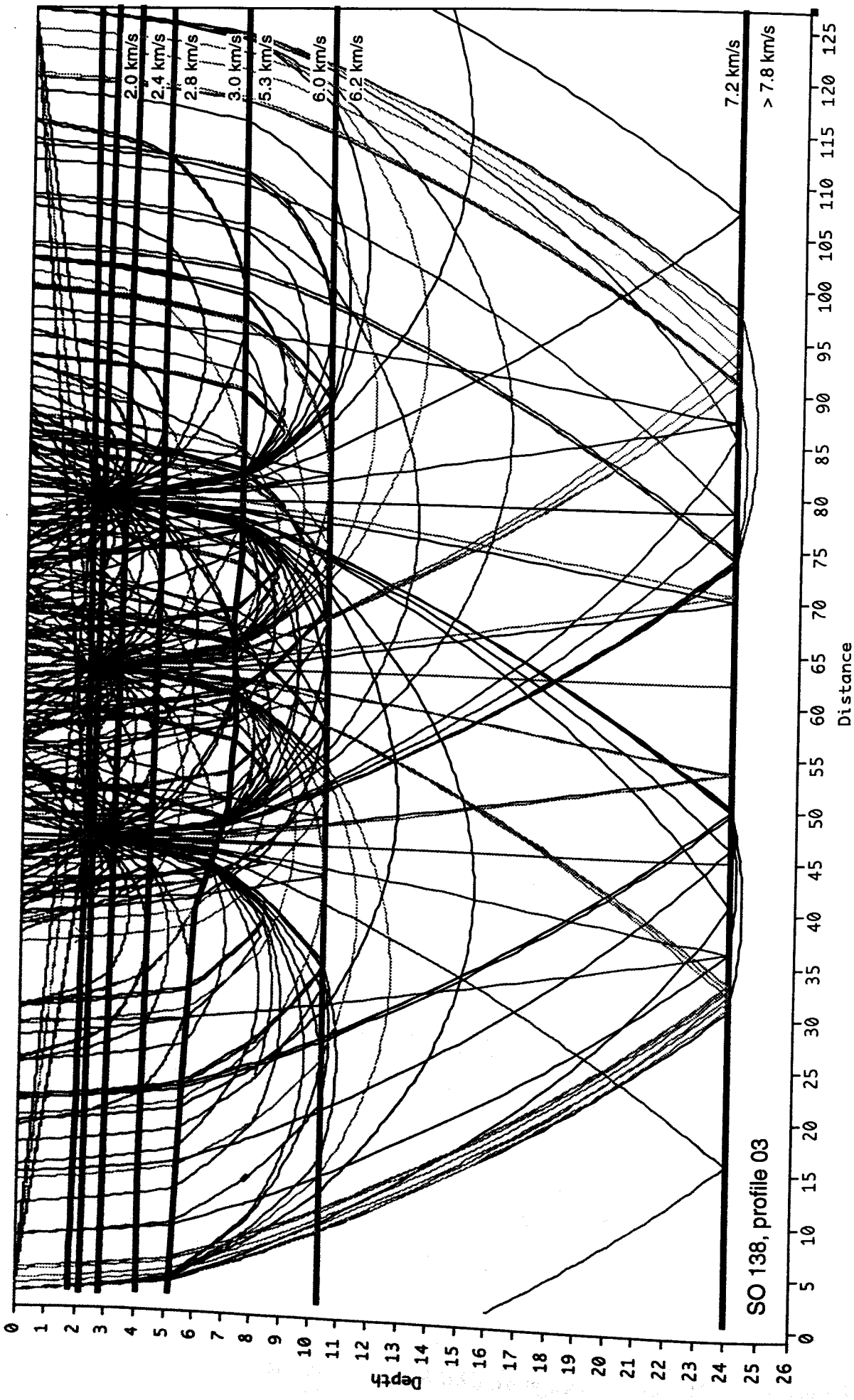

Figure 6.3.4.2.25: Ray coverage from OBH 19, 22, and 25

6.3.4.3 PROFILE SO138-04

(T. Petersen, J. Bialas, E. Flueh)

Profile SO138-04 is a dip line across the margin off Sunda Strait and was chosen coincident with MCS line SO137-42 (Reichert and shipboard Scientific party, in prep.). Sixteen instruments (OBH35 to 50) were deployed, three of them seaward of the trench. A gap of 25 miles across the trench could not be filled with instruments due to water depths in excess of 6000 m. The OBS (OBH49), the vertical array (OBH48) and a newly designed small OBS, the OBS light (OBH47) were among the instruments deployed (Figure 6.3.4.3.1). Deployment of the instruments started on 10 January 1999 at midday, and was finished on 11 January 1999 at 04:00. A transit profile with the magnetometer deployed was run to the start of the shooting line close to Krakatau volcanoe. Shooting started on 11 January 1999 at 07:55. The shot interval was 60s, and the streamer and magnetometer were also deployed. In the early evening, one of the arrays had to be pulled in after it got tangled with some fishery gear, but could be redeployed soon after. Shooting extended for about 20 miles across the first instrument and was terminated on 12 January 1999 at 18:50. All instruments were safely recovered by 18:00 on 13 January. Further details on instrumentation and shooting are given in appendices 9.1.3 and 9.2. The data recorded by the streamer are shown in Figure 6.3.4.3.2, and the record sections of the OBH that contain valuable data are shown in Figures 6.3.4.3.3 to 6.3.4.3.15. The data quality was rather poor. Severe noise problems were encountered near the trench, similar to observations made on profile SO138-01. There is no obvious explanation for this, although extensive ship traffic was noticed during deployment and shooting. The seismometer of the OBS light did apparently not touch the ground as had been anticipated.

Despite these shortcomings, several record sections contain valuable data and allow a preliminary interpretation.

Modelling and Discussion

All OBH sections are highly asymmetric due to strong topographic and structural variations. First arrival times were picked for OBH39, 40, 41, 42, 43, 45, 47 and 50. A 2D-velocity model was calculated using *MacRay* (Luetgert, 1992) and is shown in Figure 6.3.4.3.6.

The aim was to investigate the velocity distribution in the accretionary wedge. Assumptions were made about the velocity and thickness of the oceanic crust south-west of the trench.

The sedimentary cover above the trench was displayed in the MCS section and included in the modelling. The thickness varies between 0.4 and 1.2 km. An average velocity of 1.9 km/s was assumed throughout the model. Some record sections show sedimentary phases corresponding to such velocities.

For the model, the oceanic crust was divided into three layers. Beneath the sedimentary cover, a 2 km thick high gradient layer with velocities increasing from 4.5 to 6.0 km/s seaward from the trench marks oceanic layer 3a. The velocity increases laterally from 4.7 km/s below the trench to 6.3 km/s in the subducting plate. The lower part of the oceanic crust is about 5 km thick with a moderate velocity increase from 6.3 to 7.2 km/s.

The boundary between the oceanic crust and the upper mantle can not be identified, no P_MP or Moho reflections nor refractions are evident in any section. The dip angle of the subducting oceanic crust increases from 5.5 degrees in the upper part to 8.5 degrees in the lower part. The ray coverage used to construct the model constrains the downgoing slap to a depth of 19 km.

On the shelf and slope 5-6 layers can be identified. Two refraction arrivals from the slope sediment can be distinguished for each OBH section. The first sedimentary layer has a velocity of 1.7 to 1.9 km/s and covers a rough topography. Some of the basin fillings can

also be found in the MCS section, at other parts, only a thin sediment cover is present. The second layer of sediments shows velocities between 2.6 and 2.9 km/s.

The acoustic basement is marked by reflections and refractions with reasonably large amplitudes. It also has a very rough topography, which is probably the result of episodic accretion.

The lateral velocity variations along the profile range from 3.9 to 4.3 km/s with an increase towards Krakatau.

A marked velocity discontinuity (5.2 to 5.8-6.3 km/s) at 10 to 14 km depth is indicated by prominent reflections (OBH47) and refracted arrivals. A similar velocity dicontinuity was found in the working area off Sumatra further north (Profiles SO138-01 and 02). Onboard interpretation only aimed at defining some of the large scale features contained in the data. More detailed analysis will allow a better constrainment of the velocity field and its variation, especially once the coincident MCS data from line SO137-42 are processed.

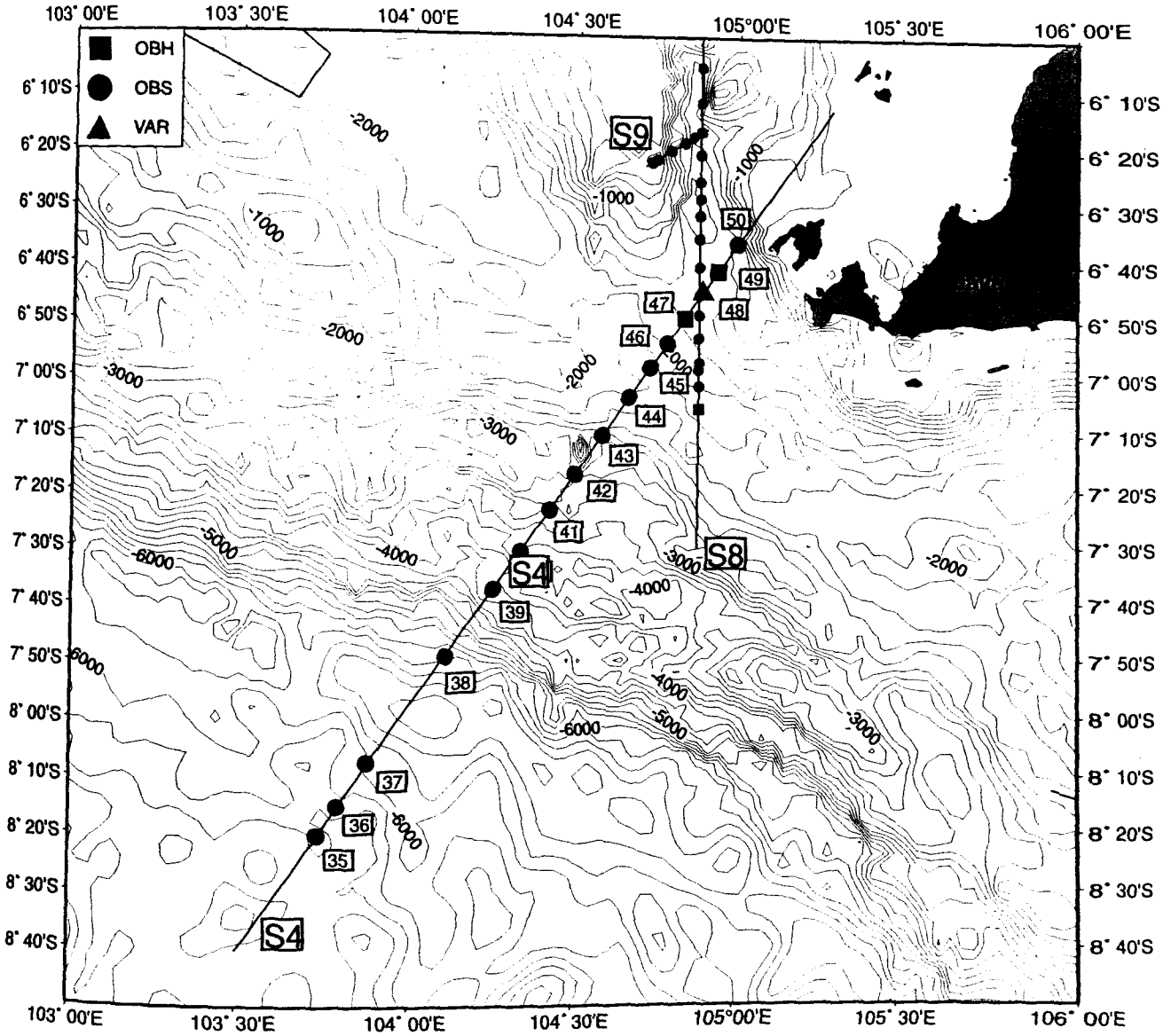

Figure 6.3.4.3.1: Location map of seismic profile S4.

Figure 6.3.4.3.2: Seismic section from MCS stack, Profile 04.

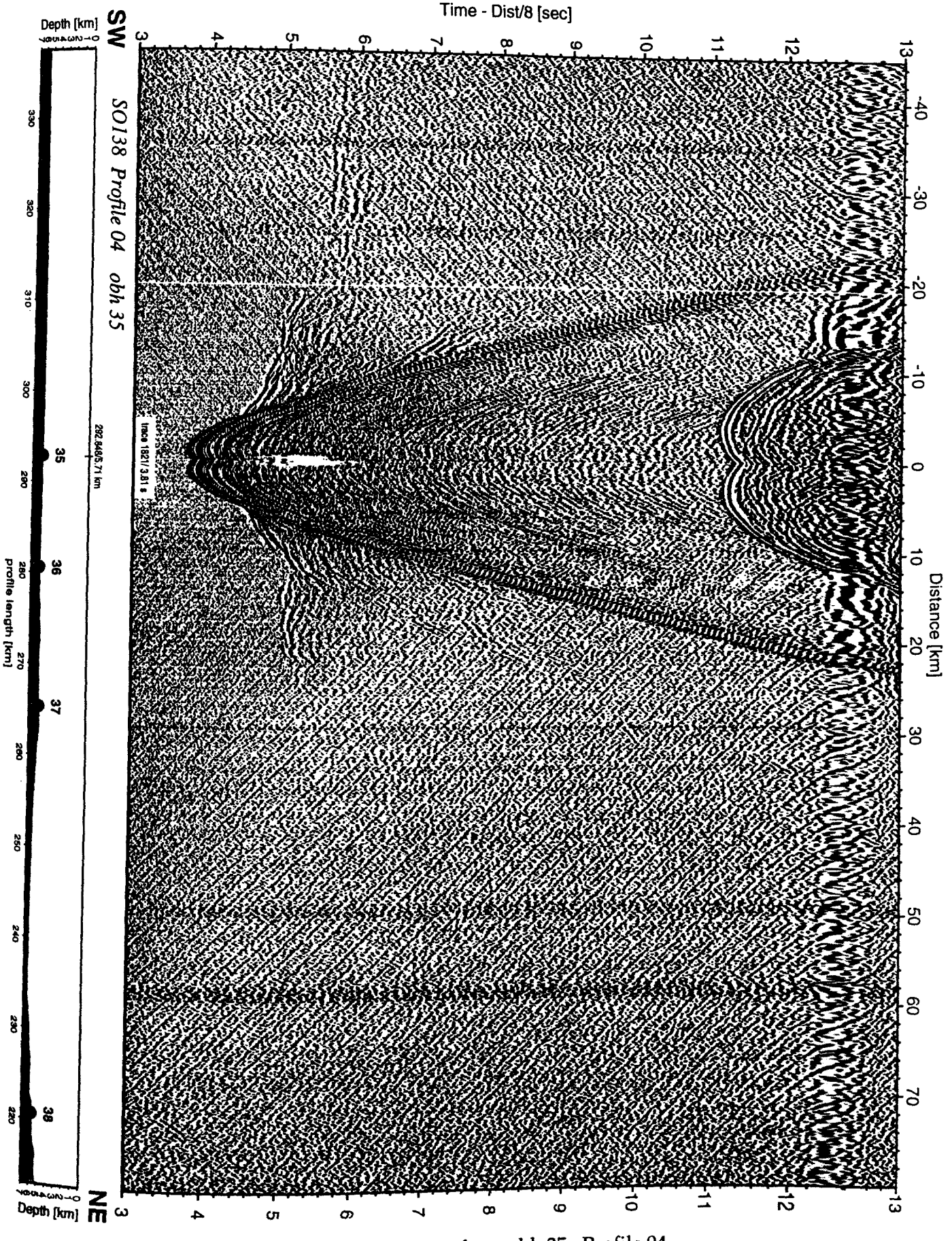

Figure 6.3.4.3.3: Record section from obh 35 , *Profile 04.*

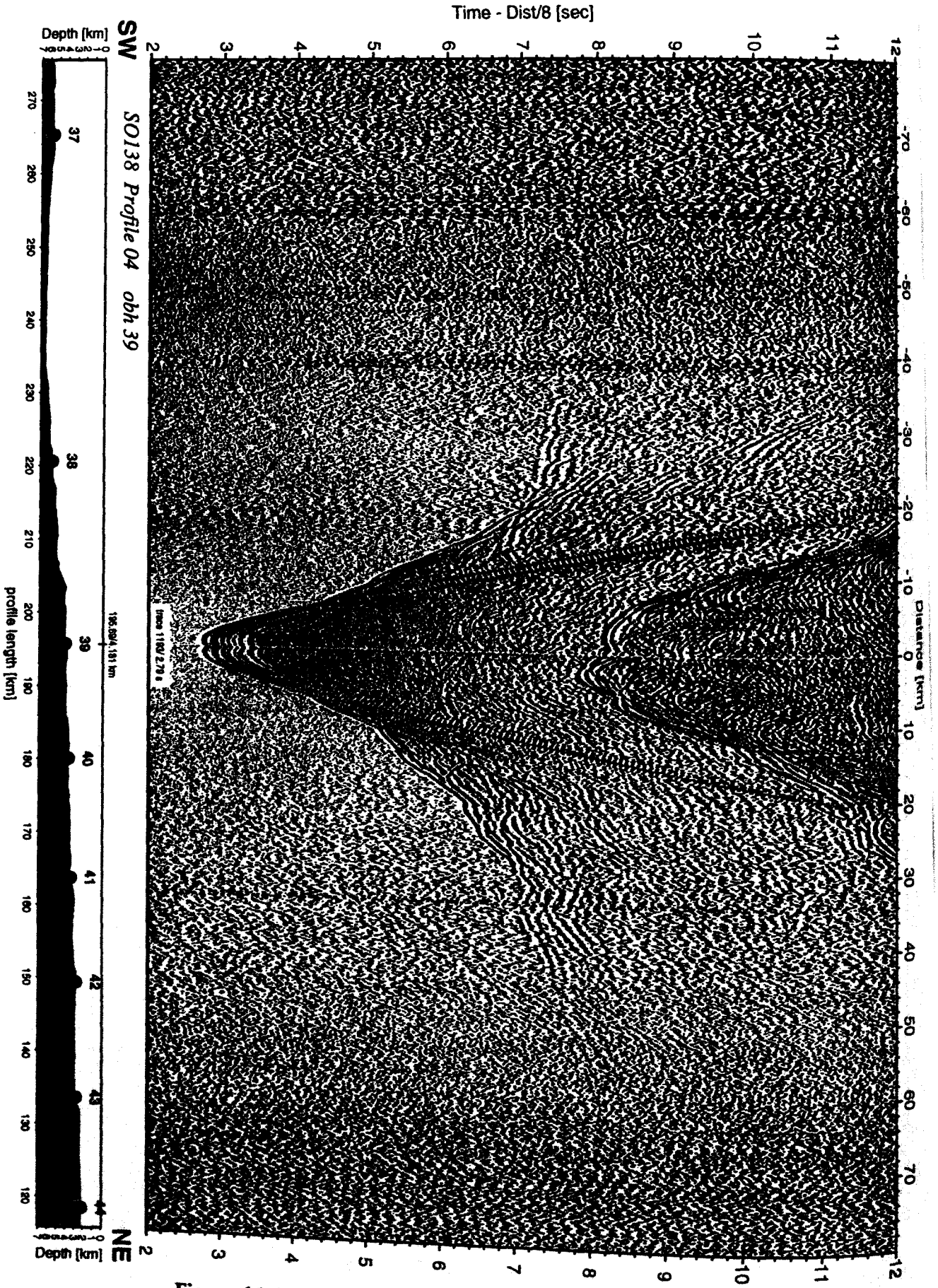

Figure 6.3.4.3.4: Record section from obh 39 , Profile 04.

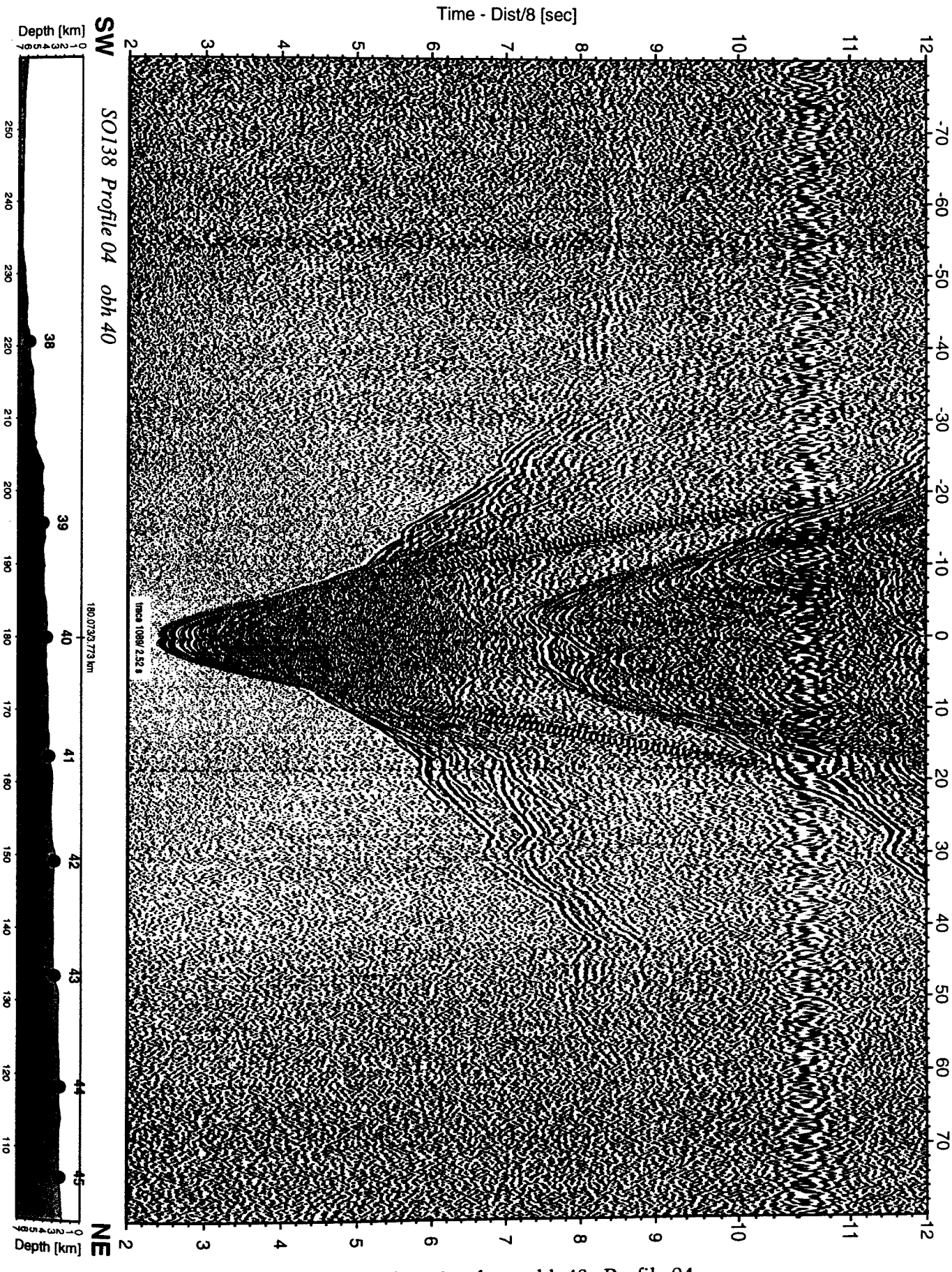

Figure 6.3.4.3.5: Record section from obh 40 , Profile 04.

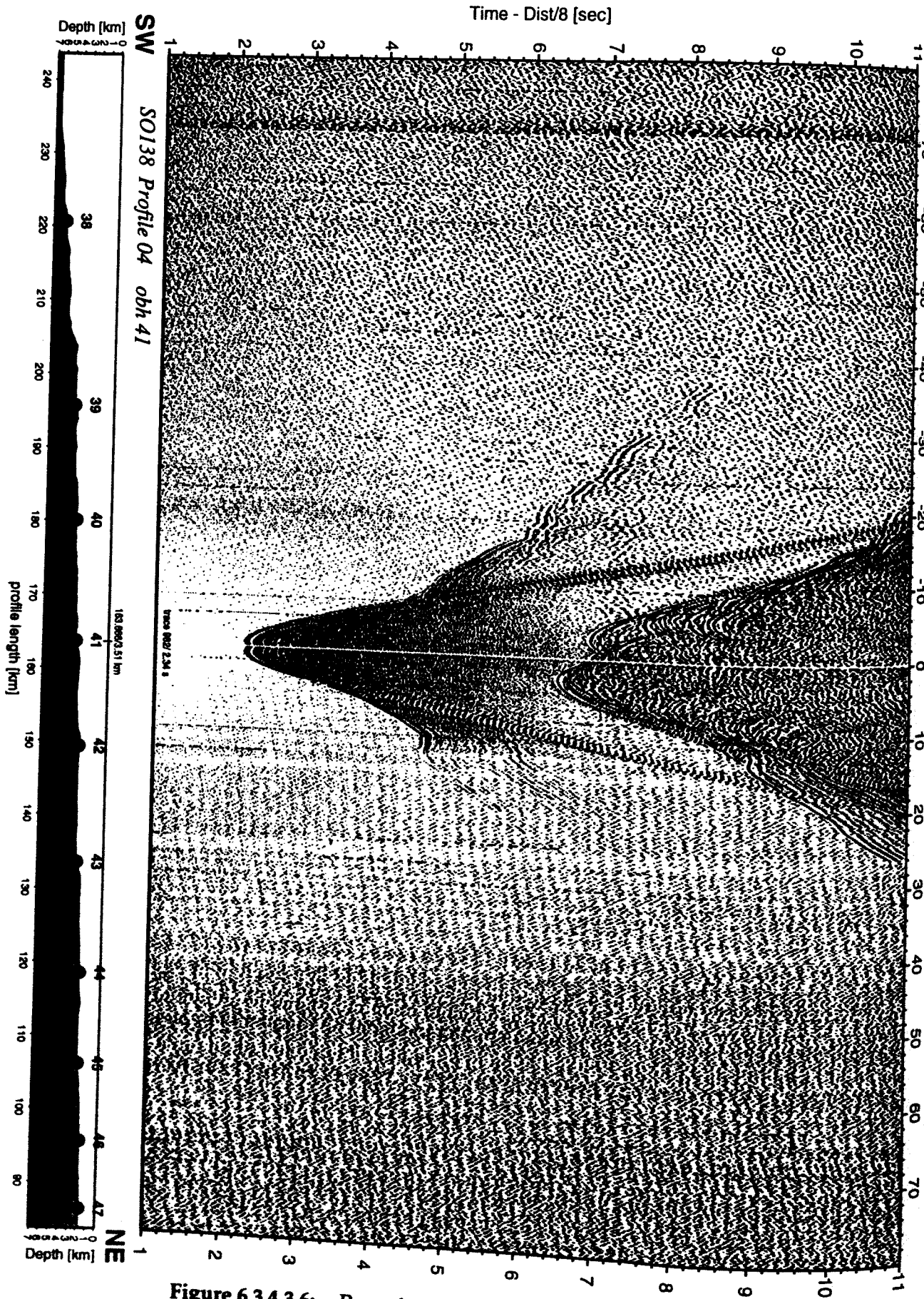

Figure 6.3.4.3.6: Record section from obh 41 , Profile 04.

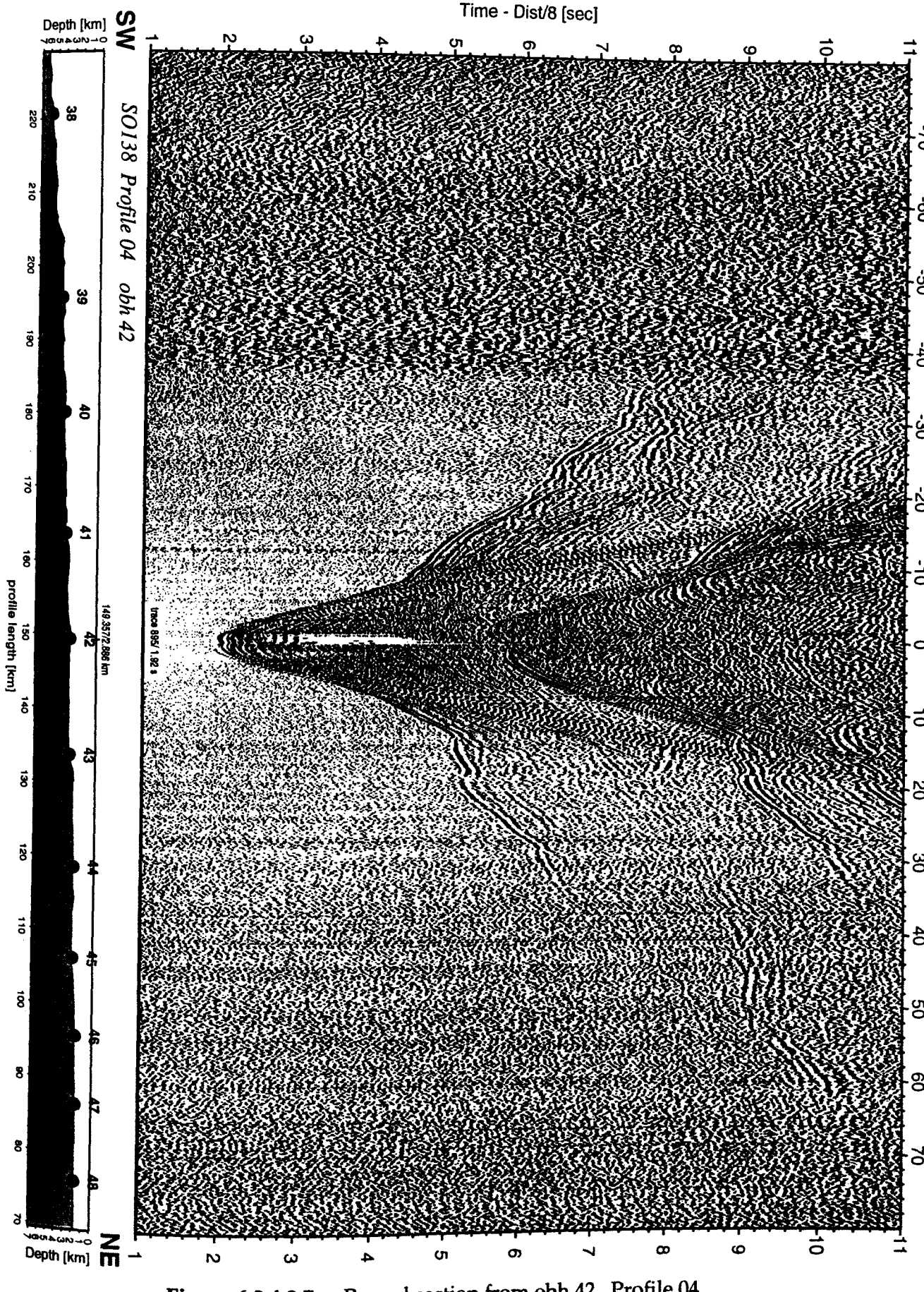

Figure 6.3.4.3.7: Record section from obh 42 , Profile 04.

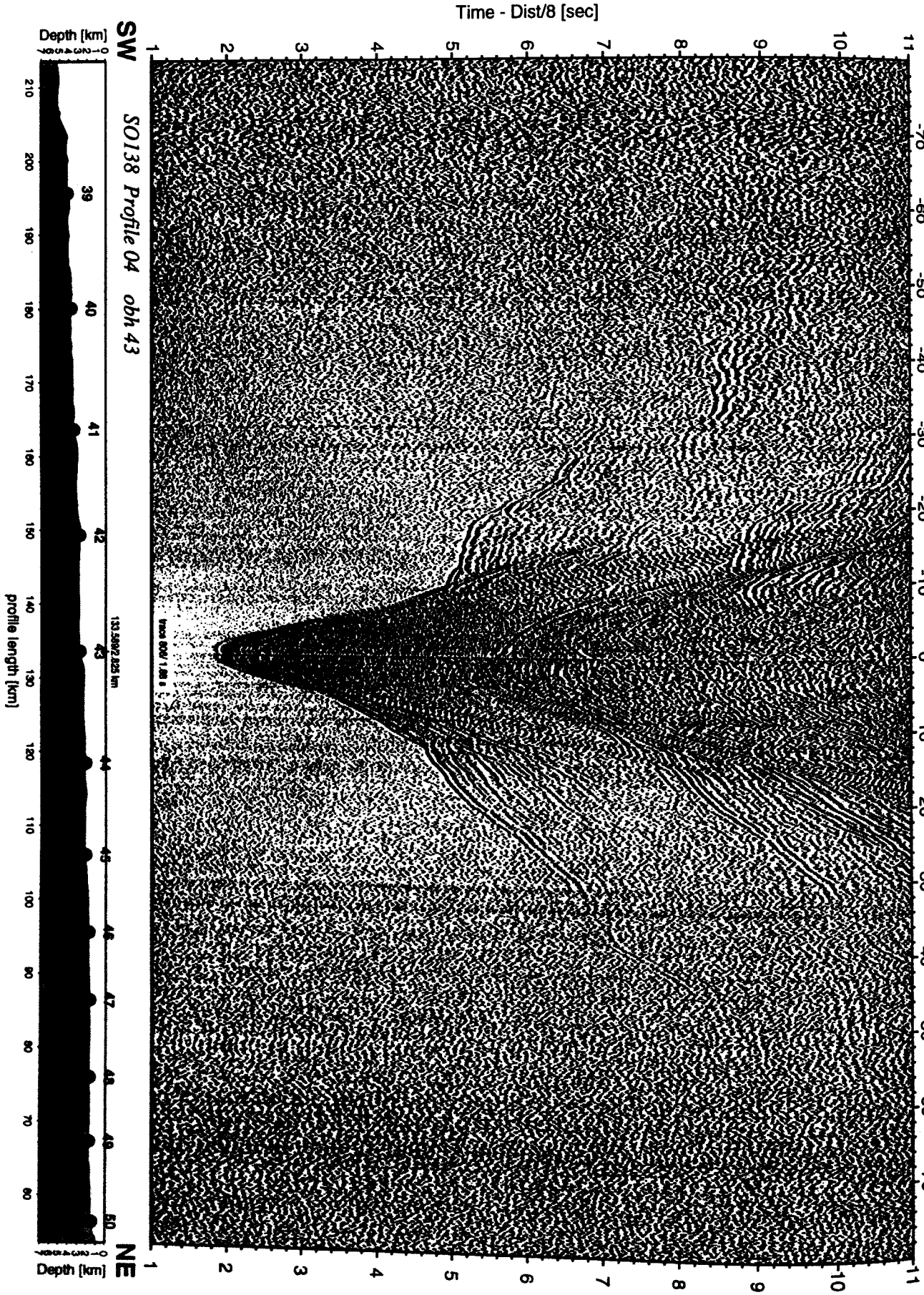

Figure 6.3.4.3.8: Record section from obh 43 , Profile 04.

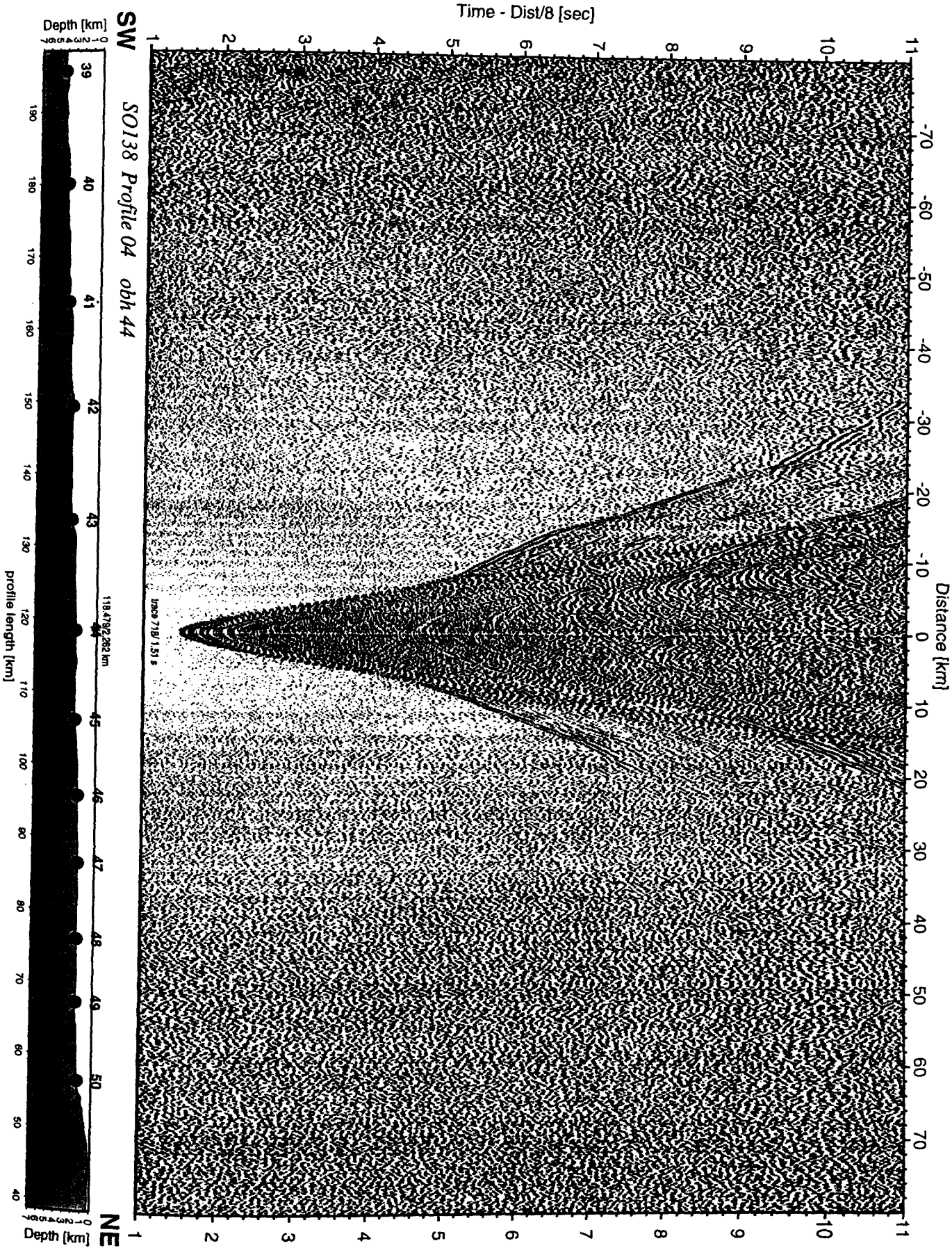

Figure 6.3.4.3.9: Record section from obh 44 , Profile 04.

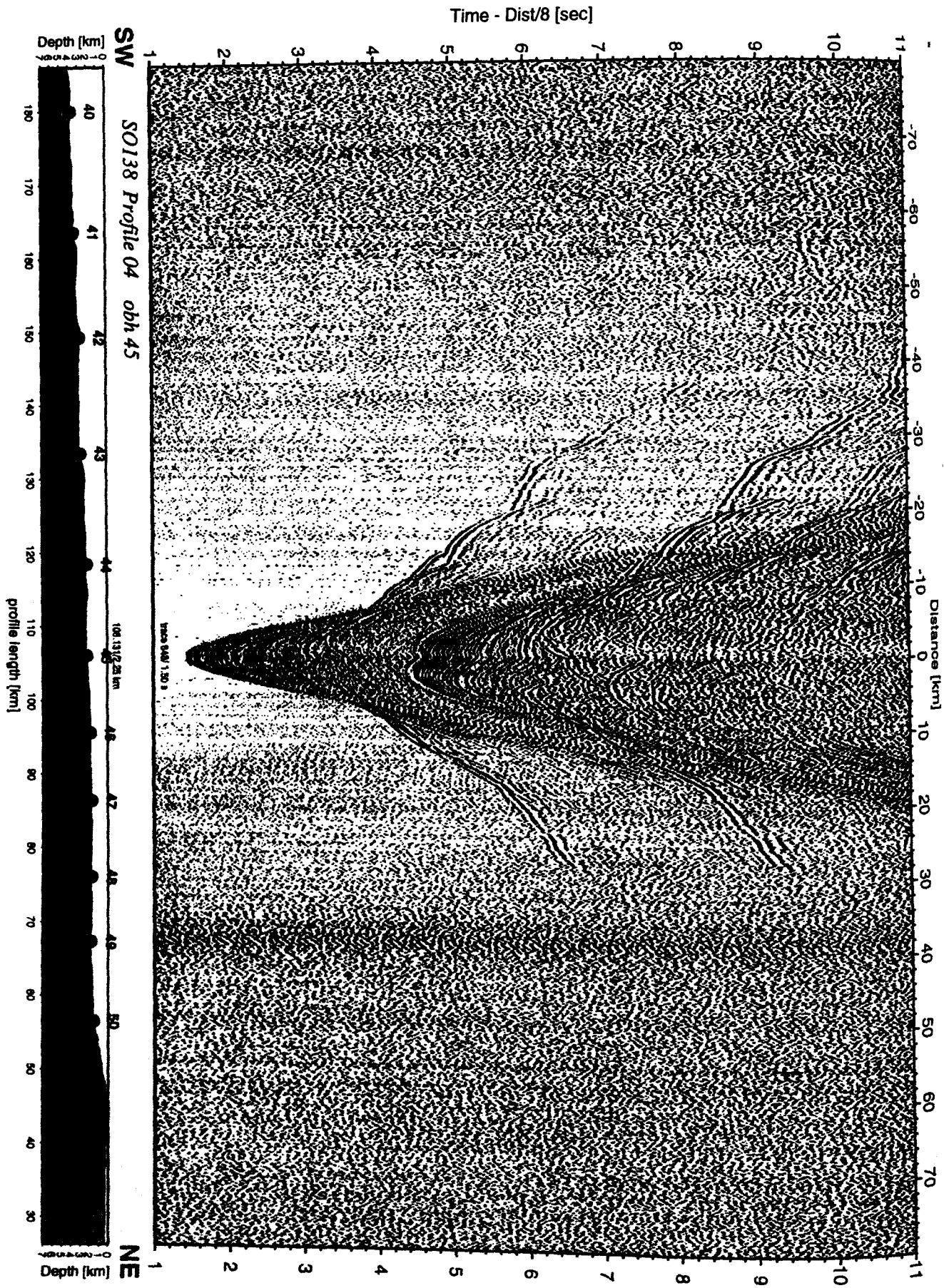

Figure 6.3.4.3.10: Record section from obh 45 , Profile 04.

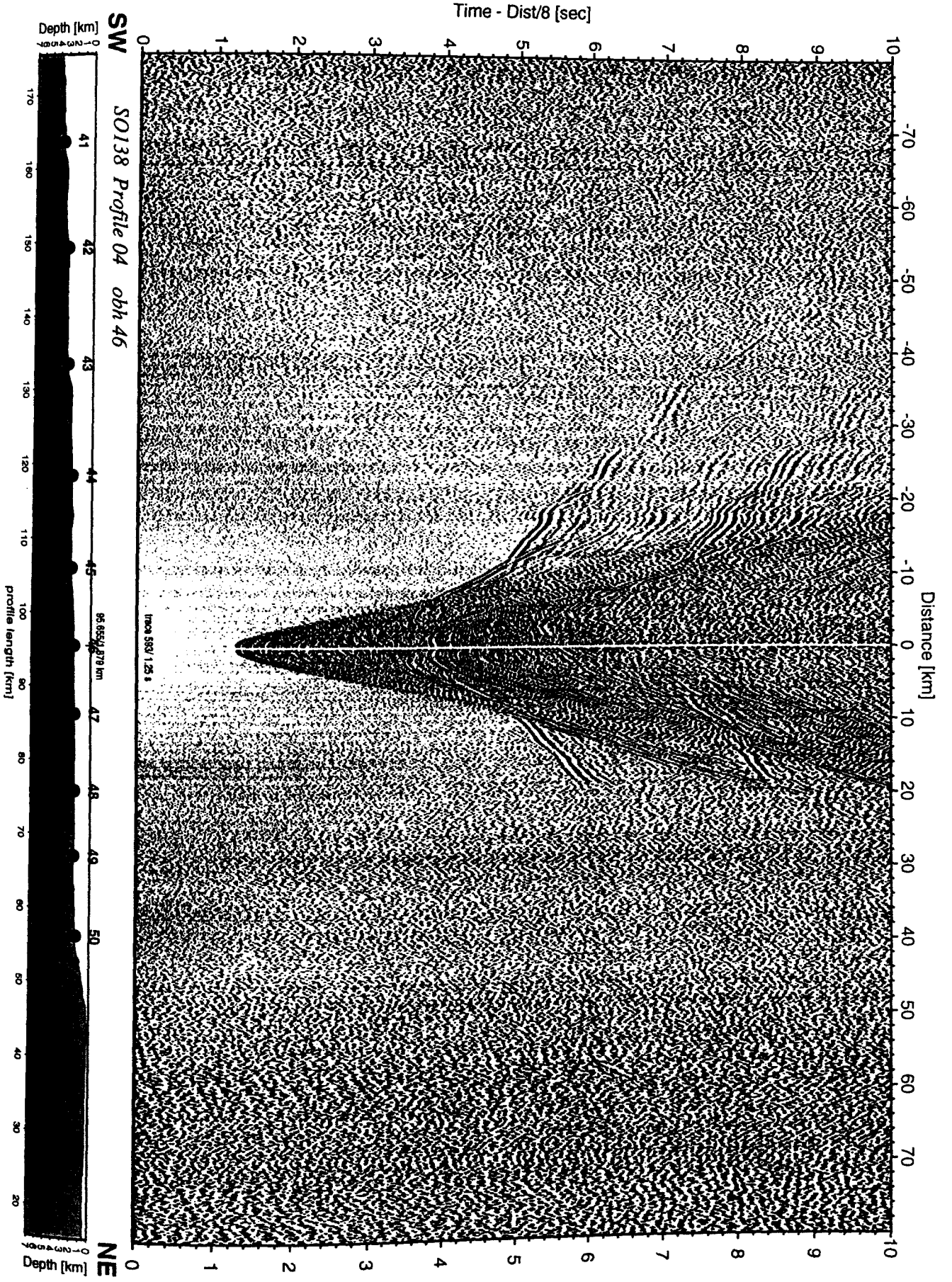

Figure 6.3.4.3.11: Record section from obh 46 , Profile 04.

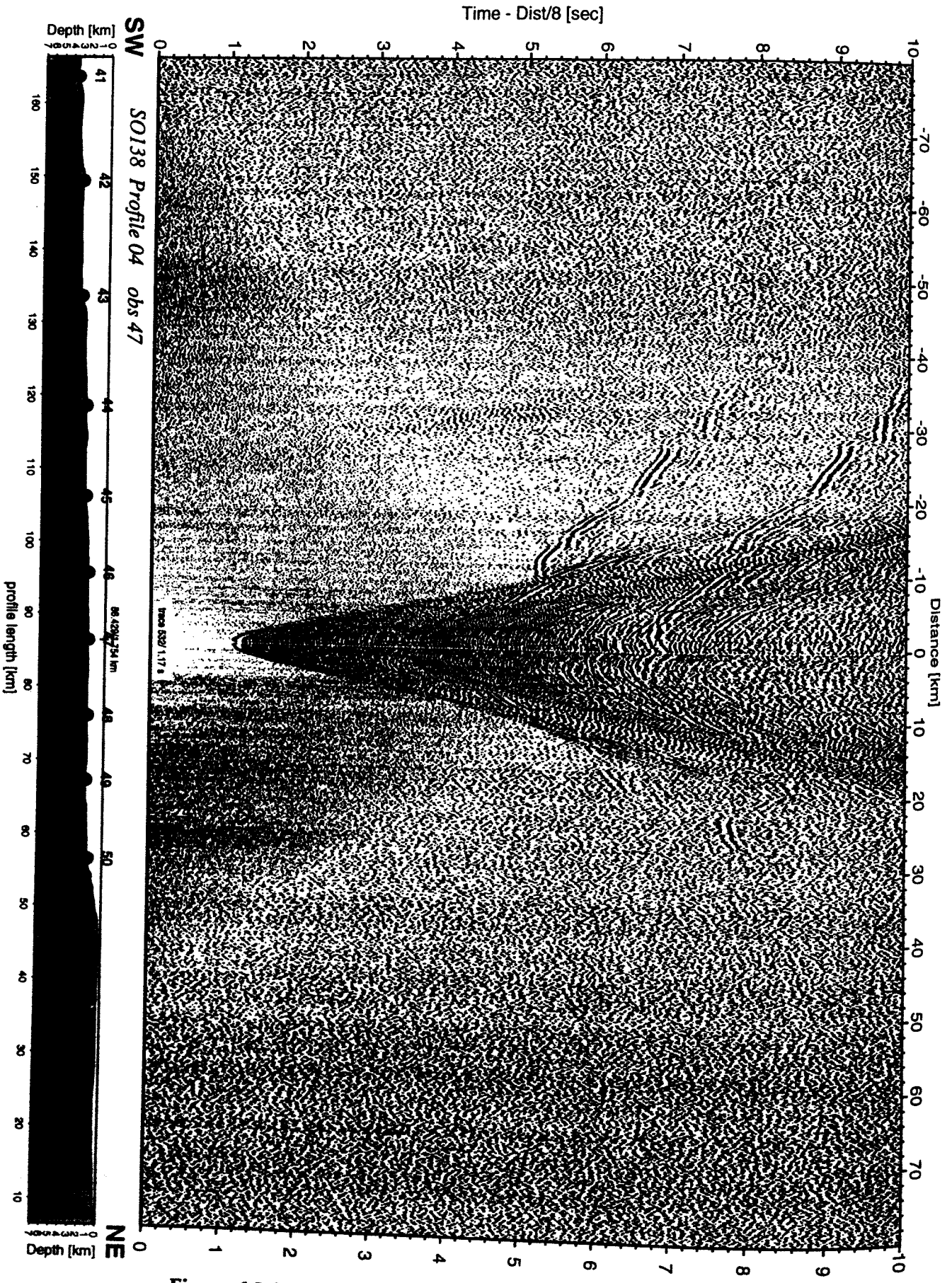

Figure 6.3.4.3.12: Record section from obs 47 hydrophone, Profile 04.

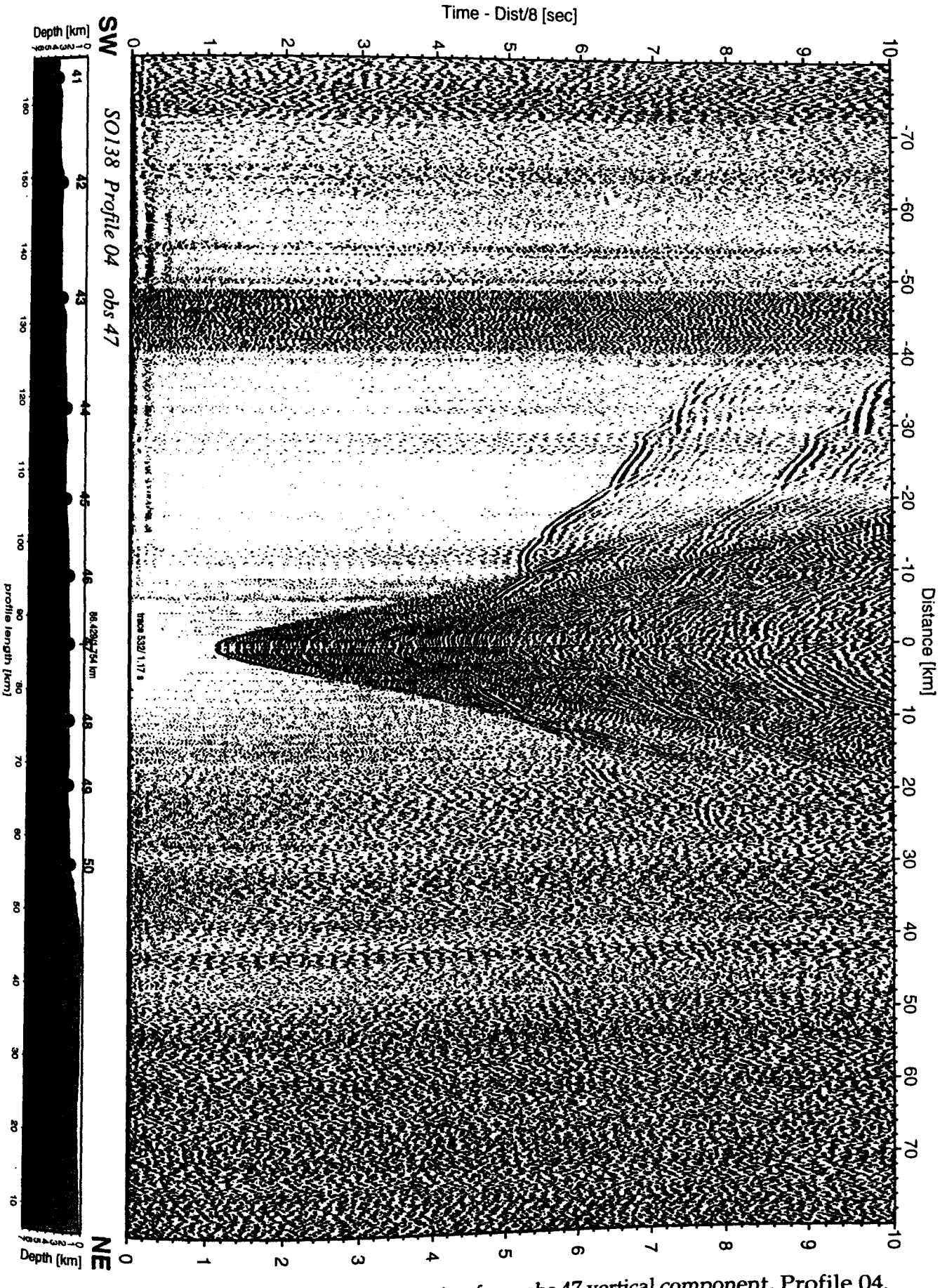

Figure 6.3.4.3.12a: Record section from obs 47 vertical component, Profile 04.

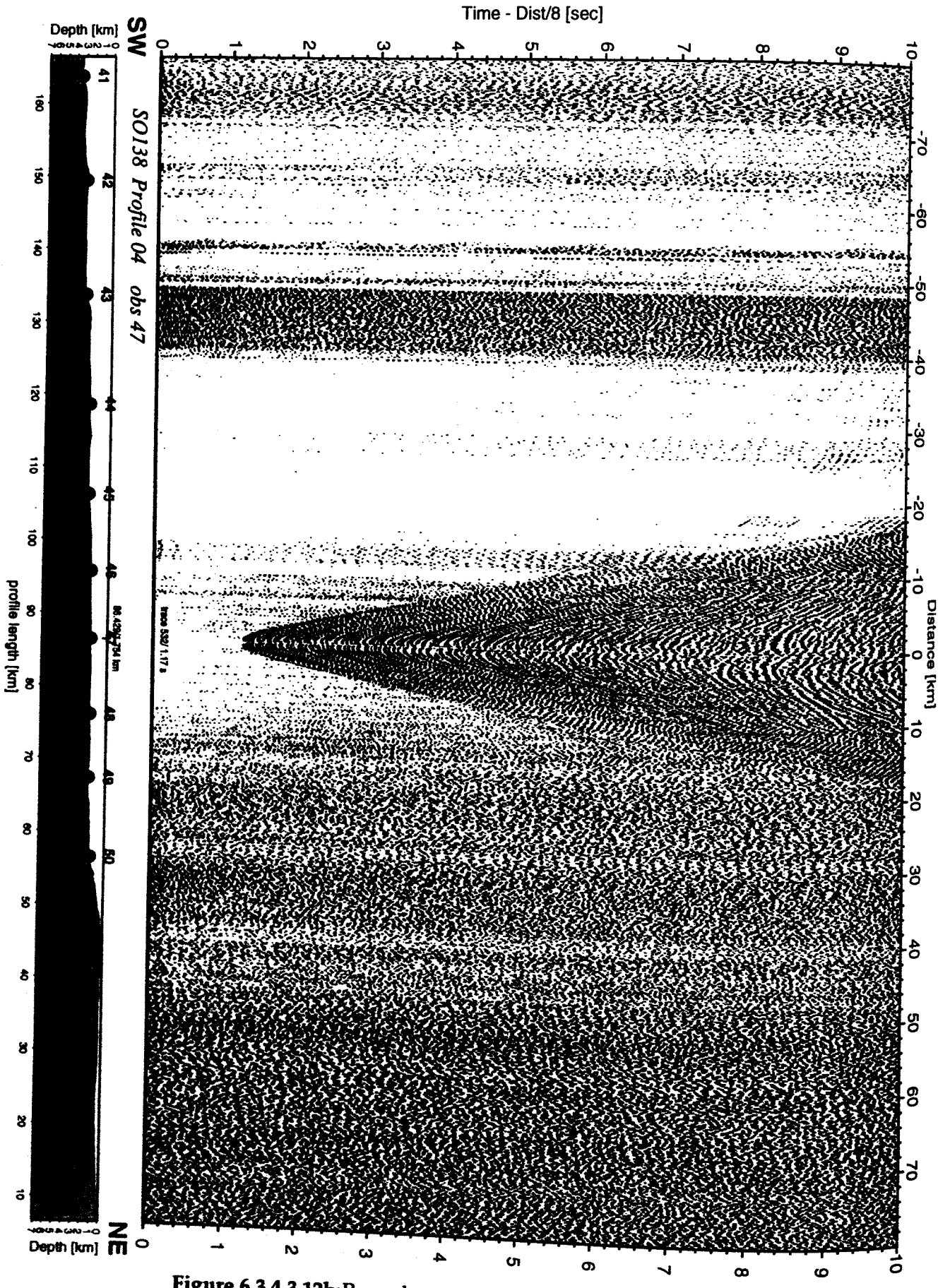

Figure 6.3.4.3.12b: Record section from obs 47 horizontal component 1, Profile 04.

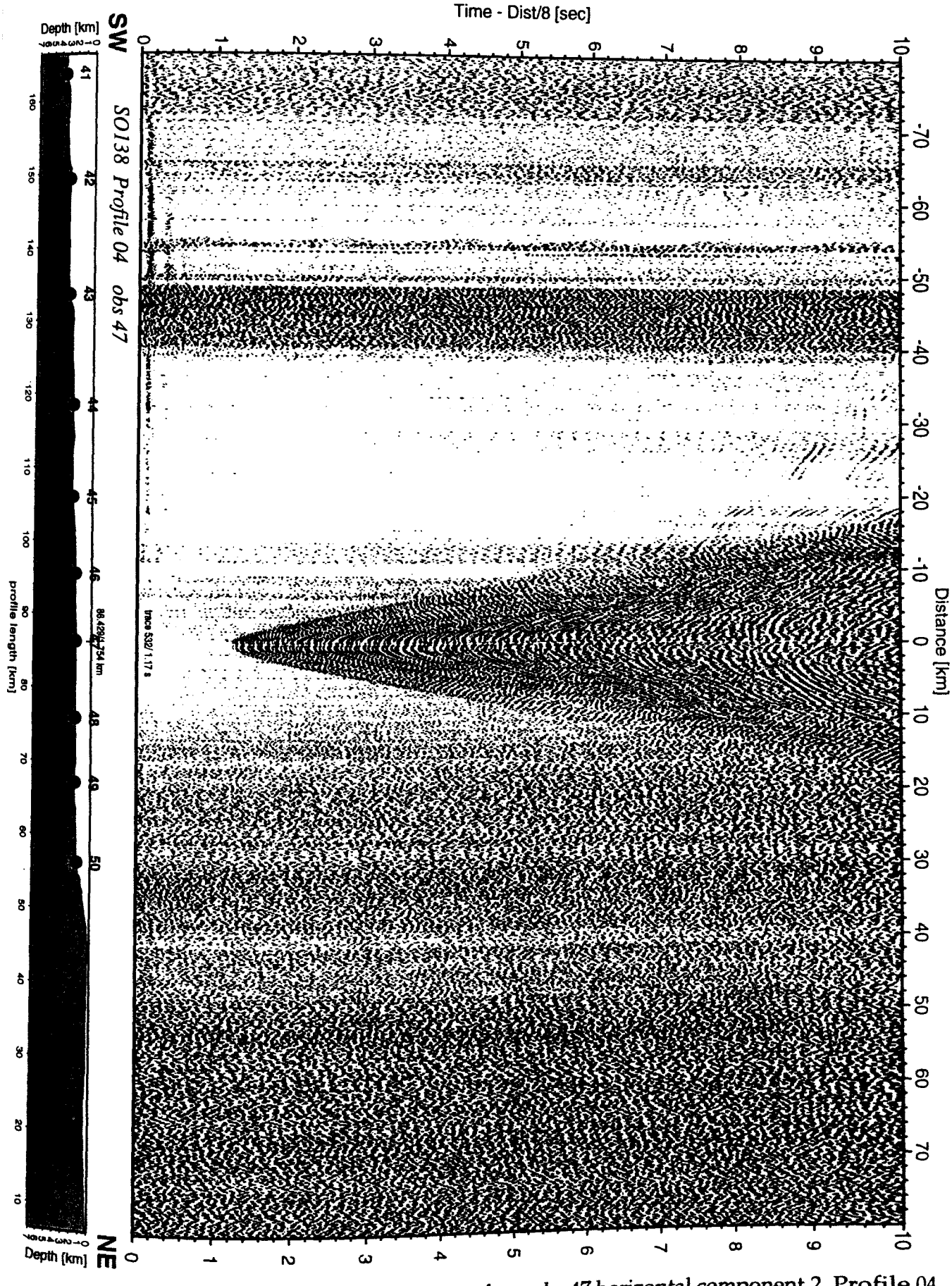

Figure 6.3.4.3.12c: Record section from obs 47 horizontal component 2, Profile 04.

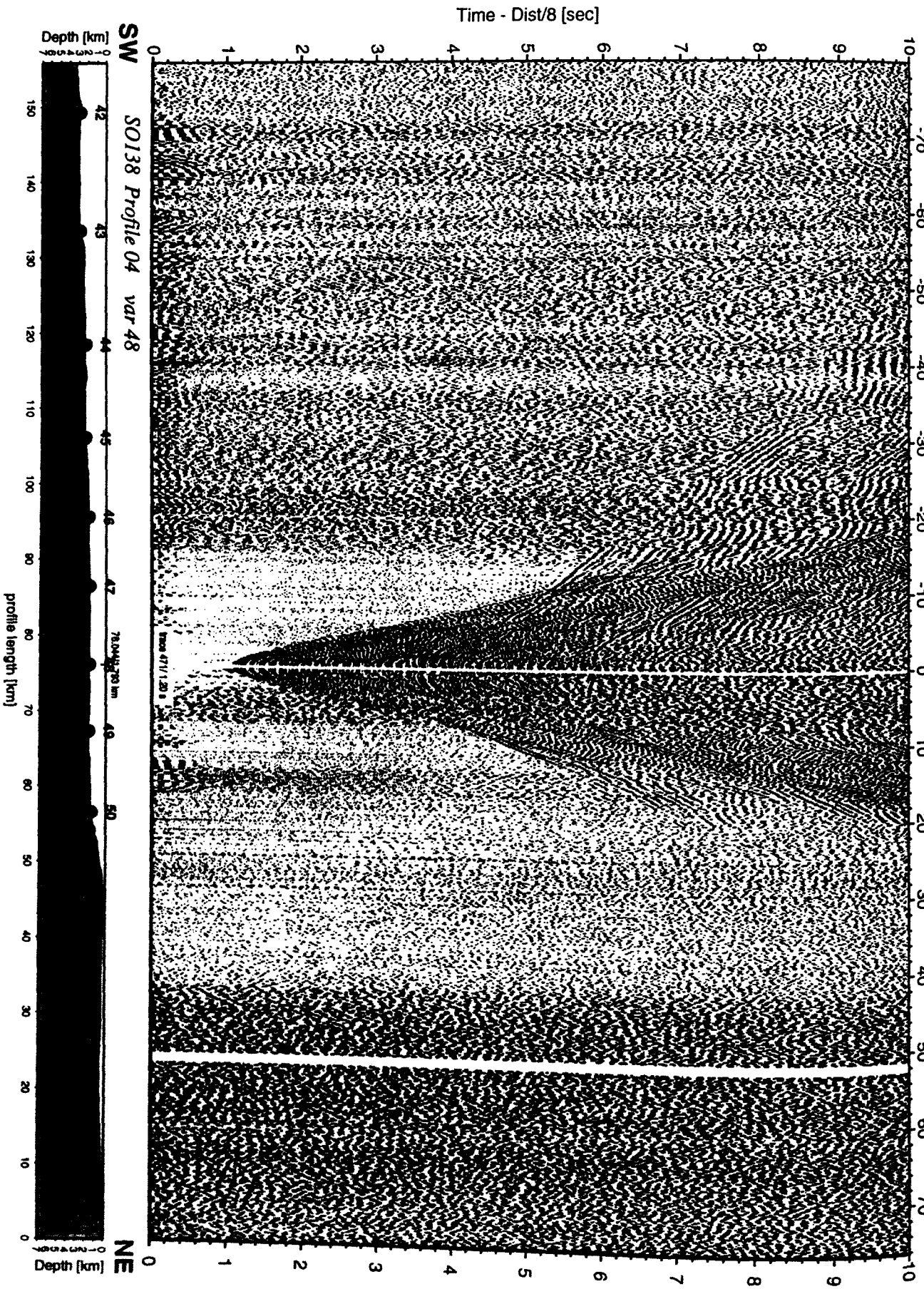

Figure 6.3.4.3.13: Record section from var 48 channel_1, Profile 04.

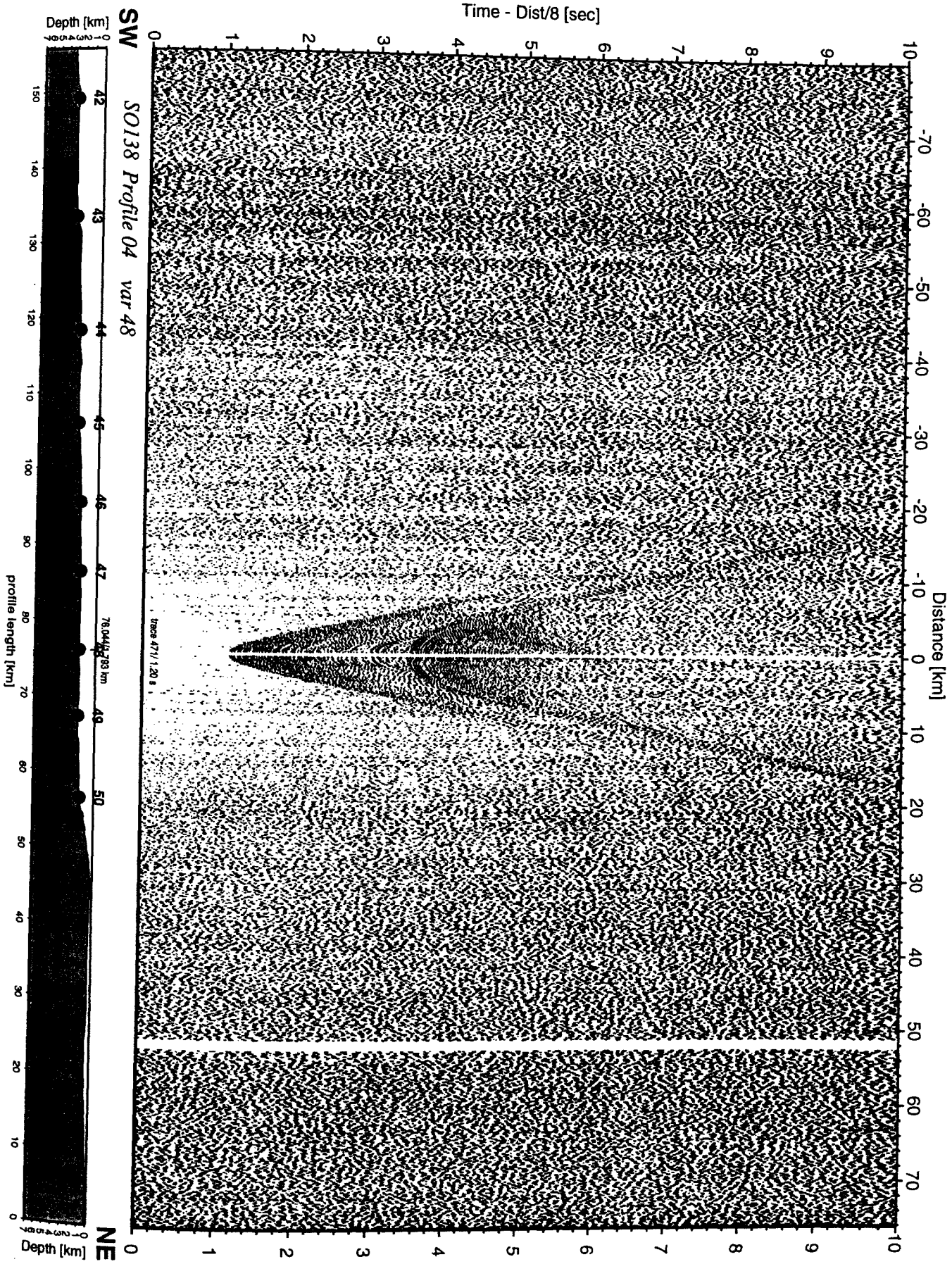

Figure 6.3.4.3.13a: Record section from var 48 channel_2, Profile 04.

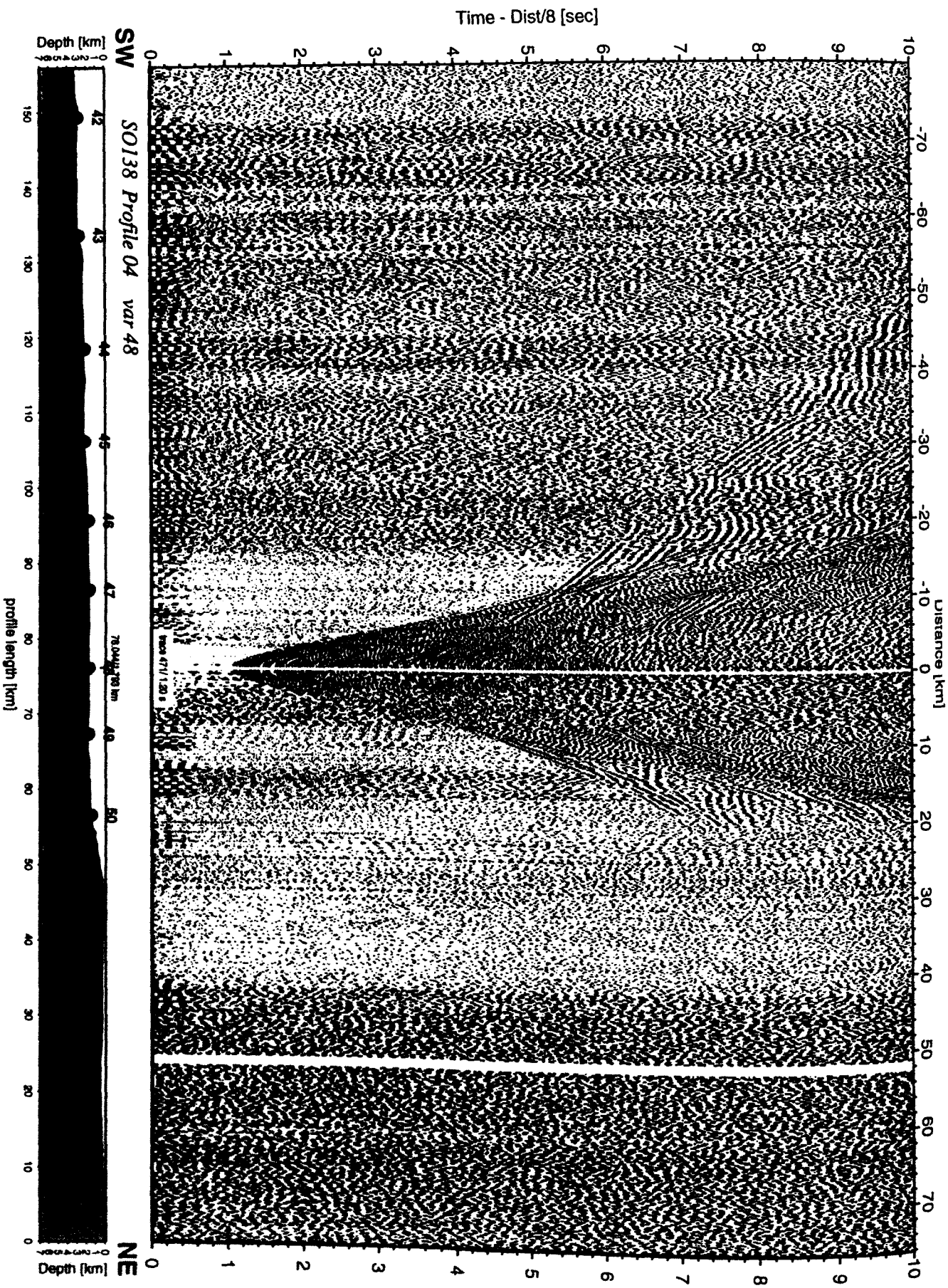

Figure 6.3.4.3.13b: Record section from var 48 channel_3, Profile 04.

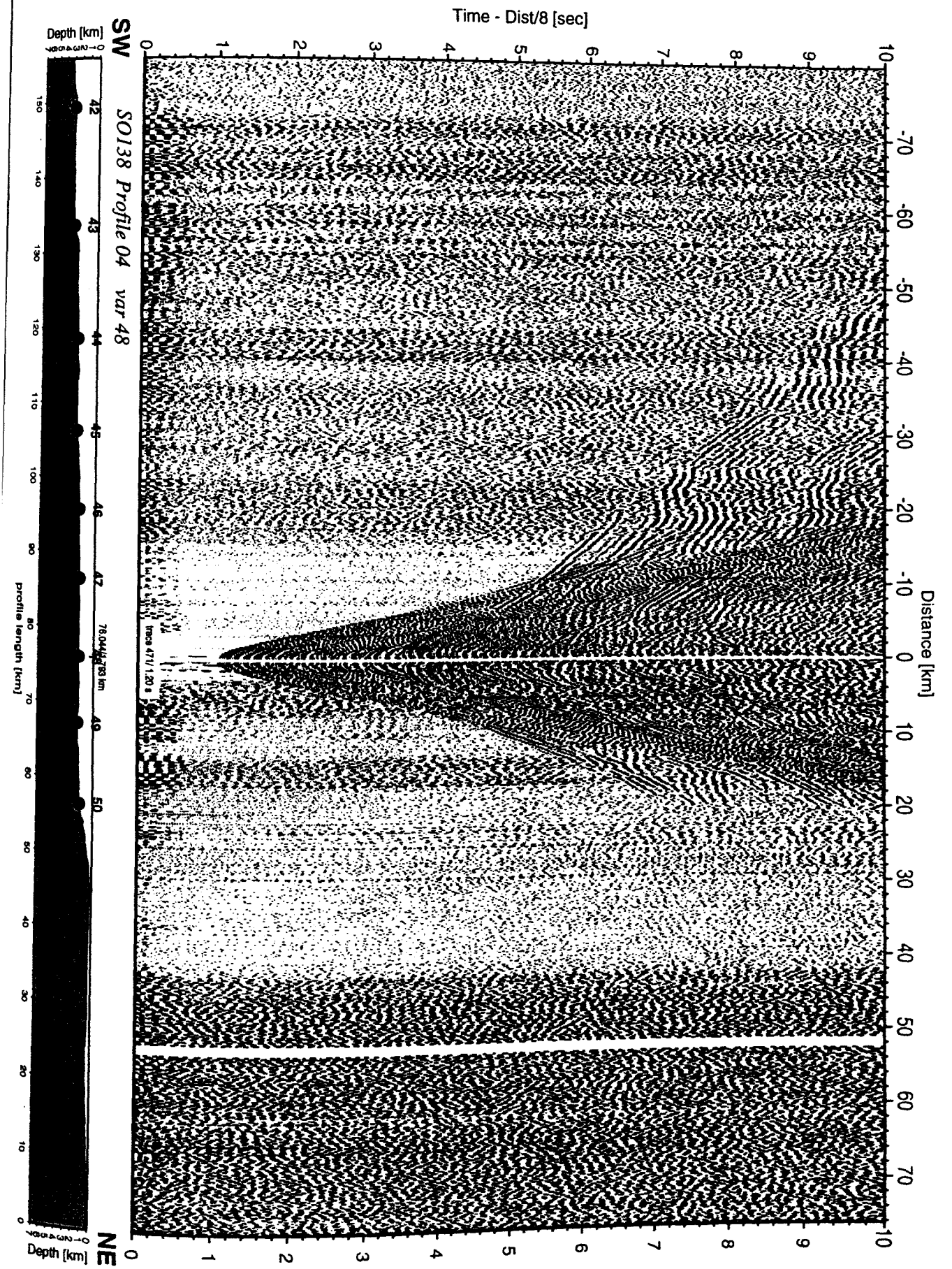

Figure 6.3.4.3.13c: Record section from var 48 channel_4, Profile 04.

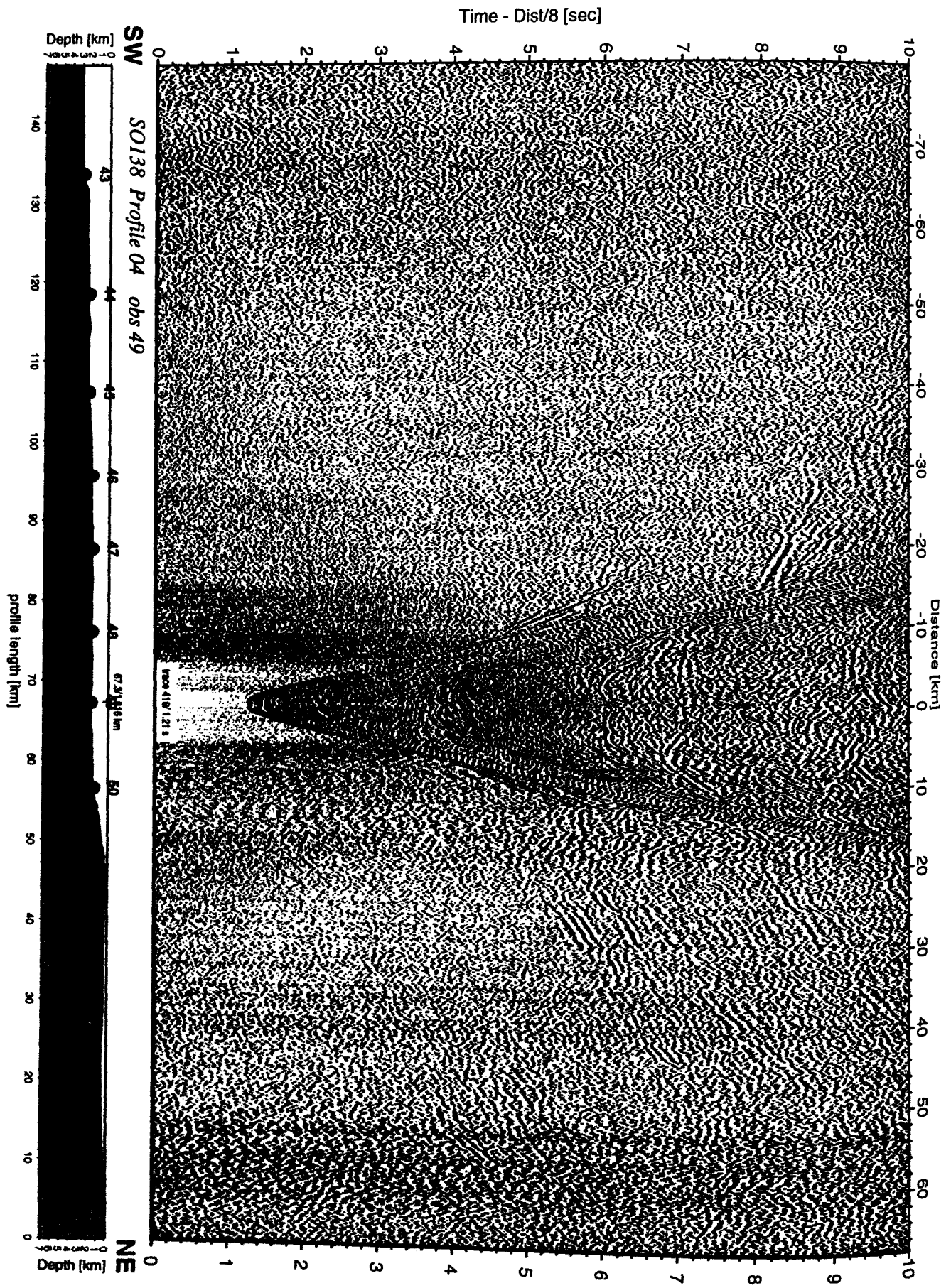

Figure 6.3.4.3.14: Record section from obs 49 hydrophone, Profile 04.

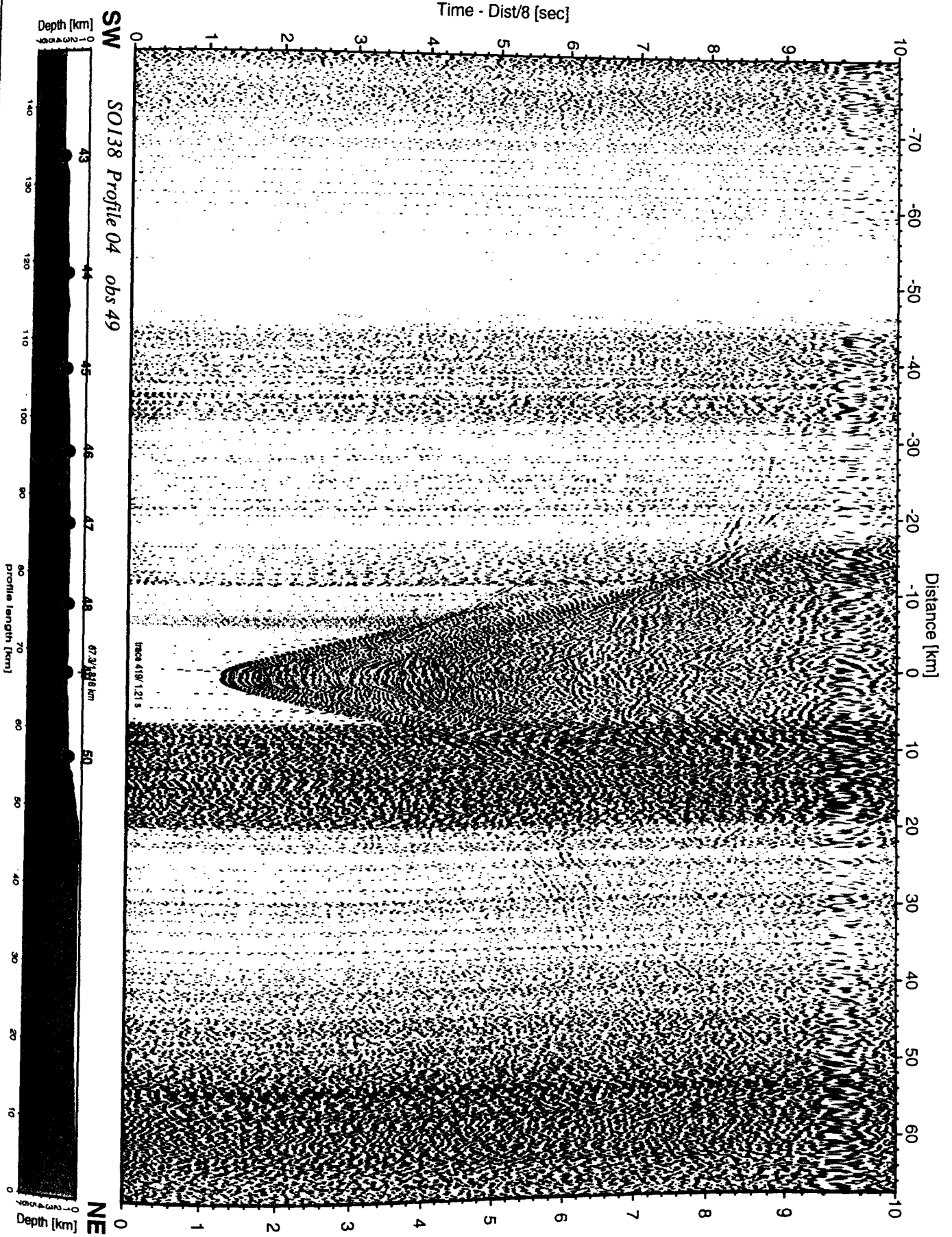

Figure 6.3.4.3.14a: Record section from obs 49 vertical component, Profile 04.

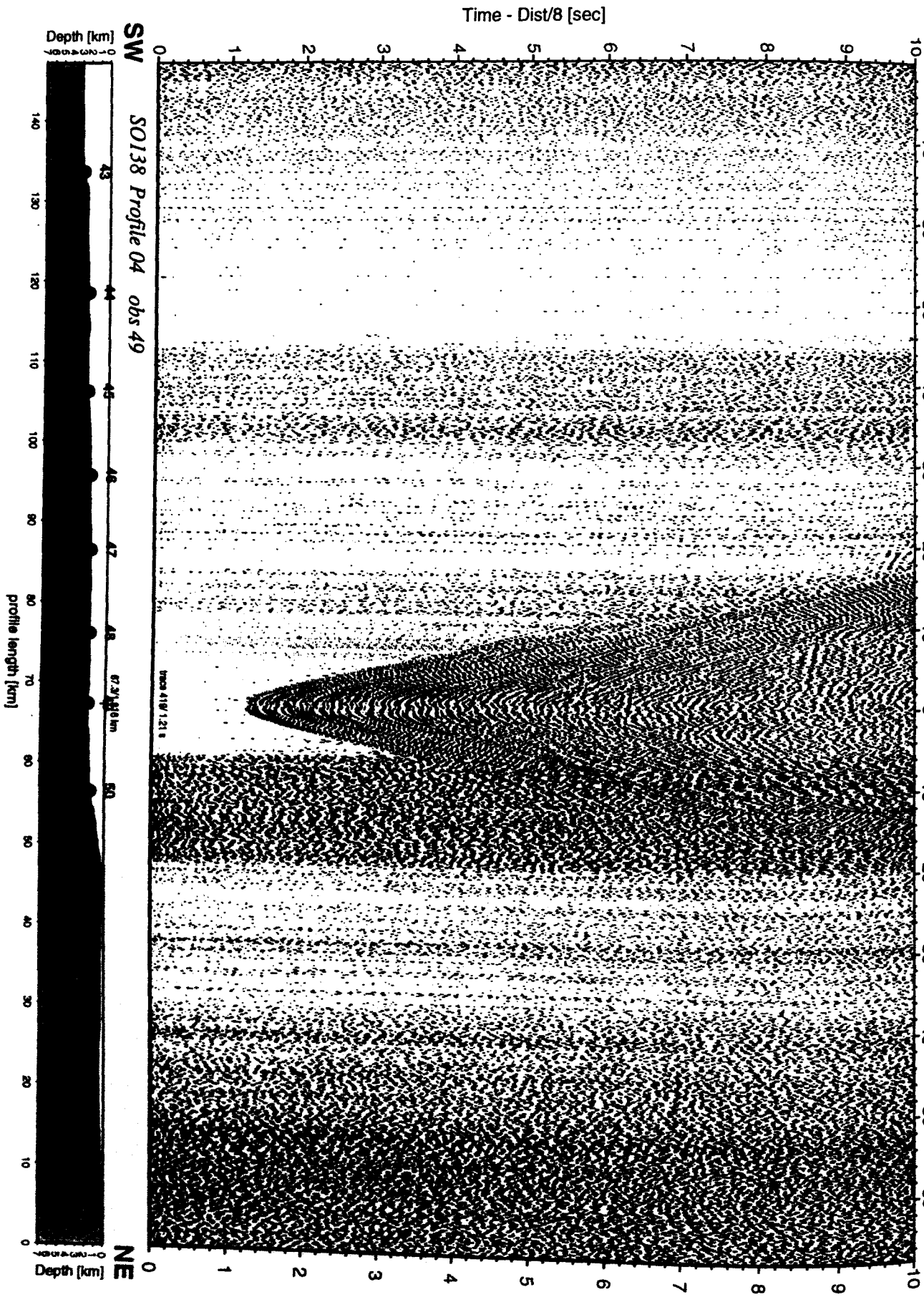

Figure 6.3.4.3.14b: Record section from obs 49 horizontal component 1, Profile 04.

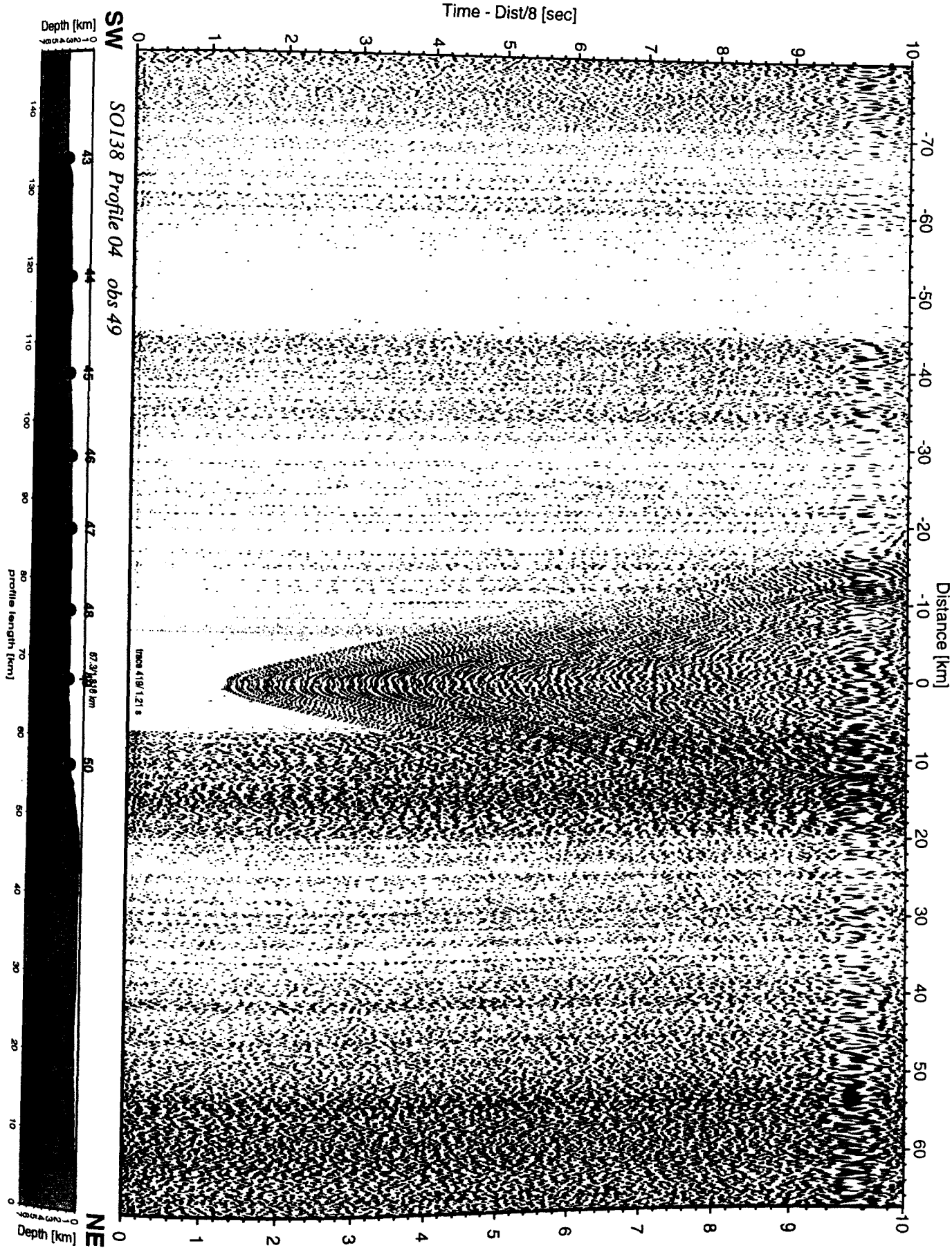

Figure 6.3.4.3.14c: Record section from obs 49 horizontal component 2, Profile 04.

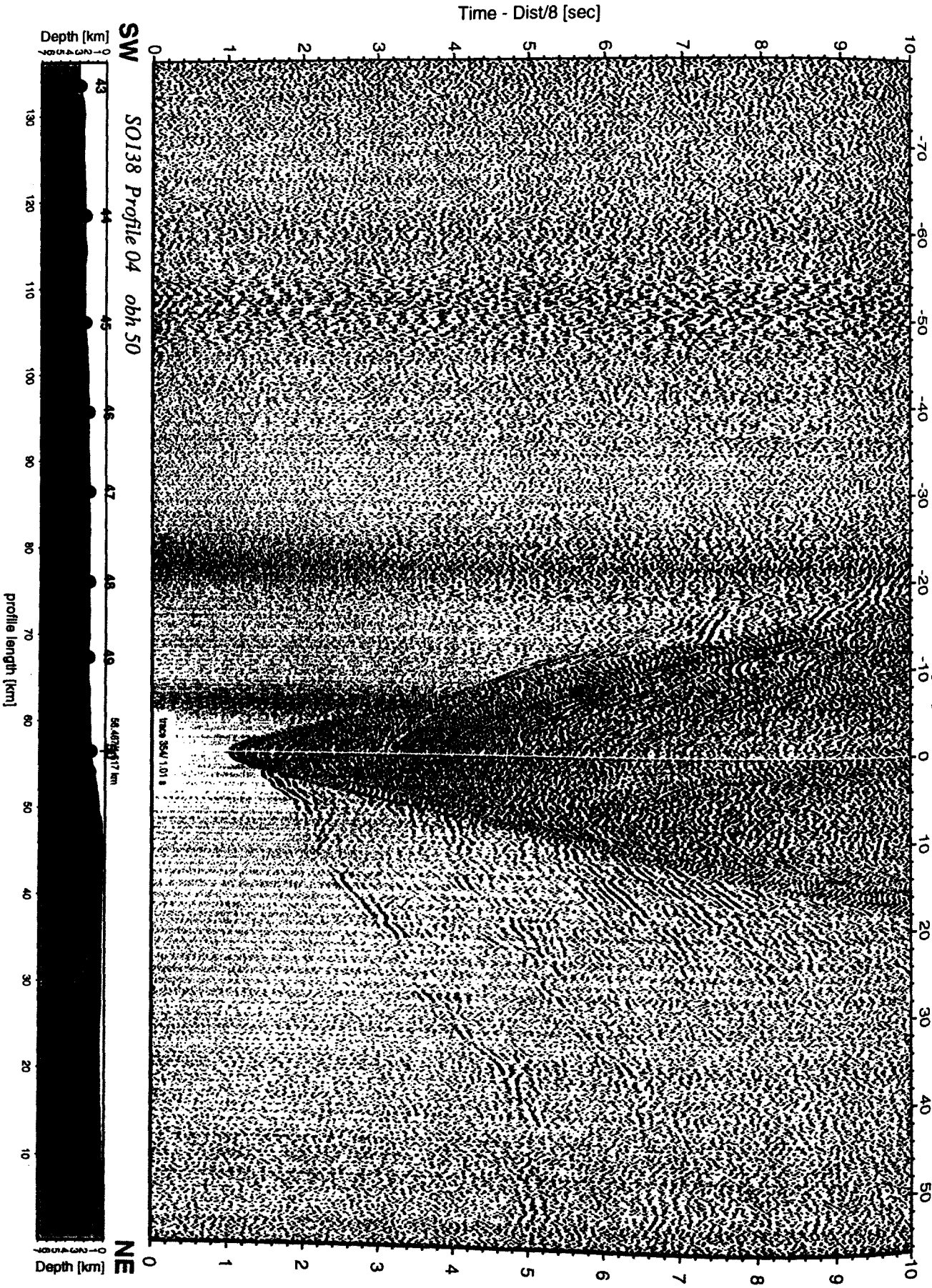

Figure 6.3.4.3.15: Record section from obh 50 , Profile 04.

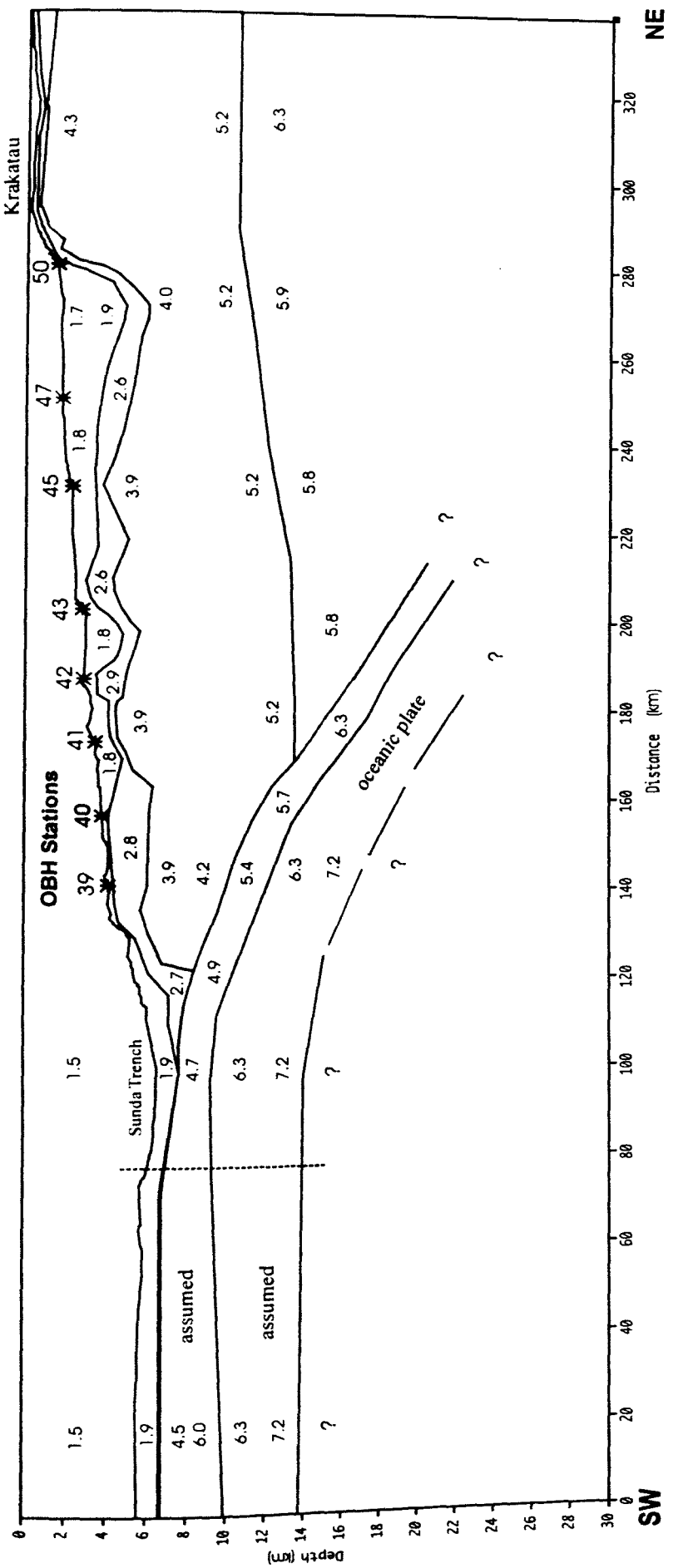

Figure. 6.3.4.3.16: 2D-velocity model of profile SO138-04

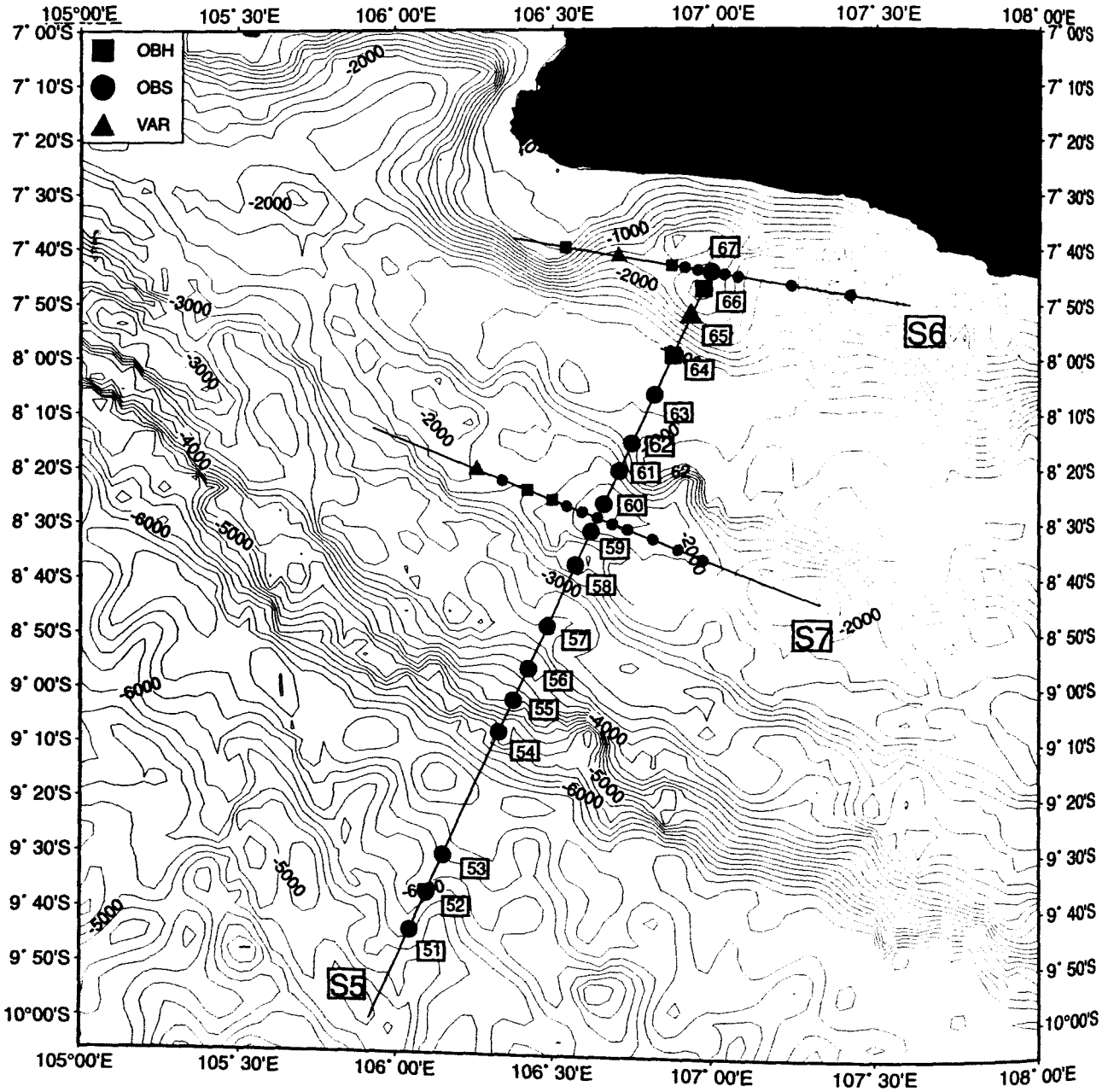

Figure 6.3.4.4.1: Location map of seismic profile S5.

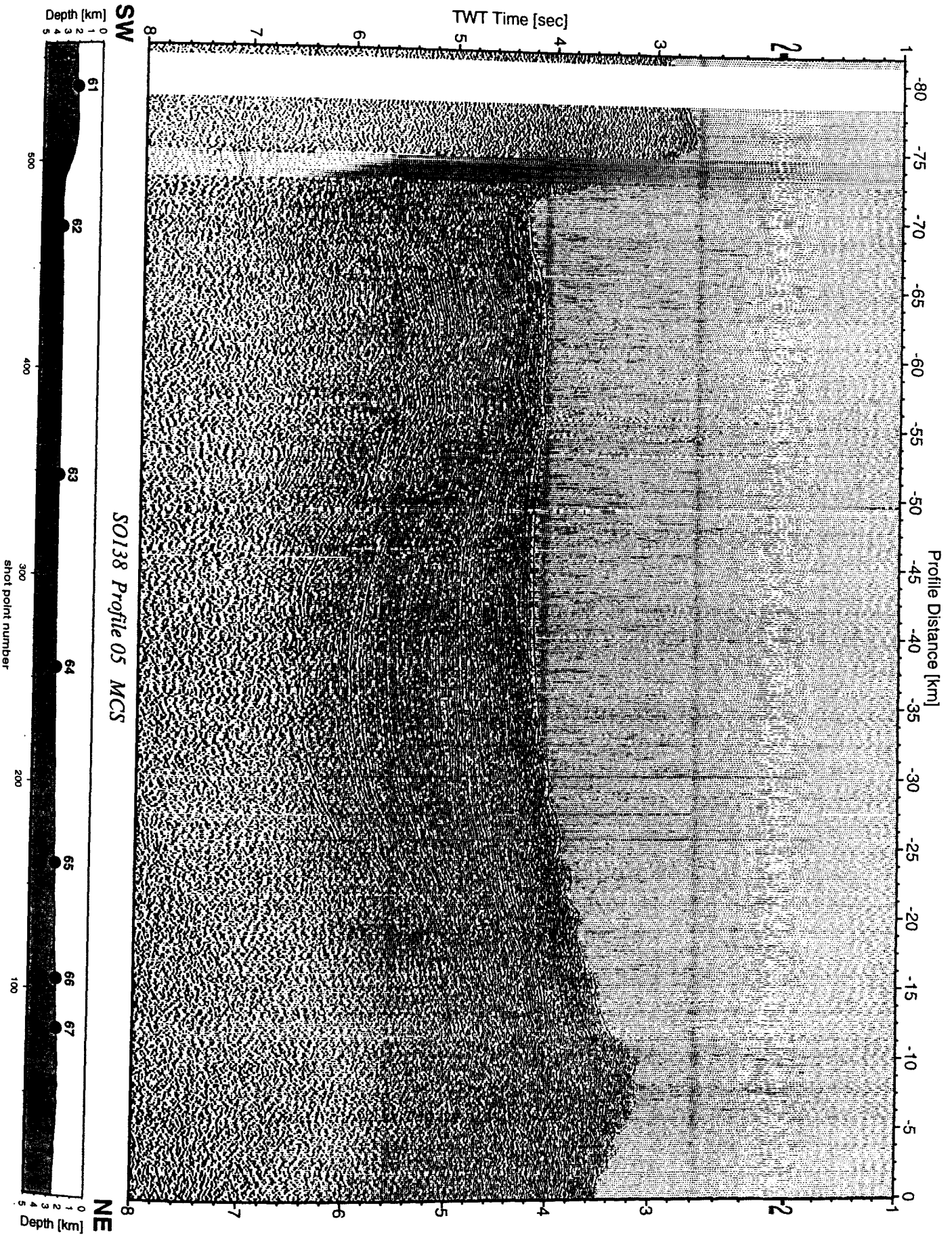

Figure 6.3.4.4.2: Seismic section from MCS stack, Profile 05.

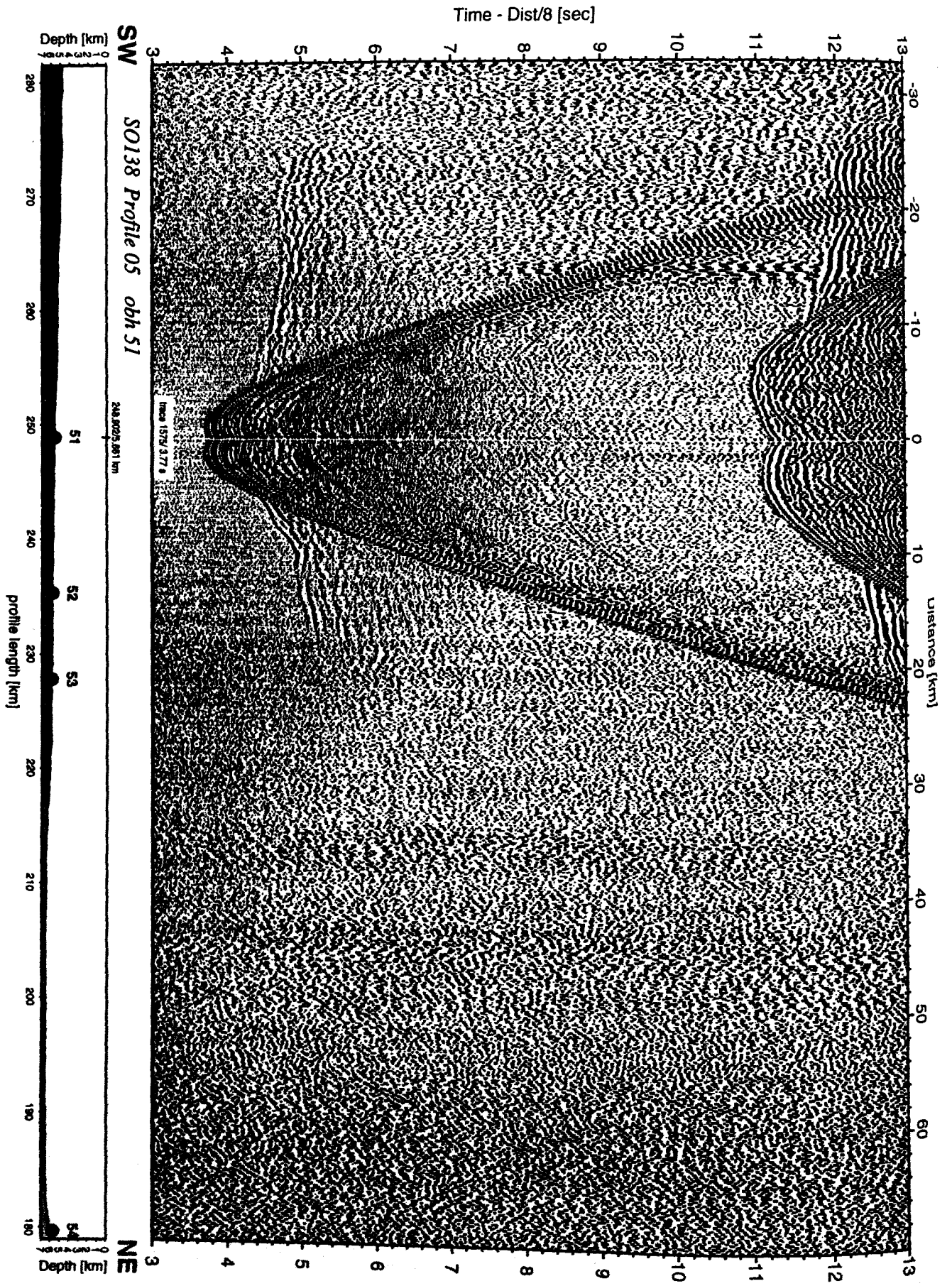

Figure 6.3.4.4.3: Record section from obh 51 , Profile 05.

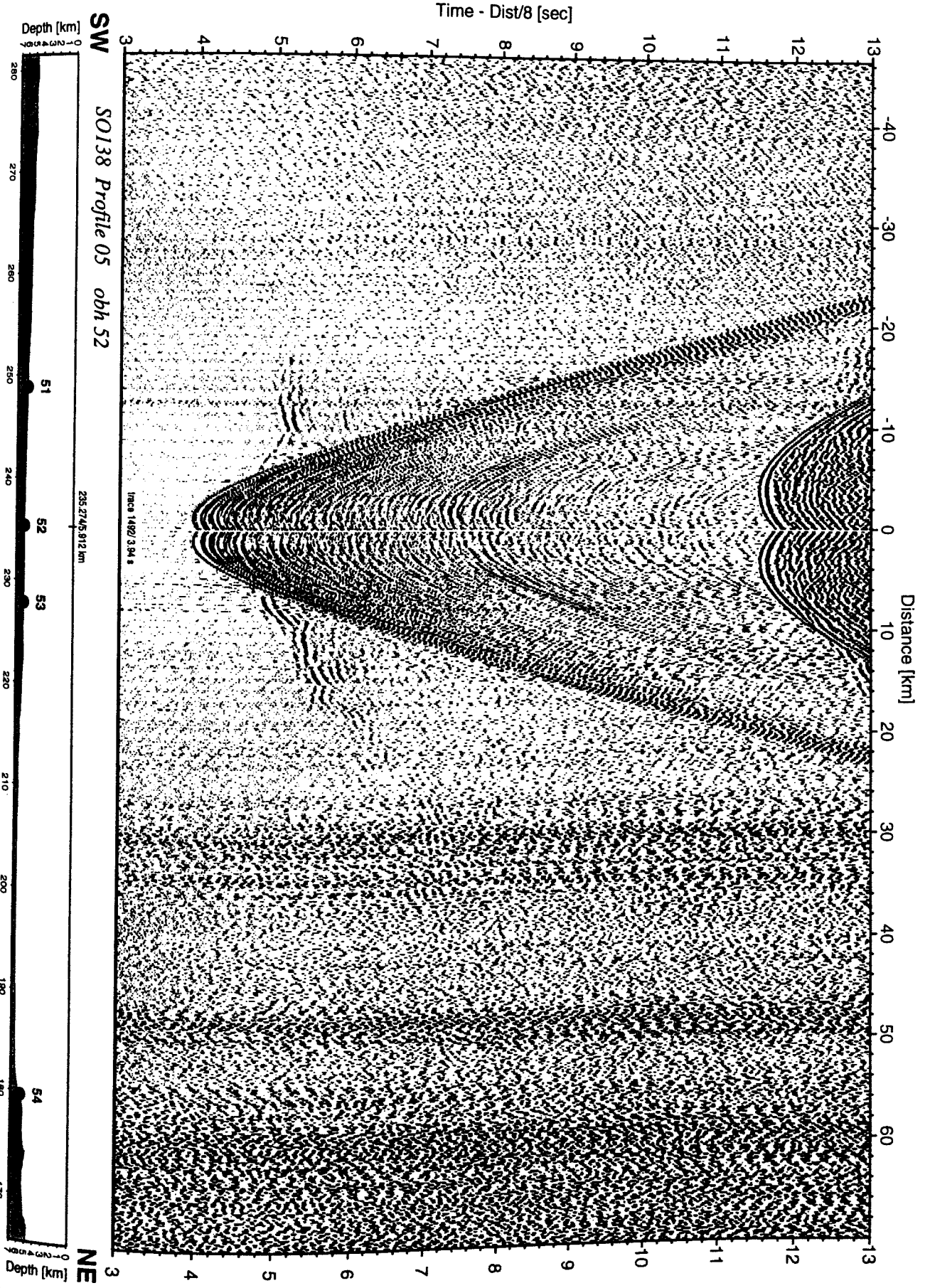

Figure 6.3.4.4.4: Record section from obh 52 , Profile 05.

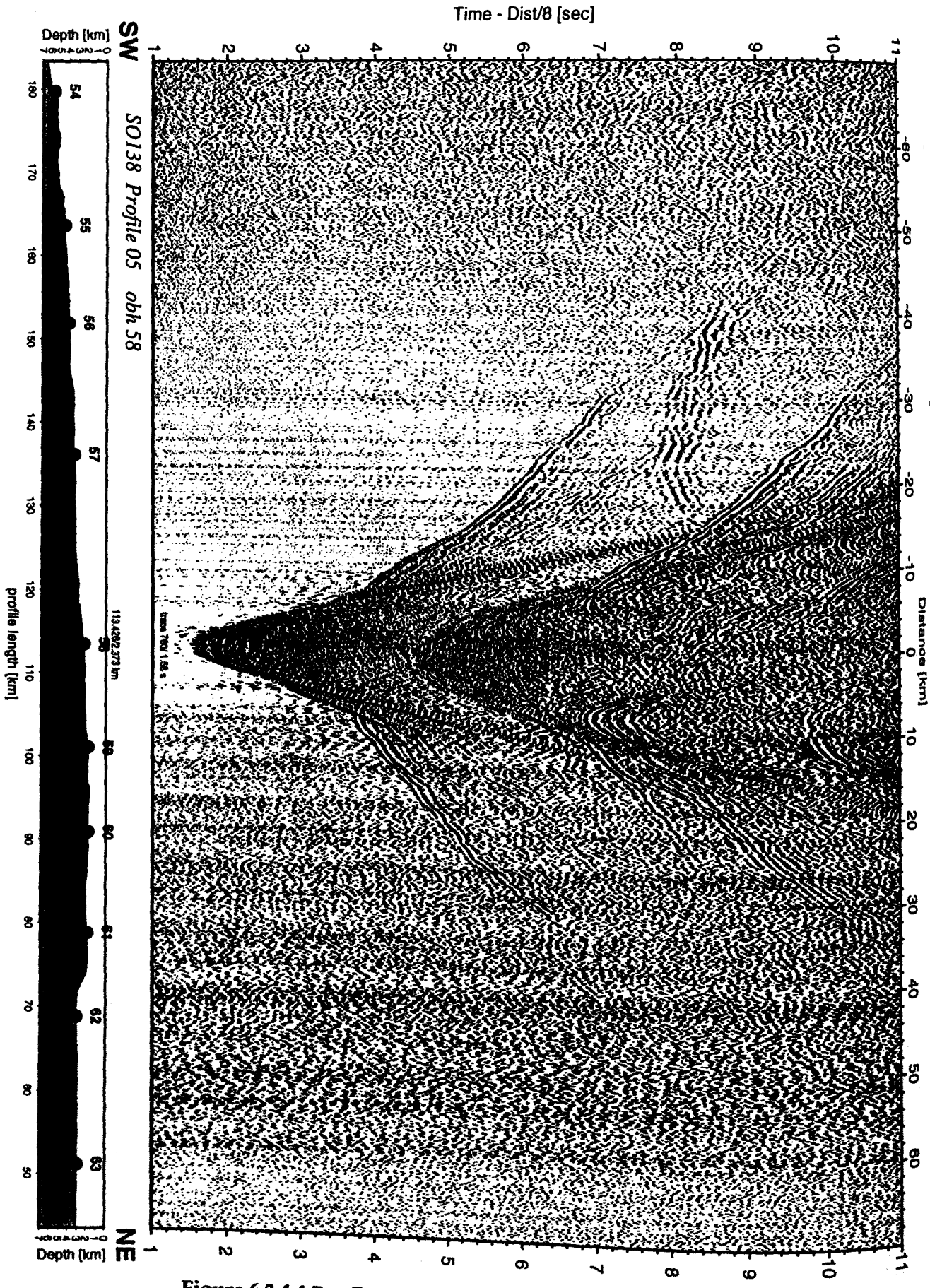

Figure 6.3.4.4.7: Record section from obh 58 , Profile 05.

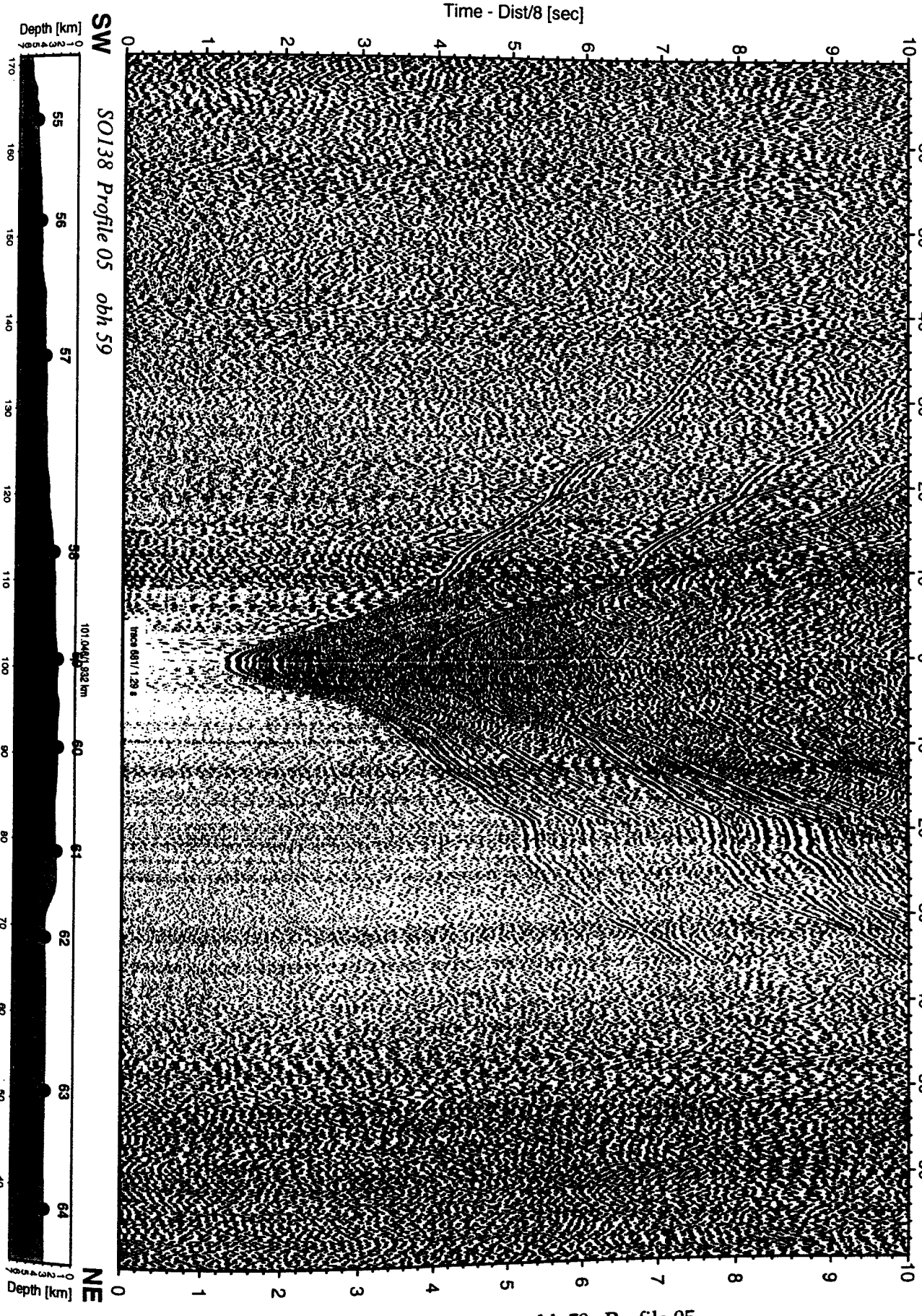

Figure 6.3.4.4.8: Record section from obh 59 , Profile 05.

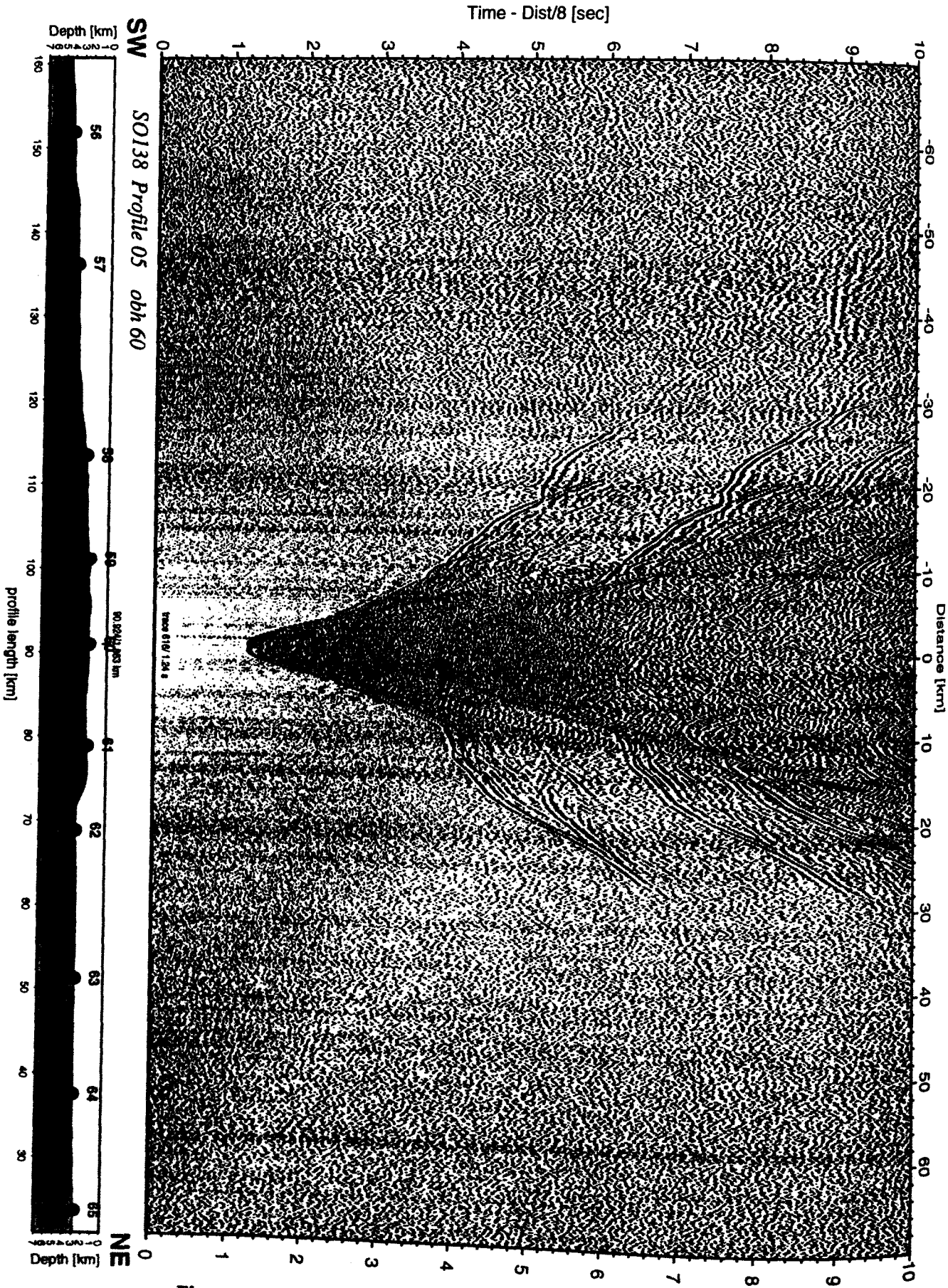

Figure 6.3.4.4.9: Record section from obh 60 , Profile 05.

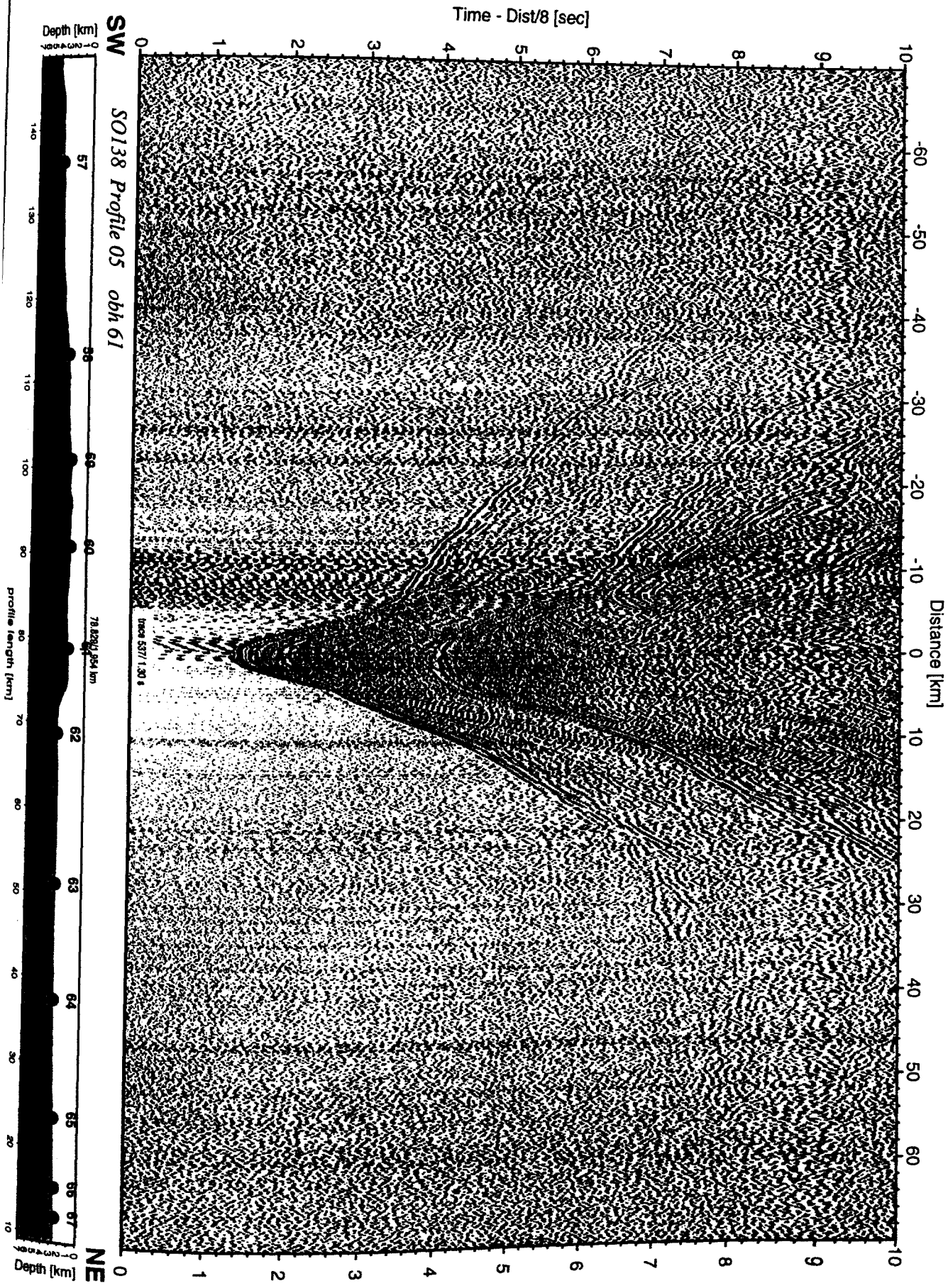

Figure 6.3.4.4.10: Record section from obh 61 , Profile 05.

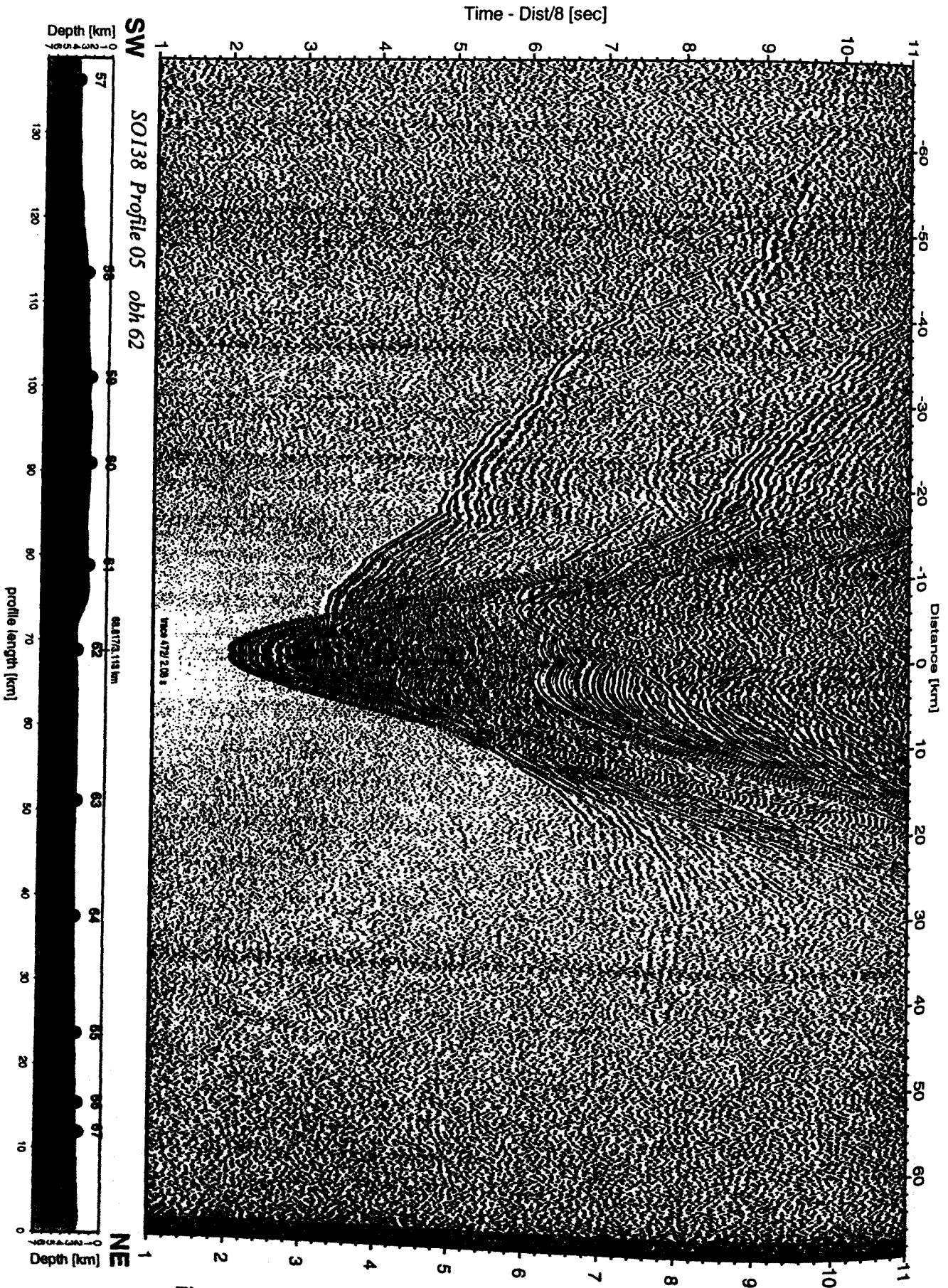

Figure 6.3.4.4.11: Record section from obh 62 , Profile 05.

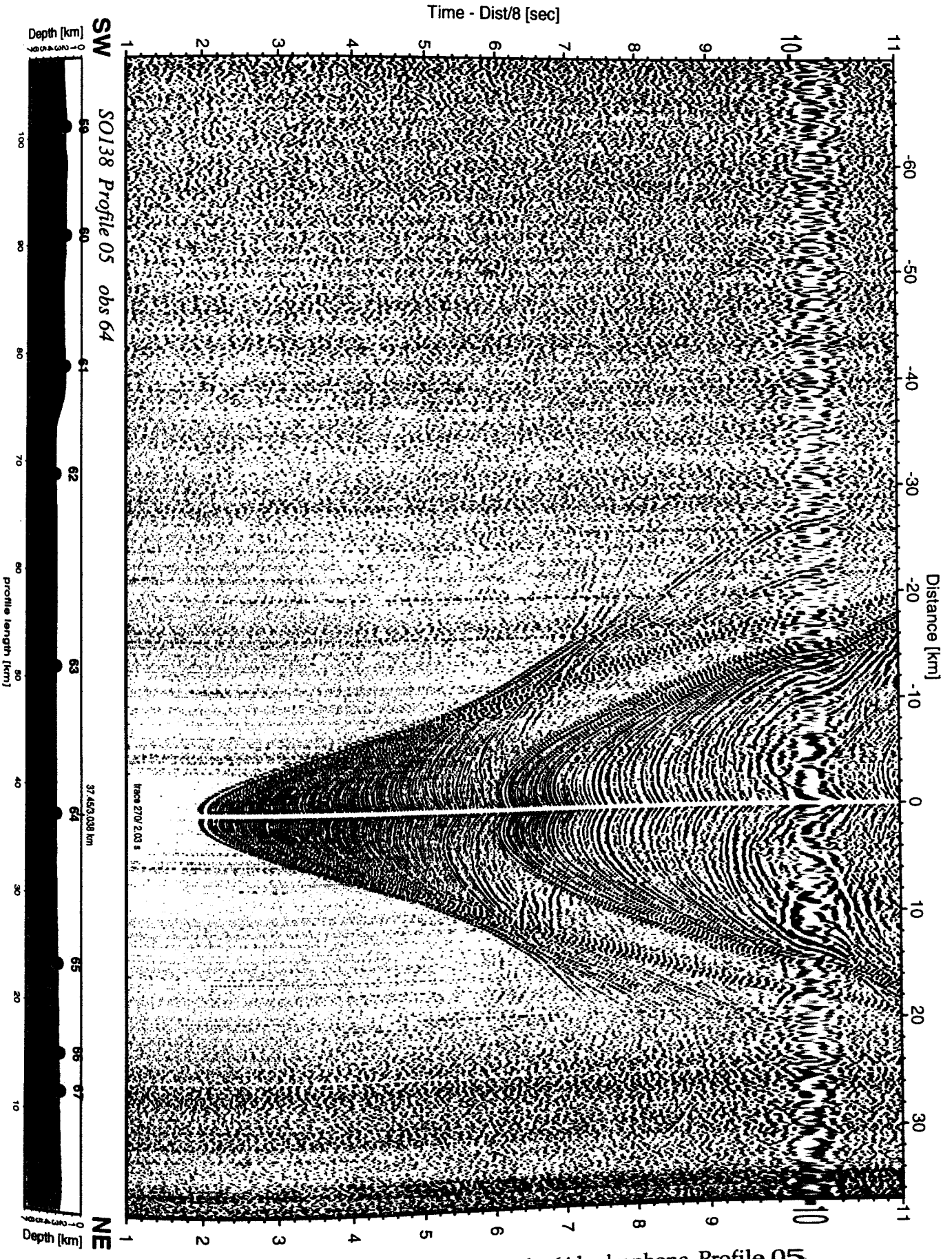

Figure 6.3.4.4.12: Record section from obs 64 hydrophone, Profile 05 -

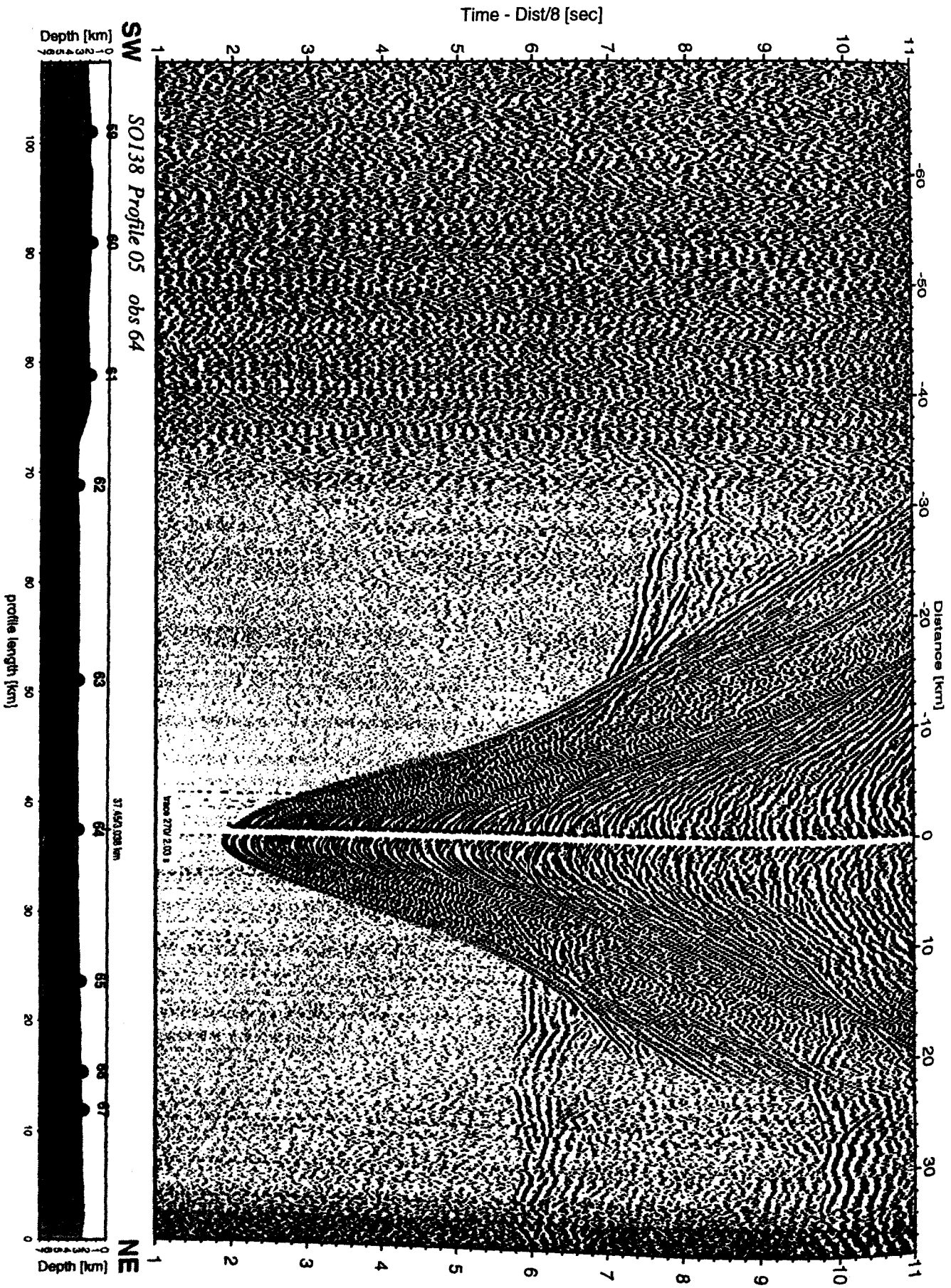

Figure 6.3.4.4.12a Record section from obs 64 vertical component, Profile 05.

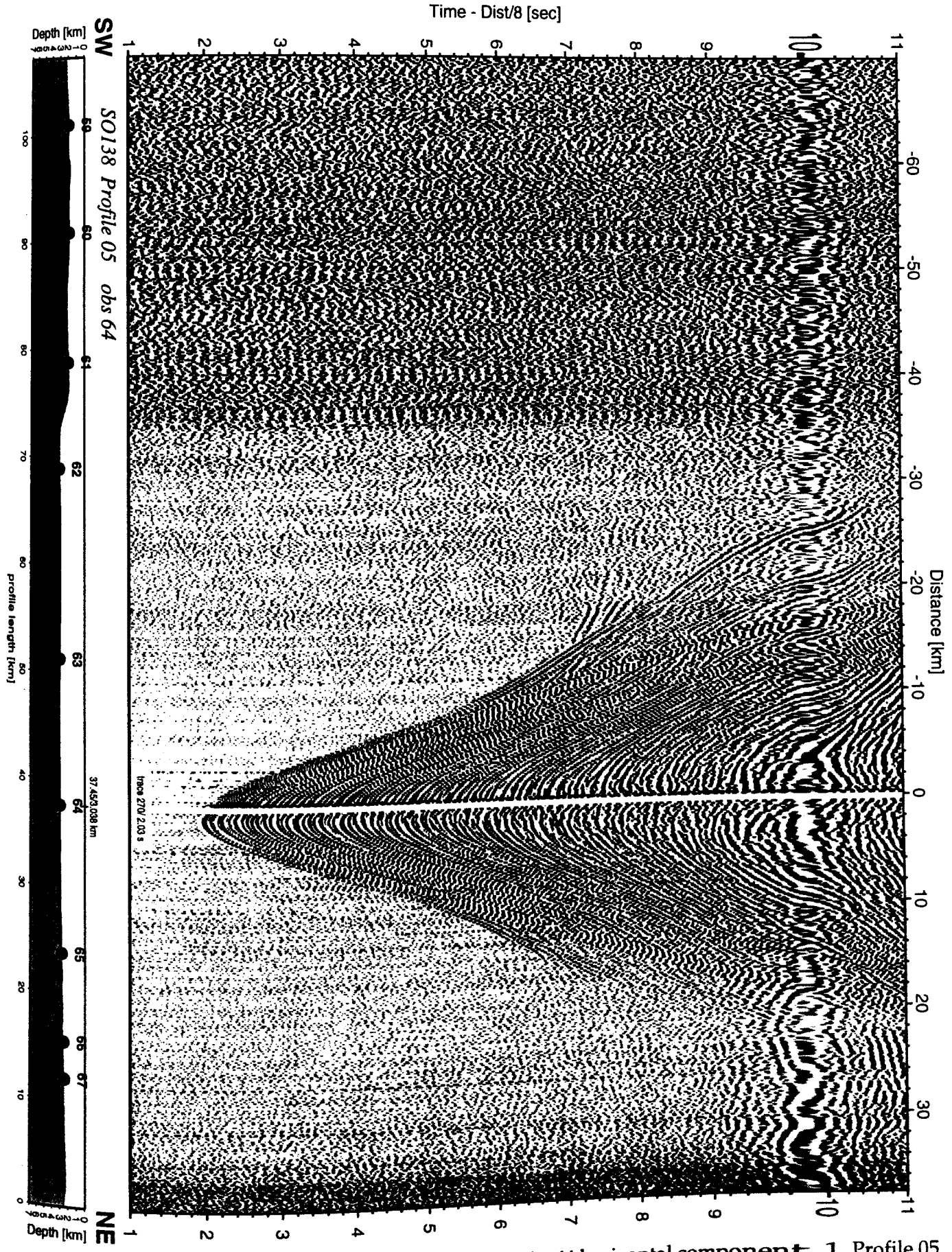

Figure 6.3.4.4.12b Record section from obs 64 horizontal component 1, Profile 05.

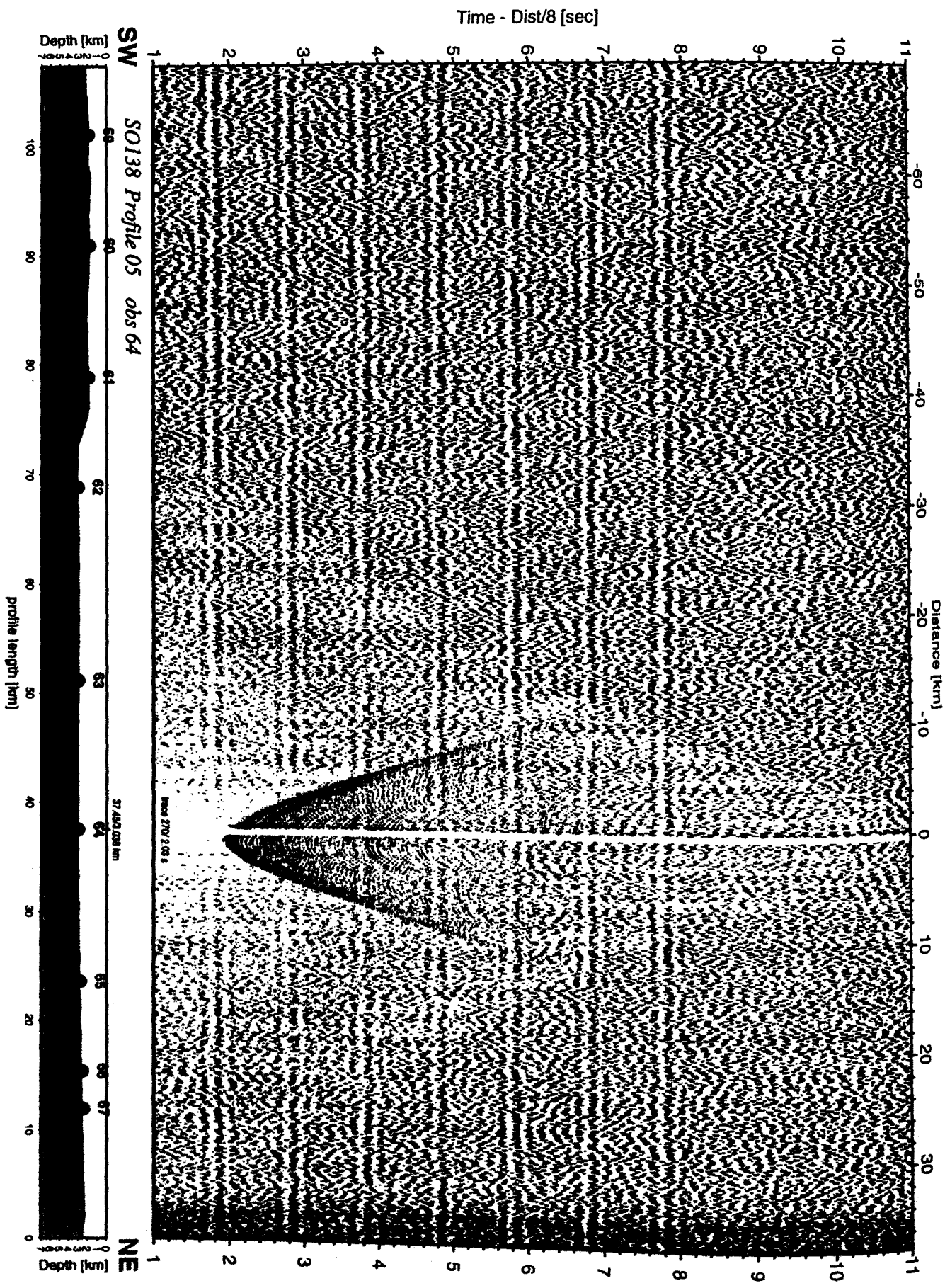

Figure 6.3.4.4.12c: Record section from obs 64 horizontal component 2, Profile 05.

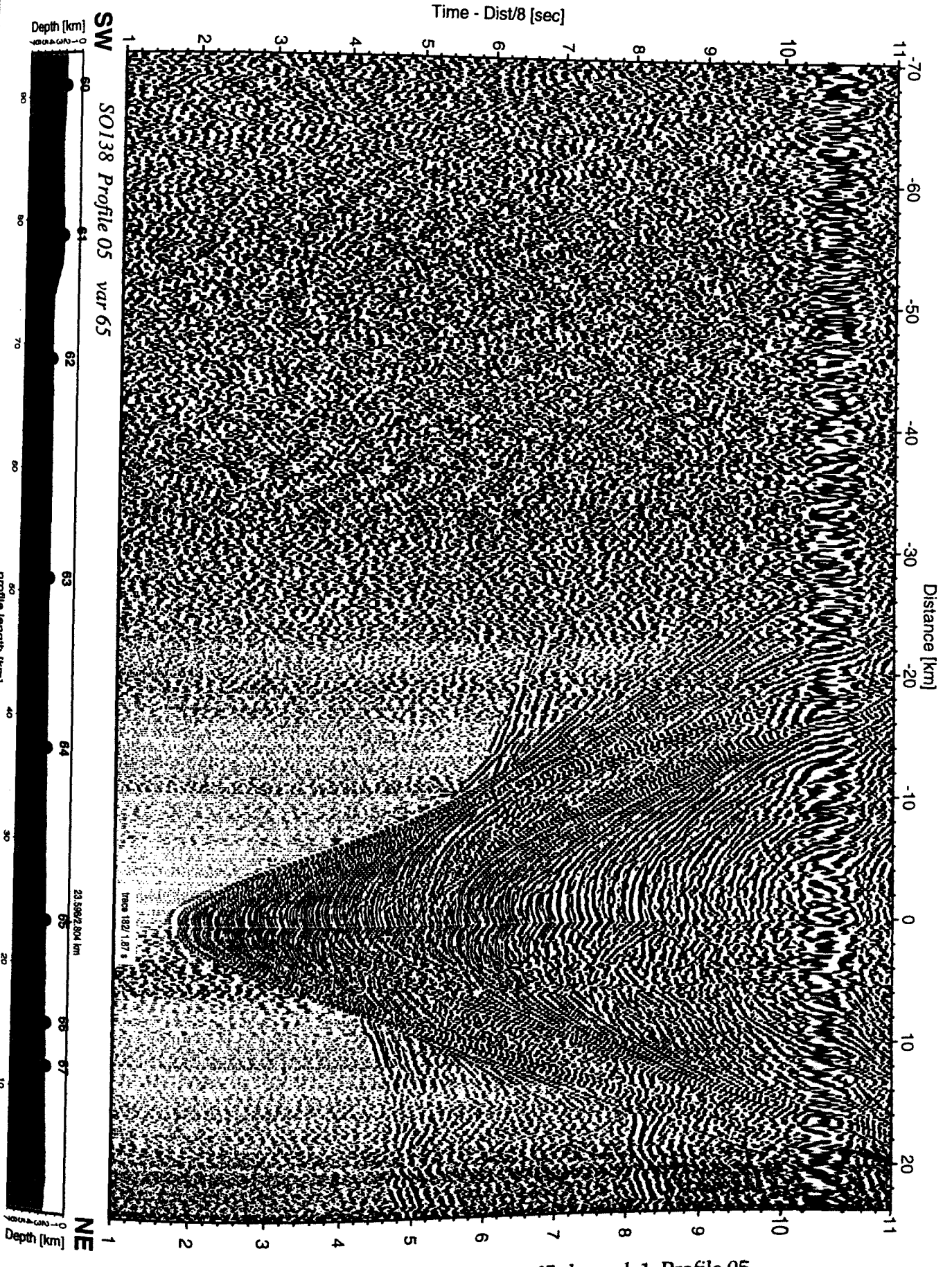

Figure 6.3.4.4.13: Record section from var 65 channel_1, Profile 05.

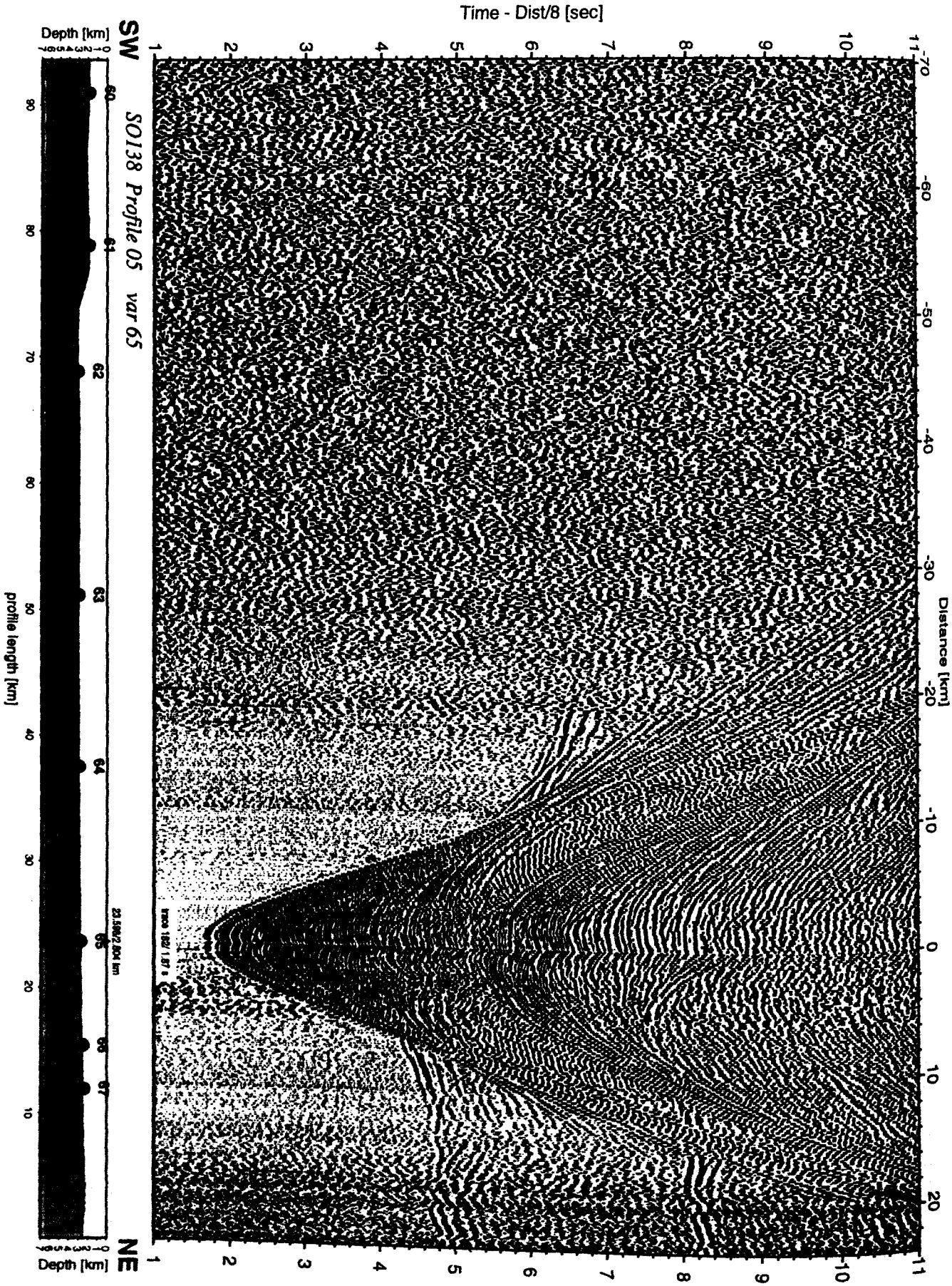

Figure 6.3.4.4.13a: Record section from var 65 channel_2, Profile 05.

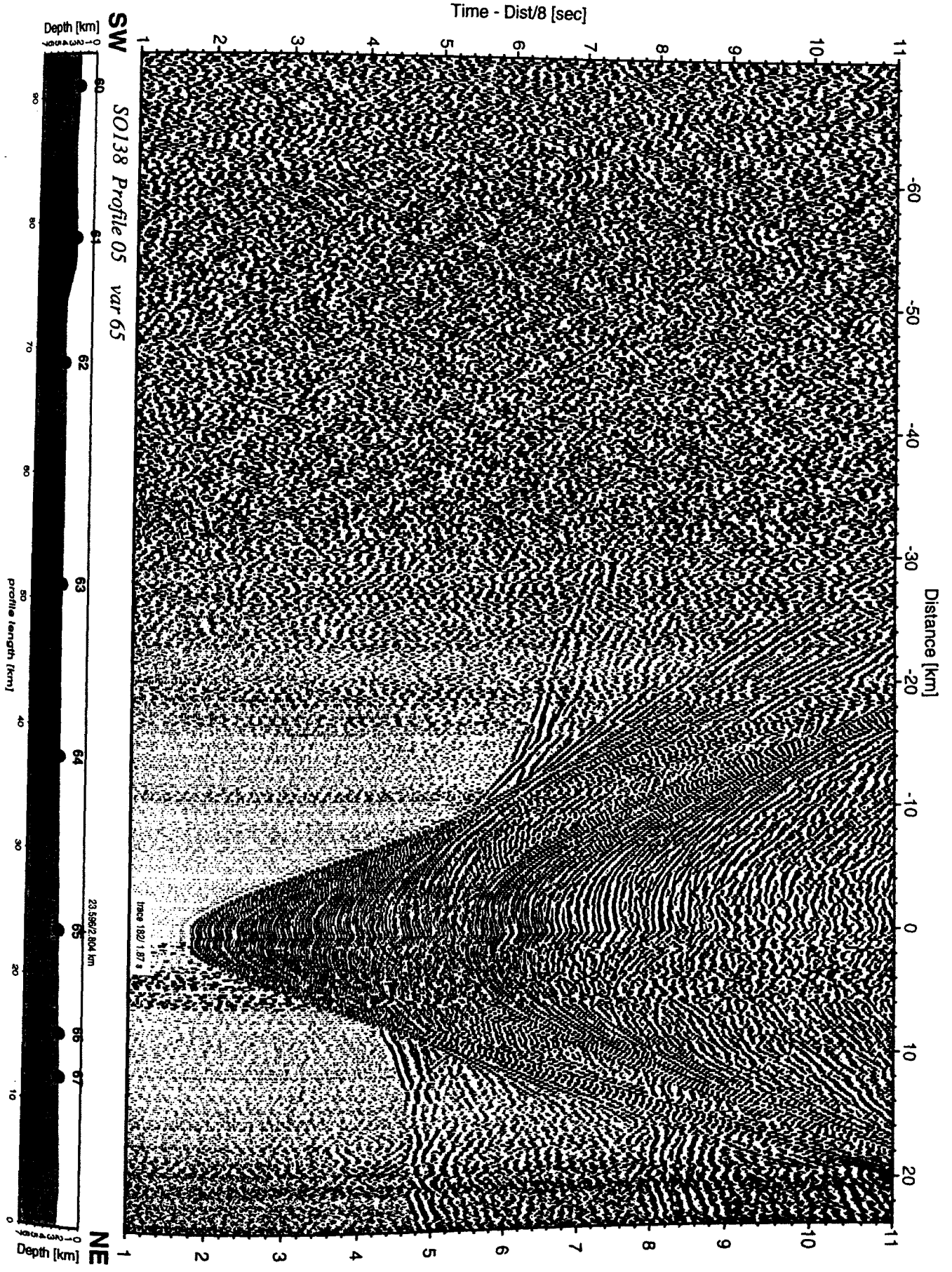

Figure 6.3.4.4.13b: Record section from var 65 channel_3, Profile 05.

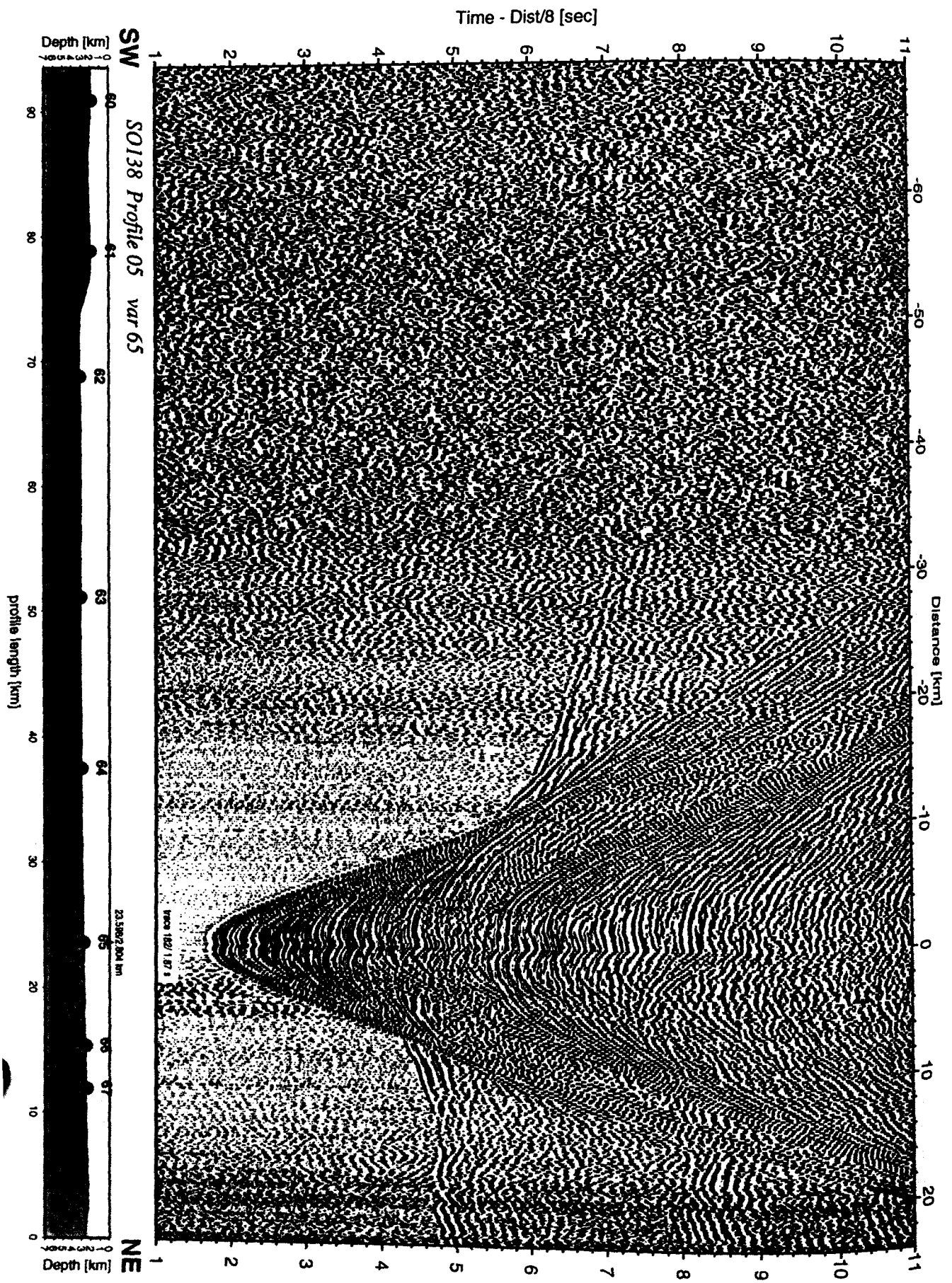

Figure 6.3.4.4.13c: Record section from var 65 channel_4, Profile 05.

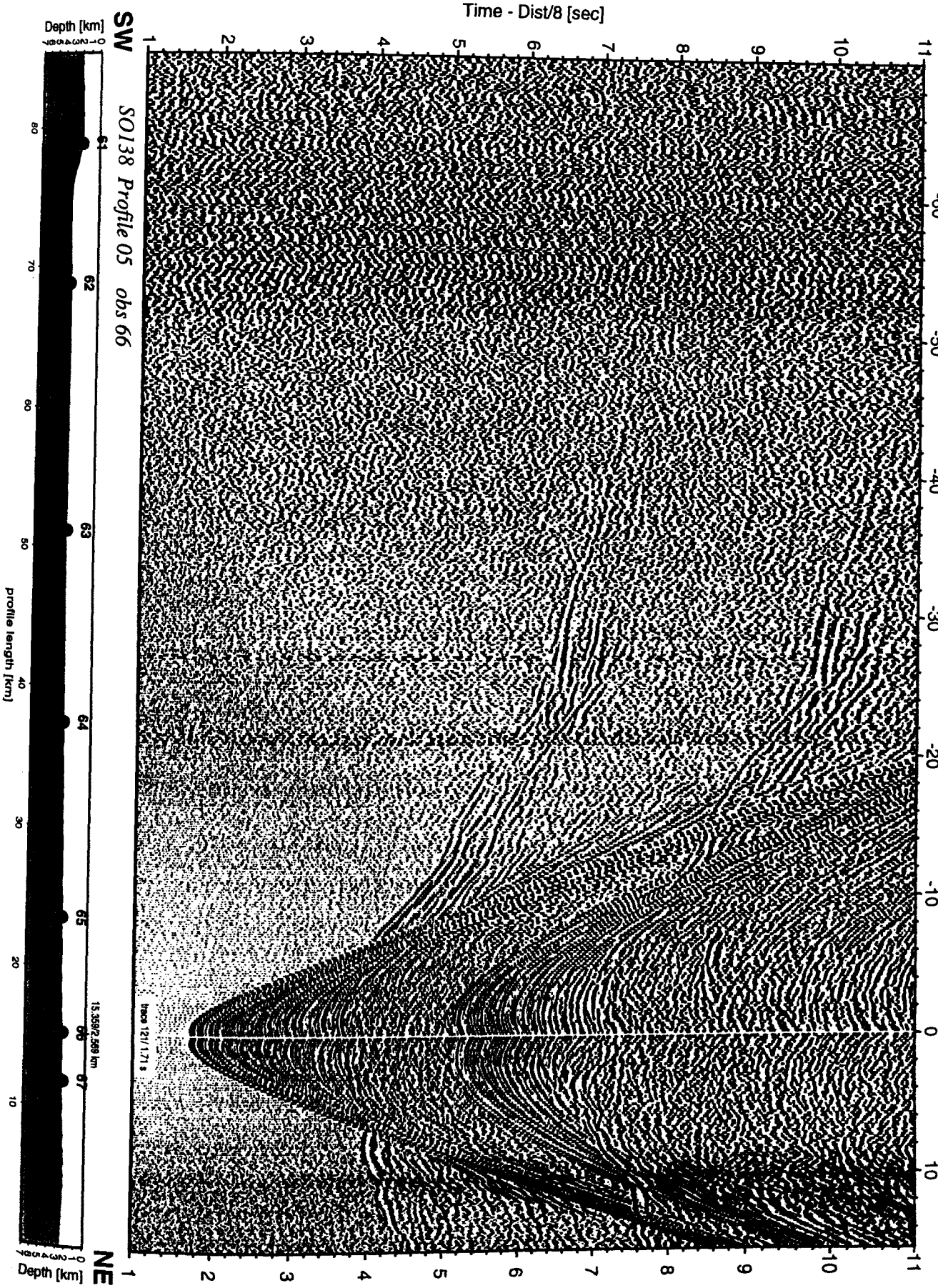

Figure 6.3.4.4.14: Record section from obs 66 hydrophone, Profile 05.

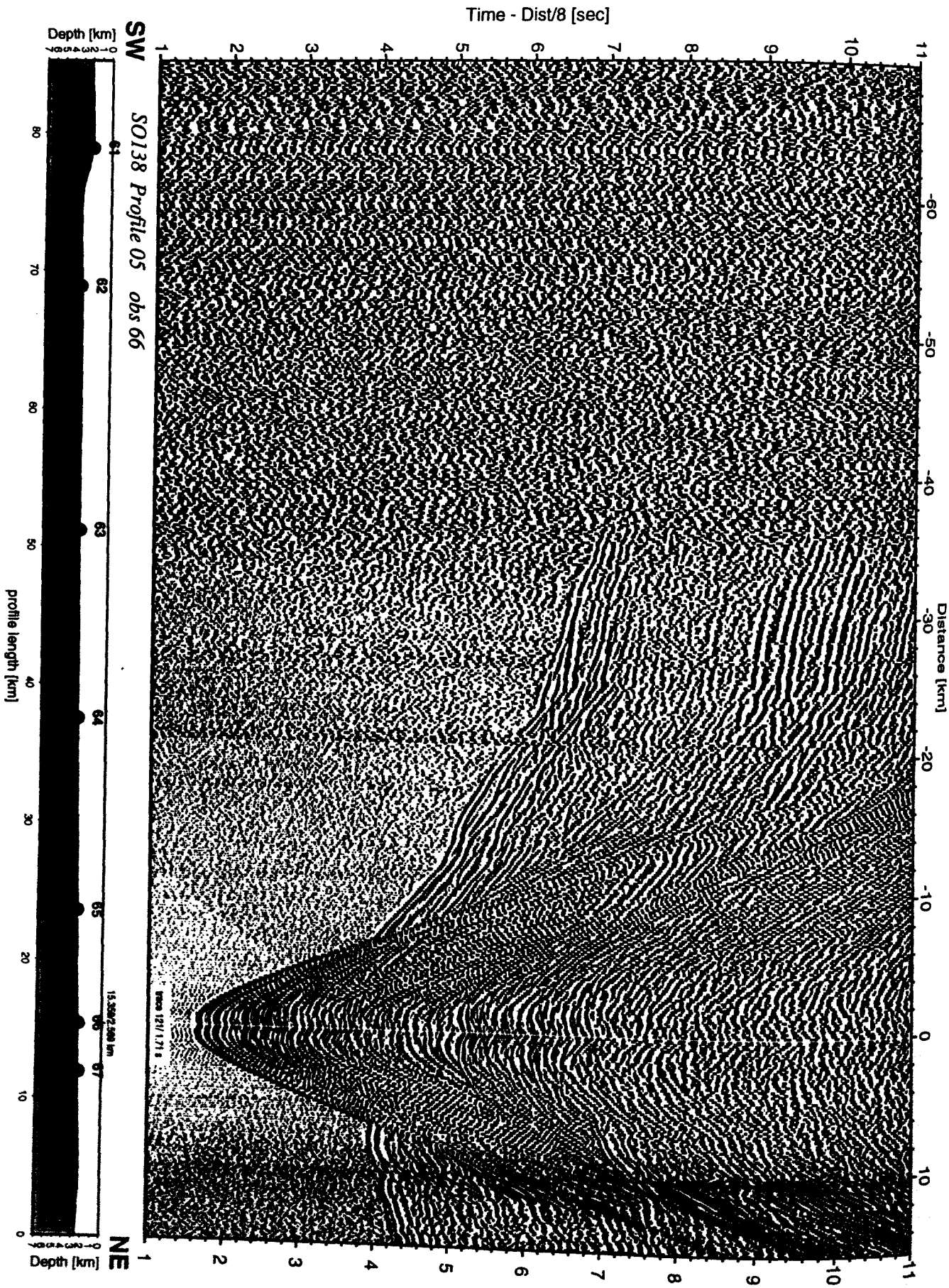

Figure 6.3.4.4.14a: Record section from obs 66 vertical component, Profile 05.

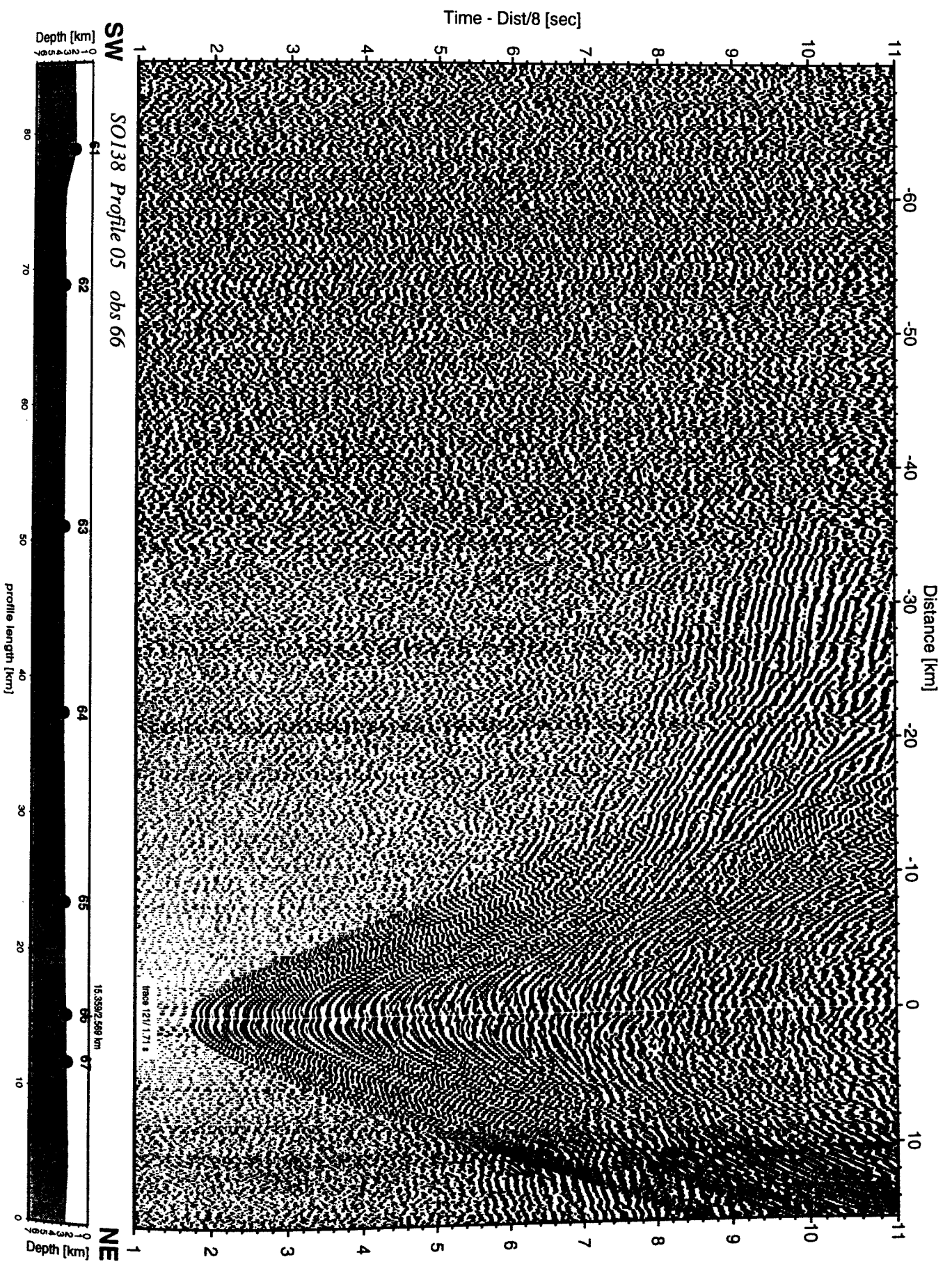

Figure 6.3.4.4.14b: Record section from obs 66 horizontal component 1, Profile 05.

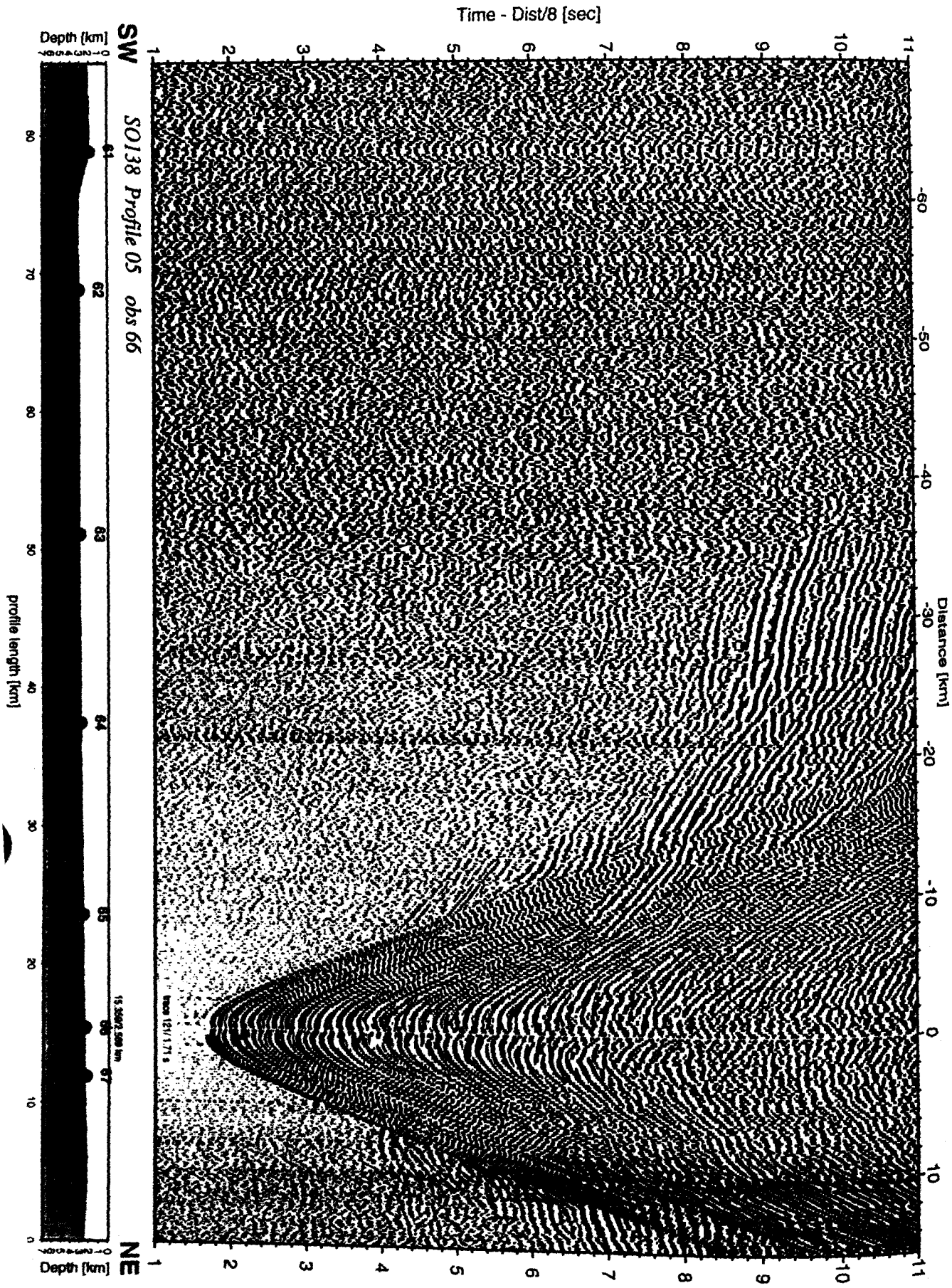

Figure 6.3.4.4.14c: Record section from obs 66 horizontal component 2, Profile 05

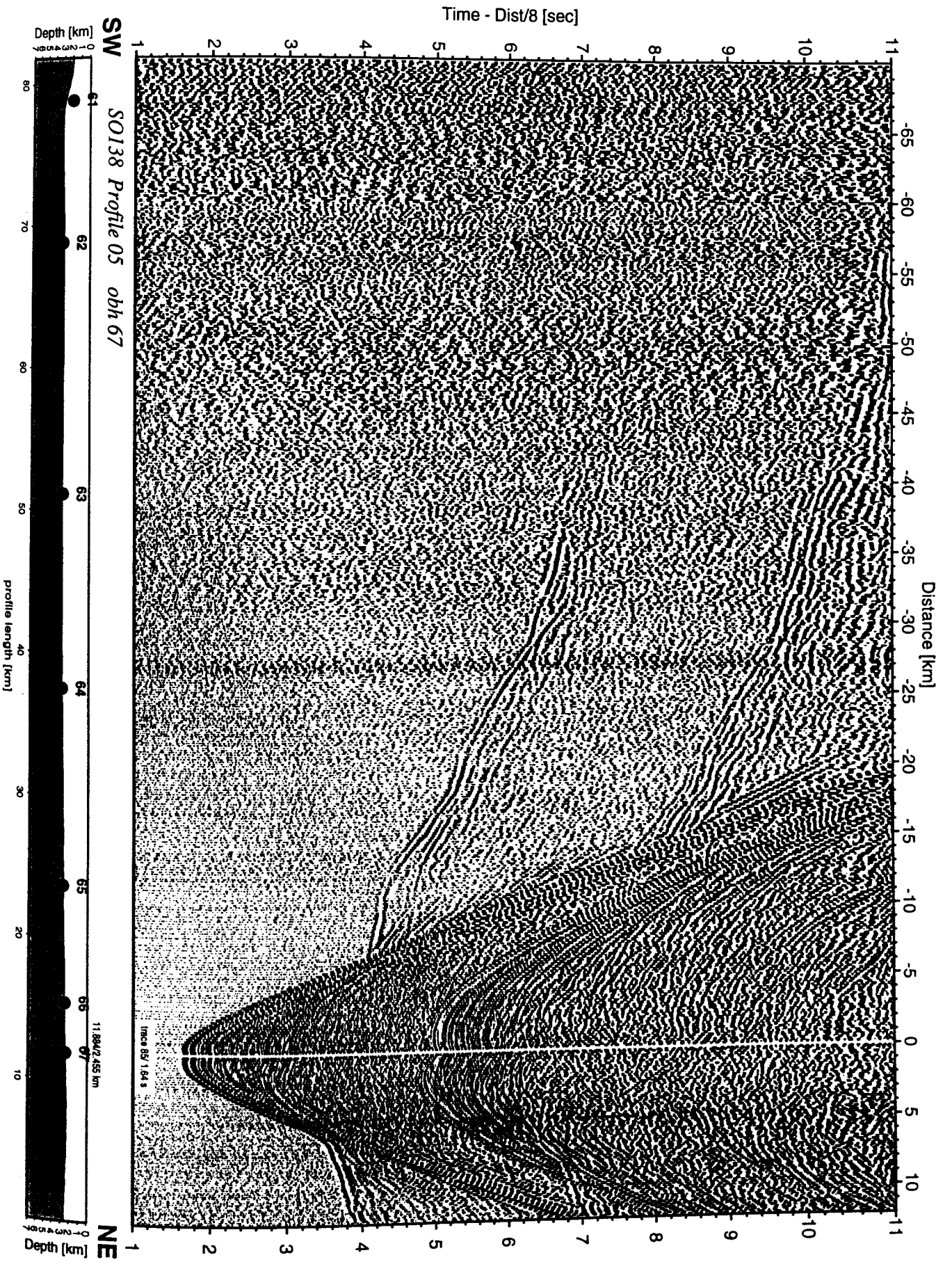

Figure 6.3.4.4.15: Record section from obh 67 , Profile 05.

6.3.4.5 PROFILE SO138-06

(J. Petersen, S. Husen, E. Flueh)

Profile SO138-06 is a strike line along the margin off Java about 12 nm from the shore. Ten instruments (OBH68 to 77) were deployed centered across profile SO138-05, at a location where MCS line SO137-03 (Reichert and shipboard Scientific party, in prep.) had indicated a rather shallow basement. The OBSes (OBH75 and 77), and a two-channel vertical array of 400 m length (OBH76) were among the instruments deployed (Figure 6.3.4.5.1). Deployment of the instruments started on 18 January 1999 at midday, and was finished shortly after midnight, interrupted by a deep tow streamer test (see 6.3.4.9). A transit profile with the magnetometer deployed was run to the start of the shooting line 12 miles away from the last instrument, and shooting this 80 nm long profile was finished in the evening of 19 Januyry 1199. The streamer was also deployed and the record section obtained is shown in Figure 6.3.4.5.2. All instruments were safely recovered by 05:00 on 20.01.1999.

From the ten instruments deployed nine provided useful information, the record sections are shown in Figures 6.3.4.5.3 to 6.3.4.5.11.

Modelling and interpretation

Along this strike line the record sections show a high degree of similarity. All sections except those from OBH 71 and VA 76 channel 2 show at least 3 refracted or reflected phases. These are the direct water-wave, a refracted arrival from the basement and a reflection from a sediment layer. Further, refracted phases and additional reflections from sediment layers can be identified in many sections. A Moho reflection (PmP) is recognized at longer offsets only in the data of OBH 73 (Fig. 6.3.4.5.7) and in the vertical component of OBS 75 (Fig. 6.3.4.5.9). These two stations in the middle of the profile show the best signal-to-noise ratio. Therefore, onboard analysis was restricted to arrivals from these two stations to yield a preliminary velocity model.

Preliminary 1D-modelling was performed on OBH 73 data using the R1D software. Because of the asymmetry between positive and negative offset phases, two different velocity-depth profiles were obtained shown in Figure 6.3.4.5.12. The solid line shows the velocity-depth profile derived from arrivals with offset to the east, the dashed line from those with offset to the west. The most evident feature is that the high velocities appear deeper in the western region than in the eastern part, and that mantle velocities are found at shallow depth.

The upper two sediment layers were assumed to have velocities of 1.6 and 2.5 km/s. The thickness of these layers was derived from the mini streamer data (Fig. 6.3.4.5.2) showing the two stations located in a trough filled with sediments, so that higher velocities should appear due to topographic effects. Especially the variation of the thickness of the second sediment layer is important to account for the asymmetry in the OBH data. Starting with the upper two sediments, the preliminary 2D-velocity model was built up using MacRay software. The result is shown in Figure 6.3.4.5.13. The model indicates 3-4 km thickness of three sediment layers with a velocity

increasing to 3.2 km/s. The basement has a high velocity gradient from 4.5 to 5.7 km/s in the uppermost two kilometers, and a moderate velocity gradient down to depths of 12-14 km, where velocities of 6.7 km/s are seen. A lower crustal layer with velocities of about 7.0 km/s gives a good explanation for the observed critical distances for the mid crustal reflections and is also in agreement with preliminary results from line SO138-05.

The Moho reflection observed at OBS 75 at an offset of –80 km indicates the Moho located in a depth of about 25 km yielding a crustal thickness of 19-21 km which is within the range of crustal thicknesses known from island arcs.

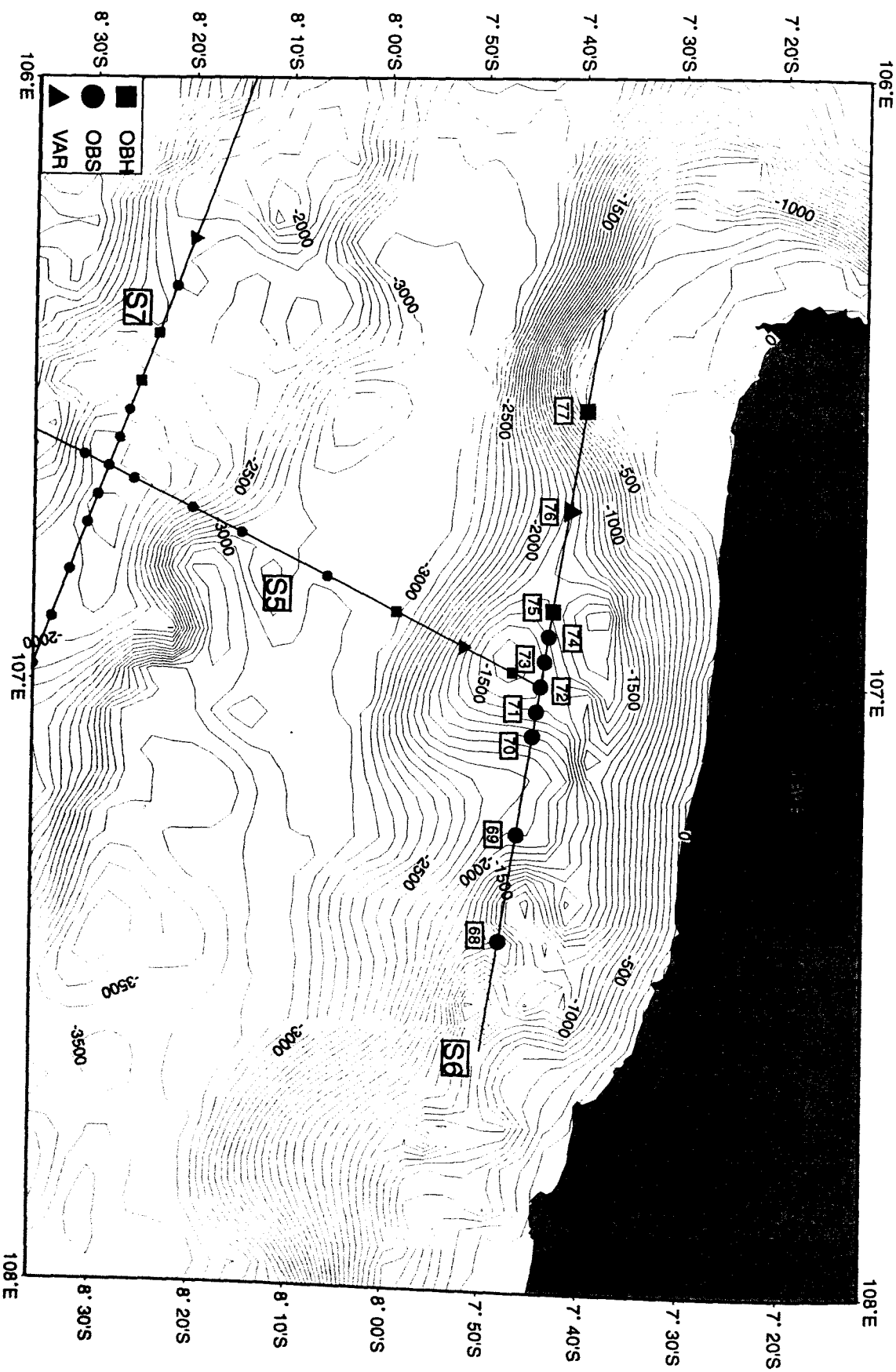

Figure 6.3.4.5.1: Location map of seismic line S6.

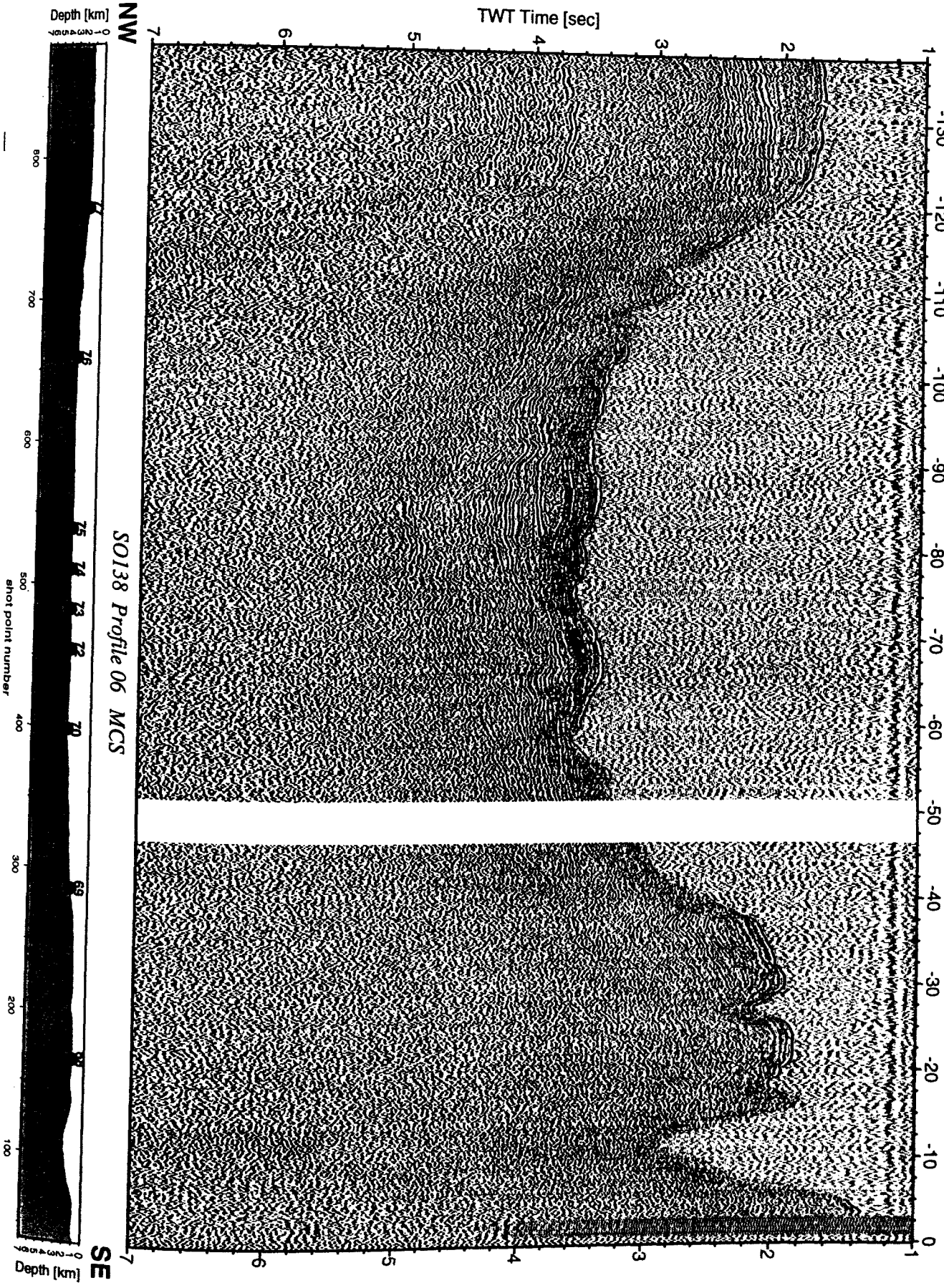

Figure 6.3.4.5.2: Seismic section from MCS stack, Profile 06.

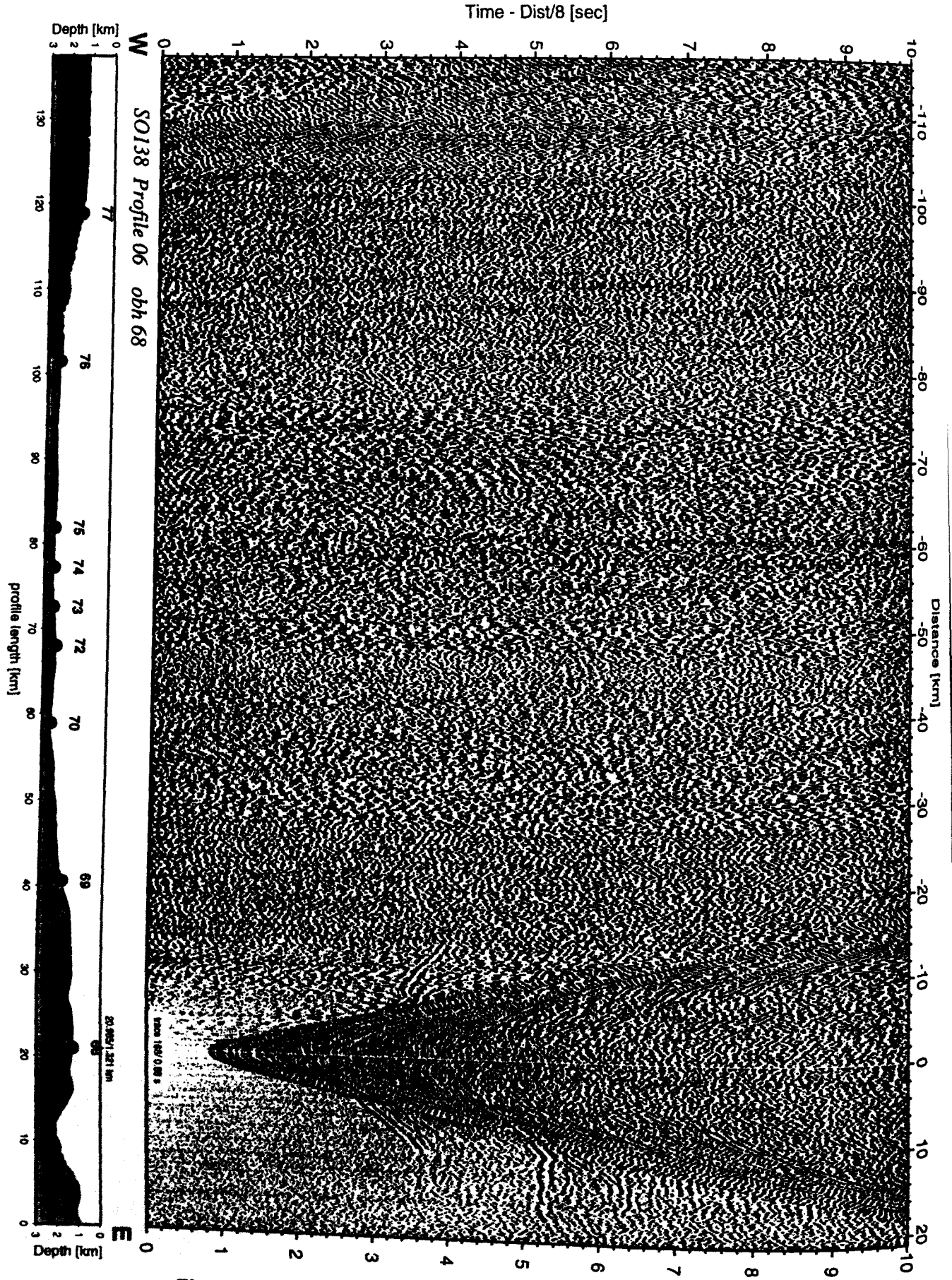

Figure 6.3.4.5.3: Record section from obh 68 , Profile 06.

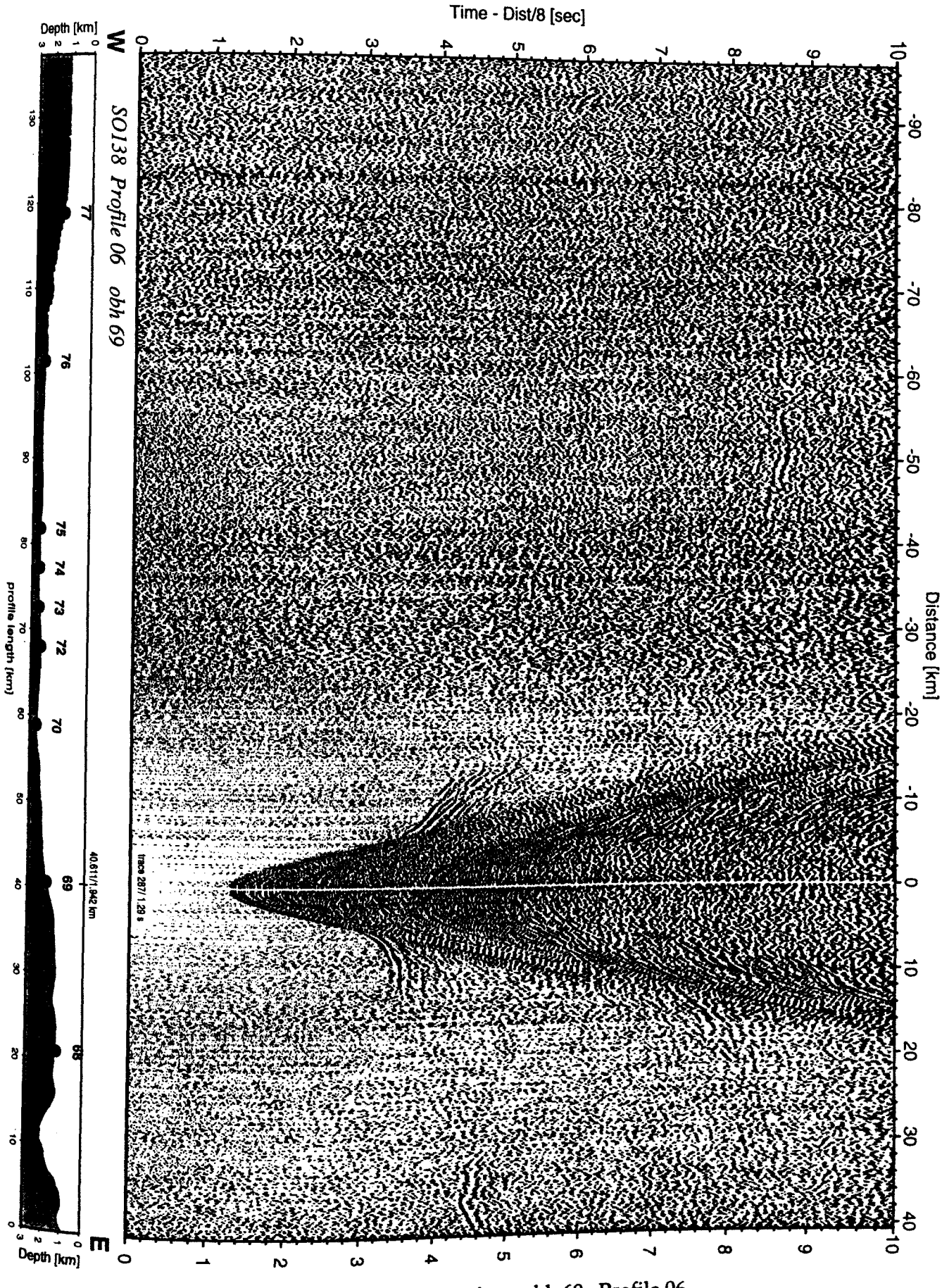

Figure 6.3.4.5.4: Record section from obh 69 , Profile 06.

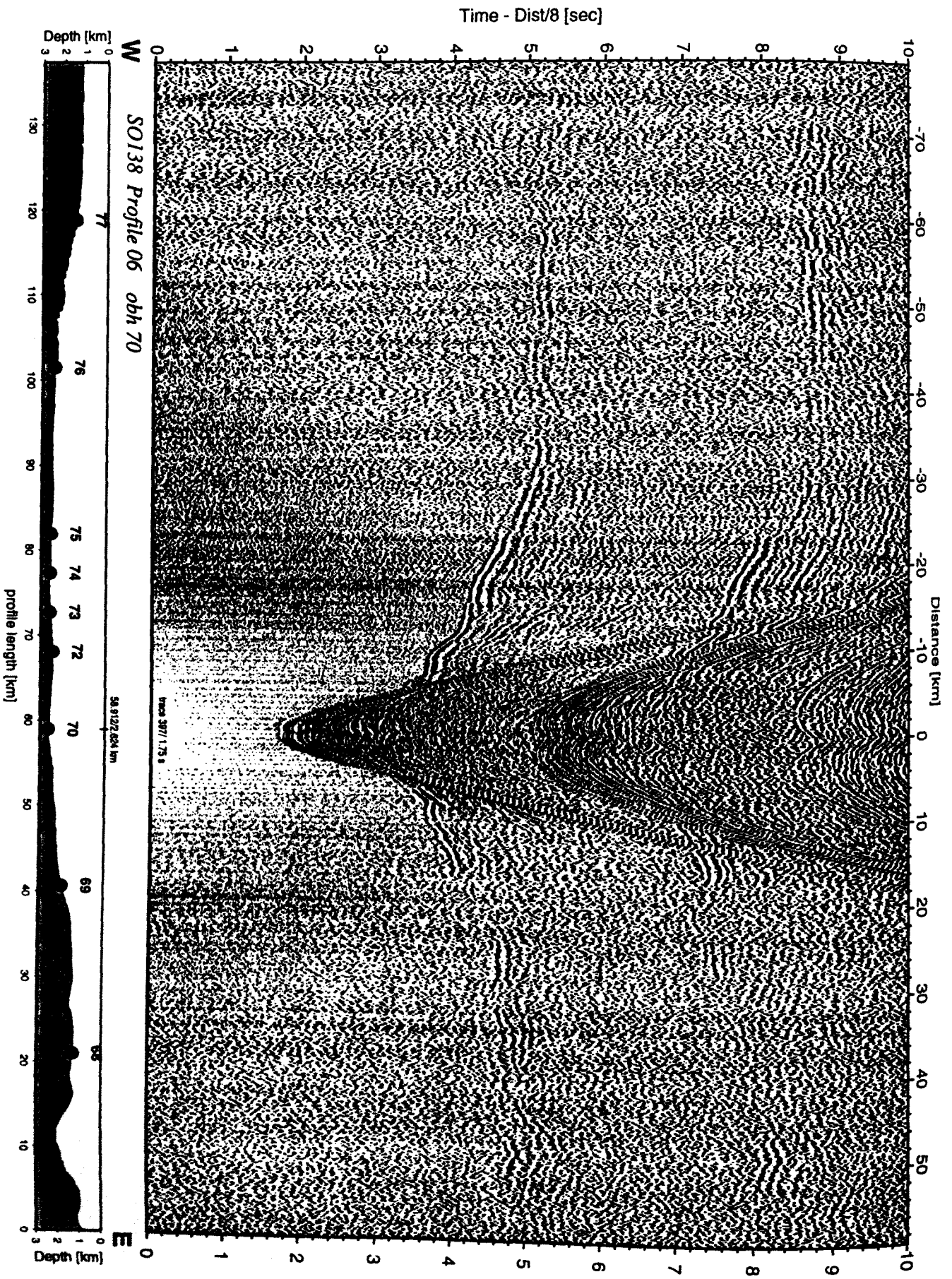

Figure 6.3.4.5.5: Record section from obh 70 , Profile 06.

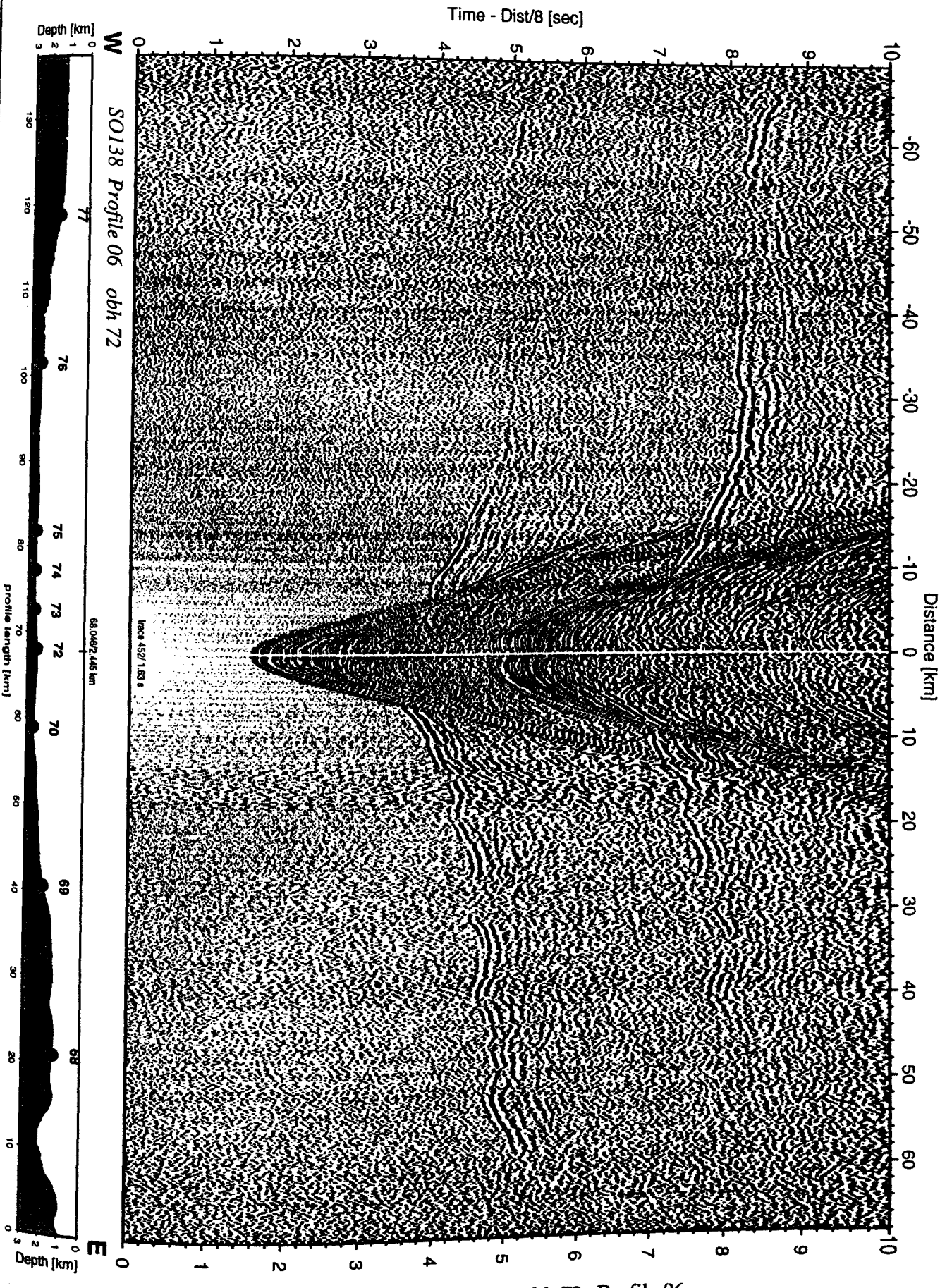

Figure 6.3.4.5.6: Record section from obh 72 , Profile 06.

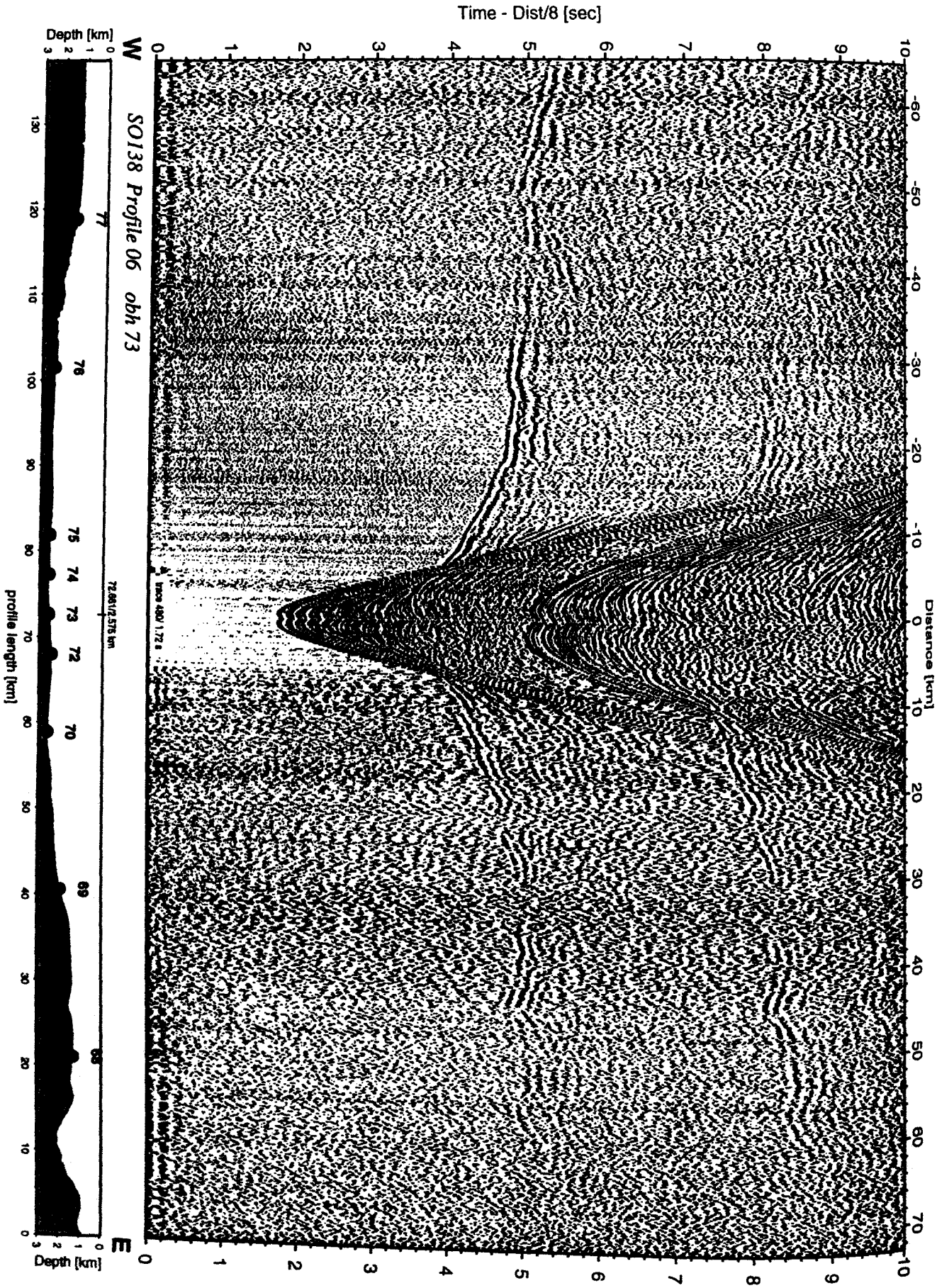

Figure 6.3.4.5.7: Record section from obh 73 , Profile 06.

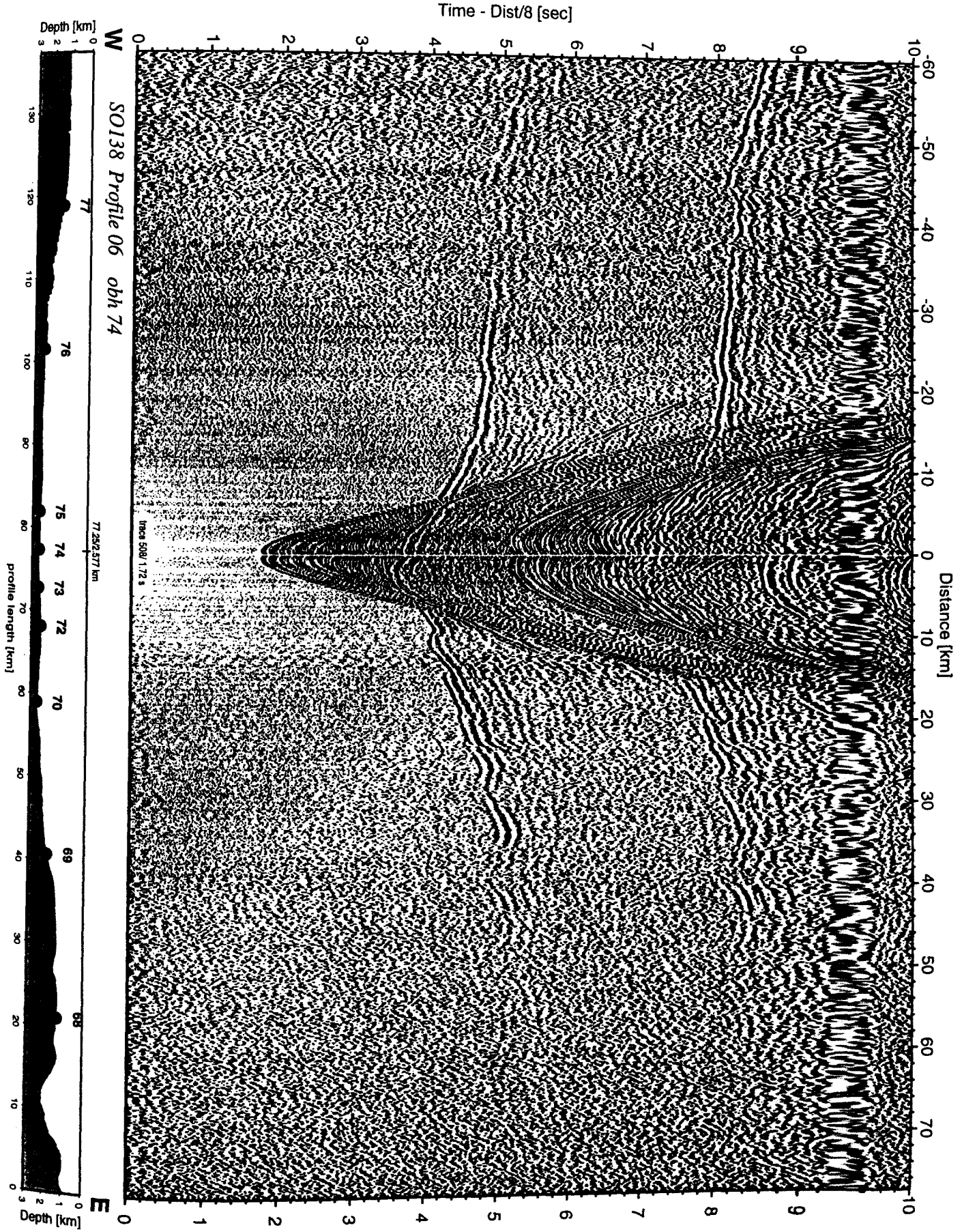

Figure 6.3.4.5.8: Record section from obh 74 , Profile 06.

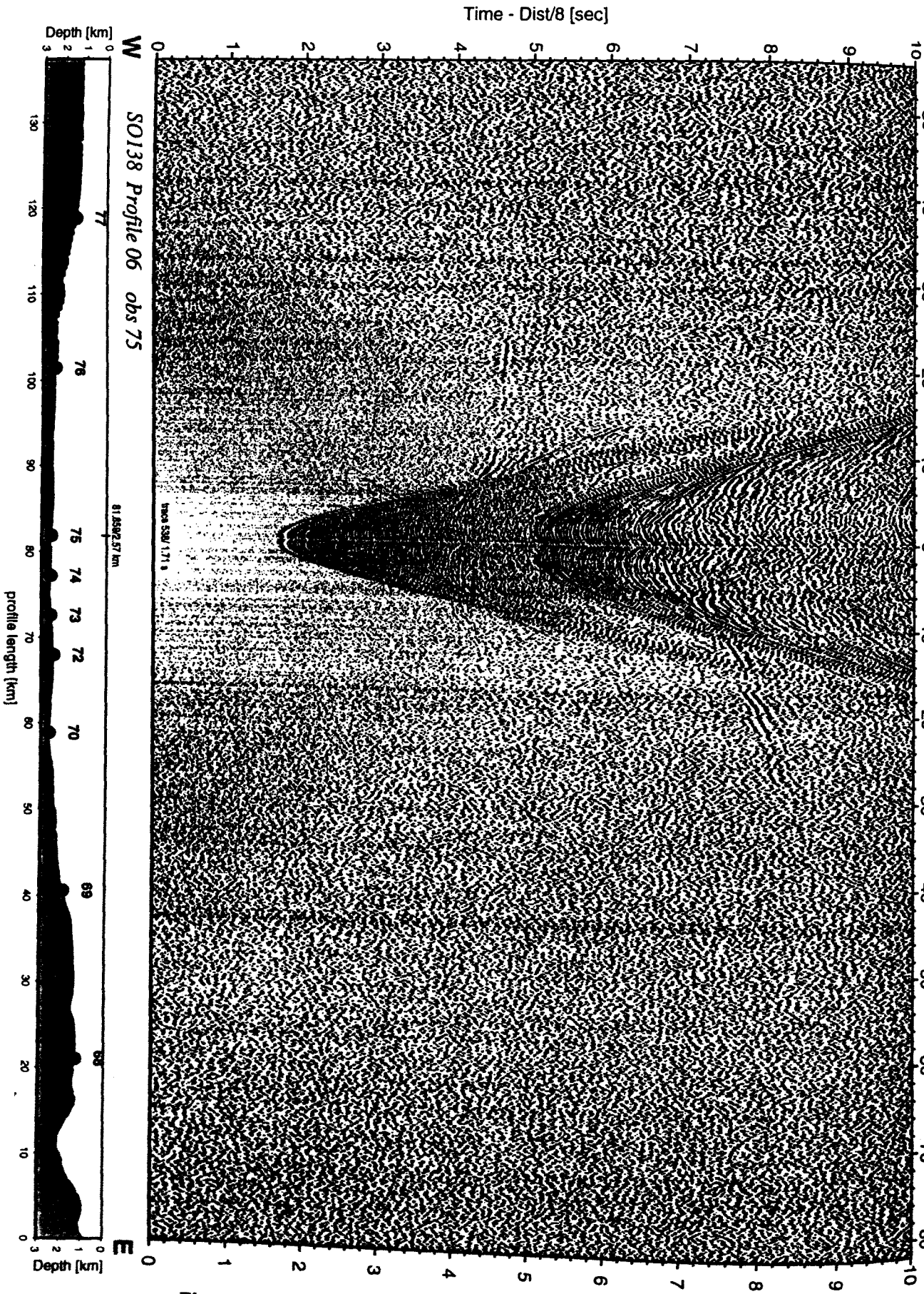

Figure 6.3.4.5.9: Record section from obs 75 hydrophone, Profile 06.

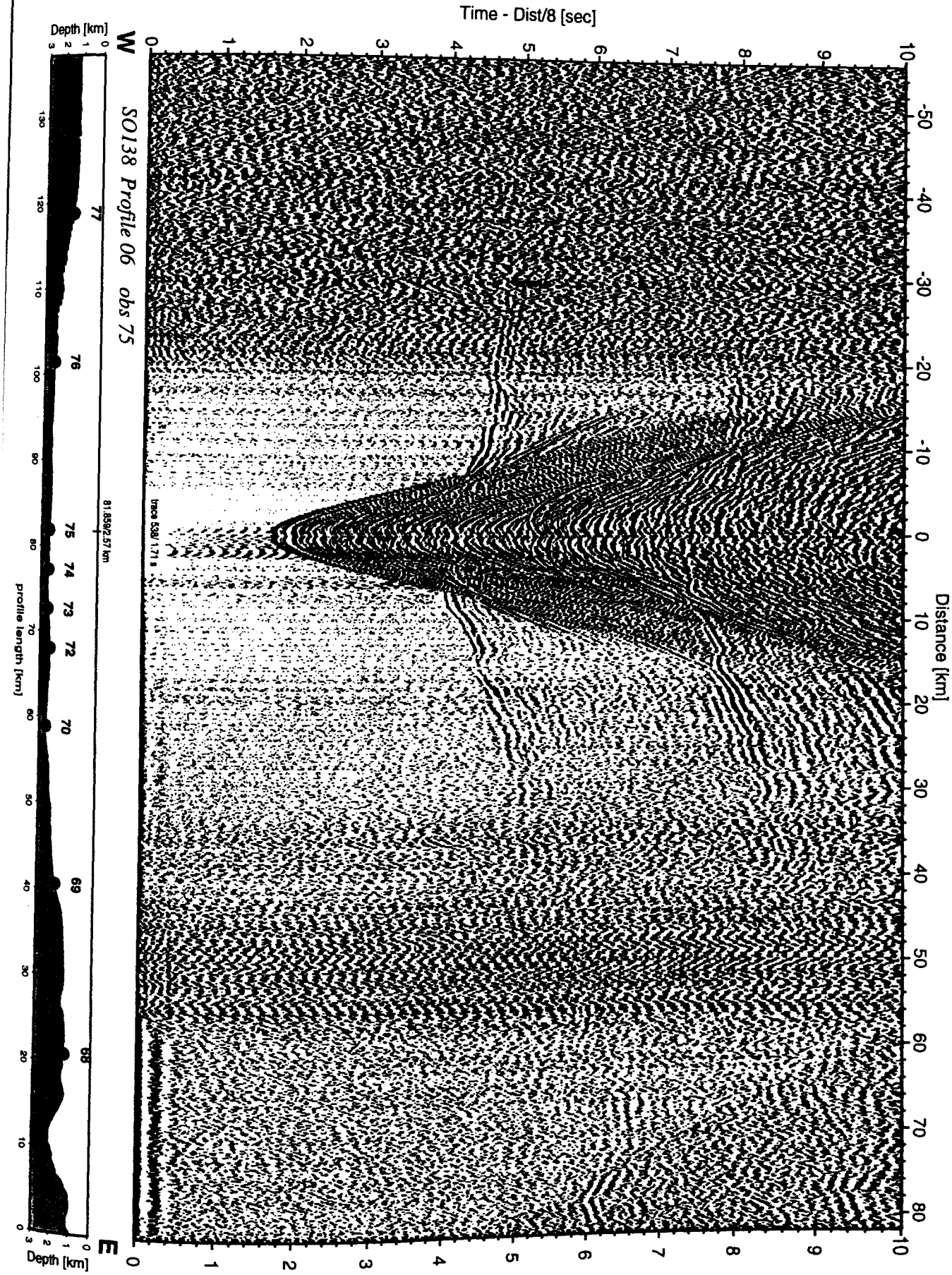

Figure 6.3.4.5.9a: Record section from obs 75 vertical component, Profile 06.

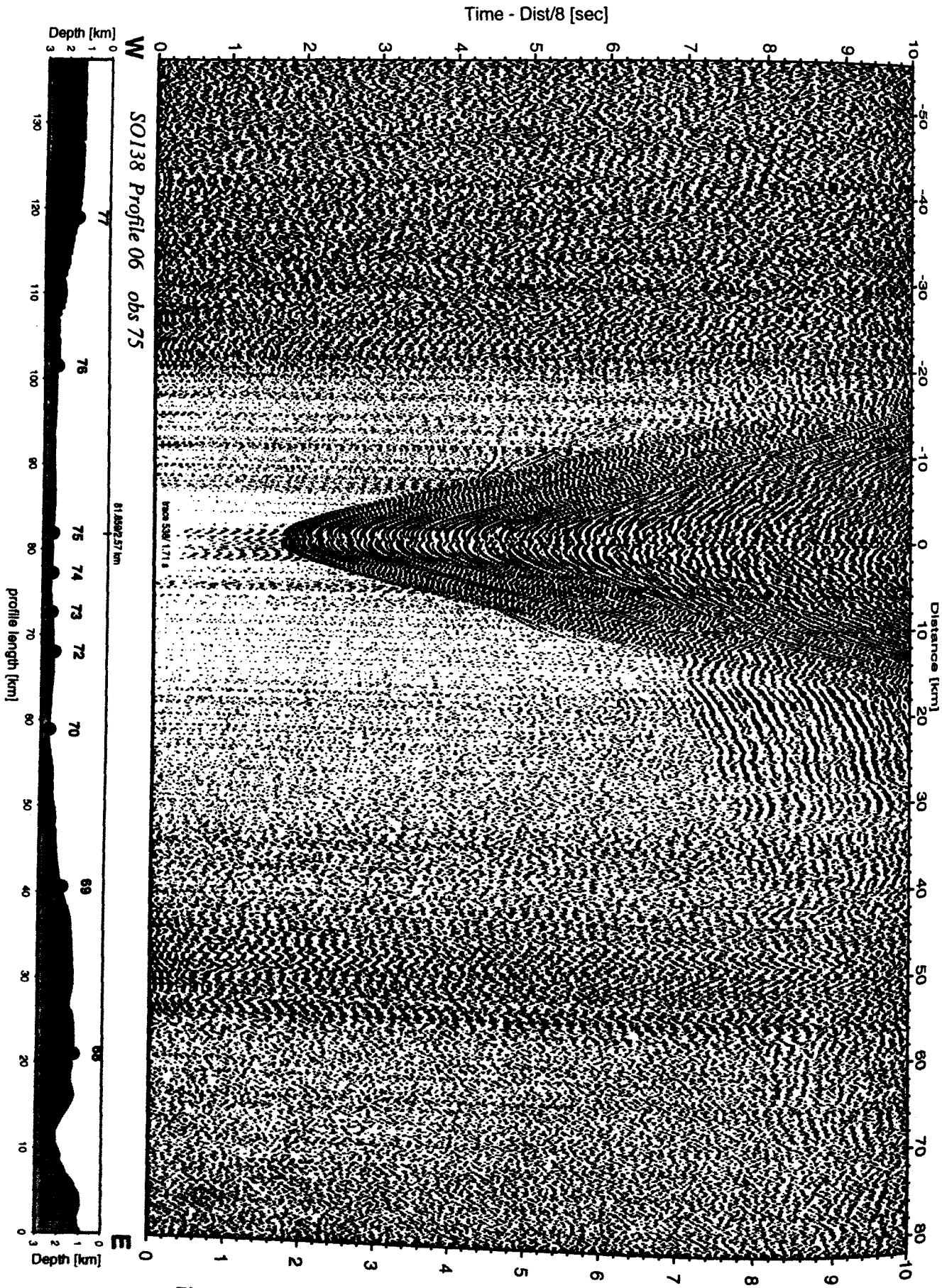

Figure 6.3.4.5.9b: Record section from obs 75 horizontal component 1, Profile 06.

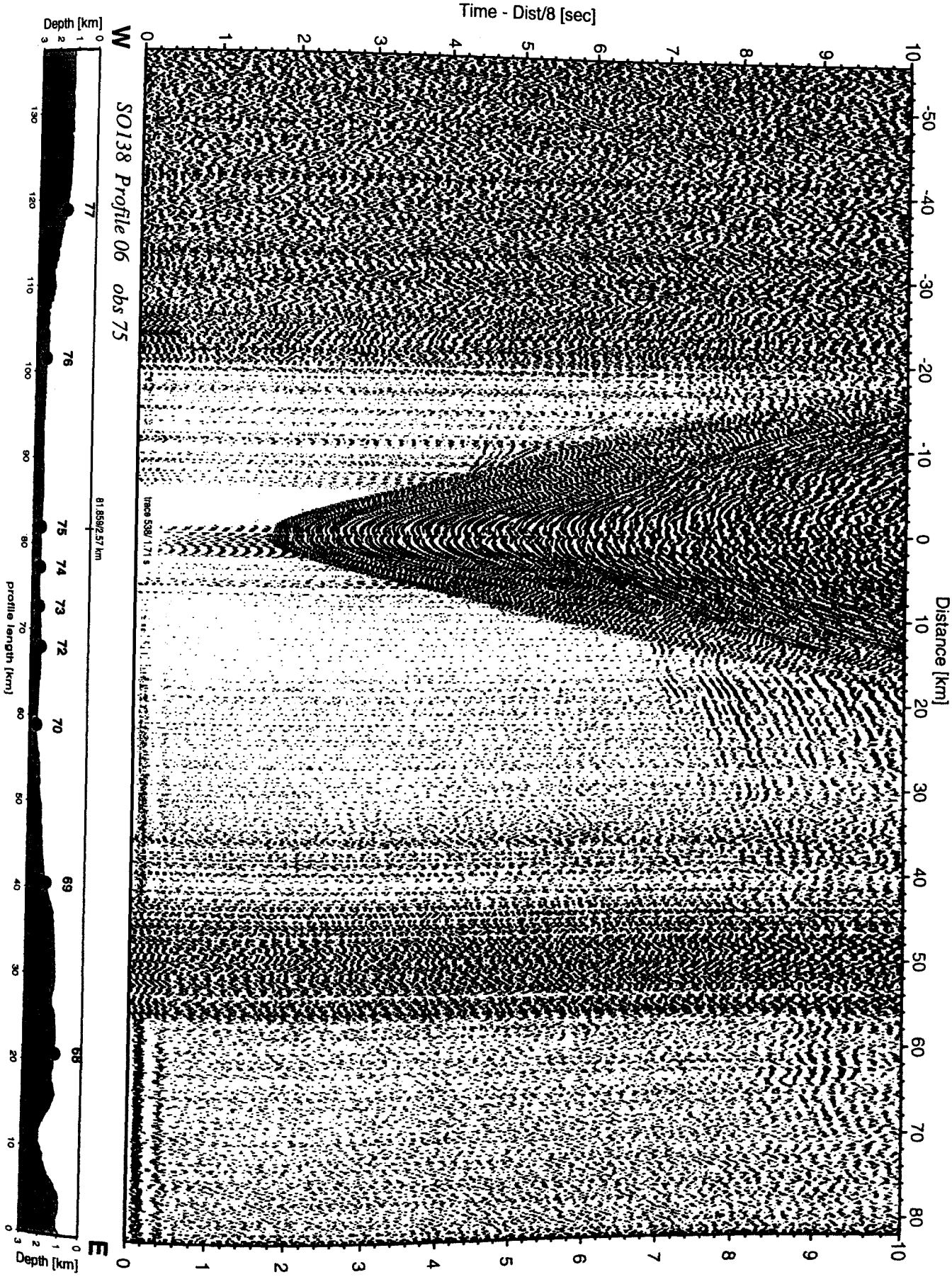

Figure 6.3.4.5.9c: Record section from obs 75 horizontal component 2, Profile 06.

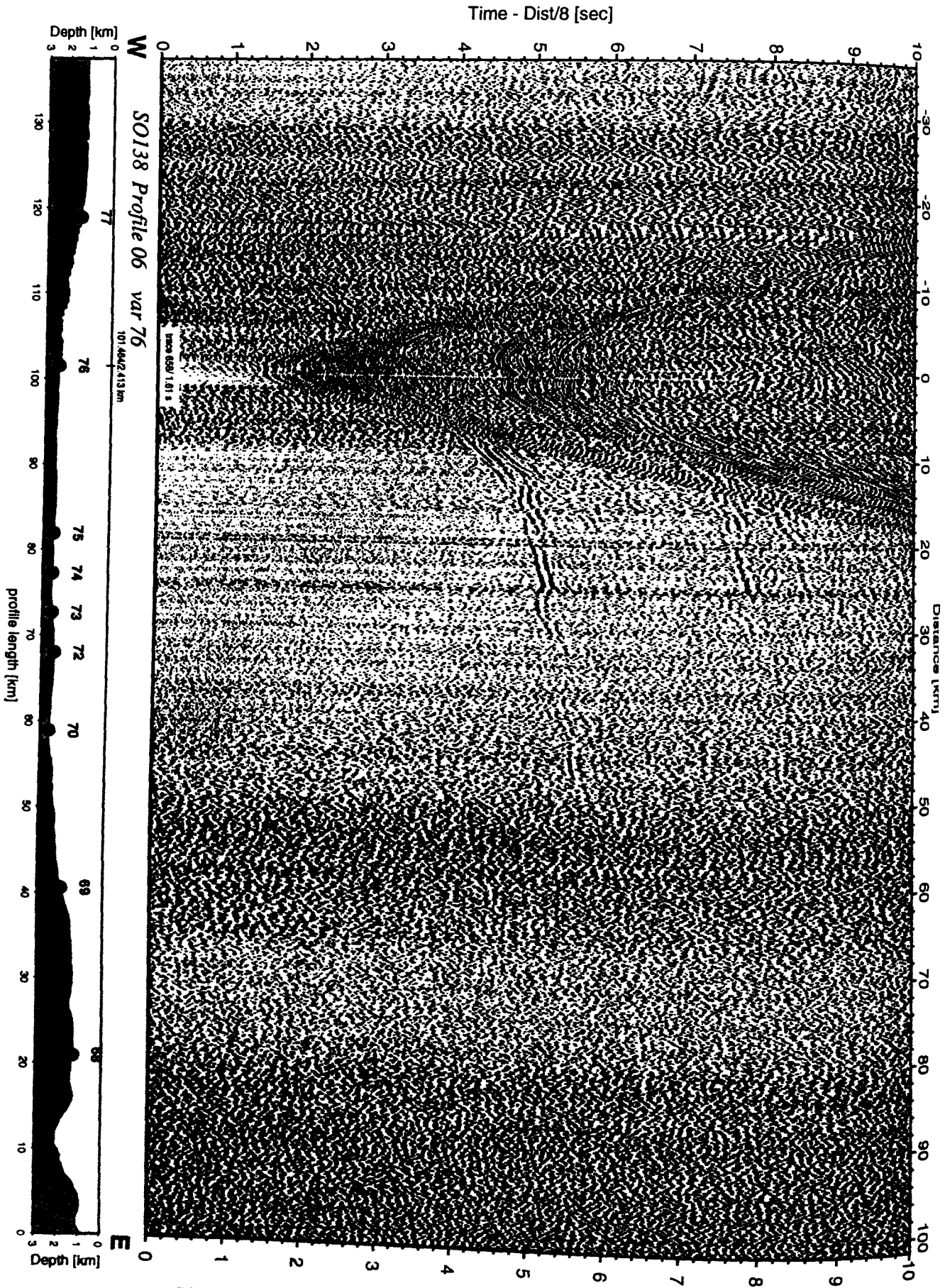

Figure 6.3.4.5.10: Record section from var 76 channel_1, Profile 06.

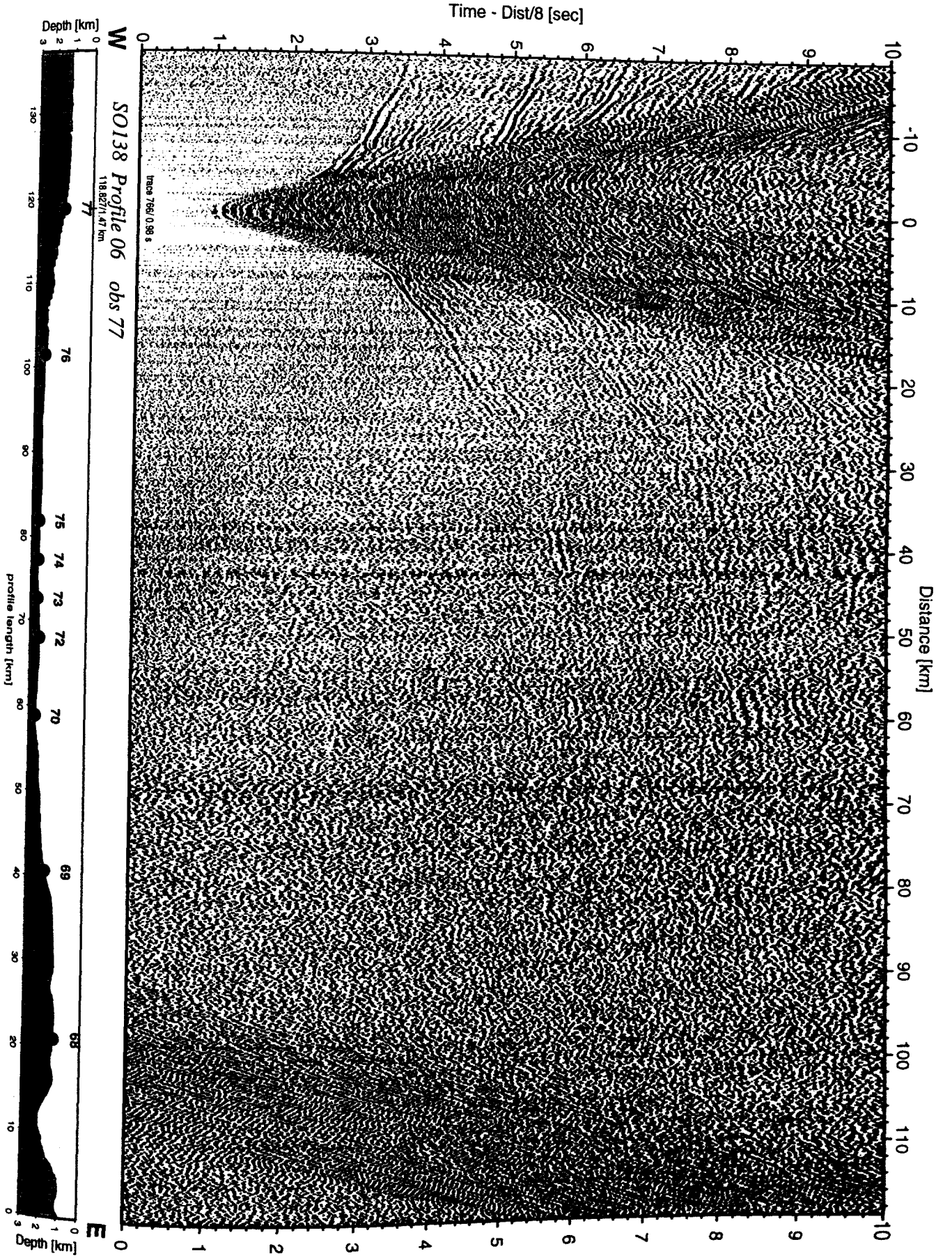

Figure 6.3.4.5.11: Record section from obs 77 hydrophone, Profile 06.

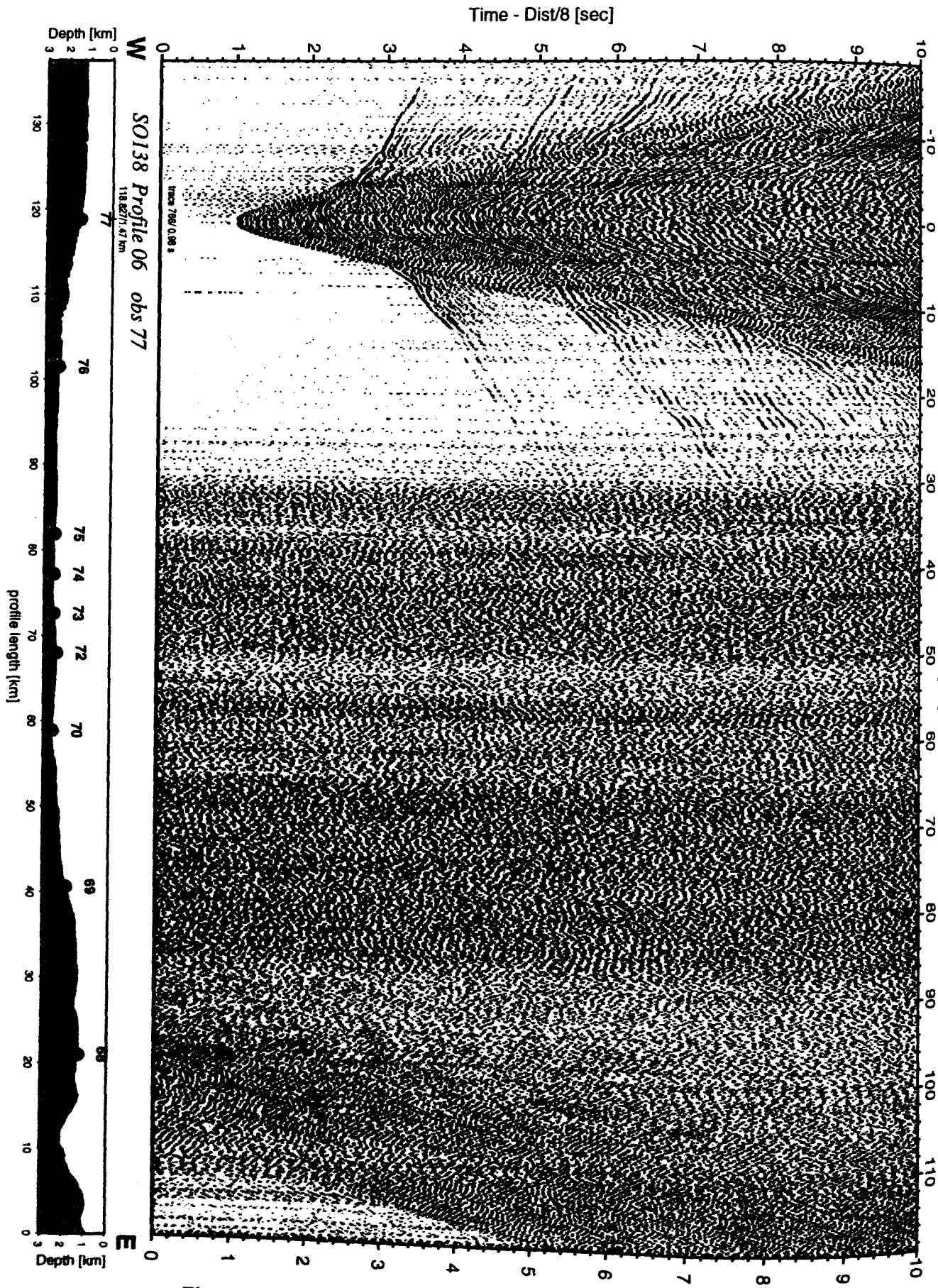

Figure 6.3.4.5.11a: Record section from obs 77 vertical component, Profile 06.

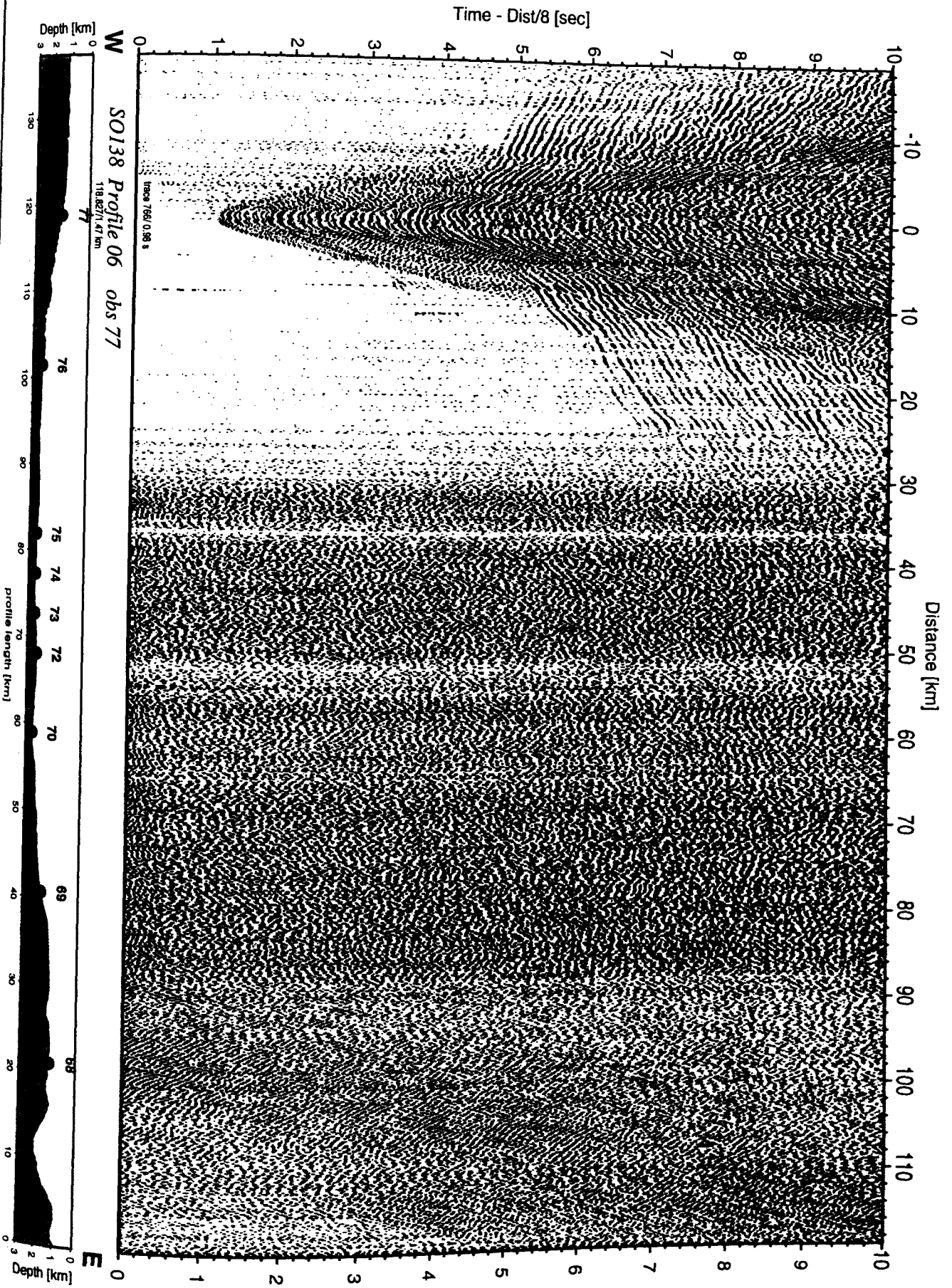

Figure 6.3.4.5.11b: Record section from obs 77 horizontal component 1, Profile 06.

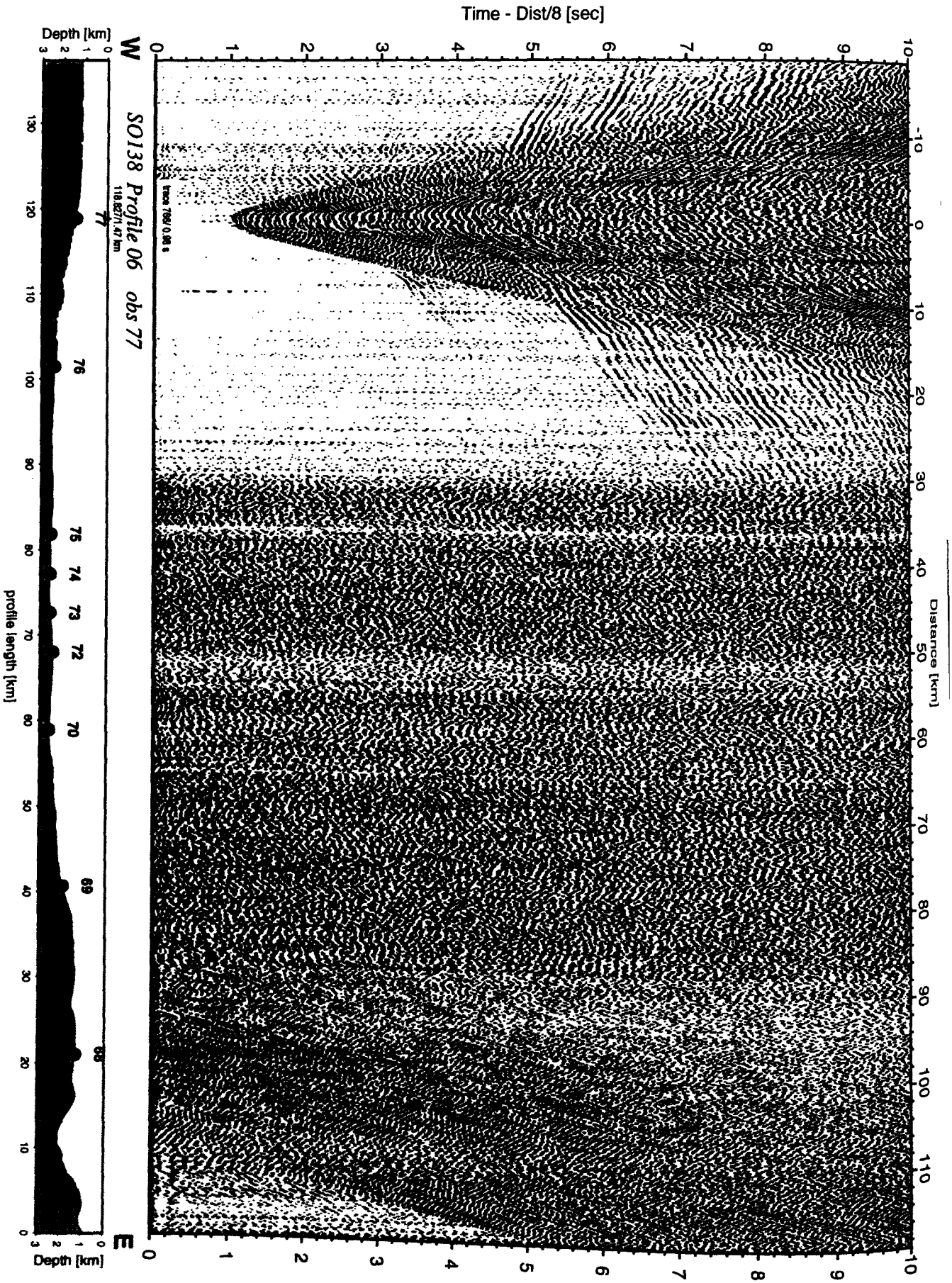

Figure 6.3.4.5.11c: Record section from obs 77 horizontal component 2, Profile 06.

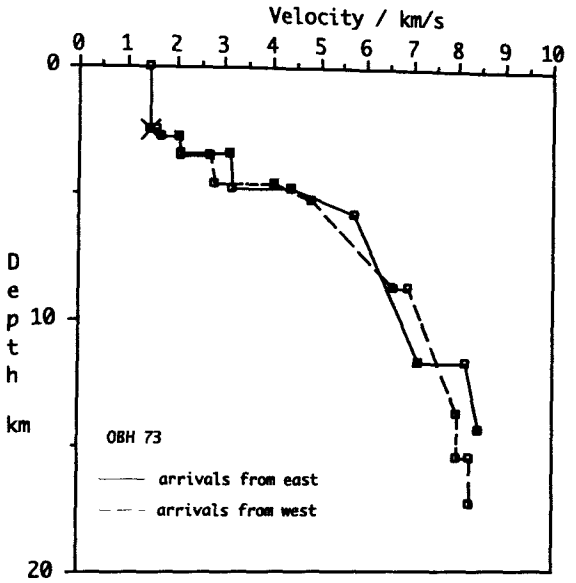

Figure 6.3.4.5.12: Velocity-depth profiles beneath OBH 73 derived from 1D-modelling of shots laying eastwards (solid line) and westwards (dashed line).

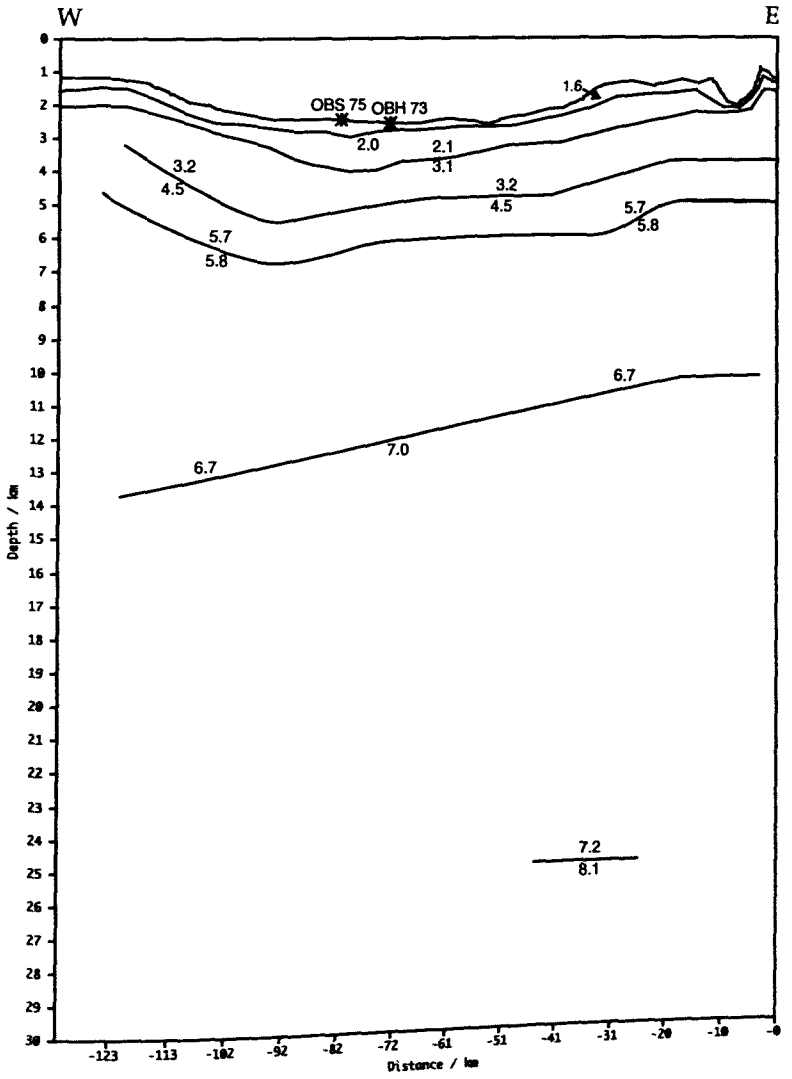

Figure 6.3.4.5.13: Preliminary velocity model along profile 6 based on ray-tracing arrivals from OBH 73 and OBS 75. Layer velocities are shown in km/s.

6.3.4.6 PROFILE SO138-07

(A. Berhorst, J. Bialas, E. Flueh)

Profile SO138-07 is another strike line on the Java margin, centered around profile SO138-05 on top of the outer arc high, aiming to determine the nature of the backstop. Twelve instruments (OBH78 to 89) were deployed between 11:00 and 18:00 on 20.01.1999, including the OBS´ses and the 400 m long vertical array (Figure 6.3.4.6.1). Shooting extended for 20 miles on both sides of the recording array and was finished in the afternoon of 21.01.1999. The record section obtained by the streamer is shown in Figure 6.3.4.6.2. All instruments were routinely recovered by 02:00 22.01.1998. Details on instrumentation and shots can be found in appendix 9.1.6 and 9.2.

The record sections are all of good quality, with one instrument failing to record the complete data set. Record sections are shown in Figures 6.3.4.6.3 to 6.3.4.6.12.

Modelling and interpretation:

Due to the relatively modest lateral variations, only a preliminary 1D velocity model was calculated for the profile SO138-07. For this analysis OBH78 (Figure 6.3.4.6.3) was selected, because this record section has a very high signal-to-noise ratio with first arrivals up to 70 km. Additional this is the only OBH of this profile with a clear moho reflection (P_mP). Velocities from the upper sedimentary layers do not show up as first arrivals and thus their velocity is difficult to determine with precision.

Despite a smooth seafloor topography, there is only one sedimentary layer imaged in the mini-streamer section (Figure 6.3.4.6.2). The thickness of this layer at the position of OBH78 is about 0.4 s (twt). This is in good agreement with the line drawing of the multi-channel seismic line SO137-03 (Figure 6.3.4.4.16) which coincides with SO138-05. These sediments are modelled as a 350 m thick layer with velocities of 1.6 kms^{-1}. Below we interpret gradually increasing velocities of up to 4.3 kms^{-1} at a depth of 7 km. Here a well marked discontinuity in the OBH section can be recognized, which is interpreted as a velocity step from 4.3 kms^{-1} to 4.7 kms^{-1}. This sudden increase is also seen in profile SO138-05, which is located about 40 km to the west of OBH78 .

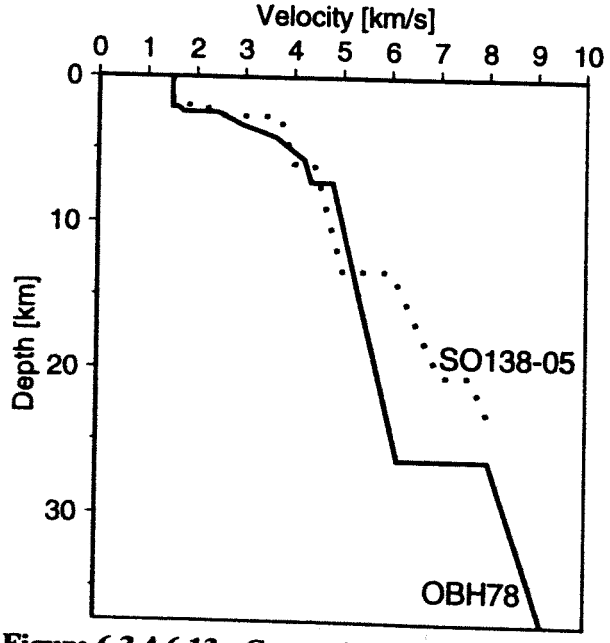

Figure 6.3.4.6.13: Comparison of the velocities from profile SO138-05 (OBH58) with the results from the 1D modelling of OBH78.

The Moho is found at a depth of 26 km, which agrees well with profile SO138-05 and profile SO138-06.

Comparing the velocity-depth profiles from OBH78 with the results from profile SO138-05 (see chapter 6.3.4.4) we find a good agreement down to 13 km, but below there is some missmatch (Figure 6.3.4.6.13). This is where the top of the downgoing plate in profile SO138-05 is imaged. The data from OBH78 do not indicate a velocity discontinuity at this depth. Further modelling will be necessary to get a better correlation between the two profiles.

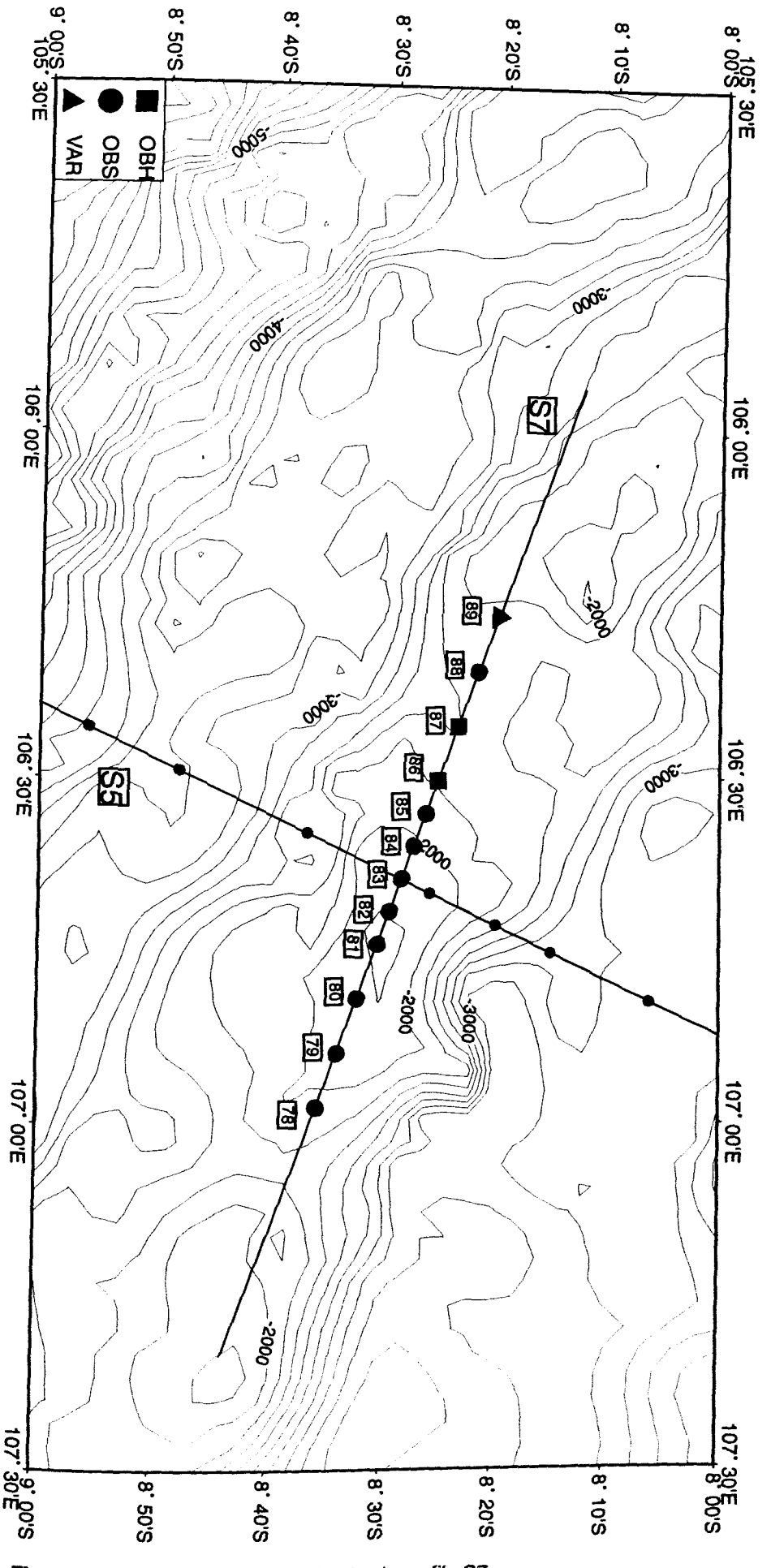

Figure 6.3.4.6.1: Location map of seismic profile S7.

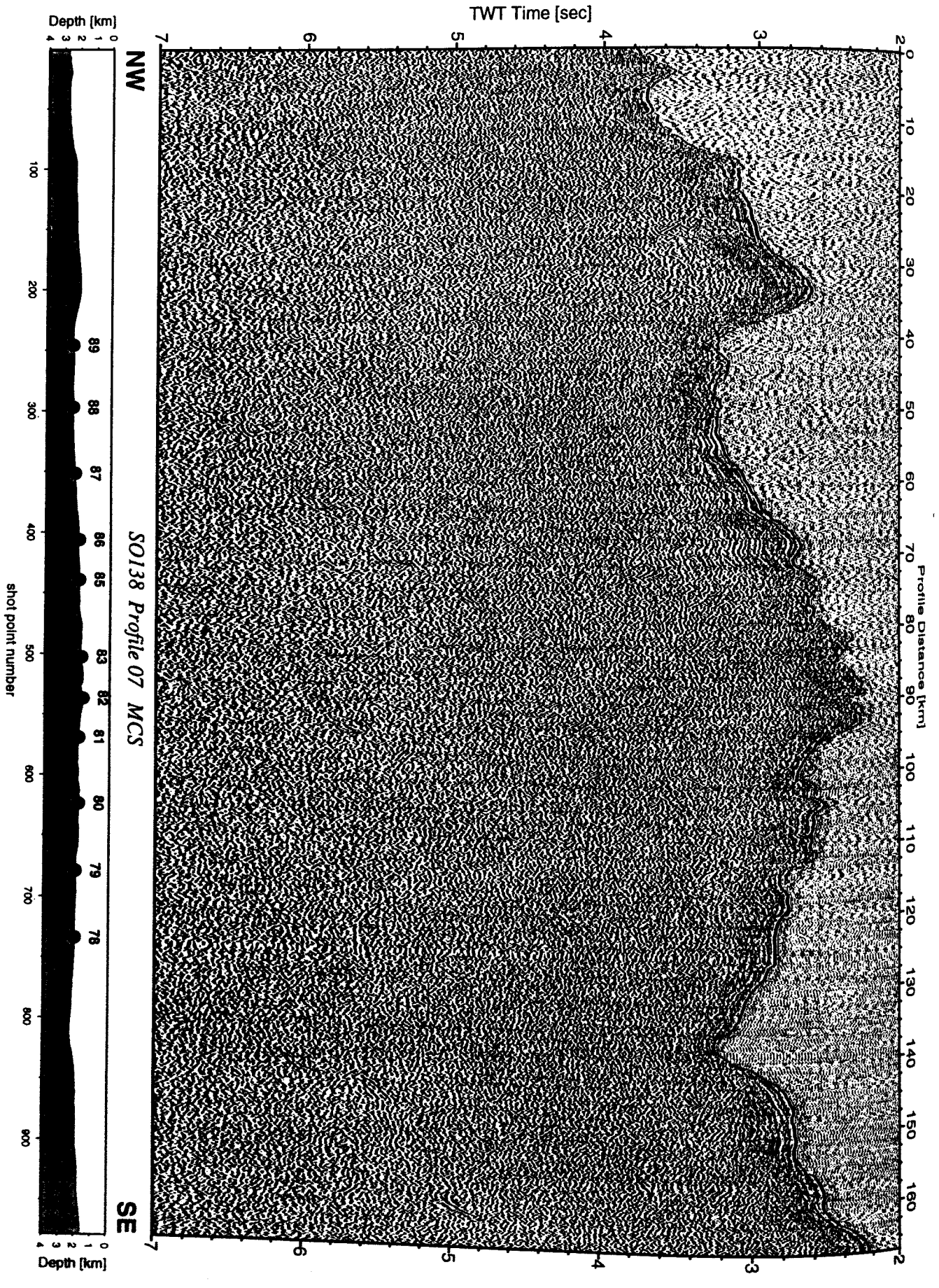

Figure 6.3.4.6.2: Seismic section from MCS stack, Profile 07.

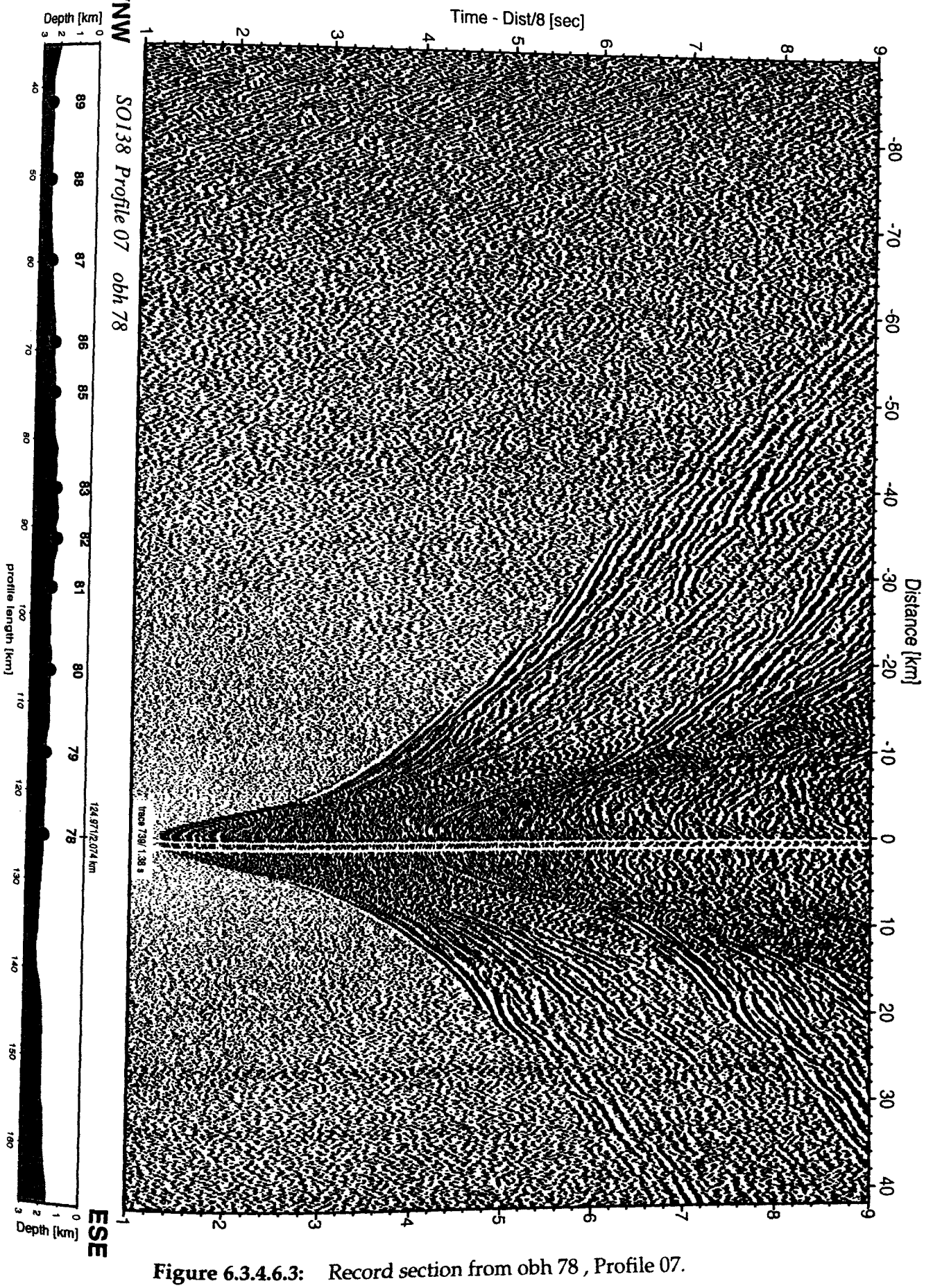

Figure 6.3.4.6.3: *Record section from obh 78 , Profile 07.*

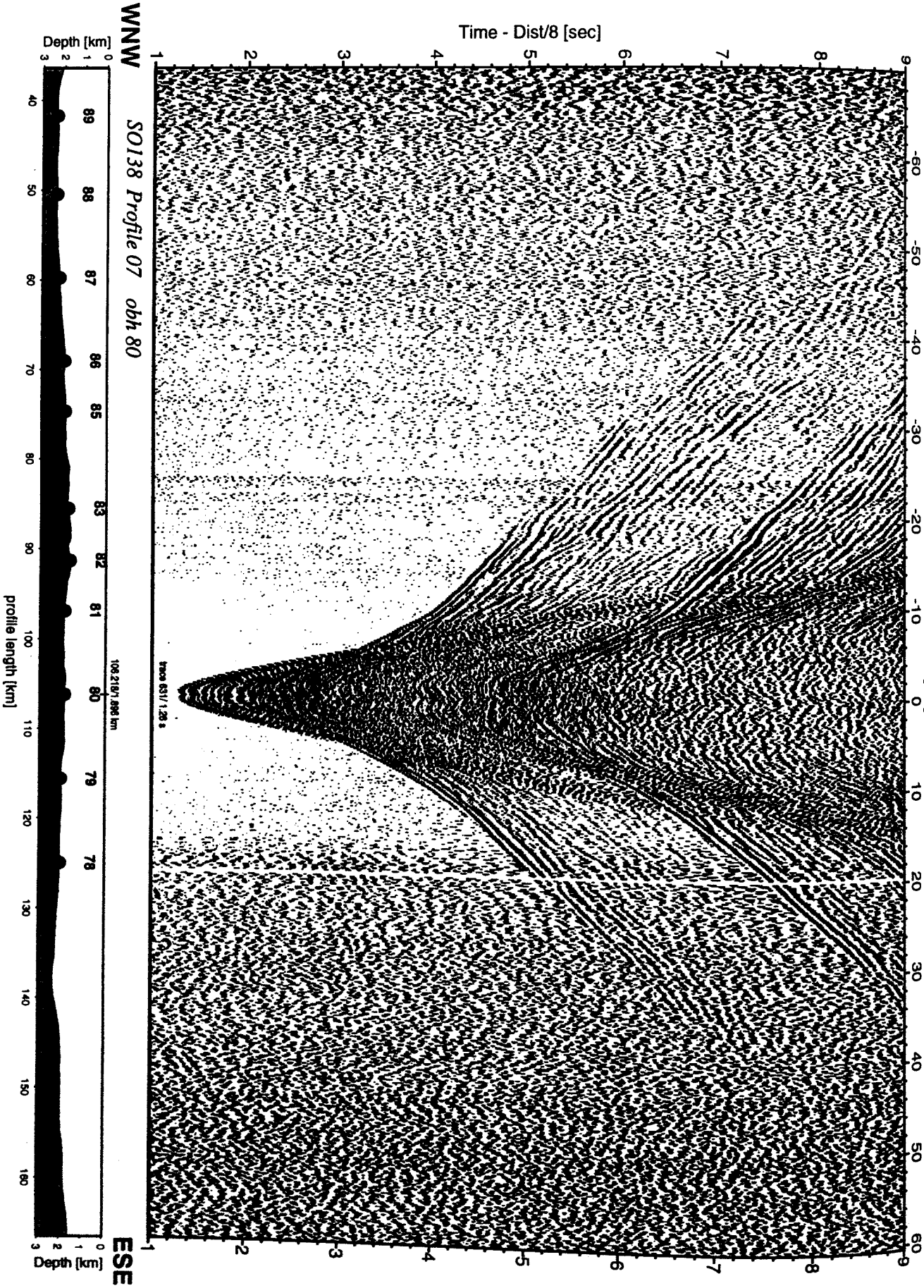

Figure 6.3.4.6.4: Record section from obh 80 , Profile 07.

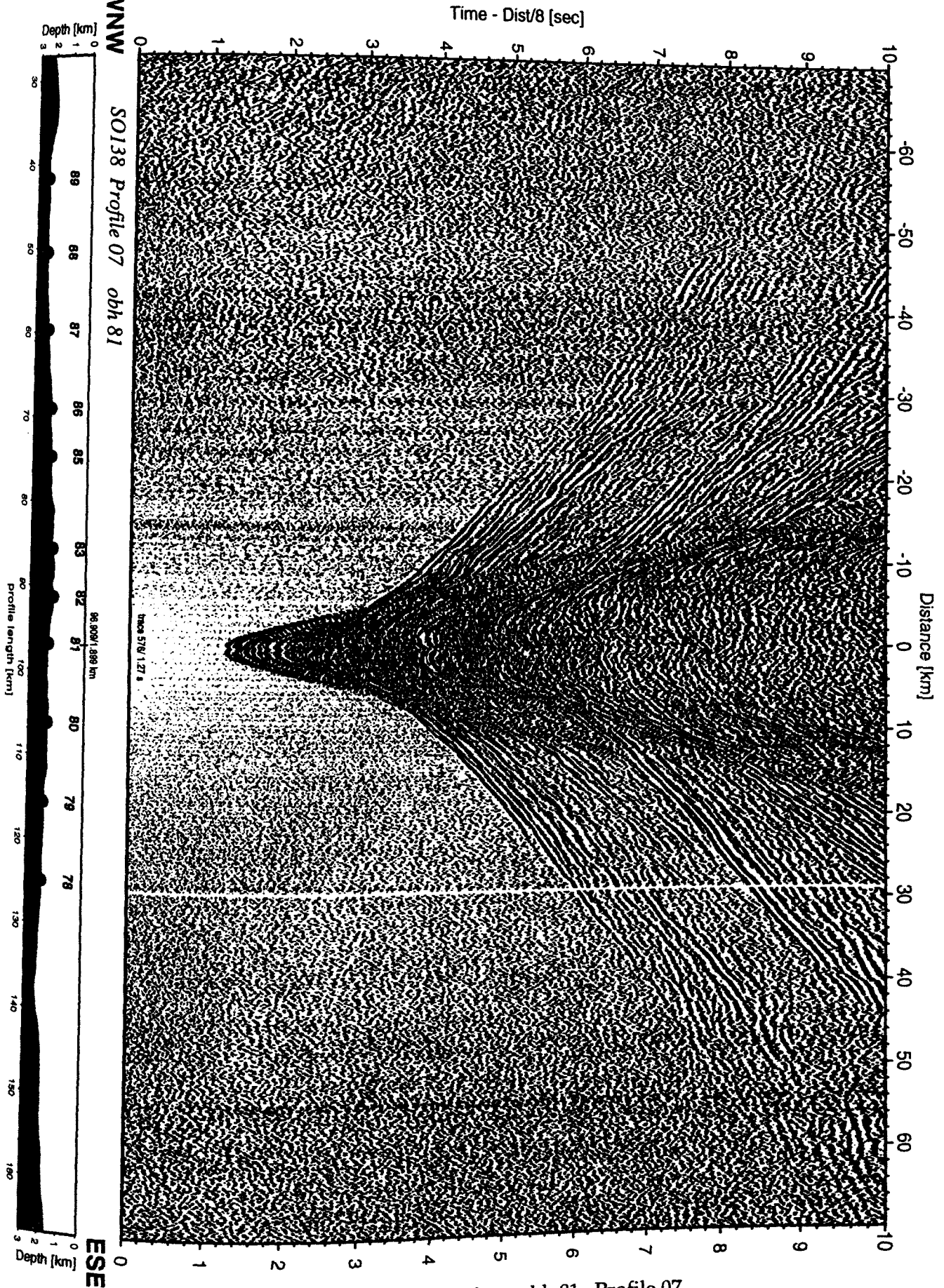

Figure 6.3.4.6.5: Record section from *obh* 81 , Profile 07.

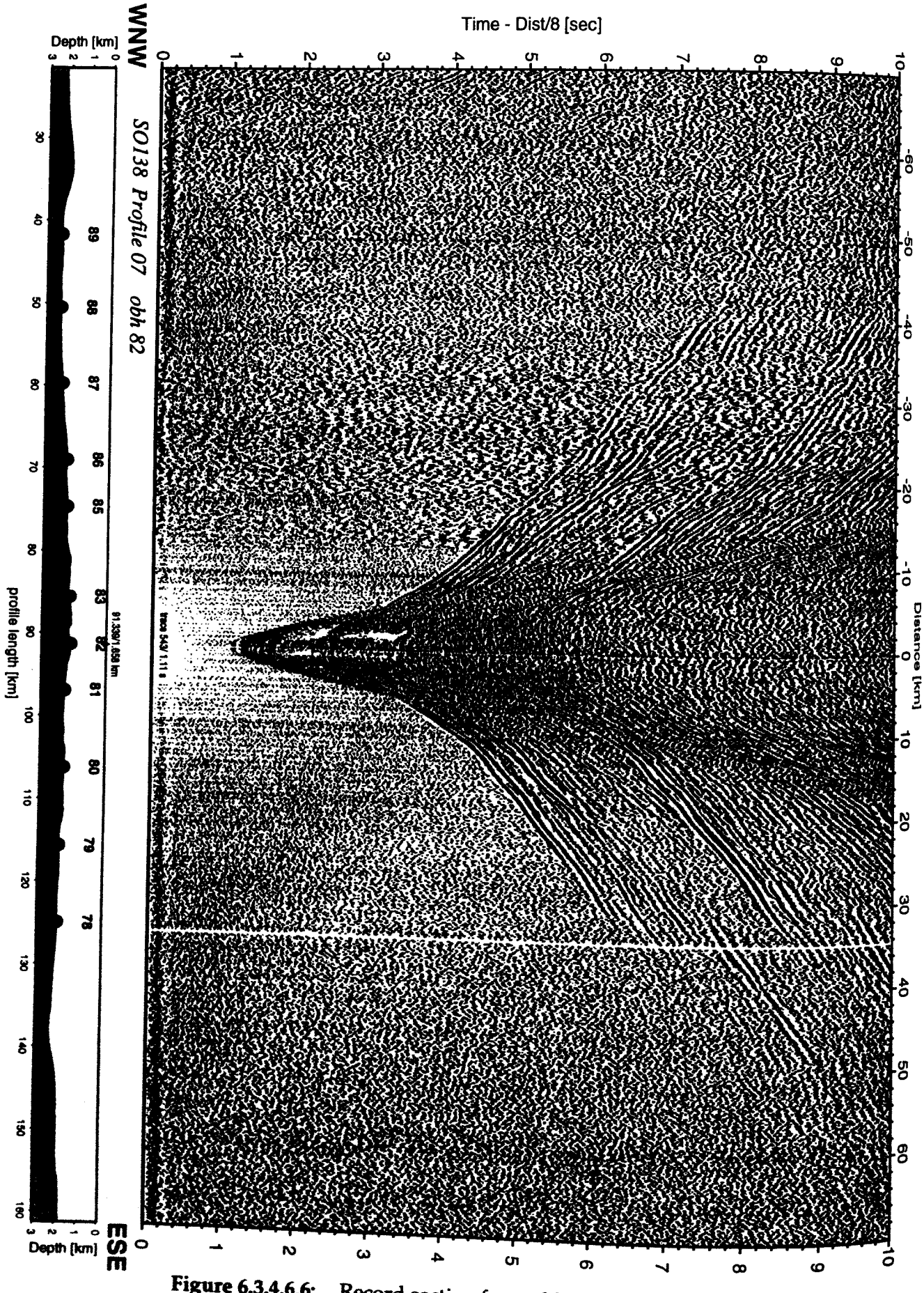

Figure 6.3.4.6.6: Record section from obh 82 , Profile 07.

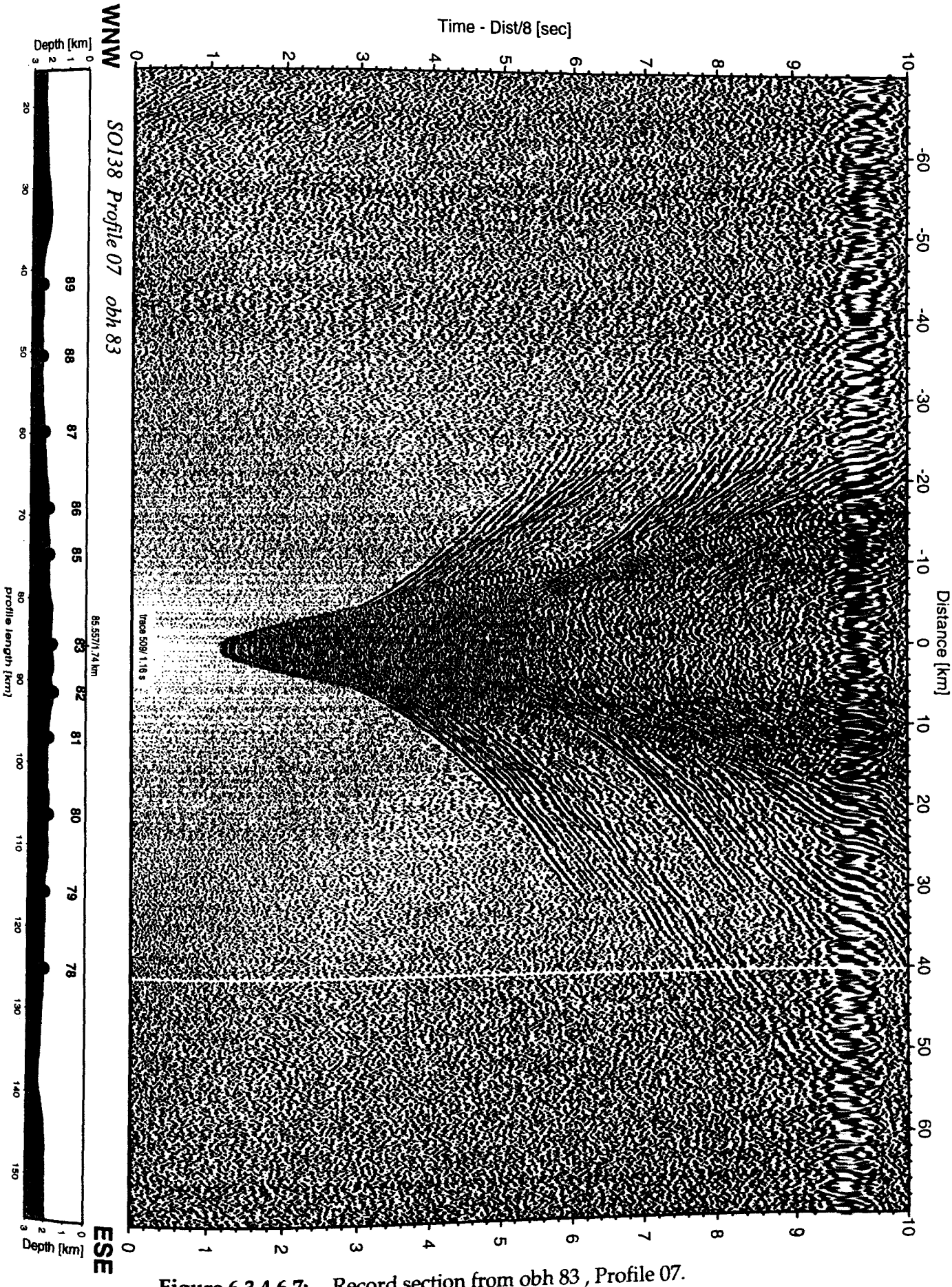

Figure 6.3.4.6.7: Record section from obh 83 , Profile 07.

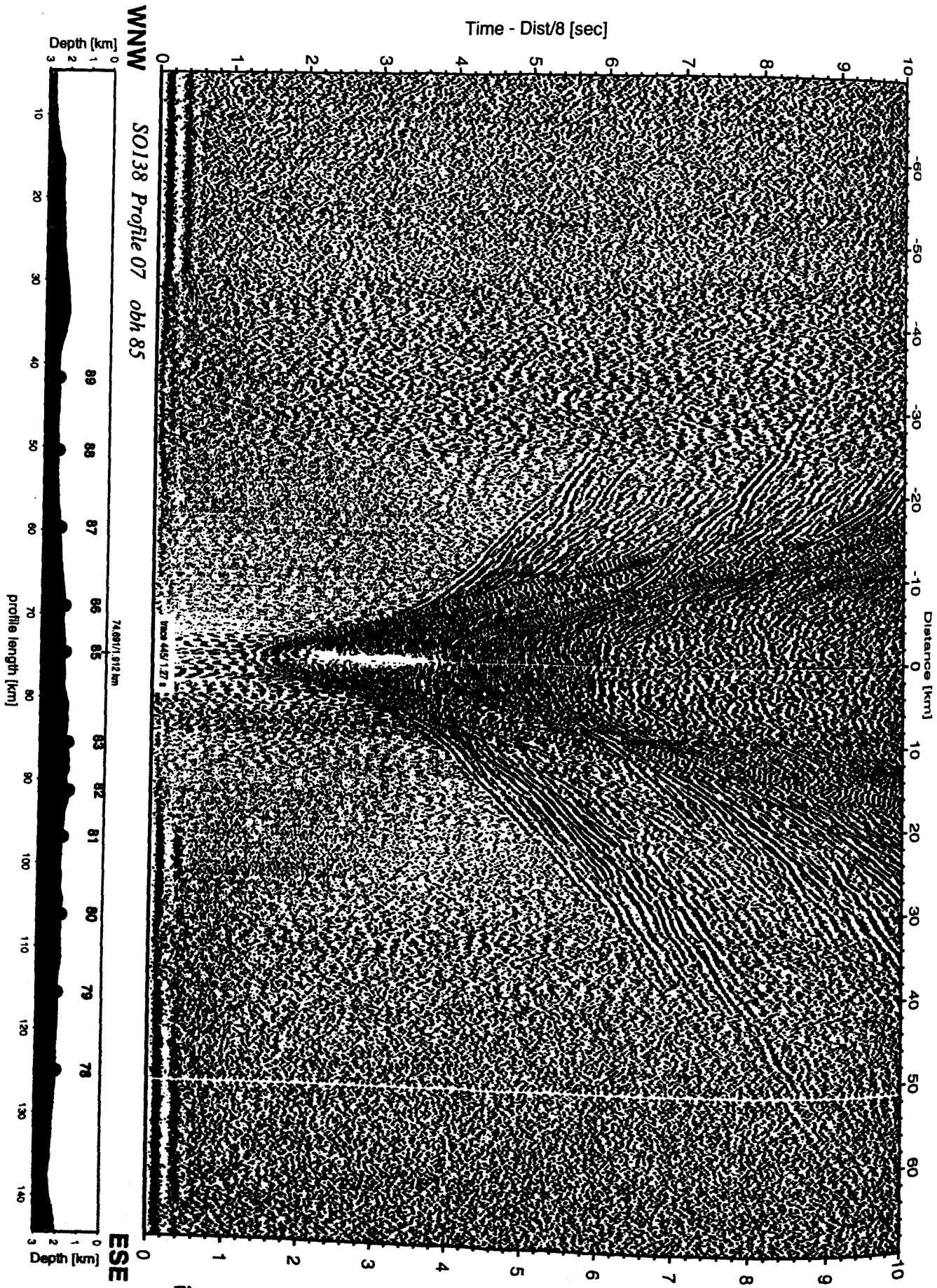

Figure 6.3.4.6.8: Record section from obh 85 , Profile 07.

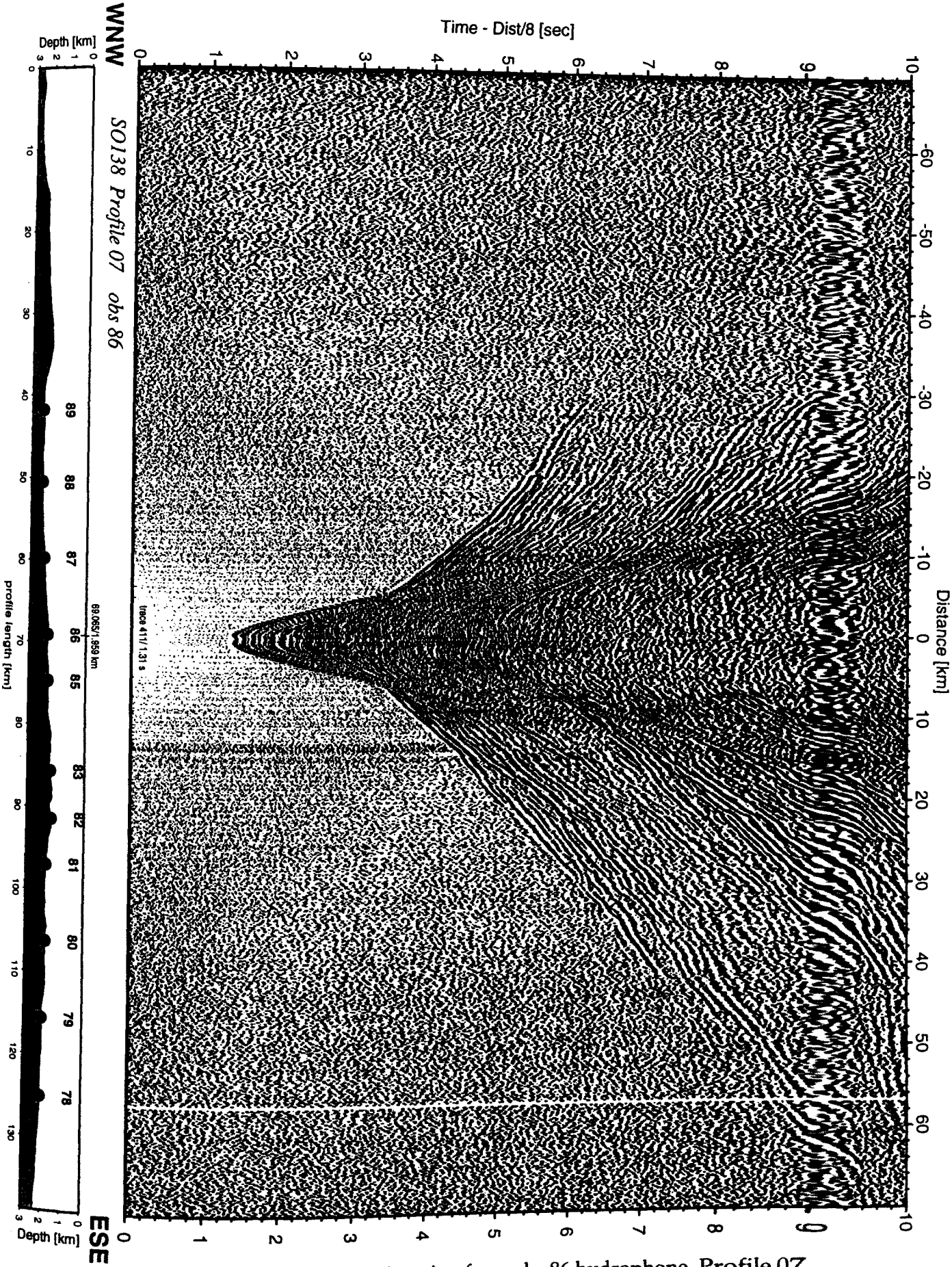

Figure 6.3.4.6.9: Record section from obs 86 hydrophone, Profile 07 _

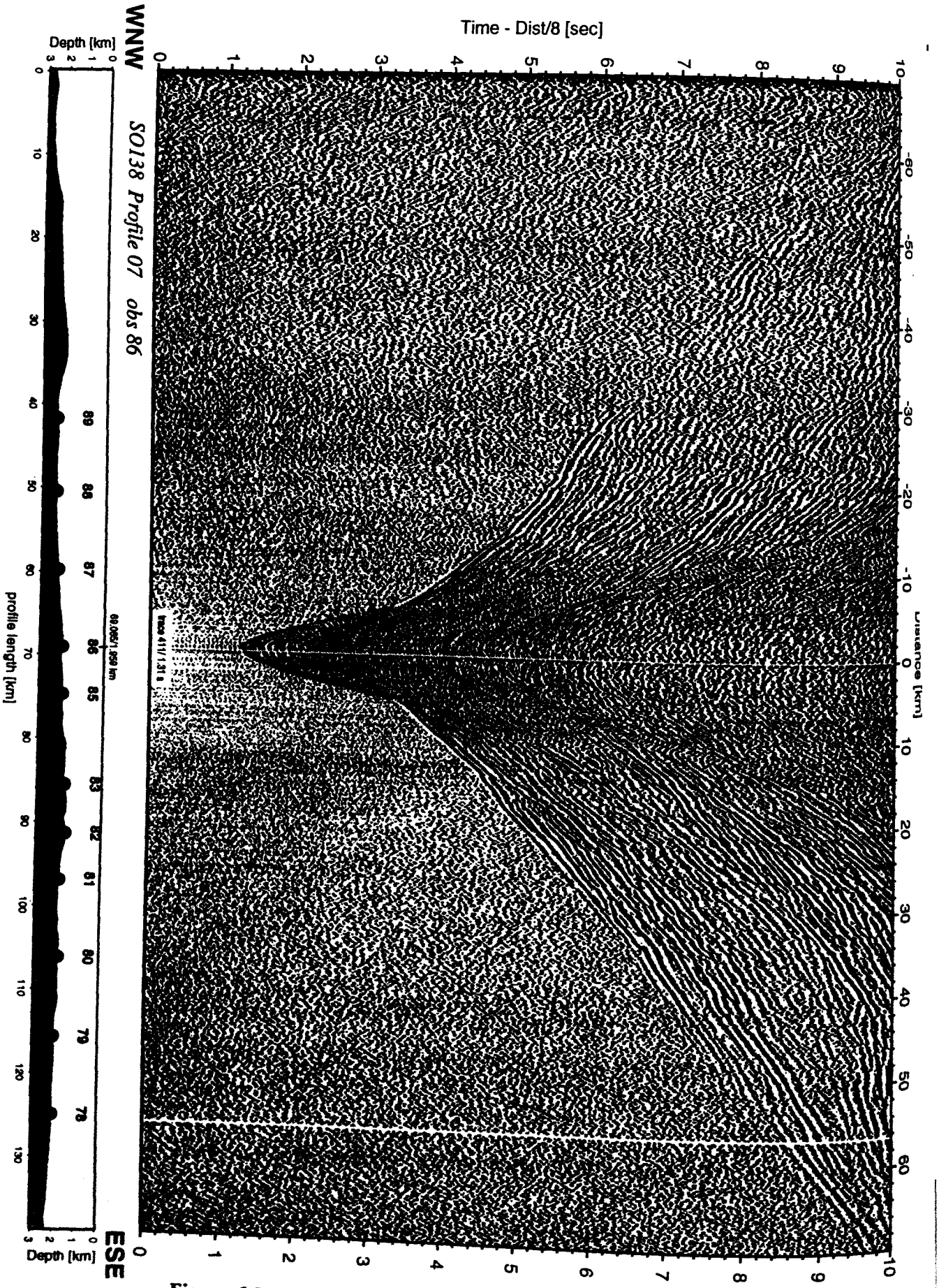

Figure 6.3.4.6.9a: Record section from obs 86 vertical component, Profile 07.

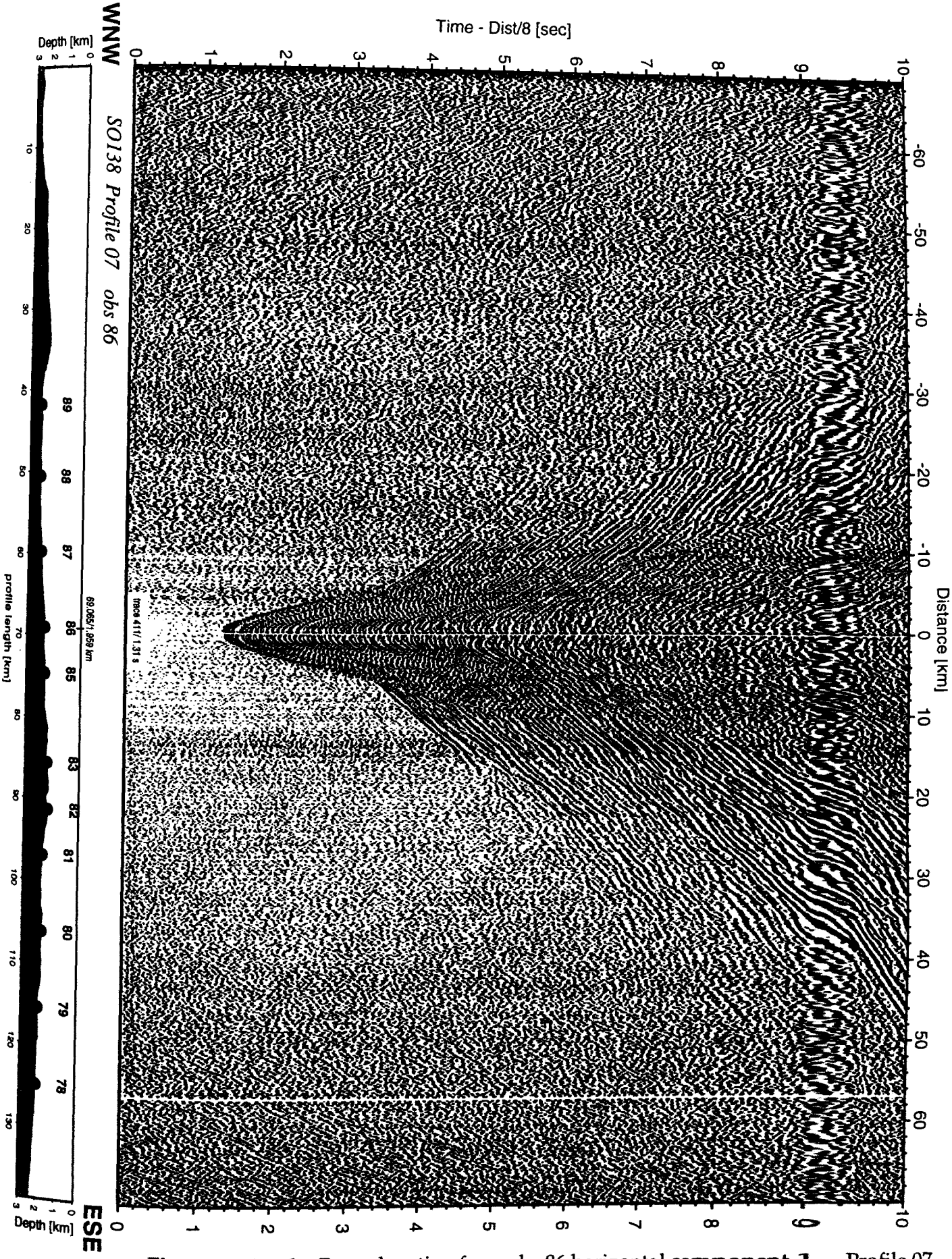

Figure 6.3.4.6.9b: Record section from obs 86 horizontal component **1**, Profile 07.

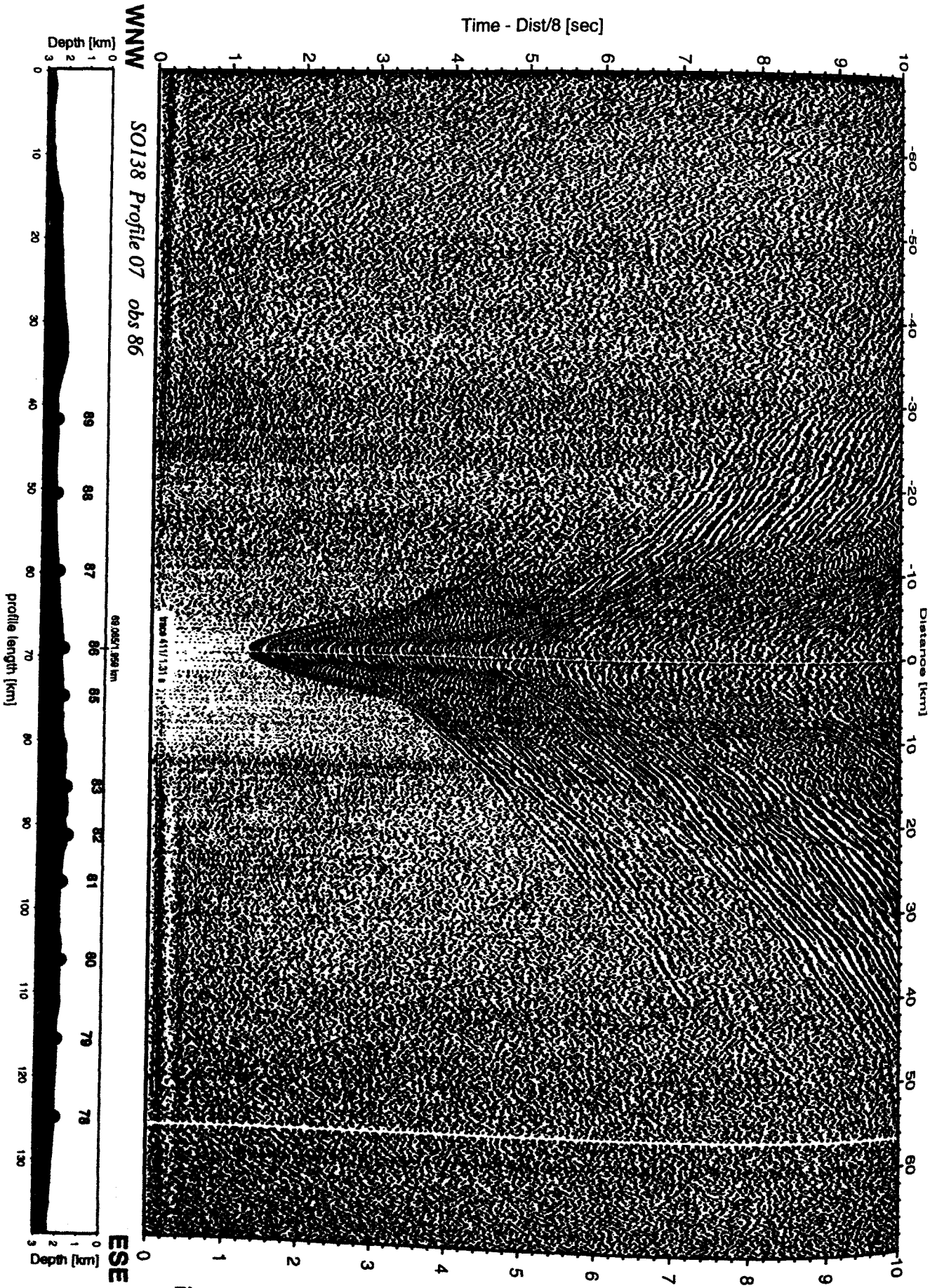

Figure 6.3.4.6.9c: Record section from obs 86 horizontal component 2, Profile 07.

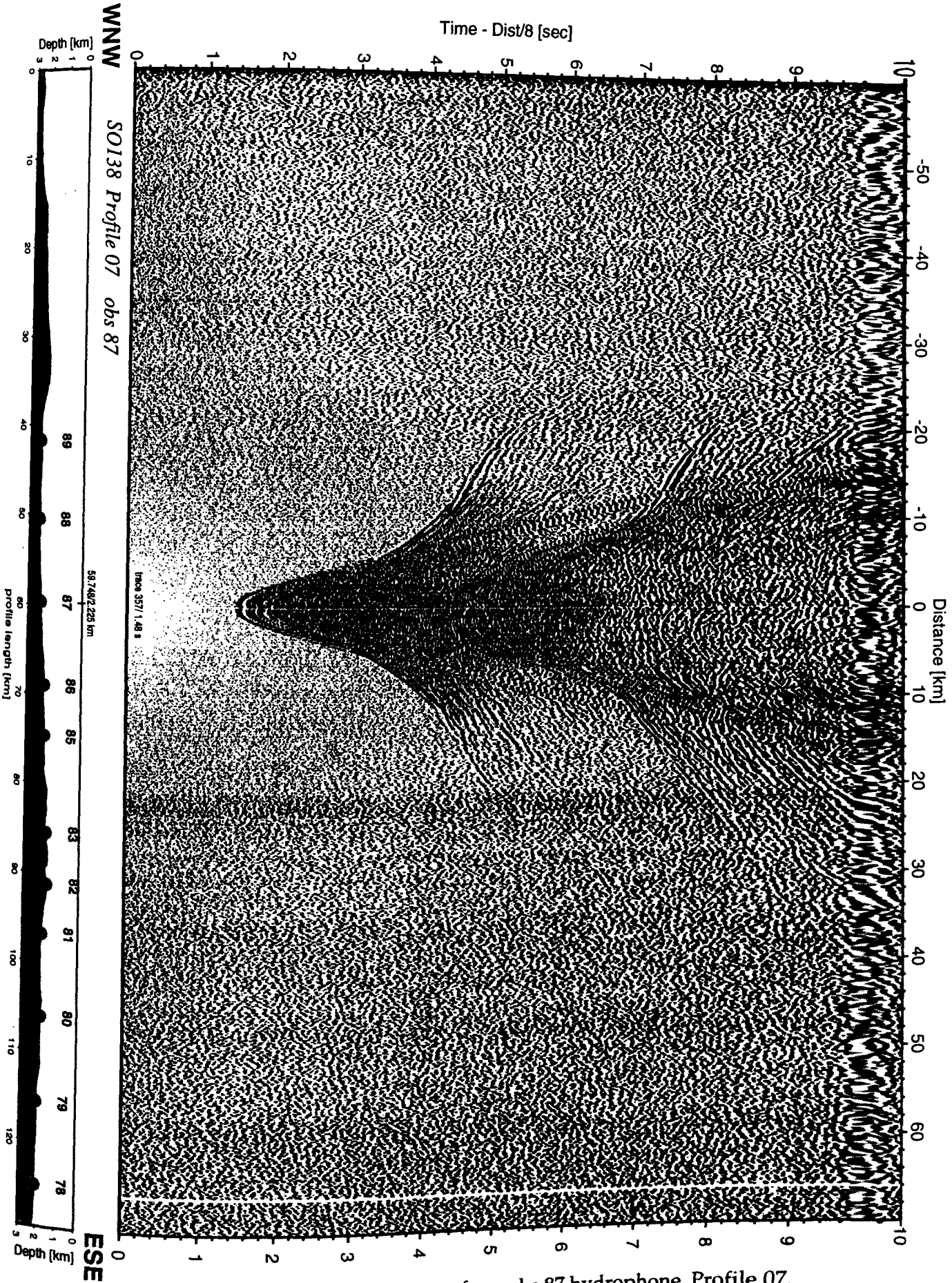

Figure 6.3.4.6.10: Record section from obs 87 hydrophone, Profile 07.

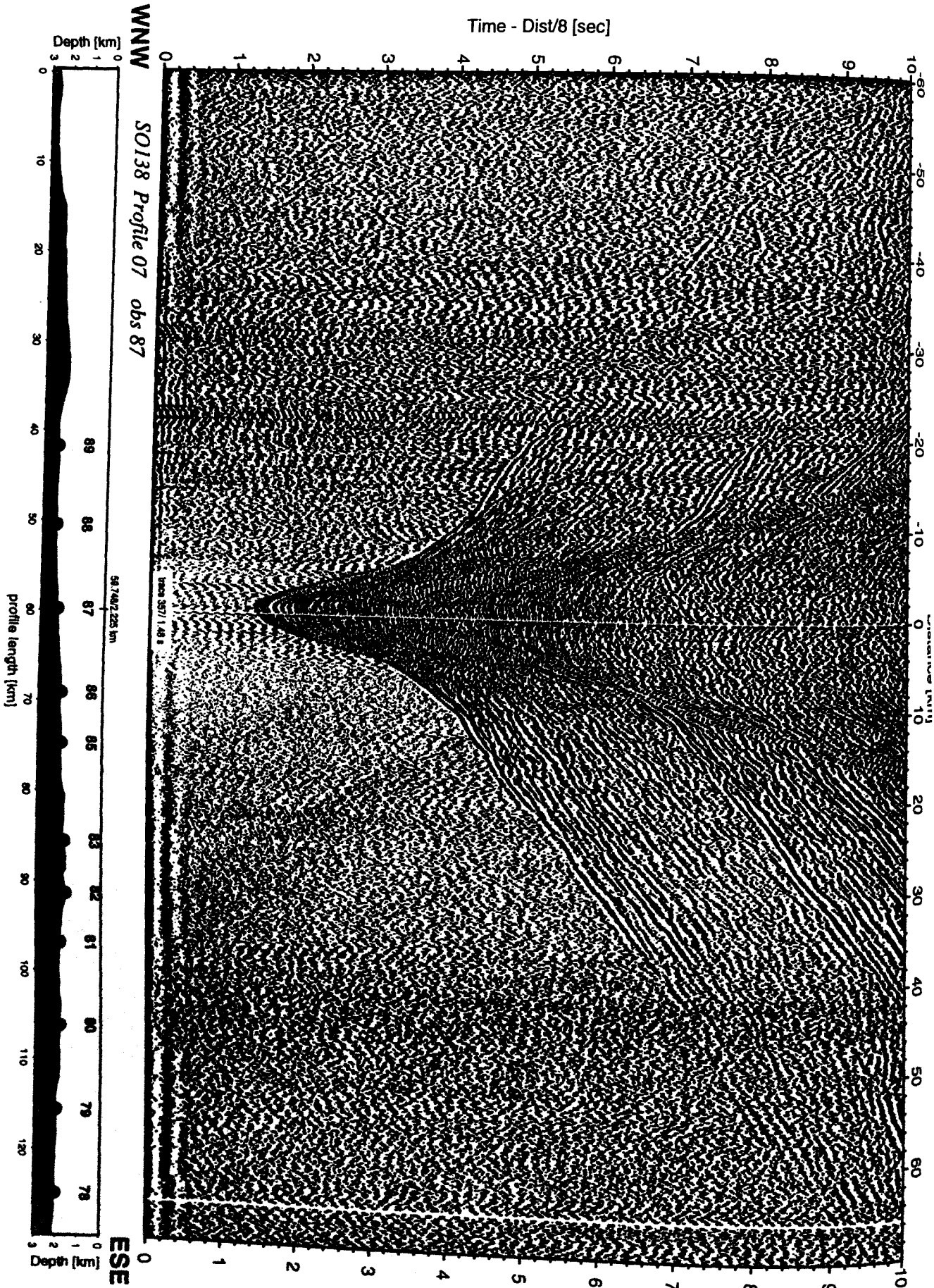

Figure 6.3.4.6.10a: Record section from obs 87 vertical component, Profile 07.

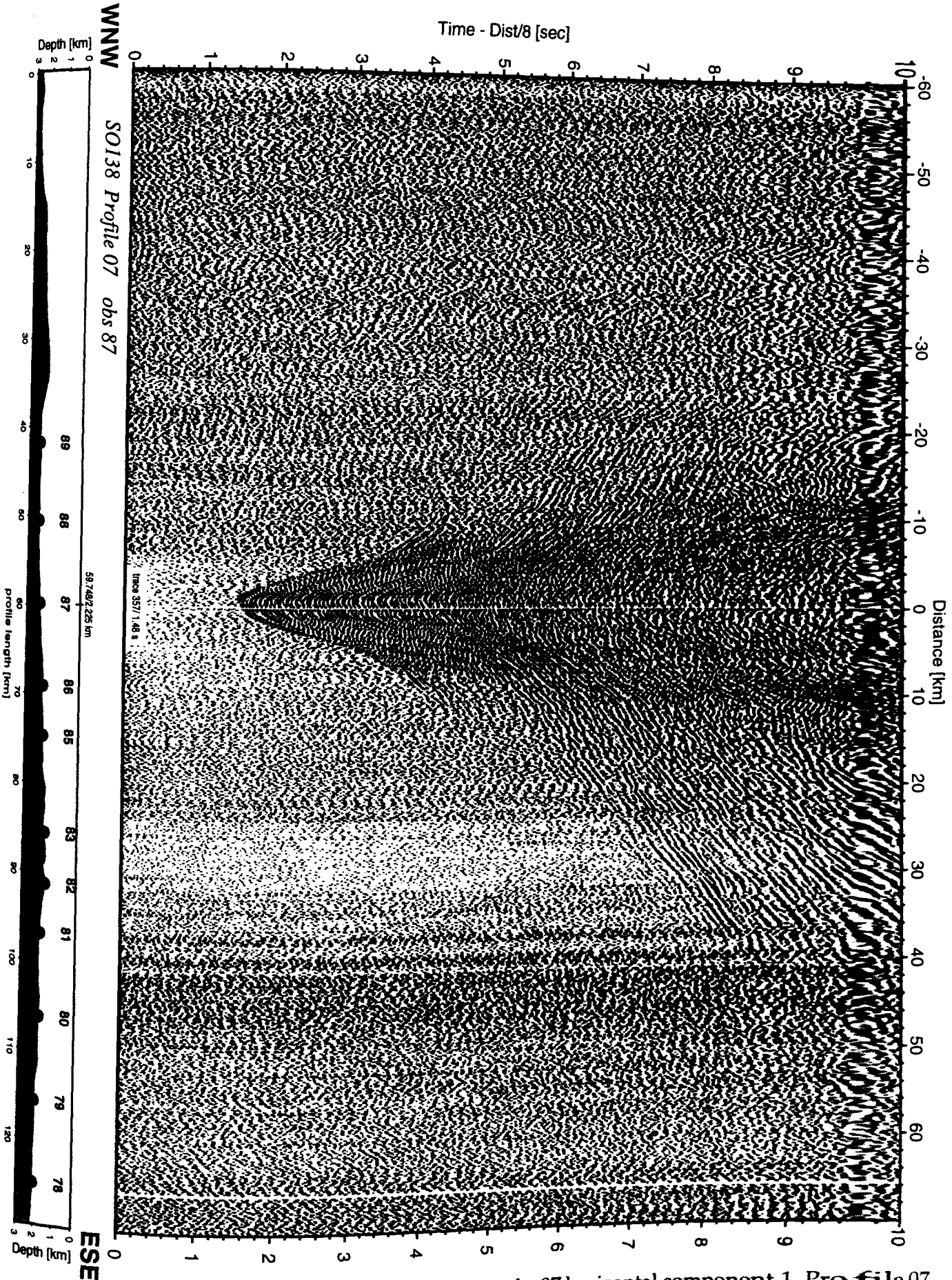

Figure 6.3.4.6.10b: Record section from obs 87 horizontal component 1, Profile 07.

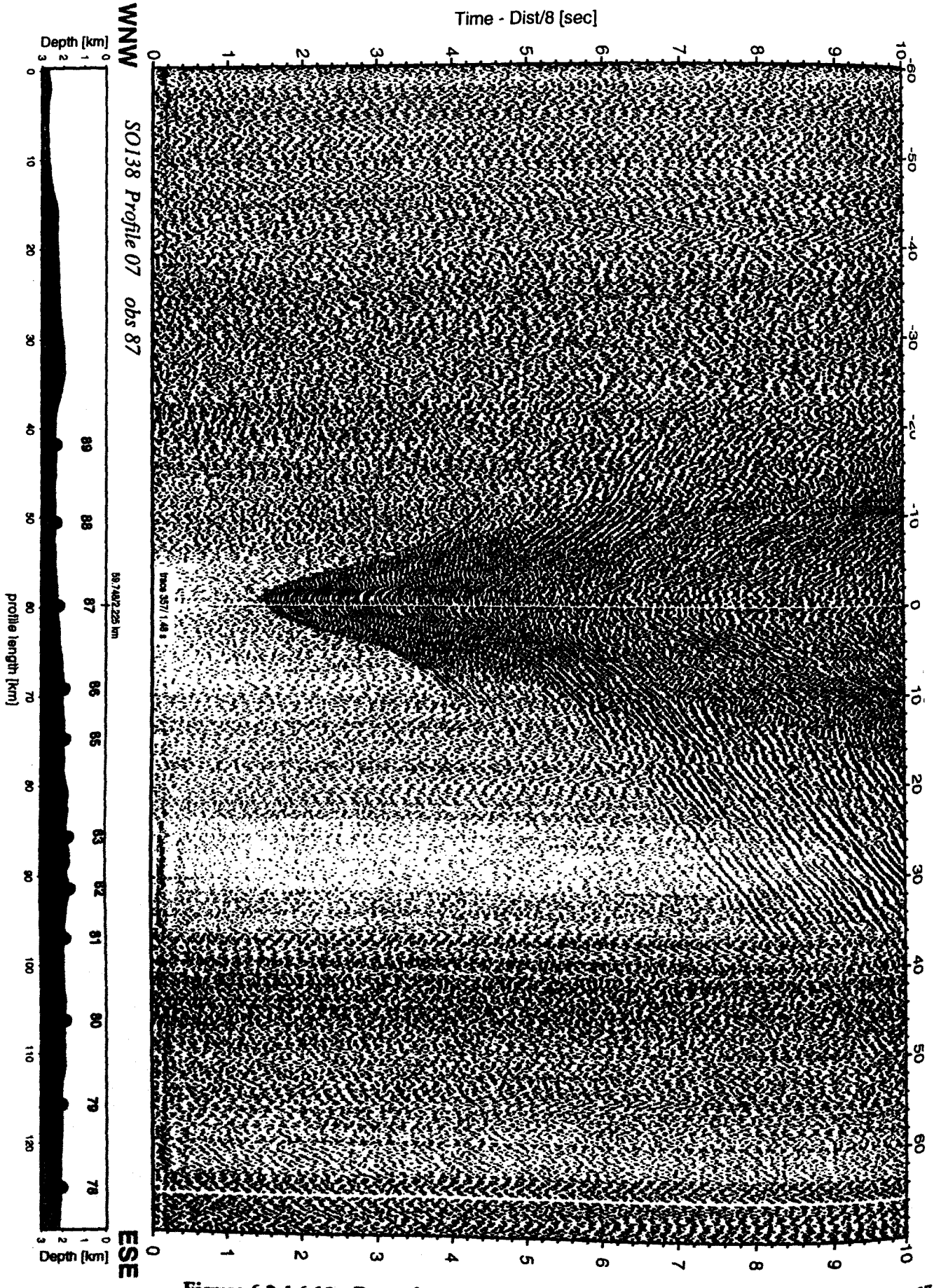

Figure 6.3.4.6.10c: Record section from obs 87 horizontal component 2, Profile 07.

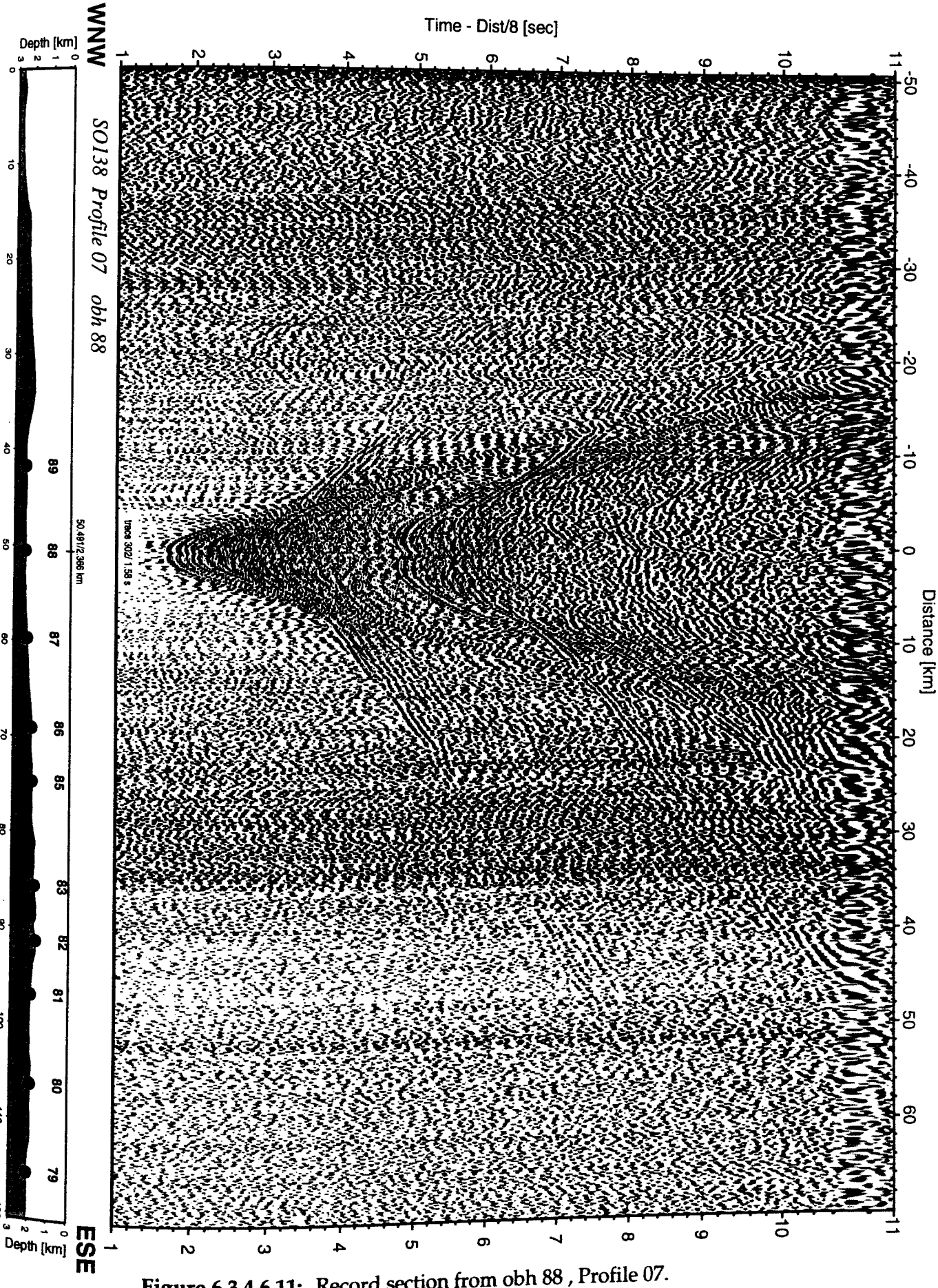

Figure 6.3.4.6.11: Record section from obh 88 , Profile 07.

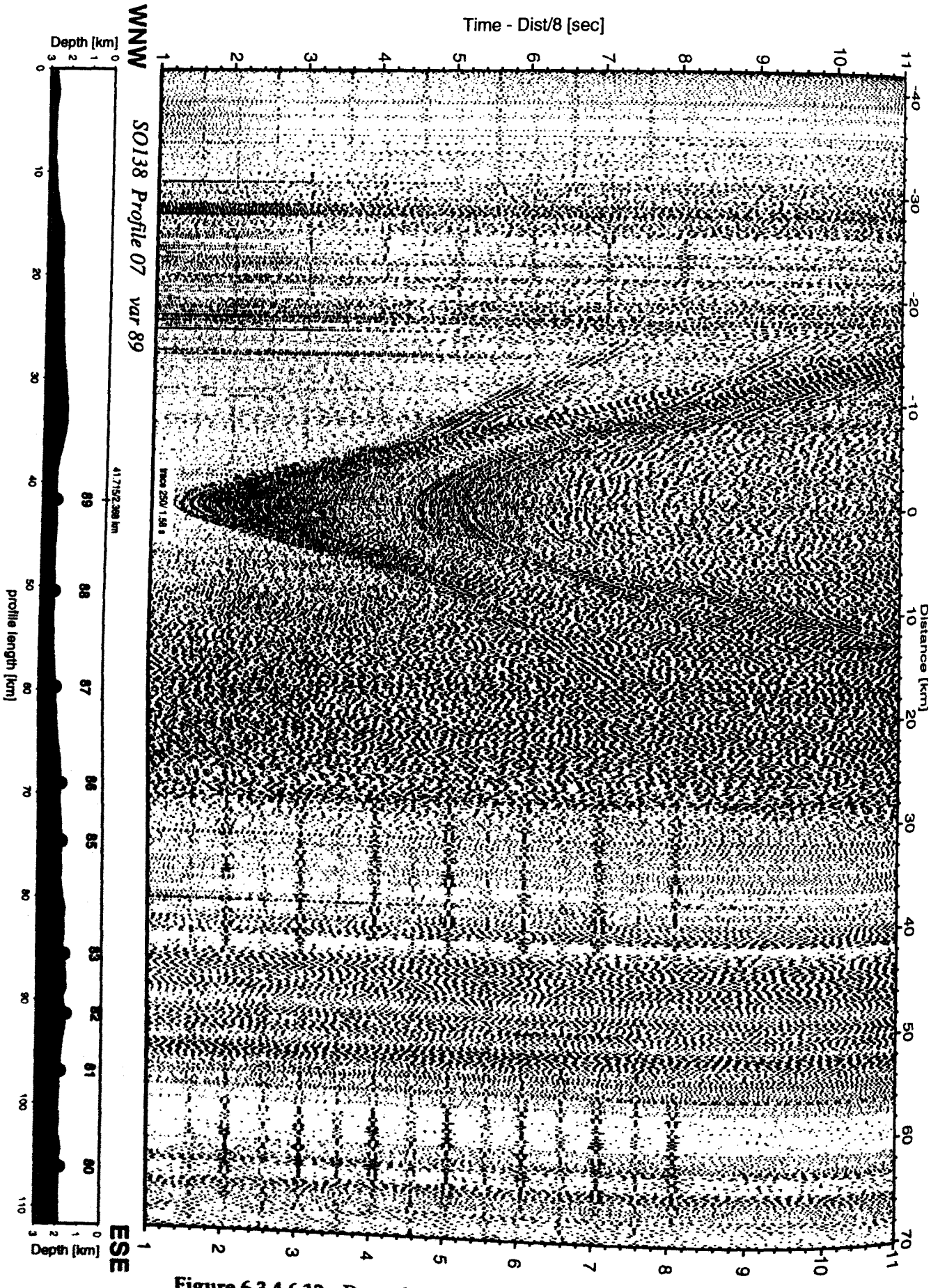

Figure 6.3.4.6.12: Record section from var 89 channel_1, Profile 07.

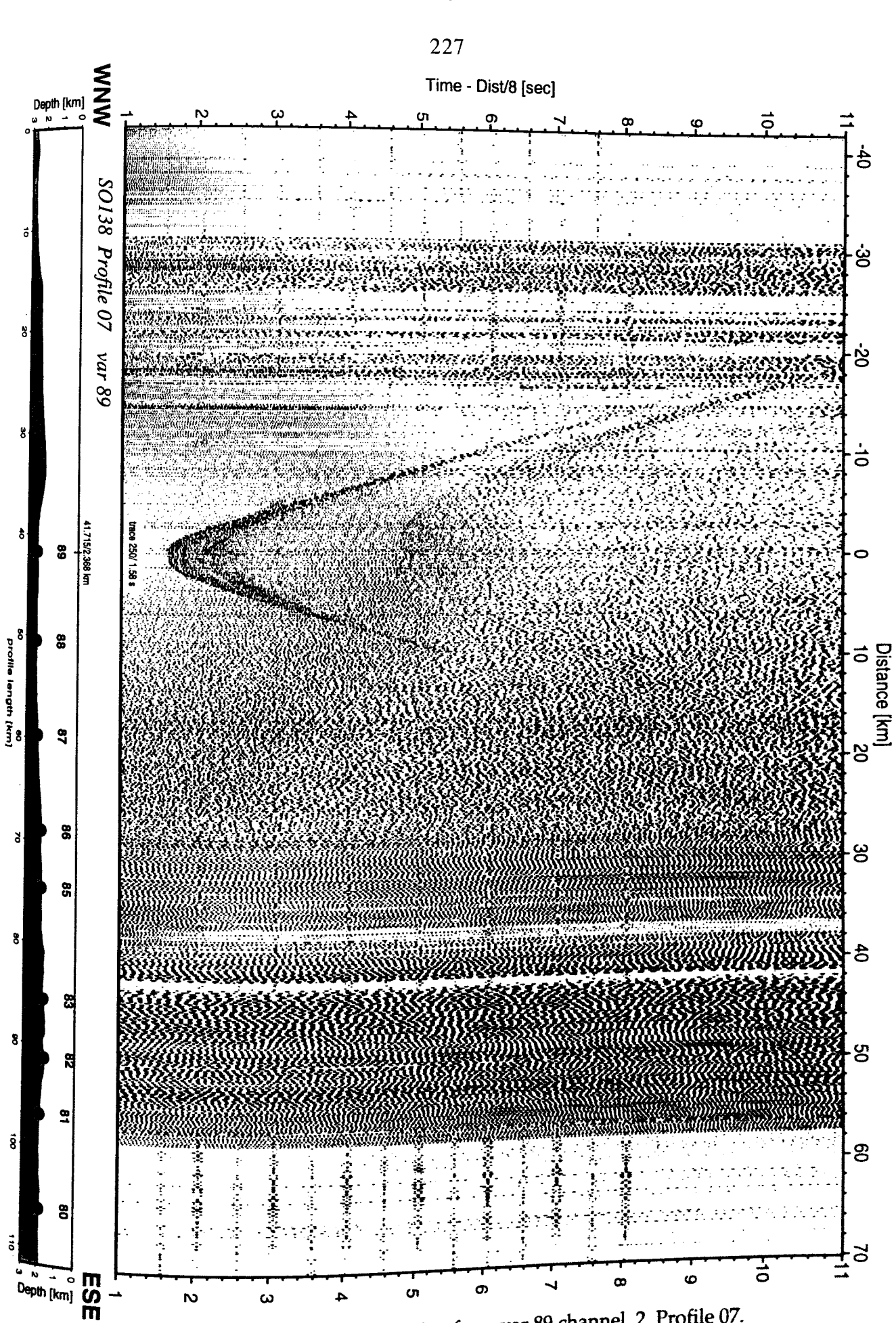

Figure 6.3.4.6.12a: Record section from var 89 channel_2, Profile 07.

6.3.4.7 PROFILE SO138-08

(S. Husen, A. Hampel, E. Flueh)

Profile SO138-008 is a north-south oriented profil aiming to investigate the crustal transition from continental Sumatera to the island arc of Java and a possible continuation of the Sumatera and Mentawai faults offshore in Sunda Strait and off Java.

As shown in Figure 6.3.4.7.1, 16 instruments including two OBS and a 800m-long vertical array were deployed in the morning of 22 January, and shooting along the 100 nm long profile was made from midday of 23 January to 24 January 1999 at 08:20. The magnetometer and the streamer were also deployed, with the magnetometer remaining deployed on the transit from the last shot to the first OBH (OBH90) to be recovered. Details on instrumentation and shots can be found in Appendices 9.1.7 and 9.2. Shooting was mainly performed under adverse weather conditions, apparently causing a high noise level. All instruments except for the 800 m long vertical array were recovered by midnight 24 January 1999. The vertical array was recovered in the afternoon of 25 January 1999, but unfortunately the cable broke after 200 m had been taken on board. A successful attempt to dredge the remaining parts was made the following day.

The data recorded along profile 8 suffer from the poor wheather conditions. The reflection section is shown in Figure 6.3.4.7.2, and all useful wide-angle sections are shown in Figures 6.3.4.7.3 to 6.3.4.7.15. The reflection data clearly indicate that a number of small basins with a thick plio/pleistocene infill of up to 1 sec TWT are transversed. In the northern edge, two volcanic ridges are apparent. The profile crosses several MCS profiles of cruise SO137 (Reichert and shipboard scientific party, in prep.) that will be useful for further evaluation of the data. During the limited time available on board, a preliminary interpretation of OBH 96, located between two basins, was made.

Modelling and interpretation of profile SO138-08

The phases identified in the record section are the water-wave, two refracted and one reflected phases from sediments and a refracted and wide-angle reflected phase from the top of the basement.

To obtain an idea of the velocity changes with depth, the record section was forward modelled using the modelling program R1D (Luetgert, 1992). The resulting model and the fit of the modelled arrivals to the observed phases are shown in figure 6.3.4.7.16. Two upper sediment layers have velocities of 1.8 km/s and 2.9 km/s. Together, they are about 4 km thick.

The top of the third layer is marked by a velocity change from 3.3 km/s to 3.9 km/s and is located in a depth of about 6 km. Its thicknes is about 8 km with an increase in velocity to 6.2 km/s, similar to values found on many other profiles.

In a depth of about 14 km, velocity changes from 6.2 km/s to 7.2 km/s, indicating an intracrustal discontinuity similar to that observed on profile SO138-05. This is constrained by a refracted phase and a wide angle reflected phase in the record section.

The seismic section from MCS stack (Fig. 6.3.4.1.2) shows sediment layers of strongly varying thickness to both sides of OBH station 96. To about 30 km to the south, the thickness increases from several undred meters to about 3 km. this could correspond to the upper two sediment layers of the model based on the OBH96 record section. Other layers can not be recognized on the seismic section. About 10 km north of OBH 96, a sediment basin is located. The thickness of the sediment layers increases to about 3 km in the center of the basin.

Necessarily, the analyses performed on board if FS SONNE remain uncompleted. More detailed modeling and in-depth studies still have to be done.

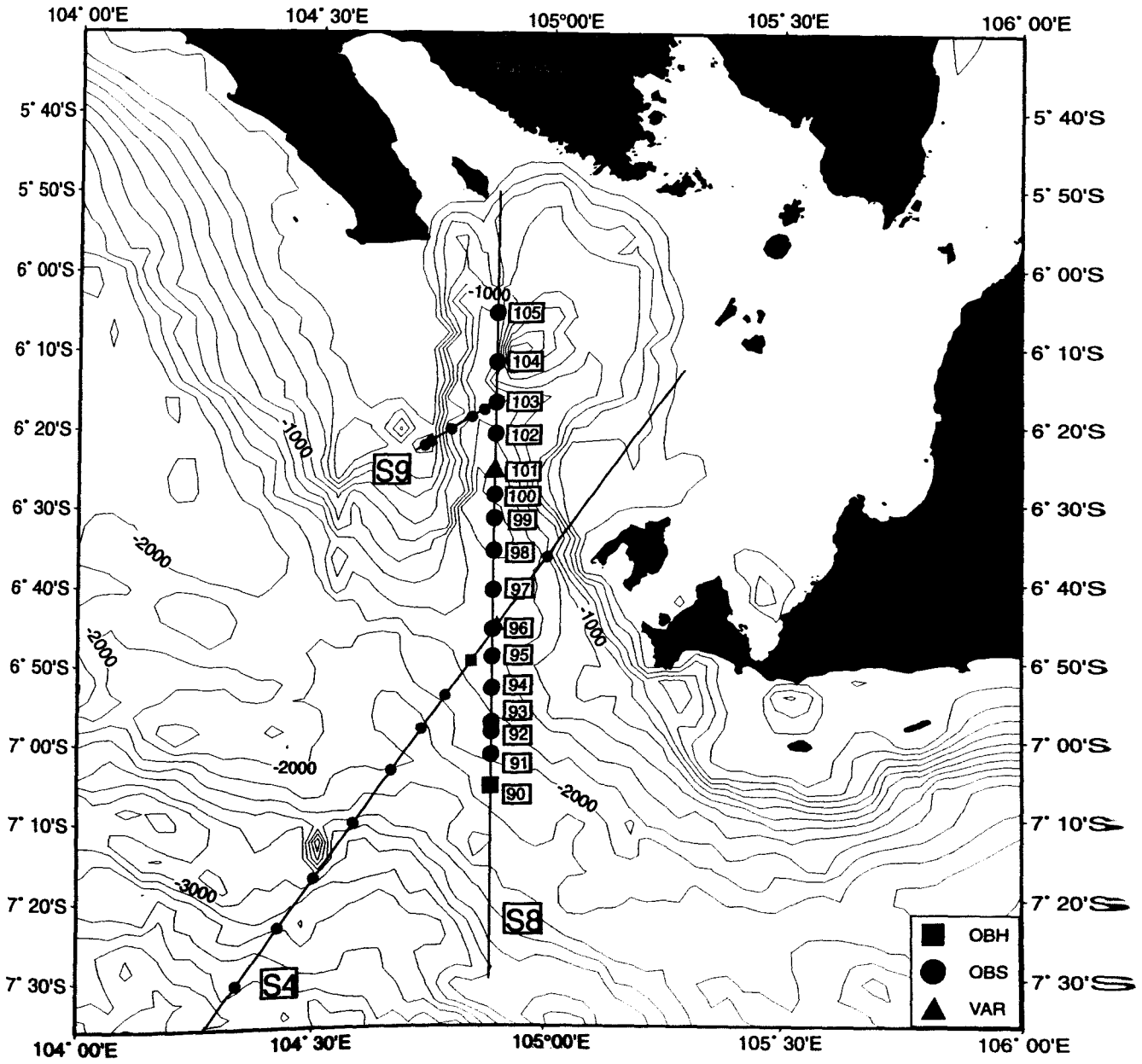

Figure 6.3.4.7.1: Location map of seismic profile S8.

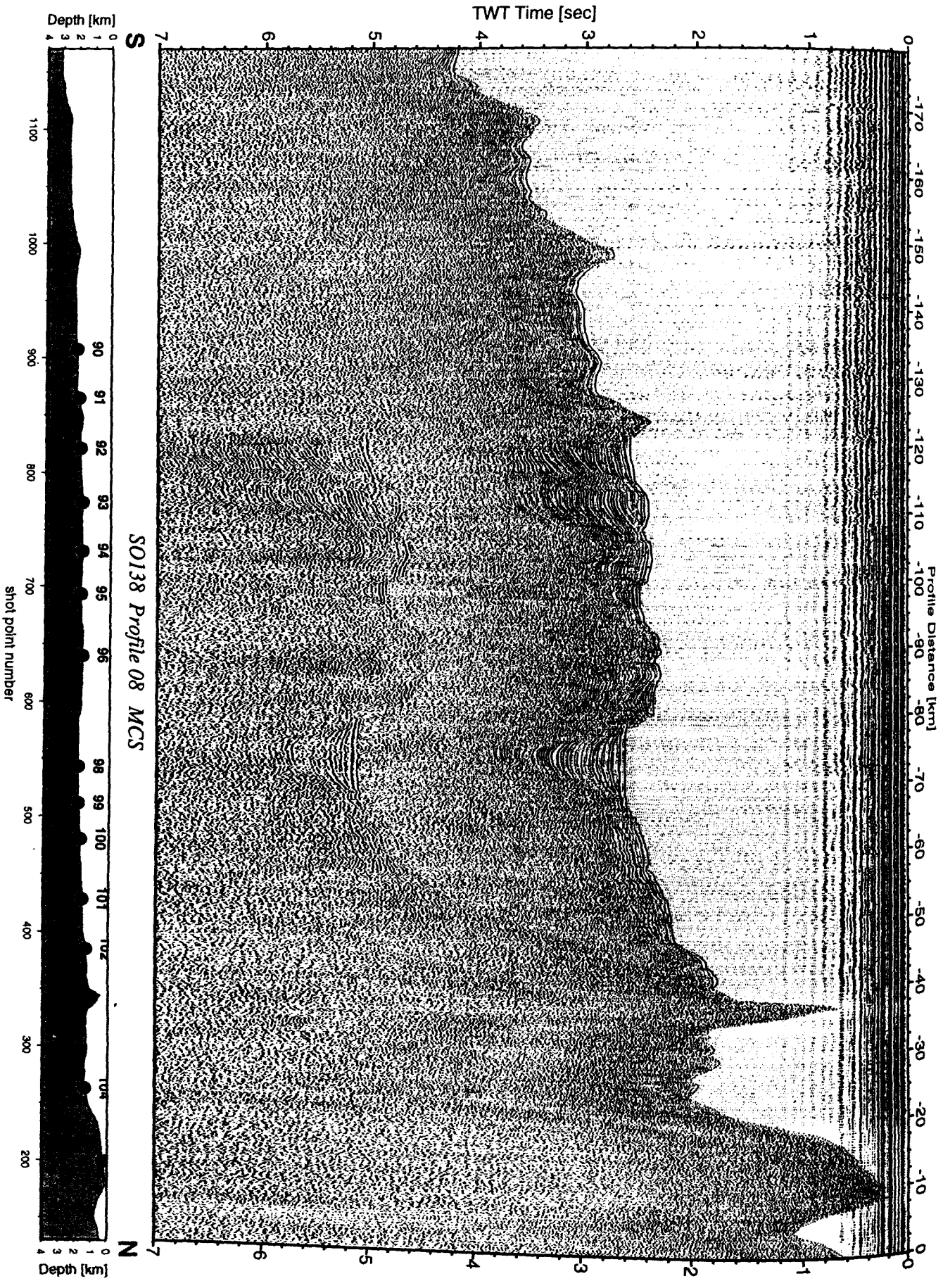

Figure 6.3.4.7.2: Seismic section from MCS stack, Profile 08.

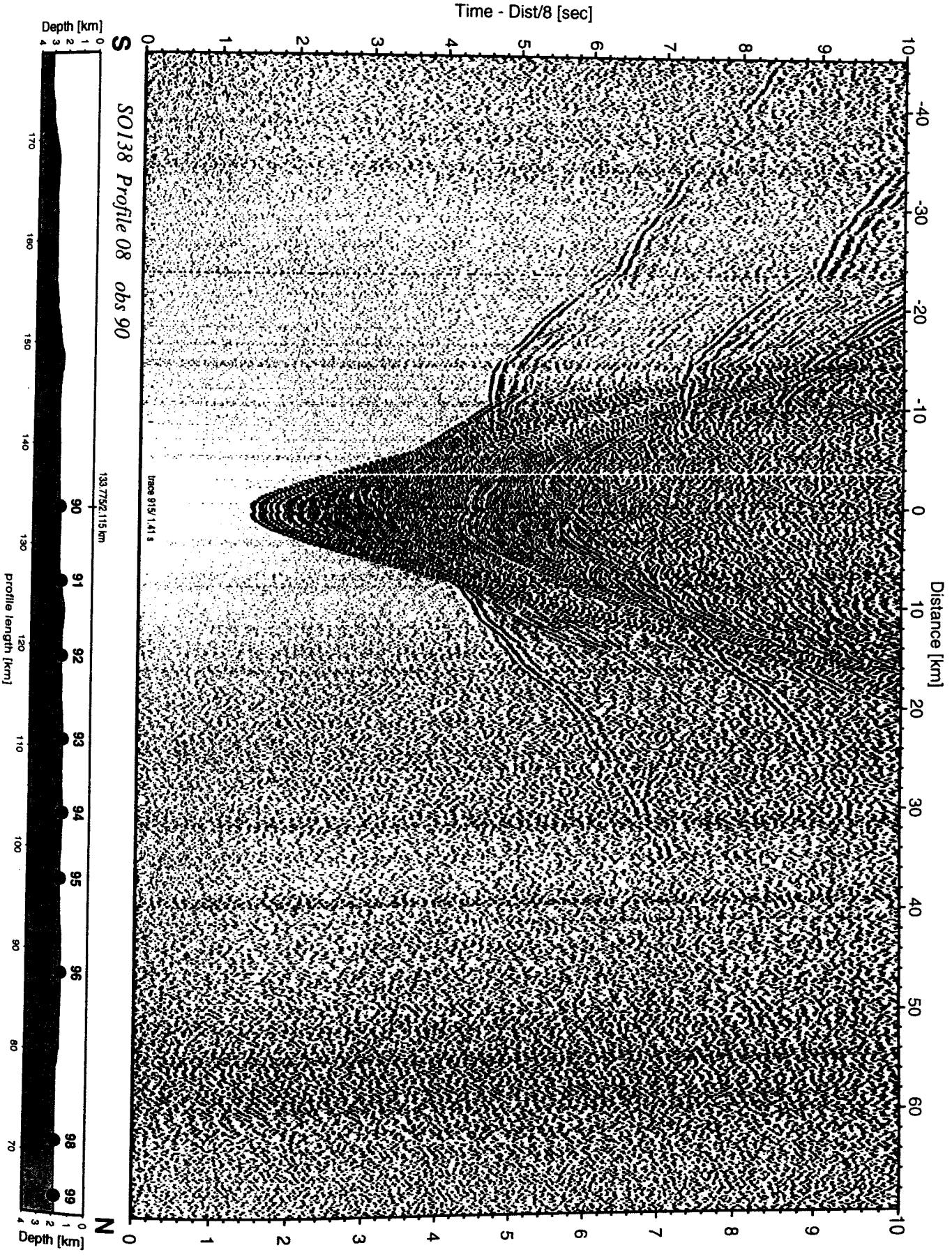

Figure 6.3.4.7.3: Record section from obs 90 hydrophone, Profile 08.

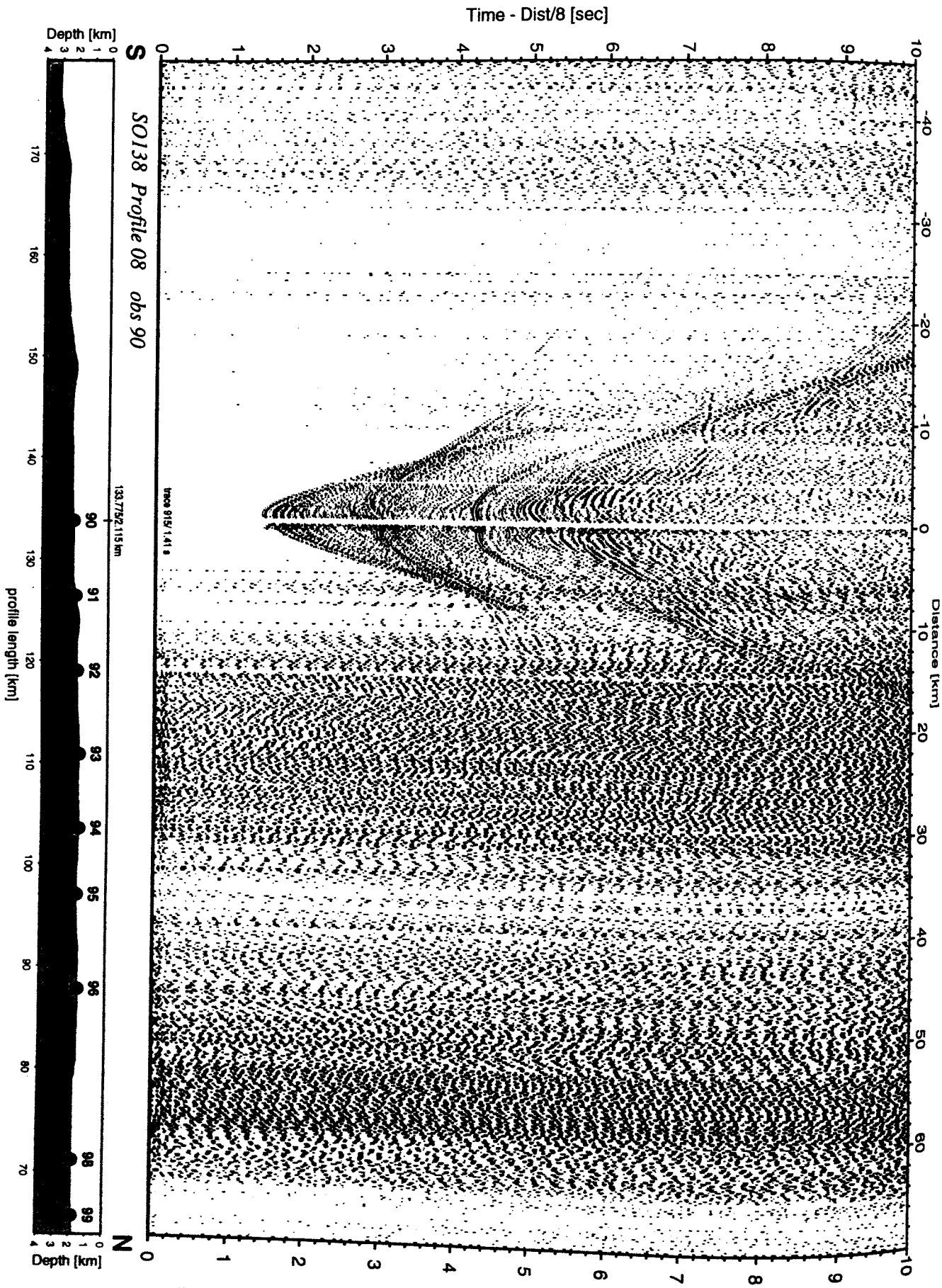

Figure 6.3.4.7.3a: Record section from obs 90 vertical component, Profile 08.

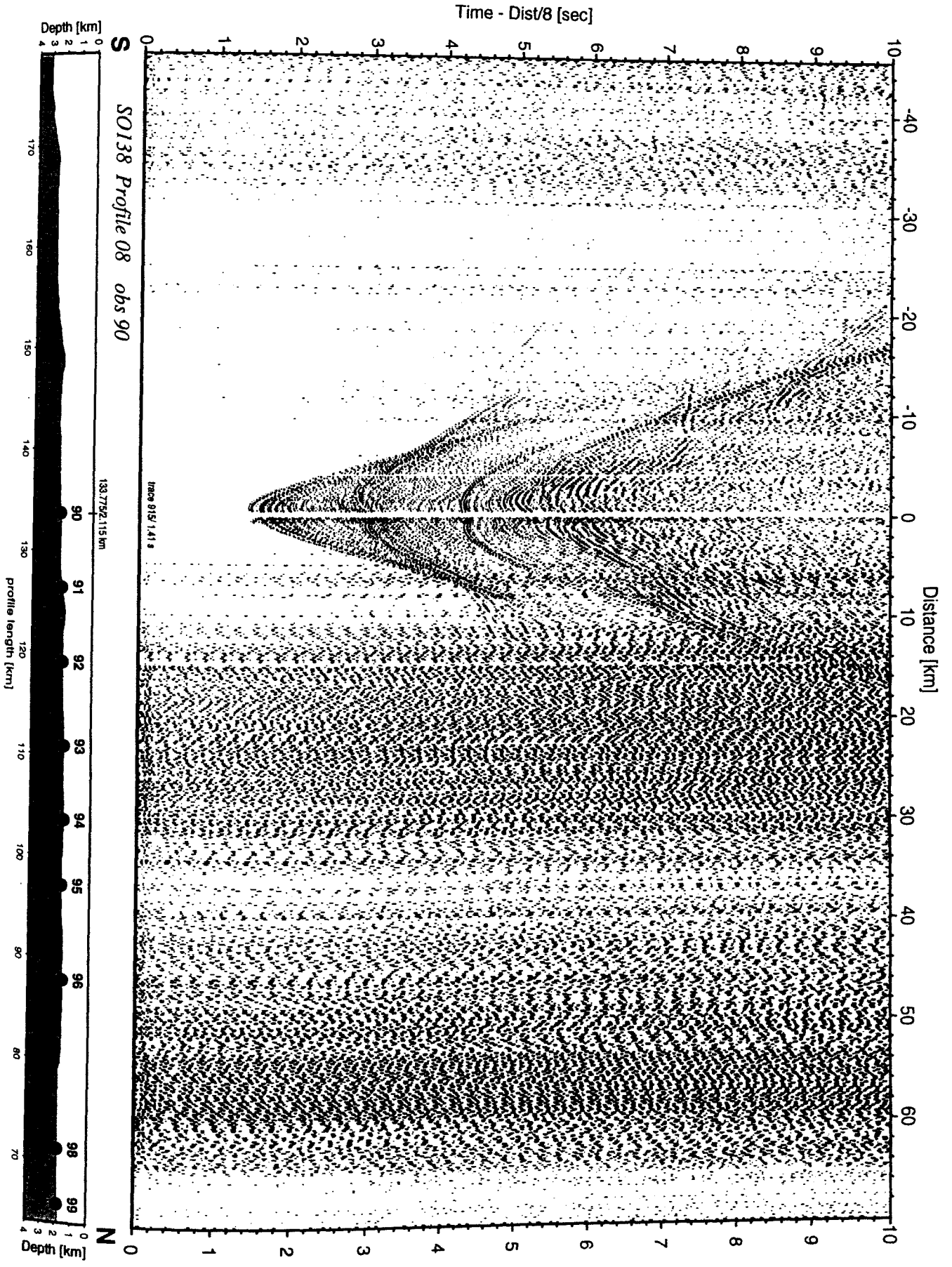

Figure 6.3.4.7.3b: Record section from obs 90 horizontal component 1, Profile 08.

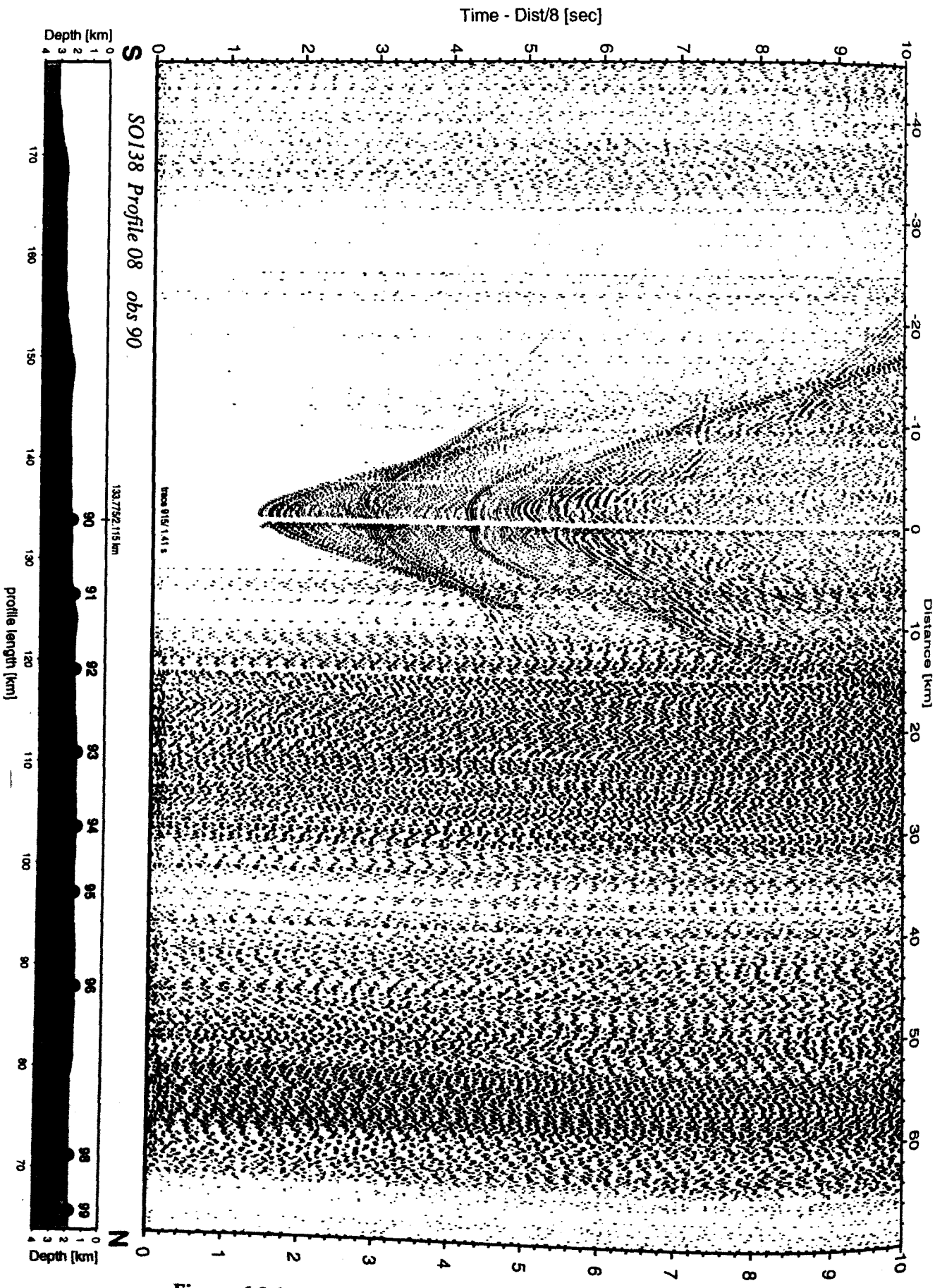

Figure 6.3.4.7.3c: Record section from obs 90 horizontal component 2, Profile 08.

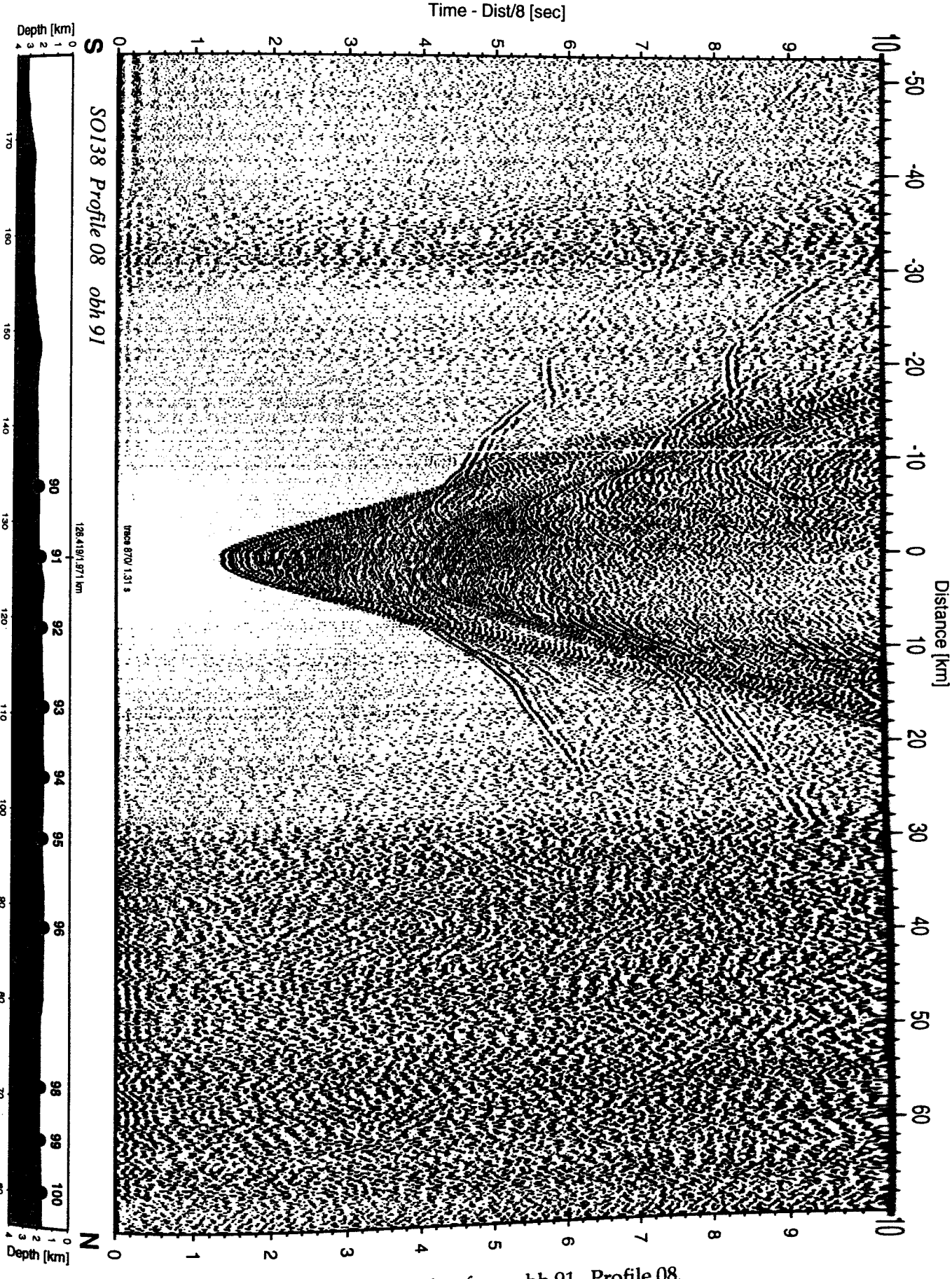

Figure 6.3.4.7.4: Record section from obh 91 , Profile 08.

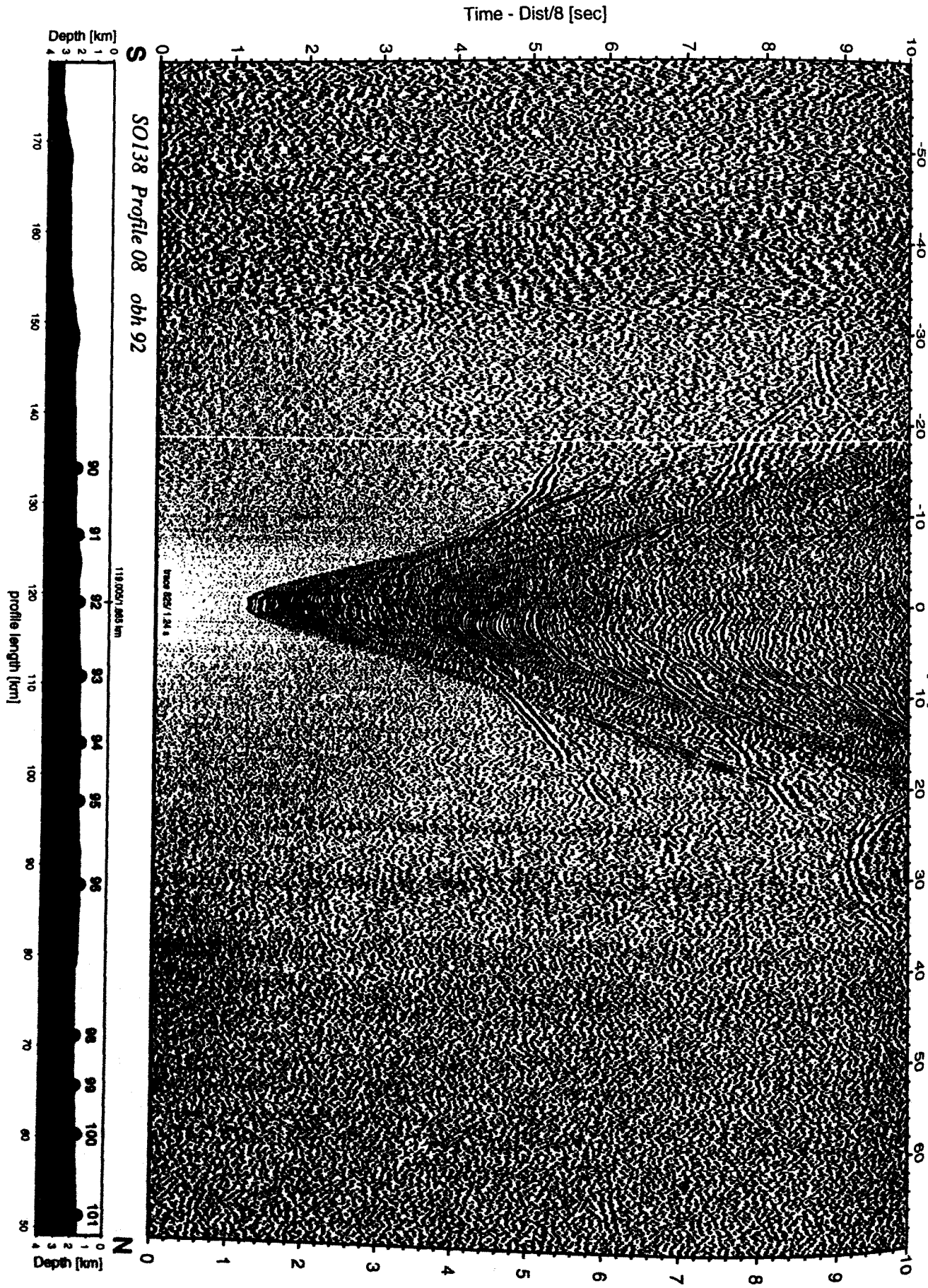

Figure 6.3.4.7.5: Record section from obh 92 , Profile 08.

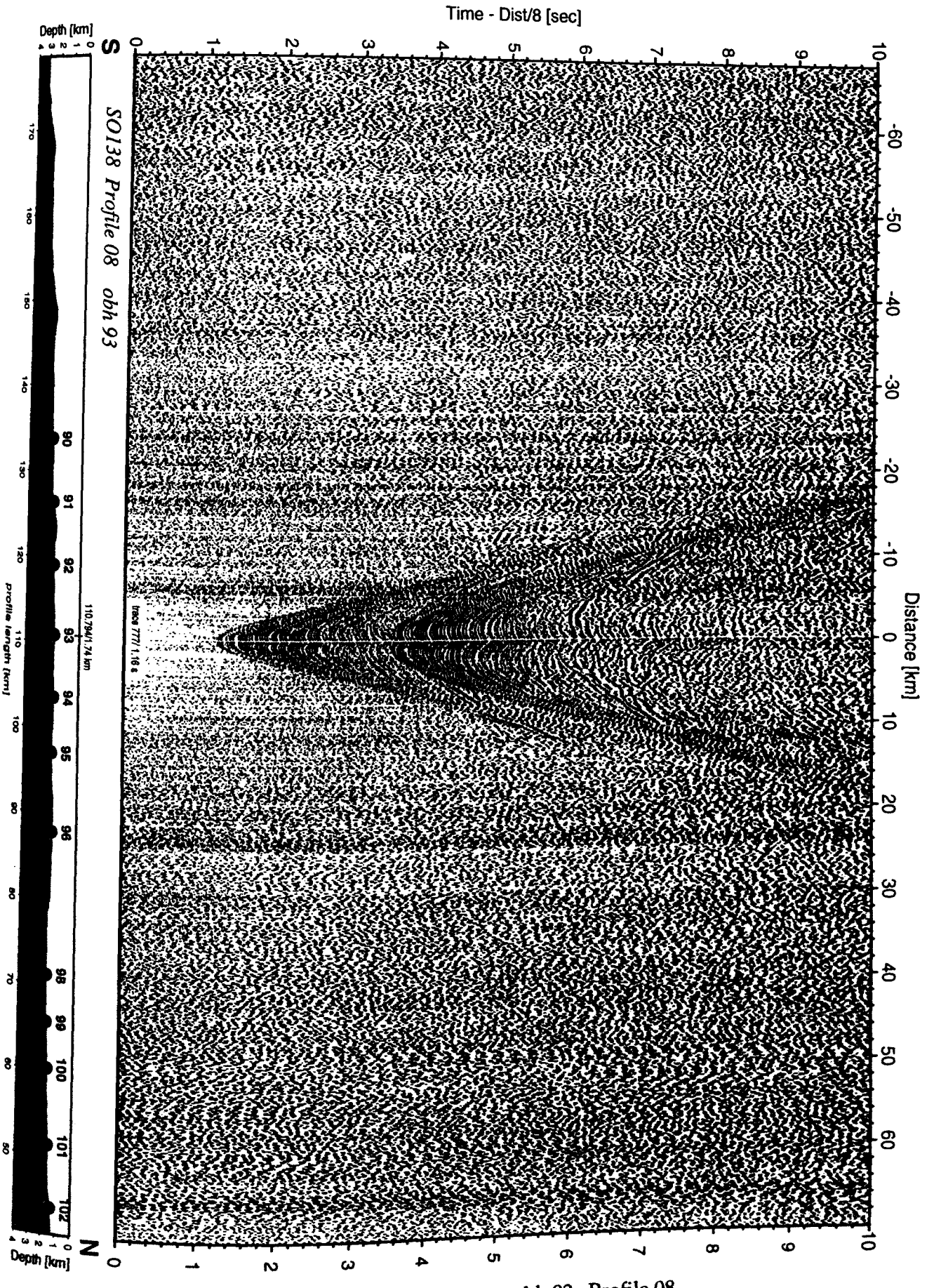

Figure 6.3.4.7.6: Record section from obh 93 , Profile 08.

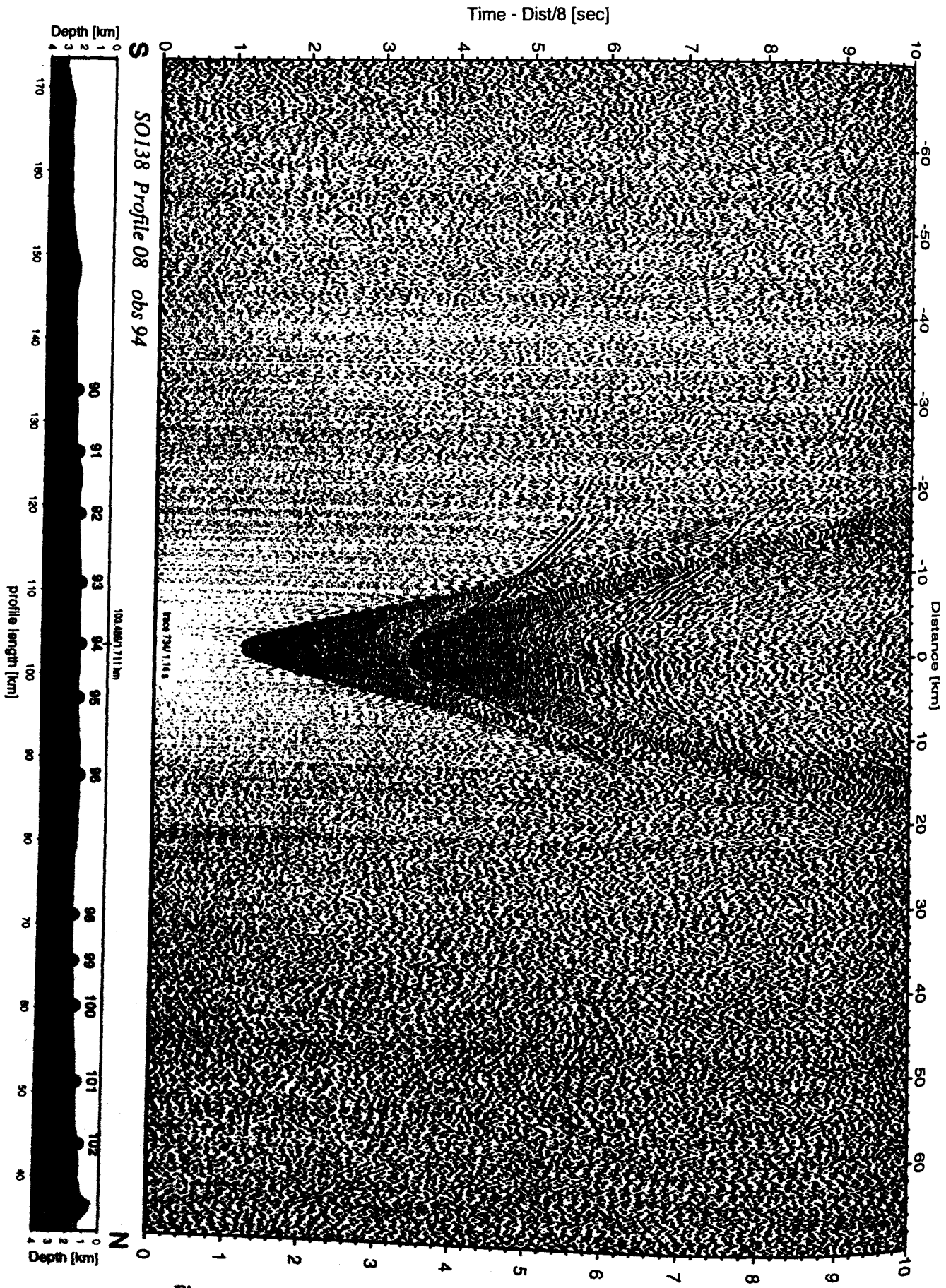

Figure 6.3.4.7.7: Record section from obs 94 hydrophone, Profile 08.

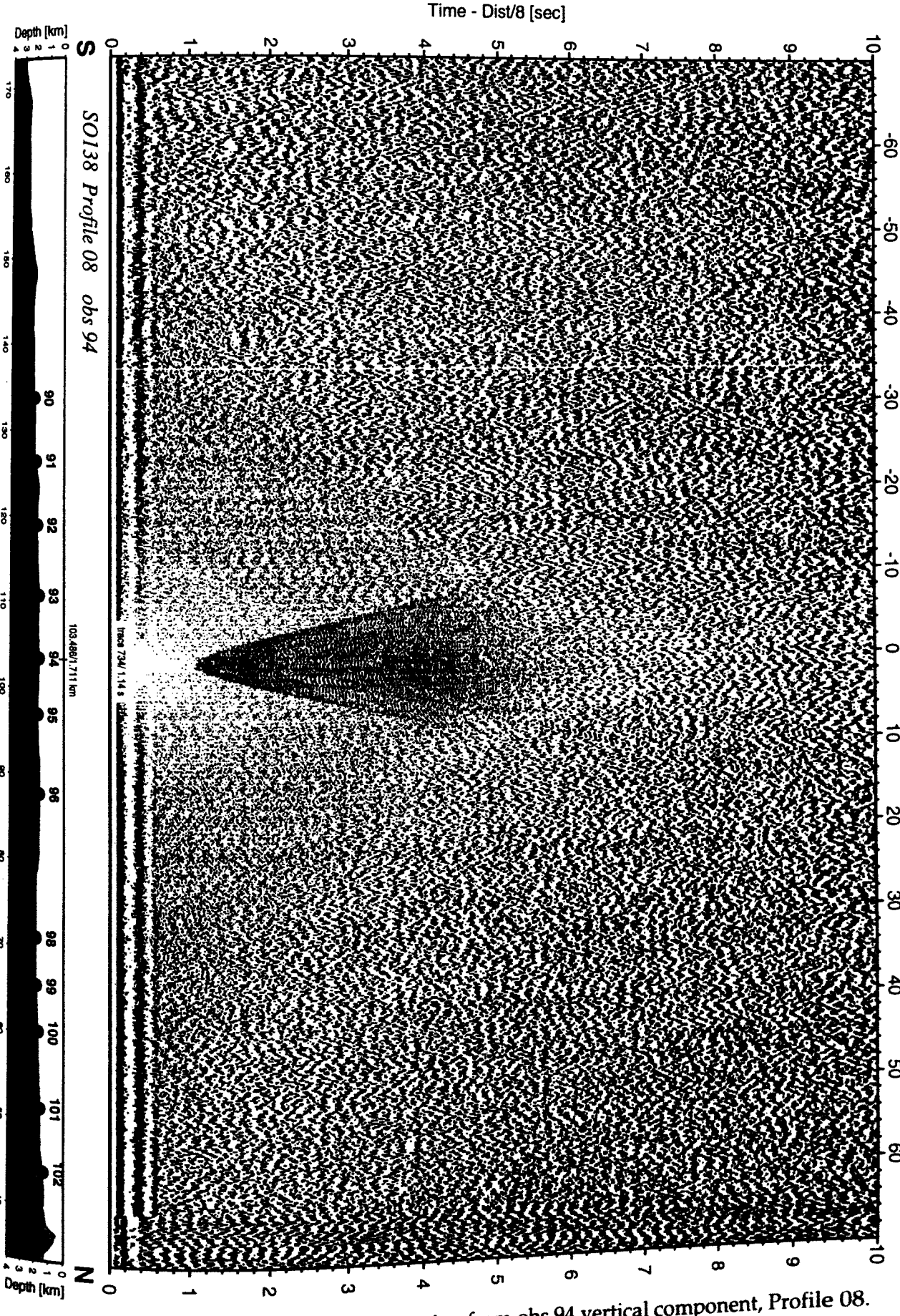

Figure 6.3.4.7.7a: Record section from obs 94 vertical component, Profile 08.

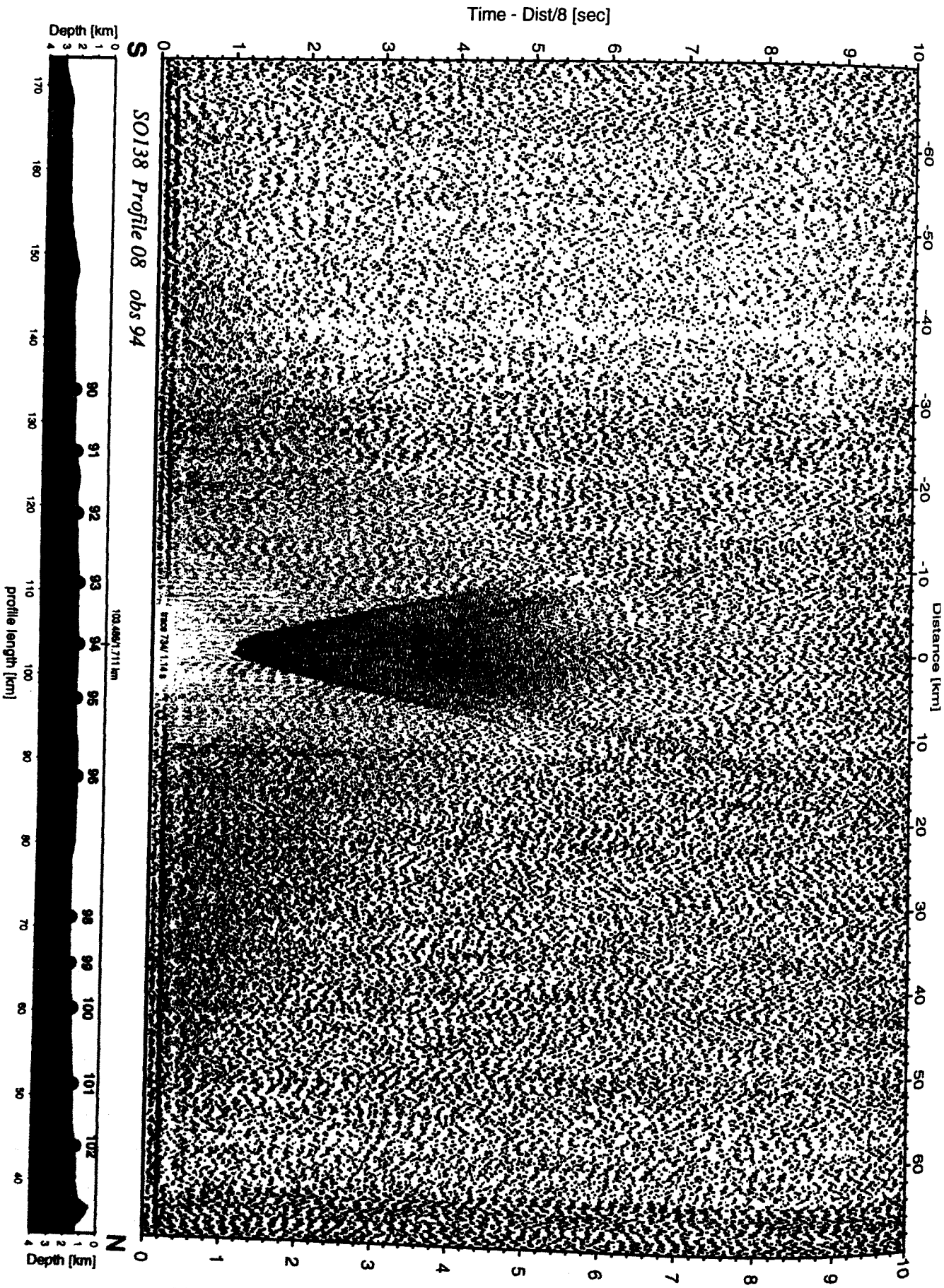

Figure 6.3.4.7.7b: Record section from obs 94 horizontal component 1, Profile 08.

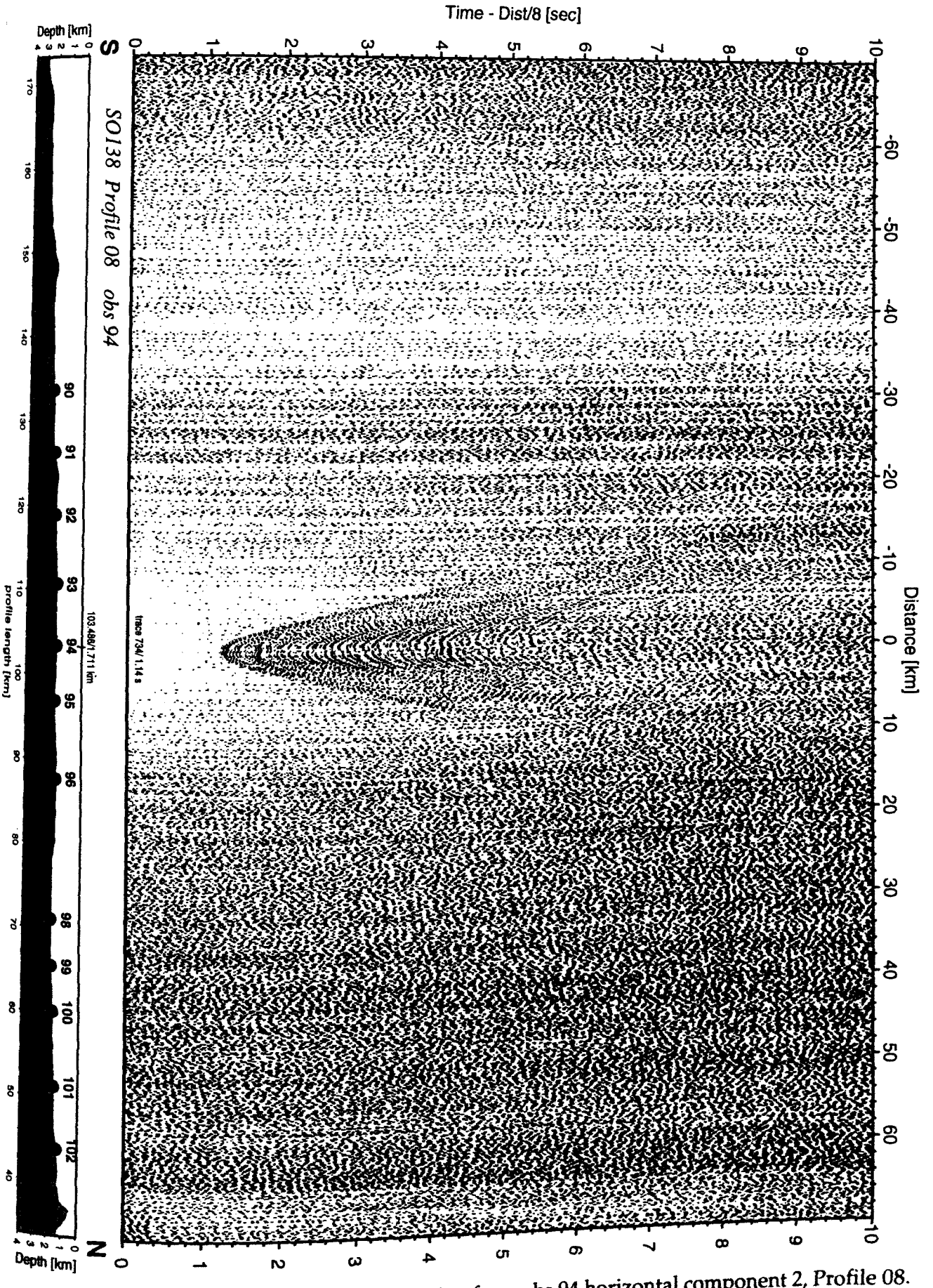

Figure 6.3.4.7.7c: Record section from obs 94 horizontal component 2, Profile 08.

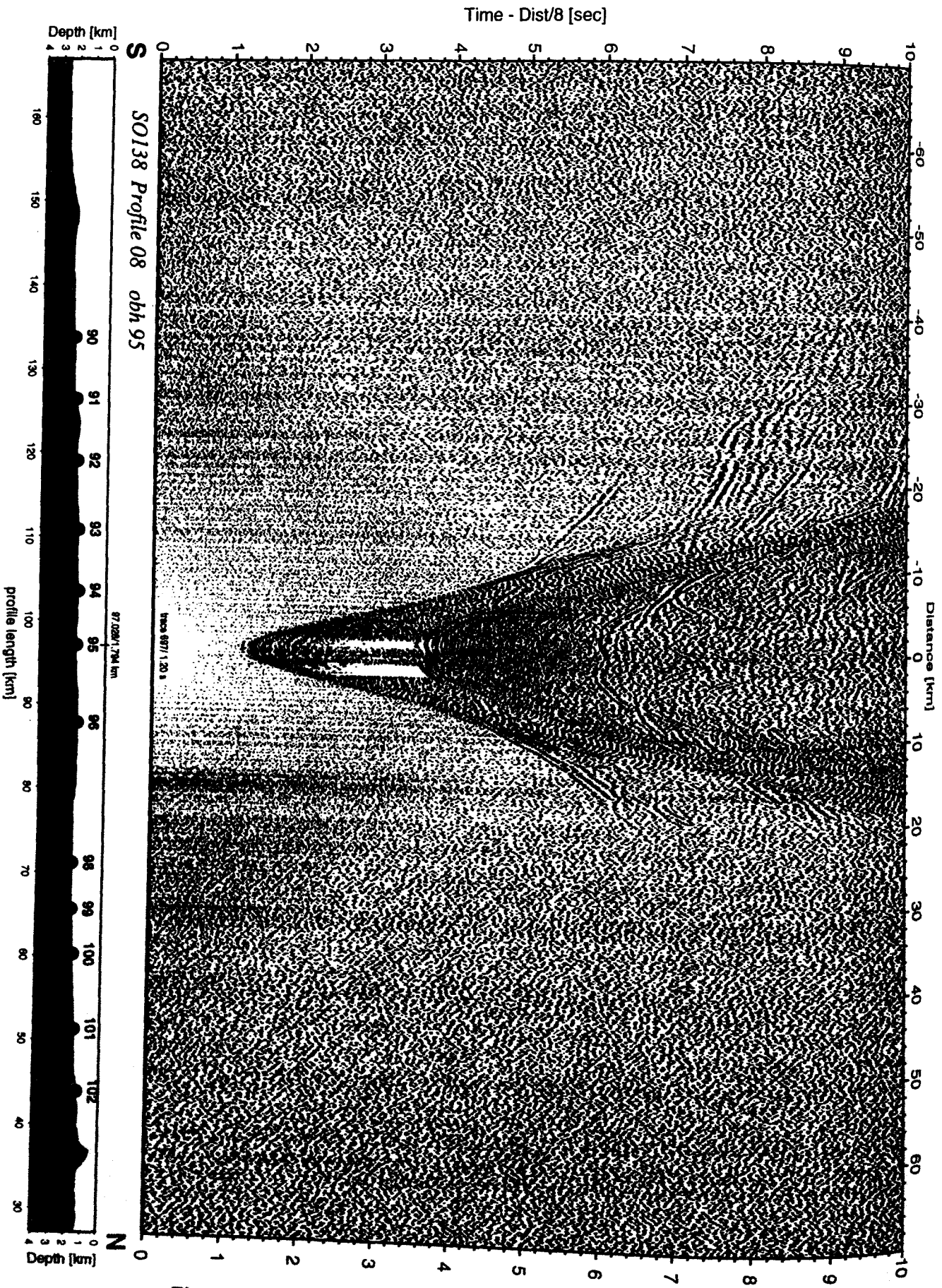

Figure 6.3.4.7.8: Record section from obh 95 , Profile 08.

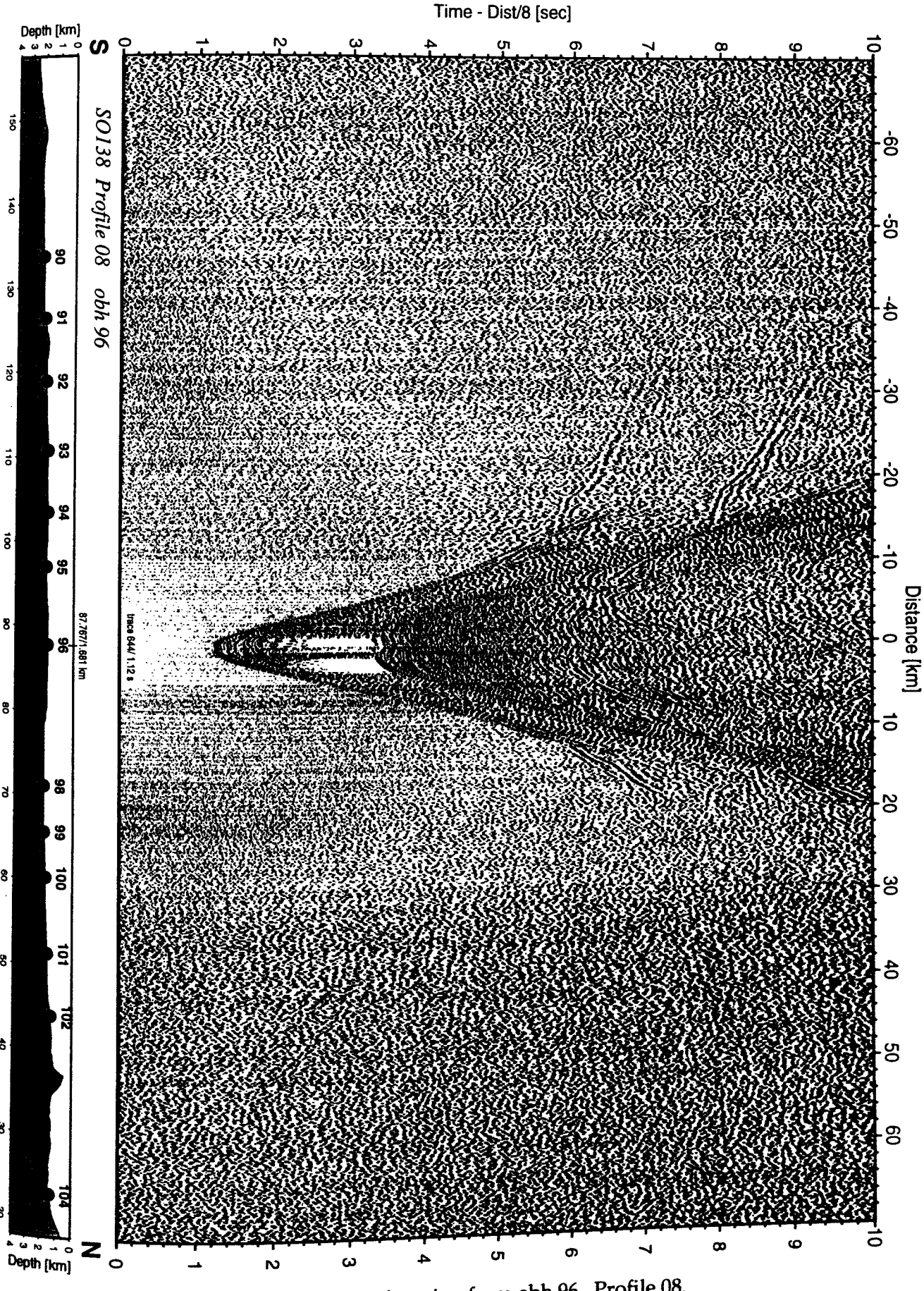

Figure 6.3.4.7.9: Record section from obh 96 , Profile 08.

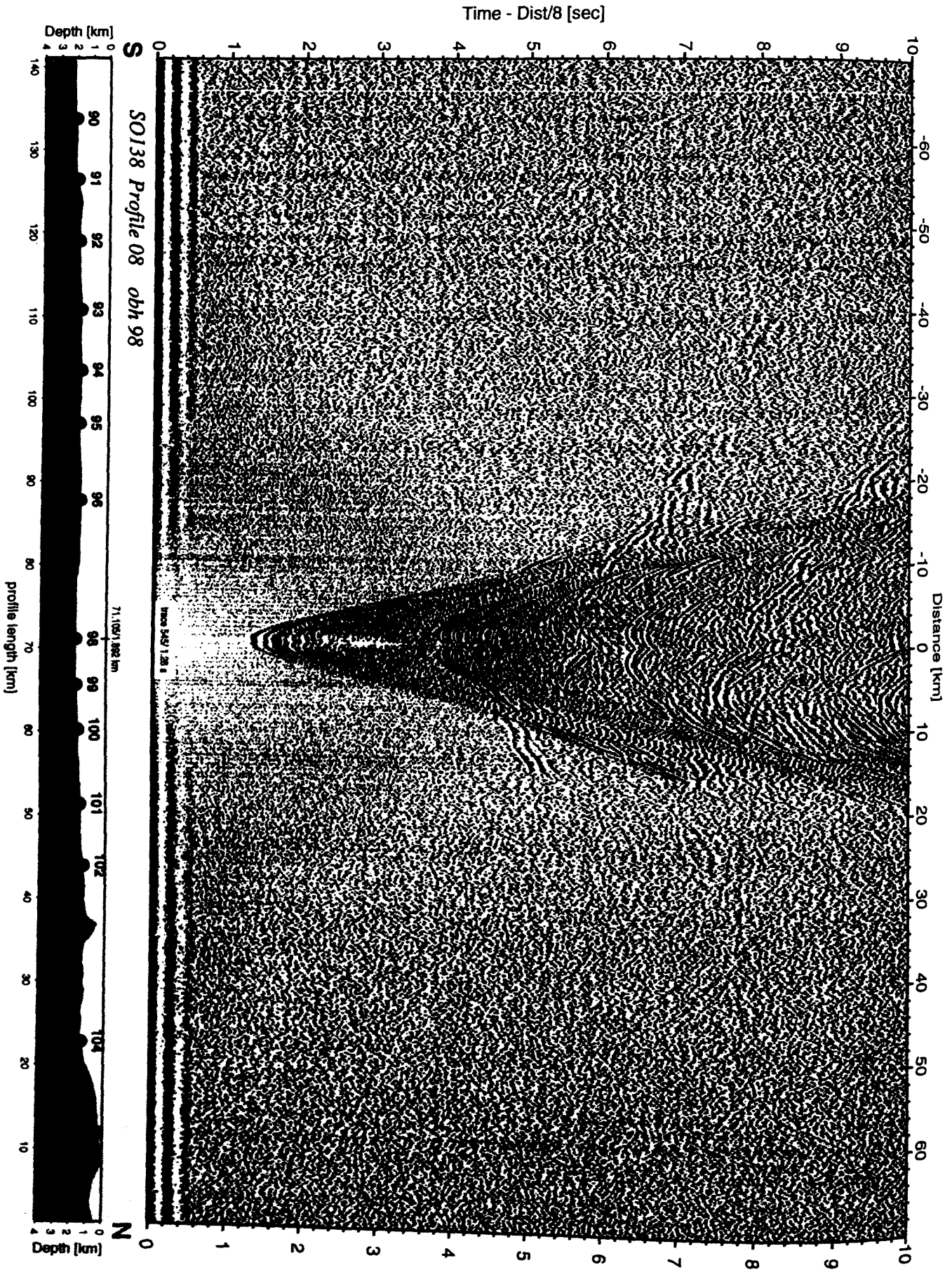

Figure 6.3.4.7.10: Record section from obh 98 , Profile 08.

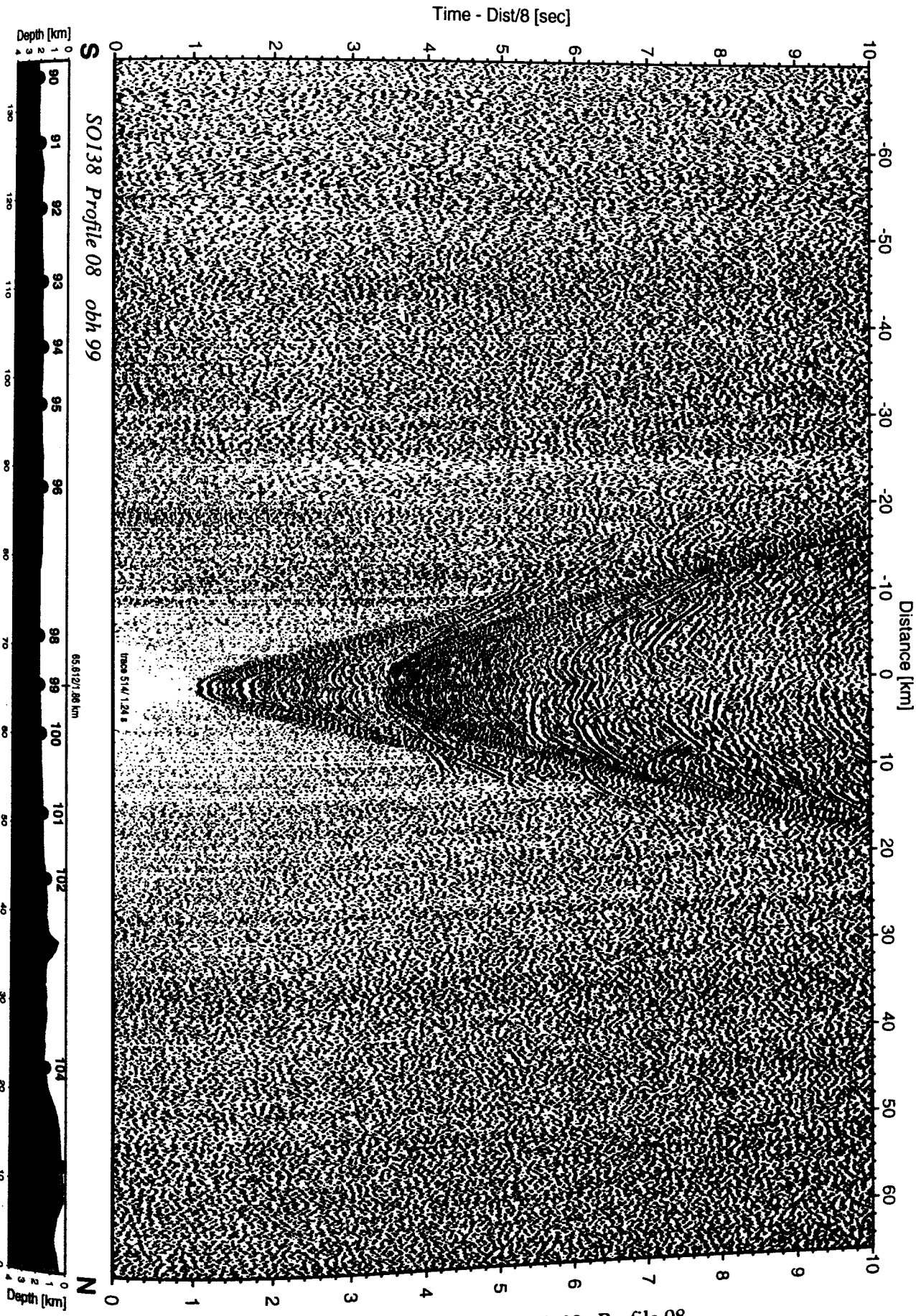

Figure 6.3.4.7.11: Record section from obh 99 , Profile 08.

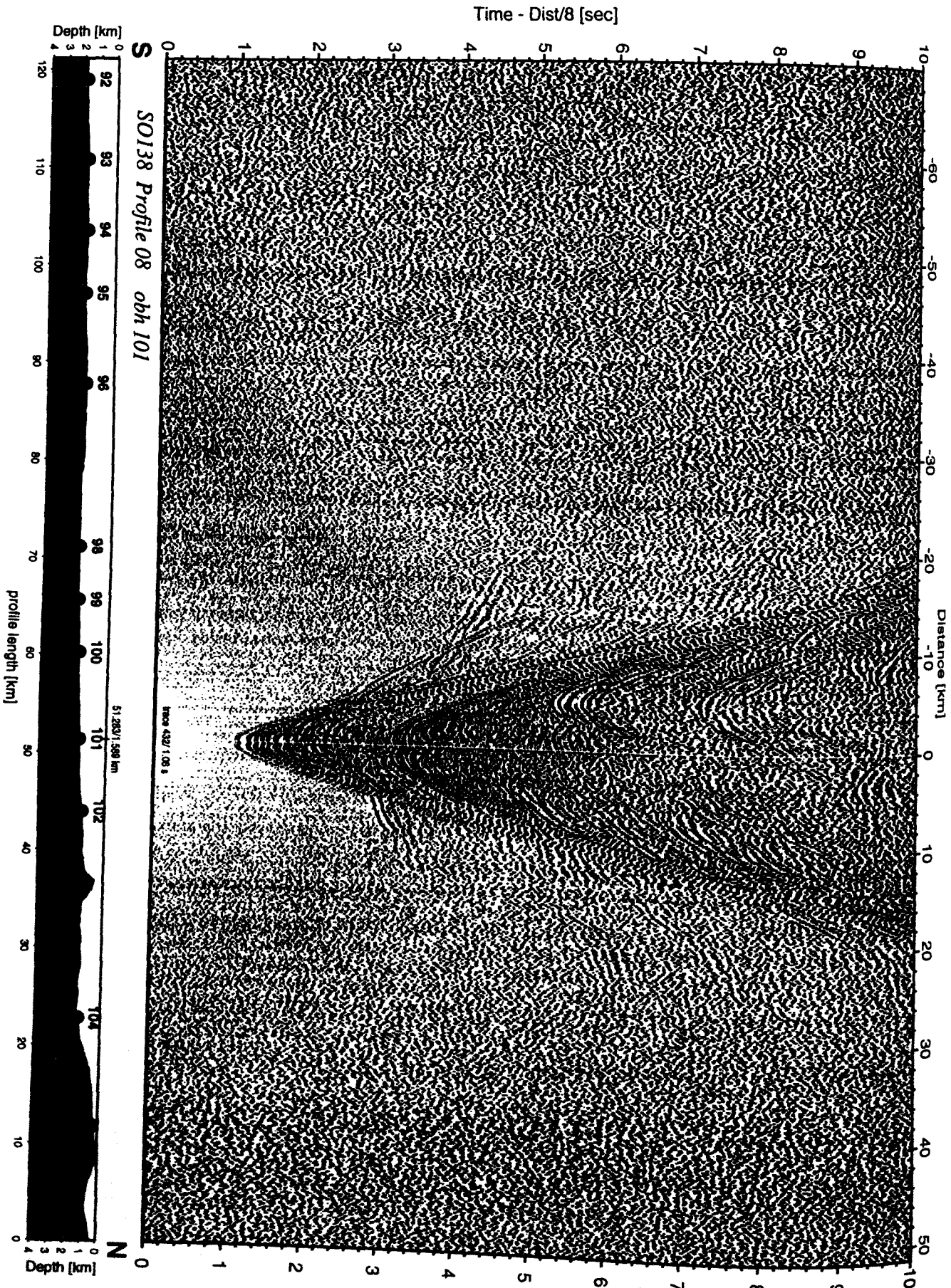

Figure 6.3.4.7.12: Record section from obh 101 , Profile 08.

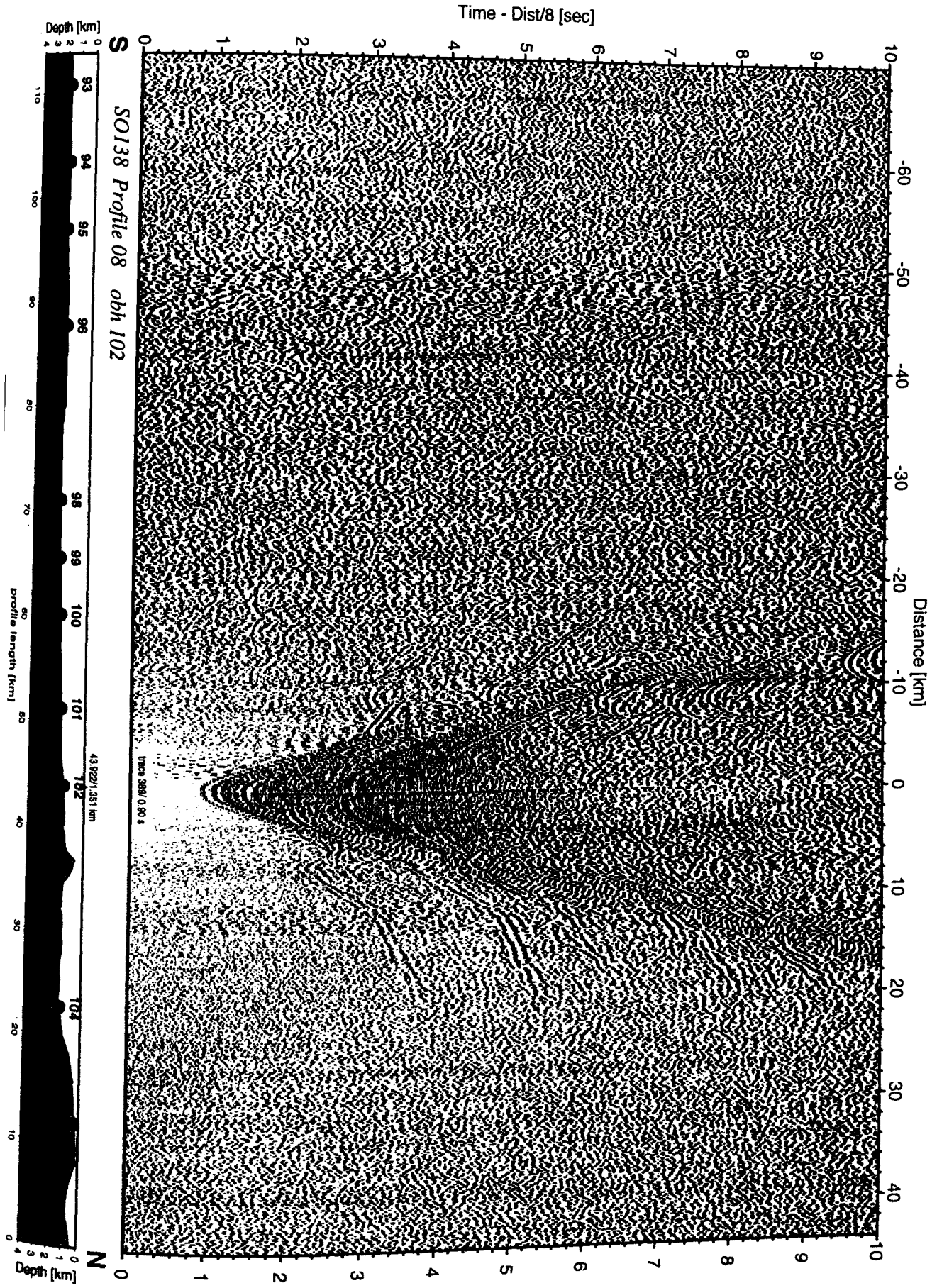

Figure 6.3.4.7.13: Record section from obh 102 , Profile 08.

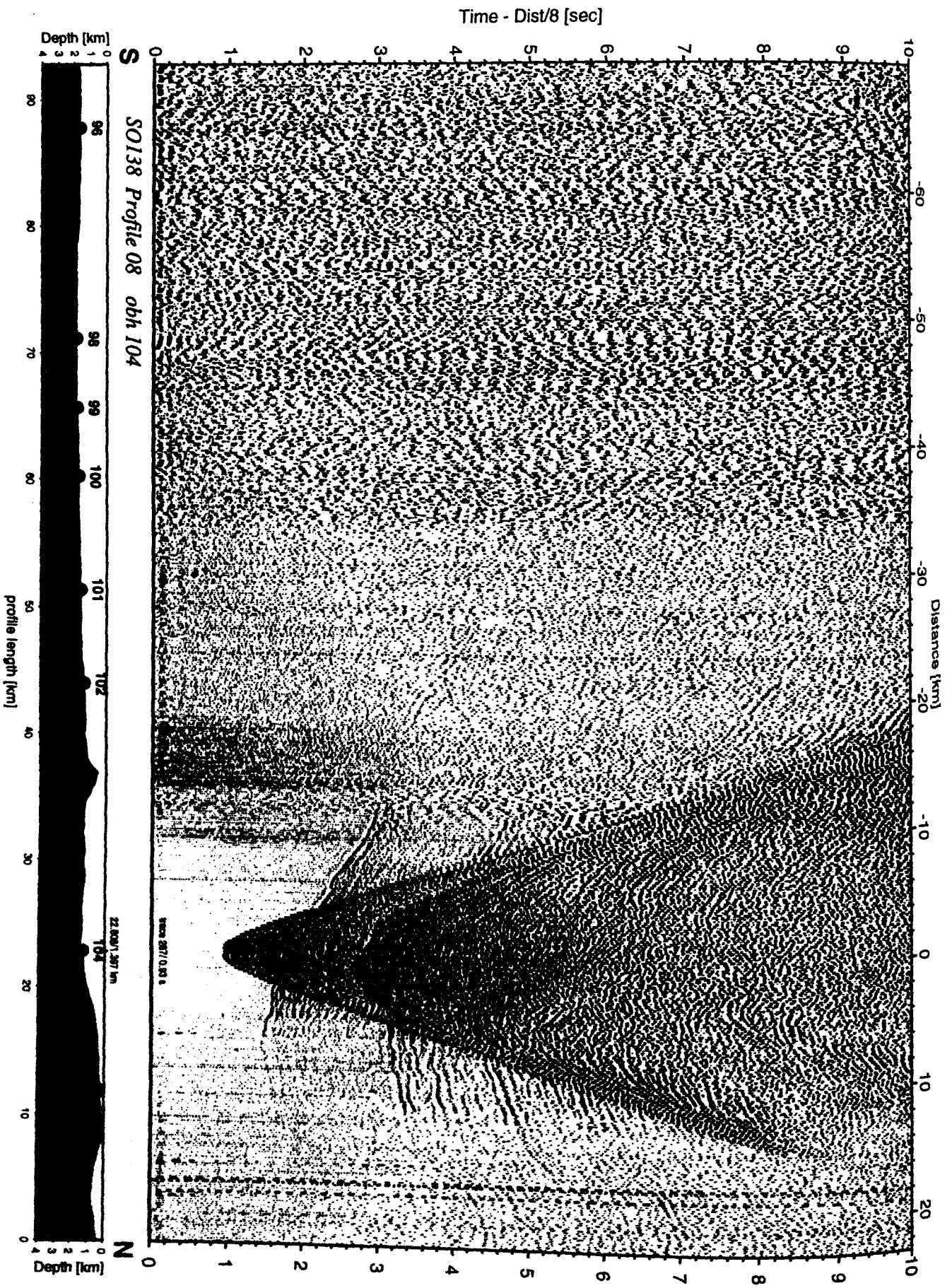

Figure 6.3.4.7.14: Record section from obh 104 , Profile 08.

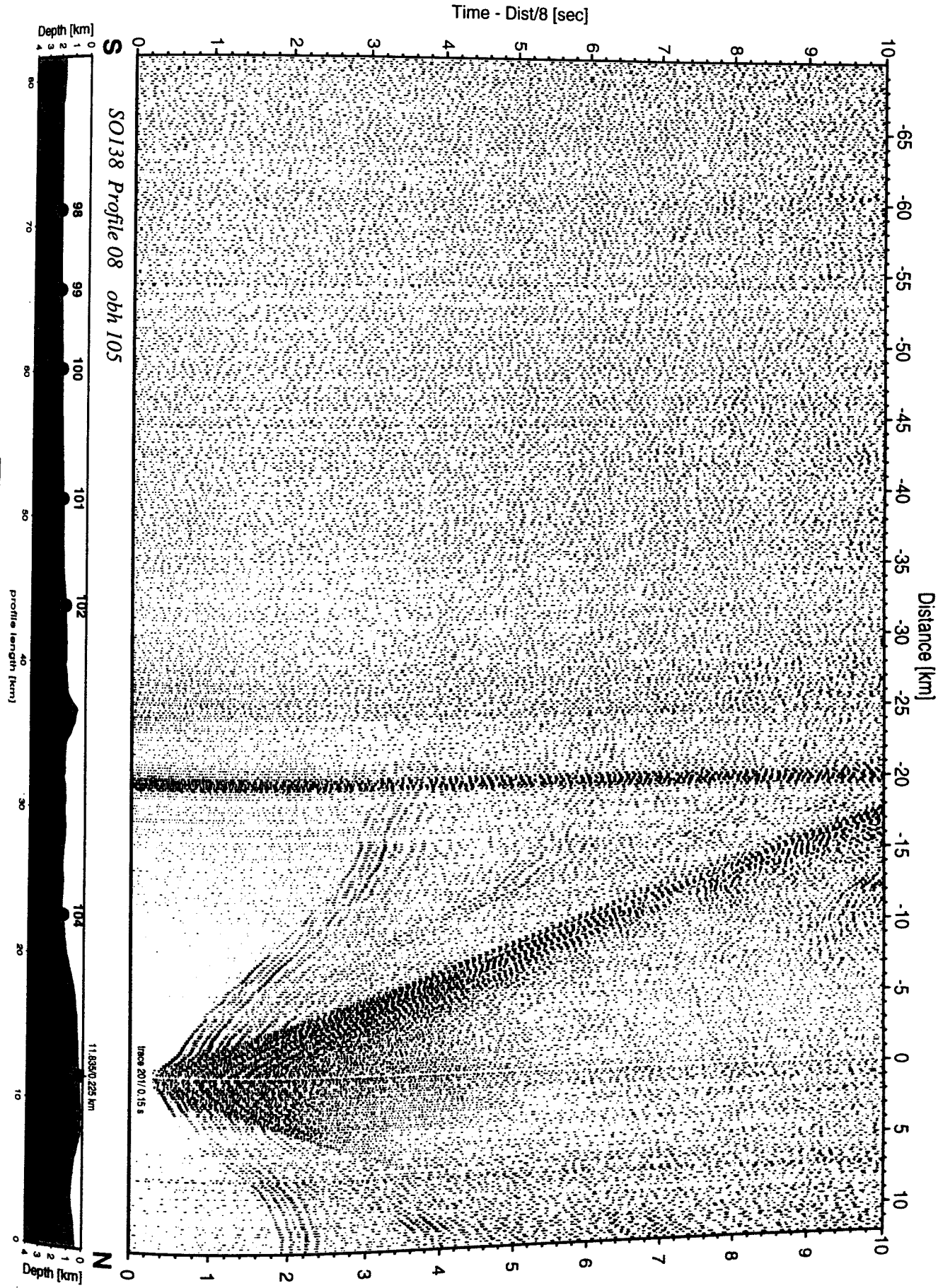

Figure 6.3.4.7.15: Record section from obh 105 , Profile 08.

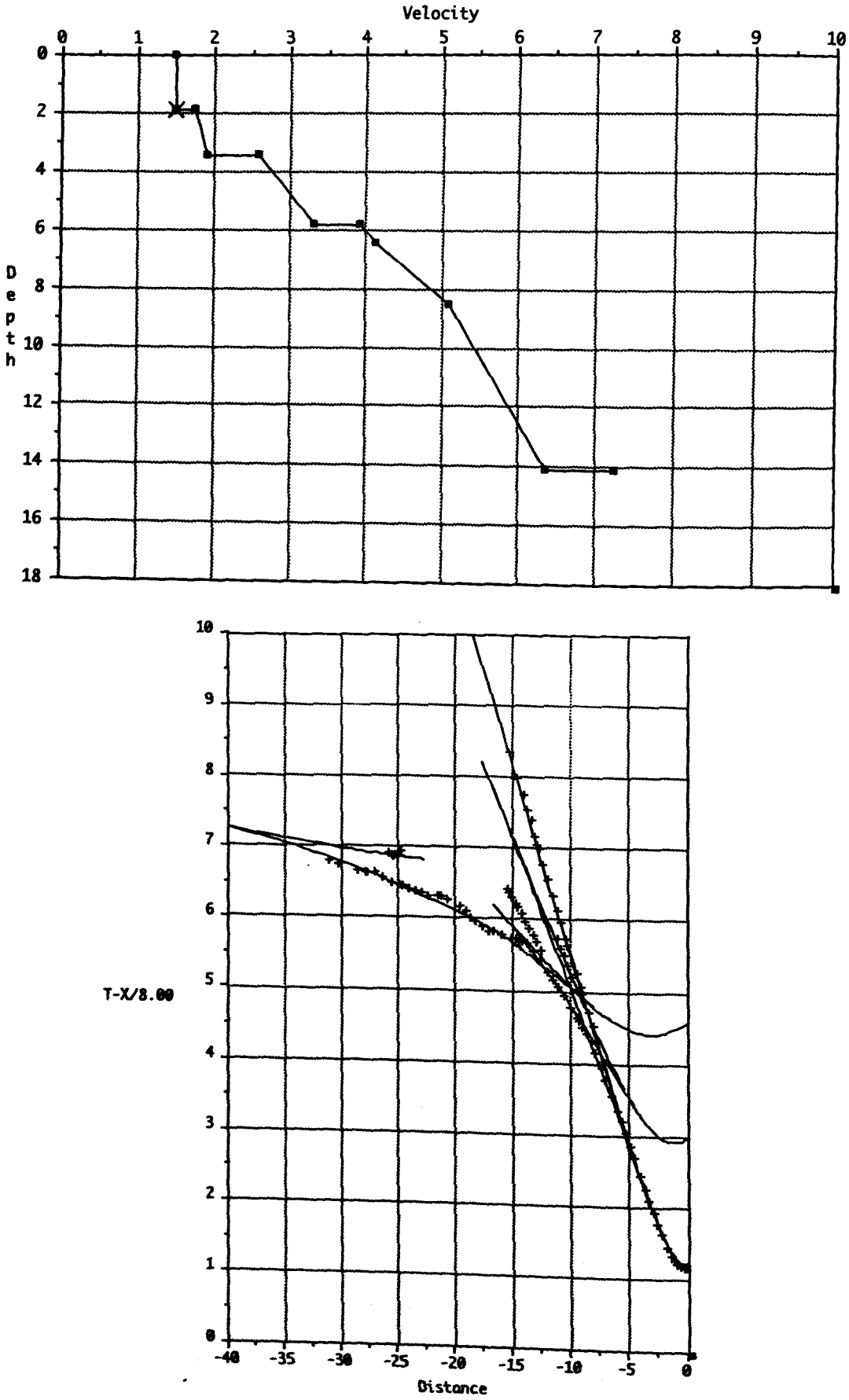

Figure 6.3.4.7.16: The velocity-depth-profile beneath OBH 96, profile SO 138-09, derived from 1D-modelling and the fit of the modelled arrivals to the observed phases in record section

6.3.4.8 PROFILE SO138-09, TEST OF THE GEOMAR AIRGUN ARRAY

(J. Bialas, E. Flueh, K.Steffen)

After shooting the final regular seismic profile SO138-08 an additional test line was occupied with OBH106 to OBS111 (Fig. 6.3.4.8.1, see also Appendix 9.1.8). Along this line a test of the small size GEOMAR airgun array was made. Using the port side gun frame, 7 airguns were aligned into one array. Fig. 6.3.4.8.2 shows the gun volumes and their corresponding bubble diameters (after Hirschleber pers. Com., Nooteboom, 1978, and others).

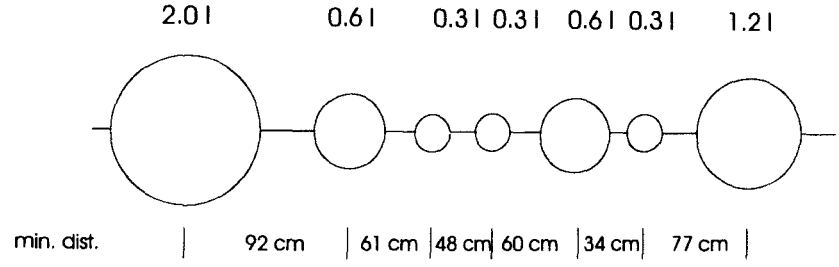

Fig. 6.3.4.8.2: Volumes and bubble diameters of GEOMAR airgun array

On the starbord side of SONNE the remaining BGR array was operated. Apart from Obh107 all stations recorded the whole test sequence. In addition, the GEOMAR streamer was deployed.

For a first run the starbord BGR array was shot at 20 seconds interval. Figures 6.3.4.8.3 to 6.3.4.8.11 show the seismic sections of the streamer and the ocean bottom stations. The stack of the three streamer channels shows a detailed resolution penetrating as deep as 2 seconds two way traveltime. Refraction seismic recordings are of varying quality. Only short distances were achieved from station 106 which was deployed at only 81 m water depth. A higher noise level than on deeper deployments restricted direct wave recordings to 10 km distance. Refracted events could be detected close to the station at 4 to 6 km offset. On all other stations direct wave arrivals were detected over the whole line (up to 22 km) due to a reduced noise level. Nevertheless, refraction events were not observed further than 4 to 6 km to the side of a station. Several reflection events could be observed in the near vertical range at all stations. As the line was acquired near the end of the cruise only standard processing routines as applied to the deep sea refraction lines were used for a first display.

For the second part of the test the GEOMAR airgun array was additionally deployed. At a final test prior to deployment the fire line of the 2 l airgun failed and it was decided to change this 2 l chamber with the neighbouring 0.6 l chamber reducing the array to 6 guns only. While deploying the string the pressure pipe of one gun broke and was shut off. As the weather conditions caused a heavy sea, the test shooting was continued using the remaining five guns. Alternating between GEOMAR port array only and both arrays shot simultaniously, the profile was reversed with 20 seconds pop interval. Due to strong sidewards currents (1 – 2 kn) the port gun array drifted towards the streamer. As streamer and the first gun tangled into each other both systems had to be pulled in. After repair of the pressure pipe the port gun array was deployed again. As the array again drifted towards the centre of the stern, the streamer was not deployed a second time. Therefore recordings of the alternating shots were only available from the ocean bottom stations. Figures 6.3.4.12 to 6.3.4.14 show the sections of OBH 109,

110 and the hydrophone of OBS 111. The stripe like pattern of the sections is due to the change between the GEOMAR array (weak events) and both arrays (strong events). The large gap was caused by the recovery of streamer and airguns as described above. The amplitude onset of arrivals from the GEOMAR array show a similar pattern as with the BGR array. This indicates the proper choosing of gun alignment as far as it could be deduced from this short test. Again, direct wave arrivals could be detected over the whole offset. Refracted energy could be detected in the 4 to 8 km offset range. Due to its smaller size the GEOMAR array events were much weaker. The near vertical penetration was obviously less than with the BGR array but also clearly on a much smaller scale due to the increased frequency content. Refraction energy could not be detected while shooting with the GEOMAR array alone.

More careful analyses of the wavefield and the frequency content will have to be done.

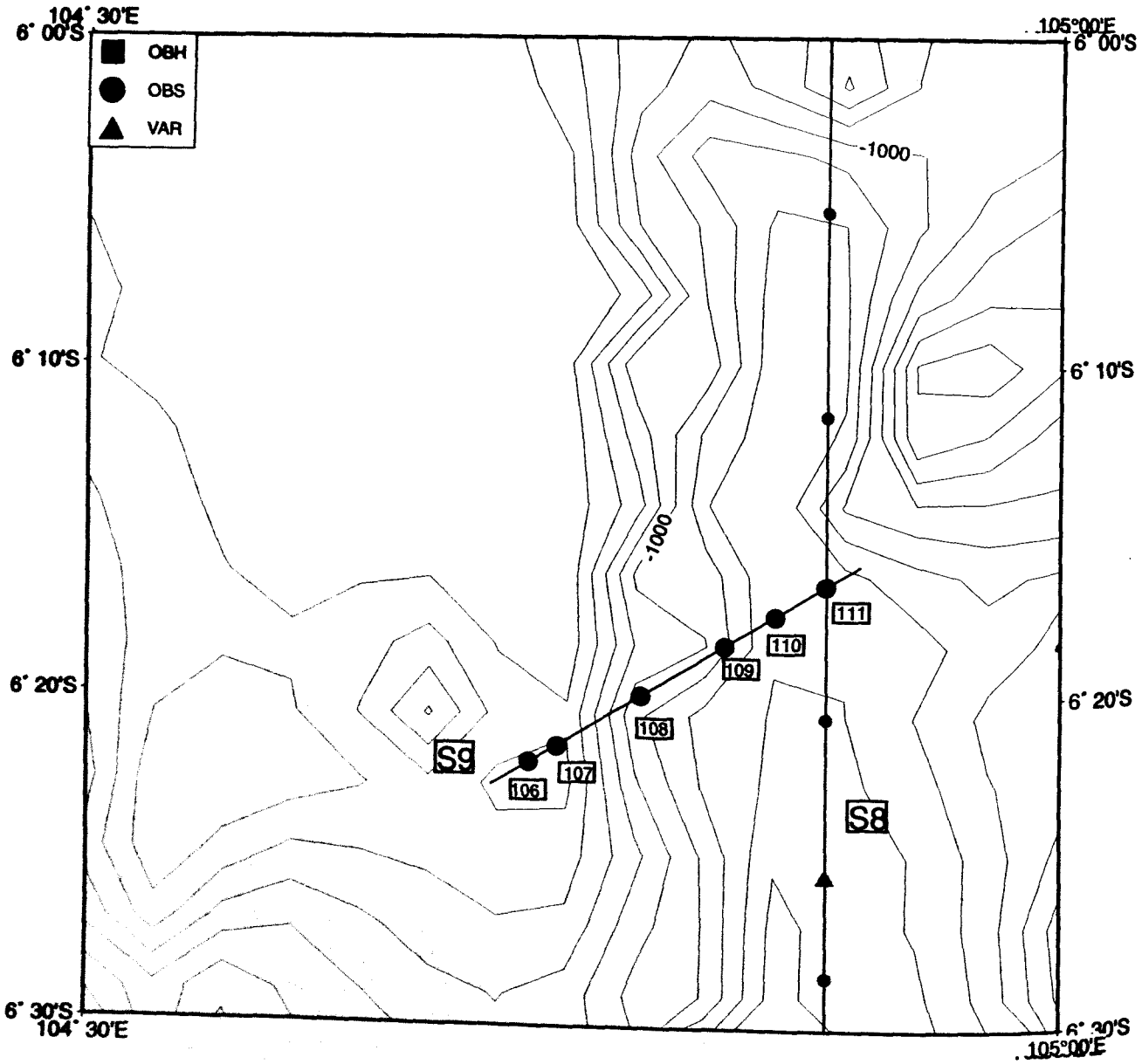

Figure 6.3.4.8.1: Location map of seismic line S9.

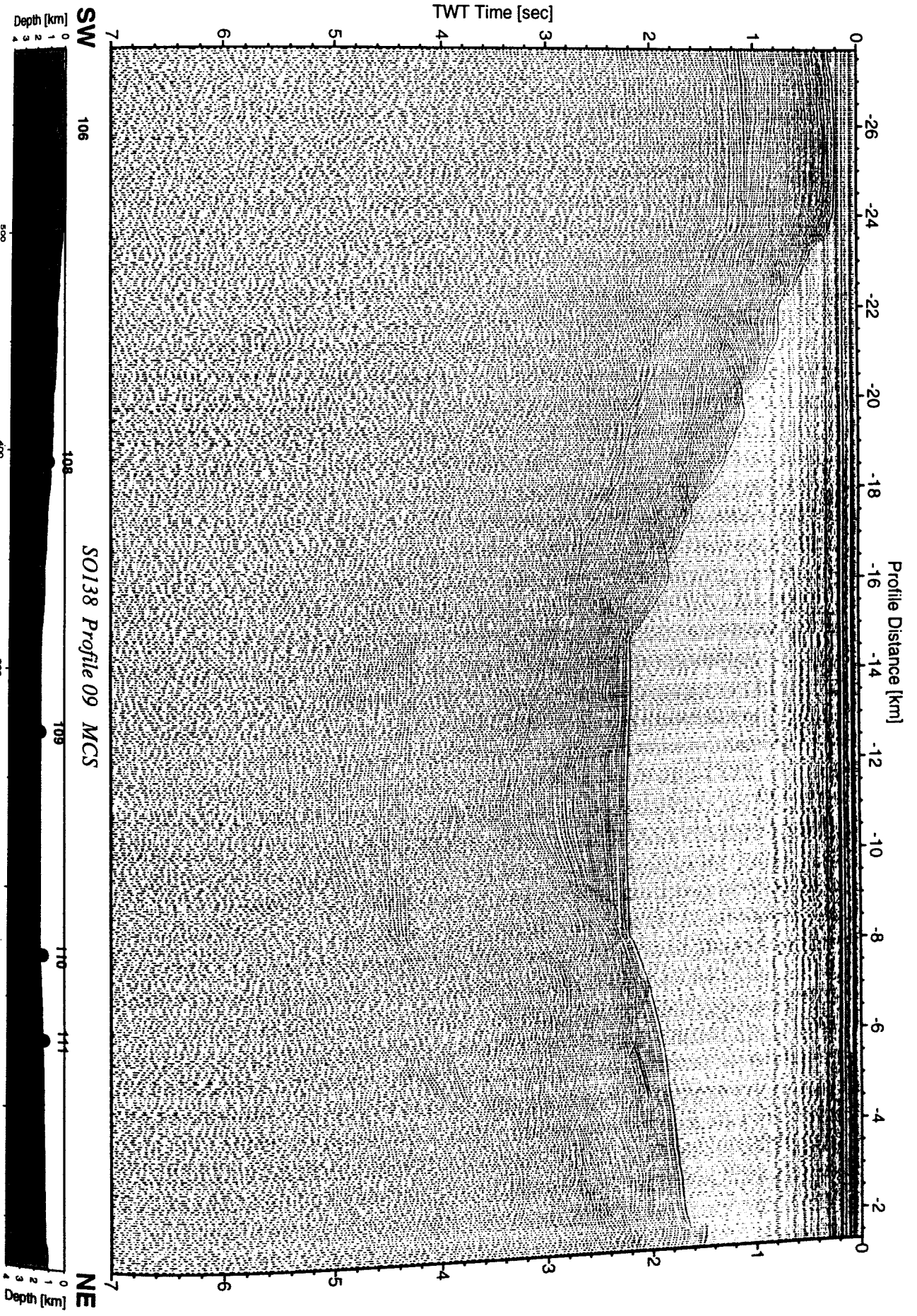

Figure 6.3.4.8.3: Seismic section from MCS stack, Profile 09.

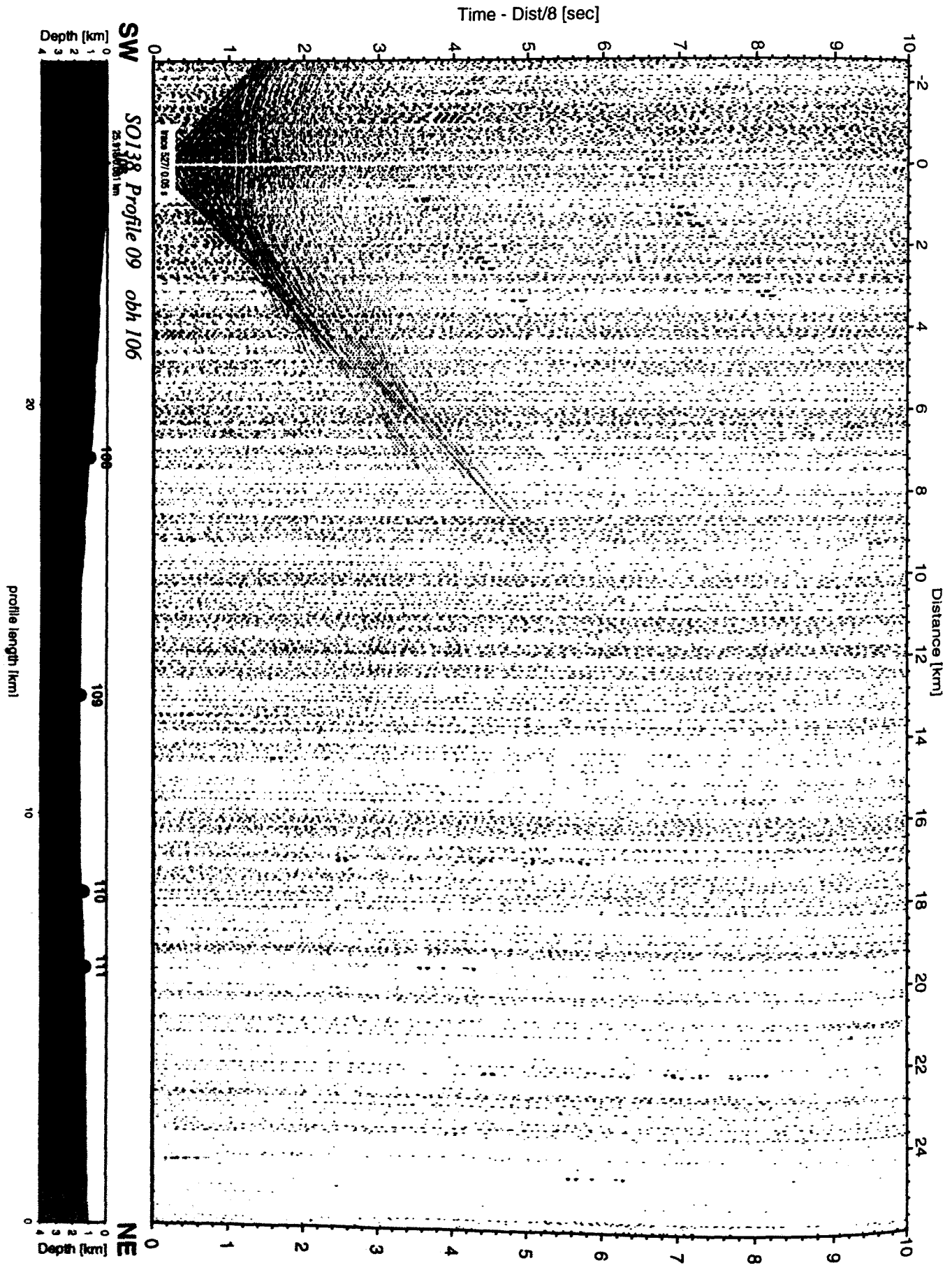

Figure 6.3.4.8.4: Record section from obh 106 , Profile 09.

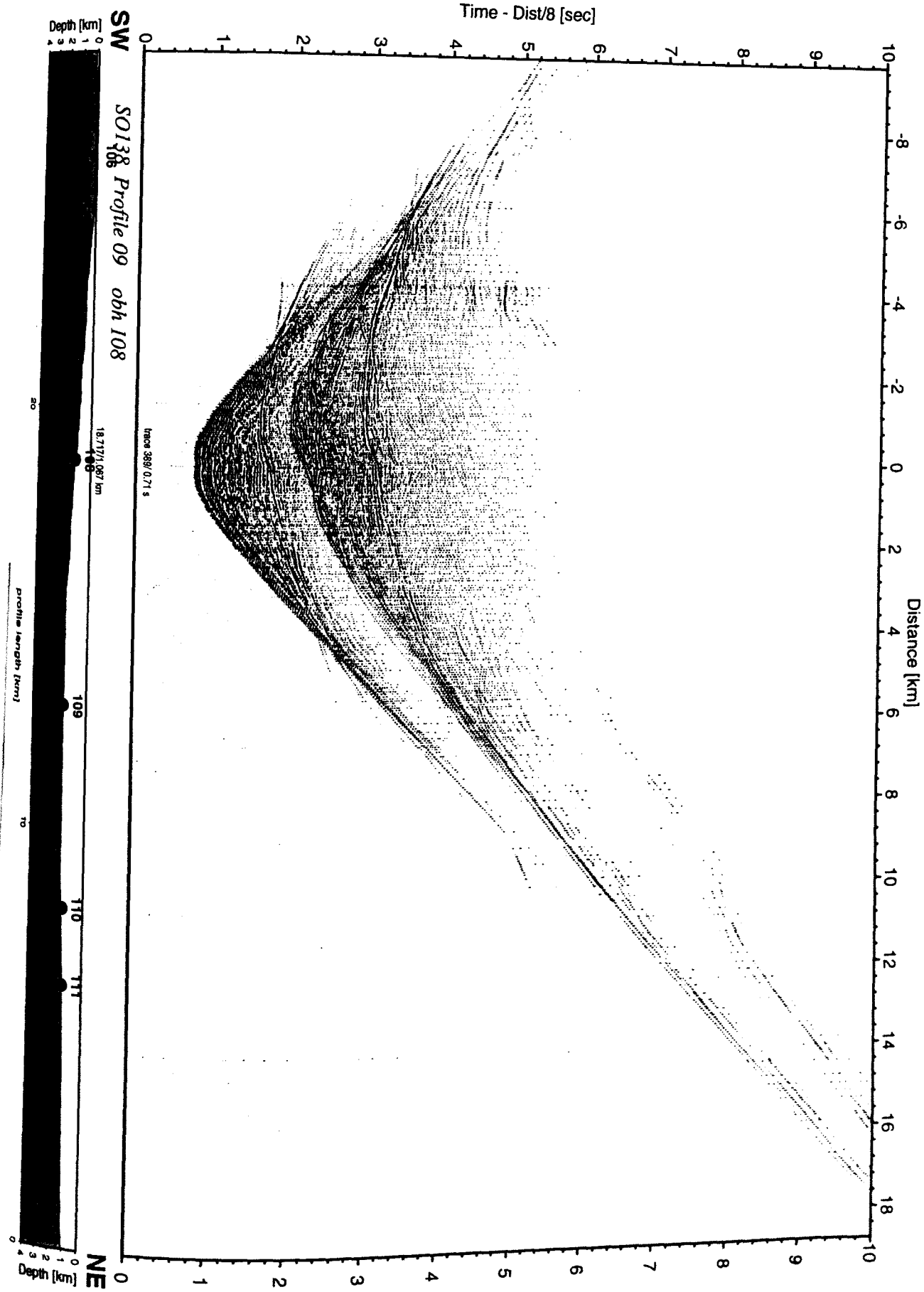

Figure 6.3.4.8.5: Record section from obh 108 , Profile 09.

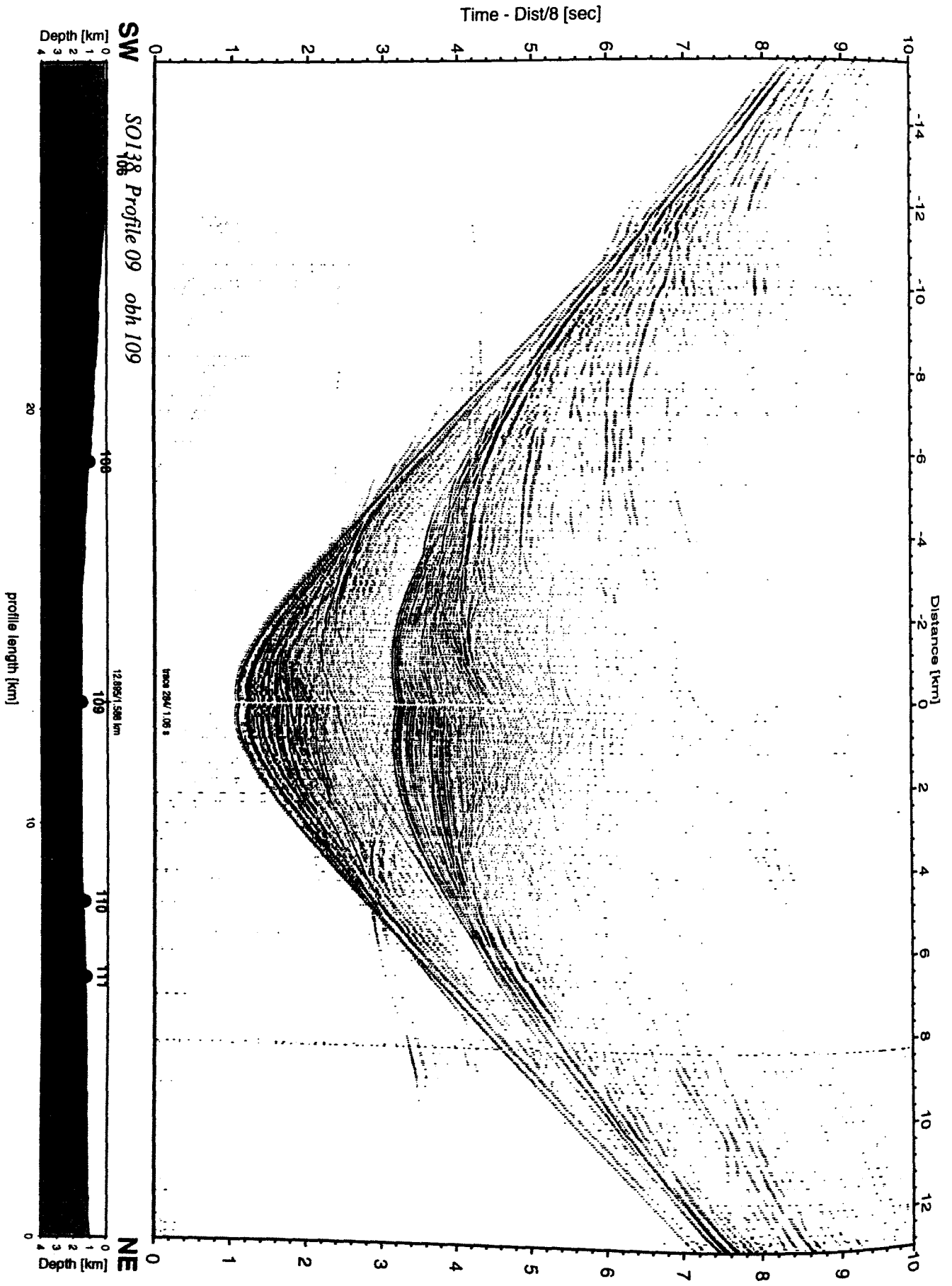

Figure 6.3.4.8.6: Record section from obh 109 , Profile 09.

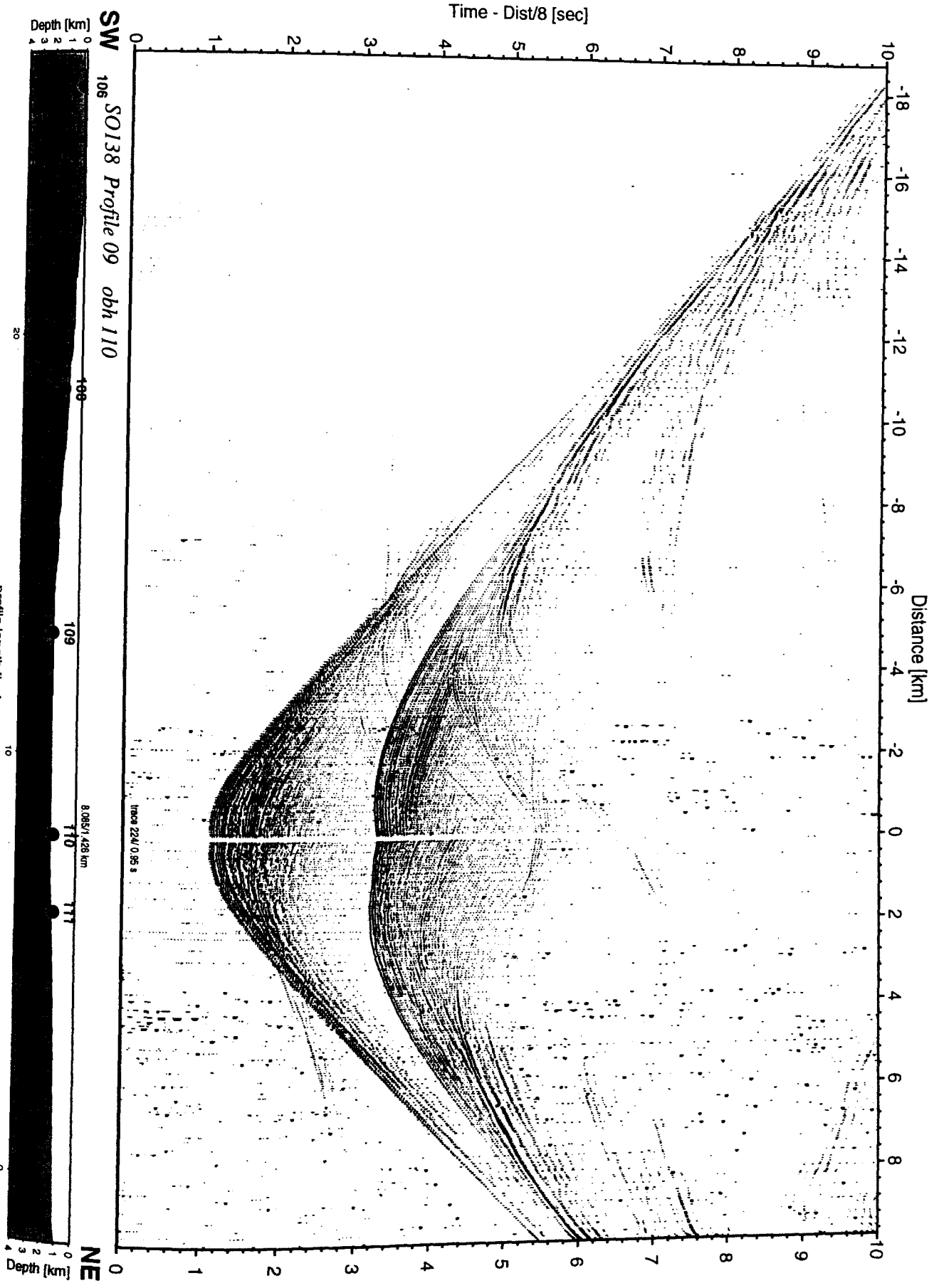

Figure 6.3.4.8.7: Record section from obh 110 , Profile 09.

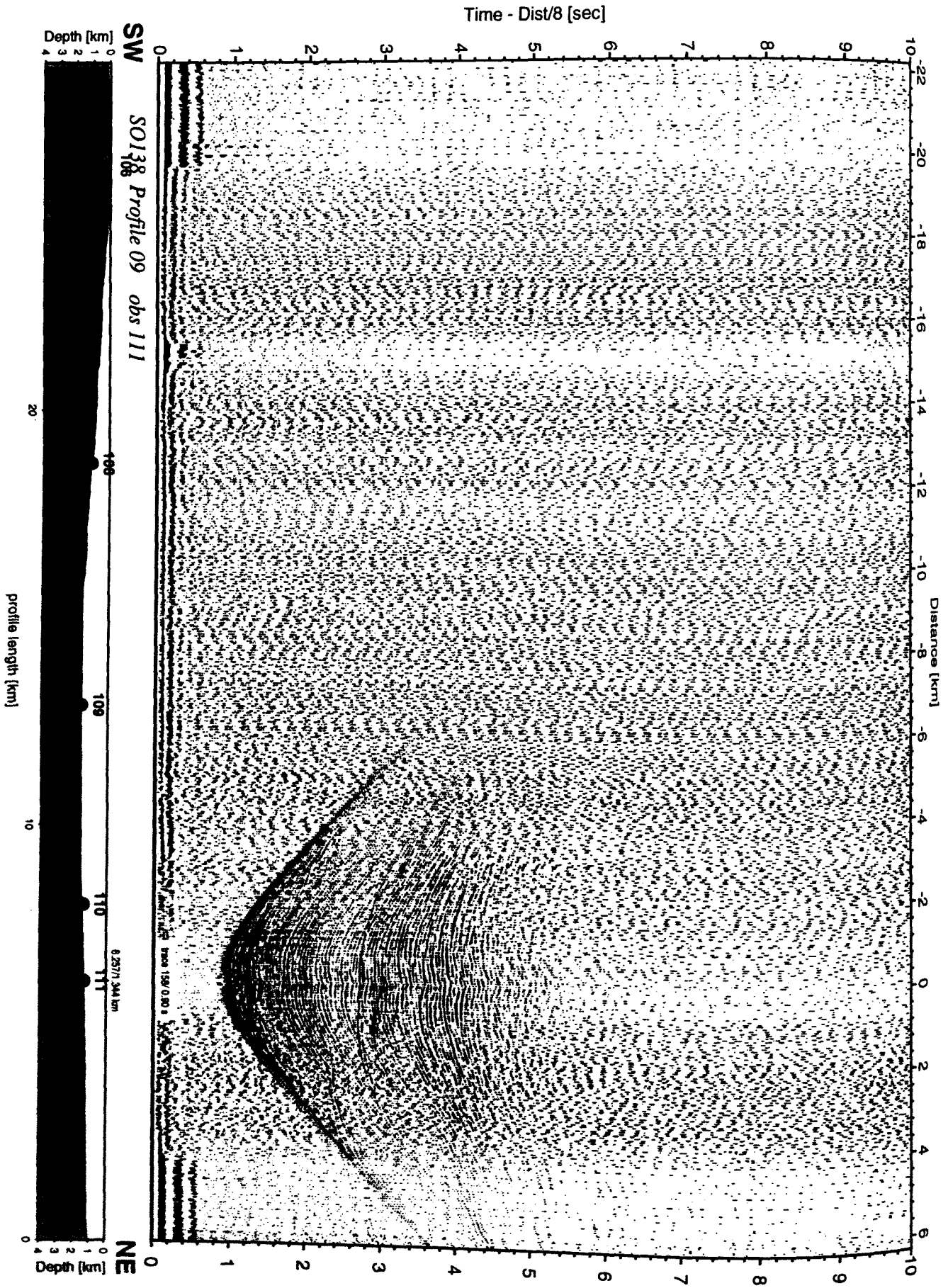

Figure 6.3.4.8.8: Record section from obs 111 horizontal component 2, Profile 09.

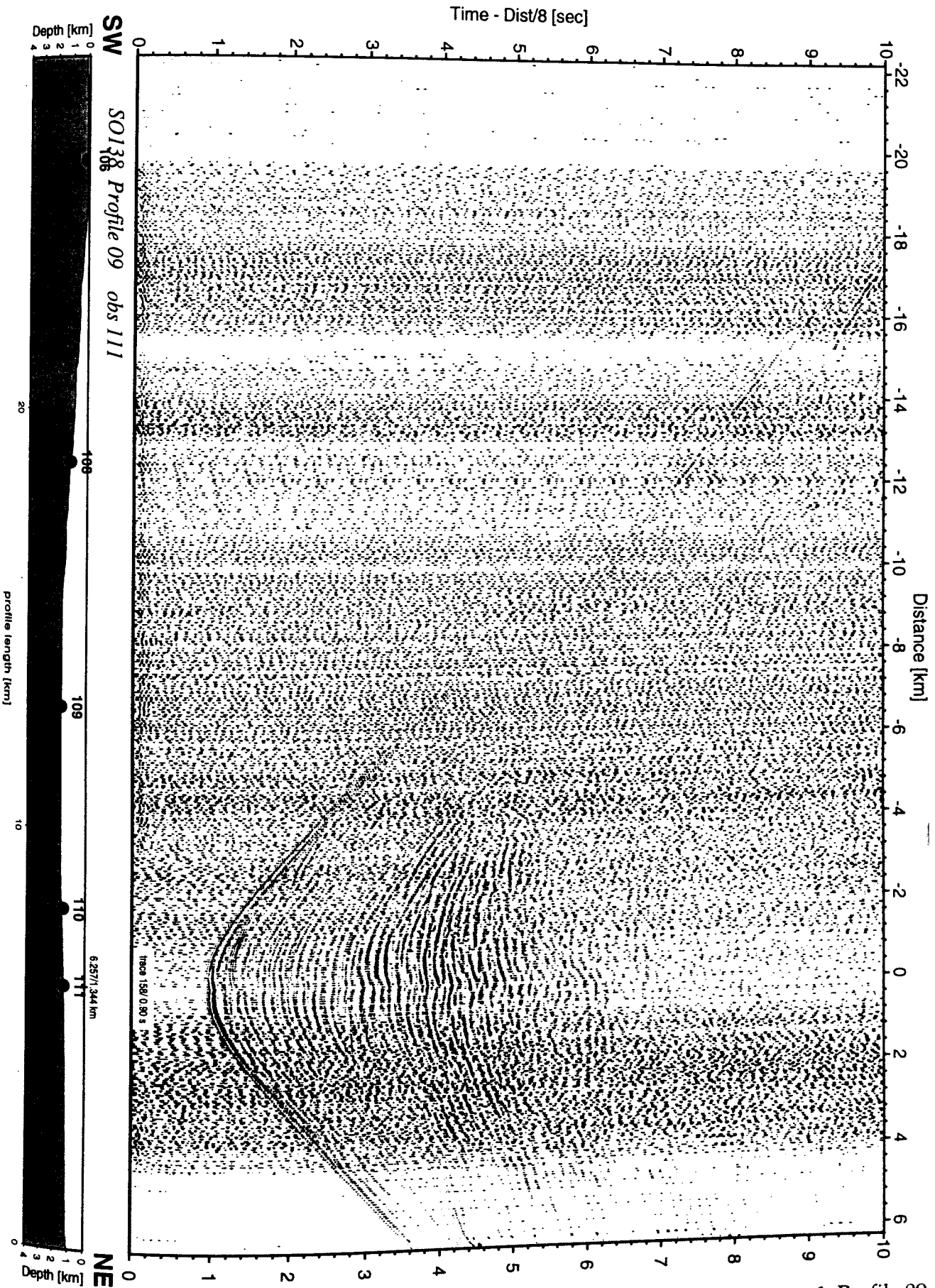

Figure 6.3.4.8.9: Record section from obs 111 horizontal component 1, Profile 09.

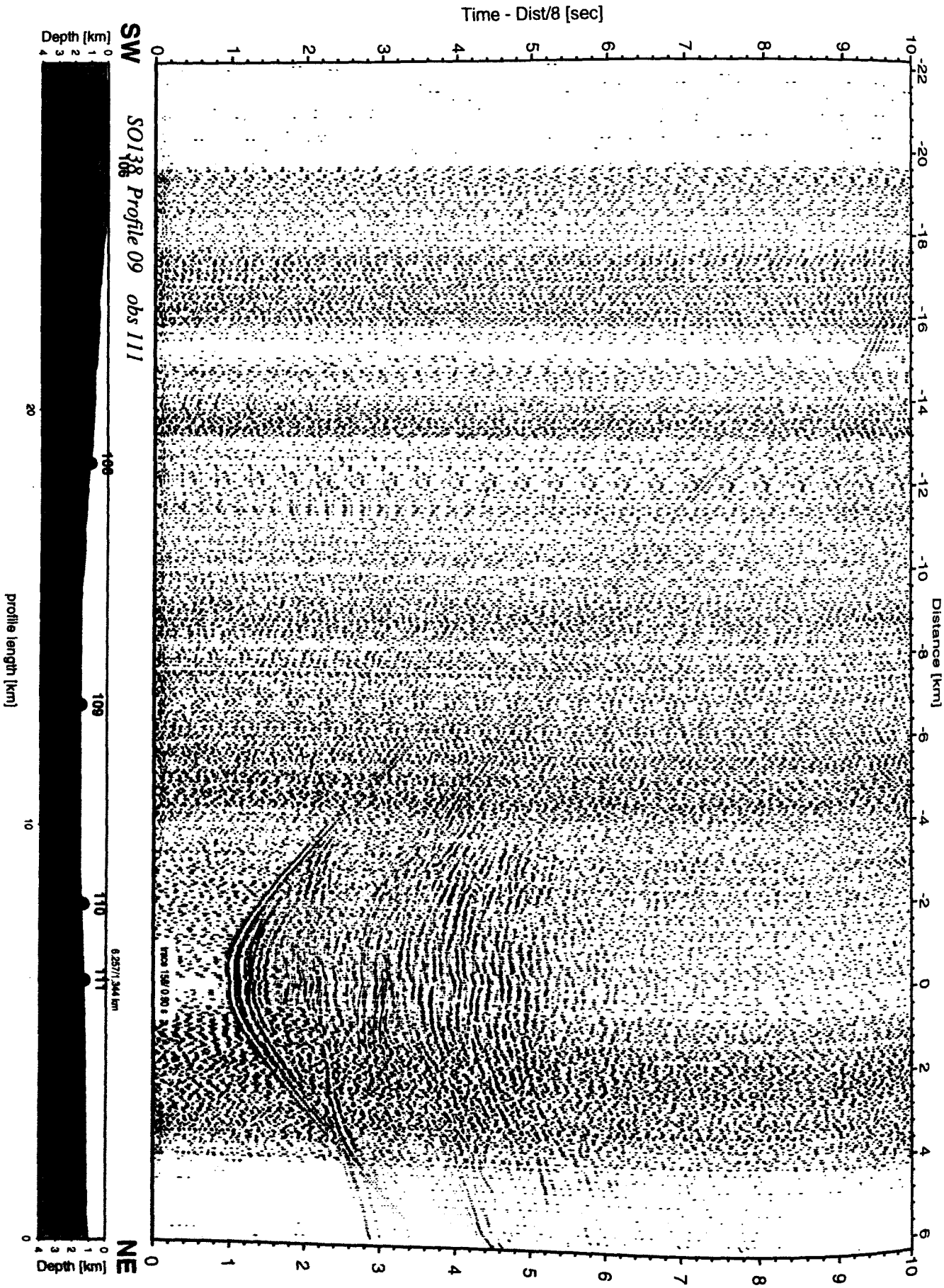

Figure 6.3.4.8.10: Record section from obs 111 vertical component, Profile 09.

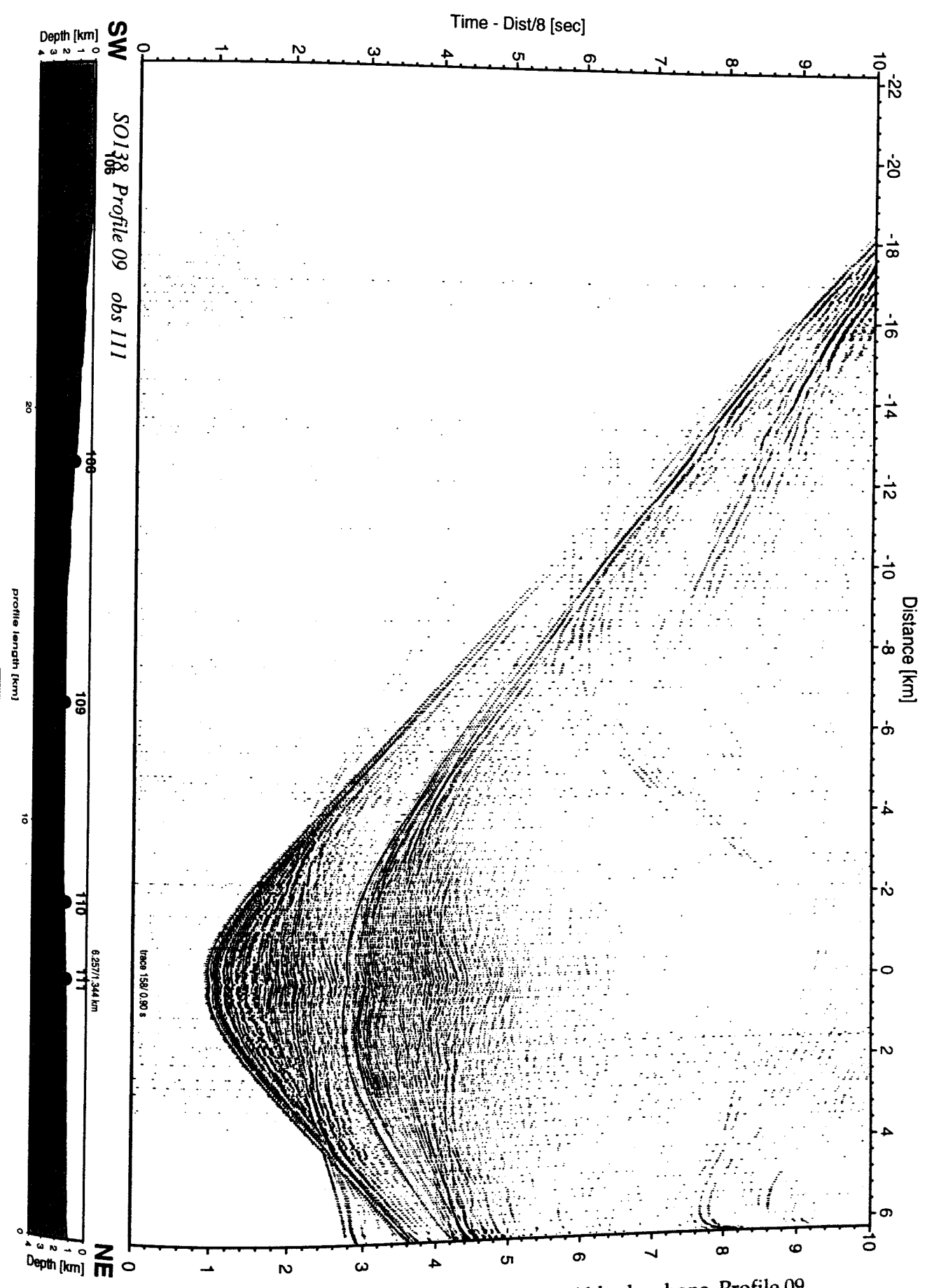

Figure 6.3.4.8.11: Record section from obs 111 hydrophone, Profile 09.

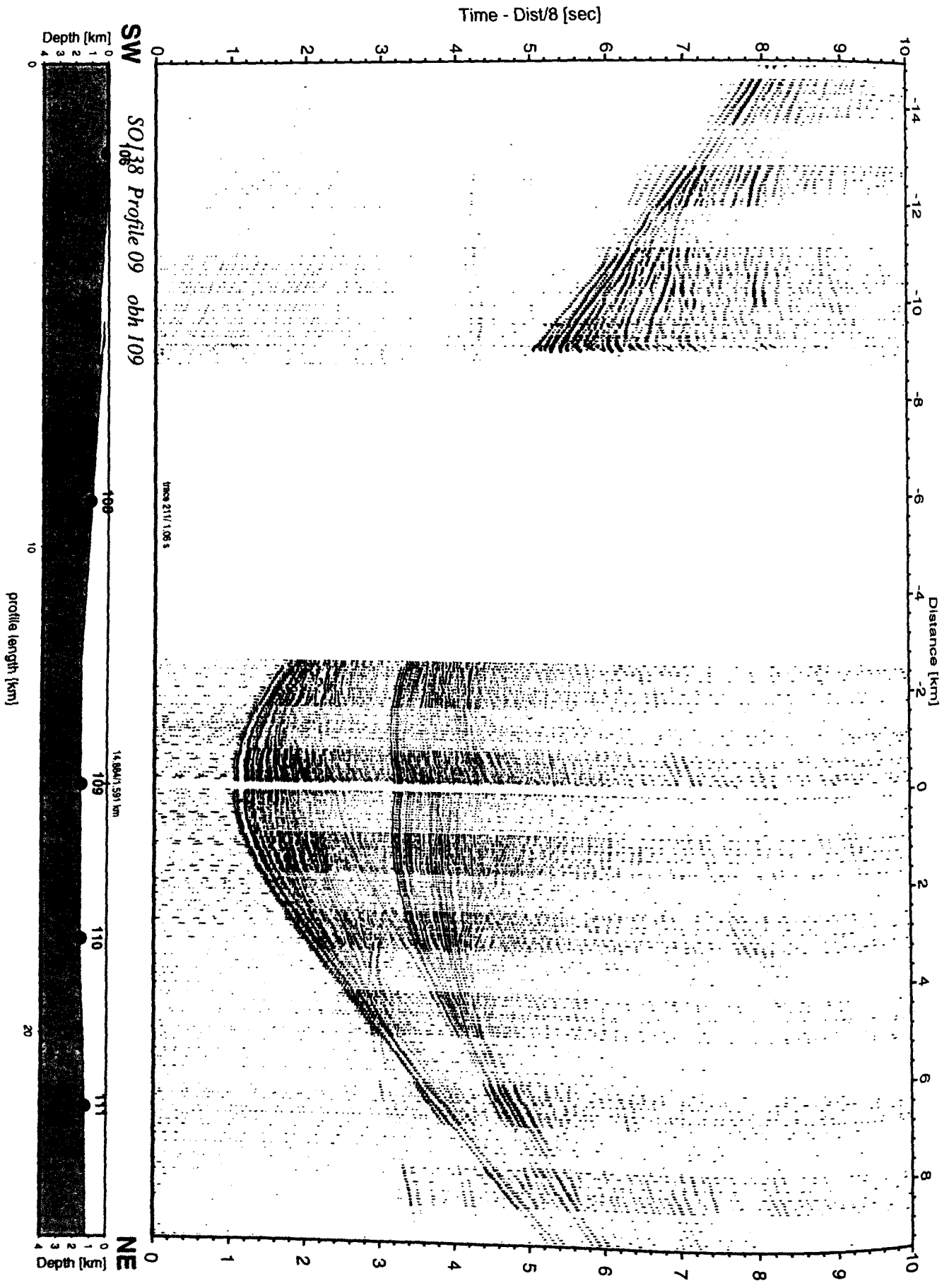

Figure 6.3.4.8.12: Record section from obh 109 , Profile 09.

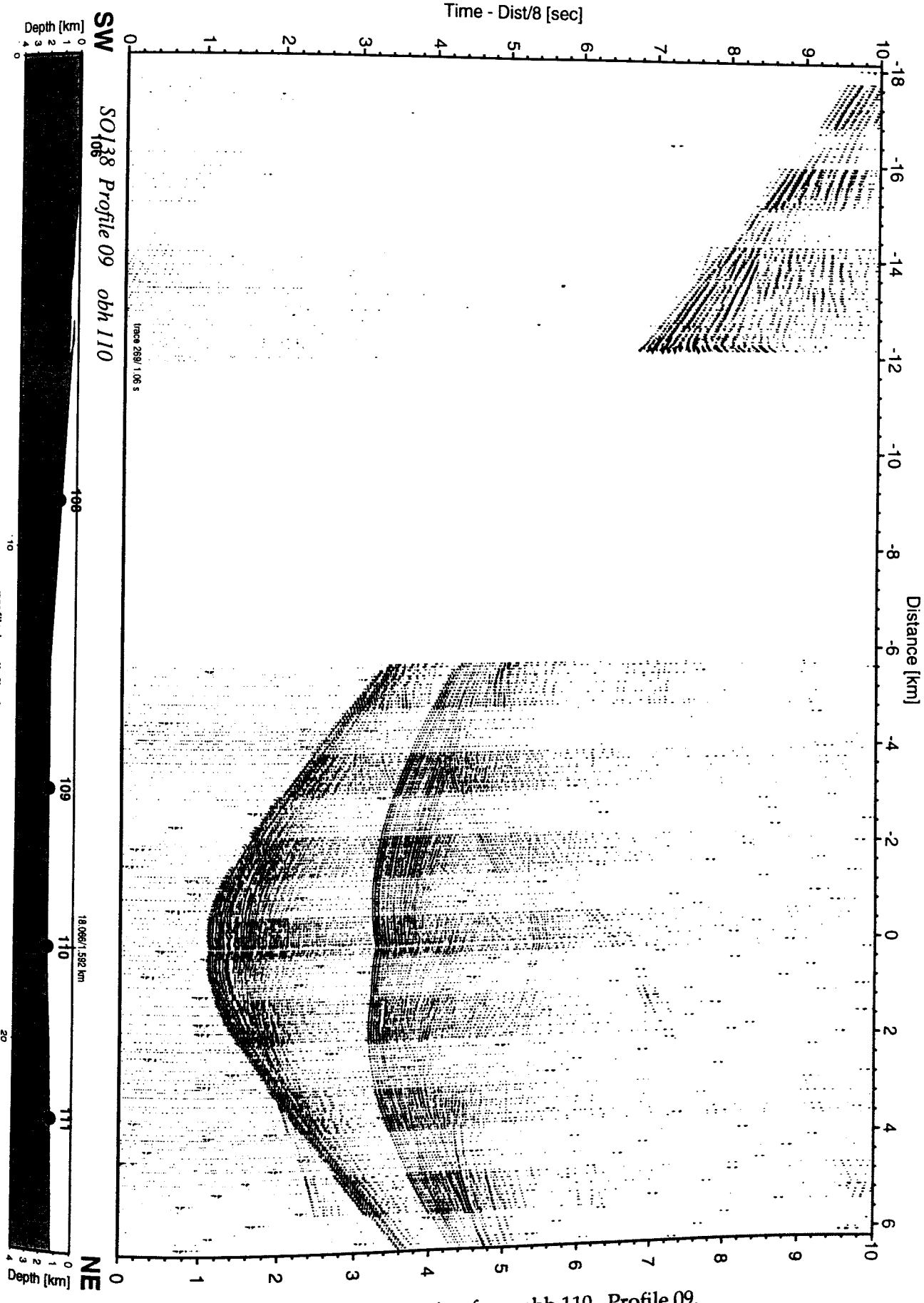

Figure 6.3.4.8.13: Record section from obh 110 , Profile 09.

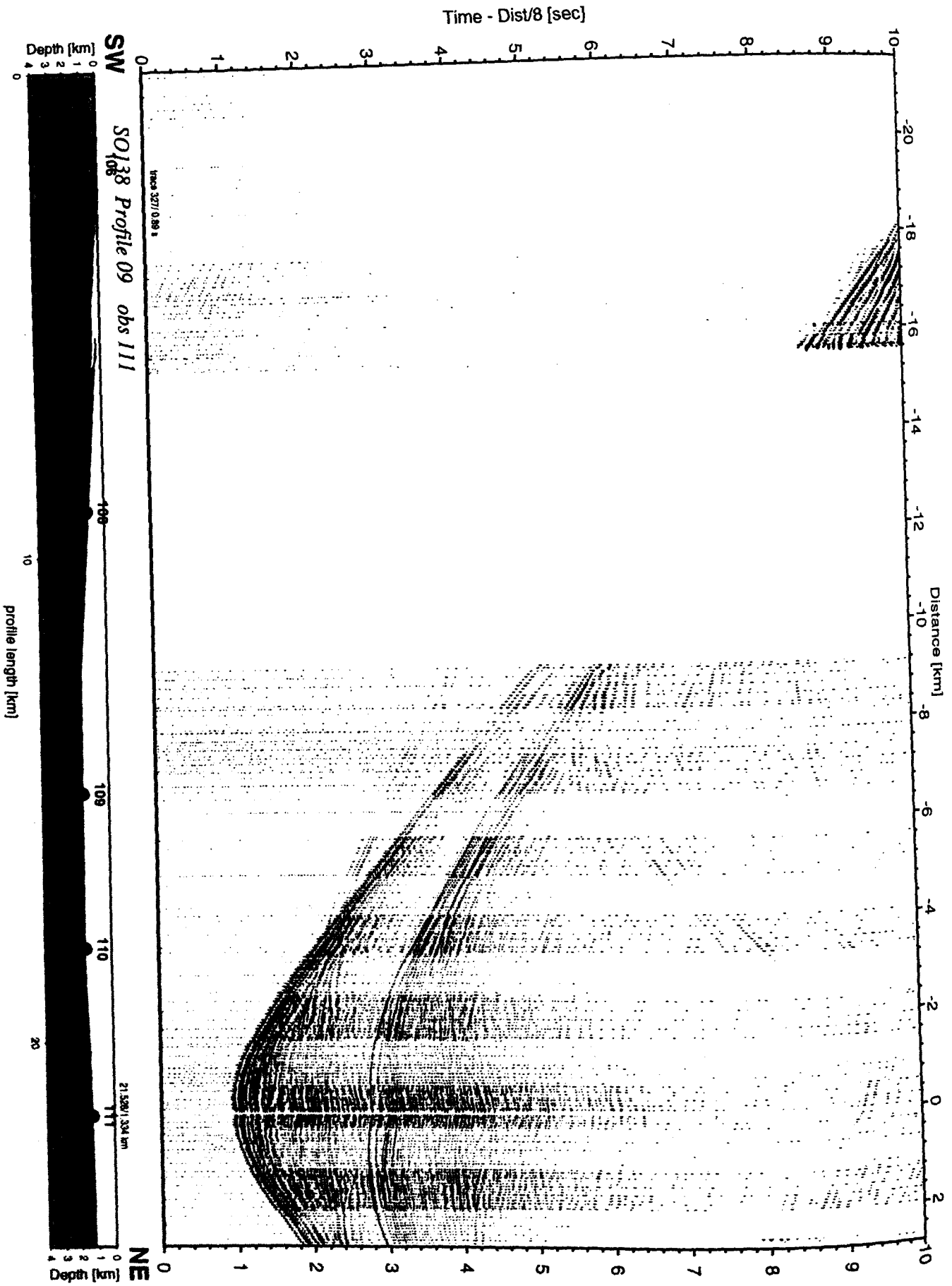

Figure 6.3.4.8.14: Record section from obs 111 hydrophone, Profile 09.

6.4 GRAVITY AND MAGNETICS

Magnetic measurements carried out during cruise SO-138 cover about 4370 profile kilometers on 68 lines. Gravimetric measurements were made on all lines and cover about 8000 km. We use the line numbering scheme for the seismic lines (SO138-01 to –09, Appendix 9.2) and an independent numbering scheme for magnetic, gravity, and hydroacoustic lines. Lines which were surveyed without seismics start at number 101 (SO138-101 to –161, Appendix 9.3). Fig. 6.4.1 shows the profile plan for all lines surveyed during cruise SO-138. Figs. 6.4.2 to 6.4.9 show the magnetic and gravimetric (free air) anomalies for selected profiles together with the water depth from the central beam of Hydrosweep. Figs. 6.4.2 to 6.4.7 display all seismic lines (except of line SO138-09) and Figs. 6.4.8 and 6.4.9 show profiles from the Sunda Strait.

6.4.1 GRAVITY TIES TO LAND STATIONS

(I. Heyde, P. Kewitsch, & B. Schreckenberger)

To compare the results of different gravity surveys the measured data have to be tied in a world-wide accepted reference system. This system is represented by the International Gravity Standardization Net IGSN71 (Morelli, 1974).

The IGSN71 was established in 1971 by the International Union of Geodesy and Geophysics (IUGG) as a set of world-wide distributed locations with known absolute gravity values better than a few tenths of mGal. It replaced the former Potsdam Gravity System which did not conform any more to the necessities of modern geodesy and geophysics. According to the recommendations of the IUGG, every gravity survey, marine or land, should be related to the datum and to the scale of the IGSN71.

Therefore, gravity measurements at land have to be carried out to connect the gravity measurements at sea with the IGSN71. The marine geophysical group of BGR uses for the gravity connections a LaCoste&Romberg gravity meter, model G, no. 480.

The point descriptions and gravity values of reference IGSN71 stations in Perth and Fremantle in Western Australia were kindly provided by the Gravimetry Group of the Australian Geological Survey Organisation (AGSO), Canberra.

Since R.V. Sonne arrived in Fremantle not before November, 20, tie measurements from reference points were done to point **A** at the entrance of the Hotel Grand Chancellor in Perth (**I, II** in Table 6.4.1.1). For this connection three reference points, two north-east of Perth (Hazelmer Store **01** and Perth-Airport **02**) and one at the University of Western Australia **03** in the south-west of Perth, were used.

R.V. Sonne moored in the Inner Harbour of Fremantle at berth 11 near bollard no. 83 (Fig. 6.4.1.1). On November, 21 and 22 two series of tie measurements to point **B** about 50 cm from bollard no. 83 to the Northeast have been made (**III, IV** in Table 6.4.1.1). Conditions were good for all measurements. In addition to the new established reference point **A** at the Hotel Grand Chancellor and the point **03** at the University of Western Australia a reference point at the main entrance of the Fremantle Port Authority **04** was used. The latter could be clearly identified as it is marked by a brass plate mentioning the AGSO station number.

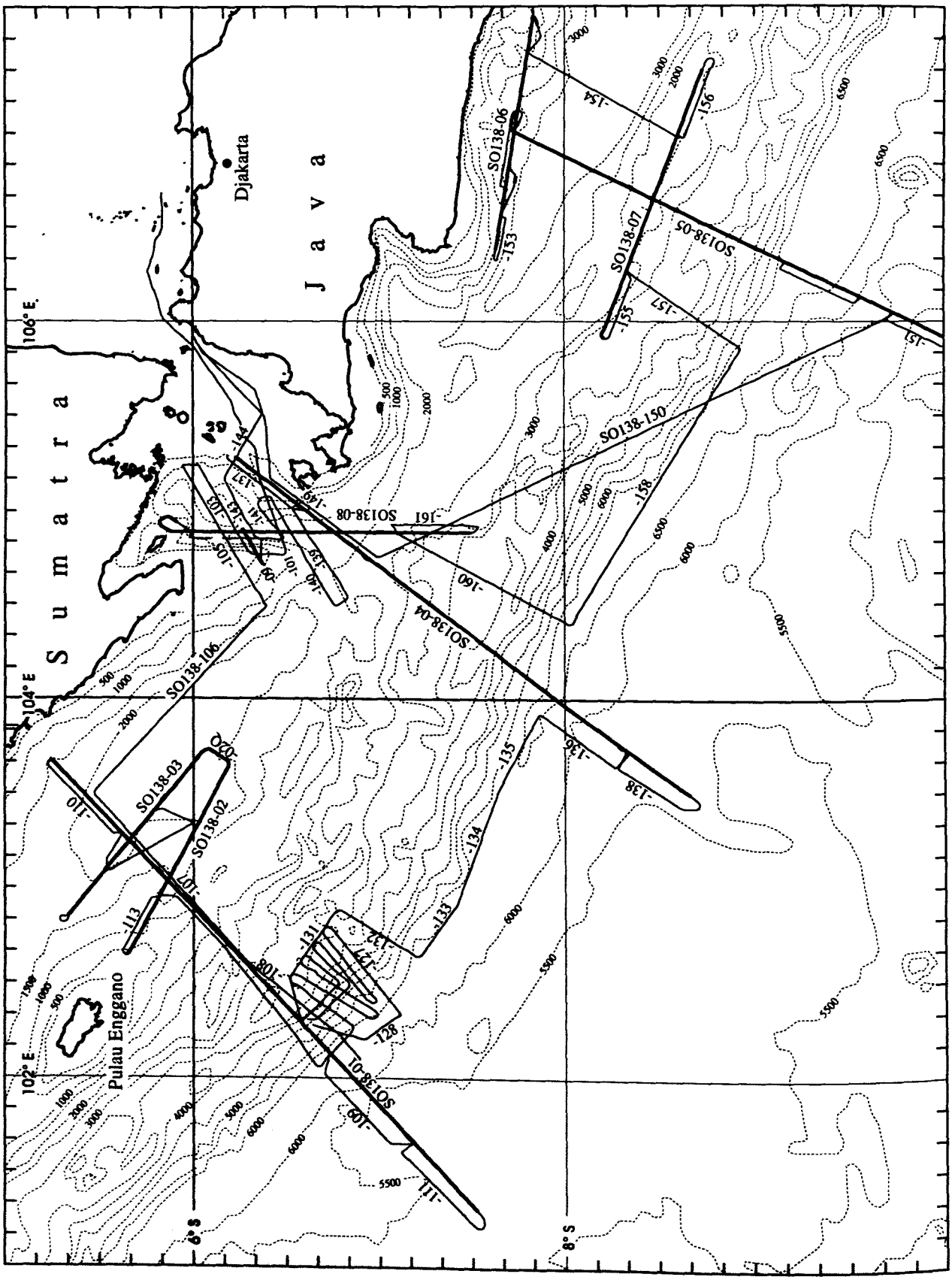

Figure 6.4.1: Profile plan of cruise SO-138 (GINCO II)

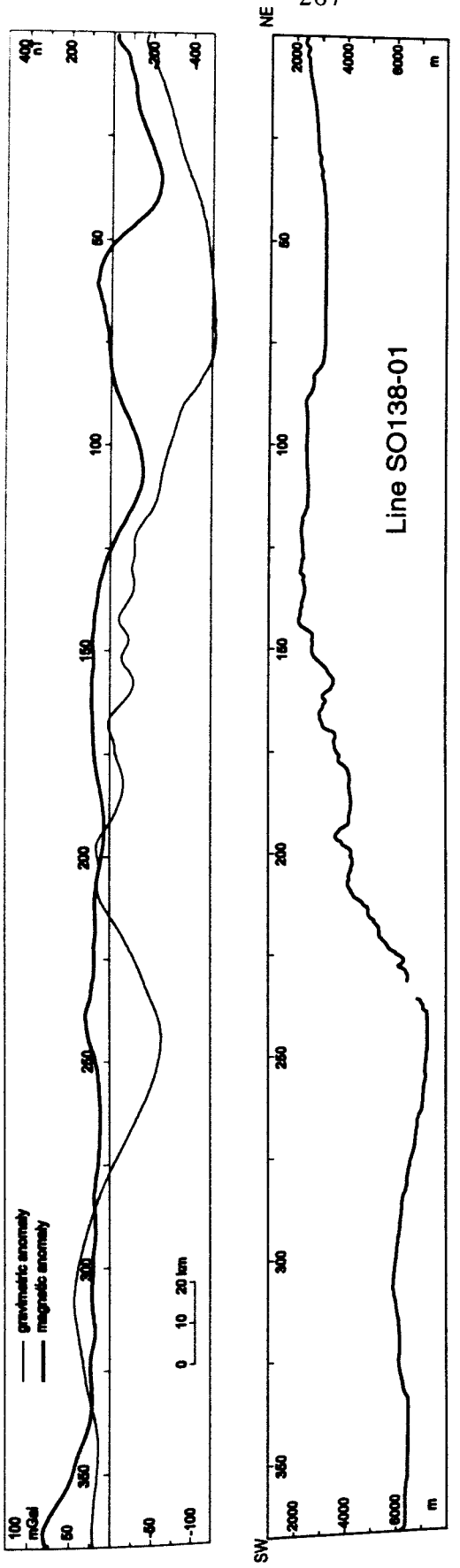

Figure 6.4.2: Potential field data combined with seafloor topography along seismic line SO138-01. The thin line in the upper part of the figure shows the free-air anomaly (scale on the left margin), the thick line the magnetic anomaly from the master sensor (scale at the right margin). The lower part of the figure shows the waterdepth in meters from the central beam of Hydrosweep.

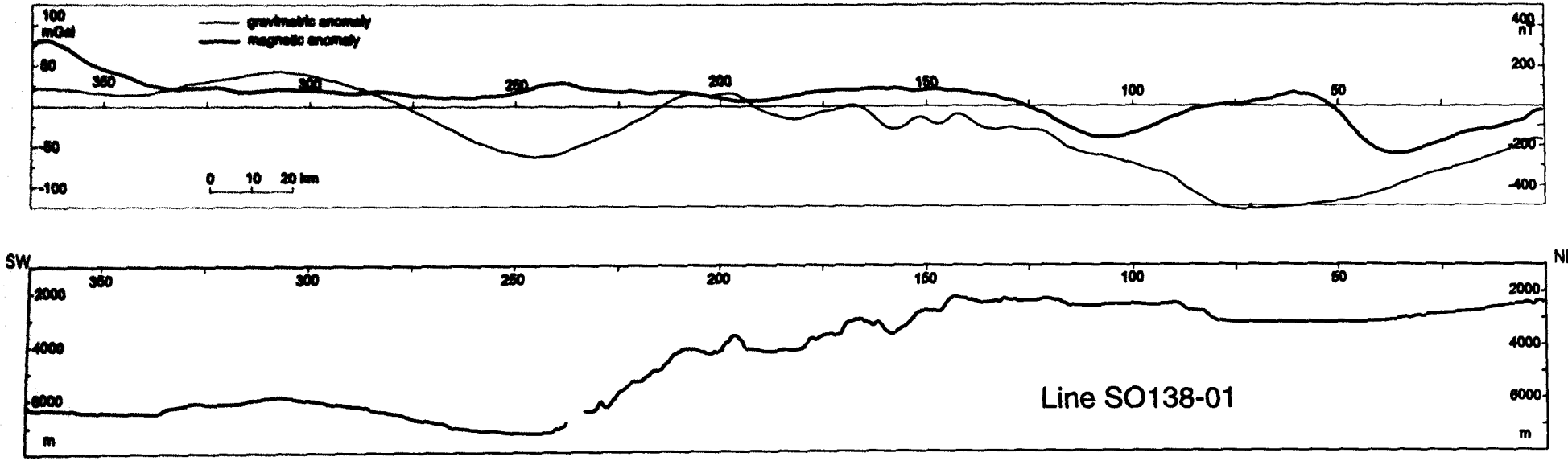

Figure 6.4.2: Potential field data combined with seafloor topography along seismic line SO138-01. The thin line in the upper part of the figure shows the free-air anomaly (scale on the left margin), the thick line the magnetic anomaly from the master sensor (scale at the right margin). The lower part of the figure shows the waterdepth in meters from the central beam of Hydrosweep.

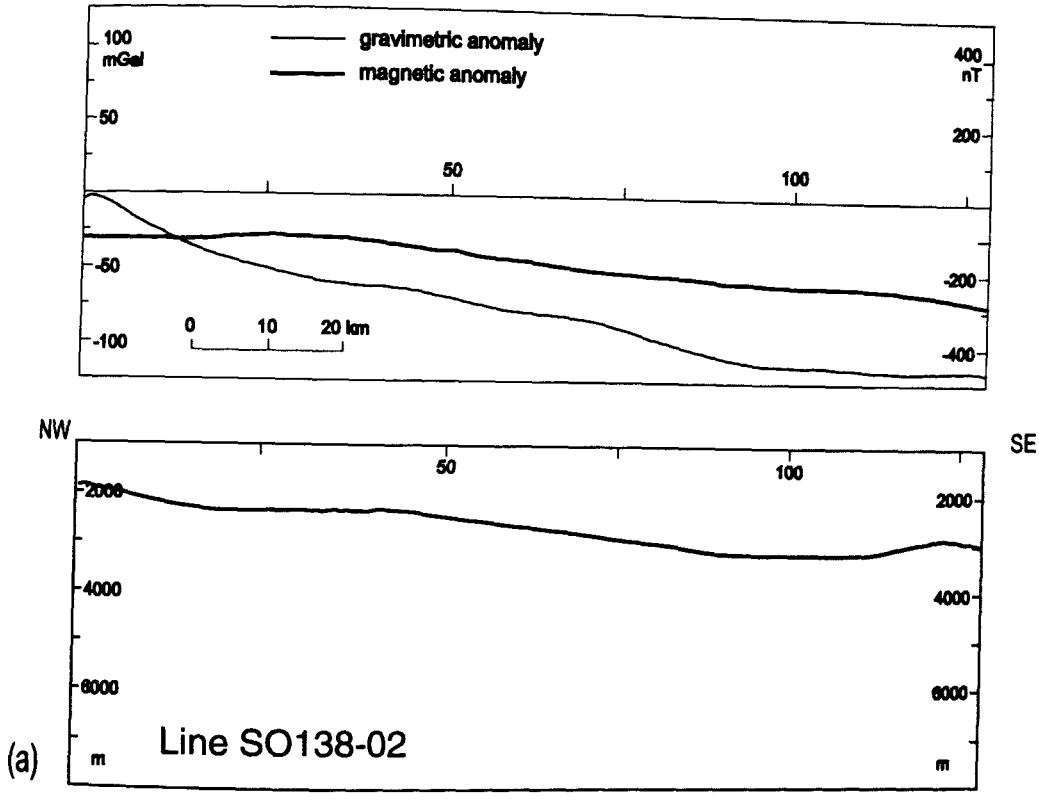

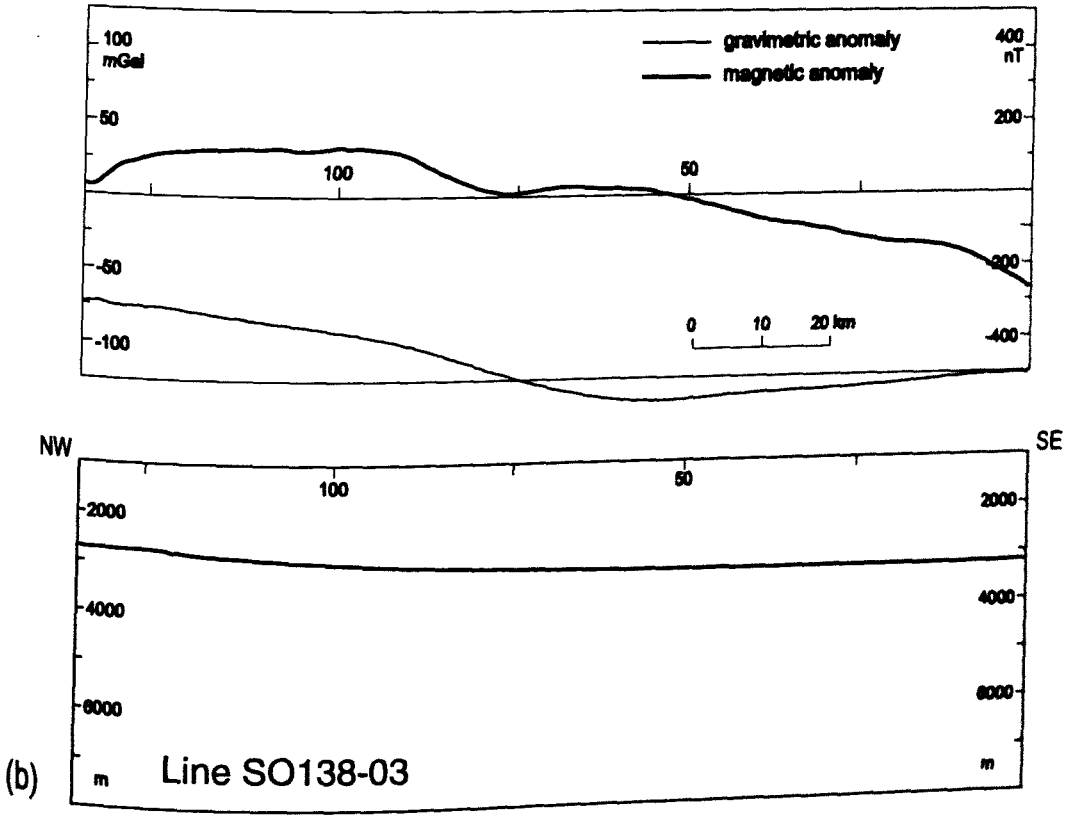

Figure 6.4.3: Potential field data combined with seafloor topography along seismic lines: (a) SO138-02 and (b) -03. Explanation see Figure 6.4.2.

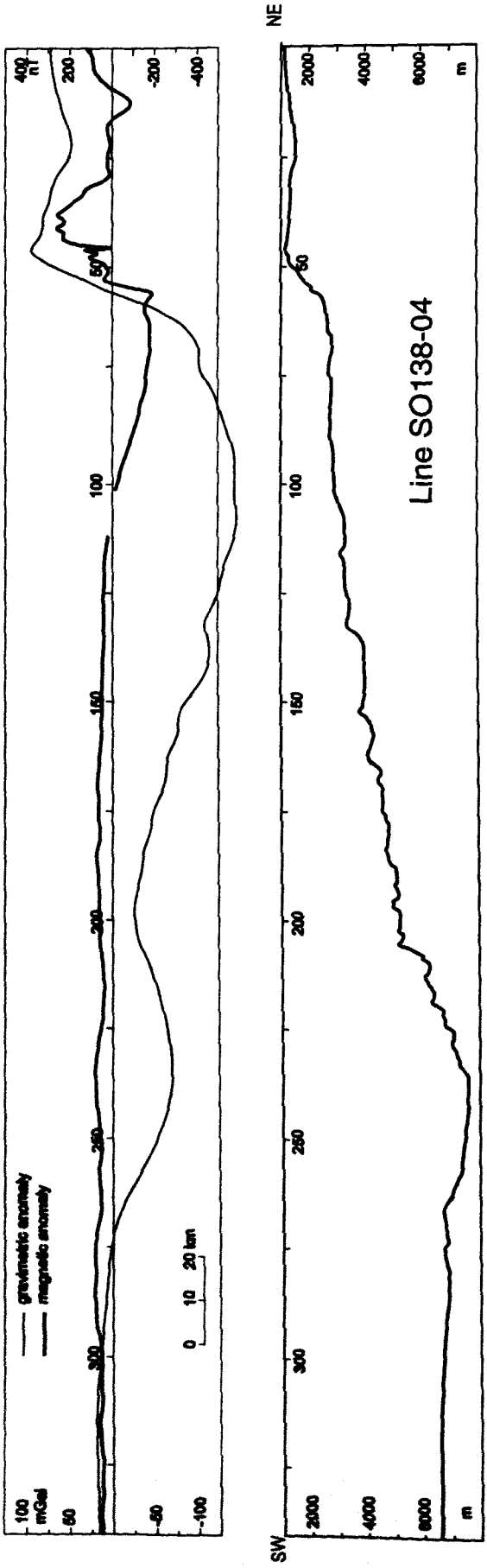

Figure 6.4.4: Potential field data combined with seafloor topography al
SO138-04. Explanation see Figure 6.4.2.

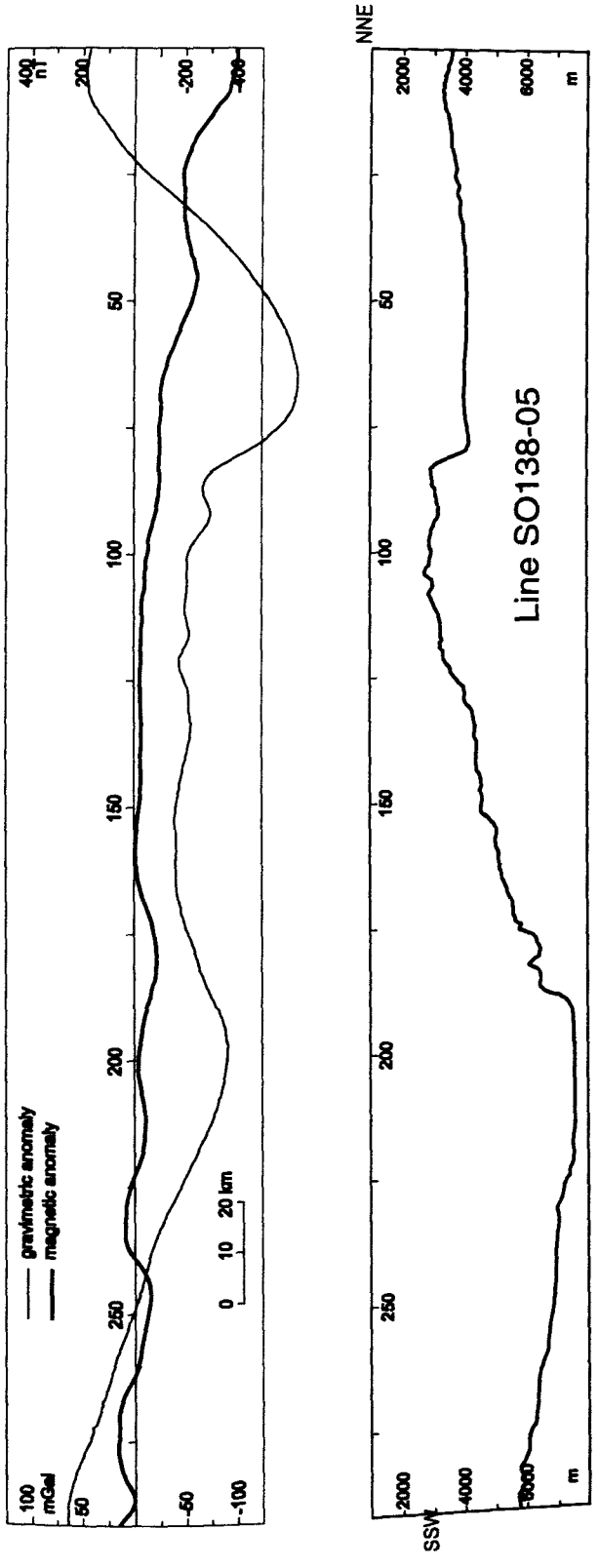

Figure 6.4.5: Potential field data combined with seafloor topography along seismic line SO138-05. Explanation see Figure 6.4.2.

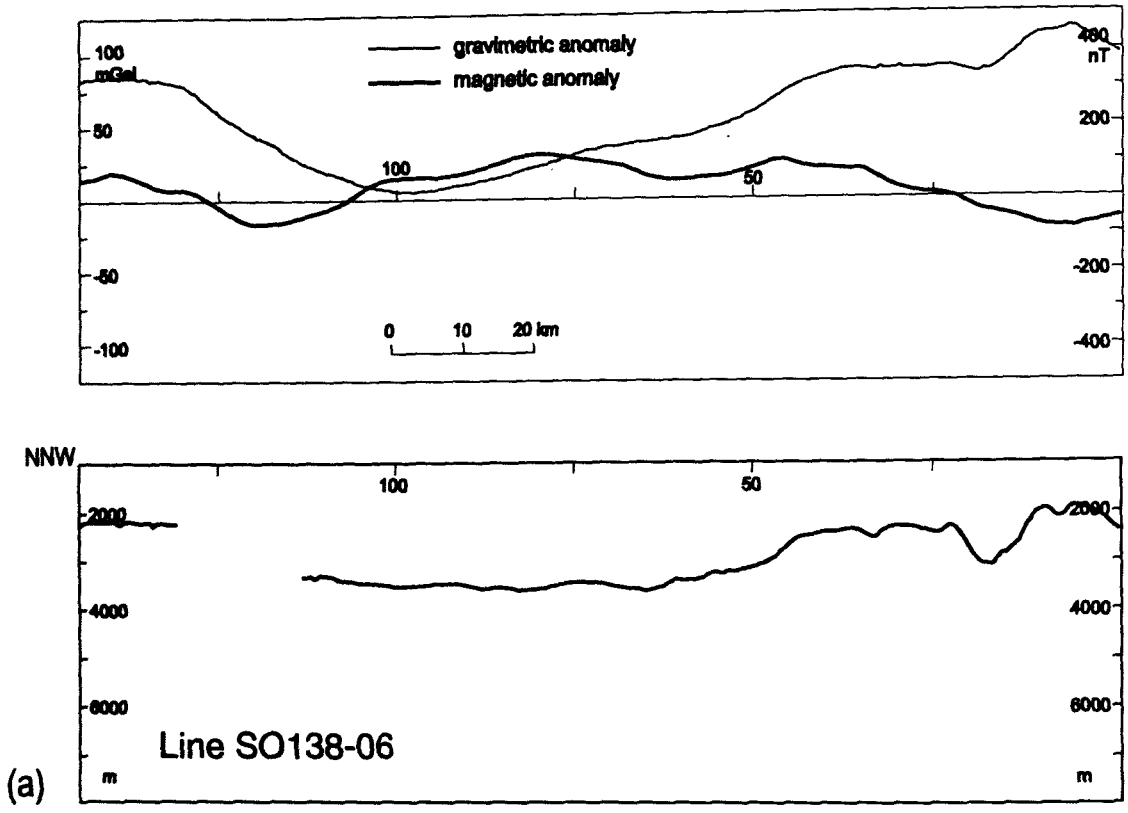

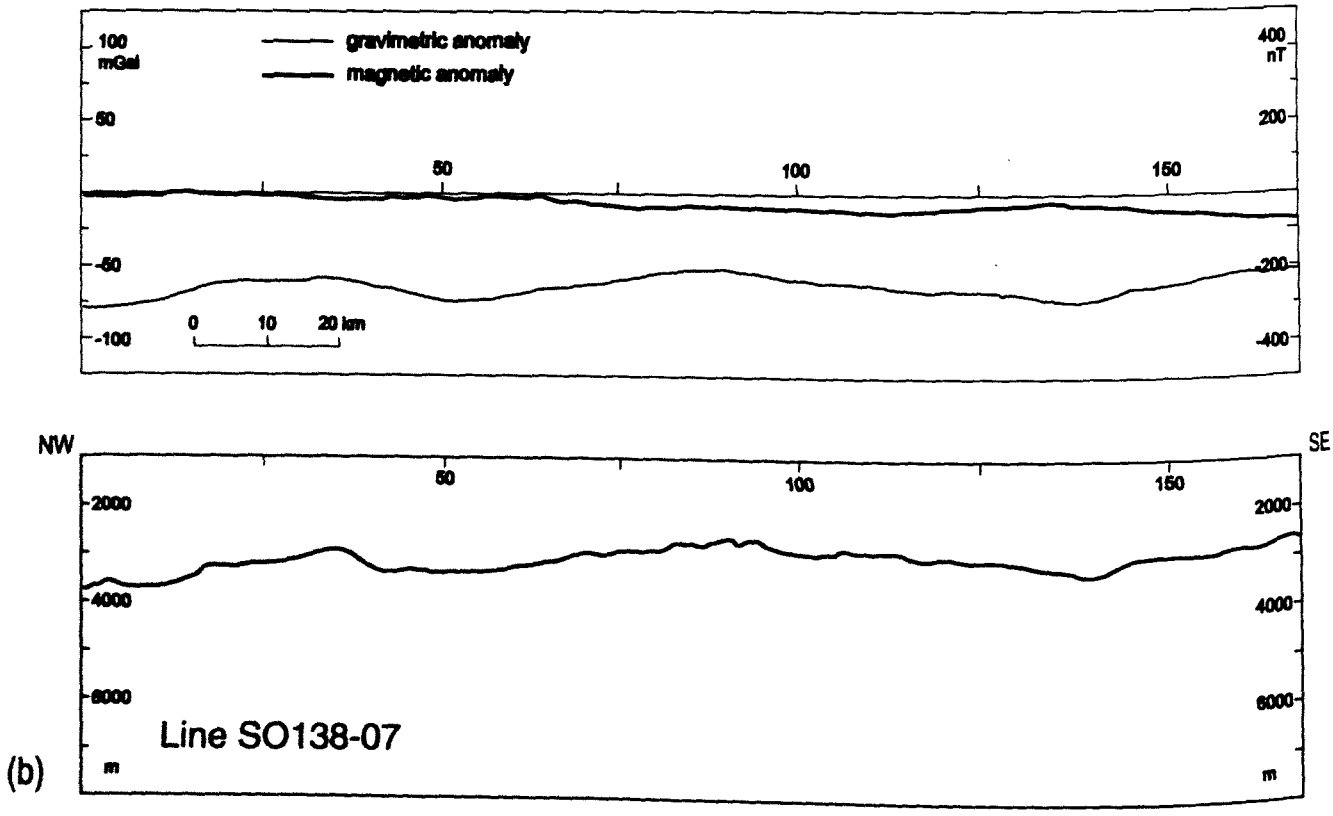

Figure 6.4.6: Potential field data combined with seafloor topography along seismic lines: (a) SO138-06 and (b) -07. Explanation see Figure 6.4.2.

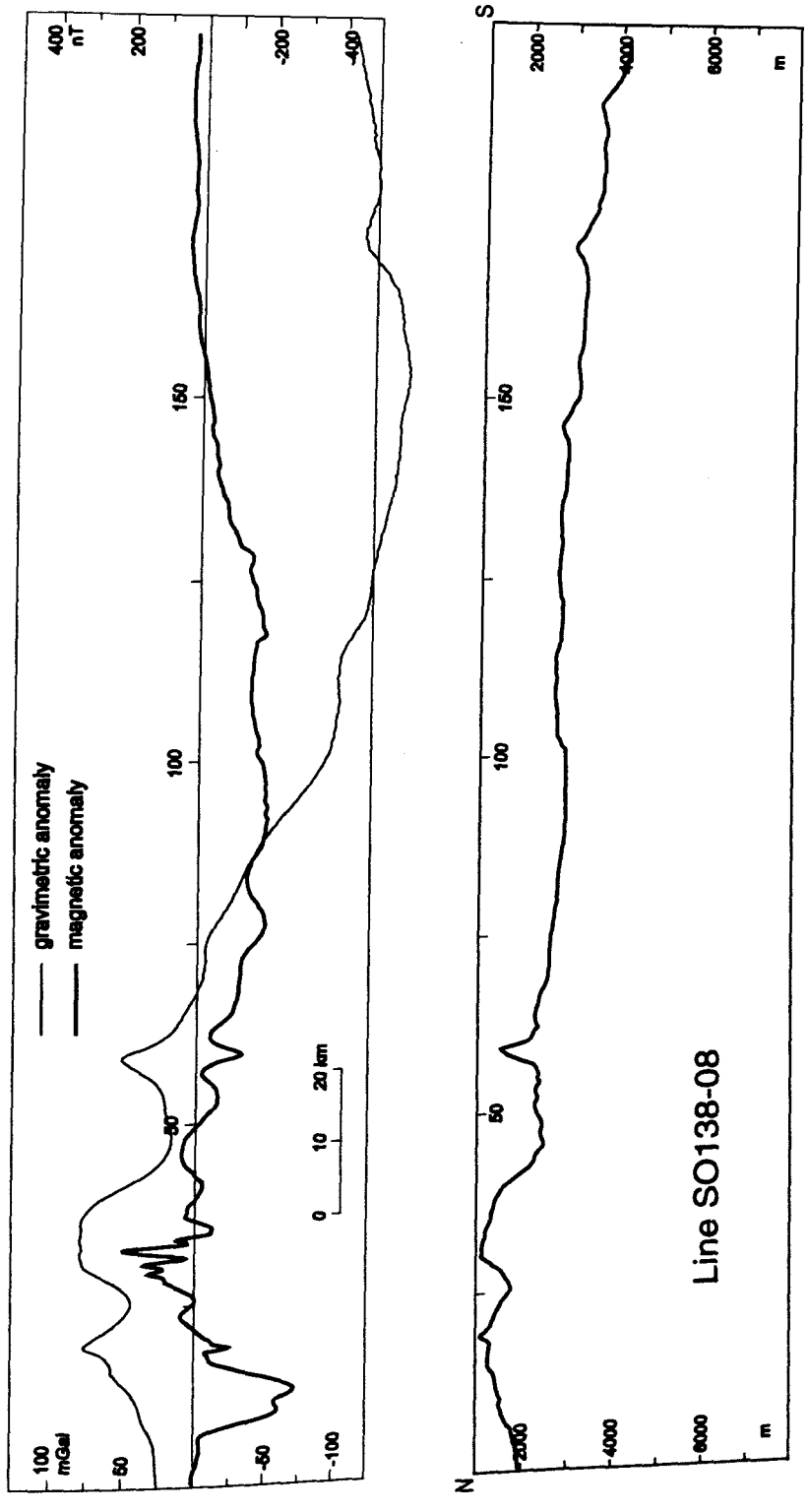

Figure 6.4.7: Potential field data combined with seafloor topography along seismic line SO138-08. Explanation see Figure 6.4.2.

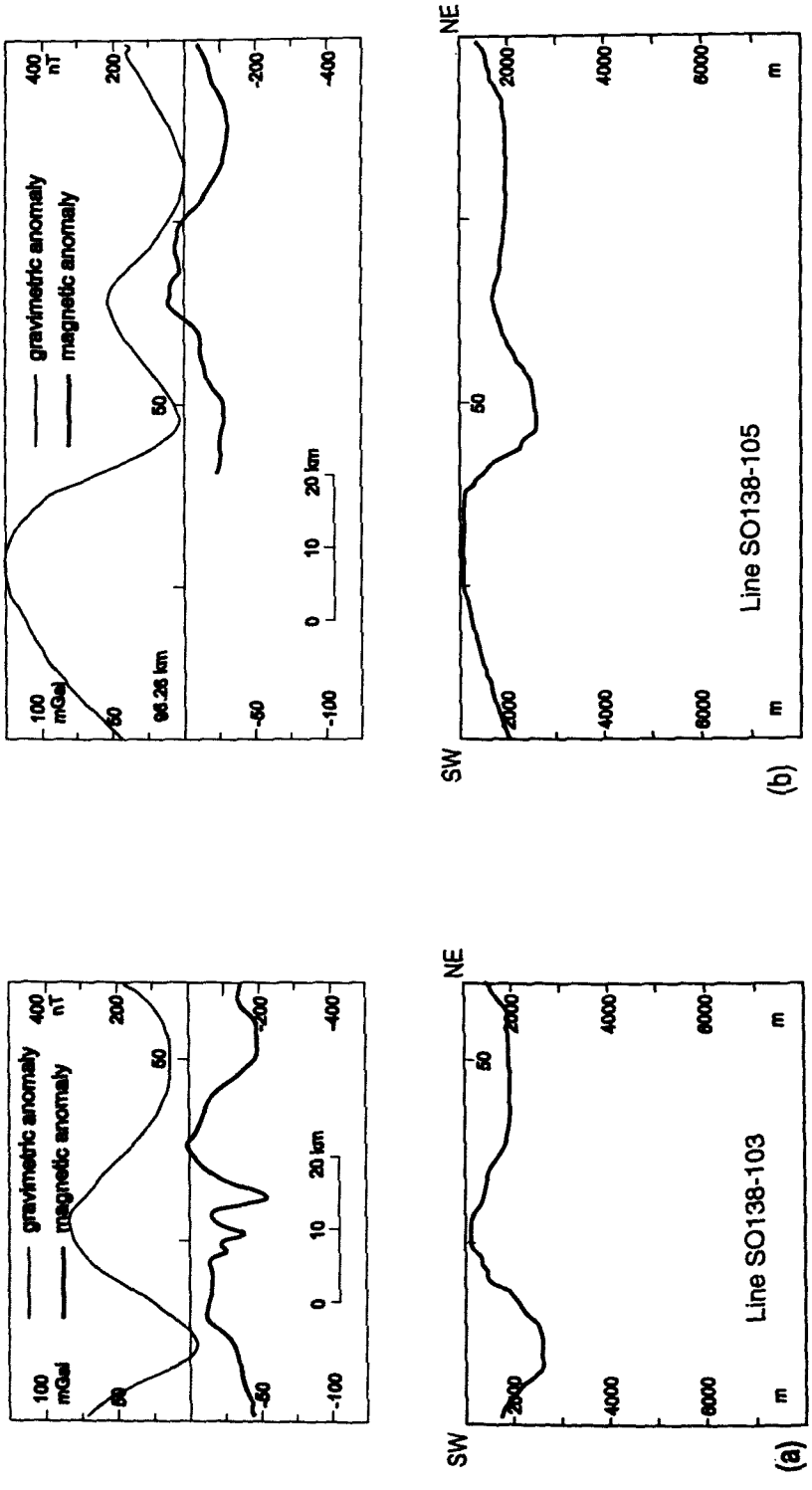

Figure 6.4.8: Potential field data combined with seafloor topography along selected lines in the Sunda Strait. (a) line SO138-103 and (b) line SO138-105. Explanation see Figure 6.4.2.

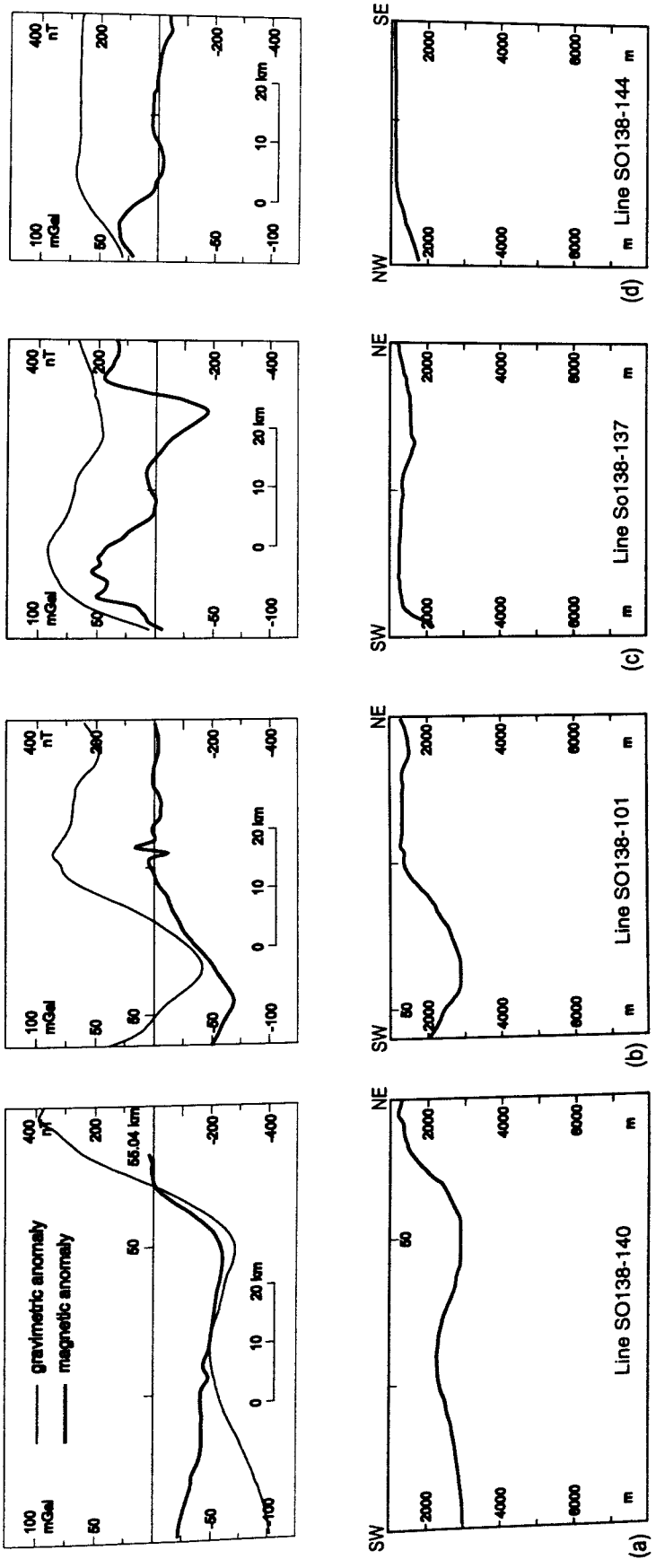

Figure 6.4.9: Potential field data combined with seafloor topography along selected lines in the Sunda Strait. (a) line SO138-140, (b) line SO138-101, (c) line SO138-137 and (d) line SO138-144. Explanation see Figure 6.4.2.

could be clearly identified as it is marked by a brass plate mentioning the AGSO station number.

All these connection measurements resulted in an average absolute gravity value of 979398.974 mGal (with water level –3.4 m, IGSN71) for point **B**. The water level was 3.4 m below the instrument during all measurements. From this the gravity value for the water level of 979399.880 mGal was calculated. The reading of the KSS31 at the leaving time (23.11.1998, 11:00 GMT) from the pier was –401.6 mGal.

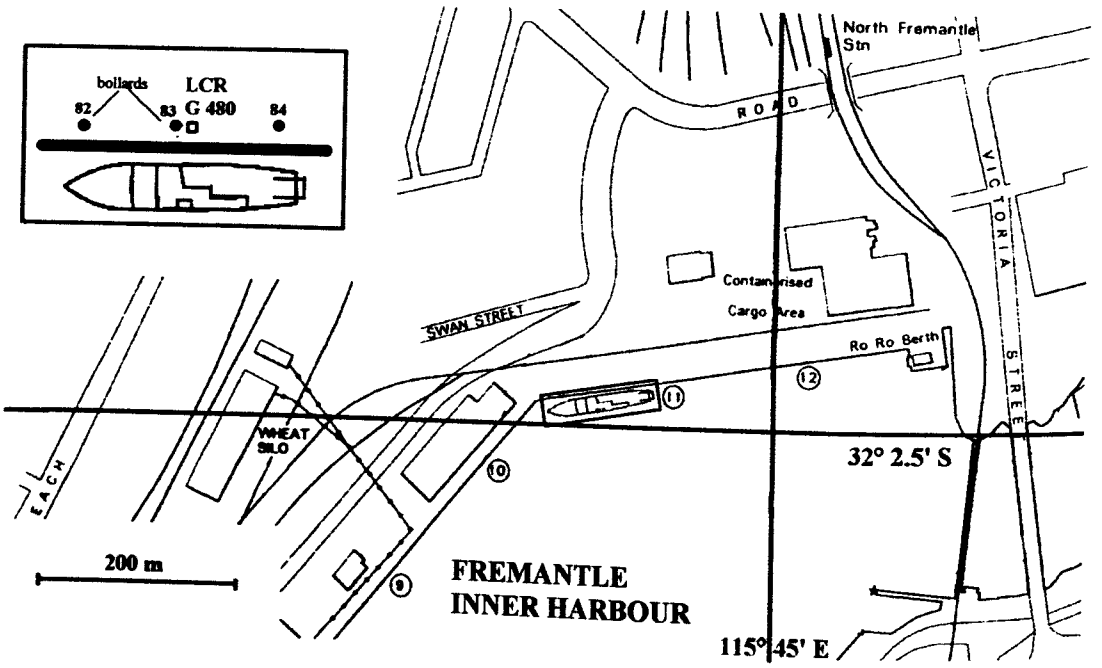

Fig. 6.4.1.1: Location of the mooring site of R.V. Sonne at berth 11 in the inner harbour of Fremantle (from the Admirality chart AUS 113 Port of Fremantle 1:7500). The inlet shows details of the gravity observation point near bollard 83 alongside R.V. SONNE.

Table 6.4.1.1: Observation report of the gravity tie measurements in Perth/Fremantle

Station	Date	Time GMT	Reading units	Measured value [mGal]	Tidal correction [mGal]	Drift correction [mGal]	Corrected gravity [mGal]
I							
A / S,K	18.11.98	06:40	2948.20	2995.328	+0.041	0 000	2995.369
01 / S,K	18.11.98	07:45	2970.66	3018.189	-0.015	+0.009	3018.183
02 / S,K	18.11.98	09:41	2962.67	3010.055	-0.079	+0.024	3010.000
A / S,K	18.11.98	12:39	2948.23	2995.358	-0.037	+0.048	2995.369
II							
A / S,K	19.11.98	02:02	2948.10	2995.218	+0.102	0.000	2995.320
03 / S,K	19.11.98	03:24	2956.34	3003.612	+0.148	-0.035	3003.725
A / S,K	19.11.98	04:05	2948.10	2995.218	+0.154	-0.052	2995.320
III							
A / S,K	20.11.98	23:28	2948.345	2995.468	-0.062	0.000	2995.406
B / S,H	21.11.98	04:11	2974.79	3022.390	+0.145	0.000	3022.535
B / S,H	21.11.98	04:41	2974.785	3022.390	+0.153	0.000	3022.543
04 / S,H	21.11.98	05:12	2978.85	3026.522	+0.155	0.000	3026.677
B / H	21.11.98	05:51	2974.79	3022.390	+0.148	0.000	3022.538
IV							
B / H	22.11.98	04:55	2974.82	3022.420	+0.142	0.000	3022.562
B / H	22.11.98	05:27	2974.84	3022.440	+0.149	-0.006	3022.583
04 / H	22.11.98	05:49	2978.885	3026.562	+0.149	-0.010	3026.701
03 / H	22.11.98	07:06	2956.275	3003.542	+0.126	-0.025	3003.643
B / H	22.11.98	07:34	2974.88	3022.480	+0.109	-0.027	3022.562

Observers: K = Kewitsch, S = Schreckenberger, H = Heyde
Gravity in mGal was calculated using LCR G 480 scaling table and scale constant BGR85/86 as 1.000447.

Reference Stations:

01: Hazelmer Store, Station 45715L AGSO 6091.0117 — 979394.583 mGal (IGSN71)
02: Perth-Airport, AGSO 9190.0317 — 979386.416 mGal (IGSN71)
03: Univ. of WA, Geology Building, Main Entrance, AGSO 7391.0417 — 979380.190 mGal (IGSN71)
04: Fremantle Port Authority, Main Entrance AGSO 9198.0617 — 979403.085 mGal (IGSN71)

Gravity stations:

A: Perth, Hotel Grand Chancellor, Entrance
B: Mooring site R.V. Sonne, Berth 11, bollard 83

Differences between reference/gravity stations

I: **A – 01** = -22.814 mGal
A – 02 = -14.631 mGal

01 – 02 = +8.183 mGal (own measurements)
= +8.167 mGal (according to AGSO values)

II: **A – 03** = -8.405 mGal

Absolute gravity at **A**: from difference to **01**: 979371.769 mGal
from difference to **02**: 979371.785 mGal
from difference to **03**: 979371.785 mGal

Absolute gravity at **A** (average): 979371.780 mGal

III: **B – A** = -27.129 / -27.137 / -27.132 mGal
B – 04 = -4.140 / -4.132 / -4.137 mGal

IV: **B – 04** = -4.139 / -4.118 / -4.139 mGal
B – 03 = +18.919 / +18.940 / +18.919 mGal

03 – 04 = +23.058 mGal (own measurements)
= +22.895 mGal (according to AGSO values)

Absolute gravity at **B**: from difference to **A**: 979398.912 mGal
from difference to **04**: 979398.948 mGal
from difference to **04**: 979398.928 mGal
from difference to **03**: 979399.109 mGal

Absolute gravity at **B** (average): 979398.974 mGal (with water level 0.00m)

Absolute gravity for **B** (reduced to water level –3.4 m) 979399.880 mGal (IGSN71 system) used for the gravity tie on 23.11.98 (11:00 GMT).

Reading of seagravimeter KSS31 at that time: -424.80 r.u. = -401.60 mGal
tidal corrected: –401.58 mGal
(scale factor 0.94542 mGal/r.u.)

On November, 29 R.V. Sonne moored in the harbour of Cilacap/Java at the General Goods Wharf. Measurements on the pier have been made with the LCR G480, but this point is not yet connected to the IGSN71 system. Hopefully we will get the absolute gravity value at this point, as tie measurements from a IGSN71 reference station in Bandung should be done by the Marine Geological Institue (MGI) in Bandung.

In the harbour of Tanjung Priok north of Jakarta, R.V. Sonne moored at shed 214 (Fig. 6.4.1.2) on December, 27 near the third bollard to the west from the north-east corner of the pier. The tie measurements where done about 50 cm to the Southeast of bollard no.3 (point **C**).

Table 6.4.1.2 gives the operation report from the mooring site to reference point **05** at Jakarta International Airport „Soekarno-Hatta", terminal B. This reference point was kindly provided by the Indonesioan National Coordination Agency for Surveys and Mapping (BAKOSUR-TANAL). Additionally a connection measurement to the mooring site **06** of R.V. Sonne at the end of cruise SO98/2 in 1994 was done.

Unfortunately the conditions for the measurements were quite bad. Especially the gravity stations in the harbour were noisy probably because of movements of the whole pier. But also the reference point at the airport was quite unstable.

For the calculation of the absolute gravity value at point **C**, only the difference to reference point **05** was used. The absolute gravity value results in 978146.350 mGal, when the water level is 1.7 m below the pier. From this the gravity value for the water level 0.0 m of 978146.803 mGal was calculated. The reading of the KSS31 on December, 27 (09:40 GMT) was –1654.94 mGal.

The instrumental drift can be derived from the readings in Fremantle and Tanjung Priok to –0.0064 mGal/day (-0.193 mGal/month). But as the reading values in Tanjung Priok and at reference station **05** were quite noisy no drift correction was applied to the data. Moreover, after the end of the cruise, we expect to take measurements at an additional reference point in Jakarta. With these measurement we hope to get the correct instrumental drift of the KSS31 over the whole period of cruises SO137 and SO138.

Leaving Tanjung Priok on December, 29 the reading of the KSS31 was –1654.70 mGal (08:35 GMT). Because this report had to be finished before the end of the cruise, it was not possible to calculate the instrumental drift from our second stay in Tanjung Priok. Experience shows that normally the drift is in the order of 1-2 mGal/month. So we conclude that the error of the measured gravity anomalies will have the same order of magnitude for a one month cruise. Final processing of the data including drift corrections will be made after the cruise.

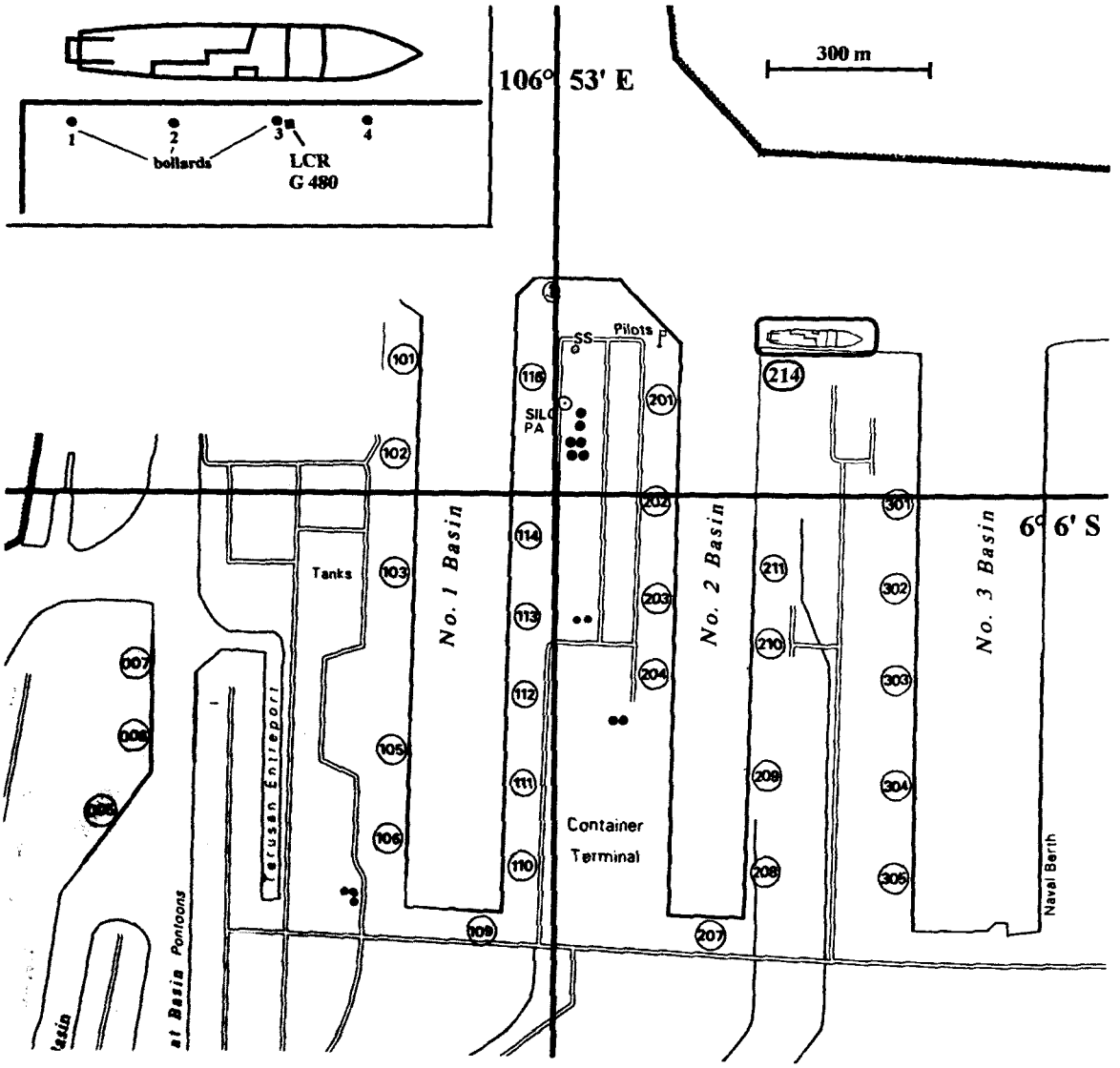

Fig. 6.4.1.2: Location of the mooring site of R.V. Sonne at shed 214 in the harbour of Tanjung Priok (from the Admirality chart 932 Tanjung Priok 1:12500). The inlet shows details of the gravity observation point near bollard 3 alongside R.V. SONNE.

Table 6.4.1.2: Observation report of the gravity tie measurements in Jakarta

Station	Date	Time GMT	Reading units	Measured value [mGal]	Tidal correction [mGal]	Corrected gravity [mGal]	sea level [m]
C / H	27.12.98	02:27	1743.75	1770.405	+0.065	1770.470	-1.5
C / K,H	27.12.98	07:16	1743.80	1770.456	-0.013	1770.443	-1.7
05 / K,H	27.12.98	07:50	1743.77	1770.425	0.000	1770.425	-1.2
06 / S,K	27.12.98	08:47	1734.97	1761.484	+0.032	1761.516	
A / S,K	27.12.98	09:40	1743.73	1770.385	+0.065	1770.450	-1.7

Observers: K = Kewitsch, H = Heyde
Gravity in mGal was calculated using LCR G 480 scaling table and scale constant BGR85/86 as 1.000447.

Reference Stations:

05: Jakarta, Airport Soekarno Hatta, Terminal B — 978137.441 mGal (IGSN71)

06: Jakarta, Tanjung Priok, shed 208, mooring site R.V. Sonne during SO-98/2 (1994) — 978146.540 mGal (IGSN71)

Gravity station:

C: Jakarta, Tanjung Priok, shed 214, mooring site R.V. Sonne

Differences between reference/gravity stations

(**C – 05** = +0.018 / +0.025 mGal)
C – 06 = +8.927 / +8.934 mGal

05 – 06 = +8.909 mGal (own measurements)
(= +9.095 mGal (according to SO98/2 measurements))

Absolute gravity at **C:** (from difference to **05**: 978146.562 mGal)
from difference to **06**: 978146.350 mGal

Absolute gravity at **C**: 978146.350 mGal (with water level –1.7 m)

Absolute gravity for **C** (reduced to water level 0.0 m) on 27.12.98 (9:40 GMT)
978146.803 mGal (IGSN71 system)

Reading of seagravimeter KSS31 at that time: -1654.94 mGal,
tidal corrected: –1654.875mGal
(scale factor 0.94542 mGal/r.u.)

Difference in absolute gravity from **B** to **C**: -1253.077 mGal (IGSN71)
in tidal corrected readings of
seagravimeter KSS31: -1253.295 mGal

instrumental drift: -0.218 mGal / 33.95 days = -0.0064 mGal/day

6.4.2 GRAVITY INTERPRETATION

(I. Heyde and B. Schreckenberger)

During the whole cruise about 8000 km of gravity profiles were measured with the seagravimeter. Considering also the about 7000 km of cruise SO137, thus altogether 15000 km of gravity profiles could be obtained. The seagravimeter is working continously and so gravity values are recorded along the complete track of the ship. Figure 2.3.1 shows the track and the profiles of cruise SO137, Figure 6.4.1 the track and the profiles of cruise SO138. The gravity value is recorded every 20 seconds as mentioned in section 5.4. Therefore around 230000 gravity values for both cruises are at hand. As well for the display as for the interpretation the filtered free-air anomalies provided by the KSS31 are taken. The quality of the data is very good. Even during sharp turns the data show little oscillations.

Although coverage of the survey area is not uniform, it is sufficient to present a map of the free-air gravity anomalies (Fig. 6.4.2.1). Isolines are drawn up to a distance of 20 nm from the run of the profiles. The values were gridded with a grid size of 2 min by 2 min. The isoline spacing comes up to 20 mGal. Positive anomalies are drawn with solid isolines, negative anomalies with dashed ones.

The gravity map is dominated by the anomalies of the main topographic features in the survey area (see Figs. 2.3.1 and 6.4.1). The oceanic crust in the SW is characterized by positive gravity values (0 to +40 mGal). The hypothesis of isostasy, however, demands that normal oceanic crust environment does not cause large free-air gravity anomalies. This is confirmed by worldwide observations of marine gravity. Free-air gravity anomalies oscillate around zero in morphologically undisturbed ocean areas. The positive gravity anomalies in this part of the survey area result from the influence of the bulge of the downgoing lithosphere. Additionally, there are topographic-high structures on the oceanic crust, as for example the Christmas Island complex, which result in an increase of the free-air gravity anomalies (106°E / 10°S).

The about 50 km wide zone of minima running from NW to SE bending towards SSE south of Java reflects the Sunda trench. Off Sumatra the values decrease to about –60 mGal, off Java down to about –80 mGal.

Landward in the area of the outer arc high, a zone of relative maxima follows. These positive anomalies reflect the decreasing water depth. Off Sumatra this zone is about 120 km wide, reaching its highest values of about +20 mGal NW of the island Enggano. Towards SE off the Sunda Strait this zone is only very slightly pronounced and reaches gravity values of -40 mGal only. South of Java values of –20 mGal are reached again, but the zone is only about 60 km wide.

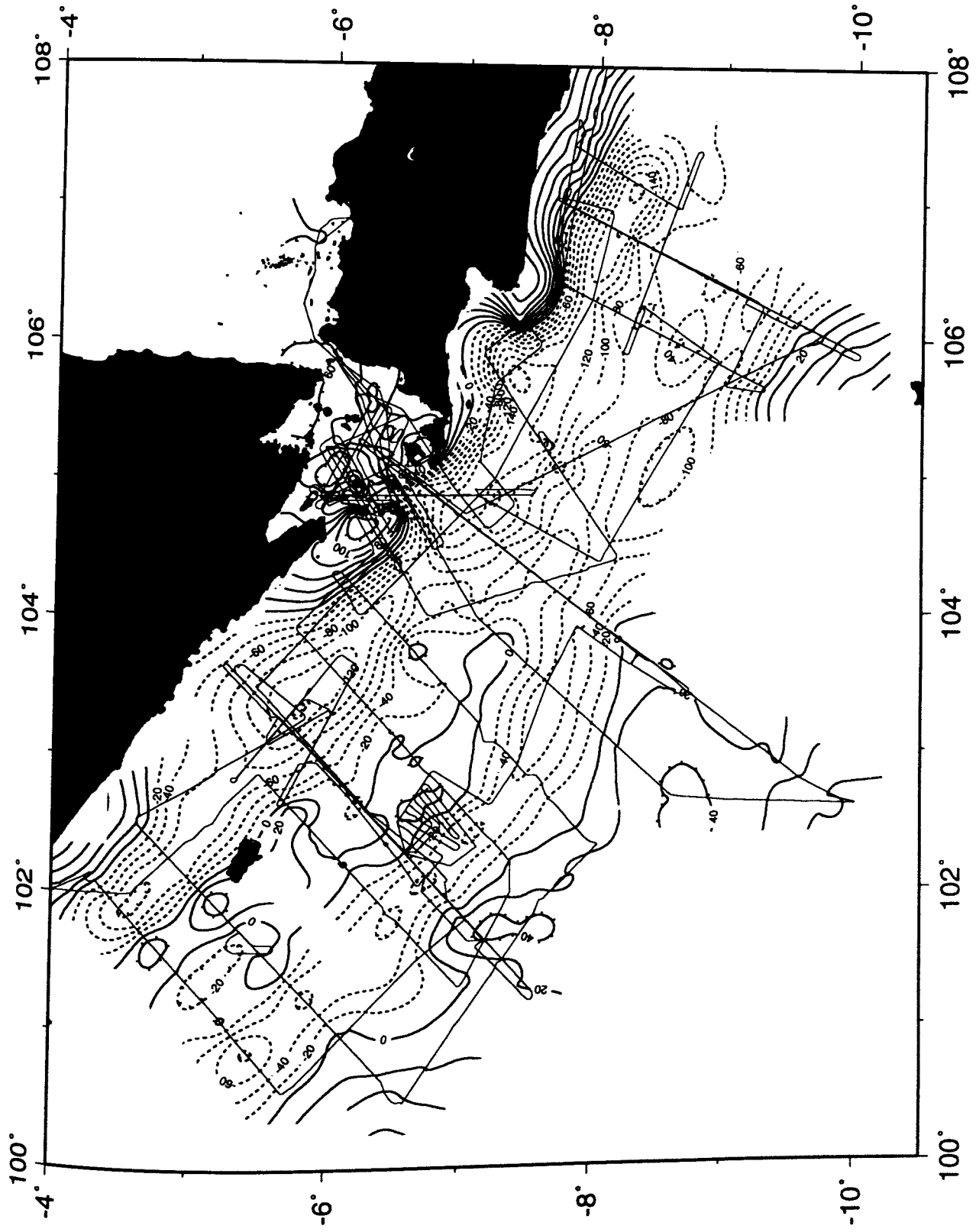

Figure 6.4.2.1: Free-air gravity anomaly map of the survey area of cruises SO137 and SO138. The survey track is marked. The isoline spacing is 20 mGal.

Further to the NE and to the N, respectively, the gravity map shows a minima zone parallel to the trench. These minima are caused by the forearc basin, filled with sediments of relatively low density. North of Enggano the values decrease to –80 mGal. SE of Enggano values of –140 mGal are reached within a basin. The lowest values have been found south of Java (-160 mGal).

Towards the islands the gravity values increase rapidly, whereby the gradient off Sumatra is much smaller (about +2 mGal/km) than off Java, where it reaches values of about +5 mGal/km. There the steep slope of the sea bottom from depths of 3000 m to less than 1000 m is reflected.

Isostatic anomalies over the trench and the arc would be probably large, too, and would exhibit the same polarity as the free-air gravity anomalies. These anomalies may result from the dynamic equilibrium imposed on the system by compression, so that the trench is forced down and the arc held up out of isostatic equilibrium by the forces driving the plates. Of course, further investigations are necessary.

Selected profiles

Only some of the profiles shown in Fig. 6.4.1 and listed in Appendices 9.2 and 9.3 are discussed in detail in the following. Fig. 6.4.2 shows the gravity and magnetic anomalies, together with the bathymetric data, along seismic profile SO138-01. This profile has a length of about 365 km and runs in SW-NE direction from the oceanic crust to the continental slope of Sumatra perpendicular to the Sunda trench. The profile thus crosses the main units of the subduction zone mentioned above. In order to interpret the data also quantitatively a 2D forward modelling of the gravity data has been carried out. Fig. 6.4.2.2 shows the resulting density model. This model considers both the results of the seismic refraction lines SO138-01,-02 and –03 and of the reflection seismic line SO137-12/12A.

Starting in the SW the oceanic crust (ρ=2.95 g/cm³) with a thickness of about 7 km is overlain by thin sediments (ρ=2.2 g/cm³, < 1 km) only. Below 13.5 km the upper oceanic mantle (ρ=3.37 g/cm³) follows. The maximum in the gravity values could be explained by the bathymetry and a slight thickening of the oceanic crust. Beginning at the trench the oceanic crust subducts gently with an angle of about 10°. The sedimental filling of the trench is not thicker than on the oceanic crust. The density of the rock units forming the accretionary wedge increases down- and eastward from 2.44 to 2.6 g/cm³. The unit in the E is named „oceanic splinter" according to the term used in the interpretation of the reflection seismics (see Fig. 2.3.3 and Reichert and the Shipboard Science Party, in prep.). However, the density is too low to be associated with massive oceanic crustal units. It can be stated only, that the density is higher than in the western part of the accretionary wedge. Small basins on the top of the wedge are filled with sediments of low density (ρ=2.2. g/cm³). The forearc basin is filled with about 3 km of sediments (ρ=2.3 g/cm³). The second sedimentary unit (ρ=2.45 g/cm³) is mainly introduced to consider the refraction seismic results. Below the sediments the continental crust (ρ=2.7 g/cm³) dipping towards SW is reached. This dipping boundary correlates with the seaward dipping reflectors found with reflection seismics (see Fig. 2.3.3 and Reichert and the Shipboard Science Party, in prep.) At a depth of 15 km the lower continental crust is reached and the continental Moho is situated at a depth of about 23 km.

Figure 6.4.2.3 shows the 2D-density model explaining the anomalies measured along seismic refraction line SO138-04. The location of this line corresponds to the one of reflection seismic profile SO137-42/A/B (see Fig. 2.3.1). The profile again runs perpendicular to the Sunda trench from the oceanic crust into the Sunda Strait crossing the elements of the subduction zone. The general built-up of the model is quite similar to the previous model. The oceanic crust is a little bit thicker. The main difference, however, is the composition of the accretionary wedge. The wedge itself is less wide and the transition to the forearc basin sediments seems to be more gradually. To explain the very steep gradient of the gravity anomalies towards the Sunda Strait, the edge of the continental crust should be very steep, too. It forms a little ridge, whereby a further sedimentary basin follows towards NE. The density of both basin sediments is rather low (ρ=2.2 g/cm^3).

Figure 6.4.2.4, finally, shows the 2D-density model along seismic refraction line SO138-05. This line corresponds to seismic reflection line SO137-03 and runs from the oceanic crust across the Sunda trench south of Java in SSW – NNE direction. The strong positive gradient seaward of the trench results from the decrease of water depth in this direction towards Christmas Island. The accretionary wedge consists of units with increasing density towards NNE (2.44 to 2.6 g/cm^3), similar to profile SO138-01 (Fig. 6.4.2.2). Again an oceanic splinter unit, covered by low density sediments, has to be considered. The following forearc basin is rather narrow, but filled with sediments to a depth of about 10 km. The transition to the continental crust is extremely steep.

Regarding the models it has to be said that they represent first approaches to explain the measured anomalies. The results of the refraction seismics were used, that means the found boundaries are mostly considered and their velocities are converted to density with a standard density-velocity relation (Ludwig et. al., 1970). But these results are preliminary only yet. Moreover the reflection seismic profiles are present until now as stacked time sections only. The results of depth migration would lead to improved density models, as according to the principle of equivalence the ambiguity would be reduced considerably with some fixed geometric structures. A further approach should be the combined interpretation of magnetic and gravity anomalies.

Gravity measurements in the Sunda Strait

The western part of the Sunda Strait was covered by a dense net of gravity profiles. In order to present the data, including many small scale features, more obvious, a detailed map of the free-air gravity anomalies in this region is given in Figure 6.4.2.5. The data were gridded with a smaller grid size of 0.5 min to 0.5 min. The isoline spacing comes up to 10 mGal. Again positive anomalies are drawn with solid isolines, negative anomalies with dashed ones.

Large positive gravity values correlate with the submarine continuation of the Semangka Peninsula. The gravity values found there (up to +130 mGal) represent the highest values in the whole survey area. East of this maximum a steep gradient leads to negative values corresponding to the Western Semangka Basin.

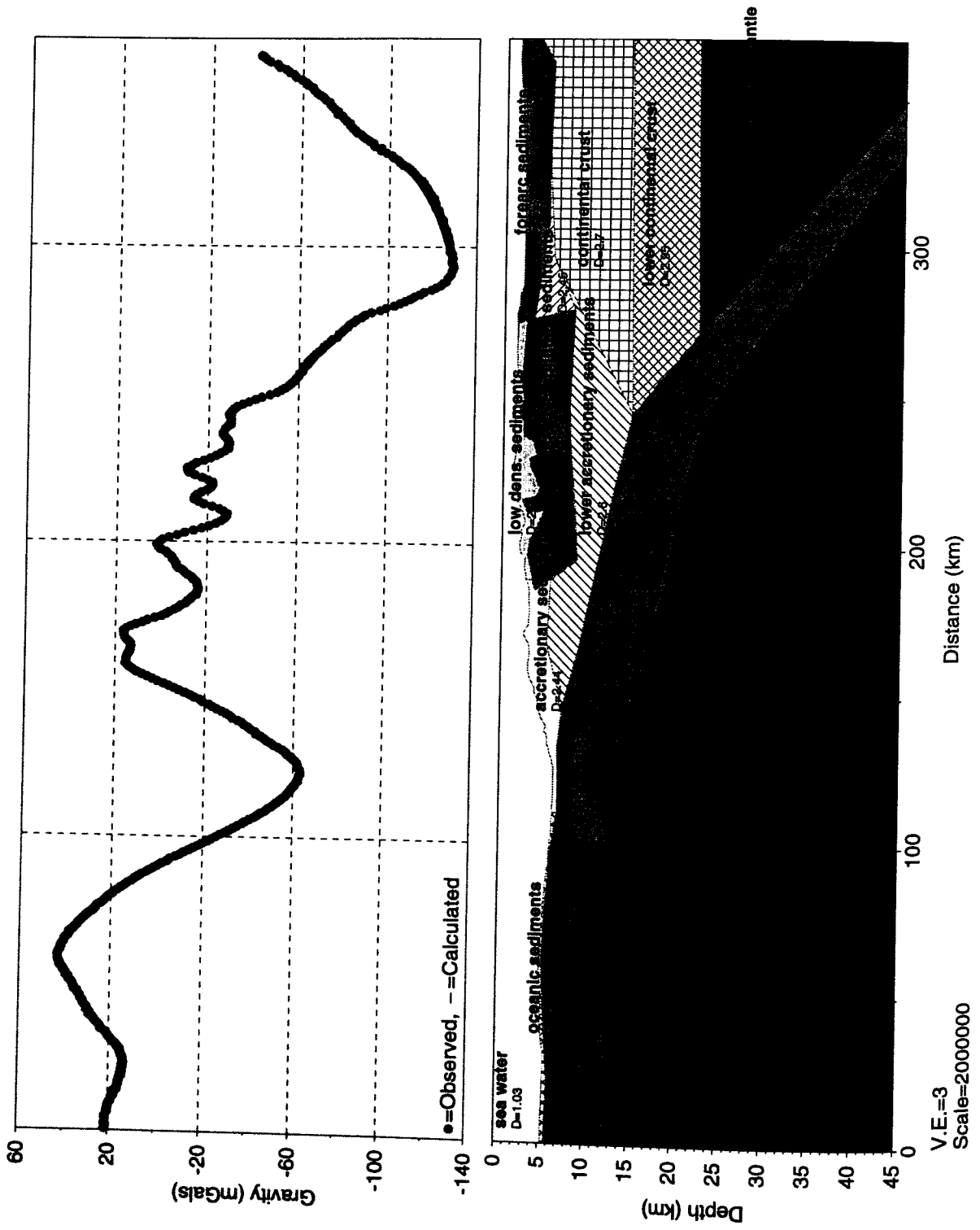

Figure 6.4.2.2: 2D density model explaining the free-air gravity anomalies along SO138-01. The observed anomalies are displayed as dots, the calculated ones as a line. Corresponding to the good fit this line is covered mostly by the dots of the observed anomalies. The density of the model units is given in g/cm³.

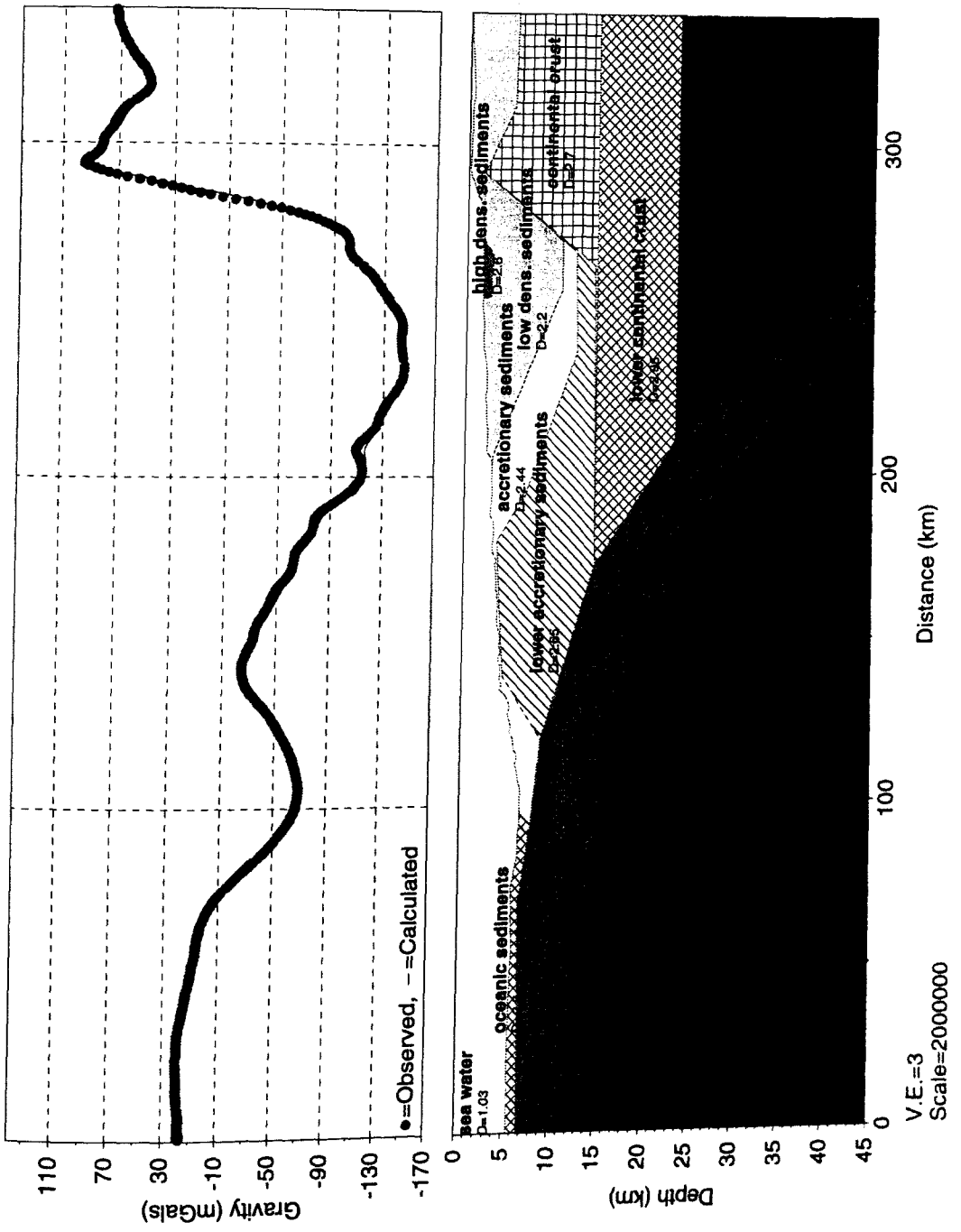

Figure 6.4.2.3: 2D density model explaining the free-air gravity anomalies along SO138-04. The observed anomalies are displayed as dots, the calculated ones as a line. Corresponding to the good fit this line is covered mostly by the dots of the observed anomalies. The density of the model units is given in g/cm³.

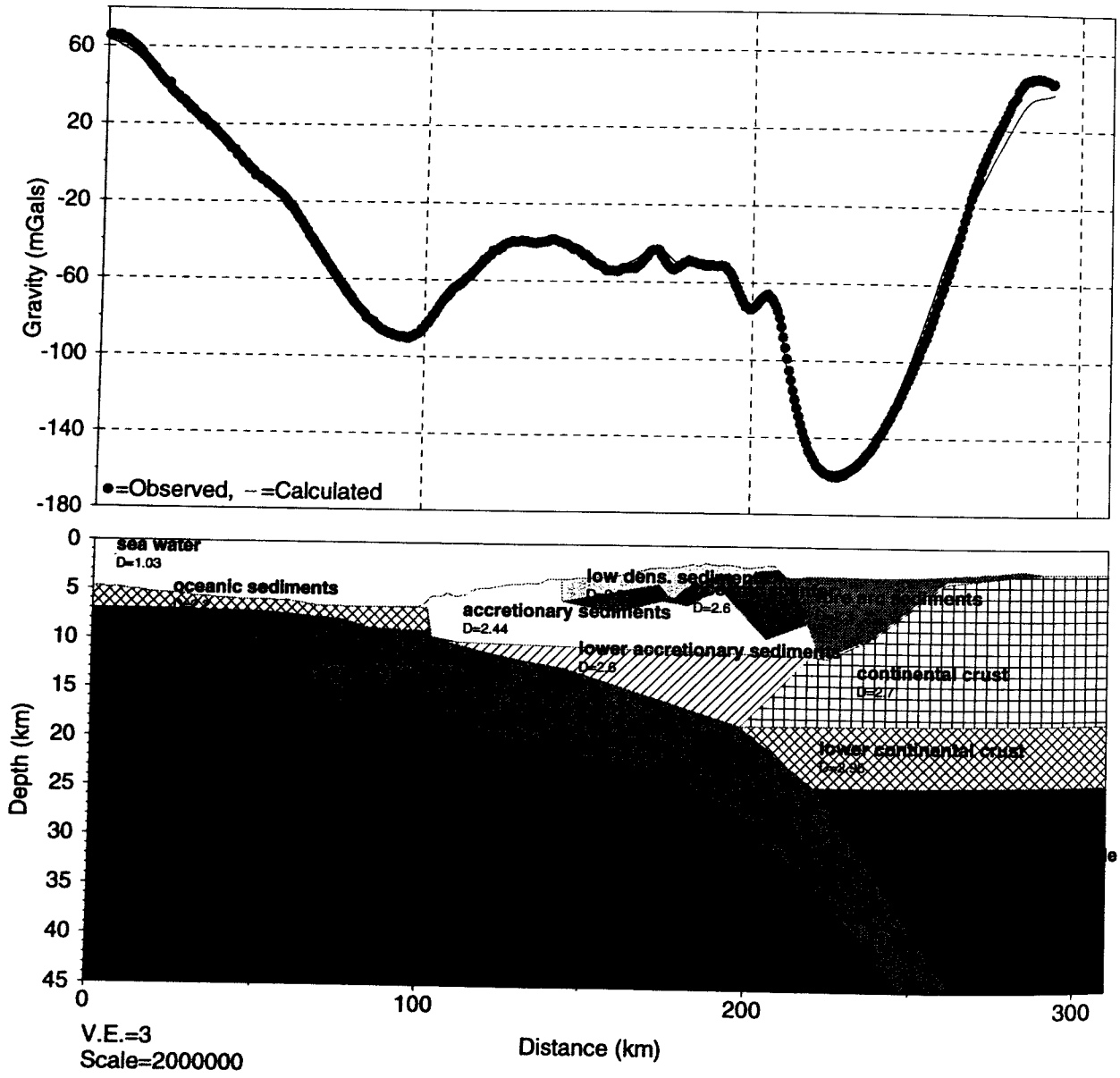

Figure 6.4.2.4: 2D density model explaining the free-air gravity anomalies along SO138-05. The observed anomalies are displayed as dots, the calculated ones as a line. Corresponding to

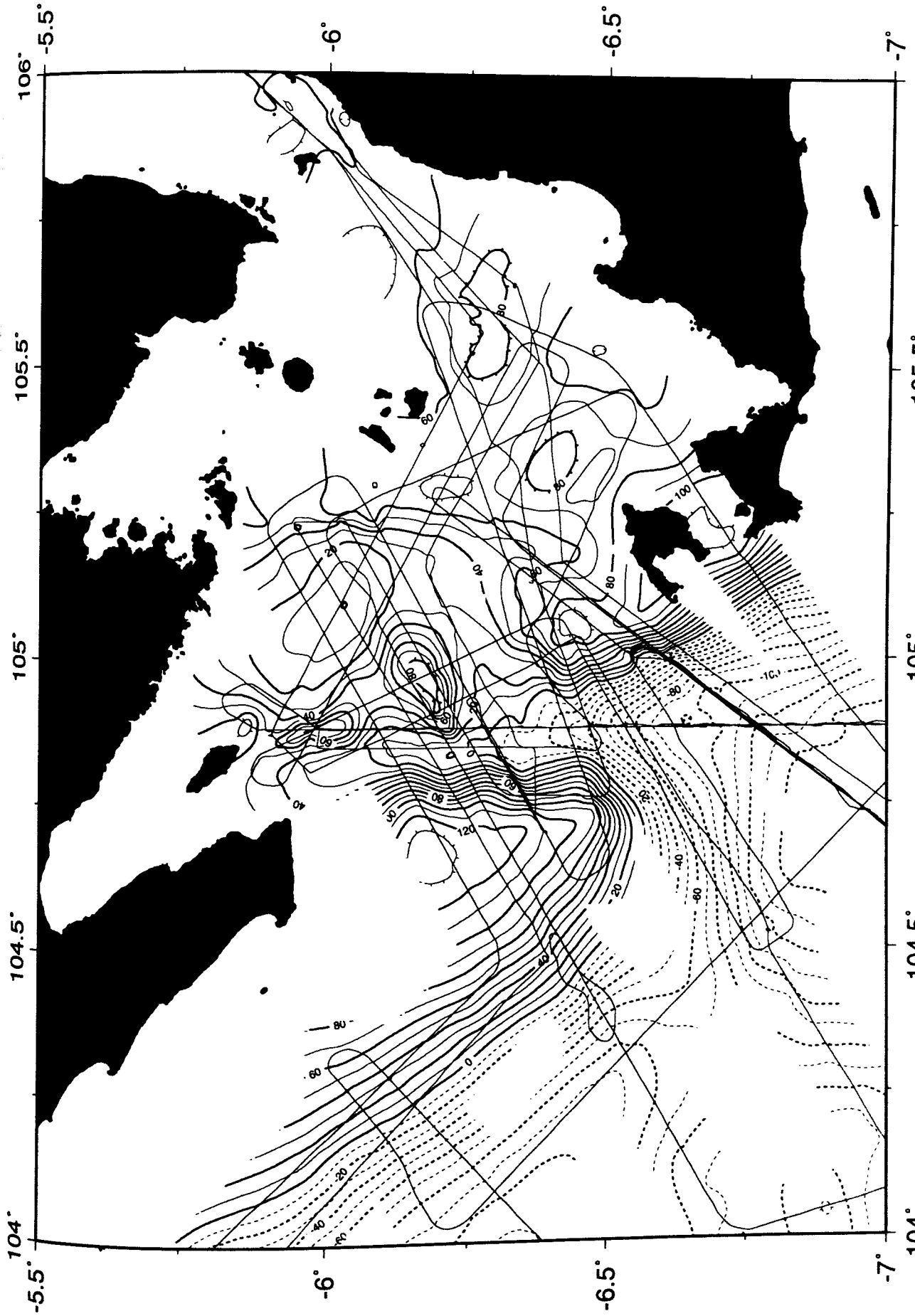

Figure 6.4.2.5: Free-air gravity anomaly map of the unda Strait area. The survey track is marked. The isoline spacing is 10 mGal.

Further to the East a chain of four areas with positive anomalies (+80 to +100 mGal) can be seen. All of them have a similar extent of about 15 km. The southermost area correlates with Panaitan island. This island is of volcanic origin, so also the other three may be interpreted as submerged volcanoes. Moreover, the northermost one was crossed by profile SO137-21 and in the reflection seismic section a submerged volcano could be seen, too (Reichert and the Shipboard Party, in prep.). The free-air gravity anomalies together with the magnetic anomalies and the bathymetry of two typical profiles crossing this area from SW to NE (lines SO138-103 and -105) are shown in Fig. 6.4.9. The assumed submerged volcano at profile km 25 or km 65, respectively, is associated as well with a gravity as with a magnetic anomaly.

Continuing in the eastern direction the water depth decreases continuously to values of about 30 to 50 m. In the map of the free-air anomalies two further maxima have been found. Possibly, they reflect volcanic units of higher density, as there is no significant change in the sea bottom topography in these regions. The Krakatau complex, however, seems not to be associated with positive gravity anomalies, as it would be expected. Possibly the profiles do not run close enough to these islands and no data were obtained North and Northeast of the complex anyway.

For the detailed interpretation of the free-air gravity anomalies in the Sunda Strait a 3D forward modeling should be performed. The anomalies could not be treated generally twodimensionally as it is mostly possible for the profiles crossing the Sunda trench. Moreover the data obtained during both cruises in the Sunda Strait represent an excellent database for detailed investigations combining the gravity results with the results of seismics, magnetics and bathymetry.

6.4.3 MAGNETIC INTERPRETATION

(B. Schreckenberger and I. Heyde)

Reconstruction of the magnetic anomaly

About 3160 km on the profiles were surveyed using the gradient magnetometer. For about 1210 km we deployed only one sensor. Mostly, the reason for not using the gradient magnetometer was the risk to interfere with fishery gear. In a few cases we had technical problems with one of the sensors.

The most simple method for the reconstruction of the magnetic field is the integration of the gradient in the space domain along the profile line. Another approach is the formulation of the problem in the frequency and in the wavenumber domain, respectively (Eilers et al., 1994). In this method the integration corresponds to a filter operation on the Fourier transform of the gradient. It provides a better insight into the problems of the reconstruction and can be combined with additional filter methods. For a first interpretation on board we used the simple integration/summation method in the space domain as well as a more sophisticated frequency method by Eilers et al. (1994).

However, our on board reconstructions showed that only very small short-period magnetic variations occured during the one month cruise. Therefore, the reconstructions did not improve the anomalies very much and we do not show the results here. The main source of

errors, visible as crossover errors, is due to long-period variations (probably diurnal variations). Theoretical considerations and experience with real data show, that the gradient method still has limitations with respect to long-wavelength anomalies, and land-based records of the variations will be needed even in the future. For this cruise, support from the Meteorological and Geophysical Agency in Jakarta, that runs the magnetic observatory Tangerang near Jakarta, could be obtained. We already received analog records of the declination and the horizontal and vertical intensity for most days of cruise SO-137. The records were digitized during this leg and they will be very helpful for the processing of the magnetic measurements. We will receive the variation records for leg SO-138 after the cruise in Jakarta. Therefore, the final processing of the magnetic data and the reconstruction of the magnetic anomalies from the gradient can only be done after the cruise.

Calculation of magnetic anomaly maps

The magnetic anomalies displayed in all figures of the report are the values from the master sensor of the magnetometer array after subtracting the appropriate reference field IGRF95 (IAGA, 1996) and an additional constant value of 100 nT which adjusts the anomalies to a level around zero. This value was determinated in the middle of cruise SO-137 by visual inspection of the anomalies. Although we calculated 83 nT as the mean of all magnetic measurements after removal of the IGRF95 reference field we kept the correction value of 100 nT because the arithmetic average of the magnetic anomalies is strongly influenced by strong negative anomalies in the NW part of our survey area (Fig. 6.4.3.1).

For the preparation of the magnetic anomaly map in Fig. 6.4.3.1 we used a gridding procedure (Wessel and Smith, 1991) to calculate a two minute grid of the anomalies from both cruises SO-137 and SO-138. In Fig. 6.4.3.1 only those parts from the grid are displayed (contoured) that have a maximum distance of 20 minutes from any profile line with magnetic measurements. In the case of magnetic anomalies this procedure is somewhat dubious when only a wide line spacing can be used. In the area over the accretionary wedge off Sumatra the line spacing is in the order of 30 nm, off Java it is even wider (Fig. 2.3.1 and Fig. 6.4.1.). Therefore, the map should be considered as very preliminary because we have a misbalance between the apparent wavelength in the direction of the lines (generally SW to NE) and in the direction of the strike of the trench. In the case of gravimetric anomalies the situation is less problematic because they usually have greater wavelengths (see Figs. 6.4.2 to 6.4.9.).

In the area of the Sunda Strait (Fig. 6.4.3.2) we have a denser coverage of profile lines and used a gridding interval of 0.5 minutes but due to the volcanic character of the area and the shallow source depth the anomalies contain much shorter wavelengths. Therefore, also here we are not able to display the full anomaly character and the anomalies displayed in Fig. 2.3.4 and Figs. 6.4.8 and 6.4.9 along the profile lines should always be taken into consideration for the interpretation of the anomaly map (Fig. 6.4.3.2).

Interpretation of the maps

In the preliminary magnetic map in Fig. 6.4.3.1 we recognize two areas with different amplitude character. Wide areas SW of the outer arc ridge have relatively smooth positive magnetic anomalies while north of the ridge strong anomalies of up to 250 nT strike from NW

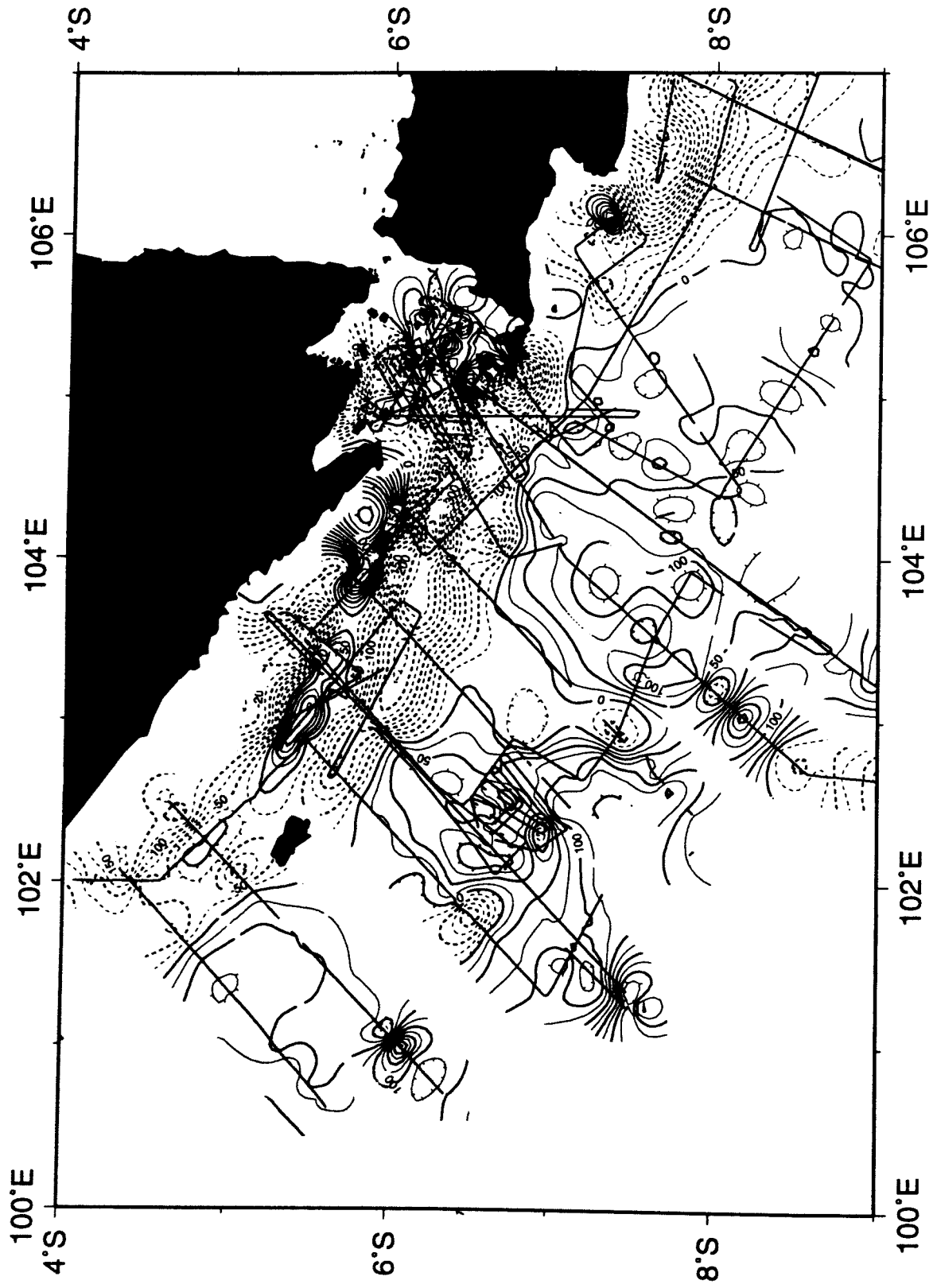

Figure 6.4.3.1: Magnetic anomaly map contoured from all data of cruises SO-137 and SO-138. Stippled contour lines denote negative anomalies, continuous contours positive anomalies in nT.

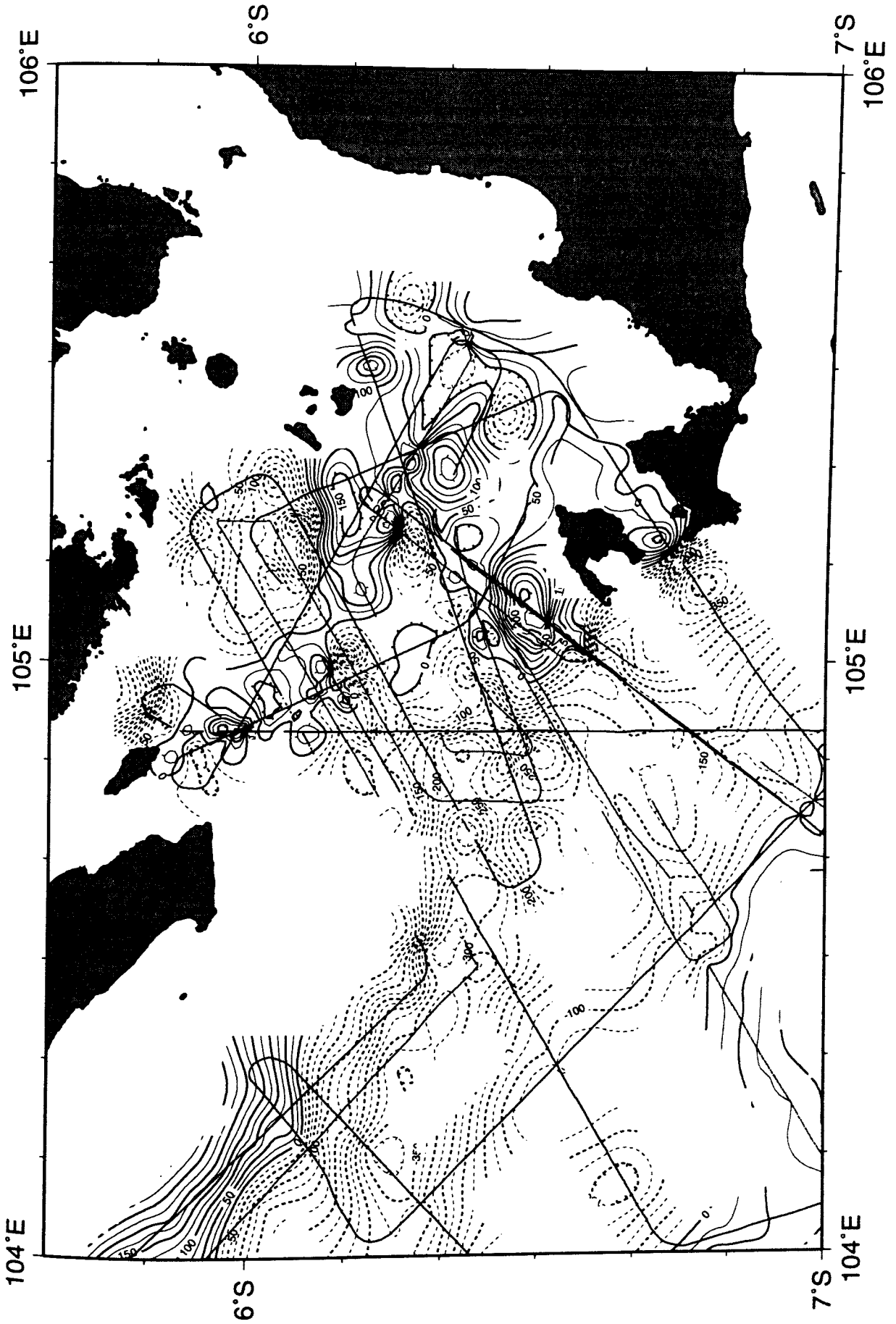

Figure 6.4.3.2: Magnetic anomaly map contoured from all data of cruises SO-137 and SO-138 in the area of the Sunda Street. Stippled contour lines denote negative anomalies, continuous contours positive anomalies in nT.

to SE. Isolated anomalies over the oceanic crust (e.g. at 6°S/101°E and 7.5°S/101.3°E) may represent seafloor-spreading anomalies 31 and 32 if we compare them with other sources like the magnetic map of East Asia by Ishihara et al. (1996) and the seafloor-spreading world map of Cande et al. (1989). From our data set we can not derive an independent determination of the age of the oceanic crust.

Landward of the outer arc ridge there is a wide low (stippled contour lines) which is more distinct east of the island Enggano (5.5°S/102.2°E). Between Enggano and the southernmost tip of Sumatra there is a strong positive anomaly within the low. The strike direction of the magnetic high is not parallel to the structural trends of the subduction zone, e.g. the forearc basin. Possible sources for that anomaly will be discussed below. The general trend of the anomalies across the subduction zone can be seen more clearly in Figs. 6.4.2, 6.4.3, 6.4.4 as well as in Fig. 2.3.2 and Fig. 2.3.3.

The magnetic map of the Sunda Strait (Fig. 6.4.3.2) also shows a magnetic low SW of the Sunda Strait. Two lines that run into the Sunda Strait NW and SE of the island Panaitan (6°40'S/105°10'E) display a steep increase from SW to NE just next to the island (SO138-04, Fig. 6.4.4) that suggests a volcanic origin of the corresponding bathymetric high. The geologic map of the Sunda Strait shows that Panaitan consists nearly entirely of volcanic rocks and we suggest that the bathymetric high (Fig. 6.4.1) on SO138-04 belongs to the same volcanic structure as Panaitan. On the other hand the anomaly may be part of a volcanic trend that runs from the Krakatau islands to the SW. An indication for that trend, that was also postulated in the literature (see chapter 2.2), are short-wavelength anomalies at 6°15'S/105°10'E. Also on the northern part of line SO137-39 (location see Fig. 2.3.1) we observe many small anomalies that indicate a volcanic trend. Because of a gap in the profile coverage it can not be decided whether the smooth zone at 6°20'S/105°00'E really interrupts the NNW-SSE trend that also points to Panaitan.

A MAGNETIC MODEL FOR LINE SO138-01

On all reflection seismic lines that cross the structures related to the subduction process off Sumatra we observed very similar features. Of special interest for the magnetic modeling is the subducting oceanic crust, the inferred oceanic crustal splinter under the outer arc high and the edge of the continental crust including the inferred seaward-dipping reflector sequence (SDRS) (see chapter 2.3, Figs. 2.3.2 and 2.3.3).

Here we present a magnetic model (Fig. 6.4.3.3) that is based on seismic reflection line SO137-12 and on line SO138-01 (Fig. 6.4.2) from this cruise. The model is different from the gravity model in Fig. 6.4.2.2. It was made to fit the magnetic anomaly and gives only a coarse fit to the free air anomaly. All bodies that have a remanent or induced magnetization are shaded, dark shading represents normal remanent magnetization ('Oceanic crust', 'Dipp2' and 'Crustal rock'), lighter shading reversed remanent magnetization ('Old oceanic crust' and 'Dipp1') and light shading induced magnetization ('Upper cont. crust' and 'Lower cont. crust').

The oceanic crust was modeled as a plate with constant magnetic polarity and does not contribute very much to the model anomaly. In order to fit the strong magnetic amplitudes over the NE part of the profile, the basement of the continental crust and its SW continuation

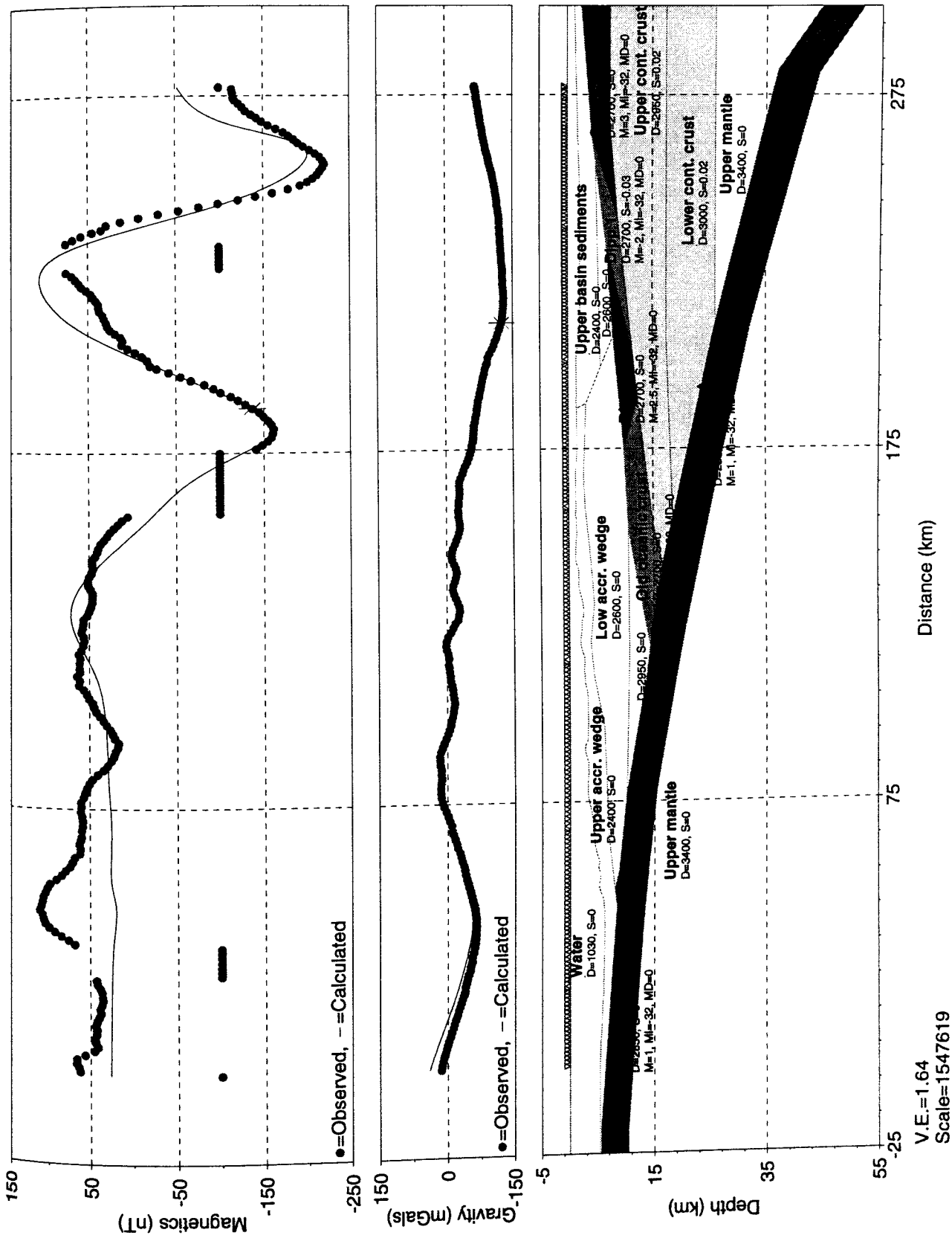

Figure 6.4.3.3: Magnetic (and gravimetric) model calculation for reflection seismic line SO138-12 and refraction line SO138-01, respectively. Labels below the names of the rock

under the forearc ridge contains strong magnetization intensities. The bodies denoted as 'Dipp1' and 'Dipp2' in Fig. 6.4.3.3 represent the dipping reflector unit identified in the reflection seismic section of SO137-12. 'Dipp2' is coincident with the seismic units but 'Dipp1' is not represented by distinct reflections. SDRS are known from many passive continental margins. They represent basalt flows that were emplaced subaerially during the breakup of continental lithosphere or during the initial stages of seafloor-spreading. Schreckenberger (1997) showed that they cause strong magnetic anomalies at various places.

There are indications (mainly from the magnetic map of East Asia by Ishihara (1996)) that the continental crust of southern Sumatra in the area of line SO138-01 is the source of strong magnetic anomalies. Therefore, we used a remanent magnetization of 3 A/m for the 'Crustal rock' unit in the model. This magnetization indicates the occurrence of basic volcanic rocks along the coast of Sumatra. Also the units 'Dipp1' and 'Dipp2' can be viewed as indications of volcanic phases that emplaced basic rocks that were magnetized at times of changing polarities of the magnetic field of the earth. Whether the unit 'Old oceanic crust' really represents a remnant of an old passive margin in the seaward continuation of the SDRS is very speculative.

The induced magnetization (0.02 SI units, equivalent to about 0.75 A/m) of the 'Upper cont. crust' and 'Lower cont. crust' units are necessary to fit the negative level of the observed anomaly in the NE of the profile compared with the slightly positive level in the SW.

The problem that the oceanic crustal splinters (Figs. 2.3.2 and 2.3.3) obviously do not cause a magnetic anomaly could not be solved with the model in Fig. 6.4.3.3. More detailed investigations will be necessary in order to estimate an upper limit for the magnetization of these structures. From comparison of all lines that cross the outer arc high it is still unlikely that they have a remanent magnetization typical for oceanic crust.

under the forearc ridge contains strong magnetization intensities. The bodies denoted as 'Dipp1' and 'Dipp2' in Fig. 6.4.3.3 represent the dipping reflector unit identified in the reflection seismic section of SO137-12. 'Dipp2' is coincident with the seismic units but 'Dipp1' is not represented by distinct reflections. SDRS are known from many passive continental margins. They represent basalt flows that were emplaced subaerially during the breakup of continental lithosphere or during the initial stages of seafloor-spreading. Schreckenberger (1997) showed that they cause strong magnetic anomalies at various places.

There are indications (mainly from the magnetic map of East Asia by Ishihara (1996)) that the continental crust of southern Sumatra in the area of line SO138-01 is the source of strong magnetic anomalies. Therefore, we used a remanent magnetization of 3 A/m for the 'Crustal rock' unit in the model. This magnetization indicates the occurrence of basic volcanic rocks along the coast of Sumatra. Also the units 'Dipp1' and 'Dipp2' can be viewed as indications of volcanic phases that emplaced basic rocks that were magnetized at times of changing polarities of the magnetic field of the earth. Whether the unit 'Old oceanic crust' really represents a remnant of an old passive margin in the seaward continuation of the SDRS is very speculative.

The induced magnetization (0.02 SI units, equivalent to about 0.75 A/m) of the 'Upper cont. crust' and 'Lower cont. crust' units are necessary to fit the negative level of the observed anomaly in the NE of the profile compared with the slightly positive level in the SW.

The problem that the oceanic crustal splinters (Figs. 2.3.2 and 2.3.3) obviously do not cause a magnetic anomaly could not be solved with the model in Fig. 6.4.3.3. More detailed investigations will be necessary in order to estimate an upper limit for the magnetization of these structures. From comparison of all lines that cross the outer arc high it is still unlikely that they have a remanent magnetization typical for oceanic crust.

7. ACKNOWLEDGEMENTS

Cruise SO 138 was funded by the German Ministery of Education, Research, Science, and Technology (BMBF) under project No. 03 G 0138 to GEOMAR and BGR within the continued and generous most commendable support for marine sciences with an outstanding research vessel such as SONNE. The travel expenses of the BGR staff for SO138 were funded by the BGR budget.

We warmly thank master H. Papenhagen and his crew for their excellent support in all work done and for the splendid working atmosphere throughout the entire cruise in spite of sometimes adverse weather conditions and the ambitious working program.

8. REFERENCES

Arifin, L., Okuda, Y., Yokokura, T., Kisimoto, K., Hakim, S., and Tamaki, K., 1987: Seismic Reflection of the Sunda Trench in Western Java, CCOP Technical Bulletin, 19, 13-23.

Audley-Charles, M.G.: Evolution of the southern margin of Thethys (North Australian region) from early Permian to late Cretaceous, in: Audley-Charles, M.G., and Hallam, A. (eds), Gondwana and Thethys, Geological Society Special Publication 37, 79-100.

Audley-Charles, M., Ballantyne, P.D., and Hall, R., 1988: Mesozoic-Cenozoic rift-drift sequence of Asian fragments from Gondwanaland, Tectonophysics, 155, 317-330.

Beaudry, D., and Moore, G.F., 1981: Seismic stratigraphic frame work off Central Sumatra, Earth and Planetary Science Letters, 54, 17-28.

Beaudry, D., and Moore, G.F., 1985: Seismic stratigraphy and cenozoic evolution of West Sumatra forearc basin, AAPG Bulletin, 69, 5, 742-759.

Beck, M.E., 1983: On the mechnism of tectonic transport in zones of oblique subduction, Tectonophysics, 93, 1-11.

Bellier, O., and Sébrier, M., 1994: Relationship between tectonism and volcanism along the Great Sumatran Fault zone deduced by SPOT image analyses, Tectonophysics, 233, 215-231.

Bellier, O., and Sébrier, M., 1995: Is the slip rate variation on the Great Sumatran Fault accommodated by fore-arc stretching?, Geophysical Research Letters, 22, 15, 1969-1972.

Ben-Avraham, Z., and Zobacu, M.D., 1992: Transform-normal extension and asymmetric basins: An alternative to pull-apart models, Geology, 1992, 20, 423-426.

Burbridge, D.R., and Braun, J., 1998: Analogue models of oblique convergent continental plate boundaries, Journal of Geophysical Research, 103, 7, 15221-15237.

Burrett, C., 1974: Plate tectonics and the fusion of Asia, Earth and Planetary Science Letters, 21, 181-189.

Burrett, C., and Stait, B., 1985: South East Asia as a part of an Ordovician Gondwanaland--a paleobiogeographic test of a tectonic hypothesis, Earth and Planetary Science Letters, 75, 184-190.

Camus, G., Gourgaud, A., and Vincent, P.M., 1987: Petrologic evolution of Krakatau (Indonesia): Implications for a future activity, Journal of Volcanology and Geothermal Research, 33: 299-316.

Camus, G., Diament, M., Gloaguen, M., Provost, A., and Vincent, P., 1992: Emplacement of a Debris Avalanche during the 1883 Eruption of Krakatau (Sunda Straits, Indonesia), GeoJournal, 28, 2, 123-128.

Cande, S.C., LaBrecque, J.L., Larson, R.L., Pitman III, W.C., Golovchenko, X., and Haxby, W.F., 1989: Magnetic lineations of the world's ocean basins, LDGO contribution 4367, AAPG, Tulsa, Oklahoma.

Caress, D.W., and D.N.Chayes, 1996: Improved processing of Hydrosweep DS Multibeam data on the R/V Maurice Ewing Marine Geophysical Researches 18, 631-650

Cardwell, R.K., and Isacks, B.L., 1978: Geometry of the subducted lithosphere beneath the Banda Sea in eastern Indonesia from seismicity and fault plane solutions, Journal of Geophysical Research, 83, 2825-2838.

Charlton, T.R., 1991: Postcollisional extension in arc-continent collision zones, eastern Indonesia, Geology, 19. 28-31.

Cloetingh, S., and Wortel, R., 1985: Regional Stress field of the Indian Plate, Geophysical Research Letters, 12. 1, 77-80.

Curray, J.R., Shor, G.G.Jr., Raitt, R.W., and Henry M., Seismic refraction and reflection studies of crustal structure of the Eastern Sunda and Western Banda arcs, Journal of Geophysical Research, 82, 17, 2479-2489.

Curray, J.R., 1989: The Sunda Arc: A model for oblique plate convergence, Netherlands Journal of Sea Research, 24, 131-140.

Daly, M.C., Cooper, M.A., Wilson, I., Smith, D.G., and Hooper, B.G.D., 1992: Cenozoic plate tectonic and basin evolution in Indonesia, Marine and Petroleum Geology, 8, 2-21.

Dardji, N., Villemin, T., and Rampnoux, J.P., 1994: Paleostresses and strike-slip movement: the Cimandiri Fault Zone, West Java, Indonesia, Jounal of Southeast Asian Earth Sciences, 9, 1/2, 3-11.

De Mets, Gordon, R. G., Argus, D. F., and Stein, S., 1990: Current plate motions, Geophysical Journal International, 101, 425-478.

Deplus, C., Bonvalot, S., Dahrin, D., Diament, M., Harjono, H., and Dubois, J., 1995: Inner structure of the Krakatau volcanic complex (Indonesia) from gravity and bathymetry data, Journal of Volcanology and Geothermal Research, 64, 23-52.

Diament, H., 1992: Mentawai fault zone off Sumatra: A new key to the geodynamics of western Indonesia, Geology, 20, 259-262.

Eilers, G., Roeser, H.A. and Kewitsch, P., 1994: Die Reduktion geomagnetischer Variationen bei seemagnetischen Messungen durch ein Gradientenmagnetometer. BGR-Report, 73 S., Hannover

Eva, C., Catianeo, M., and Merlanti, F., 1988: Seismotectonics of the Central segment of the Indonesian Arc, tectonophysics, 146, 241-259.

Fitch, T.J., 1972: Plate convergence, transcurrent faults and internal deformation adjacent to Southeast Asia and the Western Pacific, JGR, 77: 4432-4460.

Fitch, T.J., 1970: Earthquake mechanisms and island arc tectonics in the Indonesian-Philippine region, Bulletin of the Seismological Society of America, 60, 2, 565-591.

Flueh, E. R, and R. von Huene, 1994: Fahrtbericht SO96 KODIAK-SEIS, GEOMAR-Kiel.

Francis, P., and Self, S., 1983: The Eruption of Krakatau, Scientific American, 249, 173-187.

Fujinawa, Y., Ukawa, M., Eguchi, T., Sudarmo, R.P., and Robertus, U.M., 1987: Seismic observation by a pop-up type OBS array and a portable seismometer on land in and around the southwestern part of the Java island, CCOP Technical Bulletin, 19, 107-118.

Ganie, B., Syafuddin, Superman, A. and Honza, E., 1987: Geomorphological features in the eastern Sunda Trench, CCOP Technical Bulletin, 19, 7-12.

Gasparon, M., and Varne, R., 1995: Sumatran granitoids and their relationship to Southeast Asian terranes, Tectonophysics, 251, 277-299.

Ghose, R., and Oike, K., 1988: Characteristics of Seismicity Distribution along the Sunda Arc: Some New Observations, Bulletin of the Disaster Prevention Research Institute, Kyoto University, 38, 2, 29-48.

Ghose, R., Yoshioka, S., and Oike, K., 1990: Three-dimensional numerical simulation of the subduction dynamics in the Sunda arc region, Southeast Asia, Tectonophysics, 181, 223-255.

Hall, R., and Blundell, D.J., 1996: Tectonic evolution of SE Asia: introduction, in: Tectonic Evolution of Southeast Asia, R. Hall (edt), Geological Society of London Spec. Publication 106 vii-xiii.

Hall, R., 1996: Reconstructing Cenozoic SE Asia, in: Tectonic Evolution of Southeast Asia, R. Hall (edt), Geological Society of London Spec. Publication 106, 153-184.

Hamilton, E.L., 1977: Sediment velocity from sonobuoys: Bengal fan, Sunda Trench, Andaman Basin and Nicobar Fan, JGR, 1977, 82, 3003-.

Hamilton, W.B., 1979: Tectonics of the Indonesian Region, USGS Professional Paper, 1078.

Hamilton, W.B., 1988: Plate tectonics and island arcs, Geological Society of America Bulletin, 100, 1503-1527.

Hamilton, W.B., 1995: Subduction systems and magmatism, in: Smellie, J.L. (ed.), Volcanism Associated with Extension at Consuming Plate Margins, Geological Society Special Publication 81, 3-28.

Harjono, H., Diament, M., Dubois, J., Larue, M. and Zen, M.T., 1991: Seismicity of the Sunda Strait: Evidence for crustal extension and volcanological implications, Tectonics, 10, 17-30.

Harjono, H., and Tjokrosapoetros, S., 1986: Geological evolution of the Indonesian Archipelago, Geological Society of Malaysia Bulletin, 20, 97-136.

Harjono, H., Diament, M., Nouaili, L., and Dubois, J., 1989: Detection of magma bodies beneath Krakatau volcano (Indonesia) from anomalous shear waves. Journal of Volcanology and Geothermal Research, 39, 335-348.

Hawkins, J.W., Bloomer, S.H., Evans, C.A., and Melchior, J.T., 1984: Evolution of intra oceanic arc-trench systems. Tectonophysics, 102, 175-205.

Honza, E., Ganie, B.M., 1987: Japan-Indonesia Cooperative Survey in the Sunda Forearc. CCOP Technical Bulletin, 19, 1-5.

Honza, E., Joshima, M., Setiya Budhi, A, and Nishimura, A., 1987: Sediments and rocks in the Sunda forearc, CCOP Technical Bulletin, 19, 63-67.

Honza, E., and Ganie, B.M., 1987: Formation of accretionary wedge in the Eastern Sunda Trench, CCOP Technical Bulletin, 19, 119-124.

Huchon, P., and Le Pichon, X., 1984: Sunda Strait and central Sumatra fault, Geology,12, 668-672.
Hutchinson, C.S., 1989: Geological Evolution of South-East Asia, Claredon Press, Oxford.
IAGA Division V, Working Group 8, 1996: International geomagnetic reference field, 1995 revision, Geophys. J. Int., 125, p 318-321.
Ishihara, T., 1994: Magnetic anomaly map of East Asia 1:4.000.000, CD-ROM version, Geological Survey of Japan.
Jarrard, R., 1986: Relations among subduction parameters, Reviews of Geophysics, 24, 2, 217-284.
Joshima, M., 1987: Geomagnetic anomaly measurements in the Sunda Arc, CCOP Technical Bulletin, 1987, 19, 29-32.
Joshima, M., Okuda, Y., Yokokura, T., Kisimoto, K., Tamaki, K., and Supangat, A., 1987: Heatflow measurements in the Sunda Arc, CCOP Technical Bulletin, 19, 51-54.
Joshima, M. and Honza, E., 1987: Sea Bottom Photography employed in the Sunda Arc area, CCOP Technical Bulletin, 19, 55-61.
Karig, D.E., Caldwell, J.G., and Parmentier, E.M., 1976: Effects of accretion on the geometry of the descending lithosphere, Journal of Geophysical Research, 81, 6281-6291.
Karig, D.E., Moore, G.F., Curray, J.R., and Lawrence, M.B., 1980: Morphology and Shallow Structure of the Lower Trench Slope off Nias Island, Sunda Arc, in: Hayes, D. ed: The Tectonic and Geologic Evolution of Southeast Asian Seas and Islands, Geophysical Monograph 23.
Katili, J., 1973: Geochronology of west Indonesia and its implication on plate tectonics, Tectonophysics, 19, 195-212.
Kellerher, J.A., Savino, J., Rowlett, H.,and McCann, W., 1974: Why and where great thrust earthquakes occur along island arcs, Journal of Geophysical Research, 79, 4889-4899.
Kieckhefer, R.M., Shor, G.G., Curray, J.R., Sugiarta, W., and Hehuwat, F., 1980: Seismic refraction studies of the Sunda Trench and forearc basin, Journal of Geophysical Research, 85, 863-889.
Kisimoto, K., and Yokokura, T., 1987: Refraction Survey by sonobuoy in the Sunda Trench area, CCOP Technical Bulletin, 19, 33-50.
Lee, T., and Lawyer, L.A., 1995: Cenozoic late reconstruction of Southeast Asia, Tectonophysics, 251, 85-138.
Letouzey, J., Werner, P., and Marty, A., 1990: Fault reactivation and structural inversion: Backarc and intraplate compressive deformations. Example of the Eastern Sunda Shelf (Indonesia), Tectonophysics, 183, 341-362.
Levchenko, O., Merklin, L.R., and Schneider, A.A., 1986: Structural and Geodynamic Features of the Sunda Trench, Geotectonics, 20, 3, 238-244.
Linthout, K., Helmers, H., and Sopaheluwakan, J., 1997: Late Miocene obduction and microplate migration around the Southern Banda Sea and the closure of the Indonesian Seaway, Tectonophysics, 281, 17-30.
Ludwig, J.W., Nafe, J.E., and Drake, C.L., 1970: Seismic refraction, in: A.E. Maxwell (Eds.), The Sea, Vol.4, 53-84-Wiley, New York.
Luetgert, J., 1992: Interactive Two-Dimensional Seismic Raytracing for the Macintosh, USGS Open File Report, 43.
Malod, J., Karta, K., Beslier, M.O., and Zen, M.T., 1995: From normal to oblique subduction: Tectonic relationships between Java and Sumatra, Journal of Southeast Asian Earth Sciences, 12, 1/2, 85-93.
Malod, J. and Kemal, B. M., 1996: The Sumatra margin: oblique subduction and lateral displacement of the accretionary prism, in: Tectonic Evolution of Southeast Asia, R. Hall (edt), Geological Society of London Spec. Publication 106, 19-28.
McCaffrey, R., Molnar, P., Roecker, S., and Joyodiwiryo, Y.S., 1985: Microearthquake seismicity and fault plane solutions related to Arc Continent collision in the eastern Sunda arc, Journal of Geophysical Research, 90, 4511-4528.
McCaffrey, R, 1988: Active Tectonics of the eastern Sunda and Banda Arcs, Journal of Geophysical Research, 93, B12, 15163-15182.
McCaffrey, R., 1991: Slip vectors and stretching of the Sumatra forearc, Geology, 19, 881-884.
McCaffrey, R., 1992: Oblique Plate Convergence, slip vectors, and forearc deformation, Journal of Geophysical Research, 97, 6, 8905-8915.
McCaffrey, R., 1996: Slip partitioning at convergent plate boundaries of SE Asia, in: Tectonic Evolution of Southeast Asia, R. Hall (edt), Geological Society of London. Spec. Publication 106, 3-18.
McCourt, W., Crow, M.J., Cobbing, E.J., and Amin, T.C., 1996: Mesozoic and Cenozoic plutonic evolution of SE Asia: evidence from Sumatra, Indonesia, in: Tectonic Evolution of Southeast Asia, R. Hall (edt), Geological Society of London Spec. Publication 106, 321-335.
Metcalfe, I., 1996: Pre-Cretaceous evolution of Se Asian terranes, in: Tectonic Evolution of Southeast Asia, R. Hall (edt), Geological Society of London Spec. Publication 106, 97-122.
Minster, J.G., and Jordan, T.H., 1978: Present day plate motions, Journal of Geophysical Research, 83, 5331-5354.

Molnar, P., and Tapponier, P., 1975: Cenozoic Tectonics of Asia: Effects of a Continental Collision, Science, 189, 419-426.

Momma, H., Ohtsuka, K., Tanaka, T., and Ohara, T., 1987: Deep-towed sonar and camera observations at the Sunda forearc region, South of West Java, CCOP Technical Bulletin, 19, 89-105.

Moore, G.F. and Karig, D.E., 1980: Structural geology of Nias island, Indonesia: Implications for subduction zone tectonics. American Journal of Science, 280, 193-223.

Moore, G.F., Curray, J.R., Moore, D.G., and Karig, D.E., 1980: Variations in Geologic Structure along the Sunda Fore Arc, Northeastern Indian Ocean, in: Hayes, D. ed: The Tectonic and Geologic Evolution of Southeast Asian Seas and Islands, Geophysical Monograph 23.

Morelli, C., 1974: The International Standardization Net 1971. International Association of Geodesy Special Publication 4, p 194.

Mueller, D., Roest, W.R., Royer, J.Y., Gahagan, L.M., and Sclater, J.G., 1997: Digital Isochrons of the world's Ocean Floor, Journal of Geophysical Research, 102, 3211-3214.

Nagao, T., and Uyeda, S., 1995: Heat-flow distribution in Southeast Asia with consideration of volcanic heat, Tectonophysics 251, 153-159.

Newcomb, K.R., and McCann, W.R., 1987: Seismic history and seismotectonics of the Sunda Arc, Journal of Geophysical Research, 92: 421-439.

Ninkovich, D., 1976: Late Cenozoic clockwise rotation of Sumatra, Earth and Planetary Science Letters, 29, 169-275.

Nishimura, S., Nishida, J., Yokoyama, T., and Hehuwat, F., 1986: Neo-Tectonics of the Strait of Sunda, Indonesia, Journal of Southeast Asian Earth Sciences, 1, 2, 81-91.

Nishimura, S., Harjono, H., and Suparka, S., 1992: The Krakatau Islands: The Geotectonic Setting, GeoJournal, 28, 2: 87-98

Nishimura, S., and Suparka, S. 1997: Tectonic approach to the Neogene evolution of Pacific-Indian Ocean seaways, Tectonophysics, 281, 1-16.

Noteboom, J.J., 1978: Signature and amplitude of linear airgun arrays, Geophysical Prospecting, 26, 194-201.

Oba, N., Tomita, K., and Yamamoto, M., 1992: An Interpretation of the 1883 Cataclysmic Eruption of Krakatau from Geochmical Studies on the Partial Melting of Granite, GeoJournal, 28, 2, 99-108.

Packham, G., 1996: Cenozoic SE Asia: reconstructing its aggregation and reorganization, in: Tectonic Evolution of Southeast Asia, R. Hall (edt), Geological Society of London Spec. Publication 106, 123-152.

Pramumijoyo, S., and Sébrier, M., 1994: Neogene and Quaternary fault kinematics around the Sunda Strait area, Indonesia, Journal of Southeast Asian Earth Sciences, 6, 2, 137-145.

Prawirodirdjo, L., Bock, Y., McCaffrey, R., Genrich, J., Calais, E., Stevens, C., Puntodewo, S.S.O., Subarya, C., Rais, J., Zwick, P., and Fauzi, 1997: Geodetic observations of interseismic strain segmentation at the Sumatra subduction zone, Geophysical Research Letters, 24, 21, 2601-2604.

Puspito, N., and Shimazaki, K., 1995: Mantle structure and seismotectonics of the Sunda and Banda arcs, Tectonophysics, 251, 215-228.

Reichert, C., and Shipboard Science Party (J. Adam, A. Anugruhadi, H.O. Bargeloh, M. Block, V. Damm, Y.S. Djajadihardja, I. Heyde, E. Hinz, J.P. Hutagaol, G. Kallaus, P. Kewitsch, H.S. Koesnadi, A. Laesanpura, D. Muljawan, S. Mulyono, S. Neben, W. Reich, U. Schrader, B. Schreckenberger, J. Sievers, S. Widiyanto, M. Zeibig), in preparation: GINCO1 (SONNE Cruise SO-137): Geo-Scientific Investigations Along the Active Convergence Zone Between the Eastern Eurasian and Indo-Australian Plates Off Indonesia - Cruise Report.

Reed, D.L., Silver, E. A., Prasetyo, H., and Meyer, A., 1986: Deformation and sedimentation along a developing terrane suture: Eastern Sunda forearc, Indonesia, Geology, 12, 1000-1003.

Richter, B., and Fuller, M., 1996: Paleomagnetism of the Sibumasu and Indochina blocks: implications for the extrusion tectonic model, in: Tectonic Evolution of Southeast Asia, R. Hall (edt), Geological Society of London Spec. Publication 106, 203-224.

Roeser, H.A., Bargeloh, H.-O., and Schreckenberger, B., 1992: Technischer Bericht über ein kleines Navigationssystem für seegeophysikalische Arbeiten. BGR report, 31 pages, Hannover.

Royer, J., and Sandwell, D.T., 1989: Evolution of the Eastern Indian Ocean Since the Late Cretaceous: Constraints from Geosat Altimetry, Journal of Geophysical Research, 94, B10, 13755-13782.

Samuel, M.A., 1996: The Mentawai fault zone and deformation of the Sumatran Forearc in the Nias area, in: Tectonic Evolution of Southeast Asia, R. Hall (edt), Geological Society of London Spec. Publication 106, 337-351.

Schreckenberger, B., 1997: Magnetische Anomalien über seewärts einfallenden seismischen Reflektorfolgen – eine vergleichende Untersuchung verschiedener Vorkommen im Atlantik, PhD thesis, Frankfurt, 116 pages.

Schreiber, R., and H.W. Schencke, 1990: Efficient hydrographic surveying of EEZ with new multibeam echosounder technology for shallow and deep water, Ocean resources, 1, 73-87.

Scotese, C., Gahagan, L.M., and Larson, R.L., 1988: Plate tectonic reconstructions of the Cretaceous and Cenozoic ocean basins, Tectonophysics, 155, 27-48.

Self, S., and Rampino, M. 1983: The 1883 eruption of Krakatau, Nature, 294, 699-704.

Self, S., 1992: Krakatau Revisited: The Course of Events and Interpretation of the 1883 Eruption, GeoJournal, 28, 2: 109-121.

Sengupta, S., Ray, K.K., Acharyya, S.K., and de Smeth, J.B., 1990: Nature of ophiolite occurrences along the eastern margin of the Indian plate and their tectonic significance, Geology, 18, 439-442.

Sievers, J., and Adam, J., 1997: Übersicht und Beschreibung über das Digitalstreamersystem der BGR. - BGR report, archive no. 116877, Hannover

Silver, E.A., Reed, D., McCaffrey, R., and Joyodiwiryo, Y., 1983: Back arc thrusting in the Eastern Sunda Arc: A consequence of arc-continent collision, Journal of Geophysical Research, 88, 7429-7448.

Stevens, S.H., and Moore, G.F., 1985: Deformational and sedimentary processes in trench slope basins of the western Sunda arc, Indonesia, Marine Geology, 69, 93-112.

Sukmono, S., Zen, M.T., Kadir, W.G.A, Hendrajaya, L., Santoso, D., and Dubois, J., 1996: Fractal Geometry of the Sumatra active Fault system and its Geodynamical Implications, Journal of Geodynamics, 22, 1/2,1-9.

Sun, J., and Pan, T., 1995: The probability of very large Earthquakes in Sumatra, Bulletin of the Seismological Society of America, 85, 4, 1226-1231.

Tarling, D.H.: Gondwanaland and the evolution of the Indian Ocean, in: Audley-Charles, M.G., and Hallam, A. (eds), Gondwana and Thethys, Geological Society Special Publication 37, pp. 61-77.

Tregoning, P., Brunner, F.K., Bock, Y., Pntodewo, S.S.O., McCaffrey, R., Genrich, J.F., Calais, E., Rais, J., and Subarya, C, 1994: First geodetic measurement of convergence across the Java Trench, Geophysical Research Letters, 21, 19, 2135-2138.

Uyeda, S., 1982: Subduction zones: an introduction to comparative subductology, Tectonophysics, 81, 133-159.

Weinrebe, W., 1997: Fahrtbericht SO-112 HIRESBAT, GEOMAR-Report 64, GEOMAR-Kiel.

Wessel, P., and W.H.F. Smith, 1991: Free software helps map and display data, EOS transactions Am. Geophys. Union 72, 441, 445-446.

Westerveld, J., 1962: Quaternary volcanism on Sumatra, Bulletin of the Geological Society of America, 63, 561-594.

Widiyantoro, S., and van der Hilst, R.,1997: Mantle structure beneath Indonesia inferred from high-resolution tomographic imaging, Geophysical Journal International, 130, 167-182.

Widiyantoro, S., and van der Hilst, R., 1996: Structure and Evolution of Lithospheric Slab Beneath the Sunda Arc, Indonesia, Science, 271, 1566-1570.

Wilson, P., Rais, J., Reigber, Ch., Reinhard, E., Ambrosius, B.A.C., Le Pichon, X., Kasser, M., Suharto, P., Abdul Majid, Paduka Awang Haji Othman Bin Haji Yakuub, Almeda R., and Boonphakdee, C., 1998: Study provides data on active plate tectonics in Southeast Asia Region, EOS Transactions, 79, 45, 545/548.

Yokoyama, I., 1987: A scenario of the 1883 Krakatau Tsunami, Journal of Volcanology and Geothermal Research, 34, 123-132.

9. APPENDICES

9.1 DETAILS OF OBH/OBS DEPLOYMENTS AND SEISMIC PROFILES

9.1.1 GINCO SO 138 – PROFILE 01
9.1.2 GINCO SO 138 – PROFILE 02/03
9.1.3 GINCO SO 138 – PROFILE 04
9.1.4 GINCO SO 138 – PROFILE 05
9.1.5 GINCO SO 138 – PROFILE 06
9.1.6 GINCO SO 138 – PROFILE 07
9.1.7 GINCO SO 138 – PROFILE 08
9.1.8 GINCO SO 138 – PROFILE 09

9.2 SEISMIC PROFILES

9.3 MAGNETIC PROFILES

9.4 CAPTAIN'S REPORT

Appendix 9.1.1

GINCO2 - SO 138 - Profile 01

INST.	LAT (S)	LON (E)	DIST. TO	DEPTH	REL.	ANT.	REC.	SKEW	REMARKS	FIGURE
	D:M	D:M	EXT (nm)	(m)	CODE	CH.	NO.	(ms)		
OBH01	7:11.195	101:39.271	11.4	5036	C454	C	91.14	-19		6.3.4.1.3
OBH02	7:03.247	101:47.601	13.7	5181	B214	D	02.95	-7		6.3.4.1.4
OBH03	6:53.700	101:57.579	16.3	5870	C464	D	91.13	-11	data buffer overflown	
OBH04	6:42.397	102:09.366	4.3	5727	C679	B	980908	3	dc-bias	
OBH05	6:39.451	102:12.379	7.1	5075	D654	D	09.94	-46		6.3.4.1.5
OBH06	6:34.500	102:17.544	3.9	3915	B644	D	05.96		not recovered	
OBH07	6:31.809	102:20.341	8.2	3109	6A24	C	980403	0		6.3.4.1.6
OBH08	6:26.102	102:26.280	6.1	3153	A319	A	980907	3		6.3.4.1.7
OBH09	6:21.886	102:30.666	8.7	3181	4974	B	03.94	-15		6.3.4.1.8
OBH10	6:15.801	103:36.983	14.4	2014	6.969	C	92.06	-6	error - eot	
OBH11	6:05.850	102:47.448	9.4	1282	D629	D	980902	8		6.3.4.1.9
OBH12	5:59.185	102:54.240	5.4	1268	D738	B	980905	-3		6.3.4.1.10
OBH13	5:55.485	102:58.121	8.3	1538	6959	A	03.96	-12		6.3.4.1.11
OBH14	5:49.185	103:04.221	10.6	1501	4979	D	91.10	-55		6.3.4.1.12
OBH15	5:42.434	103:11.928	7.3	2160	D719	A	15.93	-68	vertical array 100m, noisy	
OBH16	5:37.263	103:17.055		2182	D634	C	980901	12		6.3.4.1.13
Streamer							980903	-2		6.3.4.1.2
Trigger							01.95	-12		

INST.	LAT (S)	LON (E)	DIST. TO	DEPTH	REL.	ANT.	REC.	SKEW	REMARKS	FIGURE
	D:M	D:M	NEXT (nm	(m)	CODE	CH.	NO.	(ms)		
OBH17	5: 32. 394	103: 06. 034	2.3	2081	D649	D	980908	3	OBS, Hydrophone defect	6.3.4.2.11
OBH18	5: 33. 794	103: 08. 023	3.0	2100	D738	A	15.93	-57	vert. array 100m, ch. 2-4 poor	6.3.4.2.12
OBH19	5: 35. 762	103: 10. 049	3.0	2140	D719	B	980902	5		6.3.4.2.13
OBH20	5: 37. 645	103: 12. 416	3.0	2160	6969	C	980403	1		6.3.4.2.14, 20, 21
OBH21	5: 39. 557	103: 14. 790	3.0	2176	D634	D	980905	0		6.3.4.2.15
OBH22	5: 41. 483	103: 17. 082	3.0	2195	4974	A	02.95	-1		6.3.4.2.16
OBH23	5: 43. 417	103: 19. 384	3.0	2208	6959	B	91.14	-15		6.3.4.2.17
OBH24	5: 45. 304	103: 21. 670	3.0	2220	4979	C	03.96	-12		6.3.4.2.18
OBH25	5: 47. 208	103: 24. 063	3.0	2228	B724	D	980402	-4		6.3.4.2.19
OBH26	6: 00. 304	103: 18. 019	3.0	2049	A319	B	03.94	-9		6.3.4.2.5
OBH27	5: 58. 874	103: 15. 306	3.0	1953	B639	D	980907	2		6.3.4.2.6
OBH28	5: 57. 412	103: 12. 589	3.0	1854	D629	A	980901	9		6.3.4.2.7
OBH29	5: 56. 004	103: 10. 001	3.0	1750	C679	D	971202	-4		6.3.4.2.8
OBH30	5: 54. 556	103: 07. 239	3.0	1659	C464	C	980401	-9	dc - bias	
OBH31	5: 53. 189	103: 04. 656	3.0	1570	6A24	B	971201	-3		6.3.4.2.9
OBH32	5: 51. 746	103: 02. 029	3.0	1470	D654	A	91.10	-27		6.3.4.2.10
OBH33	5: 50. 342	102: 59. 339	3.0	1357	B214	A	01.95	-8	data buffer overflown	
OBH34	5: 48. 893	102: 56. 726	3.0	1357	C454	A	980906	6	dc-bias	
Streamer							980903	-2		6.3.4.2.2-4
Trigger							91.15	-9		

Appendix 9.1.3

GINCO2 - SO 138 - Profile 04

INST.	LAT (S)	LON (E)	DIST. TO	DEPTH	REL.	ANT.	REC.	SKEW	REMARKS	FIGURE
	D:M	D:M	NEXT (nm)	(m)	CODE	CH.	NO.	(ms)		
OBH35	8: 19. 929	103: 44. 144	6.0	5711	6A24	C	971201	-2		6.3.4.3.3
OBH36	8: 14. 436	103: 47. 938	9.2	5876	C464	D	971202	-14	dc-bias	
OBH37	8: 07. 607	103: 52. 665	24.6	5707	C679	B	980402	-4	dc-bias	
OBH38	7: 48. 008	104: 06. 915	12.9	5735	C454	B	980906	7	dc-bias	
OBH39	7: 37. 148	104: 15. 028	8.3	4139	B214	D	980401	-11		6.3.4.3.4
OBH40	7: 30. 291	104: 20. 014	9.0	3772	D654	C	03.94	-11		6.3.4.3.5
OBH41	7: 23. 136	104: 25. 391	7.7	3497	4974	D	91.14	-23		6.3.4.3.6
OBH42	7: 16. 926	104: 29. 986	8.5	2888	6959	D	980403	-1		6.3.4.3.7
OBH43	7: 10. 037	104: 35. 065	8.2	2812	A319	C	980907	3		6.3.4.3.8
OBH44	7: 03. 441	104: 39. 939	6.5	2263	6969	A	08.94	-35		6.3.4.3.9
OBH45	6: 58. 065	104: 43. 941	5.2	2252	4979	A	03.96	-8		6.3.4.3.10
OBH46	6: 53. 956	104: 47. 985	5.5	1875	B639	D	980901	10		6.3.4.3.11
OBH47	6: 49. 473	104: 50. 307	5.6	1755	D634	xx*	980902	7	OBS light	6.3.4.3.12
OBH48	6: 45. 021	104: 53. 772	4.8	1794	D719	A	15.93	-71	vertical array 100 m	6.3.4.3.13
OBH49	6: 41. 114	104: 56. 464	5.9	1816	D649	x*	980908	6	OBS	6.3.4.3.14
OBH50	6: 36. 385	104: 59. 958		1507	D629	B	980905	-1		6.3.4.3.15
Streamer							980903	-2		6.3.4.3.2
Trigger							91.15	-7		

*x: f = 156,675 MHz

xx: f = 156,625 MHz

INST.	LAT (S)	LON (E)	DIST. TO	DEPTH	REL.	ANT.	REC.	SKEW	REMARKS	FIGURE
	D:M	D:M	NEXT (nm)	(m)	CODE	CH.	NO.	(ms)		
OBH51	9: 43. 469	106: 02. 755	7.5	5666	A319	A	980401	-9		6.3.4.4.3
OBH52	9: 36. 788	106: 05. 962	4.0	5911	6959	B	971201	-2		6.3.4.4.4
OBH53	9: 33. 117	106: 07. 734	26.1	5965	C679	A	980402	-2	dc-bias	
OBH54	9: 09. 522	106: 19. 063	8.5	5648	C464	D	971202	5	dc-bias	
OBH55	9: 01. 642	106: 22. 827	6.4	4560	6A24	A	02.95	-5		6.3.4.4.5
OBH56	8: 55. 876	106: 25. 568	8.5	4115	6969	D	980403	-1		6.3.4.4.6
OBH57	8: 48. 173	106: 29. 298	12.3	3517	4974	x*	980907	4	dc-bias in parts	
OBH58	8: 36. 995	106: 34. 657	6.6	2368	D654	A	91.14	-23		6.3.4.4.7
OBH59	8: 30. 940	106: 37. 639	5.5	1922	B214	C	03.94	-13		6.3.4.4.8
OBH60	8: 25. 942	106: 40. 011	6.6	1862	C454	D	08.94	-41		6.3.4.4.9
OBH61	8: 19. 947	106: 42. 834	5.5	1943	D629	C	03.96	-14		6.3.4.4.10
OBH62	8: 15. 026	106: 45. 259	9.8	3112	B639	D	91.10	125		6.3.4.4.11
OBH63	8: 06. 170	106: 49. 423	7.8	3044	4979	C	980901	11	dc-bias	
OBH64	7: 59. 037	106: 52. 849	7.8	3034	D634	D	980902	5	OBS light	6.3.4.4.12
OBH65	7: 51. 998	106: 56. 024	5.5	2801	D719	B	15.93	-72	vertical array 100 m	6.3.4.4.13
OBH66	7: 47. 013	106: 58. 575	3.2	2568	D649	C	980908	5	OBS	6.3.4.4.14
OBH67	7: 44. 085	106: 59. 995		2454	4949	B	980905	0		6.3.4.4.15
Streamer							980903	-1		6.3.4.4.2
Trigger							91.15	-6		

* x: f = 156.675

Appendix 9.1.5

GINCO2 - SO 138 - Profile 06

INST.	LAT (S)	LON (E)	DIST. TO	DEPTH	REL.	ANT.	REC.	SKEW	REMARKS	FIGURE
	D:M	D:M	NEXT (nm)	(m)	CODE	CH.	NO.	(ms)		
OBH68	7: 48. 169	107: 25. 334	10.6	1320	6969	D	08.94	-20		6.3.4.5.3
OBH69	7: 46. 459	107: 14. 732	9.8	1953	4979	C	980905	-1		6.3.4.5.4
OBH70	7: 44. 865	107: 04. 944	2.5	2626	C454	C	03.94	-6		6.3.4.5.5
OBH71	7: 44. 478	107: 02. 518	2.5	2512	4974	x*	980403	0	dc-bias	
OBH72	7: 44. 067	107: 00. 031	2.5	2451	4949	B	03.96	-11		6.3.4.5.6
OBH73	7: 43. 679	106: 57. 576	2.5	2565	B214	C	980401	-6		6.3.4.5.7
OBH74	7: 43. 243	106: 55. 104	2.5	2574	D654	C	971201	-2		6.3.4.5.8
OBH75	7: 42. 877	106: 52. 624	10.0	2573	D634	B	980902	3	OBS light	6.3.4.5.9
OBH76	7: 41. 156	106: 42. 176	10.0	2420	D719	D	980907	2	vert. array 400 m, ch. 2 dead	6.3.4.5.10
OBH77	7: 39. 654	106: 32. 732		1509	D649	D	980908	2	OBS	6.3.4.5.11
Streamer							980903	-33		6.3.4.5.2
Trigger							91.15	-3		

* x: f = 156.675

INST.	LAT (S)	LON (E)	DIST. TO	DEPTH	REL.	ANT.	REC.	SKEW	REMARKS	FIGURE
	D:M	D:M	NEXT (nm)	(m)	CODE	CH.	NO.	(ms)		
OBH78	8: 35. 992	106: 58. 620	5.0	2079	4949	D	03.96	-8		6.3.4.6.3
OBH79	8: 34. 169	106: 53. 853	5.0	2052	4974	C	08.94	-21	noisy	
OBH80	8: 32. 392	106: 49. 191	5.0	1897	6969	C	980901	7		6.3.4.6.4
OBH81	8: 30. 656	106: 44. 447	3.0	1901	D654	C	02.95	-6		6.3.4.6.5
OBH82	8: 29. 584	106: 41. 607	3.0	1662	6A24	C	980403	0		6.3.4.6.6
OBH83	8: 28. 526	106: 38. 704	3.0	1714	4979	D	980905	0		6.3.4.6.7
OBH84	8: 27. 488	106: 35. 950	3.0	1772	C454	B	91.10	-322	1 reset, not sync.*	
OBH85	8: 26. 391	106: 33. 123	3.0	1905	C464	A	971202	-2		6.3.4.6.8
OBH86	8: 25. 284	106: 30. 227	5.0	1960	D649	D	980908	2	OBS	6.3.4.6.9
OBH87	8: 23. 557	106: 25. 523	5.0	2221	D634	D	980902	3	OBS light	6.3.4.6.10
OBH88	8: 21. 758	106: 20. 767	5.0	2365	B214	A	980402	-2		6.3.4.6.11
OBH89	8: 20. 028	106: 16. 169		2370	D719	B	980907	1	vertical array 400m	6.3.4.6.12
Streamer							980903	-1		6.3.4.6.2
Trigger							91.15	-4		

* data to be recovered later

Appendix 9.1.7

GINCO2 - SO 138 - Profile 08

INST.	LAT (S)	LON (E)	DIST. TO	DEPTH	REL.	ANT.	REC.	SKEW	REMARKS	FIGURE
	D:M	D:M	NEXT (nm)	(m)	CODE	CH.	NO.	(ms)		
OBH90	7: 05. 144	104: 53. 007	4.0	2115	D649	A	980908	3	OBS	6.3.4.7.3
OBH91	7: 01. 481	104: 53. 018	4.1	1981	B214	D	980403	1		6.3.4.7.4
OBH92	6: 57. 431	104: 53. 007	4.4	1867	C464	A	02.95	-4		6.3.4.7.5
OBH93	6: 53. 001	104: 52. 987	4.0	1738	4979	B	980905	-1		6.3.4.7.6
OBH94	6: 49. 028	104: 53. 013	3.5	1712	D634	C	980902	4	OBS light	6.3.4.7.7
OBH95	6: 45. 508	104: 53. 008	5.0	1797	C454	D	971201	-1		6.3.4.7.8
OBH96	6: 40. 497	104: 53. 009	5.0	1678	6A24	B	980402	-3		6.3.4.7.9
OBH97	6: 35. 504	104: 53. 022	4.1	1873	D654	C	980901	7	dc-bias	
OBH98	6: 31. 411	104: 53. 003	3.0	1893	4974	D	971202	-4		6.3.4.7.10
OBH99	6: 18. 419	104: 53. 038	3.0	1862	4949	B	91.10	345		6.3.4.7.11
OBH100	6: 25. 501	104: 53. 011	4.8	1738	D719	C	980907	2	vert. array 800m, noisy	
OBH101	6: 20. 617	104: 53. 019	4.0	1586	B639	D	03.96	-6		6.3.4.7.12
OBH102	6: 16. 647	104: 53. 044	5.1	1344	6969	C	03.94	-11		6.3.4.7.13
OBH103	6: 11. 459	104: 53. 041	6.2	1282	6959	D	08.94	-23	dc-bias	
OBH104	6: 05. 175	104: 53. 015	6.0	1373	C679	B	980906	3		6.3.4.7.14
OBH105	5: 59. 255	104: 53. 018		216	A319	A	91.14	-9	AQ-12 Hydrophon	6.3.4.7.15
Streamer							980903	-2		6.3.4.7.2
Trigger							91.15	-4		

INST.	LAT (S)	LON (E)	DIST. TO	DEPTH	REL.	ANT.	REC.	SKEW	REMARKS	FIGURE
	D:M	D:M	NEXT (nm)	(m)	CODE	CH.	NO.	(ms)		
OBH106	6: 21. 983	104: 43. 885	0.9	81	4974	B	91.14	-5		6.3.4.8.4
OBH107	6: 21. 474	104: 44. 779	3.0	273	D654	C	03.96	1	noisy	
OBH108	6: 20. 012	104: 47. 257	3.0	1090	A319	D	980905	-1	AQ-12 Hydrophone	6.3.4.8.5
OBH109	6: 18. 416	104: 49. 981	1.8	1590	C679	B	02.95	-2		6.3.4.8.6, 12
OBH110	6: 15. 514	104: 51. 442	1.7	1592	6959	C	980901	1		6.3.4.8.7, 13
OBH111	6: 16. 580	104: 53. 027		1343	D649	D	980908	1	OBS	6.3.4.8.8-11,14
Streamer							980903	0		6.3.4.8.3
Trigger							91.15	-3		

Appendix 9.2

SEISMIC PROFILES

Line number	Shot points	Date	Time	Position		Course	Methods
SO138-01	1	01.01.99	13:47	05° 14.335 S	103° 40.057 E	226°	S G M P
(1)	2354	03.01.99	05:00	07° 31.523 S	101° 18.122 E		363.90 km
SO138-02	1	04.01.99	23:50	05° 38.261 S	102° 38.655 E	118°	S G M P
	705	05.01.99	11:34	06° 11.226 S	103° 39.333 E		128.45 km
SO138-02Q	706	05.01.99	11:35	06° 11.210 S	103° 39.424 E	33°	S G M P
	810	05.01.99	13:19	06° 04.406 S	103° 43.735 E		15.69 km
SO138-03	811	05.01.99	13:20	06° 04.334 S	103° 43.713 E	309°	S G M P
	1693	06.01.99	04:02	05° 19.954 S	102° 50.953 E		134.18 km
SO138-03A	1	06.01.99	05:31	05° 20.465 S	102° 51.345 E	130°	S G M P
(2)	198	06.01.99	07:42	05° 28.745 S	103° 01.639 E		24.38 km
SO138-03B	1	06.01.99	07:44	05° 28.878 S	103° 01.788 E	130°	S G M P
(3)	924	06.01.99	12:51	05° 48.909 S	103° 26.249 E		58.33 km
SO138-04	1	11.01.99	00:55	06° 11.180 S	105° 17.373 E	216°	S G M P
(4)	2096	12.01.99	11:50	08° 40.246 S	103° 30.102 E		338.29 km
SO138-05	1	15.01.99	22:26	07° 44.218 S	107° 06.413 E	206°	S G M P
	1776	17.01.99	04:01	09° 59.799 S	105° 54.893 E		291.82 km
SO138-06	1	18.01.99	19:23	07° 51.421 S	107° 34.084 E	281°	S G M P
(5)	882	19.01.99	10:04	07° 37.979 S	106° 22.513 E		144.62 km
SO138-07	1	20.01.99	13:53	08° 12.962 S	105° 54.595 E	107°	S G M P
	982	21.01.99	06:15	08° 44.050 S	107° 20.134 E		167.11 km
SO138-08	1	23.01.99	05:49	05° 54.868 S	104° 56.030 E	182°	S G M P
(6)	1172	24.01.99	01:21	07° 30.155 S	104° 52.993 E		175.72 km
SO138-09	1	24.01.99	23:05	06° 15.639 S	104° 56.007 E	242°	G M P
(7)	586	25.01.99	02:20	06° 22.707 S	104° 42.600 E		27.95 km
SO138-09A	1	25.01.99	02:49	06° 22.424 S	104° 43.035 E	53°	G M P
(8)	117	25.01.99	03:29	06° 20.422 S	104° 45.710 E		6.16km
SO138-09B	1	25.01.99	04:47	06° 19.089 S	104° 48.834 E	59°	G M P
(9)	210	25.01.99	05:56	06° 15.715 S	104° 54.441 E		12.07 km

Methods used:
G - gravity, M - magnetics, P - Hydrosweep, Parasound, S - seismics

(1) missing shots due to compressor failure around SP 260: 5 shots,SP 1983-1989, SP 2029-2031, SP 2050
(2) shot interval 40 sec.
(3) shot interval 20 sec.

(4) SP 650-663 starboard array only
(5) SP 429-478 starboard array only
(6) failure of gun 14 after SP 899
(7) shot interval 20 sec., BGR array at starboard, GEOMAR array at port
(8) shot interval 20 sec., BGR array at starboard, GEOMAR array at port
SP 0-15 both arrays, SP 16-30 port array only, 31-45 both arrays,46-60 port array, 98-148 no shots, after 149 starboard array only
(9) shot interval 20 sec., BGR array at starboard, GEOMAR array at port
SP 1-15, 31-45, 61-75, 91-105, 121-135, 151-165, 181-195 both arrays
SP 16-30, 46-60, 61-75, 76-90, 106-120, 136-150, 166-180, 196-210 port array only

Appendix 9.3

MAGNETIC PROFILES

Line number	Date	Time	Position		Course	Methods
SO138-101	29.12.98 29.12.98	20:48 23:33	06° 20.989 S 06° 29.501 S	105° 13.754 E 104° 45.923 E	250°	G M P 55.04 km
SO138-102	29.12.98 30.12.98	23:33 00:35	06° 29.501 S 06° 18.560 S	104° 45.923 E 104° 46.460 E	0°	G M P 20.83 km
SO138-103	30.12.98 30.12.98	00:35 03:17	06° 18.560 S 06° 01.744 S	104° 46.460 E 105° 14.187 E	60°	G M P 60.40 km
SO138-104	30.12.98 30.12.98	03:17 03:45	06° 01.744 S 05° 56.507 S	105° 14.187 E 105° 13.863 E	0°	G M P 9.56 km
SO138-105	30.12.98 30.12.98	03:45 08:52	05° 56.507 S 06° 23.530 S	105° 13.863 E 104° 29.488 E	239°	G M P 96.26 km
SO138-106	30.12.98 30.12.98	08:52 17:20	06° 23.530 S 05° 28.342 S	104° 29.488 E 103° 29.952 E	313°	G M P 150.71 km
SO138-107	30.12.98 31.12.98	17:20 00:17	05° 28.342 S 06° 16.999 S	103° 29.952 E 102° 36.591 E	228°	G M P 134.08 km
SO138-108	31.12.98 31.12.98	00:17 04:10	06° 16.999 S 06° 46.507 S	102° 36.591 E 102° 13.888 E	218°	G M P 69.21 km
SO138-110	01.01.99 01.01.99	10:27 13:30	05° 34.417 S 05° 13.616 S	103° 17.198 E 103° 38.936 E	46°	G M P 56.17 km
SO138-111	03.01.99 03.01.99	05:59 08:45	07° 31.100 S 07° 07.217 S	101° 13.028 E 101° 36.912 E	46°	G M P 62.21 km
SO138-113	04.01.99 04.01.99	21:31 23:37	05° 46.348 S 05° 37.456 S	102° 56.305 E 102° 39.357 E	298°	G M P 35.33 km
SO138-114	06.01.99 07.01.99	21:59 00:14	05° 34.183 S 05° 58.045 S	103° 05.749 E 103° 19.318 E	150°	G M P 51.11 km
SO138-115	07.01.99 07.01.99	05:50 07:50	05° 52.356 S 06° 08.865 S	102° 57.199 E 102° 42.166 E	225°	G M P 41.17km
SO138-116	07.01.99 07.01.99	07:50 12:19	06° 08.907 S 06° 39.347 S	102° 42.122 E 102° 03.935 E	230°	G M P 90.03 km

Methods used:

G - gravity
M - magnetics
P - Hydrosweep,Parasound

Line number	Date	Time	Position		Course	Methods
SO138-117	07.01.99	12:32	06° 41.439 S	102° 04.359 E	132 °	G M P
	07.01.99	13:44	06° 51.118 S	102° 15.041 E		26.56 km
SO138-118	07.01.99	13:55	06° 50.641 S	102° 16.917 E	330°	G M P
	07.01.99	16:10	06° 31.099 S	102° 30.448 E		43.81 km
SO138-119	07.01.99	16:34	06° 33.953 S	102° 32.032 E	210°	G M P
	07.01.99	18:52	06° 56.622 S	102° 18.899 E		48.28 km
SO138-120	07.01.99	19:14	06° 58.680 S	102° 20.982 E	30°	G M P
	07.01.99	21:51	06° 35.482 S	102° 35.081 E		50.03 km
SO138-121	07.01.99	22:23	06° 37.621 S	102° 37.487 E	217°	G M P
	07.01.99	23:18	06° 46.020 S	102° 30.883 E		20.32 km
SO138-122	07.01.99	23:29	06° 46.182 S	102° 29.118 E	315°	G M P
	08.01.99	00:29	06° 38.428 S	102° 21.442 E		20.11 km
SO138-123	08.01.99	16:20	06° 39.788 S	102° 18.927 E	135 °	G M P
	08.01.99	17:24	06° 49.719 S	102° 28.640 E		25.60 km
SO138-124	08.01.99	17:30	06° 50.000 S	102° 29.668 E	45°	G M P
	08.01.99	18:53	06° 39.063 S	102° 39.912 E		28.43 km
SO138-125	08.01.99	19:14	06° 40.446 S	102° 42.654 E	230°	G M P
	08.01.99	21:17	06° 55.148 S	102° 25.410 E		42.41 km
SO138-126	08.01.99	21:44	06° 58.613 S	102° 25.088 E	50°	G M P
	09.01.99	00:00	06° 42.039 S	102° 44.934 E		48.32 km
SO138-127	09.01.99	00:24	06° 44.493 S	102° 46.949 E	230°	G M P
	09.01.99	03:28	07° 06.395 S	102° 20.565 E		63.18 km
SO138-128	09.01.99	03:31	07° 06.478 S	102° 20.067 E	325°	G M P
	09.01.99	04:45	06° 55.367 S	102° 12.289 E		24.99 km
SO138-129	09.01.99	04:49	06° 54.722 S	102° 12.169 E	15°	G M P
	09.01.99	06:12	06° 39.514 S	102° 16.281 E		29.04 km
SO138-130	09.01.99	15:35	06° 33.178 S	102° 20.685 E	74°	G M P
	09.01.99	16:28	06° 30.758 S	102° 31.279 E		20.28 km
SO138-131	09.01.99	16:28	06° 30.751 S	102° 31.349 E	125°	G M P
	09.01.99	18:28	06° 45.634 S	102° 52.399 E		47.51 km

Methods used:

G - gravity
M - magnetics
P - Hydrosweep,Parasound

Line number	Date	Time	Position		Course	Methods
SO138-132	09.01.99 09.01.99	18:37 21:10	06° 47.176 S 07° 12.756 S	102° 52.973 E 102° 38.620 E	209°	G M P 54.05 km
SO138-133	09.01.99 09.01.99	21:12 22:50	07° 13.025 S 07° 24.804 S	102° 38.811 E 102° 54.686 E	127°	G M P 36.40 km
SO138-134	09.01.99 10.01.99	22:51 02:02	07° 24.845 S 07° 38.456 S	102° 54.740 E 103° 30.929 E	110°	G M P 71.14 km
SO138-135	10.01.99 10.01.99	02:03 04:18	07° 38.483 S 07° 51.509 S	103° 30.991 E 103° 54.916 E	119°	G M P 50.11 km
SO138-136	10.01.99 10.01.99	04:24 06:58	07° 52.484 S 08° 15.979 S	103° 55.122 E 103° 39.066 E	214°	G M P 52.40 km
SO138-137	10.01.99 11.01.99	21:55 00:38	06° 32.990 S 06° 11.370 S	105° 00.095 E 105° 16.005 E	36°	G M P 50.23 km
SO138-138	12.01.99 12.01.99	13:10 15:22	08° 36.607 S 08° 17.947 S	103° 26.679 E 103° 40.313 E	36°	G M P 42.53 km
SO138-139	13.01.99 13.01.99	11:36 14:30	06° 32.461 S 06° 49.907 S	104° 59.973 E 104° 33.038 E	237°	G M P 59.85 km
SO138-140	13.01.99 13.01.99	15:02 18:23	06° 45.472 S 06° 25.018 S	104° 30.083 E 104° 03.978 E	59°	G M P 73.65 km
SO138-141	13.01.99 13.01.99	19:00 20:01	06° 21.723 S 06° 29.149 S	104° 00.396 E 104° 51.388 E	230°	G M P 21.52 km
SO138-142	13.01.99 13.01.99	20:08 20:47	06° 28.391S 06° 21.301S	104° 50.539 E 104° 50.949 E	3°	G M P 13.09 km
SO138-143	13.01.99 13.01.99	20:56 22:40	06° 19.932 S 06° 10.512 S	104° 51.785 E 105° 08.946 E	61°	G M P 36.10 km
SO138-144	13.01.99 14.01.99	22:50 00:46	06° 10.602 S 06° 22.267 S	105° 10.890 E 105° 30.423 E	121°	G M P 42.56 km
SO138-149	14.01.99 14.01.99	09:00 13:48	06° 24.784 S 06° 59.601 S	105° 09.913 E 104° 45.318 E	215°	G M P 79.09 km
SO138-151	17.01.99 17.01.99	04:40 06:42	09° 59.929 S 09° 42.161 S	105° 51.943 E 106° 00.006 E	24°	G M P 35.92 km

Methods used:

G - gravity
M - magnetics
P - Hydrosweep,Parasound

Line number	Date	Time	Position		Course	Methods
SO138-153	19.01.99 19.01.99	10:39 11:41	07° 37.792 S 07° 40.930 S	106° 19.536 E 106° 30.512 E	106°	G M P 21.00 km
SO138-154	19.01.99 19.01.99	22:00 23:30	07° 48.114 S 08° 35.997 S	107° 25.440 E 106° 58.556 E	210°	G M P 101.13 km
SO138-155	20.01.99 20.01.99	11:48 13:29	08° 19.685 S 08° 14.753 S	106° 08.376 E 105° 55.335 E	291°	G M P 25.61 km
SO138-156	21.01.99 21.01.99	07:22 09:25	08° 46.704 S 08° 39.185 S	107° 20.262 E 107° 00.630 E	291°	G M P 38.58 km
SO138-157	21.01.99 21.01.99	19:29 23:10	08° 22.283 S 08° 55.538 S	106° 14.442 E 105° 51.839 E	214°	G M P 74.01 km
SO138-158	21.01.99 22.01.99	23:19 01:03	08° 55.660 S 08° 45.783 S	105° 50.341 E 105° 34.482 E	302°	G M P 34.30 km
SO138-158A	22.01.99 22.01.99	05:21 13:06	08° 42.273 S 08° 04.016 S	105° 28.699 E 104° 27.067 E	302°	G M P 133.31 km
SO138-159	22.01.99 22.01.99	13:07 13:40	08° 03.974 S 08° 00.806 S	104° 26.980 E 104° 24.185 E	319°	G M P 7.78 km
SO138-160	23.01.99 22.01.99	13:40 19:25	08° 00.748 S 07° 05.423 S	104° 24.213 E 104° 53.059 E	105°	G M P 116.29 km
SO138-161	24.01.99 24.01.99	01:58 04:58	07° 31.626 S 07° 05.680 S	104° 55.071 E 104° 55.510 E	1°	G M P 47.83 km

Methods used:

G - gravity
M - magnetics
P - Hydrosweep,Parasound

Line number	Date	Time	Position		Course	Methods
SO138-153	19.01.99 19.01.99	10:39 11:41	07° 37.792 S 07° 40.930 S	106° 19.536 E 106° 30.512 E	106°	G M P 21.00 km
SO138-154	19.01.99 19.01.99	22:00 23:30	07° 48.114 S 08° 35.997 S	107° 25.440 E 106° 58.556 E	210°	G M P 101.13 km
SO138-155	20.01.99 20.01.99	11:48 13:29	08° 19.685 S 08° 14.753 S	106° 08.376 E 105° 55.335 E	291°	G M P 25.61 km
SO138-156	21.01.99 21.01.99	07:22 09:25	08° 46.704 S 08° 39.185 S	107° 20.262 E 107° 00.630 E	291°	G M P 38.58 km
SO138-157	21.01.99 21.01.99	19:29 23:10	08° 22.283 S 08° 55.538 S	106° 14.442 E 105° 51.839 E	214°	G M P 74.01 km
SO138-158	21.01.99 22.01.99	23:19 01:03	08° 55.660 S 08° 45.783 S	105° 50.341 E 105° 34.482 E	302°	G M P 34.30 km
SO138-158A	22.01.99 22.01.99	05:21 13:06	08° 42.273 S 08° 04.016 S	105° 28.699 E 104° 27.067 E	302°	G M P 133.31 km
SO138-159	22.01.99 22.01.99	13:07 13:40	08° 03.974 S 08° 00.806 S	104° 26.980 E 104° 24.185 E	319°	G M P 7.78 km
SO138-160	23.01.99 22.01.99	13:40 19:25	08° 00.748 S 07° 05.423 S	104° 24.213 E 104° 53.059 E	105°	G M P 116.29 km
SO138-161	24.01.99 24.01.99	01:58 04:58	07° 31.626 S 07° 05.680 S	104° 55.071 E 104° 55.510 E	1°	G M P 47.83 km

Methods used:

G - gravity
M - magnetics
P - Hydrosweep,Parasound

R.F. Reedereigemeinschaft
Forschungsschiffahrt GmbH

F.S. "S O N N E"
Kapt. H. Papenhagen

Stationsprotokoll F.S. "S O N N E" Reise SO 138

Gebrauchtes Instrumentarium

RFL	ReFlektionsseismik mit Streamer von 300 m Länge und 2 airgun-arrays, diverse OBH, OBS und Vertikalarrays von 200 und 800 m Länge
GRA	Gravimeter
MAG	Gradiometer oder Magnetometer
HS	Hydrosweep
PS	Parasound

Eingesetzte Winden:

Winde			RF-Nr.	SO 138 Einsatz	Gesamt Einsatz	SO 138 S`länge	gefierte max.Sl	Gesamt S`lange	Zust
W 1	000	18,2	00000	000 h	0000 h	000000 m	0000 m	000000	0
W 2	LWL	18,2	865017	000 h	1201 h	000000 m	0000 m	725757	3
W 4	NSW	11,0	817141	003 h	0003 h	003892 m	3892 m	003892	1
W 5	NSW	11,0	816187	000 h	0237 h	000000 m	4228 m	217297	3
W 6	NSW	18,2	813004	008 h	0496 h	006604 m	4104 m	366244	4

Geräteverluste: 1 OBH komplett ; 2 Auftriebskörper mit Releaser ;

Abkürzungen im Stationsprotokoll:

z.W.	zu Wasser
a.D.	an Deck
Boko	Bodenkontakt
Bosi	Bodensicht
Slmax.	Seillänge
LT	Lottiefe nach Hydrosweep
W x	eingesetzte Winde
HS	Hydrosweep
PS	Parasound

Zeit : UTC + 7 Stunden

30.12.1998

Profil SO 138-101 GRA/MAG/HS/PS

0333 – 0343	Magnetometer z.W.		
0343	Beginn Profil	06 20,7 S 105 15,1 E	
0623	Ende Profil	06 30,0 S 104 47,5 E	52 sml

Profil SO 138-102 GRA/MAG/HS/PS

0637	Beginn Profil	06 28,9 S 104 45,8 E	
0728	Ende Profil	06 20,0 S 104 46,0 E	10 sml

Profil SO 138-103 GRA/MAG/HS/PS

0745	Beginn Profil	06 17,3 S 104 47,9 E	
1016	Ende Profil	06 02,0 S 105 14,0 E	30 sml

Profil SO 138-104 GRA/MAG/HS/PS

1017	Beginn Profil	06 01,6 S 105 14,2 E	
1042	Ende Profil	06 56,8 S 105 14,2 E	05 sml

Profil SO 138-105 GRA/MAG/HS/PS

1045	Beginn Profil	06 56,5 S 105 13,9 E	
1345 – 1355	hieven Magnetometer ein		
1458 – 1523	setzen Gradienten-Magnetometer aus		
1552	Ende Profil	06 23,5 S 104 29,5 E	52 sml

Profil SO 138-106 GRA/MAG/HS/PS

1554	Beginn Profil	06 23,5 S 104 29,1 E	
31.12.1998			
0010	Ende Profil	05 28,9 S 103 31,2 E	81 sml

Profil SO 138-107 GRA/MAG/HS/PS

0026	Beginn Profil	05 28,7 S 103 29,0 E	
0717	Ende Profil	06 17,0 S 102 36,5 E	72 sml

Profil SO 138-108 GRA/MAG/HS/PS

0717	Beginn Profil	06 17,0 S 102 36,5 E	
1038 – 1110	holen Magnetometer ein		
1123	Ende Profil	06 47,6 S 102 12,9 E	39 sml

Teststation 1 W 6

1130	releaser z.W.	LT = 6151 m	06 47,6 S 102 12,8 E
1244	SL = 6000 m	LT = 6150 m	06 47,5 S 102 12,8 E
1244 – 1308	12 Release-Test		
1308	Beginn hieven		
1443	Releaser a.D.		

Teststation 2 W 6

1700	Beginn Station	LT = 6176 m	06 53,5 S 102 05,8 E
1743	13 Releaser z:W.		
1935	Slmax = 6000 m	LT = 6182 m	06 52,8 S 102 05,1 E
2111	Releaser a.D.		

Auslegung OBH auf Profil 138-S 01

2157	OBH 3 z.W.	LT = 5870 m	06 53,70 S 102 57,58 E
2320	OBH 2 z.W.	LT = 5181 m	07 03,25 S 101 47,60 E
01.01.1999			
0031	OBH 1 z.W.	LT = 5034 m	07 11,19 S 101 39,27 E

Profil SO 138-109 HS/PS

0115	Beginn Profil		07 03,2 S 101 39,3 E
0328	Ende Profil		06 42,2 S 102 01,2 E 30 sml

Fortsetzung OBH-deployment auf Profil S 01

0447	OBH 4 z.W.	LT = 5742 m	06 42,39 S 102 09,36 E
0540	OBH 5 z.W.	LT = 5085 m	06 39,44 S 102 12,36 E
0636	OBH 6 z.W.	LT = 3911 m	06 34,50 S 102 17,54 E
0708	OBH 7 z.W.	LT = 3110 m	06 31,81 S 102 20,34 E
0758	OBH 8 z.W.	LT = 3153 m	06 26,10 S 102 26,28 E
0940	OBH 9 z.W.	LT = 3181 m	06 21,89 S 102 30,67 E
1032	OBH 10 z.W.	LT = 2017 m	06 15,80 S 102 36,98 E
1203	OBH 11 z.W.	LT = 1280 m	06 05,84 S 102 47,47 E
1308	OBH 12 z.W.	LT = 1267 m	05 59,19 S 102 54,23 E
1346	OBH 13 z.W.	LT = 1538 m	05 55,48 S 102 58,11 E
1437	OBH 14 z.W.	LT = 1500 m	05 49,65 S 103 04,20 E
1558	OBH 15 z.W.	LT = 2161 m	05 42,40 S 103 11,84 E
1650	OBH 16 z.W.	LT = 2179 m	05 27,26 S 103 17,06 E

1656 – 1716 bringen Magnetometer aus

Profil SO 138-110 MAG/GRA/HS/PS

1728	Beginn Profil	05 34,3 S 103 17,2 E
1945 – 1957	setzen Bb-array aus	
1959 – 2009	setzen Stb-array aus	
2020	Ende Profil	05 14,0 S 103 38,2 E 29 sml

Profil SO138-S 01 REF/MAG/GRA/HS/PS

2047	Beginn Profil	05 14,4 S 103 40,1 E
2105 – 2120	bringen Streamer aus	
2400		05 26,2 S 103 28,5 E
02.01.1999		
1200		06 09,0 S 102 44,1 E
1958 – 2010	holen Magnetometer vor	
2031 – 2041	bringen Magnetometer aus	
2400		06 50,0 S 102 01,4 E
03.01.1999		
1200	Ende Profil	07 31,5 S 101 18,2 E 194 sml

1203 – 1208 holen Streamer ein
1210 – 1218 holen Bb-array ein
1220 – 1228 holen Stb-array ein

Profil SO 138-111 MAG/GRA/HS/PS

1258	Beginn Profil	07 31,22 S 101 13,0 E
1540	Ende Profil	07 07,1 S 101 36,1 E 27 sml

1547 – 1614 holen Magnetometer ein

Bergung der OBH des Profiles SO 1

1552	OBH 01 ausgelöst	1648	aufgetaucht	1712 a.D. 07 10,9 S 101 39,1 E
1747	OBH 02 ausgelöst	1844	aufgetaucht	1854 a.D. 07 03,0 S 101 47,5 E

1941 OBH 03 ausgelöst 2041 aufgetaucht 2102 a.D. 06 53,4 S 101 57,6 E

Releaser-Teststation 3 W 6

2237 Releaser z.W. LT = 5829 m 06 42,5 S 102 09,3 E

04.01.1999

0017 Slmax = 5500 m

0018 – 0024 Test der Releaser

0150 Releaser a.D.

Fortsetzung Bergung der OBH des Profiles SO 1

0025	OBH 04	ausgelöst	0130	aufgetaucht	0213	a.D.	06 42,1 S 102 09,6 E
0119	OBH 05	ausgelöst	0226	aufgetaucht	0258	a.D.	06 39,3 S 102 53,3 E
0308	OBH 06	ausgelöst		gesendet, geantwortet, nicht aufgetaucht			
0344	OBH 07	ausgelöst	0441	aufgetaucht	0516	a.D.	06 31,7 S 102 20,9 E
0657	OBH 08	ausgelöst	0737	aufgetaucht	0746	a.D.	06 26,1 S 102 26,6 E
0800	OBH 09	ausgelöst	0841	aufgetaucht	0849	a.D.	06 21,9 S 102 31,0 E
0912	OBH 10	ausgelöst	0936	aufgetaucht	0949	a.D.	06 15,8 S 102 37,4 E
1046	OBH 11	ausgelöst	1103	aufgetaucht	1113	a.D.	06 05,9 S 102 47,9 E
1152	OBH 12	ausgelöst	1210	aufgetaucht	1243	a.D.	05 59,8 S 102 55,0 E
1303	OBH 13	ausgelöst	1317	aufgetaucht	1329	a.D.	05 55,6 S 102 58,4 E
1401	OBH 14	ausgelöst	1418	aufgetaucht	1432	a.D.	05 50,0 S 103 04,5 E
1518	OBH 15	ausgelöst	1552	aufgetaucht	1606	a.D.	05 42,7 S 103 12,1 E
1634	OBH 16	ausgelsöt	1700	aufgetaucht	1705	a.D.	05 37,3 S 103 17,2 E

Auslegung OBH auf den Profilen S 2, SQ und S 3

1833	OBH 17 z.W.	LT =	05 32,39 S	103 06,03 E
1907	OBH 18 z.W. (VA)	LT =	05 33,79 S	103 08,02 E
1939	OBH 19 z.W.	LT = 2130 m	05 35,76 S	103 10,05 E
2010	OBH 20 z.W.	LT = 2154 m	05 37,65 S	103 12,42 E
2042	OBH 21 z.W.	LT = 2177 m	05 39,56 S	103 14,79 E
2112	OBH 22 z.W.	LT = 2195 m	05 41,48 S	103 17,08 E
2141	OBH 23 z.W.	LT = 2207 m	05 43,42 S	103 19,38 E
2208	OBH 24 z.W.	LT = 2219 m	05 45,30 S	103 21,68 E
2234	OBH 25 z.W.	LT = 2228 m	05 47,21 S	103 24,06 E

Profil SO 138-112 GRA/HS/PS

2257	Beginn Profil	05 50,3 S	103 24,7 E
2346	Ende Profil	05 59,2 S	103 20,7 E 10 sm

05.01.1999

Fortsetzung Auslegung OBH auf den Prfilen S 2 SQ und S 3

0009	OBH 26 z.W.	LT = 2050 m	06 00,30 S	103 18,02 E
0037	OBH 27 z.W.	LT = 1950 m	05 58,87 S	103 15,30 E
0103	OBH 28 z.W.	LT = 1856 m	05 57,36 S	103 12,59 E
0130	OBH 29 z.W.	LT = 1752 m	05 56,03 S	103 10,00 E
0158	OBH 30 z.W.	LT = 1658 m	05 54,55 S	103 07,24 E
0224	OBH 31 z.W.	LT = 1571 m	05 53,18 S	103 04,56 E
0253	OBH 32 z.W.	LT = 1472 m	05 51,74 S	103 02,02 E
0319	OBH 33 z.W.	LT = 1356 m	05 50,34 S	102 59,33 E

FS SONNE

Stationsprotokoll SO 138

0351 OBH 34 z.W. LT = 1356 m 05 48,89 S 102 56,72 E

0400 – 0430 Magnetometer z.W.

Profil SO 138-113 MAG/GRA/HS/PS

0428	Beginn Profil	05 46,5 S 102 56,4 E	
0611 – 0620	Bb-array z.W.		
0616	Ende Profil	05 38,2 S 102 41,0 E	18 sm

0622 – 0632 Stb-array z.W.

Profil SO 138 S 2 REF/MAG/GRA/HS/PS

0650	Beginn Profil	05 38,4 S 102 38,7 E	
0705 – 0715	Streamer z.W.		
1822	Ende Profil	06 11,1 S 103 38,2 E	67 sm

Profil SO 138 S 2 Q REF/MAG/GRA/HS/PS

1841	Beginn Profil	06 11,0 S 103 40,0 E	
2006	Ende Profil	06 05,3 S 103 43,8 E	08 sm

Profil SO 138 S 3 REF/MAG/GRA/HS/PS

2040	Beginn Profil	06 03,0 S 103 43,0 E	
06.01.1999			
1102	Ende Profil	05 20,0 S 102 51,0 E	67 sm

1102 – 1220 drehen auf Gegenkurs

Profile SO 138 S 3-A/B REF/MAG/GRA/HS/PS

1226	Beginn Profil	05 20,2 S 102 50,9 E	
1513	Profilwechsel A auf B	05 30,7 S 103 04,0 E	17 sm
1951	Ende Profil	05 48,9 S 103 26,3 E	28 sm

1957 – 2003 holen Stb-array ein
2000 – 2037 holen Magnetometer ein
2005 – 2015 holen Bb-array ein
2018 – 2025 holen Streamer ein

Bergung der OBH des Profils S 3

2100	OBH 25	ausgelöst					
2138	OBH 25	ausgelöst					
2149	OBH 24	ausgelöst	2213	gesichtet	2223	a.D.	05 45,6 S 103 21,9 E
2225	OBH 25	ausgelöst	2249	gesichtet	2255	a.D.	05 47,4 S 103 24,2 E
2320	OBH 23		2344		2400		05 43,8 S 103 19,7 E
07.01.1999							
0003	OBH 22		0031		0055		05 41,7 S 103 17,5 E
0055	OBH 21		0122		0127		05 39,7 S 103 15,1 E
0127	OBH 20		0202		0222		05 37,8 S 103 12,7 E
0223	OBH 19		0240		0300		05 36,0 S 103 10,4 E
0303	OBH 18		0336		0358		05 33,9 S 103 08,2 E
0347	OBH 17		0425		0435		05 32,5 S 103 06,1 E

Profil SO 138-114 MAG/GRA/HS/PS

0456	Beginn Profil	05 34,1 S	103 05,7 E	
0714	Ende Profil	05 57,9 S	103 12,3 E	28 sm

Bergung OBH des Profiles S 2

0731	OBH 26 ausgelöst	0755	gesichtet	0802	a.D.	06 00,5 S	103 18,3 E
0808	OBH 27	0845		0852		05 59,0 S	103 15,6 E
0853	OBH 28	0914		0920		05 47,5 S	103 12,8 E
0921	OBH 29	0939		0947		05 56,1 S	103 10,1 E
0948	OBH 30	1004		1018		05 54,7 S	103 07,5 E
1022	OBH 31	1042		1048		05 53,2 S	103 04,9 E
1051	OBH 32	1112		1117		05 51,9 S	103 02,4 E
1120	OBH 33	1138		1145		05 50,5 S	102 59,6 E
1149	OBH 34	1204		1214		05 49,1 S	102 57,0 E

1221 – 1248 Magnetometer z.W.

Profil SO 138-115 MAG/GRA/HS/PS

1304	Beginn Profil	05 55,1 S	102 56,3 E	
1454	Ende Profil	06 09,0 S	102 42,0 E	20 sm

Profile SO 138-116 bis 122 MAG/GRA/HS/PS

1454	Beginn Profil 116	06 09,0 S	102 42,0 E	
1919	Ende Profil 116	06 39,3 S	102 04,0 E	35 sm
1932	Beginn Profil 117	06 41,4 S	102 04,3 E	
2044	Ende Profil 117	06 51,1 S	102 15,1 E	17 sm
2054	Beginn Profil 118	06 50,7 S	102 16,9 E	
2304	Ende Profil 118	06 32,0 S	102 29,5 E	23 sm
2334	Beginn Profil 119	06 34,0 S	102 32,0 E	
08.01.1999				
0153	Ende Profil 119	06 56,5 S	102 19,0 E	26 sm
0214	Beginn Profil 120	06 59,0 S	102 20,9 E	
0451	Ende Profil 120	06 35,5 S	102 35,0 E	27 sm
0523	Beginn Profil 121	06 37,5 S	102 37,5 E	
0619	Ende Profil 121	06 46,1 S	102 30,8 E	13 sm
0630	Beginn Profil 122	06 46,2 S	102 29,1 E	
0730 – 0758	holen Magnetometer ein			
0824	Ende Profil 122	06 34,5 S	102 17,5 E	17 sm

Bergungsversuch OBH 6 W 6

0845 – 2240 3 Bergungsversuche des OBH 06
Slmax = 7500 m

2245 – 2309 bringen Magnetometer aus

Profile SO 138-123 bis 129 MAG/GRA/HS/PS

2320	Beginn Profil 123	06 39,8 S	102 18,9 E
09.01.1999			

0027	Ende Profil 123	06 50,1 S	102 29,0 E	06 sm
0036	Beginn Profil 124	06 49,3 S	102 30,7 E	
0154	Ende Profil 124	06 39,0 S	102 40,0 E	15 sm
0214	Beginn Profil 125	06 40,5 S	102 42,5 E	
0420	Ende Profil 125	06 55,3 S	102 25,3 E	23 sm
0445	Beginn Profil 126	06 58,5 S	102 25,2 E	
0700	Ende Profil 126	06 42,0 S	102 45,0 E	27 sm
0724	Beginn Profil 127	06 44,5 S	102 47,0 E	
1029	Ende Profil 127	07 06,5 S	102 20,4 E	34 sm
1031	Beginn Profil 128	07 06,6 S	102 20,1 E	
1146	Ende Profil 128	06 55,3 S	102 12,2 E	14 sm
1149	Beginn Profil 129	06 54,7 S	102 12,2 E	
1315 – 1339	holen Magnetometer ein			
1400	Ende Profil 129	06 35,2 S	102 17,5 E	19 sm

Bergung OBH 06 W 6

1413	1. Draggen und Responder z.W.	
1438	2. Draggen und Responder z.W.	SL = 750 m
1918	Slmax = 7500 m	
2110	Seil gerissen bei SL = 7530 m	

Profile SO 138 – 130 bis 136 MAG/GRA/HS/PS

2210 – 2233	bringen Magnetometer aus			
2235	Beginn Profil 130	06 33,7 S	102 20,7 E	
2327	Ende Profil 130	06 30,8 S	102 31,3 E	27 sm
2331	Beginn Profil 131	06 31,1 S	102 31,9 E	
10.01.1999				
0128	Ende Profil 131	06 45,7 E	102 52,5 E	20 sm
0137	Beginn Profil 132	06 47,3 S	102 52,9 E	
0402	Ende Profil 132	07 11,4 S	102 38,6 E	30 sm
0412	Beginn Profil 133	07 13,0 S	102 36,9 E	
0510	Ende Profil 133	07 25,0 S	102 55,0 E	38 sm
0510	Beginn Profil 134	07 25,0 S	102 55,0 E	
0903	Profilwechsel 134/135	07 38,5 S	103 31,0 E	37 sm
1119	Ende Profil 135	07 51,6 S	103 55,0 E	28 sm
1124	Beginn Profil 136	07 52,3 S	103 55,2 E	
1240 – 1303	holen Magnetometer ein			
1400	Ende Profil 136	08 16,0 S	103 39,0 E	29 sm

Auslegung OBH 35 bis 50 auf Profil S 4

1439	OBH 35 z.W.	LT = 5713 m	08 19,93 S	103 44,14 E
1530	OBH 36 z.W.	LT = 5876 m	08 14,45 S	103 47,94 E
1620	OBH 37 z.W.	LT = 5706 m	08 07,61 S	103 52,67 E
1830	OBH 38 z.W.	LT = 5749 m	07 48,01 S	104 06,92 E
1944	OBH 39 z.W.	LT = 4139 m	07 37,15 S	104 15,03 E
2036	OBH 40 z.W.	LT = 3774 m	07 30,29 S	104 20,01 E
2130	OBH 41 z.W.	LT = 3500 m	07 23,14 S	104 25,39 E
2218	OBH 42 z.W.	LT = 2883 m	07 16,92 S	104 29,98 E
2311	OBH 43 z.W.	LT = 2810 m	07 10,04 S	104 35,07 E

11.01.1999

0008	OBH 44 z.W.	LT = 2262 m	07 03,45 S	104 39,94 E
0052	OBH 45 z.W.	LT = 2253 m	06 51,06 S	104 43,94 E
0126	OBH 46 z.W.	LT = 1873 m	06 53,95 S	104 46,88 E
0209	OBH 47 z.W.	LT = 1753 m	06 49,46 S	104 50,31 E
0305	OBH 48 z.W.	LT = 1795 m	06 45,02 S	104 53,77 E
0342	OBH 49 z.W.	LT = 1816 m	06 41,11 S	104 56,46 E
0424	OBH 50 z.W.	LT = 1504 m	06 36,37 S	104 59,96 E

0433 – 0442 bringen Magnetometer aus

Profil SO 138-137 MAG/GRA/HS/PS

0458	Beginn Profil	06 32,6 S	105 00,3 E
0650 – 0658	bringen Bb-array aus		
0701 – 0710	bringen Stb-array aus		
0738	Ende Profil	06 11,5 S	105 16,0 E 26 sm

Profil SO 138 – S 4 REF/MAG/GRA/HS/PS

0755	Beginn Schießen		
0810 – 0821	bringen Streamer aus		
0821	Beginn Profil	06 13,2 S	105 17,1 E
1430	fieren Magnetometer auf KL = 850 m		
1814 – 1821	holen Magnetometer vor		
1845 – 1857	holen Bb-array ein und kappen Longlinegeschirr		
1900	Bb-array wieder z.W.		
1900 – 1907	Magnetometer wieder auf KL = 850 m		
2400		07 23,0 S	104 25,53 E

12.01.1999

0912	kreuzen Longlin e-Geschirr		
0915 – 0922	holen Magnetometer vor		
0940 – 0950	Magnetometer auf KL = 850 m		
1851	Ende Profil	08 40,3 S	103 30,1 E 136 sm

1857 – 1906 holen Streamer ein
1907 – 1917 holen Bb-array ein
1918 – 1926 holen Stb-array ein

Profil SO 138-138 MAG/GRA/HS/PS

2010	Beginn Profil	05 36,6 S	103 26,7 E
2203	Ende Profil	08 17,5 S	103 38,4 E 22 sm

2210 – 2219 holen Magnetometer ein

Aufnahme der OBH des Profils SO 138-S 4

2223	OBH 35 ausgelöst	2321	gesichtet	2330	a.D.	08 20,1 S 103 44,1 E
2340	OBH 36 ausgelsöt					

13.01.1999

		0038	gesichtet	0106	a.D.	08 14,6 S 103 48,3 E
0133	OBH 37 ausgelöst	0136	gesichtet	0300	a.D.	08 07,6 S 103 52,9 E

FS SONNE

Stationsprotokoll SO 138

0439	OBH 38		0545	0555	07 47,9 S 104 37,0 E
0646	OBH 39		0725	0731	07 37,1 S 104 15,1 E
0752	OBH 40		0828	0832	07 30,3 S 104 20,1 E
0853	OBH 41		0934	0941	07 23,2 S 104 25,4 E
1000	OBH 42		1034	1038	07 17,0 S 104 30,0 E
1100	OBH 43		1135	1141	07 10,1 S 104 35,0 E
1203	OBH 44		1228	1304	07 03,8 S 104 39,8 E
1328	OBH 45		1348	1408	06 58,3 S 104 43,9 E
1429	OBH 46		1453	1500	06 54,0 S 104 47,1 E
1516	OBH 47		1534	1540	06 49,6 S 104 50,5 E
1543	OBH 48	VA	1618	1632	06 45,1 S 104 53,9 E
1636	OBH 49		1707	1712	06 41,2 S 104 56,5 E
1729	OBH 50		1748	1758	06 36,4 S 105 00,0 E

1801 – 1811 bringen Magnetometer aus

Profile SO 138-139 – 146 MAG/GRA/HS/PS

1836	Beginn Profil 139	06 32,4 S	105 00,0 E	
1913 – 1921	holen Magnetometer vor			
1935 – 1944	srecken wieder aus			
2130	Ende Profil 139	06 50,0 S	104 33,0 E	32 sm
2202	Beginn Profil 140	06 45,5 S	104 30,0 E	
2335 – 2342	holen Magnetometer vor			
2348 – 2355	stecken wieder aus			
0105 – 0115	hieven Magnetometer vor			
0123	Ende Profil 140	06 25,0 S	105 04,0 E	40 sm
0200	Beginn Profil 141	06 21,0 S	105 01,0 E	
0200 – 0208	stecken Magnetometer aus			
0258	Ende Profil 141	06 29,0 S	104 52,0 E	13 sm
0308	Beginn Profil 142	06 28,3 S	104 50,5 E	
0348	Ende Profil 142	06 21,1 S	104 50,9 E	9 sm
0355	Beginn Profil 143	06 20,0 S	104 51,7 E	
0415	Magnetometer vorgehievt			
0515	Magnetometer ausgesteckt			
0540	Ende Profil 143	06 10,5 S	105 09,1 E	29 sm
0550	Beginn Profil 144	06 10,6 S	105 10,9 E	
0746	Ende Profil 144	06 22,3 S	105 30,6 E	24 sm
0748	Beginn Profil 145	06 22,4 S	105 30,9 E	
0808 – 0818	holen Magnetometer ein			
0832	Profilwechsel 145 / 146	06 20,0 S	105 38,4 E	8 sm
1012	Ende Profil 146	06 03,0 S	105 50,0 E	21 sm

Profile SO 138-147 – 150 MAG/GRA/HS/PS

1148	Beginn Profil 147	06 03,0 S	105 50,0 E	
1348	Ende Profil 147	06 23,0 S	105 30,0 E	28 sm
1353	Beginn Profil 148	06 22,9 S	105 29,7 E	
1530	Ende Profil 148	06 25,0 S	105 10,0 E	20 sm
1533 – 1625	Bootsmanöver			

1628	Beginn Profil 149	06 25,0 S	105 10,0 E
1655 – 1717	bringen Garadiometer aus		
1828 – 1913	holen Gradiometer ein		
1958 – 2008	bringen Magnetometer aus		
2048	Ende Profil 149	06 59,7 S	104 45,3 E 43 sm
2053	Beginn Profil 150	07 00,5 S	104 45,3 E
2345 – 2354	holen Magnetometer ein, Defekt am Kabel		
2400		07 32,4 S	105 00,2 E
15.01.1999			
1158	Ende Profil 150	09 39,7 S	106 00,0 E 176 sm

Auslegung der OBH auf Profil SO 138-S 5

1231	OBH 51	z.W.	LT = 5666 m	09 43,47 S 106 02,75 E
1317	OBH 52	z.W.	LT = 5911 m	09 36,78 S 106 05,96 E
1414	OBH 53	z.W.	LT = 5966 m	09 33,11 S 106 07,73 E
1638	OBH 54	z.W.	LT = 5633 m	09 09,52 S 106 19,06 E
1730	OBH 55	z.W.	LT = 4560 m	09 01,64 S 106 24,89 E
1813	OBH 56	z.W.	LT = 4114 m	08 55,88 S 106 25,57 E
1907	OBH 57	z.W.	LT = 3514 m	08 48,18 S 106 29,30 E
2020	OBH 58	z.W.	LT = 2362 m	08 37,00 S 106 34,66 E
2104	OBH 59	z.W.	LT = 1923 m	08 30,94 S 106 37,64 E
2141	OBH 60	z.W.	LT = 1863 m	08 25,94 S 106 40,01 E
2227	OBH 61	z.W.	LT = 1941 m	08 19,95 S 106 42,84 E
2304	OBH 62	z.W.	LT = 3112 m	08 15,01 S 106 45,27 E
2336	OBH 62	z.W.	LT = 3113 m	08 15,03 S 106 45,26 E
16.01.1999				
0034	OBH 63	z.W.	LT = 3045 m	08 06,17 S 106 49,42 E
0135	OBH 64	z.W.	LT = 3034 m	07 59,03 S 106 52,84 E
0233	OBH 65	VA. z.W.	LT = 2801 m	07 51,99 S 106 56,24 E
0313	OBH 66	z.W.	LT = 2568 m	07 47,01 S 106 88,57 E
0342	OBH 67	z.W.	LT = 2452 m	07 44,08 S 106 59,99 E

0351 – 0420	Magnetometer z.W. KL = 850 m
0412 – 0420	Bb-array z.W.
0422 - 0430	Stb-array z.W.
0431 – 0503	Streamer z.W.
0445	Beginn Drehen über Bb

Profil SO 138-S 5 REF/MAG/GRA/HS/PS

0525	Beginn Profil	07 44,1 S	107 06,3 E
2400		09 06,3 S	106 20,7 E
17.01.1999			
1100	Ende Profil	09 59,7 S	105 54,9 E 154 sm

1102 – 1108	holen Streamer ein
1111 – 1120	holen Bb-array ein
1121 – 11228	holen Stb-array ein

FS SONNE

Stationsprotokoll SO 138

Profil SO 138-151 MAG/GRA/HS/PS

1146	Beginn Profil				
1233 – 1255	holen Magnetometer ein				
1324	OBH 51 ausgelöst				
1343	Ende Profil				09 42,0 S 106 00,0 E 18 sm

Aufnahme und Bergung OBH des Profils S 5

1424	OBH 51	gesichtet	1434	a.D.	09 43,4 S	106 02,6 E
1454	OBH 52	ausgelöst	1556	gesichtet	1603 a.D.	09 36,7 S 106 05,7 E
1532	OBH 53	ausgelöst	1645	gesichtet	1655 a.D.	09 33,2 S 106 07,5 E
1700 – 1706	Magnetometer z.W.					
1716 – 1719	holen Magnetometer ein					
1722 – 1726	bringen Magnetometer aus					
1730 – 1741	KL = 700 m					
1817 – 1827	holen Magnetometer ein					
1921	OBH 54	ausgelöst	2027	gesichtet	2037 a.D.	09 09,6 S 106 19,0 E
2107	OBH 55		2209		2222	09 01,6 S 106 22,5 E
2238	OBH 56		2323		2332	08 55,9 S 106 25,3 E
17.01.1999						
0000	OBH 57		0043		0101	08 48,2 S 106 29,0 E
0158	OBH 58		0209		0236	08 37,0 S 106 34,7 E
0300	OBH 59		0320		0336	08 30,9 S 106 37,7 E
0352	OBH 60		0417		0427	08 25,8 S 106 40,0 E
0502	OBH 61		0525		0536	08 19,9 S 106 42,9 E
0550	OBH 62		0631		0639	08 15,0 S 106 45,4 E
0722	OBH 63		0757		0805	08 06,1 S 106 49,6 E
0826	OBH 64		0858		0906	07 59,0 S 106 53,1 E
0927	OBH 65	VA	1004		1020	07 52,0 S 106 56,5 E
1034	OBH 66		1125		1128	07 47,0 S 106 58,7 E
1129	OBH 67		1200		1211	07 44,0 S 107 00,2 E

Auslegung OBH des Profils S 6 und Schlepptest mit Vertikal-array 120 m

1218	OBH 72 z.W.	LT = 2450 m	07 44,07 S	107 00,03 E
1245	OBH 73 z.W.	LT = 2567 m	07 43,67 S	106 57,57 E
1308	OBH 74 z.W.	LT = 2577 m	07 43,24 S	106 55,10 E
1332	OBH 75 z.W.	LT = 2573 m	07 42,87 S	106 52,62 E
1409	Beginn Auslegung VA 120 m mit Auftriebskörper und Rekorder am Draht der W 6			
1433	Beginn fieren	v = 1,8 kn		
1500 – 1505	1 airgun Bb z.W.			
1507	Beginn schießen			
1533	SL = 2500 m	v = 1,0 kn		
1551	v = 3,0 kn			
1600	Beginn hieven, v = 1,0 kn			
1630	Ende schießen			
1630 – 1640	holen Bb-airgun ein			
1656	alles a.D. Ende Test			
1809	OBH 77 z.W.	LT = 1509 m	07 39,65 S	106 32,73 E
1900	Beginn Auslegung OBH 76 mit VA 400 m			

2000	OBH 76	z.W.	LT = 2420 m	07 41,15 S 106 42,16 E
2212	OBH 71	z.W.	LT = 2514 m	07 44,48 S 107 02,52 E
2238	OBH 70	z.W.	LT = 2625 m	07 44,87 S 107 04,94 E
2338	OBH 69	z.W.	LT = 1951 m	07 46,46 S 107 14,73 E
19.01.1999				
0047	OBH 68	z.W.	LT = 1318 m	07 48,17 S 107 25,33 E

0053 – 0121 Magnetometer z.W.
0150 – 0200 Bb-array z.W.
0201 – 0210 Stb-array z.W.

Profil SO 138 – S 6 REF/MAG/GRA/HS/PS

0223	Beginn Schießen	07 51,35 S 107 34,30 E
0303	Beginn Profil	
0309 – 0321	Streamer z.W.	
0925	holen Gradiometer vor	
0923 – 0939	holen Bb-array vor	
0945	passieren treibenden Fischer an Leine	07 44,09 S 107 00,76 E
0952	Gradiometer a.D.	
1000 – 1022	bringen Gradiometer aus	
1012 – 1020	bringen Bb-array aus	
1704	Ende Profil	07 38,0 S 106 22,5 E 74 sm

1705 – 1715 holen Bb-array ein
1716 – 1725 holen Stb-array ein
1726 – 1733 holen Streamer ein

Profil SO 138-153 MAG/GRA/HS/PS

1750	Beginn Profil	07 39,0 S 106 21,1 E
1844 – 1906	holen Gradiometer ein	
1906	Ende Profil	07 41,3 S 106 32,8 E 12 sm

Auslösung und Aufnahme OBH des Profils S 6

1907	OBH 77	ausgelöst	1936	gesichtet	1946	a.D. 07 39,6 S 106 32,9 E
2030	OBH 76	VA 400 m	2053		2140	07 41,2 S 106 04,2 E
2225	OBH 75		2257		2306	07 42,8 S 106 52,8 E
2310	OBH 74		2333		2340	07 43,2 S 106 55,2 E
2341	OBH 73					
20.01.1999						
			0007		0015	07 43,6 S 106 57,6 E
0017	OBH 72		0045		0052	07 44,0 S 107 00,1 E
0053	OBH 71		0124		0131	07 44,4 S 107 02,6 E
0135	OBH 70		0206		0215	07 44,8 S 107 05,0 E
0303	OBH 69		0324		0336	07 46,5 S 107 15,0 E
0418	OBH 68		0430		0449	07 48,2 S 107 25,5 E

0500 – 0513 bringen Gradiometer aus

FS SONNE

Stationsprotokoll SO 138

Profil SO 138-154 MAG/GRA/HS/PS

0500	Beginn Profil	07 48,3 S 107 25,3 E
1028	Ende Profil	08 36,0 S 106 58,6 E 46 sm

1030 – 1052 holen Gradiometer ein

Auslegung der OBH des Profils S 7

1107	OBH 78	z.W.	LT = 2077 m	08 36,00 S 106 58,62 E
1146	OBH 79		2053 m	08 34,17 S 106 53,85 E
1230	OBH 80		1894 m	08 32,39 S 106 49,19 E
1312	OBH 81		1903 m	08 30,65 S 106 44,44 E
1339	OBH 82		1663 m	08 29,58 S 106 41,60 E
1409	OBH 83		1727 m	08 28,52 S 106 38,70 E
1437	OBH 84		1772 m	08 27,42 S 106 35,94 E
1504	OBH 85		1906 m	08 26,39 S 106 33,12 E
1532	OBH 86		1909 m	08 25,29 S 106 30,22 E
1609	OBH 87		2221 m	08 23,56 S 106 25,52 E
1645	OBH 88		2365 m	08 21,76 S 106 20,77 E
1713	Beginn Auslegung OBH 89 mit VA 400 m			
1734	OBH 89		2371 m	08 20,03 S 106 16,18 E
1737	OBH 89	abgetaucht		

Profil SO 138-155 MAG/GRA/HS/PS

1802	Beginn Profil	08 21,6 S 106 13,4 E
1820 – 1842	Gradiometer z:W. KL = 900 m	
1957 – 2007	setzen Bb-array aus	
2008 – 2016	setzen Stb-array aus	
2019 – 2029	bringen Streamer aus	
2030	Ende Profil	08 14,7 S 105 55,3 E 19 sm

Profil SO 138- S 7 REF/MAG/GRA/HS/PS

2054	Beginn Profil	08 12,8 S 105 44,7 E
21.01.1999		
1312	Ende Profil	08 44,0 S 107 20,0 E 89 sm

1318 – 1325 holen Streamer ein
1320 – 1336 holen Bb-array ein
1340 – 1346 holen Stb-array ein

Profil SO 138-156 MAG/GRA/HS/PS

1423	Beginn Profil	08 46,5 S 107 20,0 E
1628 – 1653	holen Gradiometer ein	
1653	Ende Profil	08 38,3 S 106 58,3 E 23 sm

Aufnahme der OBH des Profils S 7

1655	OBH 78	ausgelöst 1720	gesichtet 1729	a.D.	08 35,9 S 106 58,6 E
1747	OBH 79	1816	1828		08 34,1 S 106 53,9 E
1850	OBH 80	1913	1928		08 32,3 S 106 49,2 E
1947	OBH 81	2007	2017		08 30,5 S 106 44,4 E

2018	OBH 82	2040	2050	08 29,5 S	106 41,6 E
2051	OBH 83	2109	2116	08 28,5 S	106 38,7 E
2118	OBH 84	2136	2142	08 27,3 S	106 35,9 E
2144	OBH 85	2206	2211	08 26,2 S	106 33,0 E
2212	OBH 86	2247	2254	08 25,1 S	106 30,1 E
2307	OBH 87	2333	2343	08 23,4 S	106 25,5 E
2355	OBH 88				
22.01.1999					
		0020	0023	08 21,6 S	106 20,7 E
0041	OBH 89 VA 400	0103	0146	08 19,9 S	106 16,1 E

Profil SO 138-157 MAG/GRA/HS/PS

0200	Beginn Profil	08 20,0 S	106 16,1 E	
0200 – 0225	bringen Gradiometer aus			
0610	Ende Profil	08 55,4 S	105 51,9 E	42 sm

Profil SO 138-158 MAG/GRA/HS/PS

0619	Beginn Profil	08 55,7 S	105 50,4 E	
0800	Unterbrechung Profil	08 45,9 S	105 34,7 E	
0802 – 0828	holen Gradiometer ein			

Teststation CTD/ROS W 4

0837	CTD/ROS z.W.	08 44,5 S	105 32,3 E	
0948	Simax = 3892 m	LT = 6245 m		
1138	CTD/ROS a.D.	08 44,5 S	105 32,3 E	
1140	Fortsetzung Profil 158	08 43,6 S	105 30,8 E	
1147 – 1210	bringen Gradiometer aus			
2007	Profilwechsel 158/59	08 04,0 S	104 27,0 E	
2027	Ende Profil	08 02,8 S	104 24,3 E	101 sm

Profil SO 138-160 MAG/GRA/HS/PS

2040	Beginn Profil	08 00,9 S	104 24,2 E	
23.01.1999				
0153 – 0219	holen Gradiometer ein			
0214	Ende Profil	07 06,0 S	104 52,8 E	62 sm

Auslegung OBH des Profils S 8

0233	OBH 90 z.W.	LT = 2113 m	07 05,44 S	104 53,00 E
0307	OBH 91	1981	07 01,48 S	104 53,00 E
0341	OBH 92	1865	06 57,43 S	104 53,01 E
0416	OBH 93	1737	06 53,00 S	104 52,99 E
0452	OBH 94	1711	06 49,03 S	104 53,01 E
0520	OBH 95	1797	06 45,51 S	104 53,00 E
0555	OBH 96	1677	06 40,49 S	104 53,00 E
0634	OBH 97	1871	06 35,50 S	104 53,02 E
0710	OBH 98	1894	06 31,41 S	104 53,00 E
0738	OBH 99	1849	06 28,42 S	104 53,03 E
0805	Beginn Auslegung OBH 100 VA 800 m			

0843	OBH 100	1740 m	06 25,50 S	104 53,02 E
0917	OBH 101	1587	06 20,62 S	104 53,00 E
0945	OBH 102	1342	06 16,65 S	104 53,05 E
1023	OBH 103	1281 m	06 11,46 S	104 53,04 E
1102	OBH 104	1366 m	06 05,18 S	104 53,01 E
1141	OBH 105	215 m	05 59,26 S	104 53,02 E

Profil SO 138-S 8 REF/GRA/MAG/HS/PS

1208 – 1220	bringen Gradiometer aus	KL = 040 m	
1225 – 1232	bringen Bb-array aus		
1235 – 1241	bringen Stb-array aus		
1242 – 1253	bringen Streamer aus		
1250	Beginn Profil	05 54,8 S	104 56,0 E
1503	Gradiometer auf KL = 800 m		
1532 – 1539	Gradiometer auf KL = 400 m		
1648 – 1656	Gradiometer auf KL = 800 m		
24.01.1999			
0820	Ende Profil	07 30,0 S	104 53,0 E 98 sm

0823 – 0833	holen Bb-array ein
0835 – 0845	holen Stb-array ein
0847 – 0855	holen Streamer ein

Profil SO 138-161 MAG/GRA/HS/PS

0858	Beginn Profil	07 31,7 S	104 55,1 E
1200	Ende Profil	07 05,3 S	104 55,5 E 27 sm
1200 – 1215	holen Gradiometer ein		

Aufnahme OBH des Profils S 8

1212	OBH 90	ausgelöst	1252	gesichtet	1303	a.D.	07 05,6 S 104 53,1 E
1319	OBH 91		1341		1352		07 01,7 S 104 53,3 E
1409	OBH 92		1432		1439		06 57,5 S 104 53,2 E
1501	OBH 93		1520		1528		06 53,2 S 104 53,1 E
1542	OBH 94		1602		1606		06 49,1 S 104 53,1 E
1621	OBH 95		1644		1649		06 45,6 S 104 53,0 S
1709	OBH 96		1730		1738		06 40,7 S 104 53,1 E
1759	OBH 97		1820		1826		06 35,7 S 104 53,2 E
1916	OBH 98		1940		1946		06 31,6 S 104 53,1 E
1950	OBH 99		2012		2018		06 28,5 S 104 53,5 E
2056	OBH 101		2117		2122		06 20,7 S 104 53,1 E
2137	OBH 102		2152		2157		06 16,7 S 104 53,2 E
2221	OBH 103		2236		2242		06 11,6 S 104 53,2 E
2308	OBH 104		2325		2331		06 05,3 S 104 53,1 E
25.01.1999							
0007	OBH 105		0008		0016		05 59,2 S 104 53,1 E

Profile SO 138-162/163 HS/PS

0036	Beginn Profil 162	05 59,0 S	104 51,0 E
0225	Ende Profil 162	06 15,7 S	104 51,1 E 23 sm

0230	Beginn Profil 163	06 22,0 S	104 50,8 E
0316	Ende Profil 163	06 22,0 S	104 43,8 E 07 sm

Auslegung OBH des Profils SO 138 - S 9

0326	OBH 106 z.W.	LT =	81 m	06 21,98 S	104 43,88 E
0345	OBH 107		273 m	06 21,47 S	104 44,77 E
0416	OBH 108		1093 m	06 20,01 S	104 47,25 E
0445	OBH 109		1590 m	06 18,42 S	104 49,89 E
0505	OBH 110		1592 m	06 17,51 S	104 51,44 E
0528	OBH 111		1343 m	06 16,58 S	104 53,02 E

Profile SO 138 – S 9/A/B REF/MAG/GRA/HS/PS

0535 – 0551	Stb-array z.W.		
0558 – 0604	Streamer z.W.		
0605	Beginn Profil S 9	06 15,6 S	104 56,1 E
0920	Ende Profil S 9	06 22,7 S	104 42,6 E 13 sm
0920 – 0940	Schleife		
0941 – 0948	Bb-array z.W.		
0948	Beginn Profil S 9 A	06 22,5 S	104 42,9 E
1022	Unterbrechung Profil, drehen Schleife	06 20,9 S	104 45,6 E
1104	Fortsetzun Profil	06 20,9 S	104 45,6 E
1024 – 1040	holen Streamer und Bb-array ein, verturnt		
1140	setzen Bb-array aus		
1147	Profilwechsel S 9 A/B	06 19,1 S	104 48,9 E
1253	Ende Profil S 9 B	06 15,9 S	104 54,1 E 16 sm
1255 – 1307	holen Stb-array ein		
1309 – 1313	holen Bb-array ein		

Profil SO 138 – 164 HS/PS

1320	Beginn Profil	06 16,1 S	104 55,0 E
1428	Ende Profil	06 25,2 S	104 55,0 E 11 sm

Aufnahme des OBH 100 VA 800 m von Profil S 8 und der OBH des Profils S 9

1430 OBH 100 ausgelöst 1448 aufgetaucht
1458 aufgepickt
1515 Verankerung reißt kurz über dem 2. Auftriebskörper
06 25,725 S 104 53,291 E
1535 Ortung des Releasers : min = 1713 m LT = 1720 m
06 25,664 S 104 53,247 E

1705	OBH 106 ausgelöst	1708	gesichtet	1712 a.D.	06 22,1 S 104 44,2 E
1718	OBH 107	1722		1728	06 21,6 S 104 45,0 E
1739	OBH 108	1750		1755	06 20,2 S 104 47,4 E
1804	OBH 109	1826		1833	06 18,5 S 104 50,2 E
1833	OBH 110	1851		1858	06 17,7 S 104 51,7 E
1859	OBH 111	1925		1933	06 16,7 S 104 53,2 E

1942 – 1951 Magnetometer z-.W

FS SONNE Stationsprotokoll SO 138

Profile SO 138-165 bis 167 MAG/GRA/HS/PS

2041	Beginn Profil 165	06 25,0 S 104 52,3 E	
2221	Ende Profil 165	06 17,2 S 105 10,0 E	20 sm
2246	Beginn Profil 166	06 15,0 S 105 09,6 E	
26.01.1999			
0215	Ende Profil 166	06 27,8 S 104 42,3 E	32 sm
0237	Beginn Profil 167	06 26,2 S 104 41,6 E	
0405 – 0419	holen Gradiometer ein		
0419	Ende Profil	06 17,0 S 104 57,6 E	19 sm

Bergung OBH 100 W 6

0600 – 0710	akustische Einmessung der Position
0715	Suchdraggen z.W. fieren mit 0,7 m/sec
0802	SL = 1720 m , LT = 1713 m Draggen am Grund fahren mit diversen Kursen , v = 1,0 kn , stecken Seil nach
0926	Slmax = 4104 m OBH-Position ein Mal umrundet, r = 0,2 sml
1008	Beginn hieven, OBH-Position 1,5 mal umrundet
1035	Releaser-Messung wird kleiner
1214	Draggen an Deck
1231	Releaser und 1 Zylinder a.D.
1243	2. Schwimmboje a.D. ; Ende der Bergung

Profile SO 138-168 bis 174 HS/PS

1258	Beginn Profil 168	06 22,5 S 104 54,6 E	
1355	Ende Profil 168	06 22,5 S 105 03,0 E	08 sm
1355	Beginn Profil 169	06 22,5 S 105 03,0 E	
1410	Profilwechsel 169/170	06 25,0 S 105 03,0 E	02 sm
1648	Profilwechsel 171/172	06 37,8 S 104 48,5 E	22 sm
1815	Profilwechsel 172/173	06 29,5 S 105 01,5 E	16 sm
1907	Profilwechsel 173/174	06 39,7 S 105 01,7 E	10 sml
2024	Profilwechsel 174/175	06 28,0 S 105 09,0 E	13 sml
27.01.1999			
0003	Ende Profil 175	06 07,0 S 105 48,2 E	44 sml

Insgesamt wurden 2952 sml mit Magnetik, Gravimetrie, und/oder Hydrosweep und Parasound vermessen.

Davon wurden 961 sml seismisch vermessen.
OBH-Einsätze : 111 mal